The University of Sheffield

Novel Hybrid Permanent Magnet Interior PM Synchronous Machines

Seyedmilad Kazemisangdehi

A thesis submitted for the degree of Doctor of Philosophy

School of Electrical and Electronic Engineering

The University of Sheffield

Mapping Building, Sheffield, S1 3JD, UK

March 2025

ABSTRACT

The rising cost of rare-earth permanent magnets (REPMs) in recent years has provided a challenge in developing high performance PM machines at a competitive price. Therefore, this thesis focuses on novel hybrid PM (HPM) machines with the synergies of high energy product REPM and low-cost ferrite PM (FEPM), with a particular emphasis on enhancement of the ratio of torque to REPM volume.

Six HPM interior PM synchronous machines (IPMSMs) with different topologies using symmetrical and asymmetric rotor structures have been developed and investigated in this thesis. The electromagnetic performance, including open circuit characteristics, output torque, torque and dq-axis inductances with current advancing angle, and efficiency, as well as mechanical robustness, demagnetisation withstand capability, and PM cost, are analysed and compared with those of a REPM-based V-shape baseline using the same stator and specifications of the commercialised Nissan Leaf 2012 IPMSM. The comparison confirms that the proposed HPM machines can produce the same torque at a lower volume of REPM consumption than that of the baseline. It is worth mentioning that the proposed HPM machines have been built and tested in a small size as the proof of concept.

Meanwhile, using the frozen permeability method, the output torques of the proposed HPM machines are divided into three components, including the reluctance torque, and the FEPM and REPM torques. Any improvement in either reluctance torque, FEPM torque or both, along with the torque enhancement caused by the magnetic field shifting effect in asymmetric topologies will result in a lower required REPM torque while maintaining the desired level of output torque. Consequently, a lower volume of REPM would be required which leads to the reduction of total PM cost. As a result, at the same torque and size, the contributions of torque components and volumes of both PM types are compared. It is shown that the HPM utilisation in topologies with a combined spoke arrangement of PM with V- or delta-shape structures can effectively improve the ratio of torque to REPM volume. Meanwhile, in the topologies where spoke FEPM is not used, a combination of asymmetric rotor topology with V- and U-shape structures of PMs can also improve the ratio of torque to REPM volume. Therefore, the proposed HPM machines in this thesis are potential candidates for electric vehicle (EV) applications at a reduced cost.

ACKNOWLEDGEMENTS

Foremost, I would like to express my sincere appreciation to my supervisor, Professor Zi-Qiang Zhu, for his invaluable guidance, continuous support and encouragement during my Ph.D. study without whom I would not be able to find defects and improve. Indeed, this period has been a great one in a life-time opportunity for me to not only learn technical knowledge for my career but also learn life perceptions from him to enhance my life skills.

I would like to thank Dr. Dawei Liang, Dr. Yinzhao Zheng, Dr. Hai Xu, Dr. Ji Qi, Dr. Zhitong Ran, Dr. Dong Xiang, Dr. Yang Xiao, Mr. Furkan Tokgoz, Mr. Ankan Dey, Mr. Qiang Wei, and all my fellows from the Electrical Machines and Drive Group at the University of Sheffield for their constructive discussions in research and friendship in life. I also thank Dr. Panos Lazari and Dr. Gavin Williams, whom I had the privilege to work with at the Diamond building, and Mr. Ian Parmenter for his administrative support during this journey.

I wish to acknowledge the Midea Group Co. Ltd. for the sponsorship and their amazing hospitality during our visit to their research centre in Foshan, China. I would like to thank Dr. Liang Chen, Dr. Yang Lei, Dr. Yanjian Zhou, Mr. Hailong Liu, and Mr. Xie Feng for their valuable discussions and assistance.

My special thanks go to my parents and my brother for their unconditional love and encouragement. Their emotional support and care have been beyond any imagination and gave me the courage to go after my dreams. At last, but not least, I am deeply grateful of the love of my life Mrs. Jeiran Hajivandi for her love, companion, devotion, and encouragement which have helped me to manage going through the difficulties in my research.

CONTENTS

NOMENCLATURE

Symbols	**Descriptions**
$\emptyset_{fe}, \emptyset_{fe1}, \emptyset_{fe2}$	FEPM flux, Wb (Chapter 3)
$\emptyset_{nd}, \emptyset_{nd1}, \emptyset_{nd2}$	REPM flux, Wb (Chapter 3)
I_{ch}	Characteristic current, A (Chapter 1)
I_s	Rated current, A (Chapter 1)
$K_{T_{out}}, K_{V_{NdFeB}}, K_{T_{ripple}}$	Optimization weighting factors
K_{wp}	REPM to FEPM widths ratio in parallel HPM machine (Chapter 2)
K_{ws}	REPM to FEPM widths ratio in series HPM machine (Chapter 2)
L_d, L_q	DQ-axis inductances, H
L_g	Airgap length, mm (Chapter 3)
P_{core}	Iron loss, kW
P_{cu}	Copper loss, kW
P_{in}	Input power, kW
P_{mec}	Mechanical loss, kW
P_{out}	Output power, kW
R_{fe1}, R_{fe2}	FEPM magnetic reluctance (Chapter 3)
R_g	Airgap magnetic reluctance (Chapter 3)
R_{ir}	Rotor inner radius, mm
R_{nd1}, R_{nd2}	REPM magnetic reluctance (Chapter 3)
R_{or}	Rotor outer radius, mm
R_v	V-shape inner radius, mm (Chapter 3)
S_{fe}	Surface area of FEPM, mm^2 (Chapter 3)
S_g	Airgap cross section, mm^2 (Chapter 3)
S_{nd}	Surface area of REPM, mm^2 (Chapter 3)
T_{out}, T	Output torque, Nm
T_{pm}, T_m	PM torque, Nm
T_{rel}, T_r	Reluctance torque, Nm
k_{mec1}, k_{mec2}	Mechanical loss coefficients
w_b	Width of flux barrier, mm (Chapters 3,5)
x_c	V-shape local coordinate position, mm (Chapters 3,4)
Ψ_{pm}	PM flux linkage, Wb
α_s	Asymmetric angle, elec. deg. (Chapter 1)
θ_b	Angle of bar-shape barrier in delta-shape IPMSM, degree (Chapter 4)
θ_c	V-shape local coordinate angle, degree (Chapters 3,4)
θ_v	V-shape angle, degree (Chapters 3,4)
b_1	Displacement of barriers, mm (Chapter 3)
b_2	Thickness of empty gap, mm (Chapters 3,4)
C_{fe}	FEPM cutting off limit, mm (Chapter 6)
D_1, D_2	Displacement of barriers, mm (Chapter 4)
D_{fe1}, D_{fe2}	Displacement of FEPM, mm (Chapters 5,6)
D_{re}	Displacement of REPM, mm (Chapters 5,6)
F_{fe}	MMF of FEPMs (Chapter 3)
F_{nd}	MMF of REPMs (Chapter 3)

H_{b1}, H_{b2}	Heights of barriers, mm (Chapter 5)
h_{fe}	Height of FEPM, mm (Chapter 3)
h_{re}	Height of REPM, mm (Chapter 3)
I_a, I_b, I_c	ABC three-phase currents, A
i_d, i_q	DQ-axis currents, A
I_{DC}	DC current, A
L_{fe}, L_{fe1}, L_{fe2}	Length of FEPM, mm
l_{mr}	Width of middle iron rib, mm (Chapters 3,4,6)
l_{or}	Width of outer iron rib, mm (Chapters 3,4,6)
L_{pm}	Length of PM, mm
L_{re}	Length of REPM, mm
$T_{out\text{-}AIPMSM}$	Output torque in asymmetric IPMSM, Nm (Chapter 1)
$T_{out\text{-}IPMSM}$	Output torque in symmetrical IPMSM, Nm (Chapter 1)
T_{ripple}	Torque ripple, %
V_{NdFeB}	Volume of REPM, cm^3
W_{fe}, W_{fe1}, W_{fe2}	Width of FEPM, mm
W_{mr}, W_{or1}, W_{or2}	Widths of iron ribs, mm (Chapter 5)
W_{re}, W_{nd}	Width of REPM, mm
X_u, Y_u	U-shape centre in x-axis and y-axis, mm (Chapter 5)
X_v, Y_v	V-shape centre in x-axis and y-axis, mm (Chapters 5,6)
$\theta_{fe1}, \theta_{fe2}$	Angle of FEPMs alignment, degree (Chapters 5,6)
θ_{re}	Angle of REPM alignment, degree (Chapters 5,6)
μ_0, μ_r	Air and relative permeabilities (Chapter 6)
ρ	Resistivity of materials (Chapter 6)
$\Psi_{fd}, \Psi_{fq}, \Psi_d, \Psi_q$	DQ-axis flux linkages, Wb (Chapter 1)
f	Frequency, Hz
p	Number of pole pairs
β	Current advancing angle, elec. deg. (Chapter 1)
δ	Skin depth (Chapter 6)
η	Efficiency, %

Abbreviations	**Descriptions**
2D	Two dimensional
3D	Three dimensional
AC	Alternating current
APC	Advanced Propulsion Centre
CPM	Constant-flux PM
CPSR	Constant power speed range
DC	Direct current
DOE	Department of Energy
EV	Electric vehicle
FEA	Finite element analysis
FEPM	Ferrite PM
FMP	Flux modulation pole
FPM	Frozen permeability method
FTT	Fault tolerant tooth
HPM	Hybrid PM
IM	Induction machine
IPM	Interior PM
MFS	Magnetic field shifting
MMF	Magnetic motive force
MTPA	Maximum torque per ampere
NdFeB	Neodymium-boron-iron
PM	Permanent magnet
PM aSynRM	PM assisted SynRM
REPM	Rare-earth PM
SFPM	Switched flux PM
SPM	Surface mounted PM
SRM	Switched reluctance machine
SynRM	Synchronous reluctance machine
UK	United Kingdom
US	United States
VPM	Variable-flux PM

CHAPTER 1

GENERAL INTRODUCTION

1.1. Introduction

The first electrical machine was invented about 200 years ago by Micheal Faraday in 1822. Although this motor could transform the electricity into the movement, it did not look anything like the modern motor. However, in 1834, Thomas Davenport made the first battery-powered electrical machine with a rotary wheel. Davenport's motor was a brushed direct current (DC) motor with a commutator. Years later in 1887, Nikola Tesla introduced the first brushless alternating current (AC) induction machine (IM). Therefore, electrical machines can originally be divided into two groups including brushed and brushless machines. The electrical machines in the former group require mechanical components (brush and commutator) for commutation which suffer from short lifetime and high maintenance cost. Meanwhile, the ones in the latter group can be driven with electronically controlled inverters which can overcome the drawbacks of the brushed machines along with a higher efficiency and more compact size at the cost of the increased price of inverters. Therefore, brushless electrical machines have been used widely in many applications. These machines can be then categorized into asynchronous and synchronous types where the synchronous machine benefits from a relatively easier control than an asynchronous counterpart (e.g. IM) due to having a synchronised rotational speed of the rotor with the rotational magnetic field of the stator. The switched reluctance machine (SRM) is a type of synchronous machine which was first built in 1839 by Robert Davidson. The rotor in this machine is simple and only made of salient poles. However, the rotor of the synchronous reluctance machine (SynRM), which was first introduced in the 1920s, is simply made of multi-layers of flux barriers.

Meanwhile, the development of Alnico, ferrite, Samarium Cobalt, and Neodymium-boron-iron (NdFeB) magnets in the 1930s, the 1950s, the late 1960s, and the early 1980s were the bright points in the history of electrical machines by providing the required background of inventing the modern permanent magnet (PM) synchronous machines. Consequently, the synchronous machines can be divided into the non-PM and PM machines. Generally, the non-PM machines (e.g. SRM) have the advantages of robustness and simple structure of the rotor and the disadvantages of low torque density and low power factor [BIA09]. On the other hand, PM machines benefit from high torque density, high efficiency, and ease of control [ZHU07], [ZHU14], [CAO12], [POL13]. Different topologies of PM machines have been developed throughout the time including doubly salient PM machines, flux reversal PM machines, switched flux PM (SFPM) machines, surface mounted PM (SPM) machines, interior PM (IPM) machines, dual-PM machines, etc. As a result, these machines can be categorized based on the location of PMs into the stator-PM, rotor-PM, and dual-PM types. These machines have been used in a variety of applications ranging from robots [XU25] and servo systems [GAO22] to power generation [MIR20] and electric vehicles (EV) [CHA08]. For EV application in particular, different driving cycles demand high acceleration at low speed and wide speed range for highway driving. In addition, a high coverage distance per charge (which can be interpreted as high efficiency), and a high reliability are also needed. Consequently, various machine topologies have been proposed for this application including IM [BIL19], SynRM [BIL15], and PM machines [ZHU17A], [CHE11A]. Meanwhile, IPMs are the most promising type of PM machines for EV application and have been widely used in the commercially manufactured EVs on the market as they are capable of satisfying the torque/power requirements of traction application in Fig. 1.1. Various IPMs with different stator slot/rotor pole combinations, different rotor structures, and different stator winding types have been employed in commercialized EVs as summarized in Table 1.1 [KRI20]. A few rotor topologies of these machines are illustrated in Fig. 1.2.

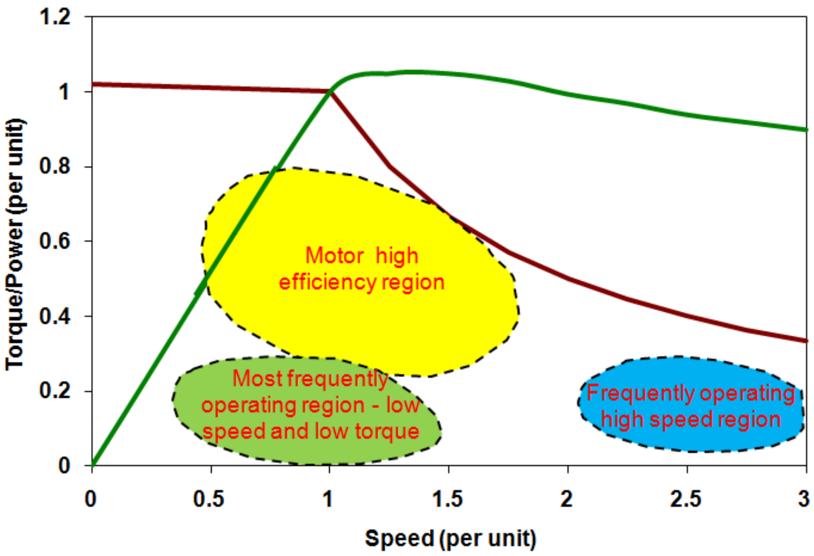

Fig. 1.1. Torque/power requirements for traction machines [ZHU07].

Table 1.1. Overview of several commercialized EVs on the market [KRI20].

EVs	**Toyota Prius Gen. III**	**Nissan Leaf**	**BMW i3**	**Chevy Bolt**	**Toyota Prius Gen. IV**	**Tesla Model 3**
Year of introduction	2010	2010	2013	2016	2017	2017
Peak torque (Nm)	207	280	250	360	163	416
Peak power (kW)	60	80	127	150	53	202
No. stator slots	48	48	72	72	48	54
No. rotor poles	8	8	12	8	8	6
Winding type	Distributed	Distributed	Distributed	Hairpin	Hairpin	Distributed

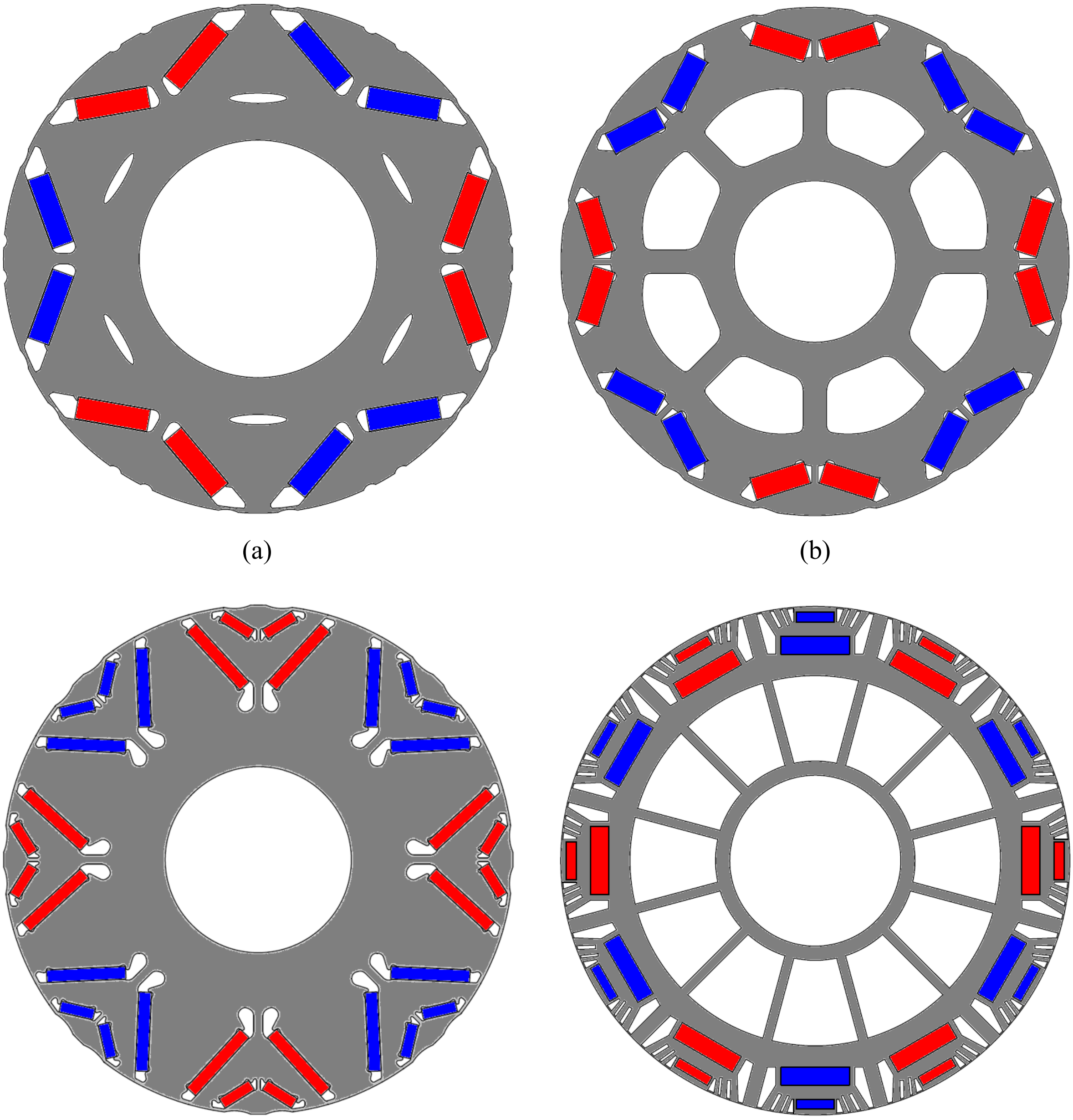

(a) (b)

(c) (d)

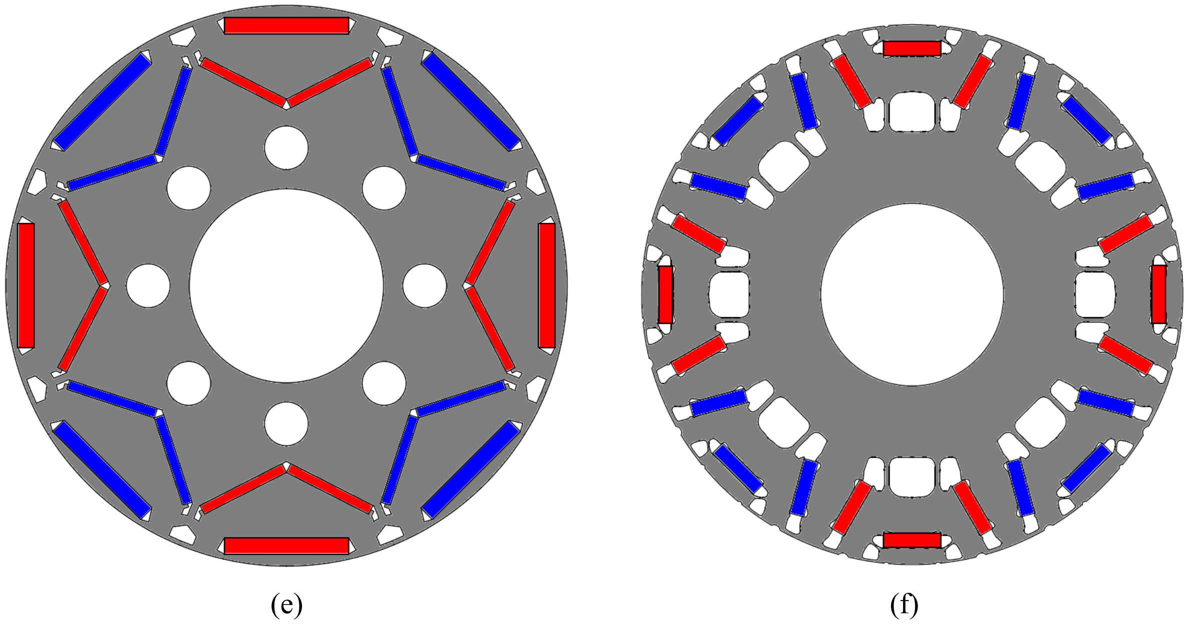

Fig. 1.2. Several rotor geometries of commercialized IPMSMs in EV industry. (a) Single-layer V-shape IPMSM with 54s/6p (Tesla Model 3). (b) Single-layer V-shape IPMSM with 48s/8p (Toyota Prius Gen. III). (c) Double-layers V-shape IPMSM with 72s/8p (Like Chevy Bolt). (d) Double-layers I-shape IPMSM with 72s/12p (BMW i3) (e) Double-layers Delta-shape IPMSM with 48s/8p (Nissan Leaf). (f) Double-layers UI-shape IPMSM with 48s/8p (Toyota Prius Gen. IV).

On the downside, the main disadvantage of the rare-earth PM (REPM) machines is their reliance on PMs made by rare-earth materials. These materials have limited resources and are generally expensive. Meanwhile, their price history shows two big spikes in 2011 and 2022 which rise a concern around the availability and affordability of REPMs. On the one hand, a report published by the United States (US) Department of Energy (DoE) shows that ~20% to 30% of the total expense of a PM machine belongs to the price of REPMs [ENE]. On the other hand, to synchronize the required specifications of PM machines with the growing market of EVs, the DOE and the United Kingdom (UK) Advanced Propulsion Centre (APC) have drafted enhanced performance targets for future [SHA20]. Therefore, designing the cost-effective high performance PM machines for EV applications becomes a hot research topic in recent years. This challenging target can be interpreted as the necessity of improving the torque with REPM volume ratio which can be done either by improving the performance at the same utilization of REPM or reducing the consumption of REPMs at the same performance (i.e. less-REPM machines). As the result of this universal attempt, several methods have been proposed in literature which are applicable in EV applications. These methods can be categorized into the stator technologies and rotor technologies based on the component that they are applied to. Using Hairpin windings on the stator structure of the PM machines in EV application is an example of stator technologies which has been proposed as a promising solution of increasing the output torque by enhancing the slot fill factor. On the other hand, the employment of ferrite PM (FEPM)-assisted SynRMs (PM aSynRMs), asymmetric rotor geometries, improving the reluctance torque component (T_{rel}), and hybrid PM (HPM) utilization have been extensively investigated in recent years as the rotor technologies for the torque enhancement. Fig. 1.3 illustrates a diagram of these methods towards less REPM usage in PM machines.

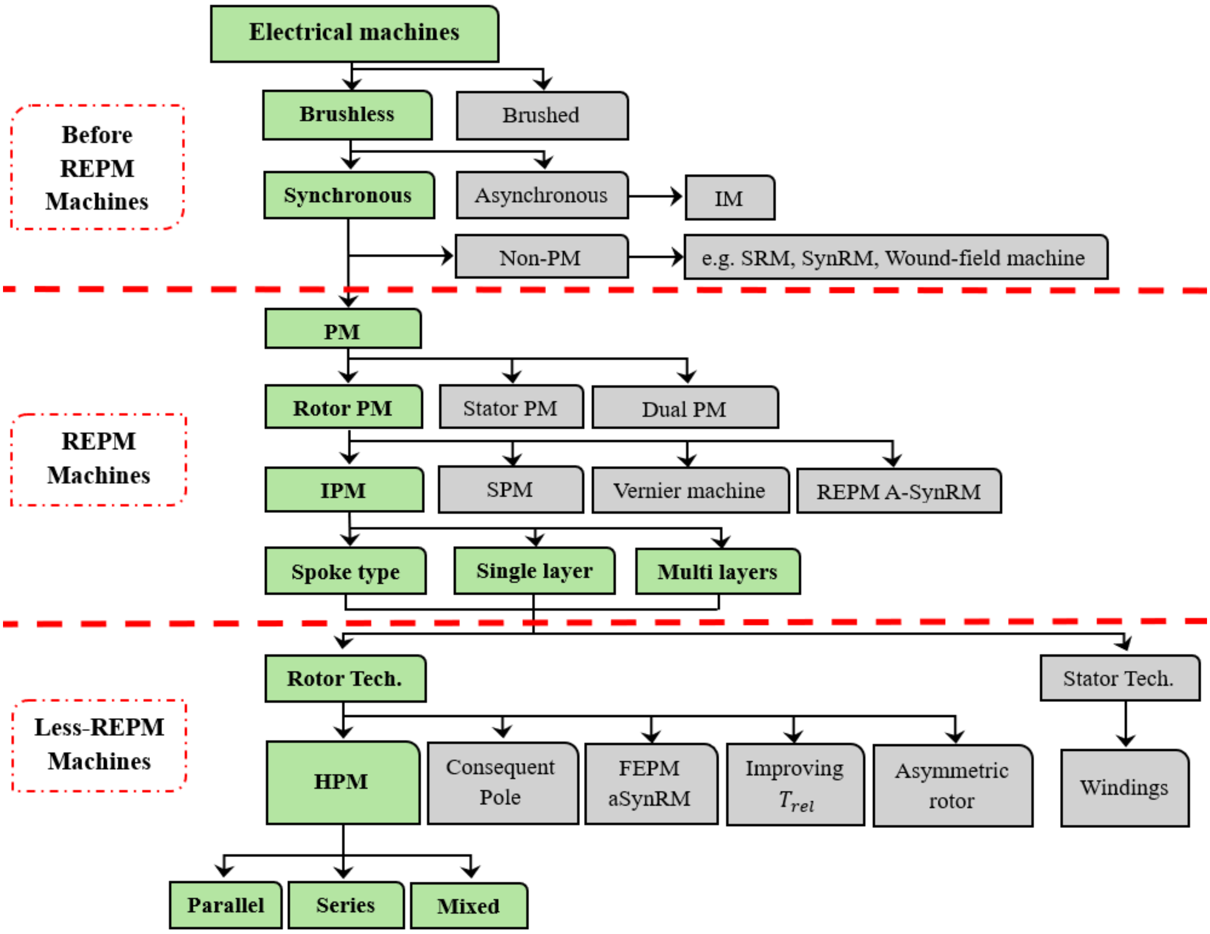

Fig. 1.3. Development of REPM and Less-REPM machines for EV application.

This thesis focuses on the HPM utilization in IPMSMs accounting for the EV application. Therefore, a detailed literature review on the HPM usage in different topologies of PM machines is enclosed in this chapter. Meanwhile, as the combination of HPM usage and the other rotor technologies methods (listed in Fig. 1.3) can also be found in literature, a brief description of them will be given in the following sections. In addition, it should be noted that HPM utilization is a new method for providing a high-performance magnetic loading at a reduced cost which is in general independent from electrical loading i.e. types of winding configuration (e.g. distributed or Hairpin). Therefore, any baseline EV IPMSM can be selected from Table 1.1 and Fig. 1.2. However, the Nissan Leaf 2012 IPMSM is selected as the main benchmark for this thesis which employs a 48-stator-slot/8-rotor-pole (48s/8p) combination as presented in Table 1.1. In addition to the benchmark's rotor structure presented in Fig. 1.2 (e), Fig 1.4 shows its stator structure and distributed winding configuration. Moreover, Table 1.2 summarizes the main specifications of this machine. In this thesis, the same stator structure, winding configuration, overall dimensions including the stack length, airgap length, and shaft diameter is used for the sake of a fair comparison. As a result, only rotor structures will be re-optimized in each chapter.

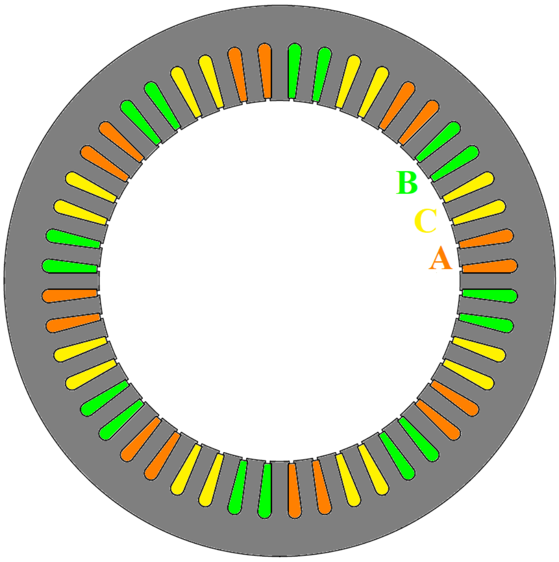

Fig. 1.4. Stator structure and winding configuration of Nissan Leaf 2012 with 48 slots and distributed winding.

Table 1.2. Specification of commercialized Nissan Leaf 2012 [YAN17A] and [BUR13].

Parameters	Values	Parameters	Values
Stator slot no.	48	Peak speed (r/min)	10000
Rotor pole no.	8	Rated speed (r/min)	2100
Stator outer diameter (mm)	200	Peak torque (Nm)	280
Stator inner diameter (mm)	131	Peak current (A_{max})	625
Rotor outer diameter (mm)	130	Peak current density (A/mm^2)	26.31
Rotor inner diameter (mm)	45	Conductor no. per slot	8
Stack length (mm)	151	Strand no. per conductor	15
Airgap length (mm)	0.5	Number of parallel branches	4
NdFeB remanence (T)	1.075	Actual volume of machine (L)	6.06
Angle of rotor skew (degree)	3.75	Peak torque per actual volume (Nm/L)	46.2

1.2. Stator Technologies

1.2.1. Concentrated and Distributed Windings

From the perspective of stator technologies, there are in general two types of winding configurations: non-overlapping concentrated windings which employ concentrated tooth coils and overlapping distributed windings in which the coil pitch is larger than two slot pitches as illustrated in Figs. 1.5 (a) and (b), respectively. The advantages and disadvantages of concentrated and distributed windings are summarized in Table 1.3.

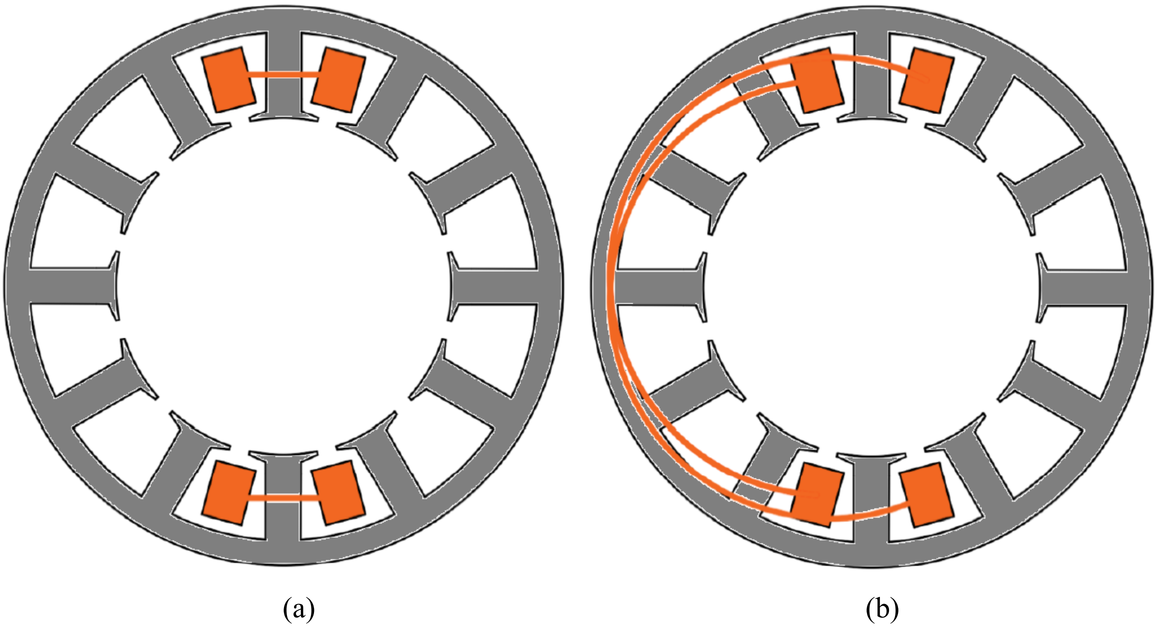

Fig. 1.5. General windings configurations. (a) Non-overlapping. (b) Overlapping.

Table 1.3. Comparison of winding configurations [ELR10] [ZHU11].

Characteristics	Non -overlapping concentrated windings	Overlapping distributed windings
Slot fill factor	0.5-0.65	0.35-0.45
Length of end winding	Short	Long
Reluctance torque	Small	Large

To benefit from the reluctance torque component in EV applications, distributed windings are widely employed. However, as listed in Table 1.3, using the stranded round wires leads to a low slot fill factor ranging from 0.35 to 0.45 in distributed windings. Meanwhile, the development of preformed rectangular wire windings (e.g. Hairpin windings) with a high slot fill factor (0.6-0.7) has gained a lot of attention for EV application in recent years [ZHA19].

1.2.2. Hairpin Windings

EVs have attracted a great deal of attention during the last few decades as a response to the global concerns on increasing greenhouse gas emissions and fossil fuel consumptions. Consequently, with the aim of being employed in an EV, many researches have been carried out on the design of electrical machines (e.g. power density enhancement) which has the most impact on energy-efficiency map and travel distance of EVs. As summarized in Table 1.4, the power density enhancement methods can be categorized in three groups including speed increase, torque enhancement, and winding technology [ARZ20]. The preformed wire windings, also known as rectangular wire windings (e.g. Hairpin and I-pin types), are growing fast in the winding technology sector especially for EV applications. These windings consist of multi-layer rectangular conductors and are located inside stator slots which lead to a higher fill factor than the conventional stranded wire windings. This section briefly describes the characteristics, benefits and drawbacks of this winding technology for EV application.

Table 1.4. Summary of key enablers for power density maximization in electrical machines [ARZ20].

Power density maximization		
Speed increase	**Torque enhancement**	**Winding technology**
• Mechanical properties of materials E.g. increasing the yield strength without negative effect on magnetic properties	• Airgap flux density E.g. improving the magnetic properties of materials	• Decreasing winding resistance E.g. reducing end winding length
• Optimal machine design E.g. optimal pole pair number	• Linear current density E.g. enhanced cooling	• Increasing fill factor E.g. preformed wires

1.2.2.1. Concept

The preformed wire windings are made of rectangular conductors instead of round wires as shown in Fig. 1.6 and are classified into two groups including Hairpin and I-pin configurations as can be seen in Fig. 1.7. I-pin windings benefit from ease of shaping and assembly but suffers from increased number of twisting and welding ports which results in a longer end winding. Therefore, hairpin windings are more suitable for EV applications and have been used in Chevy Bolt 2016, Toyota Prius IV 2017, and Jaguar I-Pace 2019 as the commercialized examples [KRI20].

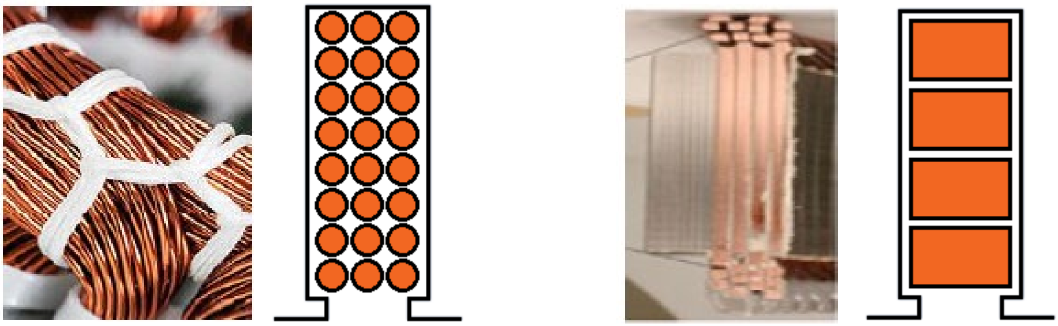

(a) (b)

Fig. 1.6. Comparison of different winding types [ZHA19]. (a) Round wires. (b) Rectangular wires.

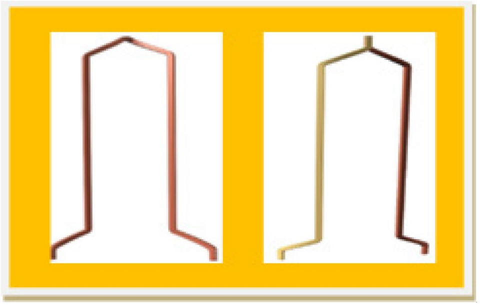

Fig. 1.7. Comparison of Hairpin (left figure) and I-pin (right figure) wires [ZHA19].

1.2.2.2. Electromagnetic Performance

Generally, a hairpin winding benefits from a higher fill factor than a stranded winding which leads to a higher electrical loading at low speed and results in a higher torque density and efficiency. Having a higher thermal dispatching capability due to the enhanced ratio of copper to insulation, high automation capacity, and high rigidity are other advantages of hairpin windings in EV application. However, on the downside, it suffers from high AC copper loss due to a big cross section area of copper which leads to the higher skin and proximity effects at high speeds [BER20].

In [FYH17], three IPMSMs with different winding types including distributed windings, concentrated windings, and hairpin windings are compared where only stator slot shape is modified in all designs. The results show the superior electromagnetic performance of the design with hairpin windings over the others as illustrated in Fig. 1.8. As can be seen, this machine benefits from higher torque and efficiency at low speed due to higher fill factor and reduced DC copper loss. However, the efficiency will be deteriorated at high speed due to the increased AC copper loss at high frequency.

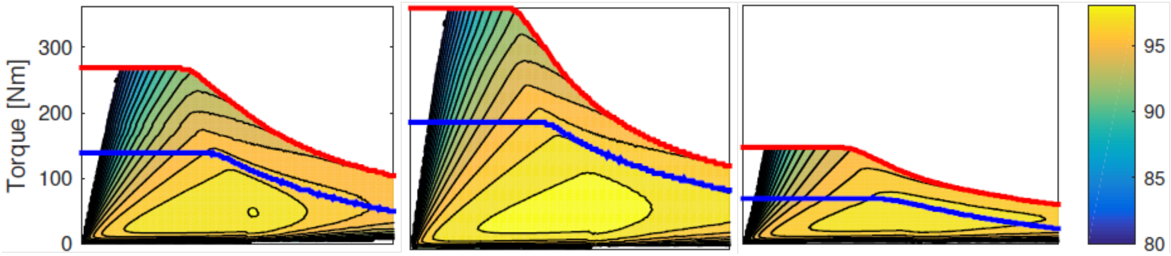

(a) (b) (c)

Fig. 1.8. Comparison of efficiency maps in different IPMSMs using various winding types [FYH17]. (a) Distributed. (b) Hairpin. (c) Concentrated.

1.2.2.3. Reduction of AC Copper Loss

Several methods have been proposed for AC copper loss mitigations in literature.

A. Free Spacing

It is known that the proportion of AC copper loss in each layer of conductors reduces with the position of layers towards the slot bottom which means the AC copper loss of conductor at slot opening is higher than that of the others due to the ununiform current density distribution caused by leakage flux at slot opening. Therefore, in [DUB18], decreasing the height of conductors is presented as the simplest way of reducing AC copper loss by taking away the layers from the slot opening as presented in Fig. 1.9 (b). Although the results show the effectiveness of this method, it reduces the slot fill factor and the resultant advantages of hairpin winding usage.

B. Parallel Conductors

It is shown in [PRE21] that as the AC copper loss is more severe near the slot opening, dividing the conductors near the airgap into several conductors (as shown in Fig. 1.9. (c)) can effectively reduce the total copper loss. It is concluded that the higher the number of segments, the lower the AC copper loss. However, a higher number of conductors leads to the higher number of welding ports and difficulty of manufacturing.

C. Asymmetric Conductors

In [ISL19], the asymmetric dimensional design of conductors is presented with the aim of reducing the cross section of conductors near the airgap without any changes in the number of conductors, number of welding ports, and reduction of slot fill factor as shown in Fig. 1.9 (d). Although this method does not increase the mechanical difficulties, it is less effective than the parallel conductors' method as compared in [ARZ20].

D. Hybrid Conductors

The hybrid conductors made by copper and aluminium are proposed for AC loss reduction in [CUT23], [VID24]. As can be seen in Fig. 1.9 (e), the copper conductors near slot opening are replaced with aluminium. It is shown that the skin depth of a conductor made by aluminium is higher than that of a copper conductor at the same frequency due to having a higher resistivity. As a result, the AC loss in a Hairpin winding made by hybrid conductors is expected to be lower than that of a copper conductor counterpart at the cost of an increased DC loss. Meanwhile, using aluminium brings the advantages of the reduced cost and mass of windings as the price and mass density of aluminium are considerably lower than those of copper.

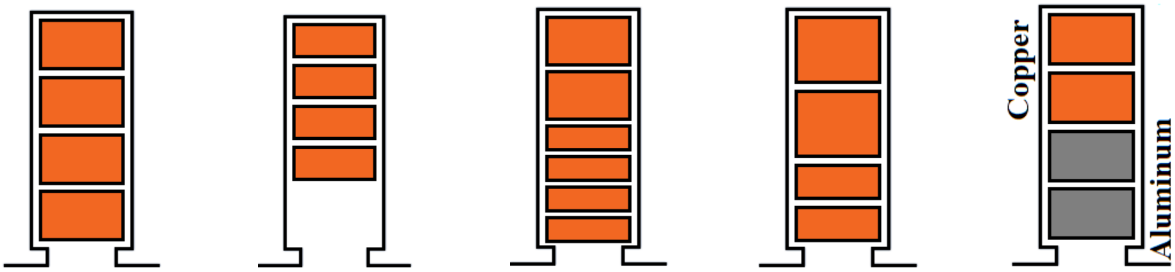

(a) (b) (c) (d) (e)

Fig. 1.9. Methods of reducing AC copper loss. (a) Reference Hairpin conductors [ZHA19]. (b) Free spacing [DUB18]. (c) Parallel conductors [PRE21]. (d) Asymmetric conductors [ISL19]. (e) Hybrid conductors [VID24].

1.3. Rotor Technologies

1.3.1. Consequent Pole PM machines

In a consequent pole PM machine, the magnetic field circuit is formed by removing the PMs of either north or south poles as shown in Fig. 1.10. Therefore, the remaining PMs generate the flux lines in the same direction. Meanwhile, the returning path of the flux lines in a magnetic loop is forced to go through the removed poles (also known as induced poles). Consequently, this machine has the same number of poles as a conventional PM machine whereas half of the poles are actual poles, and the other half are the induced poles [POU21]. As a result, the volume of REPM can be effectively reduced at the cost of slight reduction in output torque.

The consequent pole structure is also used in inset PM [LI18] and PM vernier machines [ALL20]. In [CHU15], a consequent pole 48-slot/4-pole inset PM machine is proposed which is capable of producing the same performance as a baseline at the rated condition with 33% reduced volume of REPM (see Fig. 1.11 (a)). In [CHU11], a PM vernier machine with modular inner stator and consequent pole outer rotor is proposed which benefits from a lower volume of REPM compared to a baseline (see Fig. 1.11 (b)). Meanwhile, it is worth mentioning that none of these machines have been proposed for EV industry as they are not suitable for high-speed applications. For example, a PM vernier machine works based on the magnetic gearing effect where the modulated harmonics can contribute with the fundamental component of magnetic field in generating a higher output torque [KWO18]. However, this type of consequent pole machines has higher winding inductance compared to the conventional PM machines which results in a higher reactance, low overload capability, and poor power factor [LI16A]. Therefore, the PM vernier machines are generally recommended for applications with high-torque and low-speed requirements.

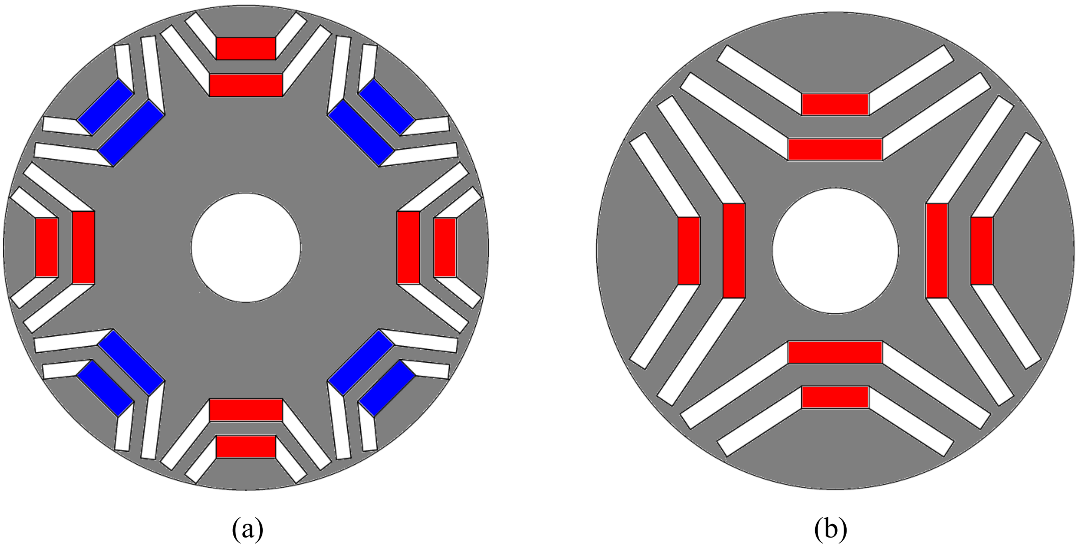
(a) (b)

Fig. 1.10. Comparison of PM machines [POU21]. (a) Conventional PM. (b) Consequent pole PM.

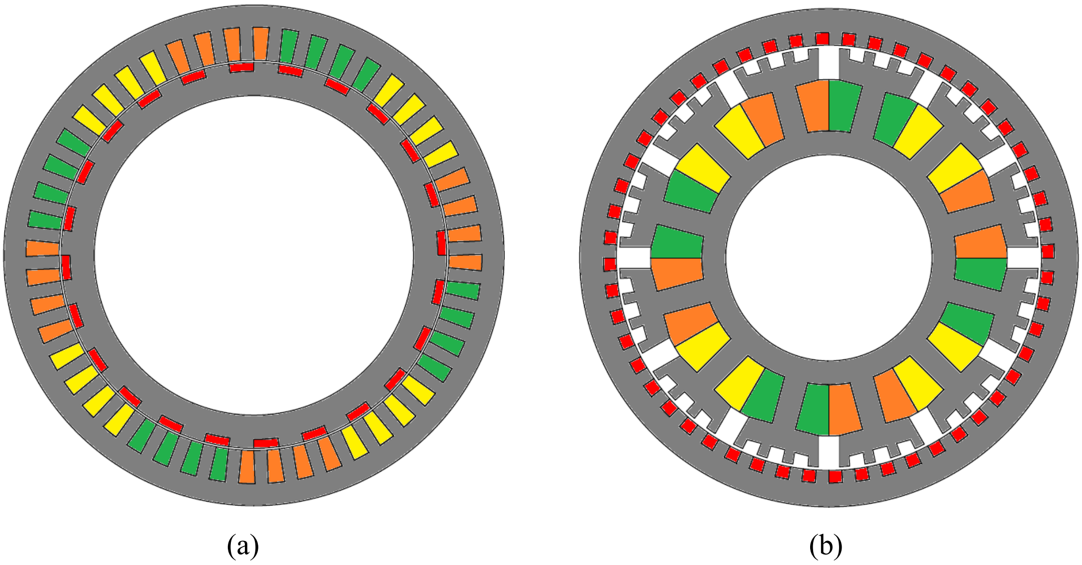
(a) (b)

Fig. 1.11. Examples of consequent pole PM machines. (a) Inset PM machine [CHU15]. (b) PM vernier machine [CHU11].

1.3.2. FEPM aSynRM

1.3.2.1. Concept

The SynRMs benefit from a simple and robust rotor structure consists of multi-layers of flux barriers and flux carriers as can be seen in Fig. 1.12. In these machines having a high anisotropy is desirable as it increases the reluctance torque component and the resultant torque. Therefore, an important parameter is introduced as the insulation ratio which is defined as the ratio of the summation of flux barriers width to the total width of flux carriers [VAG14]. It can be said that a higher insulation ratio results in a higher saliency ratio and a higher reluctance torque. Meanwhile, the saturation level of the flux carriers is a limitation for excessive increase in this ratio. The effect of insulation ratio on the performance of a SynRM accounting for the saturation level of flux carriers is investigated in [FER15]. In addition, it is shown in [WAN15], [WAN17] that increase in the number of layers of flux barriers at the same insulation ratio has low impact of average torque but is highly effective on torque ripple mitigation.

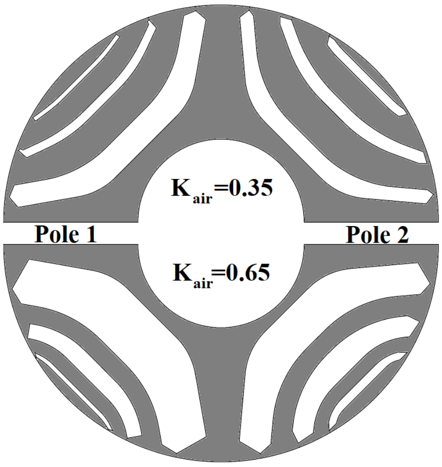

Fig. 1.12. Illustration of insulation ratio in SynRM [FER15].

On the downside, SynRMs suffer from low power factor and efficiency. To address this issue, PM aSynRMs are introduced which are assisted either by REPMs or FEPMs. It is shown in [HUY18] that the arrangement of PMs inside the flux barriers is affecting the performance meaning that the PM in the 1st layer, the closest layer to the shaft (see Fig. 1.13 (a)), contributes more to the output torque. However, it is shown in [GUG13] that the dimensions of PMs in each layer can be optimized separately to achieve a reduced volume of REPM usage as shown in Fig. 1.13 (b). However, although the volume of REPM can be reduced, having a high number of magnets with different sizes increases the labour cost of PMs. Therefore, in an attempt of reducing the reliance on the high-cost REPMs, FEPM aSynRM is introduced. Although this machine can similarly benefit from an improved power factor and efficiency, it cannot produce a comparable torque to that of a REPM-based counterpart. This is because the residual flux density of a FEPM can be 67% less than that of a REPM.

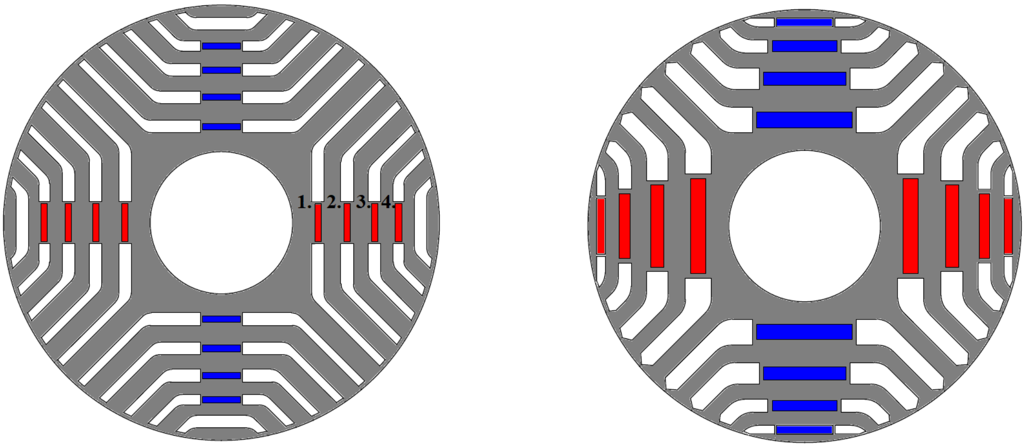

(a) (b)

Fig. 1.13. Arrangement of PMs in PM aSynRM. (a) Positions of PMs [HUY18]. (b) Dimensions of PMs [GUG13].

1.3.2.2. High-speed Application

For high-speed applications including EVs, the PM machines should provide a wide-speed range of operation which is also known as the constant power speed range (CPSR). The CPSR capability can be compared using the rated current (I_s) and the characteristic current (I_{ch}) as following:

$$I_{ch} = \frac{\Psi pm}{L_d} \tag{1.1}$$

where Ψ_{pm} and L_d are the PM flux linkage and the d-axis inductance, respectively.

Therefore, PM machines can be categorized into three groups:

- $I_{ch} > I_s$: limited speed range and fast power drop
- $I_{ch} < I_s$: wide speed range with power drop
- $I_{ch} \approx I_s$: wide speed range without power drop

For example, I_{ch} in SPMs is bigger than I_s. Therefore, these machines are not suitable for high-speed applications [CAR14]. Meanwhile, the CPSR capabilities of IPM and PM aSynRM are compared in [HUY17]. It is concluded that in general I_{ch} of PM aSynRM is lower than its I_s. Therefore, this machine can satisfy the wide-speed range operation at the cost of power drop at high speed. Meanwhile, the $I_{ch} \approx I_s$ in IPM implies that this machine can operate at high speed without a reduction of output power. It should be noted that the CPSR capability of PM aSynRM can be improved by the increase in the volume of PMs and the resultant Ψ_{pm}. However, having a high number of flux barriers introduces the geometrical limit to accommodate a high volume of REPMs as the saturation level of flux carriers should be considered.

1.3.3. Improving Reluctance Torque

FEPMs are introduced as the low-cost alternative to REPMs in literature which can be at least ten times cheaper. However, as the energy-product of FEPMs can be 67% lower than that of the REPMs, a FEPM machine cannot typically generate the same performance as a REPM counterpart. Meanwhile, the spoke-type IPMSM topology can provide a massive space for accommodating a large volume of FEPMs to compensate their low energy-product and benefits from flux focusing effect. However, these machines suffer from a relatively low reluctance torque contribution. Therefore, in [KAK13], a triangle flux barrier is added between adjacent spokes in d-axis as shown in Fig. 1.14 (a). It is shown that the total torque is increased about 23 Nm (7.7 %) due to the increase in the reluctance torque component by 72 Nm. However, it is achieved at the cost of 49 Nm reduction of PM torque component at the same magnet usage. Therefore, the PM utilization, i.e. the ratio of PM torque to PM usage, is significantly reduced. In [NAG16], the shape of rotor core is modified as shown in Fig. 1. 14 (b). It is shown that this modification helps with the torque enhancement at high-speed region compared to the base model. However, similar to the previous machine, the PM torque contribution is suppressed by using flux barriers in d-axis.

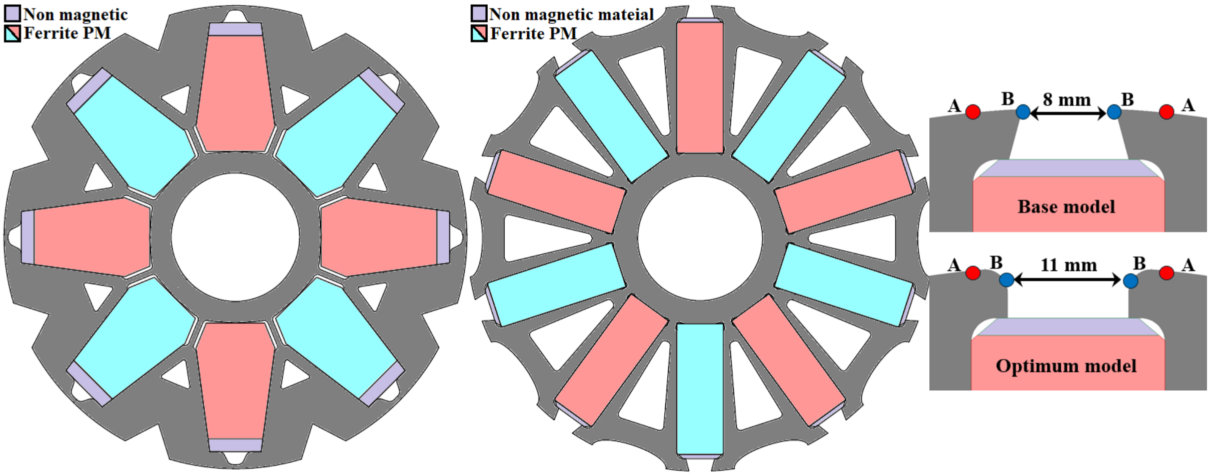

(a) (b)

Fig. 1.14. Improving the reluctance torque of the spoke-type IPMSM. (a) Extra flux barrier in d-axis [KAK13]. (b) Shaping the rotor core when d-axis flux barrier is used [NAG16].

1.3.4. Asymmetric Rotor

On the one hand, the output torque of a PM machine has a unique optimum current advancing angle at each current amplitude which can be obtained using the maximum torque per ampere (MTPA) control strategy. On the other hand, it is known that the output torque of a PM machine is the summation of PM torque and reluctance torque components whereas the peak values of these components are achievable at different current advancing angles. Therefore, in general, the amplitude of either PM torque component or reluctance torque component needs to be increased to improve the output torque of a symmetrical PM machine.

However, in an asymmetric PM machine, the corresponding current advancing angles of PM torque and reluctance torque components are forced to merge towards each other thanks to the magnetic field shifting (MFS) effect. Therefore, as two torque components are reaching to their maximum towards a unique current advancing angle, the resultant torque will increase even at the same amplitudes of these components. Consequently, an asymmetric PM machine can produce a higher torque at the same volume of REPM or the same torque at a lower REPM usage compared to a symmetrical counterpart.

1.3.4.1. Theoretical Analysis of MFS Effect

In this section, the principle of the MFS effect in asymmetric IPMSMs will be discussed by employing a simplified analytical model without considering saturation, cross-magnetization, and harmonics [ZHU22].

On the one hand, Fig. 1.15 compares the vector diagrams of stator current and PM flux linkage in symmetrical and asymmetric IPMSMs in the dq-axis coordinates. In this figure, i_s, i_d, and i_q are the vectors of stator and dq-axis currents. Similarly, Ψ_{pm}, Ψ_{fd}, and Ψ_{fq} are the vectors of resultant PM flux linkage, and dq-axis flux linkages, respectively. Finally, β is the current advancing angle in both machines, and α_s is the asymmetric angle in asymmetric IPMSM only. On the other hand, the dq-axis flux linkages can be generally written as:

$$\begin{cases} \Psi_d = \Psi_{fd} + L_d i_d \\ \Psi_q = \Psi_{fq} + L_q i_q \end{cases} \tag{1.2}$$

where Ψ_d and Ψ_q are the dq-axis PM flux linkages, and L_d and L_q are the dq-axis inductances, respectively.

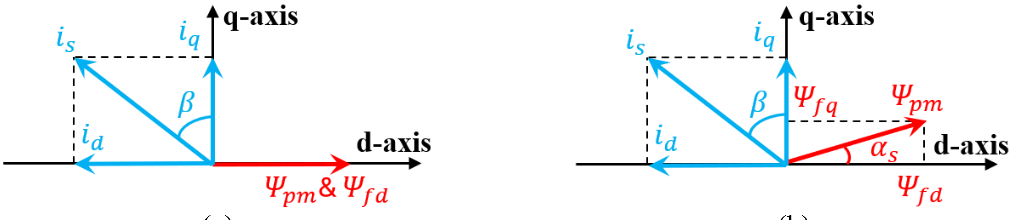

(a) (b)

Fig. 1.15. Comparison of vector diagrams in dq-axis coordinates. (a) Symmetrical IPMSM. (b) Asymmetric IPMSM.

Therefore, considering Fig. 1.15 and (1.2), the equation of Ψ_d and Ψ_q for the symmetrical and asymmetric IPMSMs can be re-written as (1.3) and (1.4), respectively:

$$\begin{cases}\Psi_d = \Psi_{pm} - L_d i_s \sin\beta \\ \Psi_q = L_q i_s \cos\beta\end{cases} \tag{1.3}$$

$$\begin{cases}\Psi_d = \Psi_{pm}\cos\alpha_s - L_d i_s \sin\beta \\ \Psi_q = \Psi_{pm}\sin\alpha_s + L_q i_s \cos\beta\end{cases} \tag{1.4}$$

Meanwhile, considering a PM torque component corresponding to the interaction of q-axis flux linkage (Ψ_{fq}) and d-axis current (i_d), the output torque of a 3-phase IPMSM (T_{out}) can generally be written as a summation of PM torque (T_m) and reluctance torque (T_r) as below:

$$T_{out} = T_m + T_r = \tfrac{3p}{2}\left((\psi_{fd} i_q + \psi_{fq} i_d) + (L_d - L_q) i_d i_q\right) \tag{1.5}$$

where p is the number of pole pairs.

Finally, by substituting (1.3) and (1.4) into (1.5), and after simplification, the output torques of the symmetrical ($T_{out\text{-}IPMSM}$) and the asymmetric ($T_{out\text{-}AIPMSM}$) IPMSMs can be expressed as:

$$\begin{cases}T_{out-IPMSM} = T_{pm}\cos\beta + T_{rel}\sin 2\beta \\ T_{out-AIPMSM} = T_{pm}\cos(\beta - \alpha_s) + T_{rel}\sin 2\beta\end{cases} \tag{1.6}$$

where T_{pm} and T_{rel} are the amplitudes of PM and reluctance torque component which can be shown as:

$$\begin{cases}T_{pm} = \tfrac{3p}{2}\Psi_{pm} i_s \\ T_{rel} = \tfrac{3p}{4}(L_q - L_d) {i_s}^2\end{cases} \tag{1.7}$$

In theory by assuming that the peak reluctance torque component of an IPMSM reaches at β=45 elec. deg., it can be concluded from (1.6) that the PM torque component of a symmetrical IPMSM reaches its maximum at $\beta=0$ elec. deg. Meanwhile, that of an asymmetric IPMSM happen at $\beta=\alpha_s$ elec. deg. Therefore, the current advancing angle difference ($\Delta\beta$) between the maximum PM torque and reluctance torque components of an asymmetric IPMSM is less than that of the symmetrical IPMSM counterpart with a positive α_s due to the MFS effect. It means, the resultant torque of an asymmetric IPMSM can be improved even with the same PM and reluctance torque amplitudes.

1.3.4.2. Categorization and Examples

In general, the asymmetric PM machines can be classified into 4 groups [ZHU22] as shown in Fig. 1.16. This categorization includes symmetrical rotor core structure and PM configuration (group 1), asymmetric rotor core structure and symmetrical PM configuration (group 2), symmetrical rotor core structure and asymmetric PM configuration (group 3), and asymmetric rotor core structure and PM configuration (group 4).

A. Group 1

The asymmetric PM machines in group 1 consist of a rotor with several parts whereas each part has a symmetrical core structure and PM configuration. For example, the proposed two-part rotor asymmetric PM machine in Fig. 1.16 (a) is made of a SPM part and a multi-layer reluctance part with the same axial length [YAN17B]. Meanwhile, a displacement angle between two parts can be employed to adjust the MFS effect and enhance the output torque [BES12]. In addition, to eliminate the unbalanced axial force in the two-part rotors, the rotor structure, with three parts using the same part at both axial ends, is proposed in [ZHA18].

B. Group 2

The asymmetric PM machines in this group are made of asymmetric rotor structure and symmetrical PM configuration as shown in Fig. 1.16 (b). For example, the proposed machine in Fig. 1.16 (b-1) employs an additional flux barrier outside the V-shaped PM cavity to improve the torque by utilizing the MFS effect. Similarly, an additional flux barrier towards the centre of the V-shaped PM cavity is used in [HAY19] as can be seen in Fig. 1.16 (b-2). Finally, Fig 1.16 (b-3) presents another topology in this group where asymmetric rotor core geometry is applied to a spoke-type IPMSM [XIA20A].

C. Group 3

The asymmetric PM machines in this group are made of symmetrical rotor structure and asymmetric PM configuration as shown in Fig. 1.16 (c). The first asymmetric PM machine in this category is made by asymmetric positioning of PMs in an inset PM machine as shown in Fig. 1.16 (c-1) [ALS15]. Similarly, a hybrid pole topology with symmetrical rotor structure can be found in Fig. 1.16 (c-2) [LIU17]. As can be seen, although the V-shape arrangement of PM is symmetrical, the inset PMs are asymmetrically positioned. Finally, a multi-layer asymmetric PM machine with asymmetric PM usage is investigated in [ZHE19] and presented in Fig. 1.16 (c-3).

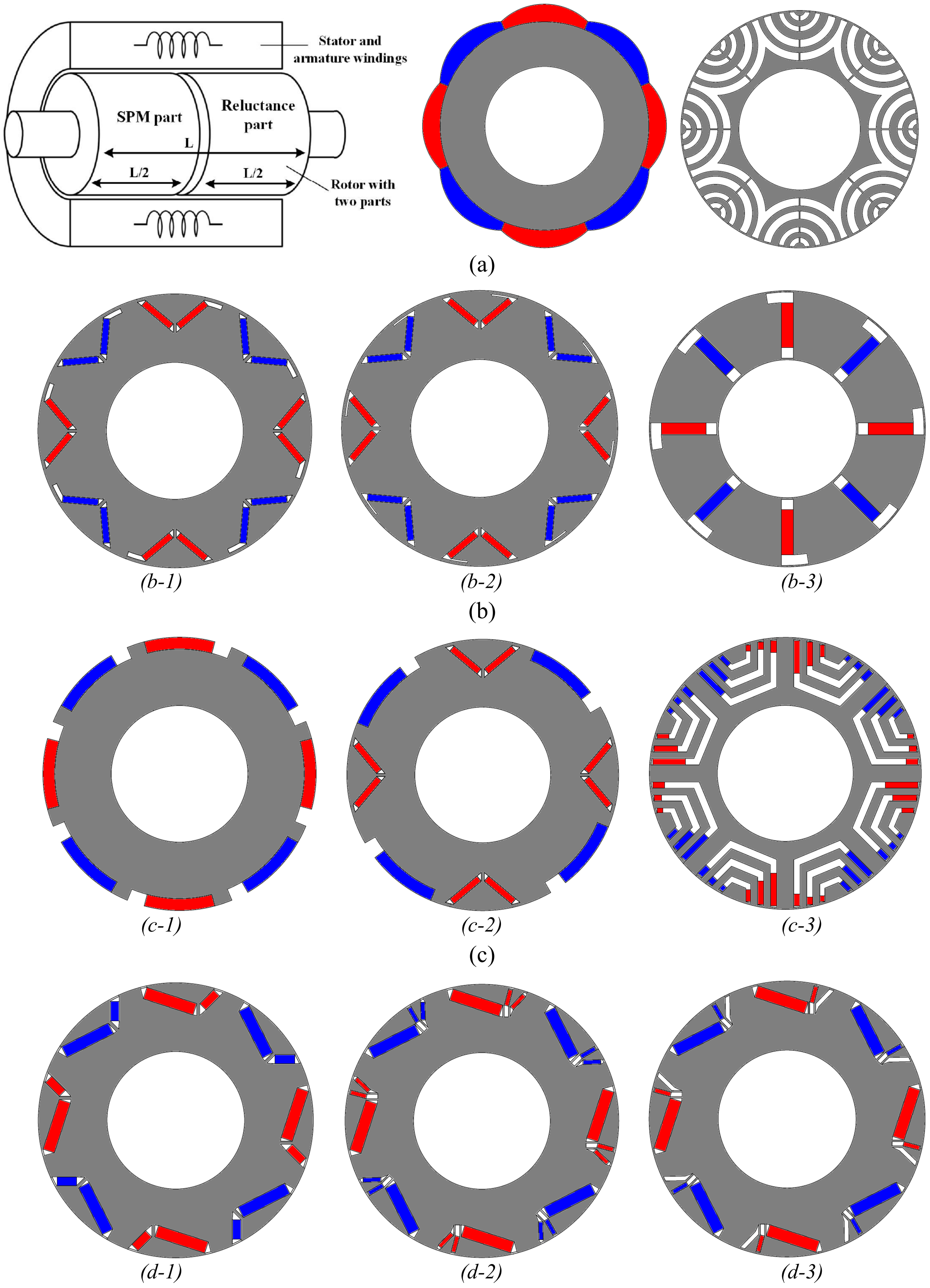

(a)

(b-1) *(b-2)* *(b-3)*

(b)

(c-1) *(c-2)* *(c-3)*

(c)

(d-1) *(d-2)* *(d-3)*

(d)

Fig. 1.16. Categorization of asymmetric PM machines. (a) Symmetrical core structure and symmetrical PM configuration (group 1). (b) Asymmetric core structure and symmetrical PM configuration (group 2). (c) Symmetrical core structure and asymmetric PM configuration (group 3). (d) Asymmetric core structure and asymmetric PM configuration (group 4).

D. Group 4

The rotor structure and PM configuration are both asymmetric in the proposed PM machines in group 4 as shown in Fig. 1.16 (d). As the axes of both PM field and reluctance torque components can be adjusted, the asymmetric PM machines in this group have more freedom of design to enhance the output torque. Fig. 1.16 (d-1) presents a single layer asymmetric V-shape IPMSM which has a negligible torque improvement due to a poor MFS effect [REN15]. Meanwhile, the hybrid-layer counterpart [XIA20B] (see Fig. 1.16 (d-2)) and the single layer asymmetric V-shape counterpart with extra flux barrier [XIA21A] (see Fig. 1.16 (d-3)) benefit from a significant torque enhancement due to an improved MFS effect.

1.3.5. Hybrid PM Utilization

Typically, the PM machines with HPM utilization are similar to the memory machines as they both employs two PM types in the same structure. Meanwhile, a memory machine simultaneously employs the constant-flux PM (CPM) and the variable-flux PM (VPM) in one structure. However, a HPM machine employs two CPM types with different residual flux densities. In general, the consumption of FEPM and NdFeB magnets in HPM machines are common. These machines are first introduced in 2011 when Jin-Tao Chen and Zi-Qiang Zhu filled a European patent application for SPM machines with HPM utilization [CHE11B] as shown in 1.17 (a). In this patent, different arrangement of two PM types are proposed. Similarly, As can be seen in Fig. 1. 17 (b), the application of HPM utilization in SPM machines with different modular structures of Halbach magnets is presented in [SHE12]. As can be seen, different sizes of magnets with either equal or unequal heights are considered. In addition, for the modular T-type designs with unequal height PMs, a non-magnetic base (e.g. aluminium) is adopted to reduce the interpolar leakage flux. At almost the same time, an outer rotor IPM machine with HPM utilization is proposed in [ISH13] as shown in Fig. 1.17 (c). A year later, two HPM SFPMs with different arrangements of two PM types are proposed in [AFI14] as shown in Fig. 1.17 (d). Therefore, the invention of HPM machines backs to only a dozen of years ago. However, they gained an excessive attention in recent years as price of REPM materials unboundedly increased.

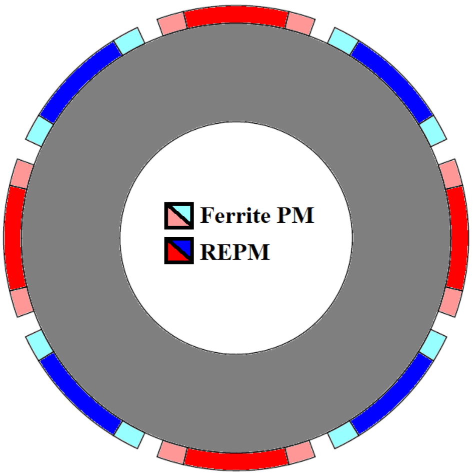
Ferrite PM
REPM

(a)

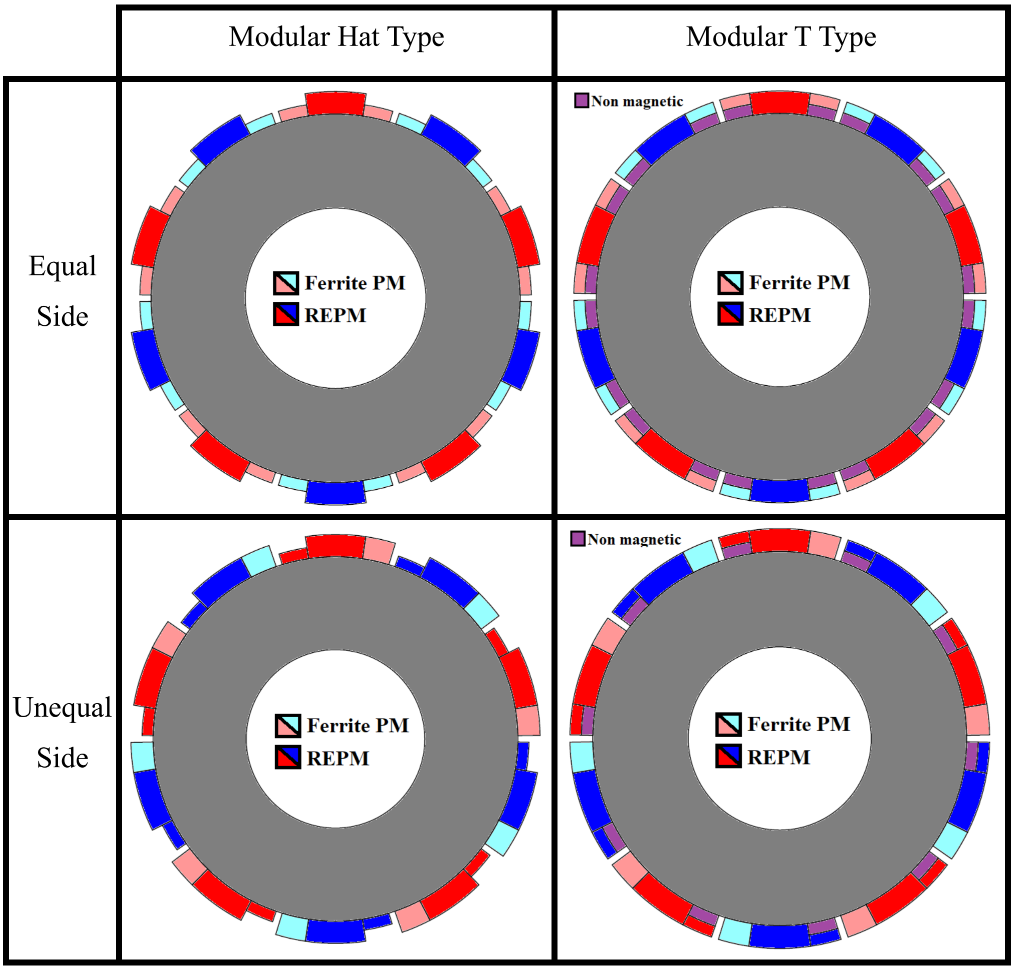
Modular Hat Type
Modular T Type
Equal Side
Unequal Side
Non magnetic
Ferrite PM
REPM

(b)

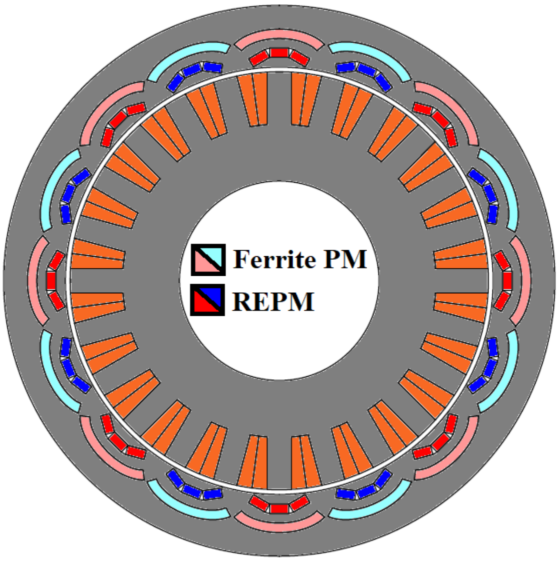

(c)

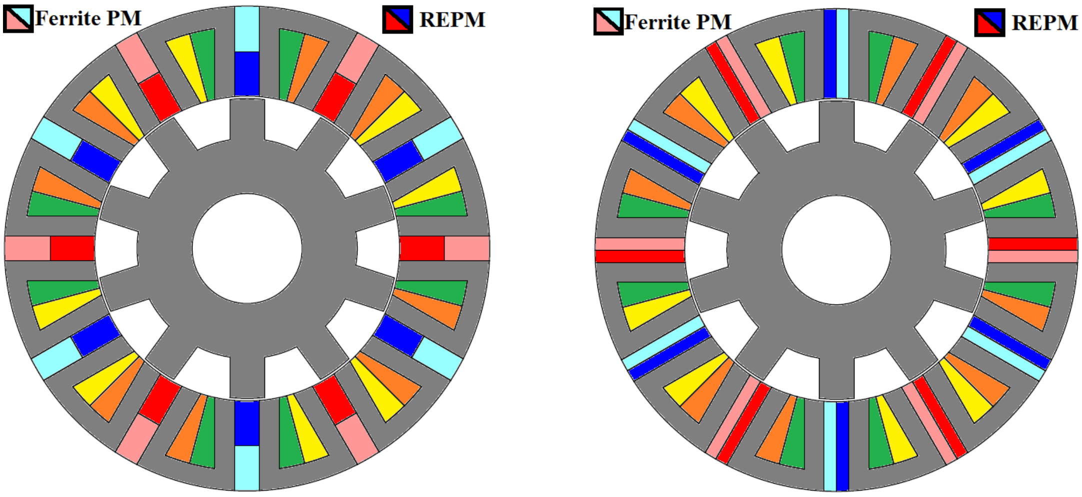

Parallel HPM

Series HPM

(d)

Fig. 1.17. Invention of HPM machines in literature. (a) Using different arrangements of two PM types in SPM machines [CHE11B]. (b) Using modular arrangements of two PM types in SPM machines [SHE12]. (c) An outer rotor HPM IPMSM [ISH13]. (d) Two HPM SFPM machines [AFI14].

Table 1.5 summarizes the torque enhancement methods in rotor technologies group as described in this section. Despite from having different features, all these methods can be used to improve the torque with REPM usage ratio in PM machines. Meanwhile, as the HPM utilization is the main objective of this thesis, a detailed literature review of HPM machines will be presented separately in the following section. As will be shown, the combinations of HPM utilization with other methods have also been proposed in some papers which can result in further reduction of REPM usage and PM cost at the same performance.

Table 1.5. Summary of torque enhancement methods in rotor technologies.

Section	Title	Example	Reference	Remark
1.3.1	Consequent Pole	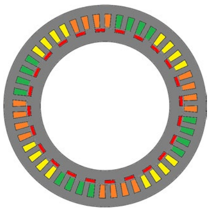	[CHU11] [CHU15] [LI16A] [LI18] [KWO18] [ALL20] [POU21]	• Reduced REPM usage • Wider constant power range than SPM machines • Modulated torque at high number of rotor poles • Low power factor • Slight reduction of average torque • Suitable for high-torque low-speed applications
1.3.2	FEPM aSynRM	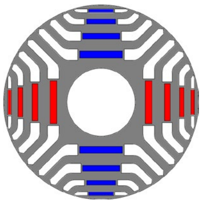	[GUG13] [CAR14] [VAG14] [FER15] [WAN15] [WAN17] [HUY17] [HUY18]	• High reluctance torque component • Improved power factor and efficiency due to being assisted by PM • Lower PM torque than a REPM aSynRM • Wide speed range with power drop • Low space for FEPM usage due to the required width of flux carriers accounting for saturation
1.3.3	Improving T_r	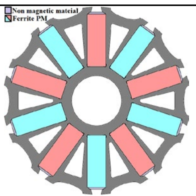	[KAK13] [NAG16] [TAH20]	• High FEPM usage • Improved reluctance torque by d-axis flux barrier • Reduced PM utilization (i.e. PM torque with PM volume ratio) due to d-axis flux barrier
1.3.4	Asymmetric Rotor	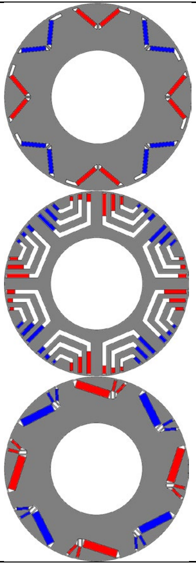	[BES12] [ALS15] [REN15] [YAN17B] [LIU17] [ZHA18] [HAY19] [ZHE19] [XIA20A] [XIA20B] [XIA21A] [ZHU22]	• Improved resultant torque due to MFS effect even at the same reluctance torque, PM torque, and PM usage • Can be categorized into 4 groups based on rotor structure and PM configuration • More flexibility for torque enhancement in topologies of group 4 with both asymmetric rotor structure and asymmetric PM configuration
1.3.5	HPM	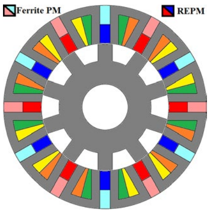	[CHE11B] [SHE12] [ISH13] [AFI14]	• New type of PM machines with first introduction in 2011 • Employs two CPMs, i.e. FEPM and REPM • Reduced volume of REPM at same performance • Mutual effect of two CPMs with different magnetic properties defines main features of HPM machines

1.4. HPM Machines

As discussed, PM machines benefit from high torque/power densities and high efficiency due to high energy-product of REPM but suffer from high cost due to the expensive REPMs. On the contrary, the FEPMs are extremely cheap but cannot produce a comparable performance to the REPMs due to low energy-product. In [TAH20], a review of FEPM usage in electrical machines is presented in terms of pros and cons. Meanwhile, the HPM machines are introduced to utilise the synergies of high energy-product REPMs and low-cost FEPMs in one structure. As two PM types with different magnetic properties are used, the relative positions of these PMs can define the general features of HPM machines and categorize them into three groups which will be discussed in section 1.4.1. In addition, they can be utilized in all PM machines including stator PM machines (section 1.4.2), dual-PM machines (section 1.4.3), and rotor PM machines (section 1.4.4).

1.4.1. Configuration of HPM Machines

In general, HPM machines can be categorized into three configurations including parallel, series, and mixed (a mixture of parallel and series magnetic connections) accounting for the relative positions of two PM types. These configurations can be defined based on the equivalent magnetic circuit at open circuit condition. In [CHE20] [CHE21] [ZHE21A], different configurations of HPM utilization are compared. The schematic and equivalent magnetic circuits of the proposed parallel, series, and mixed HPM machines in [CHE21] are shown in Figs. 1.18 and 1.19, respectively. As can be seen, each magnet is modelled with a magnetic motive force (MMF) in a series connection with a magnetic reluctance. In addition, from Fig. 1.19 (a), it can be concluded that the PM flux produced by either REPM or FEPM will not face the magnetic reluctance of the second PM type in a parallel HPM configuration. Meanwhile, as two PM types with different magnetic properties are used, the flux produced by the high energy-product REPM can form a leakage flux path through the low-coercive FEPM. On the contrary, from Fig. 1.19 (b), it can be said that the flux produced by both PM types needs to flow through the other magnet in a series connection. In addition, the magnetic field produced by REPM can support the magnetic field produced by FEPM. As a result, a parallel HPM configuration generally benefits from a higher electromagnetic performance and suffers from a higher risk of irreversible demagnetization in FEPM compared to those of a series HPM counterpart. Finally, as the name of the mixed HPM configuration suggests, it is a mixture of the parallel and series magnetic connections and may have the synergies of both features at the cost of a complicated structure as shown in Fig. 1.19 (c). It is also worth mentioning that the proposed mixed HPM topology in [CHE20] and [CHE21] employs an asymmetric arrangement of PMs which results in two different equivalent magnetic circuits in adjacent poles as can be seen in Fig. 1. 19 (c). As can be seen in both magnetic circuits, a parallel HPM part is in a series magnetic connection with another PM. However, a mixed HPM configuration can also be made by a series HPM part in a parallel magnetic connection with another PM as shown in Fig. 1.20 (b). Figs. 1.20 (a) and (b) present the schematic and the equivalent magnetic circuit of the proposed mixed HPM spoke-type IPMSM in [ZHE21A].

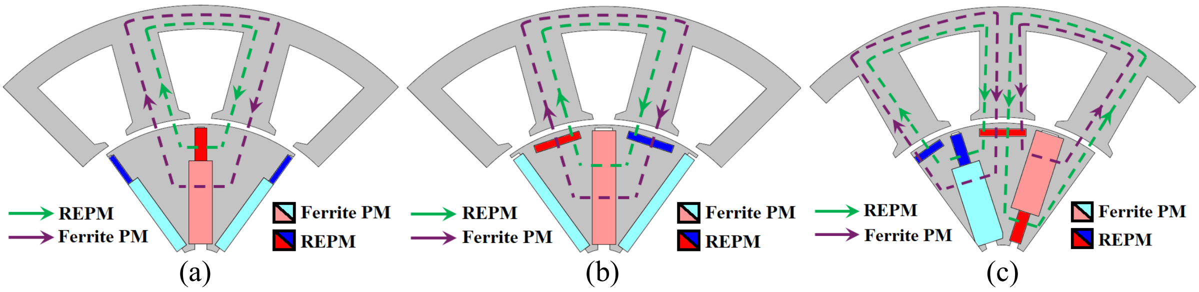

Fig. 1.18. Schematics of different HPM configurations in spoke-type IPMSMs [CHE21]. (a) Parallel. (b) Series. (c) Mixed.

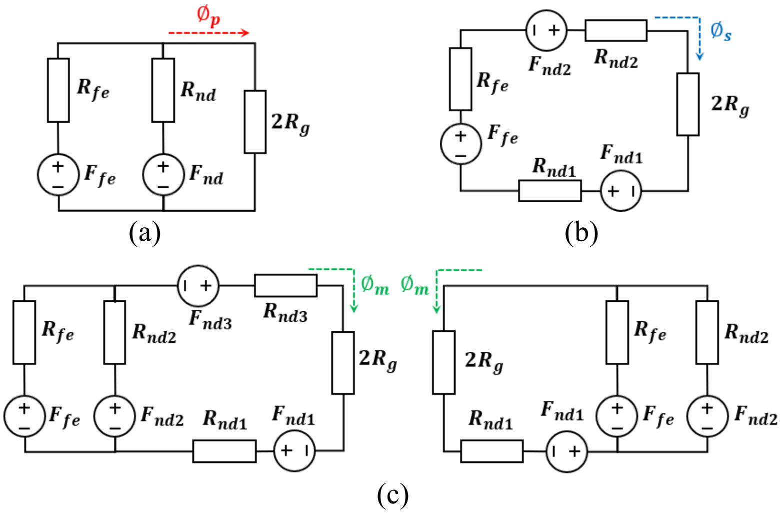

Fig. 1.19. Equivalent magnetic circuits of different HPM configurations in spoke-type IPMSMs [CHE21]. (a) Parallel. (b) Series. (c) Mixed.

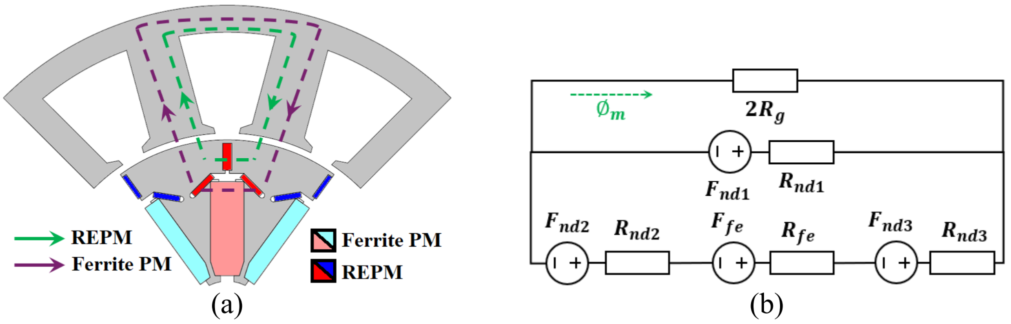

Fig. 1.20. Mixed HPM spoke-type IPMSM in [ZHE21A]. (a) Schematic model. (b) Equivalent magnetic circuit.

Table 1.6 compares the main features of different HPM configurations.

Table 1.6. Summary of main features in different HPM configurations.

Configuration	Schematic	Advantage	Disadvantage
Parallel	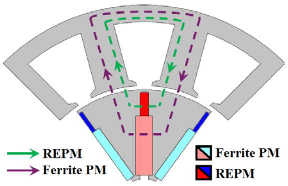	• Low magnetic reluctance of PM flux paths • High electromagnetic performance	• Reduced working point of FEPM by REPM • Increased demagnetization risk of FEPM
Series	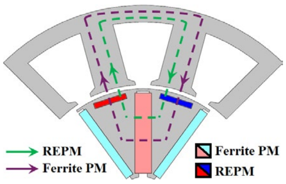	• Improved working point of FEPM by REPM • Increased demagnetization withstand capability of FEPM	• High magnetic reluctance of PM flux paths • Low electromagnetic performance
Mixed	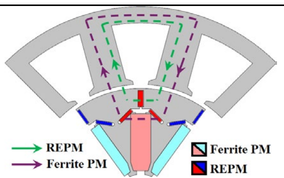	• Trade-off of the advantages in other HPM configurations	• Complicated rotor structure in most designs

1.4.2. Stator PM Machines with HPM Utilization

In [AFI16], the application of HPM utilization in a SFPM machine is investigated by comparing a REPM-based, a FEPM-based, and two parallel and series HPM configurations (see Fig. 1.14.(d)), all in the same size. On the one hand, the available space for accommodating FEPMs at the same machine dimension is limited. On the other hand, the residual flux density of the FEPM is considerably lower than that of REPM. Therefore, it is shown that the output torque of the REPM-based and FEPM-based designs at the same size are the highest and the lowest, respectively. Meanwhile, the output torque of the HPM counterparts can vary in this range depending on the volumes of each PM type. However, on the upside, it is shown that the topologies with more volume of FEPM benefit from improved flux weaking capability and efficiency at a reduced cost.

In [ALQ21], a mixed HPM partitioned stator SFPM machine is proposed which consists of an outer stator with AC windings and inner stator with two PM types (T-shape REPM and rectangular ferrite segments) as shown in Fig. 1.21 (a). In addition, the rotor is made of the flux modulation pole (FMP) pieces which are similar to those of the magnetically geared machines. As a result, these machines can generally benefit from less saturation on stator teeth and enhanced space utilization for accommodating FEPMs in the inner stator compared to those of the conventional SFPM machines. However, on the downside, they may require improved electrical and magnetic loadings as they have two airgaps. Fig. 1.21 (b) presents a similar partitioned stator SFPM machine whereas a parallel HPM configuration and the DC field windings are employed [LI16B]. As a result of hybrid excitation, this machine benefits from an improved flux regulation capability. In [CHE18A] and [CHE18B], two HPM hybrid excited partitioned stator SFPM machines are proposed with one stator filled by PMs and DC windings whereas the other stator is filled by AC windings only. In both machines, the DC windings have embraced the FEPMs to improve the demagnetization withstand capability of this magnet at overload conditions. However, they are expected to suffer from an additional copper loss in DC windings and a compensated flux weaking capability due to the position of PMs. It should be noted that the proposed topology in [CHE18A] has an inner stator with AC windings whereas that of the [CHE18B] employs an outer stator with AC windings.

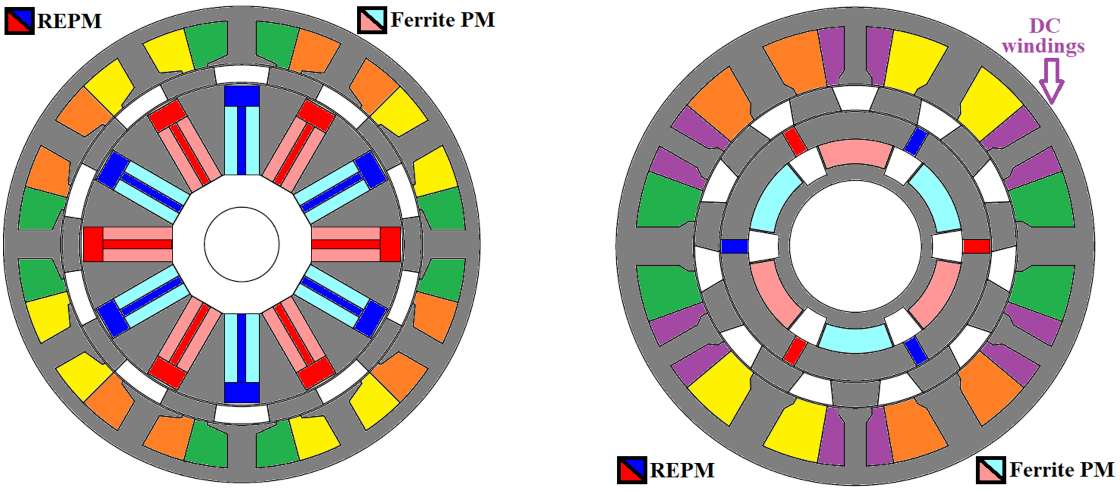

(a) (b)

Fig. 1.21. HPM partitioned stator SFPM machines. (a) Mixed HPM without DC windings [ALQ21]. (b) Parallel HPM with DC windings (hybrid excited) [LI16B].

In [LU16], a HPM double stator SFPM machine is proposed. In the proposed machine, the salient pole rotor has different numbers of poles in each side and is magnetically separated into two parts by using a non-magnetic insulating material in the middle of the rotor structure. In addition, each stator has its own set of AC winding which can be excited separately. Therefore, this topology can be considered as the combination of two machines where the inner machine has an inner stator and an outer rotor, and the outer machine employs an outer stator and an inner rotor. It is discussed that the outer and inner machines can work solely for the low-speed and high-speed operations, respectively. However, for the high-power operation at overload condition, both machines can work together. The proposed machine suffers from a highly complicated structure whereas a parallel HPM configuration is only used in the inner machine. In [WAN22], a HPM double stator SFPM machine is proposed where the rotor is made of the FMP pieces with REPMs. Meanwhile, the stators are built with different split tooth combinations whereas the FEPMs are filled between the split teeth and in the slot openings. It is concluded that the proposed machine has the advantage of high torque density and high demagnetization withstand capability of FEPMs due to the series HPM connection. However, as a high number of magnets are used near the airgap, the manufacturing difficulty and the increased labour cost are expected.

In [XIA18] and [FAN17] two partitioned rotor SFPM machines with different configurations of HPMs are proposed as can be seen in Fig. 1.22. In [XIA18], the parallel and series configurations of HPMs are considered as illustrated in Figs. 1.22 (b) and (c), respectively. It is shown that the parallel configuration benefits from a higher torque density but suffers from a lower overload capability and a lower demagnetization withstand capability of FEPMs compared to those of the series HPM counterpart. Meanwhile, as can be seen in Fig. 1.22 (a), the employed FEPM is shaped with a thinner width towards the inner side which suffers from an increased risk of irreversible demagnetization. Therefore, as shown in Fig. 1.22 (d), two small segments of REPM are used to improve the demagnetization withstand capability of FEPM and enhance the torque density to some extent in [FAN17].

Table 1.7 compares the application of HPM utilization in different SFPM machines. As can be seen, the partitioned stator SFPM machines can provide more space for accommodating a higher volume of FEPMs.

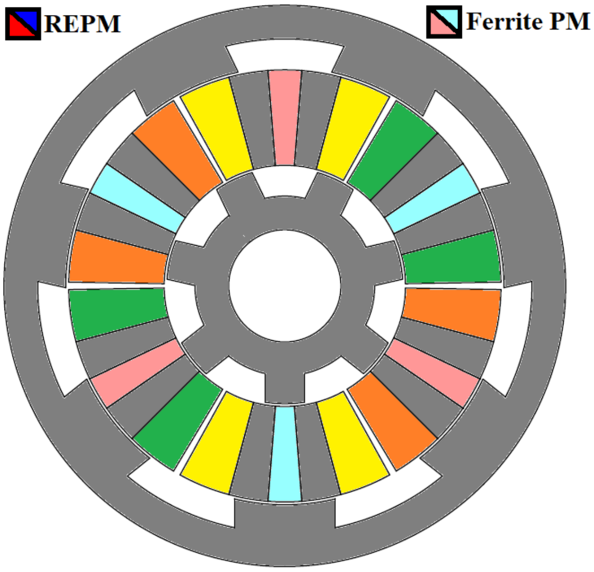

(a)

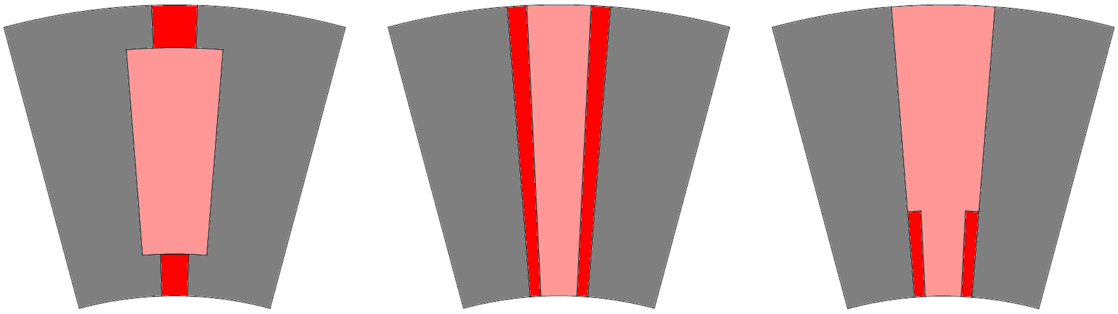

(b) (c) (d)

Fig. 1.22. HPM double rotor SFPM machines. (a) Cross section of proposed machine. (b) Parallel HPM configuration [XIA18]. (c) Series HPM configuration [XIA18]. (d) Mixed HPM configuration [FAN17].

Table 1.7. HPM utilization in different SFPM machines.

Type of SFPM	**Example**	**Reference**	**Remark**
Conventional	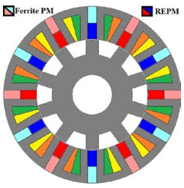	[AFI16]	• Low space for FEPM usage in SFPM machines • Lower space for FEPM usage in hybrid excited SFPMs • Higher torque if using a higher volume of REPM • Improved efficiency if using a higher volume of FEPM due to a reduced PM eddy current loss
Partitioned rotor	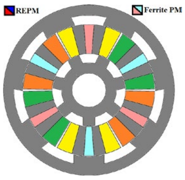	[FAN17] [XIA18]	• Low space for FEPM usage • High torque density • Low leakage flux in stator due to yoke-less design • Two airgaps
Partitioned stator	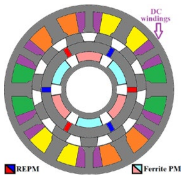	[LI16B] [CHE18A] [CHE18B] [ALQ21]	• Less saturation in stators due to separated PM and AC winding • More space for FEPM usage in both PM-excited and hybrid excited SFPM machines • AC/DC windings in one stator and HPMs in the other • AC winding in one stator and DC winding/HPMs in the other • Improved anti-demagnetization of FEPMs if they are embraced by DC windings • Two airgaps

1.4.3. Dual PM Machines with HPM Utilization

In [XU17A], a unipolar dual PM vernier machine with HPM utilization is presented as shown in Fig. 1.23 (a). As can be seen, the inset REPMs are used on the rotor structure whereas FEPMs are located between the flux-modulation poles on the stator structure. Both PM types are magnetized in the same radial direction which defines the series HPM configuration and increases the demagnetization withstand capability. It is shown that by adding FEPMs to this structure, the output torque increases by ~11% compared to that of an equivalent machine without FEPMs at the same size, specifications, and REPM usage. Unlike the proposed machine in [XU17A], a dual PM vernier machine with HPM utilization is proposed in [KAN22] (Fig. 1.23 (b)) which consists of an outer stator and an inner rotor. As can be seen, the inset FEPMs are used on the rotor structure whereas a Halbach array of REPMs are employed between the flux-modulation poles on the stator structure. This machine can produce a high torque density at low speed at the cost of manufacturing difficulties by using the Halbach array.

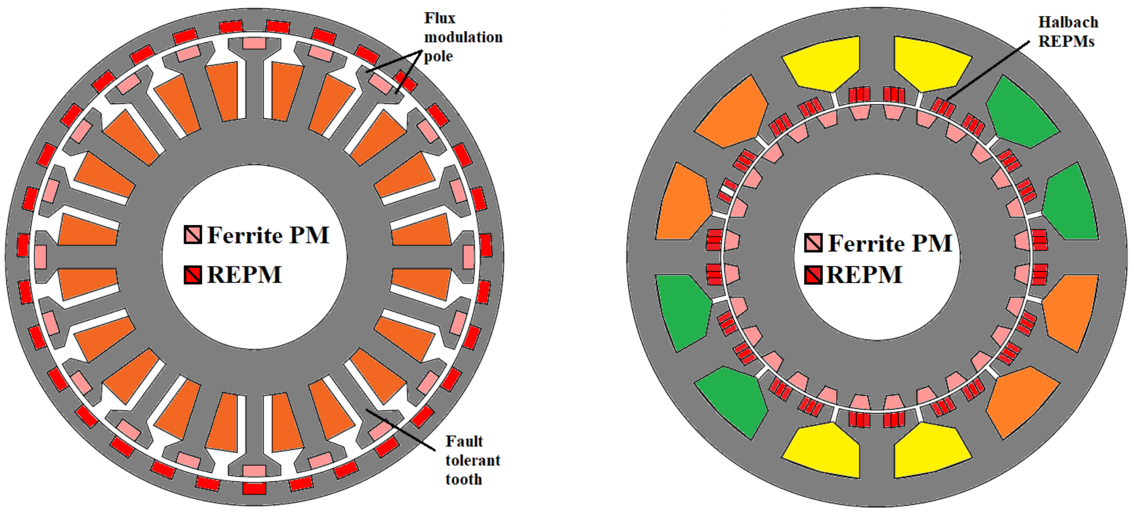

(a) (b)

Fig. 1.23. Dual PM vernier machines with HPM utilization. (a) With inner stator and outer rotor [XU17A]. (b) With outer stator and inner rotor [KAN22].

1.4.4. Rotor PM Machines with HPM Utilization

The HPM utilization has been applied to the different topologies of rotor PM machines in literature as will be presented in the following subsections.

1.4.4.1. HPM SPM

In [LIU14], three Halbach SPM machines with one series and two mixed HPM configurations are compared. The proposed mixed HPM structures have a T-shape, or a hat-shape arrangement of FEPMs as can be seen in Figs. 1.24 (a) and (b). Meanwhile, the REPM magnets are filled above the hat-shape FEPMs near the airgap, or beneath the T-shape FEPMs near the shaft. It is shown that although the generated torques of the proposed HPM machines are slightly lower than that of a REPM-based baseline at the same size, the torque per REPM usage ratios of these machines are higher. Meanwhile, it is shown that the mixed HPM with T-type FEPMs has an inferior performance than that of the other counterpart with hat-type

FEPMs. It is because when REPMs are located near the shaft, they face a thinner FEPM in the middle which increases the risk of leakage flux from the shaft side. However, when REPMs are located near the airgap, the thickness of FEPM is higher which reduces the risk of leakage flux near the airgap. In addition, the risk of leakage flux near the shaft is also reduced by the Halbach arrangement of FEPMs in the shaft side. In [KNY14], a SPM machine with HPM utilization is proposed as shown in Fig. 1.24 (c) which is similar to the equal-side modular T-type SPM machine in [SHE12] (see Fig. 1.17 (b)). However, a parallel HPM utilization is used in the proposed machine which is different from the Halbach array in [SHE12]. In addition, the beneath space of the short-height FEPM is filled by rotor core instead of non-magnetic aluminium base in Fig. 1.17 (b). Therefore, the proposed machine is expected to suffer from the interpolar leakage flux. Meanwhile, a parallel HPM configuration is applied to a SPM machine and compared with a series HPM counterpart in [CHE14]. In this machine, the height of FEPM is higher than that of the REPM. As expected, it is shown that the parallel HPM design benefits from a higher electromagnetic torque but suffers from a lower demagnetization withstand capability of FEPMs compared to those of the series counterpart.

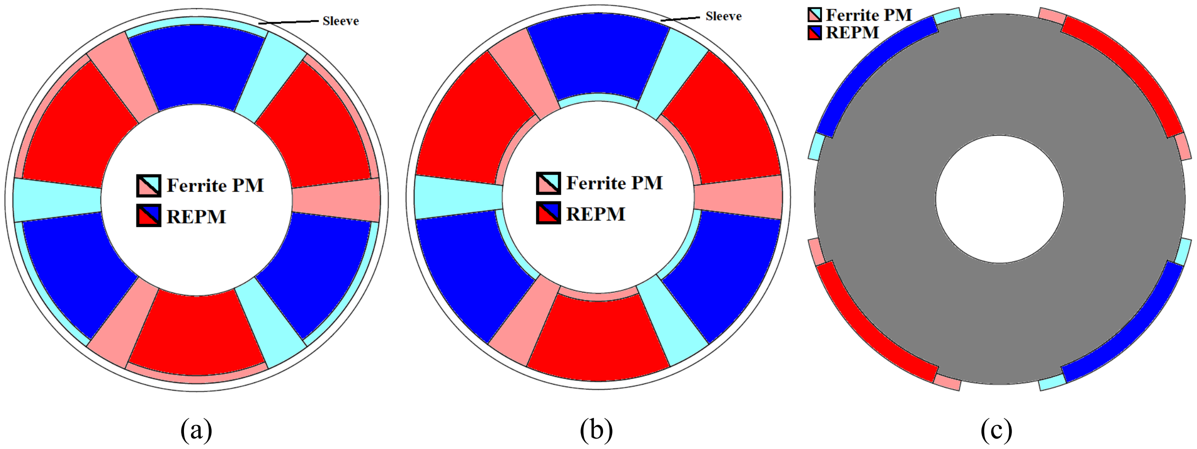

Fig. 1.24. SPM machines with HPM utilization. (a) Mixed HPM with T-type FEPMs [LIU14]. (b) Mixed HPM with hat-type FEPMs [LIU14]. (c) Parallel HPM T-type without aluminium base [KNY14].

In [POU22], a combined method of analytical derivation and optimization algorithm is applied to a SPM machine with parallel HPM utilization with the aim of reducing the cogging torque in a reduced computational time compared to that of a finite element analysis (FEA) optimization. The proposed machine in this paper employs the same height for REPM and FEPM whereas the widths of two PM types are optimized independently.

1.4.4.2. HPM aSynRM

As discussed in section 1.3.2, the SynRMs benefit from high reluctance torque due to a high anisotropy while suffering from a low power factor and efficiency. Therefore, the PM aSynRMs are introduced to overcome the drawbacks. Meanwhile, the REPM aSynRM generates a higher electromagnetic performance at the cost of being more expensive than a FEPM aSynRM. As a result, the HPM aSynRMs are proposed to combine the advantages of both PM types.

In [KUM20], the positioning effect of two PM types in a three-layer PM aSynRM is investigated as illustrated in Fig. 1.25 (a). It is shown that the combinations with REPM in the 3rd layer (closest flux barrier to the shaft) can generate a higher torque compared to the others. This is because the magnet in the last layer is expected to contribute more to torque production as it was concluded in [HUY18] (see Fig. 1.13 (a)). In addition, two cases are selected as the promising combinations in this paper. The first one employs NdFeB in the 2nd and 3rd layers whereas FEPM is filled in the 1st layer (closest flux barrier to the airgap). Meanwhile, the other topology employs NdFeB in the 1st and 3rd layers whereas FEPM is filled in the 2nd layer. Then, it is concluded that the former design benefits from a higher torque whereas the latter topology, with FEPM in middle layer, benefits from a lower PM cost at the cost of a higher torque ripple due to the higher distortion of PM flux in the airgap. It should be noted as the series HPM configuration is used, no significant demagnetized area of FEPMs could be found. A similar study with the same conclusion is conducted in [WAN24] where only two layers of flux barriers are used as shown in Fig. 1.25 (b). In summary, it can be said that employing REPM in the inner layer closer to the shaft is beneficial for generating a higher torque but employing FEPM in this layer brings the advantage of more reduction in PM cost.

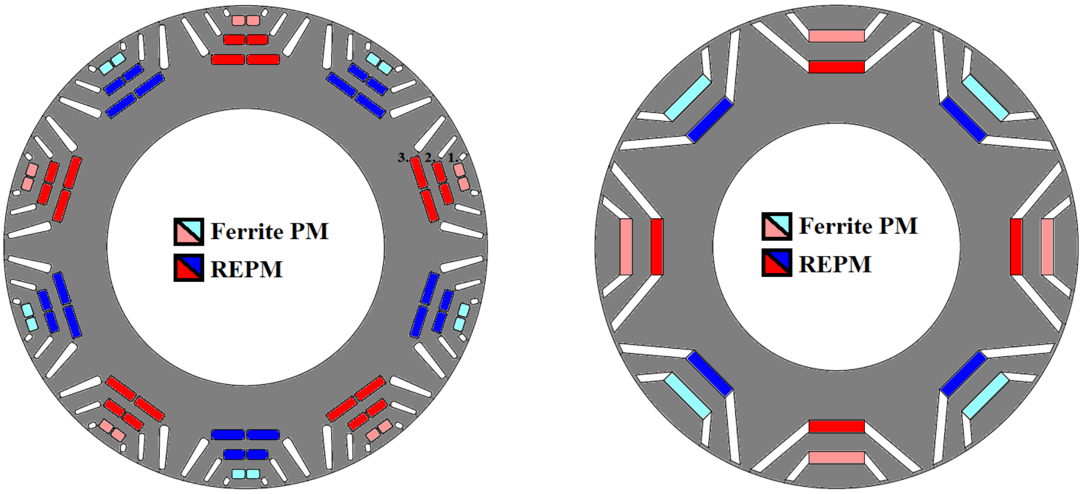

(a) (b)

Fig. 1.25. Positioning effect of two PM types in series HPM aSynRM. (a) With three-layers of flux barriers [KUM20]. (b) With two-layers of flux barriers [WAN24].

In [LIN22] a series HPM aSynRM is proposed with two inner layers of FEPMs and one outer layer of REPM as can be seen in Fig. 1.26 (a). The proposed design is compared with the FEPM-based and the REPM-based counterparts. It is shown that this machine can generate a comparable torque to that of the REPM-based topology with a PM cost close to that of the FEPM-based machine. Unlike the proposed topologies with one PM type per flux barrier in [KUM20] [WAN24] and [LIN22], the proposed series HPM aSynRM in [WU17A] employs two PM types in each flux barrier of rotor structure as shown in Fig. 1.26 (b). In this paper, the saliency ratio is first maximized by the proper design of flux barriers. Then, the area of each flux barrier is shared between two PM types. In this regard, the ratio of REPM height to the total height of flux barrier is defined followed by a parametric analysis in open circuit condition by separating the flux linkage and leakage flux. It is shown that for the ratios above 30%, the flux linkage going through airgap will be higher than the leakage flux going through the ribs. Therefore, it is concluded that the height of REPM should be at least 30% of the flux barrier height to achieve a low-cost design with improved electromagnetic performance.

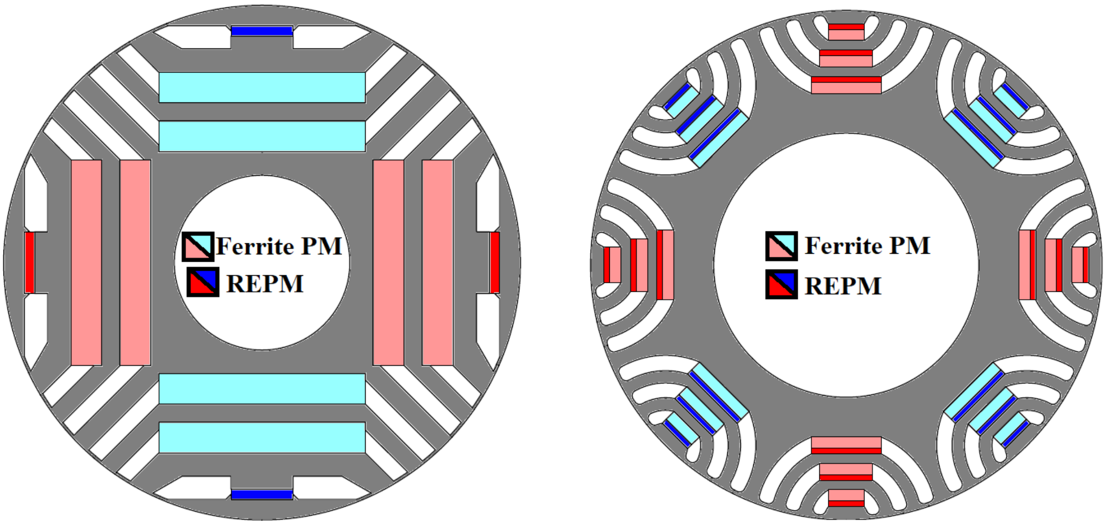

(a) (b)

Fig. 1.26. Different insertions of two PM types. (a) One PM type per flux barrier [LIN22]. (b) Two-PM types per flux barrier [WU17A].

In [WU17B], a three-layer parallel HPM aSynRM is proposed as presented in Fig. 1.27 (a). Although the proposed machine shows a high electromagnetic performance at a reduced cost due to using a parallel HPM configuration, the risk of irreversible demagnetization of FEPM is high. It is due to locating these magnets near airgap which makes them more vulnerable to the demagnetizing d-axis current. As a result, the safe range of overload current is reduced to 1.3 times the rated current. On the contrary, as illustrated in Fig. 1.27 (b), the proposed three-layer parallel HPM aSynRM in [ZHU17A] employs FEPMs in the central flux barriers. Meanwhile, as can be seen, both sides of flux barriers are filled with REPMs only. In [MA21A], a three-layer parallel HPM aSynRM is proposed as illustrated in Fig. 1.27 (c) and compared to a double-layer REPM based V-shape IPMSM. As can be seen, the FEPMs are not only filled in the middle flux barriers of the proposed design but also partially located in the side barriers with a parallel HPM connection to REPMs. Meanwhile, with the aim of improving the demagnetization withstand capability of FEPMs, they are separated from REPMs by the introduced air pockets. It is concluded that the proposed design can generate the same torque as the baseline with ~42% reduction of REPM volume and ~20 % reduction of total PM cost with a reduced demagnetization risk ratio in FEPMs. It is worth noting that the demagnetization risk ratio in FEPMs is measured by comparing the back-EMFs before and after applying the demagnetization current. A similar study with a series configuration of HPM is carried out in [MA21B]. It is shown that the output torque of the proposed series HPM topology is slightly reduced. In addition, it is concluded that the FEPM demagnetization withstand capability at low temperature in series HPM topology is improved compared to that of the parallel HPM counterpart. However, the REPM demagnetization withstand capability at high temperature in series HPM topology is deteriorated as the thickness of REPM is reduced. In addition, it is worth mentioning that the number of PM segments in the proposed series HPM machine is twice of that in the parallel HPM counterpart.

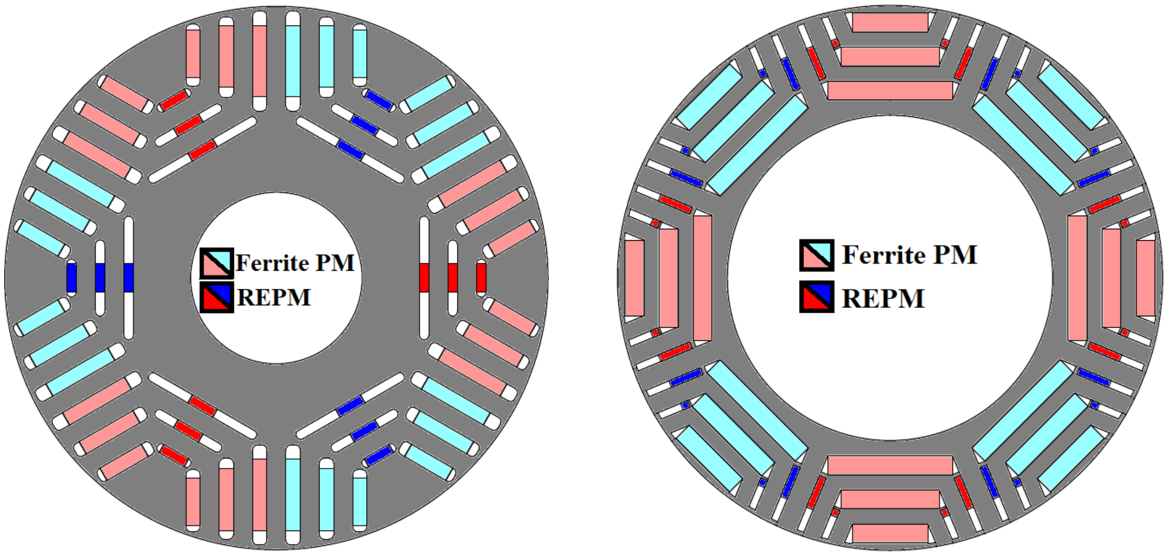

(a) (b)

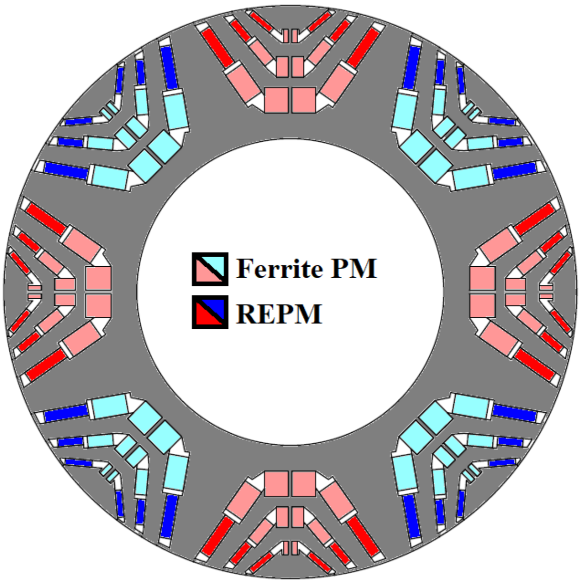

(c)

Fig. 1.27. Parallel HPM aSynRMs. (a) With FEPMs in the side barriers near airgap [WU17B]. (b) With REPMs in the side barriers near airgap [ZHU17A]. (c) With two PM types in the side barriers when REPMs are near airgap [MA21A].

A new topology is proposed in [LIU23A] which combines a two-layer FEPM aSynRM and a REPM-based spoke-type IPMSM as shown in Fig. 1.28 (a). It is shown that after adding the REPM spokes, the output torque is increased by ~8% compared to that of the two-layer FEPM aSynRM counterpart. However, the REPM volume usage is not given. In addition, the open circuit flux lines in Fig. 1.28 (b) shows a mixed HPM configuration for two PM types along with a considerable leakage flux of REPM-spokes. Therefore, the REPM utilization (the ratio of REPM torque with REPM usage) is expected to be low.

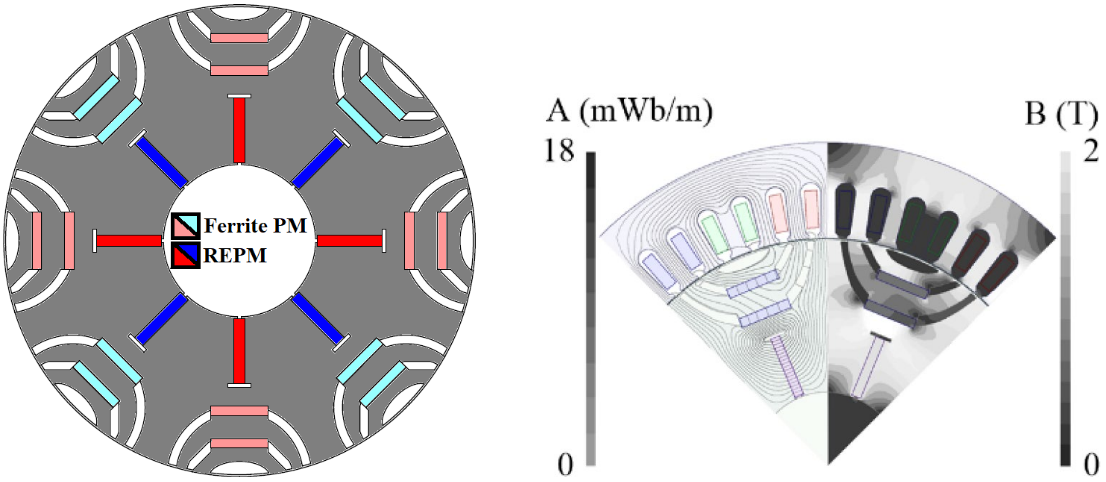

(a) (b)

Fig. 1.28. Mixed HPM aSynRM [LIU23A]. (a) Rotor geometry. (b) Open-circuit flux density and flux lines distributions.

1.4.4.3. HPM Spoke-type IPMSM

In [TAH20], it is shown that when it comes to utilizing low-energy product FEPM, a high volume of this magnet is required for which the spoke-type IPMSM is advantageous. In addition, this machine benefits from flux focusing effect which can increase the airgap flux density and the resultant PM torque. Meanwhile, it is known that a higher FEPM usage in HPM machines leads to a less required volume of REPMs. Therefore, many researches on HPM spoke-type IPMSMs have been investigated in literature. For example, a series HPM spoke-type IPMSM with ferrite spokes and bar-shape REPMs is proposed and compared with a REPM-based V-shape IPMSM in [ZEN18] as presented in Fig. 1.29 (a). It is shown that the proposed machine is capable of producing a comparable torque at ~30% reduction of PM cost. Meanwhile, a similar topology is investigated for the effect of the rib thickness and the pole arc (defined by the barrier of the bar-shape REPM) on the torque and torque ripple in [ZHA20].

In [MA20], a parallel HPM spoke-type IPMSM is proposed (see Fig. 1.29 (b)) as the most cost-effective design compared to a REPM-based double-layer V-shape baseline. The cost saving benefit of this machine is due to the application of high performance parallel HPM configuration and the employment of high volume of low-cost FEPM. However, the proposed machine has higher PM torque but lower reluctance torque components than those of the baseline with double layers PM arrangement. In addition, it is also concluded that having a smaller width of REPM than that of FEPM (in this case ~30% less) can satisfy the torque requirement and is advantageous for the demagnetization withstand capability improvement of FEPM in a parallel magnetic connection.

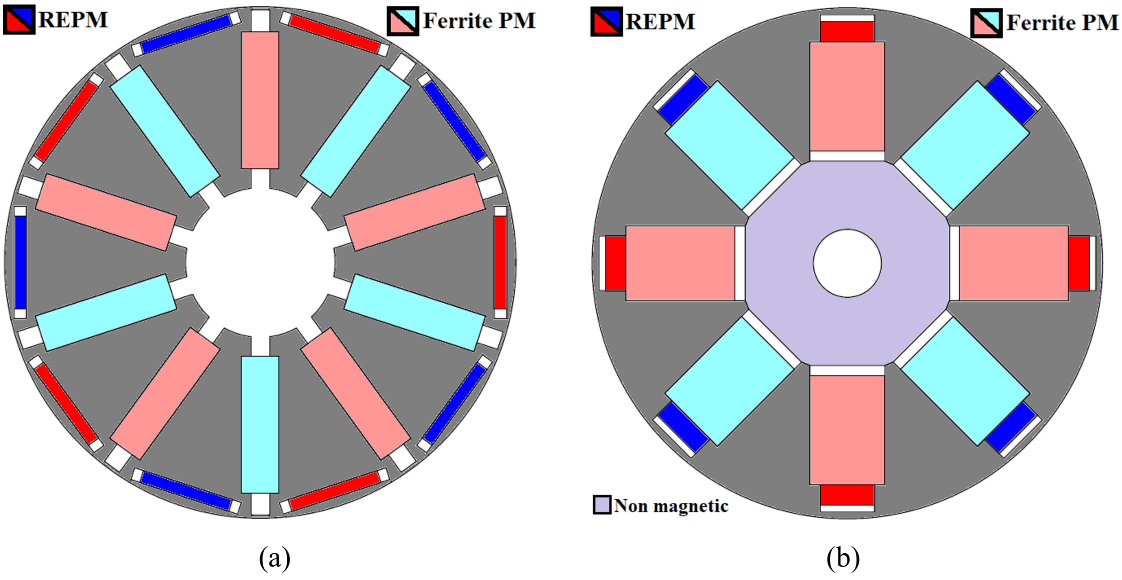

(a) (b)

Fig. 1.29. HPM spoke-type IPMSMs. (a) Series connection [ZEN18]. (b) Parallel connection [MA20].

In [ZHU19], a parallel HPM spoke-type IPMSM is proposed where the REPM in each spoke is divided into two segments with a V-shape arrangement as illustrated in Fig. 1.30 (a). It is shown that the employed V-shape arrangement of REPM can contribute to enhance the natural flux focusing effect of spoke-type machine to some extent. It is also shown that the proposed design benefits from ~22% less PM cost compared to a REPM-based V-shape baseline. In [JEO19], a parallel HPM spoke-type IPMSM is proposed with the bended spokes. It is shown that as the thicknesses of two PM types are almost the same, FEPMs are at a high risk of irreversible demagnetization. Therefore, alternative PM types are used near the airgap as shown in Fig. 1.30 (b). It is shown that the proposed design can reduce the PM cost by ~20% whereas the risk of demagnetization in FEPMs is considerably reduced.

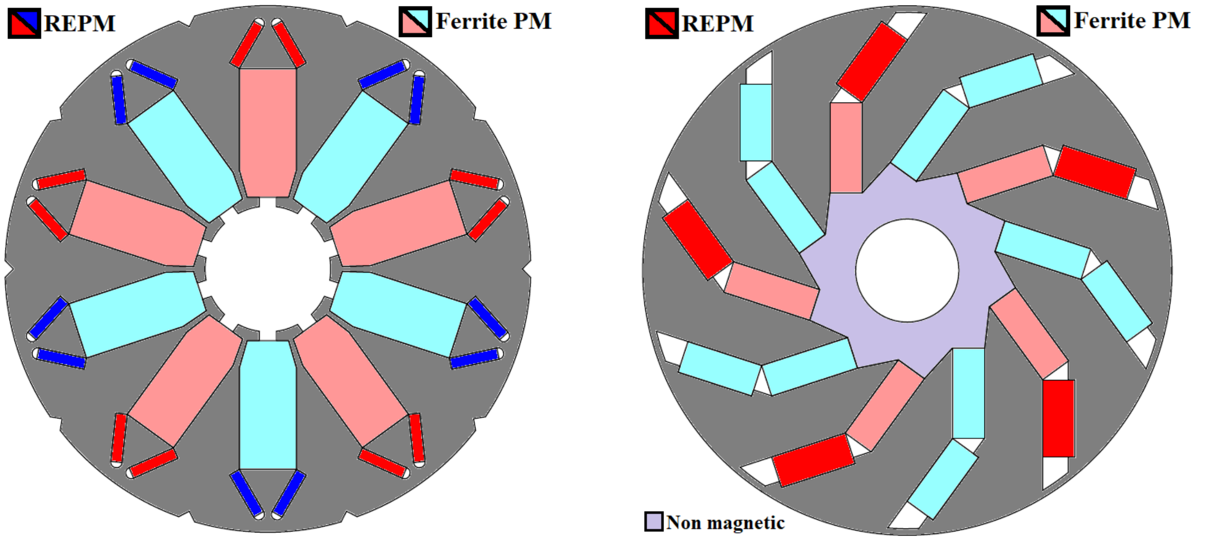

(a) (b)

Fig. 1.30. Parallel HPM spoke-type IPMSMs. (a) With V-shape REPM [ZHU19]. (b) With Bended spokes [JEO19].

In [ZHU17B], a parallel HPM spoke-type IPMSM is proposed where the FEPMs are divided into two segments as presented in Fig. 1.31 (a). The proposed machine is compared to a FEPM-based spoke-type IPMSM, and it is concluded that this machine benefits from a higher flux weakening capability and reluctance torque component compared to those of the baseline. Meanwhile, the effect of expanded q-axis cross section (see Fig. 1.31 (b)) on the reduced q-axis saturation and the resultant q-axis inductance is not investigated. Therefore, the higher reluctance torque component of the proposed machine is suspected to be because of the thinner REPM rather than the segmented FEPMs. Consequently, comparing the proposed machine with an equivalent parallel HPM topology with 1 ferrite segment per spoke could have been fairer and more clearly proven the conclusion. Using the proposed machine in Fig. 1.31 (a), a method for demagnetization withstand capability improvement and a robust optimization method accounting for the PM materials uncertainties are investigated in [ZHA21] and [WU21], respectively.

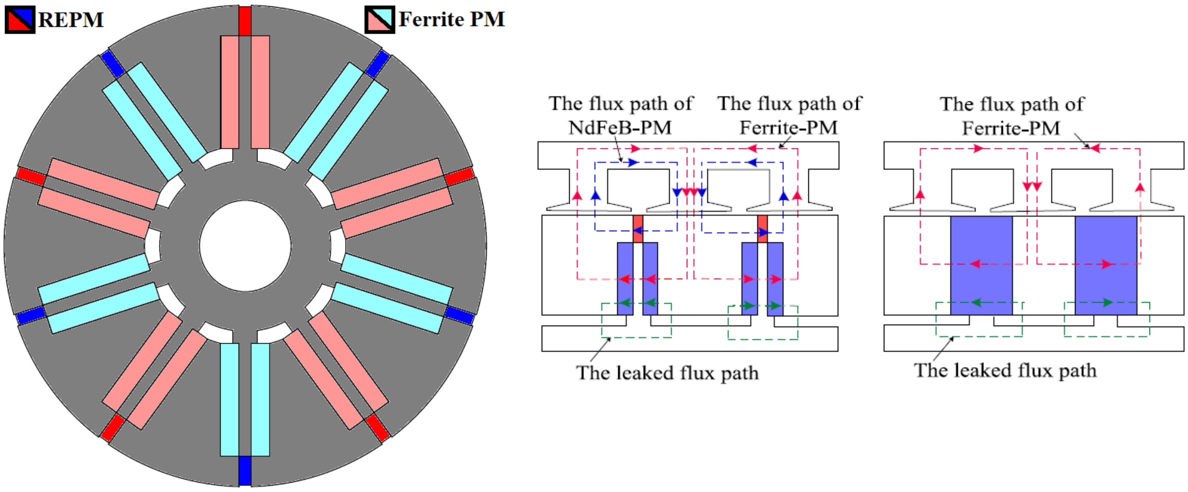

(a) (b)

Fig. 1.31. Parallel HPM spoke-type IPMSM with segmented ferrite spoke in [ZHU17B]. (a) Cross section. (b) Comparison of flux paths between the proposed machine and a FEPM-based baseline.

In [ALQ19], the application of tapered FEPM in a series HPM connection is investigated and applied to the spoke PM arrangement of the high-speed inner rotor of a magnetic gear. It is shown that the electromagnetic performance of the magnetic gear with tapered FEPMs towards the shaft would be deteriorated due to the increased leakage flux near the shaft compared to a rectangular PM counterpart. In [PAR21], the application of tapered FEPM in spoke-type IPMSM is analysed where both parallel and series HPM configurations are considered as shown in Fig. 1.32. Although the results show that the proposed method can effectively improve the reluctance torque component in both machines, the parallel HPM topology suffers from a reduced PM torque contribution due to using a large flux barrier in d-axis and locating REPMs away from airgap.

In [YAN24A], one parallel HPM and one series HPM spoke-type IPMSMs are proposed and compared with a conventional REPM-based V-shape IPMSM. Fig. 1.33 (a) presents the proposed parallel HPM design with narrow flux barriers to regulate REPM flux towards the airgap and reduce the downgrading effect of this magnet on the working point of FEPMs. This kind of flux barriers are also suggested in memory machines with parallel magnetic connection to avoid unintentional demagnetization in the variable flux PMs, e.g. [WAN19]. Meanwhile, the proposed series HPM counterpart with V-shape REPMs in consequent poles is shown in

Fig. 1.33 (b). It is shown that both machines can improve the torque with REPM volume ratio compared to the baseline.

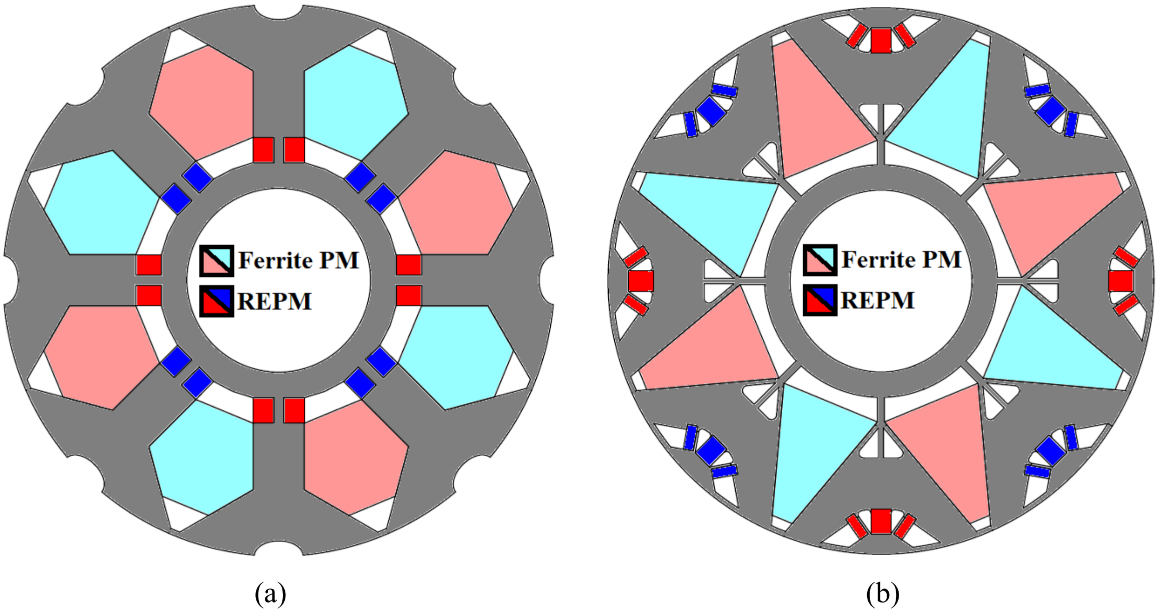

(a) (b)

Fig. 1.32. HPM spoke-type IPMSMs with tapered FEPMs [PAR21]. (a) Parallel configuration. (b) Series configuration.

A similar design to the proposed series HPM configuration in Fig. 1.33 (b) is presented in [CHE24] whereas the FEPM-based spokes are changed to the parallel HPM spokes. As a result, this machine employs a mixed configuration of HPMs using V-shape REPMs in consequent poles as illustrated in Fig. 1. 33 (c). It is shown that using the combination of spoke-type arrangement and consequent pole structure can improve the magnetic field modulation effect. At the same volume of both PM types, this machine is compared with a conventional series HPM spoke-type IPMSM (see Fig. 1.29 (a)) as the baseline and it is revealed that the output torque of the proposed machine with 34.5 Nm is higher than that of the baseline with 28.5 Nm. This enhancement is not only because of the mixed HPM utilization, but also due to the enhanced modulation torque component to ~4.2 Nm. It is worth mentioning that the modulation torque component of the series HPM baseline is ~2.2 Nm.

In [ZHE21A], a mixed HPM spoke-type IPMSM is presented (see Fig. 1.20) and optimized accounting for different magnetic properties of two PM types at different operating modes in EVs. The rotor structure is optimized for three objectives including high torque, low torque ripple, and improved demagnetization withstand capability. Using the optimization results of the abovementioned objectives at different operational conditions, the final design is defined by making a trade-off optimum combination. In [SEO22], a combined method, using the analytical equations and magnetic equivalent circuit, is proposed to accurately obtain the airgap flux density by a two dimensional (2D) FEA in HPM spoke-type IPMSMs. It is shown that due to the axial leakage flux in spoke-type machines, the airgap flux density in 2D FEA suffers from a considerable error compared to the airgap flux density obtained from a three dimensional (3D) FEA. However, the proposed method can achieve a more accurate result.

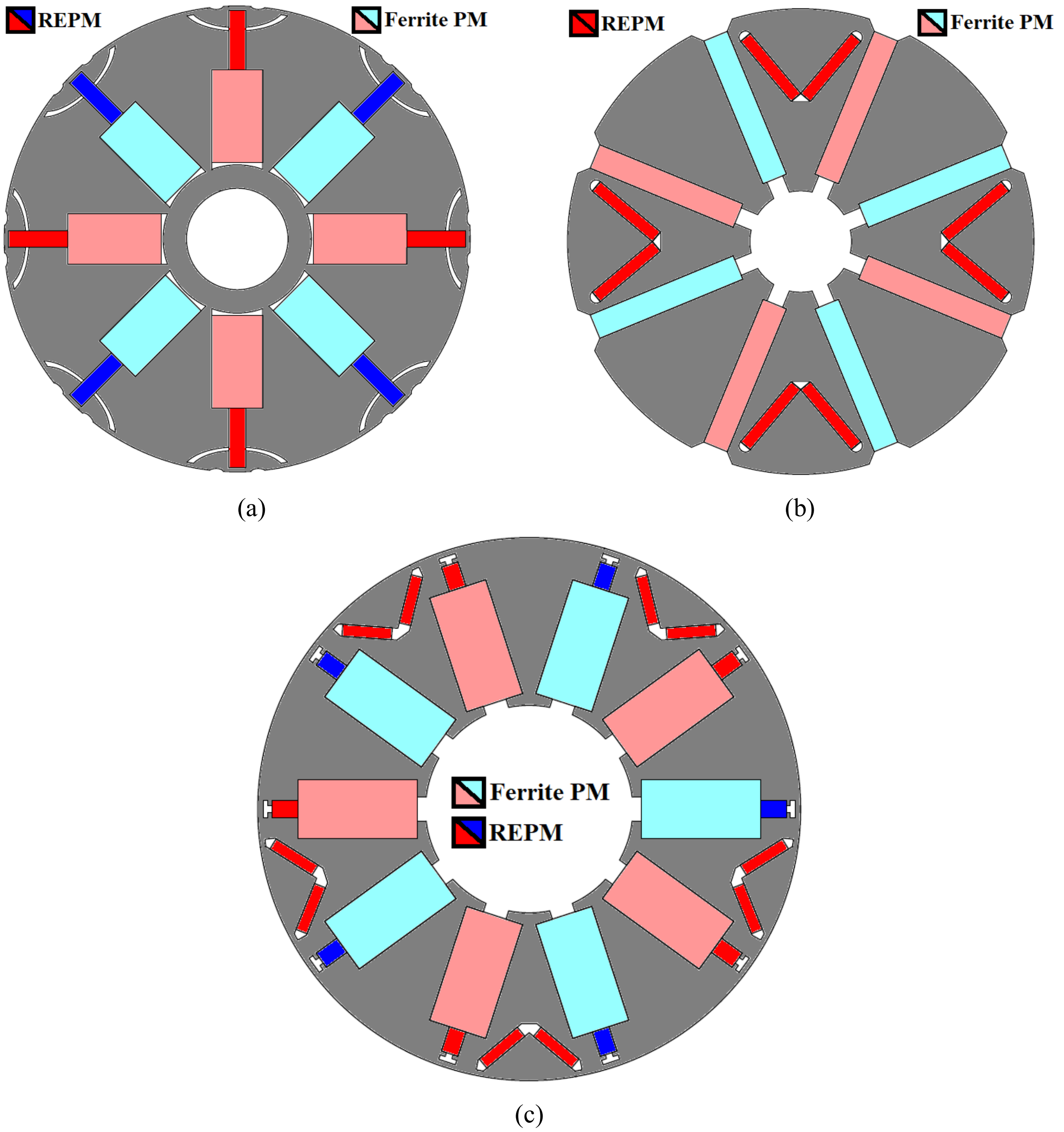

(a)

(b)

(c)

Fig. 1.33. Structural comparison of HPM spoke-type IPMSMs. (a) Parallel configuration with flux regulating barriers [YAN24A]. (b) Series configuration with V-shape REPMs in consequent poles [YAN24A]. (c) Mixed configuration with V-shape REPMs in consequent poles [CHE24].

1.4.4.4. HPM IPMSM

As discussed, HPM spoke-type IPMSMs are suitable for using an excessive volume of FEPMs. However, they utilize a relatively low reluctance torque and have not been used in EV application as they, for example, may raise mechanical concerns in a high-speed application. Meanwhile, as presented in Fig. 1.2, other IPMSM topologies including V-shape, U-shape, UI-shape, and delta-shape can already be found in the widespread manufactured EVs on the market. Therefore, the application of HPM utilization in these machines will be presented in this section.

In [WU16] and [DU20], two parallel HPM U-shape IPMSMs are proposed as illustrated in Figs. 1.34 (a) and (b), respectively. The main difference between these two topologies is in the position of REPMs. In [WU16], REPMs are located on the top of a ferrite segment whereas in [DU20], these magnets are filled on both sides of a ferrite segment. As a result, the length of FEPM in the proposed machine in [WU16] can be wider whereas the thickness of REPMs should be limited to a thin width to avoid blocking the flux path of FEPM. On the other hand, the length of FEPM in the proposed machine in [DU20] is shorter whereas the width of REPM has more flexibility to be thicker. Finally, Unlike the proposed machine in [DU20], there are no ribs and flux barriers between REPMs and FEPM in [WU16]. Consequently, the proposed machine in [DU20] is expected to have a higher mechanical strength and less mutual demagnetization effect between two PM types. It is also worth noting that the proposed machine in [DU20] can produce the same torque as Toyota Camry 2007 with 30% reduction of REPM usage and 20% reduction of total PM cost. In [YAN24B], several flux barriers with two shapes are applied to a similar parallel HPM U-shape IPMSM to [DU20] with the aim of reducing the self-leakage flux of REPMs in one pole and mutual leakage flux of REPMs between two adjacent poles as shown in Fig. 1.34 (c). The results show that by applying these flux barriers, the d-axis flux linkage at open circuit condition can increase to some extent. Fig. 1.34 (d) presents a parallel HPM U-shape IPMSM which is introduced in [JEO17]. Unlike the other U-shape topologies, the central FEPM is divided into two segments with V-shape arrangement. Meanwhile, due to the geometrical limits, the thickness of FEPM has inevitably reduced. Therefore, these FEPMs will be at a higher risk of irreversible demagnetization in a parallel HPM configuration. It is also shown that in the absence of stator structure (for example at the stage of prototyping the rotor), the interpolar flux circulation can increase the demagnetization risk of low-coercive FEPMs by the high energy-product REPMs. Therefore, it is advised that using a ring core around rotor structure can reduce the risk of open circuit demagnetization during the assembly progress.

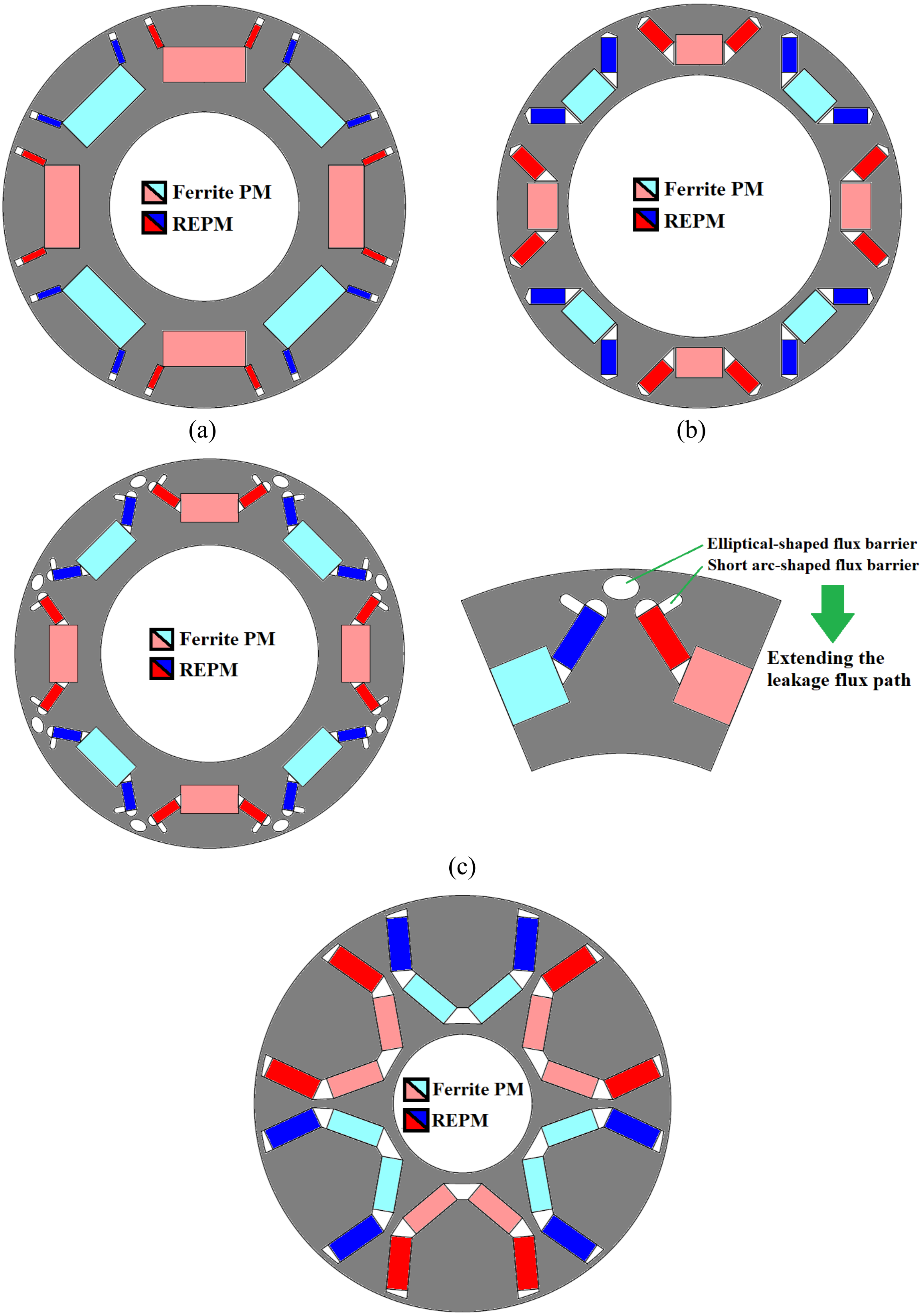

(a) (b) (c) (d)

Fig. 1.34. Parallel HPM U-shape IPMSMs. (a) With REPMs on top of a FEPM in [WU16]. (b) With REPMs on both sides of a FEPM in [DU20]. (c) With extra flux barriers to reduce leakage flux [YAN24B]. (d) With segmented FEPMs in a V-shape arrangement [JEO17].

In [HUA19] and [CUI22], two mixed HPM IPMSMs with delta-shape and UI-shape arrangement of PMs are proposed as shown in Figs. 1.35 (a) and (b), respectively. As can be seen, the parallel HPM configurations in V-shape and U-shape parts are magnetically connected to a bar-shape REPM in a series connection. As a result, the parallel REPM in V-shape and U-shape parts may reduce the working point of FEPMs but the series bar-shape REPM would increase it. Therefore, the demagnetization withstand capability of FEPMs can be preserved in an appropriate design. It should also be noted that the proposed designs in Fig. 1.35 are utilizing a double layer of PM arrangement compared to the single layer designs in Fig. 1.34 which naturally results in a higher reluctance torque component. In addition, the proposed design in [CUI22] is compared with an equivalent REPM-based baseline whereas both machines employ fractional slot concentrated windings. It is known that these windings bring the advantages of short end winding, low copper loss, and small torque ripple at the cost of high eddy current loss in rotor, especially in NdFeB magnets. Meanwhile, this paper shows that using FEPMs can not only reduce the PM cost but also can reduce the magnet eddy current loss due to a higher resistivity of FEPMs to eddy current compared to that of the REPMs. However, on the downside, the output torque may reduce due to the low energy-product of FEPMs, and torque ripple may increase due to the distortion of magnetic field and increase in harmonics. A similar study to [CUI22] is carried out in [CUI23] where the bar-shape REPM in Fig. 1.35 (b) is changed to a V-shape arrangement of two REPM segments in Fig 1.35 (c). The proposed machine is compared with the same baseline in [CUI22] (see Fig. 1.35 (b) and (c)). It is shown that the baseline suffers from a high magnet eddy current loss (17% of total loss) under sinusoidal current which can be even worse by 7% if current harmonics by PWM inverter is included. It is shown that the FEPM utilization, dividing the radial REPM into two segments in V-shape arrangement, and the angle between two REPM segments can effectively be used to reduce the magnet eddy current loss of the proposed machine by 78%.

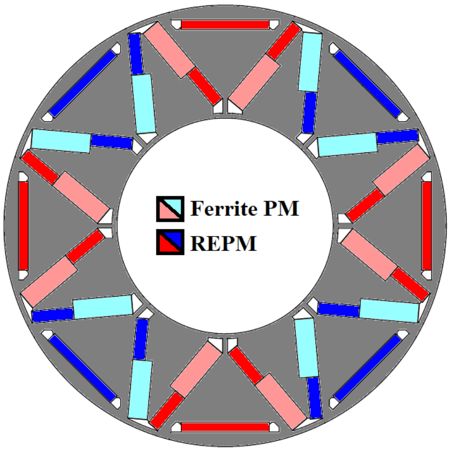

(a)

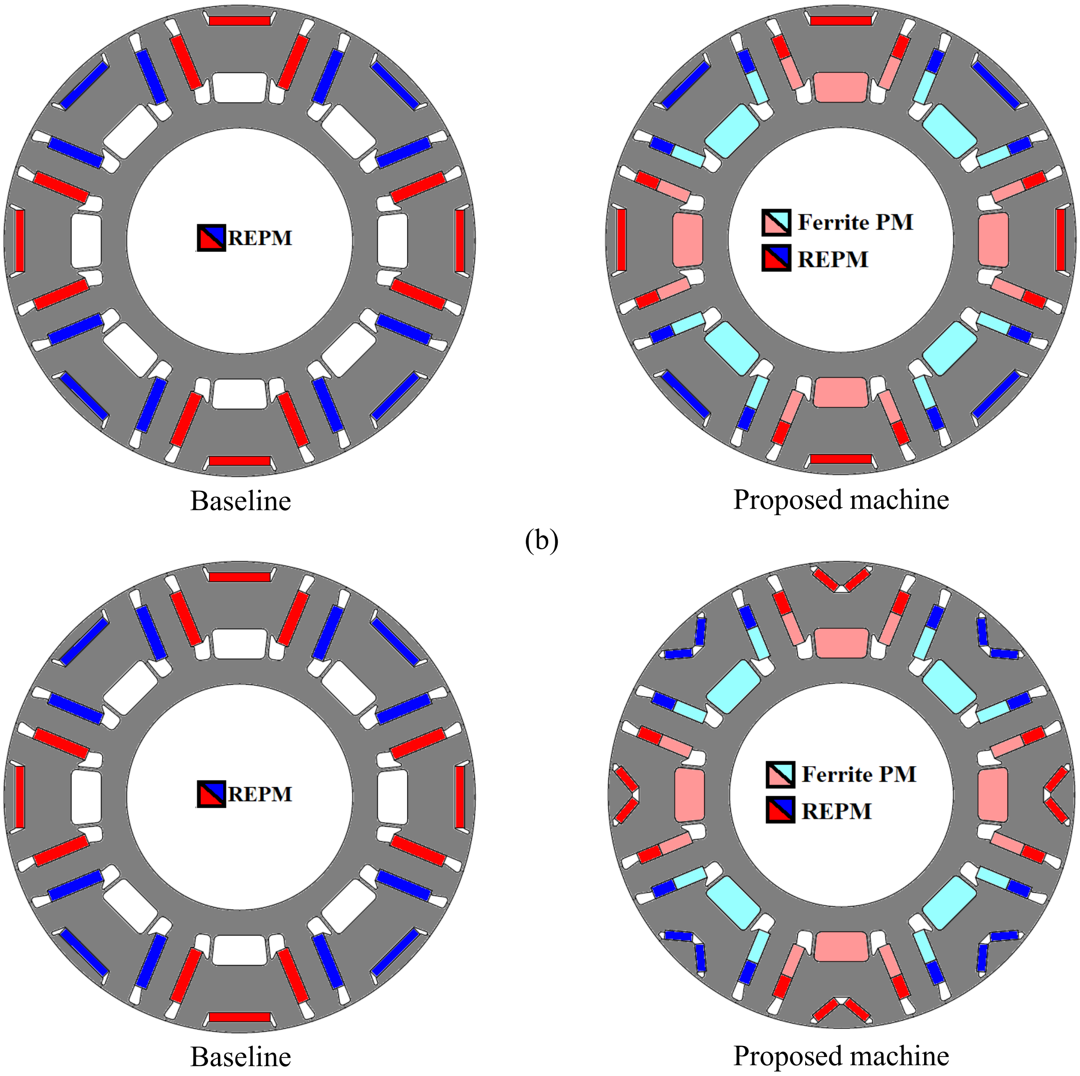

(c)

Fig. 1.35. Mixed HPM IPMSMs. (a) Delta-shape [HUA19]. (b) UI-shape [CUI22]. (c) UV-shape [CUI23].

As discussed, a series HPM machine is naturally expected to have the advantage of a better demagnetization withstand capability and the disadvantage of a lower electromagnetic performance compared to a parallel HPM counterpart. Therefore, several researches on improving the performance of series HPM machines have been studied in literature. For example, in [PAR22], a new series HPM machine is presented as shown in Fig. 1.36 (a) which benefits from an improved reluctance torque due to the enhanced q-axis inductance. It is shown that this machine can produce the same torque as a REPM-based benchmark with 38% reduction of REPM usage. [JIA22] and [ZHU23A] investigate the application of HPM utilization in consequent pole PM machines. The proposed design in [JIA22] employs consequent-pole yoke FEPMs which is assisted by slot REPMs. Meanwhile, the proposed design in [ZHU23A] presents a mixed HPM consequent pole U-shape IPMSM as shown in Fig.

1.36 (b). As discussed earlier, the HPM utilization can effectively improve the torque per REPM volume ratio in PM machines. However, it may cause distortion in airgap flux density and increase the harmonics. Consequently, [ZHU23A] focuses on the torque quality enhancement including increase in the average torque and decrease in the torque ripple. In the proposed machine, the large FEPM segment is in parallel to the REPMs and used to enhance the average torque. Meanwhile, the small FEPMs with a shorter length than REPMs are partially in series connection with these magnets. As a result, by changing the dimensions of the small FEPMs, the overall MMF of HPMs in the series connection flux path can be adjusted. Therefore, the small FEPMs can be used to suppress the torque ripple by reducing the harmonics of airgap flux density.

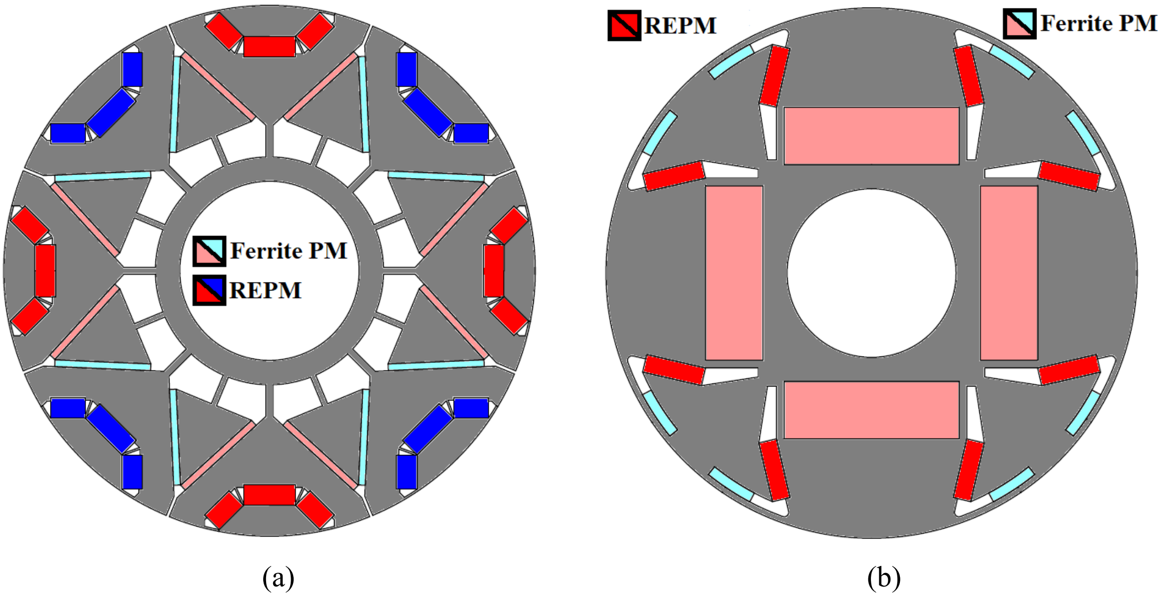

(a) (b)

Fig. 1.36. HPM IPMSMs. (a) Series configuration with enhanced reluctance torque in [PAR22]. (b) Mixed configuration with a large parallel FEPM for torque enhancement and two small series FEPMs for torque ripple reduction [ZHU23A].

In [LIU18] and [SHI24], two parallel HPM flux intensifying IPMSMs with reverse saliency are proposed with a U-shape arrangement of PMs. Unlike the conventional IPMSMs, these machines employ external q-axis flux barriers to make the d-axis inductance larger than the q-axis inductance. Consequently, MTPA control strategy in the conventional IPMSMs leads to a maximum torque being achieved at a negative d-axis current with a positive current advancing angle. On the contrary, the maximum torque of a flux intensifying IPMSM is achievable at a positive d-axis current with a negative current advancing angle. Therefore, under the MTPA control strategy, the working point of FEPMs in conventional IPMSMs will be reduced (due to the negative d-axis current) but that of flux intensifying IPMSMs will be enhanced (due to the positive d-axis current). It should be noted that this comparison is only valid under MTPA control strategy. However, when it comes to the flux weaking capability, both machines will utilize the negative d-axis current with a positive current advancing angle. Meanwhile, the proposed machine in [SHI24] is compared with a REPM-based V-shape IPMSM. It is shown that maximum torque of the proposed machine at low-speed region is less than that of the baseline. However, this machine benefits from superior performance at high-speed performance leading to a better flux weakening capability. It should be noted that the torque per REPM ratios of both machines presented in [LIU18] and [SHI24] are improved due the HPM utilization. A similar investigation in [ZHE21B] is presented in a flux-intensifying IPMSM with V-shape arrangement of PMs. Although the same results are concluded, the proposed machine employs FEPMs in alternative poles. Consequently, this machine may suffer from axial leakage flux.

An outer rotor parallel HPM IPMSM is investigated in [YU19]. The cross section of this machine is similar to the proposed series HPM machine in [ISH13] which is illustrated in Fig. 1.17 (c). However, as this machine utilizes a parallel configuration of two PM types, it benefits from a higher electromagnetic performance, but a lower demagnetization withstand capability of FEPMs compared to the series HPM counterpart.

1.4.4.5. Asymmetric HPM Machines

As mentioned, the asymmetric rotor topology and HPM utilization can lead to a less REPM usage at the same performance. The former method employs the MFS effect to force PM torque and reluctance torque components merge to a unique current advancing angle which leads to the total torque enhancement at the same PM and reluctance torque amplitudes. Meanwhile, the latter method uses low-cost FEPMs to reduce the reliance on REPM materials. To further reduce the volume of REPM in PM machines, these two methods can be combined to benefit from the synergies of the MFS effect and HPM utilization. Therefore, an asymmetric HPM machine has shifted reluctance and PM torque components whereas a portion of PM torque contribution is provided by FEPMs.

In [CHE19], an asymmetric HPM machine with multi-parts rotor is proposed as shown in Fig. 1.37. The HPM feature of the proposed machine is due to a FEPM-based spoke-type rotor part and a REPM-based SPM rotor part. Meanwhile, the MFS effect is adjustable by the alignment angle between two rotor parts. Therefore, this machine can be categorized in the group 1 of asymmetric PM machines in Fig. 1.16. As the magnetic flux path of two rotor parts are separated, REPMs and FEPMs are in a parallel HPM configuration. It is worth mentioning that generating a higher torque or reducing the PM cost can easily be traded off by adjusting the lengths of two rotor parts, e.g. a higher torque requirement leads to a longer REPM-based SPM rotor part.

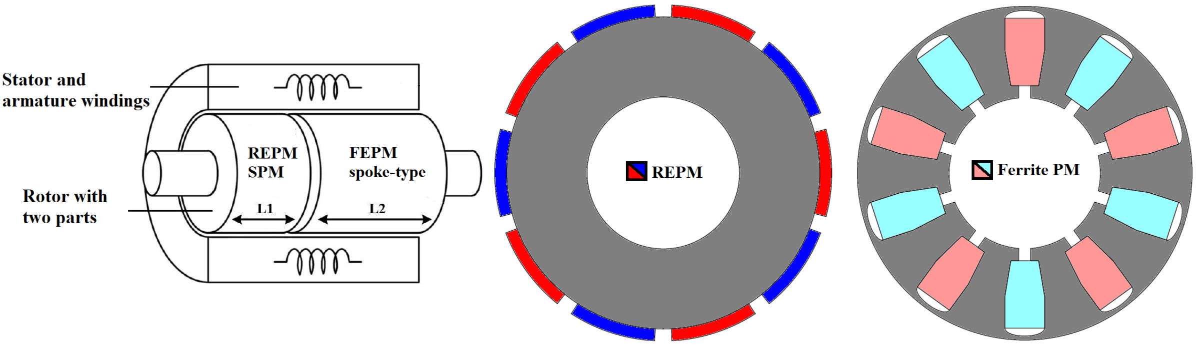

Fig. 1.37. Asymmetric HPM machine with two-parts rotor structure with symmetrical rotor core structure and symmetrical PM usage in [CHE19].

In [LI19], an asymmetric mixed HPM IPMSM with a delta-shape arrangement of PMs is proposed as illustrated in Fig. 1.38 (a). This machine can be placed in group 3 of asymmetric machines in Fig. 1.16 due to having a symmetrical rotor structure and asymmetric PM usage. In general, the asymmetric PM usage in this group is achievable by using PMs with different sizes in a REPM-based machine. However, using two PM types with different magnetic properties, e.g. REPM and FEPM, can cause MFS effect even at the same size if they are placed properly, e.g. the proposed cross-section in Fig. 1.38 (a). The results show that this machine can increase the torque per REPM cost by 8% compared to the IPMSM in BMW i3. The effectiveness of the MFS is illustrated by the comparison of open circuit airgap flux densities and flux lines distributions and decomposing the PM torque and reluctance torque components in these two machines. In [XIE22], an asymmetric multi-layer mixed HPM aSynRM is proposed. The rotor is made of symmetrical core structure and asymmetric PM usage which results in this machine being categorized in group 3 of asymmetric PM machines. However, Unlike the proposed design in [LI19], the dimensions of FEPMs are optimized separately in this paper. It is shown that the proposed design can reduce the PM cost by 22%. However, the risk of irreversible demagnetization in FEPMs is increased to some extent as the small segments of this PM type are employed.

A hybrid pole asymmetric PM machine with HPM utilization is proposed in [XU17B]. This machine which can also be categorized in group 3 of asymmetric machines, utilizes an asymmetric inset REPM module and a symmetrical multi-layer FEPM-based module as shown in Fig. 1.39. Although the results show that the proposed machine can effectively improve the torque per REPM usage ratio, it may suffer from axial leakage flux as the unequal north and south poles are used.

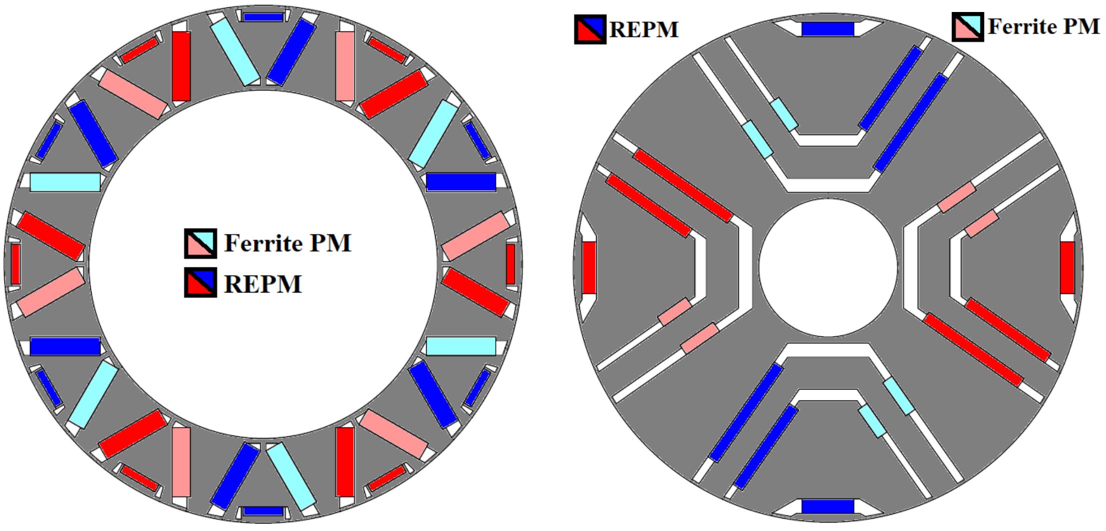

(a) (b)

Fig. 1.38. Asymmetric HPM machines with symmetrical rotor core structure and asymmetric PM usage. (a) Asymmetric PM configuration by two different PM types at the same size [LI19]. (b) Asymmetric PM configuration by two different PM types at different sizes [XIE22].

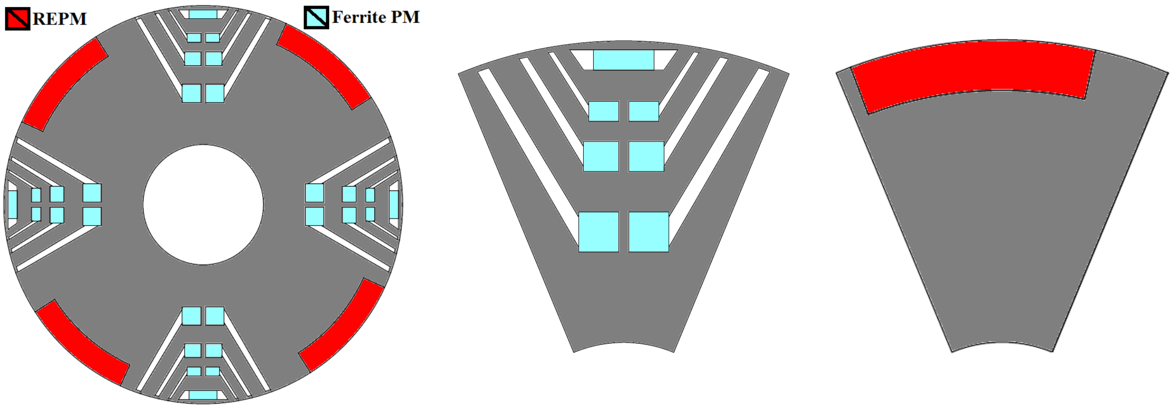

(a) (b) (c)

Fig. 1.39. Proposed hybrid pole asymmetric HPM machine in [XU17B]. (a) Cross section. (b) Symmetrical multi-layer FEPM -based module. (c) Asymmetric inset REPM-based module.

An asymmetric HPM aSynRM is presented in [QIA24] which is in general similar to the proposed topology in [XIE22]. However, as asymmetric PM usage with asymmetric flux barriers is used, this machine will be categorized in group 4 of asymmetric PM machines as shown in Fig. 1.40. As can be seen, not only a semi-enclosed flux barrier is used in the first layer, but also the width of the 2nd flux carrier in the left hand-side is bigger than that of the right hand-side. This results in early saturation of this flux carrier in the clockwise direction and regulate the PM flux path towards the anticlockwise direction. Therefore, the MFS effect will be achieved by both asymmetric HPM usage and asymmetric rotor core structure. Although the results show that the PM field in the proposed design is shifted by ~23 elec. deg., the torque per REPM usage ratio is improved only by 4.3 % compared to that of the baseline. This can be partially because of the low FEPM usage due to the limited space in a multi-layer PM aSynRM. This is why a high FEPM usage in HPM machines is more preferrable.

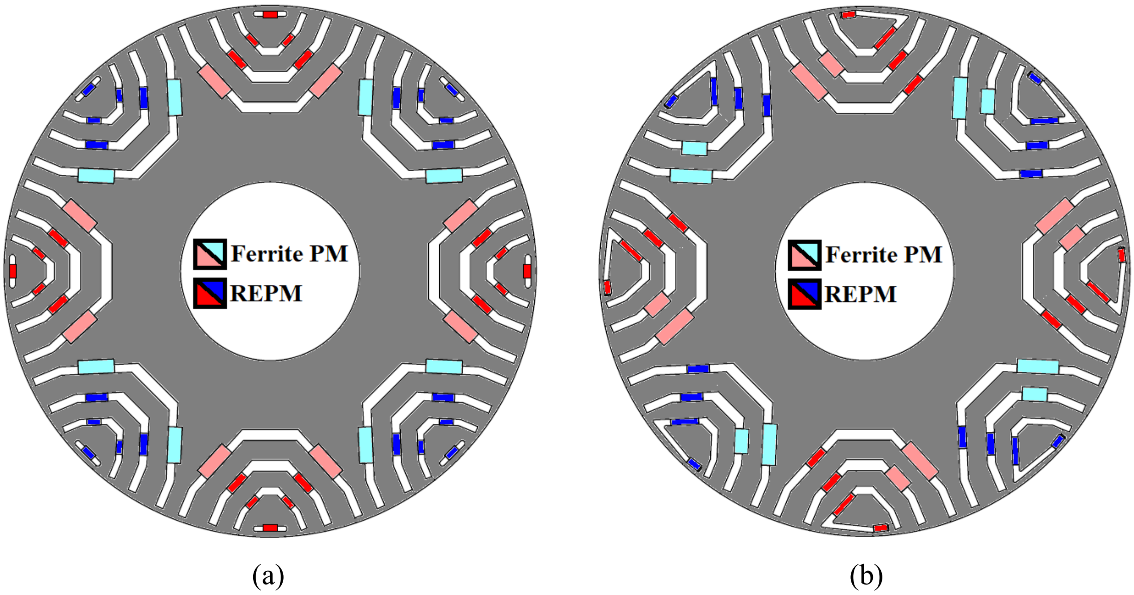

Fig. 1.40. Structural comparison of presented machines in [QIA24]. (a) Baseline. (b) Proposed asymmetric HPM aSynRM.

Consequently, several papers in literature investigate the feasibility of adding MFS effect to the HPM spoke-type IPMSMs where the FEPM usage are maximized. For example, in [ZEN19] and [ZHU23B], the bar-shape REPM in a series HPM spoke-type IPMSM is shifted as shown in Fig. 1.41 (a). [ZEN19] focuses on the feasibility study of the proposed method, and it is shown that by displacing the bar-shape barrier and REPM at the same volume of both PM types, the output torque can be increased by ~16%. In [ZHU23B], a more detailed investigation and optimization are proposed whereas not only the shifting parameters but also the dimensions of both PMs are optimized. The results show that the output torque can be increased by ~20%. In addition, the proposed design shows a better demagnetization withstand capability not only in flux weaking region but also under rated current. This is partially because the current advancing angle of the maximum torque in the proposed machine with 24 elec. deg. is less than that of the symmetrical baseline with 30 elec. deg. This means that under the MTPA control strategy at the rated current, the FEPMs in the proposed machine encounter less d-axis current. As a result, the demagnetization withstand capability of FEPMs under rated condition will be improved. In [CHE23], a continuous work to [CHE21] is presented where different magnetic properties of two PM types at different operation conditions of EV are considered when optimizing the rotor structure. Similar to [ZHE21A], improved torque performance and demagnetization withstand capability are considered as the main objectives in this paper. Meanwhile, the third objective is changed from low torque ripple in [ZHE21A] to the high efficiency in [CHE23]. Using the optimization results of the abovementioned objectives at different operational conditions, the final design is defined by making a trade-off optimum combination. Fig. 1.41 (b) illustrates the optimum cross section of the proposed machine in this paper. In [HAN22] a series HPM consequent-pole spoke-type IPMSM is presented whereas the pole arc of the inset REPM part can be optimized differently from the pole arc of the FEPM spokes. This machine is compared with a conventional series HPM spoke-type IPMSM with inset REPMs. It is shown that at the same volume of REPM and overall dimensions, the proposed machine can produce a higher torque per REPM usage ratio than that of the conventional series counterpart. It is worth noting that all proposed asymmetric HPM machines in Fig. 1.41 can be categorised in group 4 of asymmetric machines (see Fig. 1.16) due to the employment of asymmetric rotor structure and asymmetric PM usage. Although the MFS effect is achievable in the asymmetric HPM spoke-type IPMSMs and their FEPM usage is generally higher than that of the multi-layer counterparts in Figs. 1.38 (b) and 1.40, these machines are not often suitable for high-speed applications including EVs due the mechanical concern and low reluctance torque component.

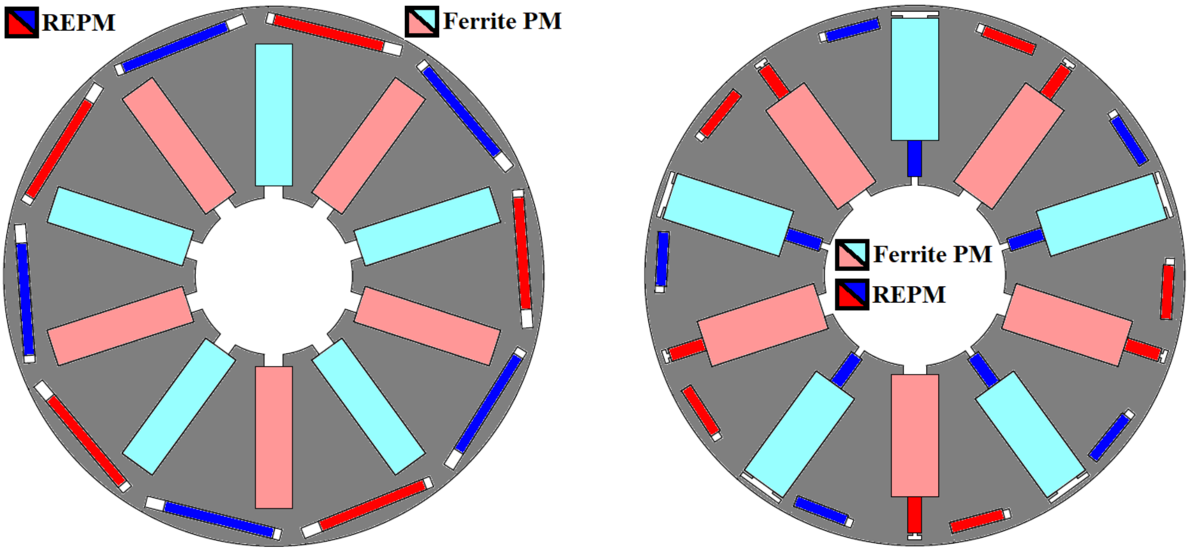

(a) (b)

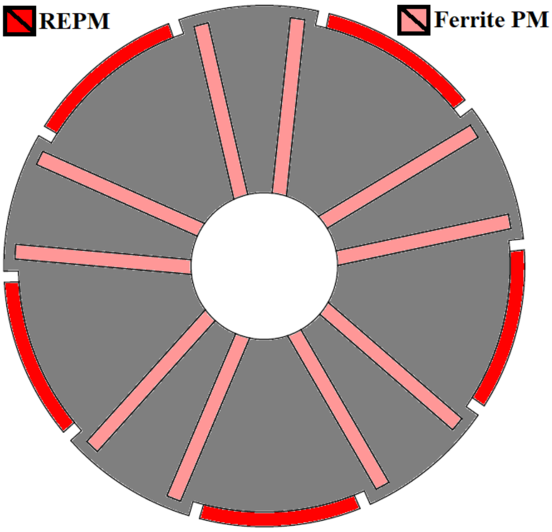

(c)

Fig. 1.41. Asymmetric HPM machines with spoke FEPMs. (a) Series HPM configuration in [ZEN19] and [ZHU23B]. (b) Mixed HPM configuration in [CHE21] and [CHE23]. (c) Series HPM configuration with consequent-pole structure in [HAN22].

Therefore, a single-layer or double-layer asymmetric HPM IPMSMs are expected to have a more favourable trade-off between the high FEPM usage and high reluctance torque contribution for EV applications. Unlike the proposed design with symmetrical rotor structure and asymmetric PM usage in Fig. 1.38 (a), the following papers are investigating the asymmetric HPM IPMSM topologies with asymmetric rotor structure and asymmetric PM usage. In [LIU23B] and [LV23], two parallel HPM asymmetric V-shape IPMSMs are proposed with FEPM in the middle (Fig. 1.42 (a)) and on the side (Fig. 1.42 (b)) of the V-shape arrangement of REPMs, respectively. As discussed in Fig. 1.16 (d-1), a single layer asymmetric V-shape IPMSM is expected to have a negligible torque enhancement due to the poor MFS effect. However, as can be seen in Fig. 1.42 (a), two types of PMs with four different sizes of REPMs and one size of FEPM are used to enhance the MFS effect to some extent in the proposed design in [LIU23B]. It is concluded that the volume of REPM at the same torque can be reduced by 18% at the cost of using multiple sizes of PMs which increases the labour cost and complexity of the rotor structure. Meanwhile, as shown in Fig. 1.42 (b), the proposed design in [LV23] employs two sizes for REPMs and one size for FEPM which result in a less complicated structure compared to that of [LIU23B]. It is shown that the required volume of REPM at the same torque is reduced by 19% compared to a symmetrical REPM-based V-shape baseline. Although the open circuit performances of [LIU23B] and [LV23] show the signs of MFS effect, the effectiveness of the employed methods on the torque enhancement in on-load condition is not clearly separated by the MFS effect and HPM utilization. Therefore, it is not clear that how much improvement in the MFS effect is achieved compared to the negligible torque enhancement conclusion of Fig. 1.16 (d-1). In addition, as the FEPMs and REPMs have almost the same thickness in a parallel magnetic connection, the risk of irreversible demagnetization in FEPMs is generally high in both designs.

Consequently, the parallel HPM configuration in the clockwise side of the V-shape arrangement of magnets in [LV23] is divided into two segments in a series magnetic connection as shown in Fig. 1.42 (c) and investigated in [LIU24]. In this paper, a REPM-based asymmetric V-shape IPMSM with extra flux barrier is selected from [XIA21A] (see Fig. 1.16 (d-3)) as the asymmetric reference machine with REPMs only. Then, the empty flux barrier is filled with FEPM as presented in Fig. 1.42 (c) and compared with the REPM-based symmetrical V-shape and the abovementioned asymmetric REPM-based machines. The results show that the proposed mixed HPM asymmetric hybrid-pole IPMSM can improve the torque with REPM usage ratio by ~4.5% and ~6.5% compared to those of the REPM-based asymmetric and symmetrical IPMSMs, respectively.

Similarly, [JI23] proposes a HPM asymmetric hybrid-pole IPMSM in which two FEPMs are used in small barriers instead of the series connection in [LIU24]. It means the proposed machine employs a parallel HPM configuration within one pole and a series HPM configuration accounting for two adjacent poles as shown in Fig. 1.42 (d). Therefore, it can still be considered as a mixed HPM utilization. In addition, a consequent pole topology with a similar arrangement of PMs is also introduced as shown in Fig. 1. 42 (e). The results show that the conventional structure can produce the same torque as the baseline with a reduced volume of REPMs. Meanwhile, the consequent pole structure cannot generate a comparable torque. However, on the contrary, the torque with REPM usage ratio of the consequent pole machine with 0.41 Nm/cm^3 is 24% higher than that of the conventional counterpart with 0.33 Nm/cm^3. It should be noted that considering the variations of torques with current advancing angle, it can be concluded that the conventional topology has considerably low MFS effect which results in a negligible torque improvement. Therefore, any PM cost reduction in this machine is mainly due to the HPM utilization. Meanwhile, the proposed consequent pole topology benefits from both HPM utilization and the PM cost saving advantage of the consequent pole structure with no MFS effect. In [JI24], different optimization methods are applied to the consequent-pole topology in Fig. 1. 42 (e) and a novel method using hierarchical multi-objective optimization algorithm is proposed. Table 1.8 summarizes the features of the abovementioned HPM asymmetric IPMSMs in this section.

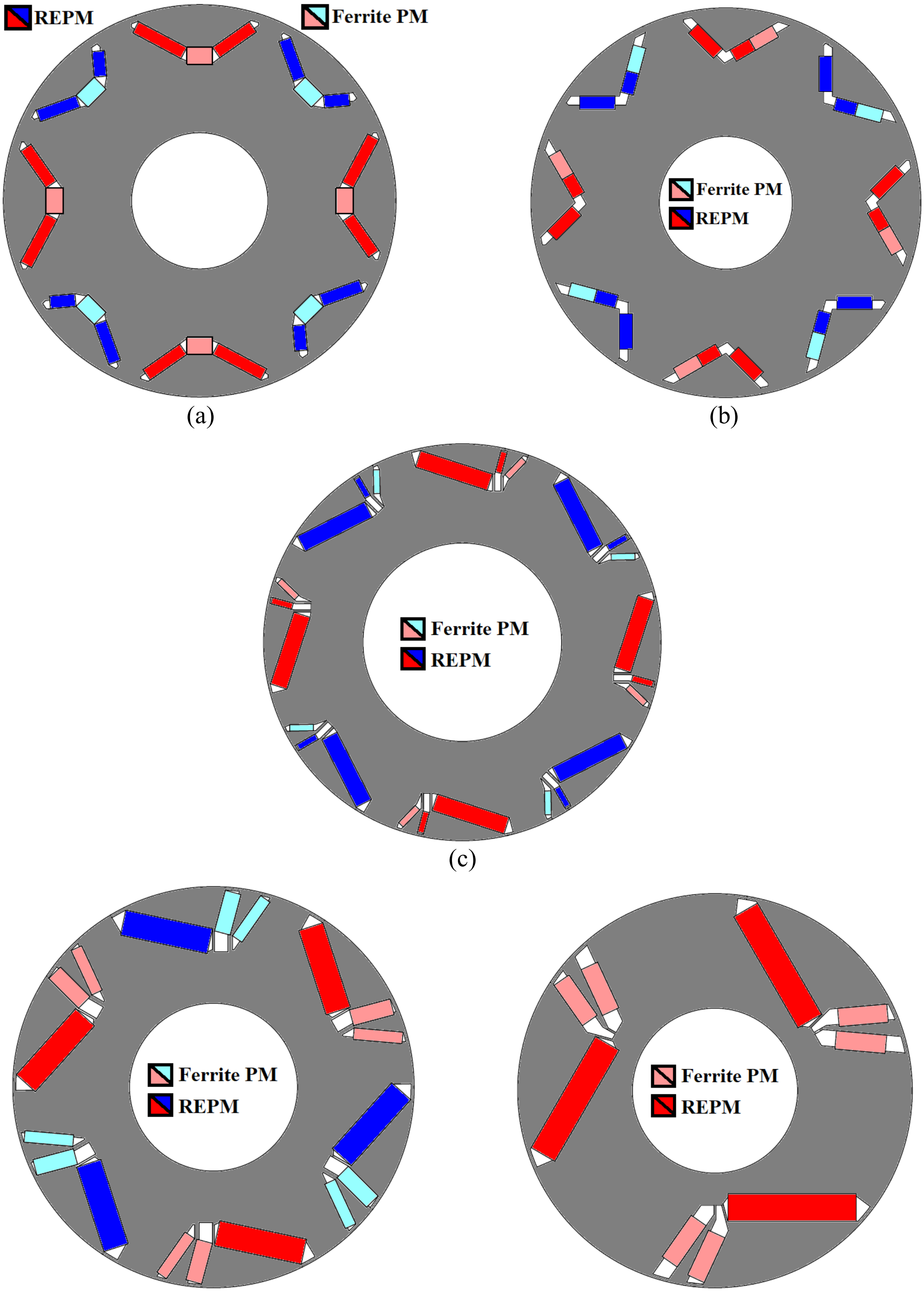

(a) (b) (c) (d) (e)

Fig. 1.42. Asymmetric HPM IPMSMs with different arrangement of two PM types. (a) Parallel HPM V-shape IPMSM with a central FEPM [LIU23B]. (b) Mixed HPM V-shape IPMSM with a parallel connection on the clockwise side of PM arrangement [LV23]. (c) Mixed HPM hybrid-pole IPMSM with a series connection on the clockwise side of PM arrangement [LIU24]. (d) Mixed HPM hybrid-pole IPMSM with two FEPMs in the clockwise side of PM arrangement [JI23]. (e) Mixed HPM consequent hybrid-pole IPMSM with two FEPMs in the clockwise side of PM arrangement [JI23], [JI24].

Table 1.8. Summary of asymmetric HPM machines.

Rotor type	**Example**	**Reference**	**Remark**
Multi-parts	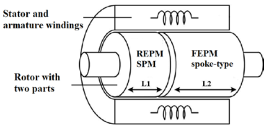	[CHE19]	• Group 1 in asymmetric machines • FEPM-based spoke-type rotor part • REPM-based SPM rotor part • Torque enhancement by the length ratio • Adjustable MFS effect by alignment angle
Multi-layers HPM aSynRM	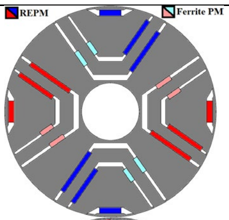 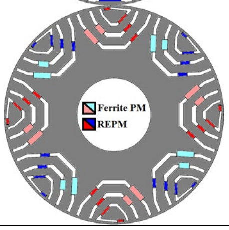	[XIE22] [QIA24]	• Group 3 with symmetrical barriers [XIE22] • Group 4 with asymmetric barriers [QIA24] • Small FEPMs at different sizes • Increased demagnetization risk of FEPMs due to using small segments • Not suitable for employing a high volume of FEPMs due to geometrical limitations • Low HPM utilization
Hybrid-pole	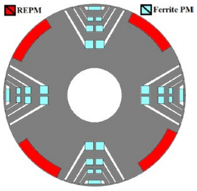	[XU17B]	• Group 3 in asymmetric machines with hybrid poles • Small FEPM segments • Unequal north and south poles • Axial flux leakage
Two-layers delta-shape	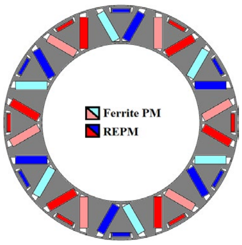	[LI19]	• Group 3 in asymmetric machines • MFS with symmetrical barriers and asymmetric PM configuration at the same dimension • Difference in the magnetic properties of two PM types can introduce MFS if they are properly placed
Spoke-type	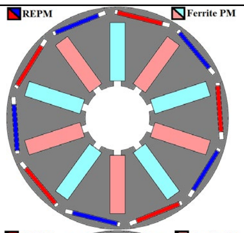 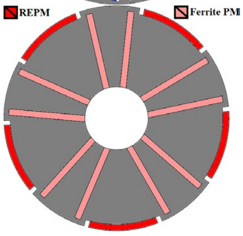	[ZEN19] [CHE21] [HAN22] [CHE23] [ZHU23B]	• Group 4 in asymmetric machines • High FEPM usage • Series HPM in [ZEN19] and [ZHU23B] • Mixed HPM in [CHE21] and [CHE23] • Using three optimizations accounting for different operational modes and magnetic properties in [CHE23]. The final optimum design is a trade-off combination of those optimizations. • Series HPM with consequent pole in [HAN22]

V-shape	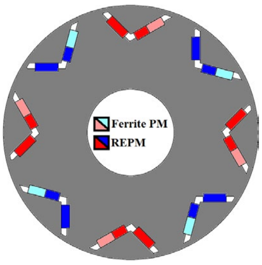	[LIU23B] [LV23]	• Group 4 in asymmetric machines • Parallel HPM V-shape IPM with two PM types in parallel at clockwise position • Low MFS effect • Low HPM utilization • Increased demagnetization risk of FEPMs due to using small size segments in parallel HPM
hybrid pole-shape	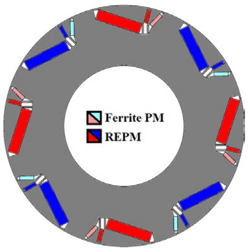	[LIU24]	• Group 4 in asymmetric machines • Mixed HPM V-shape IPM with two PM types in series at clockwise position • Improved MFS effect • Improved anti-demagnetization of FEPMs • Low HPM utilization
consequent hybrid pole-shape	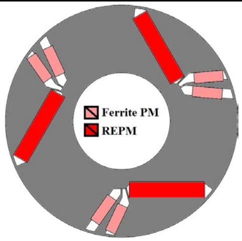	[JI23] [JI24]	• Group 4 in asymmetric machines • Parallel HPM • Consequent pole structure • Low FEPM volume • No MFS effect due to consequent pole structure

1.4.4.6. Axial Flux HPM Machines

The application of parallel and series HPM configurations in a dual rotor axial flux PMSM is proposed and compared in [DIA23]. It is shown that the proposed parallel HPM design can produce almost comparable torque at a reduced PM cost compared to a REPM-based baseline at the same size. Meanwhile, the performance of the series counterpart is lower than the others which is also expected based on literature.

1.4.5. Discussion and Research Direction

As discussed, HPM machines are new topologies of PMSMs which have been introduced in response to a global attempt towards less-REPM usage in PM machines. These machines are first introduced in 2011 with a fast growing in recent years as the price of REPM materials unboundedly increased. In general, HPM machines can be categorized in three groups including parallel, series, and mixed. Naturally, as two types of PMs with different magnetic properties are used, the parallel HPM machines benefit from higher electromagnetic performance but suffers from lower demagnetization withstand capability of FEPMs compared to those of series HPM counterpart. Meanwhile, a mixed HPM configuration can have a trade-off performance at the cost of more complicated structure. Generally, as shown in literature, these merits are always applicable to the specific HPM configuration despite from the topology. Meanwhile, the degrees of the effectiveness in each feature can be varied depending on the topology and the quality of the HPM machine design.

On the other hand, rotor-HPM machines including spoke-type, multi-layers aSynRM, single- and double- layers PM arrangements, and asymmetric IPMSMs can be used for EV applications. In general, the output torque of HPM machines can be the resultant of PM torque (FEPM torque plus REPM torque), reluctance torque, and enhanced torque by MFS (in asymmetric machines only). On the other hand, it is worth mentioning that for an effective HPM utilization a higher FEPM usage is preferred. Although a simultaneously maximizing all these three components leads to an enhanced torque at very low REPM usage, it is a highly challenging objective to be achieved. Table 1.9 provides an example for each machine and some summarized features from torque components point of view. It should be noted that the comparison of features is generally made relatively and not numerically.

Table 1.9. Summary of HPM machines for EV applications.

Topology	**Symmetricity**	**Example**	**Remark**
Spoke-type	Symmetrical Or Asymmetric	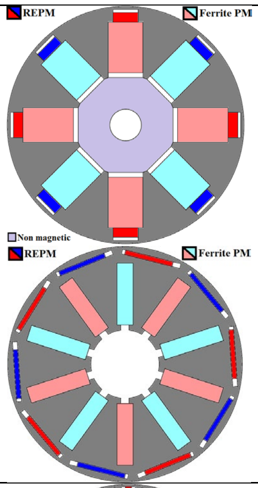	• High FEPM usage and torque • Big FEPM segments • High anti-demagnetization of FEPM • Low reluctance torque • Enhanced torque by MFS effect in asymmetric counterparts
Multi-layer aSynRM	Symmetrical Or Asymmetric	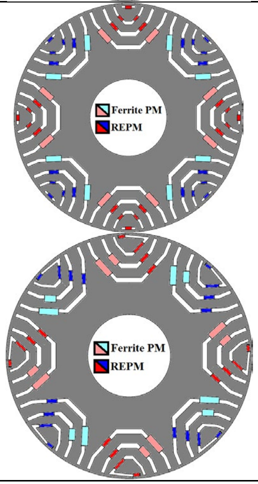	• Low FEPM usage and torque • Small FEPM segments • Low anti-demagnetization of FEPM • High reluctance torque • Enhanced torque by MFS effect in asymmetric counterparts

Single-layer/ double-layers IPMSM	Symmetrical	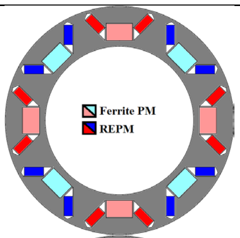 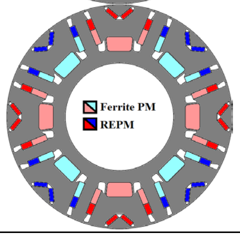	• Moderate FEPM usage and torque • Small and medium FEPM segments • Moderate anti-demagnetization of FEPM • Moderate reluctance torque • No enhanced torque by MFS
Single-layer IPMSM	Asymmetric	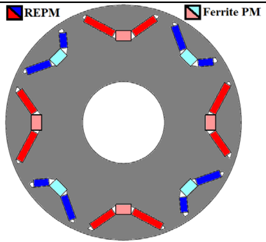	• Low FEPM usage and torque • Small FEPM segments • Low anti-demagnetization of FEPM • Moderate reluctance torque • Low torque enhancement by MFS
Hybrid-layers IPMSM	Asymmetric	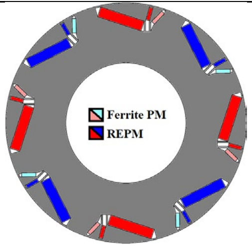	• Low FEPM usage and torque • Small FEPM segments • High anti-demagnetization of FEPM • Moderate reluctance torque • High torque enhancement by MFS

It is shown that the combination of HPM utilization with reluctance torque improvement, multi-layer flux barrier, consequent pole structure, and asymmetric rotor design are proposed in literature for more reduction of REPM usage at the same performance in HPM machines. For example, the spoke-type IPMSM is a promising topology for HPM utilization as it can excessively provide a massive space for a higher volume of low energy-product FEPMs. However, this topology has not been used in EV application due to the mechanical concerns at high speeds and low reluctance torque contribution. Meanwhile:

A) From [KAK13], [KAK13]:
  - Adding d-axis flux barrier improves the reluctance torque
  - Adding d-axis flux barrier reduces the PM torque and PM utilization

B) From [ALQ19]:
  - Tapered FEPM towards shaft reduces the output torque

C) From [PAR21]:
  - Tapered FEPM towards airgap with d-axis flux barrier leads to a poor performance in parallel HPM topology

D) Consequently, a proper reluctance torque improvement in HPM spoke-type IPMSMs yet to be introduced.

In addition, the single layer IPMSMs with V-shape and U-shape arrangement of PMs have already been used in EV application on the market. The advantages of HPM utilization in these structures will be supported by a higher reluctance torque component than the spoke-type IPMSMs. Meanwhile:

A) From [WU16], [DU20], and [YAN24B]:
   - Improved reluctance torque compared to the spoke-type topology
   - Low cross section area of FEPM (perpendicular to the magnetization direction)
   - Low or moderate FEPM usage due to not using the inner space of rotor core in full

B) From [JEO17]:
   - Dividing the middle FEPM into two segments in V-shape arrangement
   - Full use of rotor space, but with low FEPM usage due to the geometrical limitations
   - Increased risk of FEPM demagnetization due to using small FEPM segments

C) Consequently, introducing the V-shape or U-shape IPMSM with increased FEPM utilization yet to be investigated.

In multi-layers HPM aSynRMs, the reluctance torque can be maximized due to a high saliency ratio which can result in the less reliance on PM torque component. Meanwhile, the target PM torque can be partially provided by FEPMs when HPMs are used. This leads to a further reduction of required REPM torque and REPM usage. Meanwhile, as the thickness of flux carriers should be preserved considering the saturation on rotor core, the available space for accommodating FEPMs is very limited which results in low FEPM usage. Therefore, these machines may not be suitable for an effective HPM utilization. As a result, the two-layers IPMSMs (e.g. delta-shape, UI-shape, and double V-shape) can be considered as more suitable topologies for HPM utilization. Although the spatial limitations for FEPM usage will be eased to some extent, preserving the widths of flux carriers still needs to be carefully considered when designing HPM IPMSMs. For example:

A) From [KUM20], [WAN24], [LIN22], [WU17A], [WU17B], [MA21A] and [MA21B]:
   - Improved torque with REPM ratio is mainly due to the high reluctance torque in these symmetrical topologies
   - Low FEPM usage with small segments may increase the risk of demagnetization

B) From [LI19], [XIE22], and [QIA24]:
   - Improved torque with REPM ratio is mainly due to the reluctance torque component and MFS effect in these asymmetric topologies
   - Low FEPM usage with small segments may increase the risk of demagnetization

C) From [HUA19], [QUI22], and [QUI23]:
   - Reduced number of layers provides more space for FEPM usage
   - Some FEPM segments have low thickness in a parallel magnetic connection with REPM which may increase the risk of demagnetization

D) Consequently, a proper two-layers IPMSM with a preserved flux carrier and high FEPM usage is yet to be introduced.

Finally, asymmetric HPM IPMSMs are introduced to benefit from the synergies of HPM utilization and improved torque by MFS effect. Meanwhile:

A) From [LIU23B], [LV23], [JI23], and [JI24]:
   - Torque enhancement is due to reluctance torque, HPM utilization, and MFS effect
   - FEPM torque contribution is moderate where torque enhancement by MFS effect is negligible

B) From [LIU24] and [JI23]:
   - Torque enhancement is due to reluctance torque, HPM utilization, and MFS effect
   - FEPM torque contribution is reduced as the small FEPM segments are used
   - Torque enhancement by MFS effect is increased

C) Consequently, a novel design of asymmetric HPM IPMSMs with either U-shape or V-shape arrangement of PMs with effective MFS and HPM utilization yet to be proposed.

1.5. Research Scope and Major Contributions

1.5.1. Research Scope

This thesis focuses on the HPM utilization, i.e. FEPM and REPM, in IPMSMs for EV application. Different configurations of HPMs, i.e. parallel, series, and mixed, are considered and applied to different IPMSM topologies including spoke-type, V-shape, delta-shape, and asymmetric V- and U-shape IPMSMs. The arrangement of all chapters in this thesis are illustrated in Fig. 1.43.

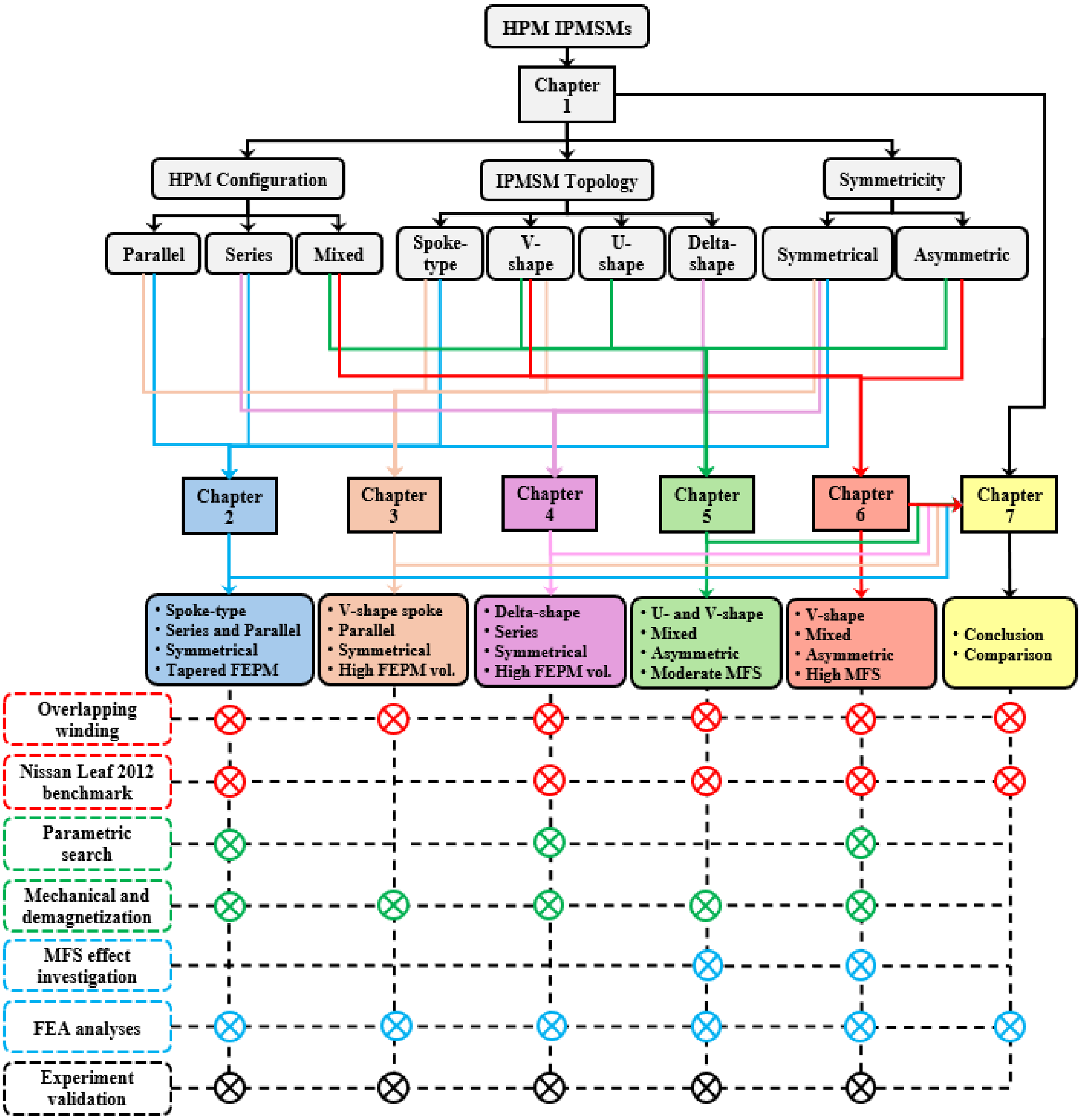

Fig. 1.43. Arrangement of chapters in this thesis.

Chapter 1

This chapter presents the introduction and the literature review on the development of less-REPM machines with a specific focus on HPM machines.

Chapter 2

In this chapter, the proper method of tapering FEPM with the aim of reluctance torque enhancement is investigated in both parallel and series HPM spoke-type IPMSMs. Unlike the proposed methods in literature which affect the d-axis inductance, we have targeted the q-axis cross section area to be expanded which results in a lower q-axis saturation and increase in q-axis inductance without introducing flux barriers in d-axis. It is shown that the proposed method is more effective in the series HPM spoke-type IPMSM and less effective in the parallel counterpart due to using a thinner REPM than FEPM in the latter topology. Therefore, the q-axis cross section area of the parallel HPM spoke-type IPMSM is already improved, and tapering FEPM can cause a minor improvement. The open-circuit and on-load electromagnetic performances, mechanical strength, and demagnetization withstand capability of FEPMs are compared using FEA. A small size prototype is manufactured and tested as the proof of concept for the proposing design with the highest torque with REPM usage ratio.

Chapter 3

As the method of chapter 2 was less effective in a parallel HPM spoke-type IPMSM, we proposed a novel design to benefit from the synergies of high reluctance torque component in a V-shape IPMSM and a high FEPM usage in a spoke-type structure. As it is shown, the proposed parallel HPM V-shape spoke IPMSM employs a high reluctance torque contribution. In addition, using V-shape spoke structure with the shaped FEPMs effectively improves the FEPM consumption which results in a high reduction of REPM usage. The open-circuit and on-load electromagnetic performances, mechanical strength, and the demagnetization withstand capability of FEPMs are investigated using FEA and compared with a REPM-based baseline. A small size prototype is manufactured and tested to validate the findings.

Chapter 4

This chapter investigates the performance improvement of a series HPM delta-shape IPMSM. It is shown that in a multilayer IPMSM, preserving the thickness of flux carriers considerably reduces the feasibility of increasing the volume of FEPMs by the structural limitations when one segment of magnet is used in the V-shape arrangement of PMs. Meanwhile, the proposed series HPM delta-shape IPMSM with split spoke (by diving each FEPM spoke into two FEPM segments with different sizes in rotor cross section) not only benefits from an increased reluctance torque component but also gains the advantage of more feasibility for FEPM usage. As a result, the proposed HPM machine with split spoke benefits from a higher torque with REPM usage ratio than that of the other counterpart with one magnet segment per spoke. The open-circuit and on-load electromagnetic performances, mechanical strength, and the demagnetization withstand capability of FEPMs are compared with a commercialized IPMSM using FEA. A small size prototype is manufactured and tested as the proof of concept and validation of the analyses.

Chapter 5

In this chapter two mixed HPM asymmetric V-shape and U-shape IPMSMs with two segments of FEPMs are investigated at first. It is shown that both machines can effectively improve the torque with REPM usage ratio by the high FEPM usage and MFS effect. However, on the downside, it is found that the small segments of FEPM in anticlockwise location in both machines are at a high risk of irreversible demagnetization even at open-circuit condition without a stator. Therefore, to avoid the open circuit self-demagnetization risk of FEPMs, these designs are modified by removing the small FEPMs and re-optimizing the rotor structures for the same torque. The modified mixed HPM V-shape and U-shape IPMSMs feature an improved demagnetization withstand capabilities at the cost of compromising the REPM usage and PM cost. It is also shown that the torque with REPM usage ratio of the proposed mixed HPM V-shape IPMSM is slightly higher than that of the mixed HPM U-shape counterpart at the same performance. Meanwhile, the MFS effect of the latter topology is twice of that in the former machine. Therefore, it can be concluded that although the MFS effect of the proposed mixed HPM asymmetric U-shape IPMSM is higher than that of the proposed mixed HPM asymmetric V-shape IPMSM, it cannot effectively be used for torque enhancement. In addition, the effective cross section of FEPM, i.e. perpendicular to the magnetization direction, in U-shape HPM machine is less than that of the V-shape counterpart which results in a lower FEPM torque contribution. For validation, two small prototypes are built, tested, and compared.

Chapter 6

In this chapter, with the aim of improving the MFS effect of the mixed HPM asymmetric V-shape IPMSM in chapter 5, a novel mixed HPM asymmetric V-shape IPMSM is proposed. This machine employs a shaped FEPM instead of the rectangular FEPM in the previous design. It is shown that the combination of the displaced centre in V-shape arrangement of PMs with the shaped FEPM can artfully cause a high intentional saturation between each two adjacent poles. This saturation regulates the produced flux by REPM to flow through the narrow edge of FEPMs which brings the following advantages. At first, the MFS effect in the proposed machine can improve to twice of that in the previous design. Secondly, as more REPM flux flows through the narrow part of FEPMs near the airgap, the demagnetization withstand capability of FEPM enhances. Thirdly, as REPM faces a lower magnetic reluctance by a thinner FEPM in the series connection, the REPM utilization ratio (i.e. the ratio of REPM torque to REPM volume) improves. Consequently, the proposed novel mixed HPM asymmetric V-shape IPMSM with the shaped FEPM benefits from the high FEPM usage as the previous V-shape counterpart using rectangular FEPMs whereas its MFS is effectively increased to the same level as the mixed HPM asymmetric U-shape IPMSM in chapter 5. Therefore, the electromagnetic performance of this machine is higher than the others. A small size prototype is manufactured and tested as the proof of concept and validation of the analyses.

Chapter 7

In this chapter, the general conclusions will be summarized, and potential future works will be given.

The cross sections of the proposed HPM machines in chapters 2 to 6 are listed and compared with a closest rotor cross section in literature in Table 1.10.

Table 1.10. Proposed HPM machines in this thesis.

Chapter	Features	Proposed rotor topology in this thesis	Closest rotor topology in literature
2a	• Tapered FEPM series spoke type IPMSM • Improved torque due to increase in reluctance torque component • [ALQ19] suffers from reduced torque	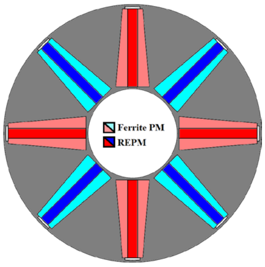	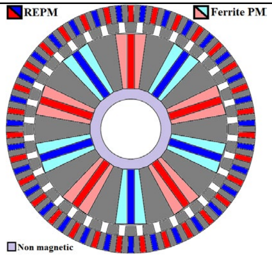 [ALQ19]
2b	• Tapered FEPM parallel spoke type IPMSM • High electromagnetic performance • [PAR21] suffers from low PM torque contribution due to d-axis flux barrier	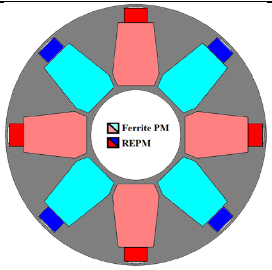	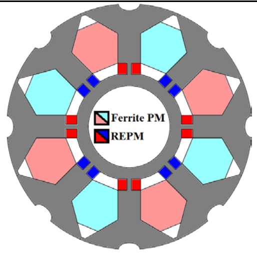 [PAR21]
3	• V-shape spoke IPMSM • Full utilization of rotor space for FEPM usage • Considerable FEPM torque component • [JEO17] suffers from low FEPM usage and increased demagnetization risk due using a narrow width	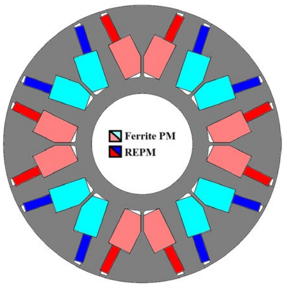	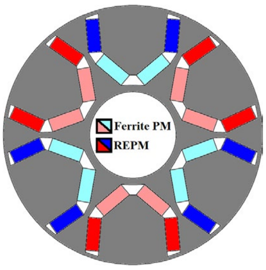 [JEO17]

4	• Delta-shape IPMSM • Less geometrical limitations for a higher FEPM usage without causing saturation in flux carriers • [PAR22] suffers from thin FEPM in the side barriers due to the geometrical limitations	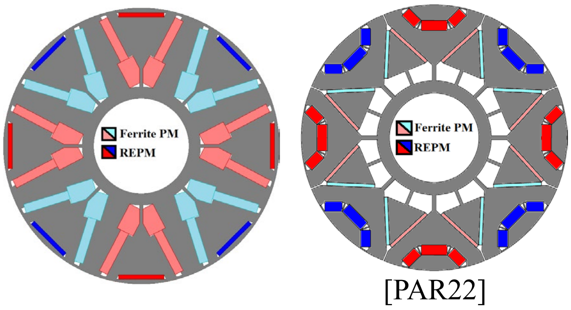 [PAR22]
5a	• Asymmetric U-shape IPMSM • High MFS effect • Moderate FEPM usage • High demagnetization withstand capability of FEPMs • [LIU23B] suffers from low MFS effect, low FEPM usage, and a high demagnetization risk	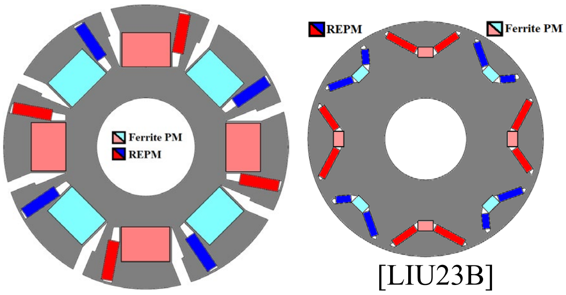 [LIU23B]
5b	• Asymmetric V-shape IPMSM • Moderate MFS effect • High FEPM usage • High demagnetization withstand capability of FEPMs • [LV23] suffers from low MFS effect and low FEPM usage	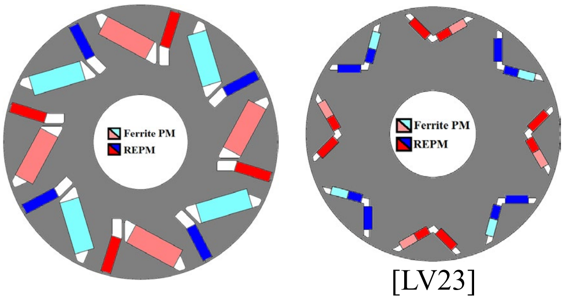 [LV23]
6	• Asymmetric V-shape IPMSM • High MFS effect • High FEPM usage • [LIU24] benefits from high MFS effect but employs 1.5 times higher number of PM segments • [LIU24] suffers from a very low FEPM torque contribution due to using low volume of FEPMs	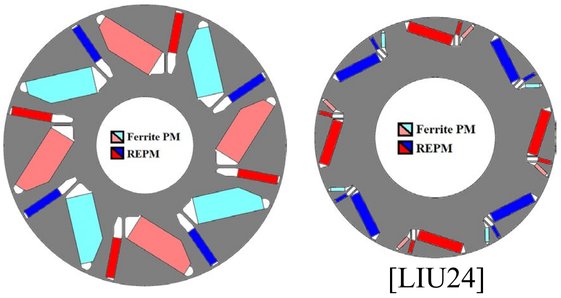 [LIU24]

1.5.2. Major Contributions

The main contribution of this thesis can be summarized as follows:

1. A reluctance torque improvement method using tapered FEPM is investigated and applied to both series and parallel HPM spoke-type IPMSM without a negative impact on PM utilization and d-axis PM flux. The proposed method is shown to be less effective in the proposed parallel HPM topology.
2. Introducing a novel parallel HPM V-shape spoke IPMSM to benefit from the synergies of a higher reluctance torque component by the V-shape arrangement, and a higher utilization of rotor volume by accommodating more FEPMs in the spoke structures.
3. Improving the FEPM usage of a series HPM delta-shape IPMSM without losing the width of flux carriers which results in a high FEPM usage and torque contribution along with a high reluctance torque component leading to an improved torque with REPM usage ratio.
4. Proposing a new mixed HPM asymmetric V-shape IPMSM with a balanced HPM usage and MFS. In addition, introducing a new mixed HPM asymmetric U-shape IPMSM with an excessive MFS effect (twice of that in the V-shape counterpart) which has not been fully utilized for the torque enhancement along with a slight reduction of FEPM torque due to the reduced effective cross section of FEPMs.
5. Introducing a novel mixed HPM asymmetric V-shape IPMSM with the shaped FEPMs which not only benefits from a large segment of FEPM and high FEPM torque contribution but also can fully utilize the MFS effect for the torque enhancement purpose.

CHAPTER 2

SPOKE-TYPE SERIES AND PARALLEL HYBRID MAGNET IPMSMS WITH TAPERED FERRITE MAGNETS

2.1. Introduction

The increased price of rare-earth permanent magnet (REPM) in recent years has introduced torque per REPM volume ratio enhancement methods, e.g. hybrid PM (HPM) utilization and asymmetric rotor, as hot research topics [KAZ23C], [ZHU22]. The former method uses two PM materials in the same structure to reduce the volume of high cost REPM by substituting with low-cost ferrite magnet (FEPM) at the same performance. Whereas, in the latter method, the difference between the corresponding current advancing angles of maximum PM and reluctance torque components will be reduced by utilizing the magnetic field shifting (MFS) effect. Therefore, as the maximums of both torque components merge towards a unique current advancing angle, the resultant torque will be increased [XIA21A].

Consequently, the employment of these methods gained a lot of attraction in high performance applications including electric vehicles (EVs). This is not only because the enhanced goals being targeted for the future of EVs, but also a cost-effective design challenge being raised as the price of REPM is reported by the US Department of Energy (DoE) to cost from 20% to 30% of the total expense in PM machines [ENE]. Therefore, universal attempts towards less REPM usage at a high performance have been provoked in recent years [POU21]. As a result, the low-cost FEPM became a popular alternative to high-cost REPMs. However, as the energy-product of FEPM is lower than that of REPM, a high volume of FEPM will be needed to replace a certain volume of REPMs at the same performance. Meanwhile, the spoke-type IPMSM can provide more space than the other IPMSMs to accommodate a higher volume of FEPM materials and is advantageous for this purpose. This is because the utilization of large PM spoke is beneficial to increase the surface area of PM, leading to an increased PM torque component. However, on the downside, this machine suffers from relatively low reluctance torque component, which can be addressed. For example, the reluctance torque of the ferrite-based spoke-type IPMSMs is improved by cavity introduction and rotor core shaping in [KAK13] and [NAG16], respectively. In the proposed design, the length of spokes is reduced whereas a proportion of spoke area is filled by non-magnetic material for the demagnetization withstand capability improvement at the cost of PM torque reduction. In addition, a W-shape arrangement of FEPM spokes is introduced in [CHI13] with an enhanced efficiency. Nonetheless, the difference in the magnetic properties of REPM and FEPM, i.e. the remanence of REPM can be ~3 times higher, is noticeable. Therefore, designing a FEPM based IPMSM with a comparable performance to a REPM based counterpart is still challenging.

To address this issue, with the aim of utilizing the synergies of high performance of REPM and low cost of FEPM, many studies were carried out leading to the invention of HPM machines in a dozen of years ago [CHE11B], [SHE12], [ISH13], [AFI14]. The combination of high performance but low-cost features of HPM machines make them a cost competitive candidate for high performance applications, i.e. EV [KAZ23D]. However, the relative positions of these two PM materials can affect the overall performance and categorize the HPM configurations into series, parallel, and mixed [AFI16], [ZHE21A], [KAZ23B]. Generally, a series HPM machine benefits from higher demagnetization withstand capability at the cost of lower electromagnetic performance than a parallel HPM counterpart. Whereas a trade-off of these features with a more complicated structure can be found in mixed HPM configurations [CHE21], [ALQ19].

As a conclusion, it can be said that the combination of HPM utilization and spoke-type IPMSMs is a cost profitable design approach. In [MA20], it is shown that a parallel HPM spoke-type IPMSM has higher torque per REPM volume ratio than the others due to the possibility of employing a high volume of low-cost FEPM. It is revealed in [ZHU17B], [ZHU19] that the performance of a parallel HPM spoke-type IPMSM can be further improved by either splitting the FEPM or REPM in each spoke. In [KAZ23A], a novel parallel HPM V-shape spoke IPMSM is designed with a high reluctance torque component and an enhanced mechanical strength at high speed. In [FAN17], HPM spokes are used in the rotor structure of a dual-stators switched flux PM machine (DS-SFPMM). In addition, the application of HPM spokes in magnetically geared machines is investigated in [ALQ19], [ALQ21]. It is shown that using a tapered magnet towards shaft leads to increase in leakage flux and reduce in performance compared to a rectangular magnet counterpart. However, the effect of tapering PM on reluctance torque and change of tapering direction towards airgap are not considered. In [PAR21], two HPM spoke-type IPMSMs using tapered magnets are investigated. The proposed parallel HPM structure suffers from low torque production due to locating the REPMs away from airgap along with using a flux barrier on the surface of rotor in d-axis. Besides, the risk of ferrite demagnetization in both designs is reduced by introducing large flux barriers on top of all spokes which caused further decrease in PM torque component due to limiting the space for magnet utilization.

This chapter focuses on the appropriate method of tapering FEPM with the aim of torque enhancement and cost reduction in both series and parallel HPM spoke-type IPMSMs. The conclusion is made by analysing the reluctance torque and PM torque components of HPM machines with and without tapered FEPMs using the frozen permeability method (FPM) in [CHU12]. Section 2.2 introduces different HPM spoke-type IPMSMs with or without tapered FEPMs. In section 2.3, the genetic algorithm (GA) and finite element analysis (FEA) are employed to investigate and compare the electromagnetic performances. The results show the effectiveness of the appropriate tapering FEPM method on electromagnetic torque enhancement in both series and parallel HPM machines. Section 2.4 presents mechanical strength and demagnetization withstand capability investigations. Finally, sections 2.5 and 2.6 summarize the experimental validation and conclusion, respectively.

This chapter is presented in IEMDC2023 conference. [S. Kazemisangdehi, Z. Q. Zhu, Y. Zhou, and H. Liu, "Improved performance of series and parallel hybrid permanent magnet spoke-type PM machines using tapered magnets," *in 2023 IEEE Int. Electric Machines & Drives Conference (IEMDC)*, 2023, pp. 1-7, IEEE.

2.2. HPM Spoke-Type IPMSMs

Spoke-type IPMSMs with single or hybrid PM types using either series or parallel HPM configurations are illustrated and compared to the benchmark in Fig. 2.1. In the following subsections, all topologies will be introduced in more detail.

2.2.1. Benchmark

The benchmark to this study is selected from a commercialized EV, using a 48-slot/8-pole (48s/8p) IPMSM as shown in Figs. 2.1 (a) and (b). From the specifications of the benchmark listed in Table 2.1, it can be observed that this machine generates 280 Nm peak torque at its peak current whereas 249.4 cm^3 of REPM (N28AH) is used in its structure. Sharing the same stator (Fig. 2.1 (a)) and specifications, the rotors of all spoke-type IPMSMs with single PM type, and HPM counterparts with or without tapered FEPMs will be re-designed. The design criterion is to achieve the same torque as benchmark with lower volume of REPMs by substituting a part of REPMs with FEPMs type TDK- FB13B.

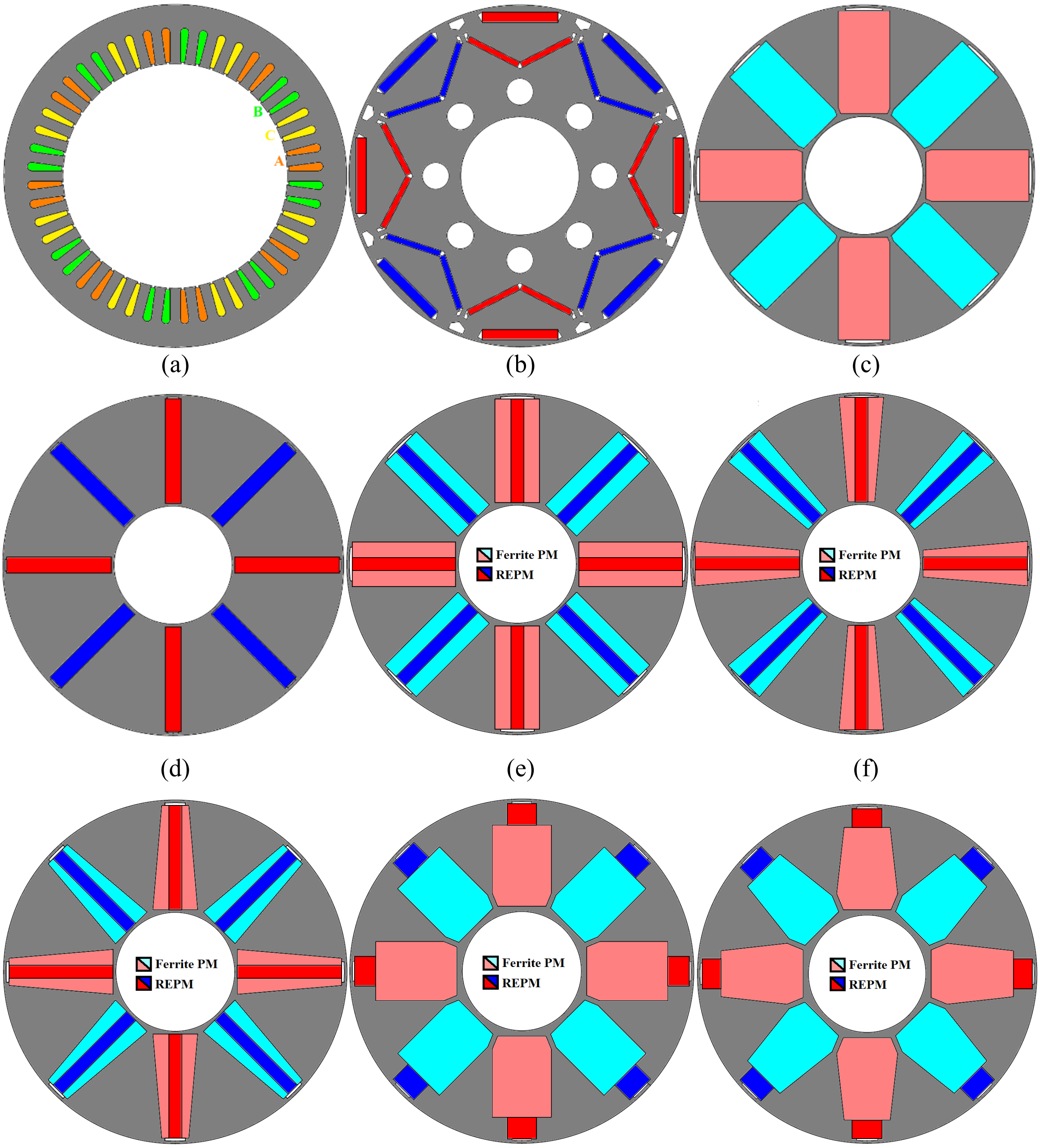

(a) (b) (c)

(d) (e) (f)

(g) (h) (i)

Fig. 2.1. Comparison of IPMSM topologies. (a) Benchmark’s stator. (b) Benchmark’s rotor. (c) FEPM-based spoke-type rotor. (d) REPM-based spoke-type rotor. (e) Series HPM spoke-type rotor with rectangular FEPM. (f) Series HPM spoke-type rotor with narrower FEPM towards shaft (Similar to [ALQ19] [ALQ21]). (g) Series HPM spoke-type rotor with narrower FEPM towards airgap. (h) Parallel HPM spoke-type rotor with rectangular FEPM. (i) Parallel HPM spoke-type rotor with narrower FEPM towards airgap.

Table 2.1. Specification of Benchmark IPMSM

Parameters	Values	Parameters	Values
Stator slot no.	48	Peak speed (r/min)	10000
Rotor pole no.	8	Rated speed (r/min)	2100
Stator outer diameter (mm)	200	Peak torque (Nm)	280
Stator inner diameter (mm)	131	Peak current (A_{max})	625
Rotor outer diameter (mm)	130	Conductor no. per slot	8
Rotor inner diameter (mm)	45	Number of parallel branches	4
Stack length (mm)	151	NdFeB volume (cm^3)	249.4
Airgap length (mm)	0.5	NdFeB remanence (T)	1.075
Angle of step skew with 3 steps (degree)	3.75	Ferrite remanence (T)	0.475

2.2.2. Conventional Spoke-Type IPMSM

The conventional spoke-type IPMSM Benefits from flux focusing effect. In addition, when it comes to replacing high energy-product REPMs with low energy-product FEPMs, a spoke-type design provides the possibility of high FEPM utilization. Therefore, two conventional spoke-type IPMSMs with single PM type (REPM or FEPM) are designed and optimized to generate the same peak torque as the benchmark with lower volume of REPM at peak current and rated speed. For the sake of comparison, overall dimensions, stack length, stator structure, and machine specifications are kept constant.

Figs. 2.1 (c) and (d) present the IPMSMs with FEPM (TDK-FB13B) only, and REPM (N28AH) only, respectively. The former rotor with 227 Nm torque can generate 81% of the desired torque and cannot satisfy the torque requirement. However, this machine utilizes 929.7 cm^3 of FEPM only and is very cheap compared to the benchmark. On the contrary, the latter rotor with REPM-based topology can satisfy the desired peak torque by using 294.5 cm^3 of REPM which is 18 % higher than that of benchmark. Therefore, the REPM-based conventional spoke-type IPMSM can be considered as a torque-competitive topology compared to the benchmark, but it is not cost-effective. To address this issue, the HPM utilization is used as shown in Figs. 2.1 (e)-(i).

2.2.3. Series HPM Spoke-Type IPMSM

In [ALQ19] and [ALQ21], the application of series HPM spokes in a magnetically geared machine is investigated where the magnets are either rectangular (like Fig. 2.1 (e)) or shaped towards shaft (like Fig. 2.1 (f)). It is concluded that the design with tapered FEPMs towards shaft generates lower torque than the rectangular magnet one due to a higher PM leakage flux in the shaft side. However, using a narrower PM towards airgap (like Fig. 2.1 (g)) is not considered. To reveal whether a narrower FEPM edge in airgap side would have different impact on torque compared to a narrower FEPM edge in shaft side, a series HPM spoke-type IPMSM with rectangular magnet is optimized first as shown in Fig. 2.1 (e). Then, the effect of tapering FEPMs in both directions on the developed torque is analysed. As will be shown, only tapering FEPMs towards airgap is beneficial for the torque enhancement.

Figs. 2.2 (a) to (c) show the cross sections of one pole in the series HPM spoke-type IPMSMs using rectangular FEPM, tapered FEPM towards shaft, and tapered FEPM towards airgap, respectively. Where L_{pm} is the length of both PMs, W_{re} is the width of REPM, and W_{fe1} and W_{fe2} are the thicknesses of FEPM in shaft side and airgap side, respectively. As can be seen, the shape of REPM is kept rectangular whereas the FEPM can be tapered in either direction. It is worth noting that the reduced area of FEPMs after tapering will be filled by rotor core. Therefore, the flux barrier slots will also be changed. Figs. 2.1 (f) and (g) show the rotor geometries when FEPMs are tapered towards shaft or airgap, respectively. The following conditions can be applied to achieve the series HPM spoke-type machines with rectangular, tapered towards shaft, and tapered towards airgap FEPMs, respectively:

$$\begin{cases} W_{fe1} = W_{fe2} \\ W_{fe1} < W_{fe2} \\ W_{fe1} > W_{fe2} \end{cases} \tag{2.1}$$

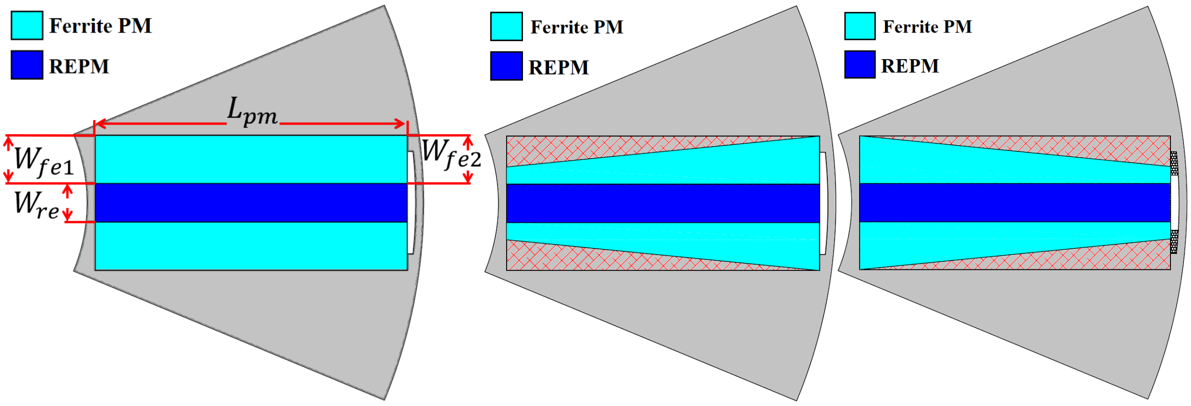

(a) (b) (c)

Fig. 2.2. Series HPM spoke-type IPMSMs using. (a) Rectangular FEPMs. (b) Tapered FEPMs towards shaft. (c) Tapered FEPMs towards airgap.

2.2.4. Parallel HPM Spoke-Type IPMSM

As will be presented later, the results of series HPM spoke-type IPMSMs show that only tapering FEPM towards airgap is beneficial for torque enhancement. Therefore, the effect of narrowing FEPM towards airgap will only be investigated in the parallel HPM spoke-type IPMSM. In this regard, two parallel HPM spoke-type IPMSMs are optimized with rectangular and narrowed FEPMs towards airgap as shown in Figs. 2.1 (h) and (i), respectively. The FEA results, which will be given in the next section, show that the parallel HPM machine with tapered FEPM towards airgap has the highest torque per REPM volume ratio among all investigated machines.

2.3. FEA Results

This section focuses on finite element analysis (FEA) results. The aim is to investigate the feasibility of torque enhancement using tapered FEPMs. In this regard, a series HPM spoke-type IPMSM with rectangular FEPM is optimized to deliver 280 Nm torque with lower volume of REPM than that of the benchmark at 625 A_{max} and 2100 r/min rotor speed. Then, the influence of tapering FEPMs in either shaft or airgap direction is investigated. It is shown that only narrowing FEPM towards airgap can lead to the torque enhancement due to increase in reluctance torque caused by a higher q-axis inductance. Consequently, a similar tapering technique is applied to the parallel HPM counterpart, where two spoke-type IPMSMs are optimized with rectangular and tapered FEPMs towards airgap. The main objective is to deliver the same torque with a lower volume of REPM compared to that of the benchmark. The results show that the proposed tapered FEPM parallel HPM spoke-type IPMSM has the least required volume of REPM among all machines and benefits from a cost-competitive performance compared to the benchmark.

2.3.1. Rectangular FEPM Series HPM Spoke-Type IPMSM

A series HPM spoke-type IPMSM with rectangular FEPMs is optimized to deliver 280 Nm torque with lower volume of REPM than that of benchmark at 625 A_{max} and 2100 r/min using the model shown in Fig. 2.2 (a). The range of the REPM thickness (W_{re}) is defined using the thickness of REPM to FEPM ratio (K_{ws}) as below:

$$W_{re} = K_{ws}.2W_{fe} \quad , \quad 0 \leq K_{ws} \leq 1 \tag{2.2}$$

where $K_{ws}=0$ refers to a ferrite-based machine, and $K_{ws}=1$ refers to a HPM machine with $W_{re}=2W_{fe}$.

Figs. 2.3 (a) and (b) show the torque with REPM volume optimization result of the series HPM spoke-type IPMSM using rectangular FEPMs and its optimum cross section, respectively. Whereas the optimum values of design parameters are listed in Table 2.2.

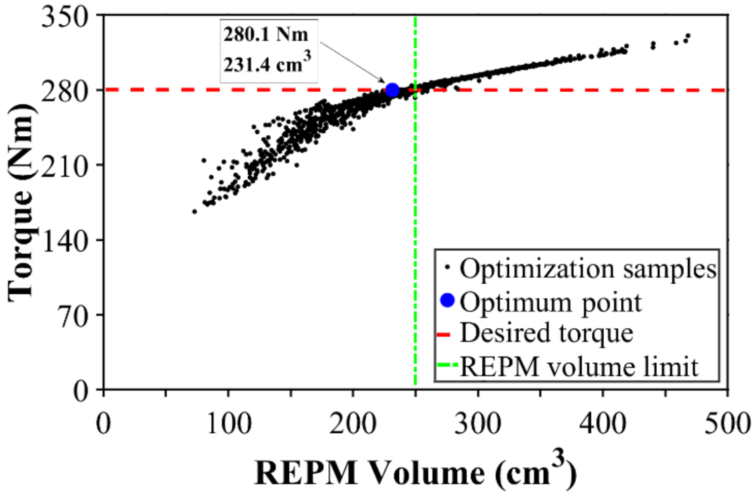

(a)

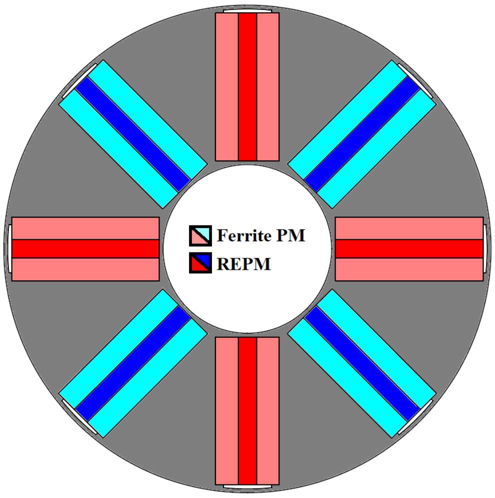

(b)

Fig. 2.3. Optimization of a rectangular FEPM series HPM spoke-type IPMSM at 625 A_{max} and 2100 r/min. (a) Result. (b) Optimum cross section.

Table 2.2. Design Parameters and Optimum Values of Series HPM Spoke-Type IPMSM with Rectangular FEPM

Parameters	**Symbols**	**Unit**	**Value**
Length of both PM types	L_{pm}	mm	39.41
Width of REPM	W_{re}	mm	4.86
Width of FEPM	W_{fe}	mm	6.05
Ratio of REPM width to FEPM width	K_{ws}	-	0.4

A comparison of the volumes of PMs in this machine with those of the benchmark is carried out in Table 2.3. As can be seen, this machine requires 231.4 cm^3 of REPM and 575.9 cm^3 of FEPM, to generate the same torque as benchmark. Therefore, the volume of REPM in this machine is only reduced by ~7.2 %.

Table 2.3. Comparison of Torque and PM Volume in Series HPM Spoke-Type IPMSM with rectangular FEPM and Benchmark

Results	**Benchmark**	**Series HPM spoke-type IPMSM with rectangular FEPM**
Torque (Nm)	280	280.1
REPM Volume (cm^3)	249.4	231.4
FEPM Volume (cm^3)	-	576

Fig. 2.4 compares the torque components of the REPM-based conventional spoke-type IPMSM, the rectangular FEPM series HPM spoke-type IPMSM, and benchmark. As can be seen, the reluctance torque components of spoke-type machines are lower than that of the benchmark, meaning that these machines will need more PM torque components to deliver the same total torque. However, almost half of the PM torque in the rectangular FEPM series HPM spoke-type IPMSM is generated by FEPMs. Although the required REPM torque component of this machine with 74.87 Nm is 48 % less than that of REPM-based conventional spoke-type IPMSM with 144.03 Nm, its REPM consumption is only reduced about 21.4 %. In other words, it can be concluded that the REPM utilization of the rectangular ferrite series HPM spoke-type IPMSM with 0.324 Nm/cm^3 is lower than that of REPM-based conventional spoke-type IPMSM with 0.489 Nm/cm^3. This is due to the high reluctance of REPM flux path caused by the high utilization of FEPMs in a series configuration of HPM. Therefore, the series HPM spoke-type IPMSM with rectangular FEPM is not a cost-effective competitor to the benchmark.

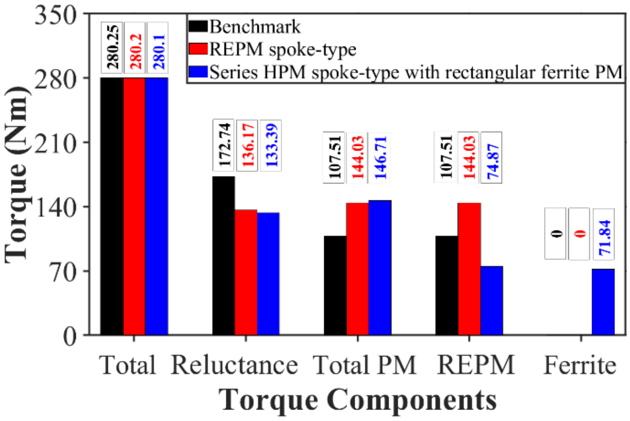

Fig. 2.4. Comparison of torque components in REPM-based conventional spoke-type IPMSM, rectangular FEPM series HPM spoke-type IPMSM, and benchmark at 625 A$_{max}$ and 2100 r/min.

2.3.2. Tapered FEPM Series HPM Spoke-Type IPMSMs

In this section, the effect of tapering FEPM in either shaft or airgap direction on the electromagnetic performance of a series HPM spoke-type IPMSM is investigated using the optimum design in Fig. 2.3 (b). A parametric study is carried out by independently changing the W_{fe1} or W_{fe2} parameters with the same intervals whereas all other parameters are kept constant. This is to normalize the variation of FEPM volume when either W_{fe1} or W_{fe2} changes by one step. Therefore, any effect on performance caused by narrowing FEPMs can be linked to the direction of tapering. Consequently, the appropriate tapering method will be revealed. Fig. 2.5 compares the variations of open circuit flux linkage, when W_{fe1} and W_{fe2} are reducing from the optimum value of 6.05 mm, respectively. As can be seen, by tapering FEPMs in both directions, the flux linkage increases slightly due to the reduced reluctance of REPM flux path caused by a thinner FEPM (Figs. 2.2 (b) and (c)). It is worth mentioning that in this case, tapering FEPM towards shaft would not increase the leakage flux as a non-magnetic shaft is used. In contrast, when tapering FEPM towards airgap, the variation of flux linkage is lower as the leakage flux increases. In addition, the airgap harmonics will also be changed.

The comparisons of open-circuit back-EMF waveforms and spectra with variations of W_{fe1} and W_{fe2} at 2100 r/min are presented in Fig. 2.6. When tapering FEPM towards shaft, the pole surface remains unchanged from airgap side leading to the same harmonic components. Therefore, the increase in the flux linkage (Fig. 2.5) leads to an increase in the fundamental component of back-EMF as shown Fig. 2.6 (b). However, on the contrary, the pole surface from airgap side will be wider by narrowing the FEPM towards airgap leading to the change of harmonics as shown in Fig. 2.6 (d). Therefore, by reducing W_{fe2}, the back-EMF waveforms become wider at almost the same fundamental components but with the higher 3rd harmonics.

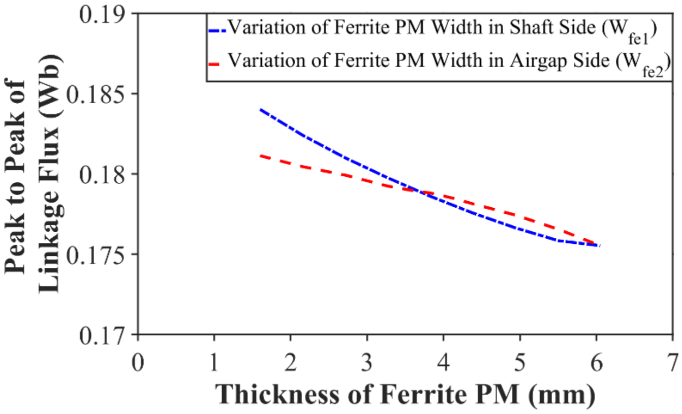

Fig. 2.5. Comparison of open circuit flux linkages with tapering FEPMs towards shaft or airgap in a series HPM spoke-type IPMSM.

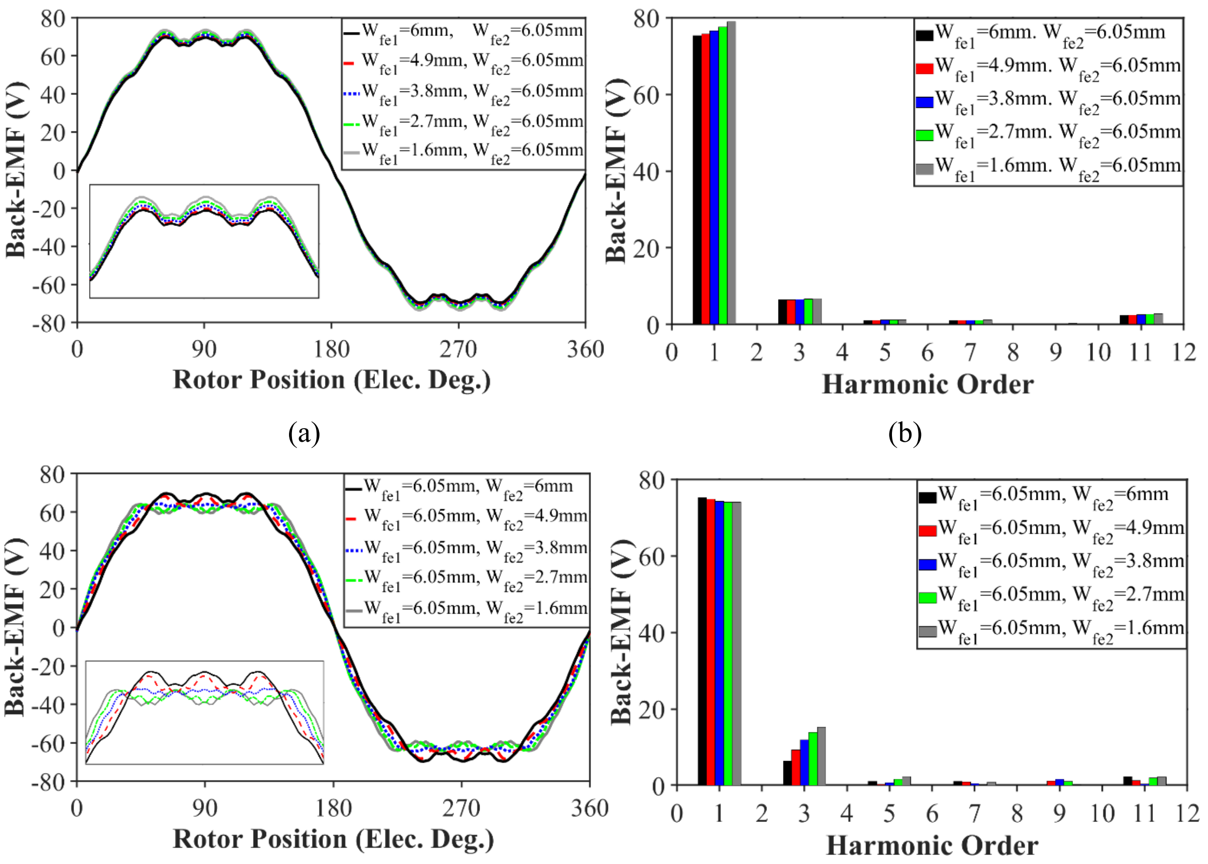

(a) (b)

(c) (d)

Fig. 2.6. Comparison of open circuit back-EMFs with tapering FEPMs in a series HPM spoke-type IPMSM at 2100 r/min rotor speed. (a) Waveforms with tapering towards shaft. (b) Spectra with tapering towards shaft. (c) Waveforms with tapering towards airgap. (d) Spectra with tapering towards airgap.

Figs. 2.7 (a) and (b) show the effect of tapering FEPM towards different directions on the total torque and dq-axis inductances (L_d and L_q) in a series HPM spoke-type IPMSM at 625 A_{max} and 2100 r/min rotor speed. The dashed lines show the references when the rectangular FEPMs are used. Then, the blue and red figures correspond to the tapering (or narrowing) FEPM towards shaft and airgap, respectively. As can be seen in Fig. 2.7 (a), the torque has reduced when the FEPM is narrowed towards shaft. In contrast, by tapering FEPM towards airgap, torque increases to a maximum value and then reduces gradually. In addition, by tapering FEPM in both directions, the magnetic reluctance of the d-axis reduces by using a thinner FEPM leading to a higher d-axis flux. Therefore, L_d increases in both cases as shown in Fig. 2.7 (b). However, the change of L_q depends on the FEPM tapering direction. When FEPMs are tapered towards shaft by reducing W_{fe1}, the cross section of q-axis flux remains unchanged (see Fig. 2.8 (a)) leading to a constant L_q as shown in Fig. 2.7 (b). On the contrary, when FEPMs are tapered towards airgap by reducing W_{fe2}, the cross section of q-axis flux is enhanced with a small increase in the length of q-axis flux (see Fig. 2.8 (b)) leading to a reduced saturation level, improved q-axis flux and increased resultant L_q as shown in Fig. 2.7 (b). Therefore, by narrowing FEPM towards shaft, the reluctance torque is expected to reduce due to having a higher L_d and a constant L_q. However, by narrowing FEPM towards airgap, the reluctance torque is expected to enhance until a certain point due to the variations of L_d and L_q. As can be seen, L_q will be decreased after W_{fe2} reduces to less than 3.83 mm leading to the reduction of reluctance torque.

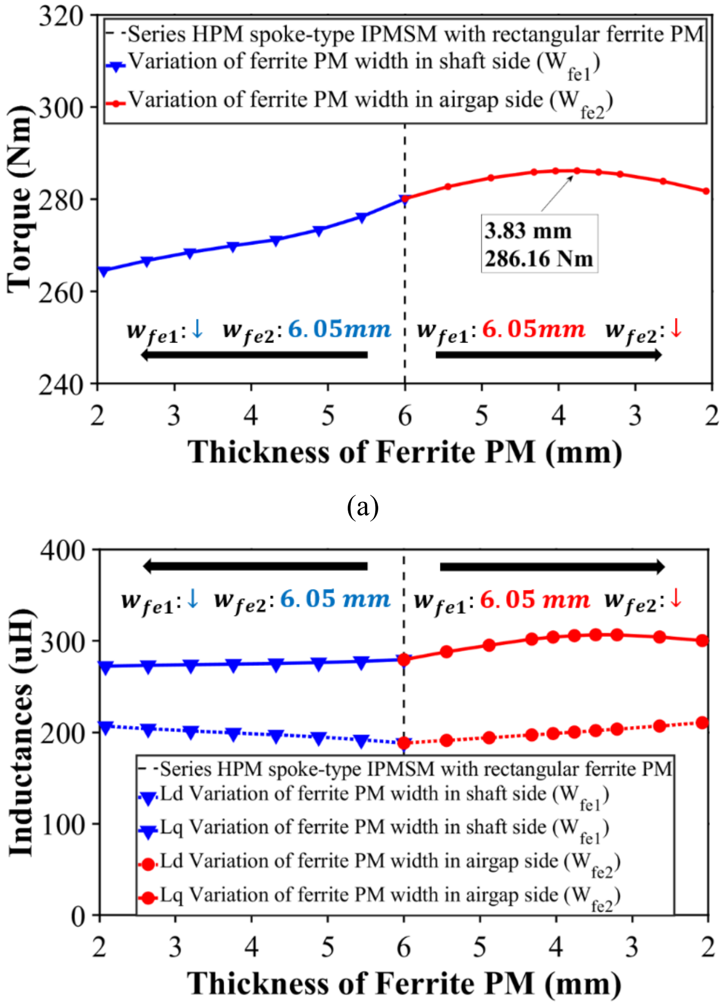

(a)

(b)

Fig. 2.7. Comparison of on-load performances at 625 A_{max} and 2100 r/min influenced by tapering FEPMs in series HPM spoke-type IPMSM. (a) Average torque. (b) Dq-axis inductances.

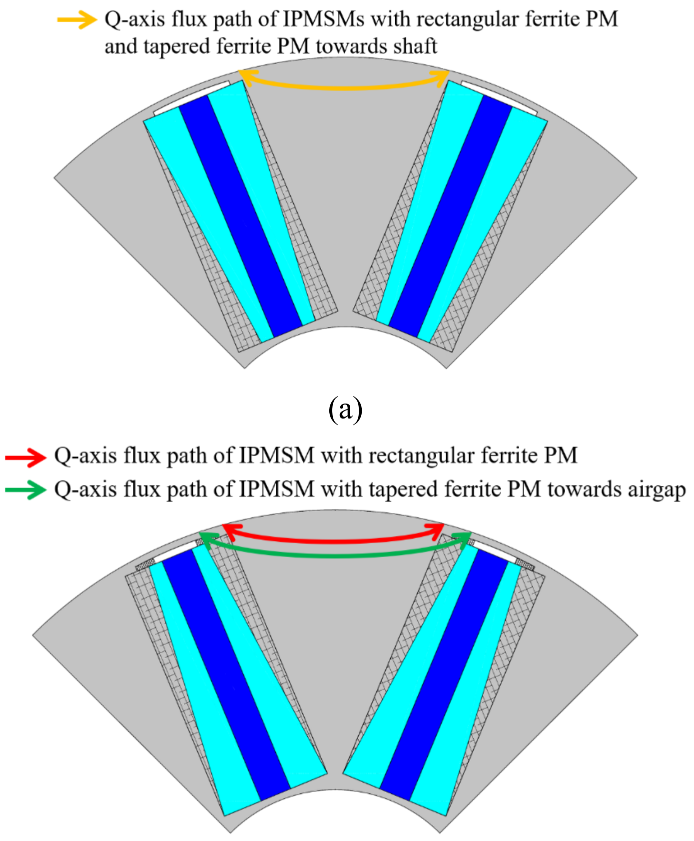

(a)

(b)

Fig. 2.8. Comparison of q-axis cross sections and flux paths in series HPM spoke-type IPMSM. (a) By tapering FEPMs towards shaft. (b) By tapering FEPMs towards airgap.

The developed torque (T) of a PM machine can be decomposed into the PM torque (T_{PM}) and reluctance torque (T_{rel}) components as presented below:

$$T = T_{PM} + T_{rel} = \frac{3p}{2}\left(\psi_{pm} i_q + (L_d - L_q) i_d i_q\right) \tag{2.3}$$

where p is the number of pole pairs, ψ_{pm} is the PM flux linkage, L_d and L_q are the d- and q-axis inductances, and i_d and i_q are the d- and q-axis currents, respectively.

Then, the frozen permeability method (FPM) is used to investigate the variation of each torque component by tapering FEPMs towards shaft and airgap as shown in Figs. 2.9 (a) and (b), respectively. Going from A to B by tapering FEPM towards shaft (reducing W_{fe1}), total torque reduces mainly due to the reduction of reluctance torque component as discussed in Fig. 2.7 (b). However, it can be seen in Fig. 2.9 (a) that the PM torque component enhances. Although the FEPM torque component has decreased by lowering the volume of this magnet, the REPM torque component is increased. This is due to the lower magnetic reluctance of REPM flux path by using a reduced FEPM thickness towards the shaft at the same pole arc.

Meanwhile, it should be noted that in this case using a non-magnetic shaft prevents an increased leakage flux at inner ribs. On the contrary, going from A to C by tapering FEPM towards airgap (reducing W_{fe2}), total torque increases mainly due to the increase in the reluctance torque component as discussed in Fig. 2.7 (b). However, the total PM toque component reduces in this case. Although a lower FEPM torque component is expected by decreasing the volume of this magnet, this reduction is more significant (Fig. 2.9 (b)) due to the increased in the leakage flux at outer rib in the presence of stator teeth. In addition, a higher REPM torque could have been expected due to the reluctance of REPM flux path being reduced by reducing W_{fe2}. However, the variation of REPM torque component is ignorable due to the increased leakage flux caused by lowering the width of outer rib in the presence of stator teeth. Finally, by going from C to D with further reduction of W_{fe2}, the total torque reduces as both reluctance torque and PM torque components are decreasing.

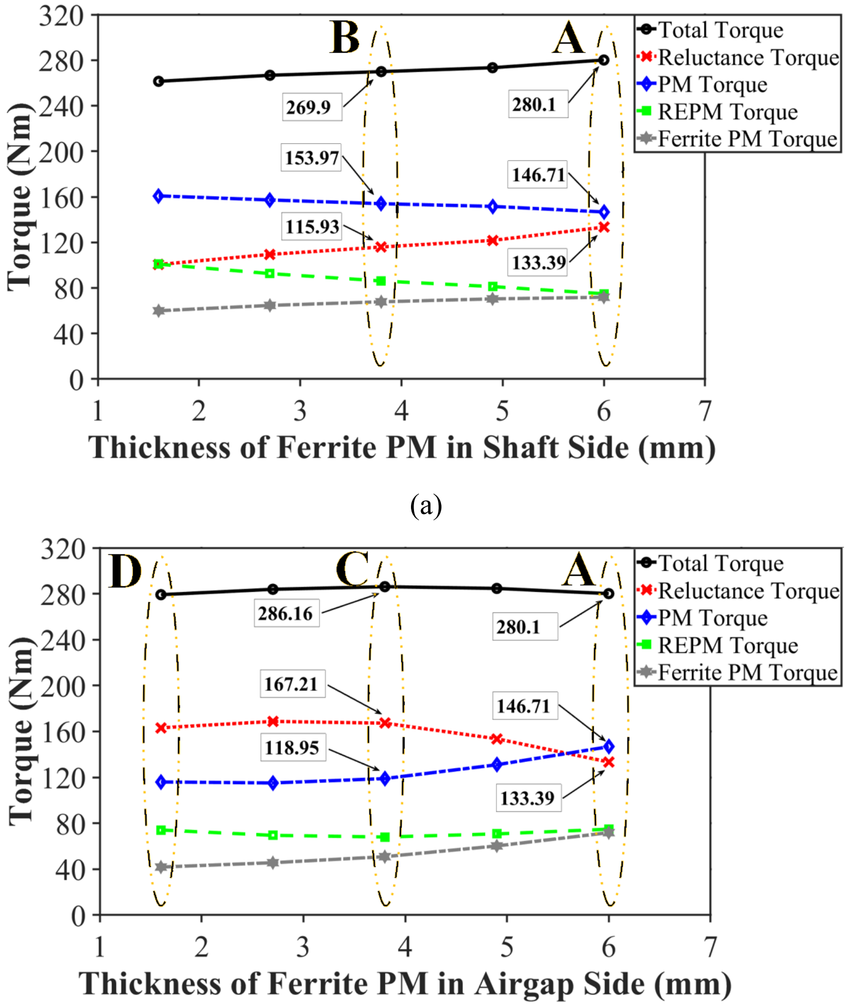

(a)

(b)

Fig. 2.9. Comparison of torque components in series HPM spoke-type IPMSMs using tapered FEPMs at 625 A_{max} and 2100 r/min. (a) Tapered FEPM towards shaft. (b) Tapered FEPM towards airgap.

2.3.3. Parallel HPM Spoke-Type IPMSMs with Rectangular and Tapered FEPMs

In this section, the application of tapered FEPMs towards airgap in a parallel HPM spoke-type IPMSM is investigated. In this regard, two parallel HPM machines without and with narrowed FEPMs towards airgap are optimized to deliver 280 Nm torque with lower volume of REPM than that of benchmark at 625 A_{max} and 2100 r/min rotor speed. Figs. 2.10 (a) and (b) illustrate the parametric designs of both machines. As can be seen, in the topology with rectangular FEPM, W_{fe1} equals to W_{fe2}, and in the machine with tapered FEPM, W_{fe1} is bigger than W_{fe2}. In addition, the thickness of REPM (W_{re}) can be defined using the REPM width to FEPM width ratio (K_{wp}) as following:

$$W_{re} = K_{wp}.W_{fe2} \quad , \quad 0 < K_{wp} \leq 1 \tag{3.4}$$

Figs. 2.10 (c) and (d) present the optimization results and the optimum cross sections of the parallel HPM spoke-type IPMSMs without and with tapered FEPMs, respectively.

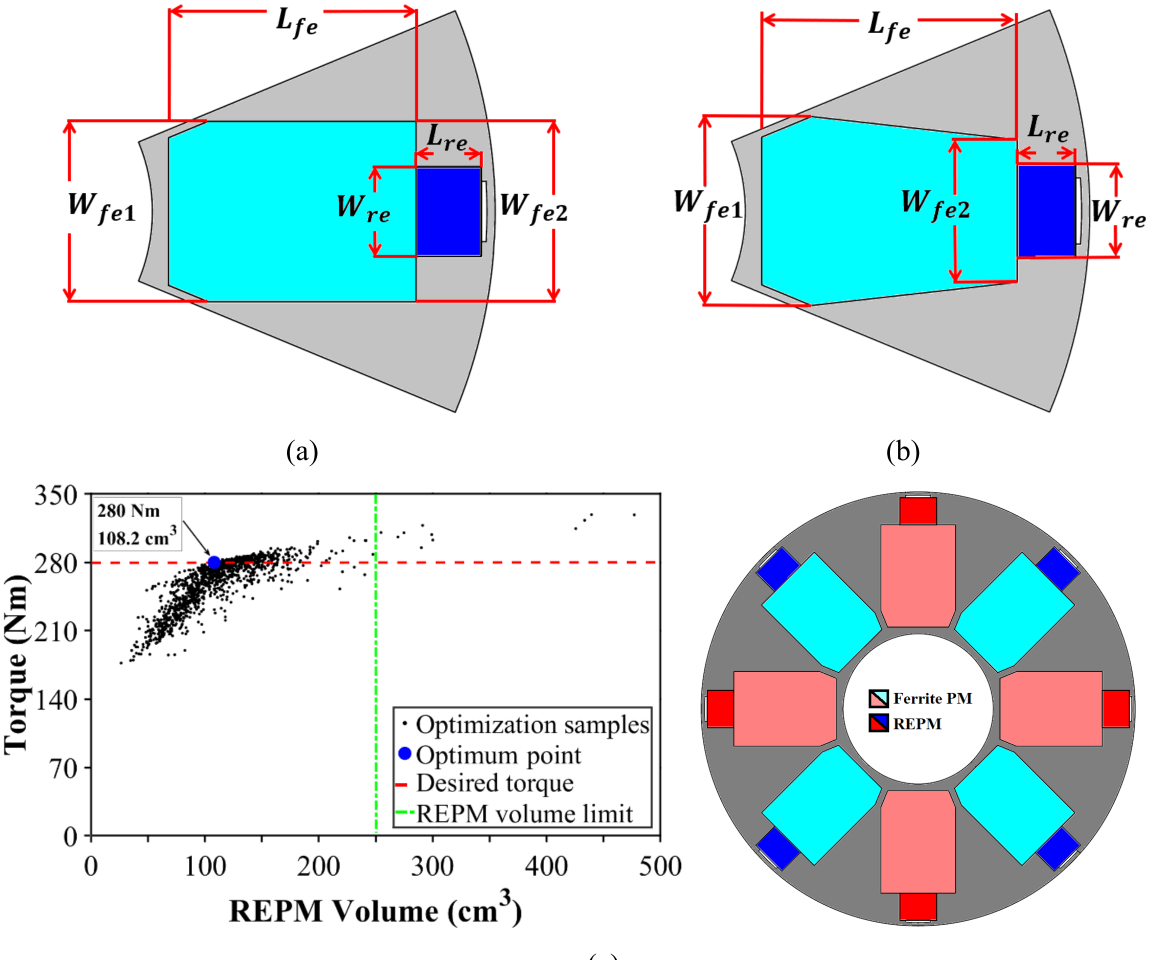

(a)

(b)

(c)

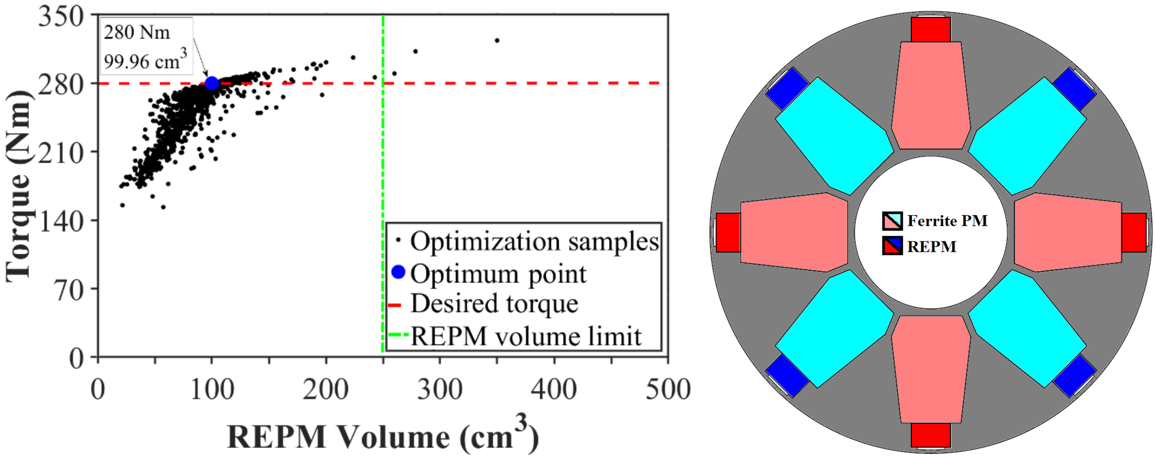

(d)

Fig. 2.10. Optimization of parallel HPM spoke-type IPMSMs at 625 A_{max} and 2100 r/min speed. (a) Parametric model of the rotor with rectangular FEPM. (b) Parametric model of the rotor with tapered FEPM towards airgap. (c) Optimization result of the machine with rectangular FEPM. (d) Optimization result of the machine with tapered FEPM towards airgap.

Table 2.4 summarizes the optimum values of the design parameters shown in Figs. 2.10 (a) and (b). Meanwhile, Figs. 2.11 (a) and (b) compare the torques and dq-axis inductances of the parallel HPM spoke-type IPMSMs with rectangular and tapered FEPM towards airgap, and those of the benchmark at 625 A_{max} and 2100 r/min, respectively. As can be seen, they can reach the desired torque at different current advancing angles. In addition, the PM torques at zero current advancing angle, and variation of dq-axis inductances are also different. Therefore, they are expected to have different PM torque and reluctance torque contributions.

Table 2.4. Optimum Values of Design Parameters in Parallel HPM Spoke-Type IPMSMs without and with Tapered FEPMs.

Parameters	**Symbols (Units)**	**Parallel HPM IPMSM with rectangular FEPM**	**Parallel HPM IPMSM with tapered FEPM**
Width of FEPM in inner side	W_{fe1} (mm)	22.38	23.38
Width of FEPM in outer side	W_{fe2} (mm)	22.38	17.65
Length of FEPM	L_{fe} (mm)	30.7	31.56
Width of REPM	W_{re} (mm)	11.11	11.525
Length of REPM	L_{re} (mm)	8.06	7.18

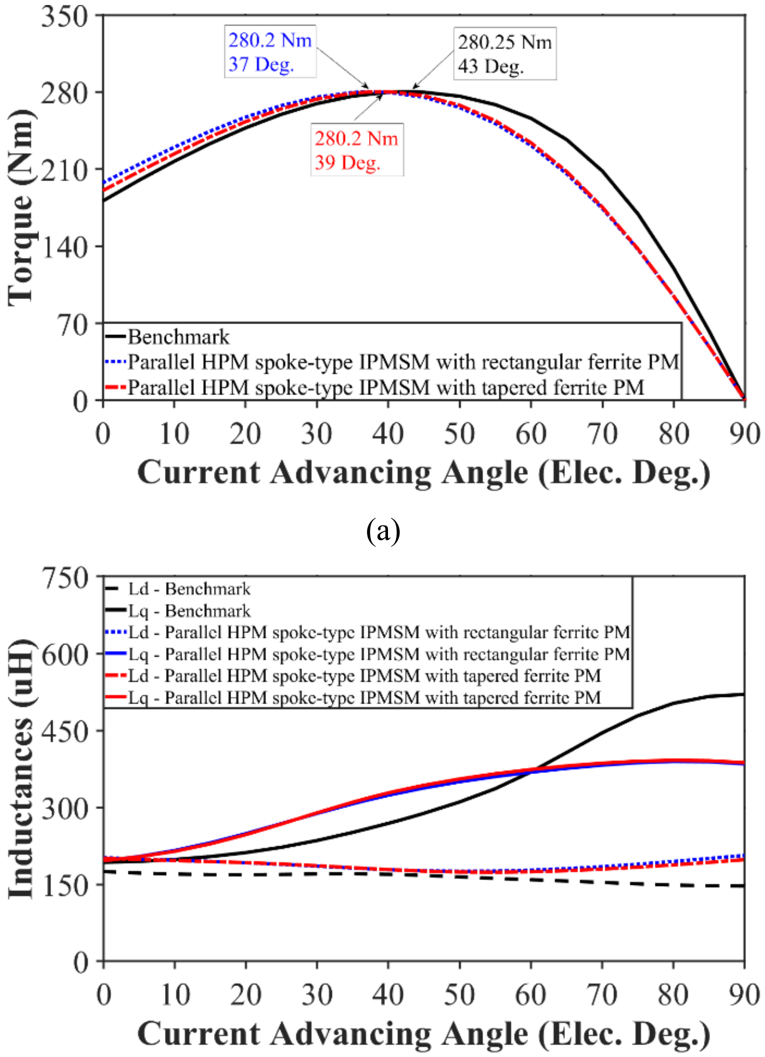

(a)

(b)

Fig. 2.11. Comparison of on-load characteristics with current advancing angle at 625 A_{max} and 2100 r/min. (a) Torque. (b) Dq-axis inductances.

Fig. 2.12 compares the torque components of these three machines at 625 A_{max} and 2100 r/min, using FPM. As can be seen, the HPM machine with tapered FEPM towards airgap has higher reluctance torque, but almost the same FEPM torque components compared to its rectangular FEPM counterpart. Therefore, at the same total torque, it requires less REPM torque leading to a less REPM volume utilization as listed in Table 2.5. It is worth mentioning that the torque enhancement effect of tapered FEPM utilization in the parallel HPM spoke-type IPMSM can be lower than that of a series counterpart. The reason is that the cross section of q-axis flux in a parallel HPM spoke-type IPMSM with a thinner REPM than FEPM is already increased (compare Figs. 2.10 (a) and 2.8 (b)), leading to a lower saturation, improved q-axis inductance, and higher resultant reluctance torque. In addition, FEPMs are distanced from airgap by the employed REPMs in the parallel magnetic connection. Consequently, tapering FEPM can add extra improvement to the q-axis flux cross section leading to a further enhancement of reluctance torque component. Table 2.5 compares the volumes of magnets in the parallel HPM machines with those of benchmark when they deliver 280 Nm torque at the same size and specifications. The proposed parallel HPM machine with tapered FEPM towards airgap is the most cost-effective competitor to the benchmark. As can be seen, the parallel HPM machine with tapered FEPM requires 60% less REPM volume than the benchmark. In addition, the volumes of REPM and FEPM are reduced 8.2 cm^3 (~8%) and 33.1 cm^3 (~4%), respectively, compared to those of the parallel HPM spoke-type IPMSM with rectangular FEPM.

It should be noted that the Nissan Leaf 2012 IPMSM is selected as the benchmark for this chapter as the aim of this thesis is to propose novel HPM machines for EV application. However, this is a commercialized IPMSM which may not be optimized against the same conditions and the same objectives as the proposed HPM machines in this chapter. As a result, the direct comparisons of the volumes and the cost of PMs may not be fair enough. Therefore, it is essential to declare that the benchmark is used as a reference only. Meanwhile, the effectiveness of the proposed method can be validated by comparing the volumes and the total cost of PMs in the proposed HPM machines without and with tapered FEPMs, which are optimized at the same conditions and objectives. Meanwhile for a fair comparison in conclusion chapter, a REPM-based baseline rotor will be optimized at the same conditions and objectives as the proposed HPM machines using the same stator, specifications, and overall dimensions of the Nissan Leaf 2012 IPMSM.

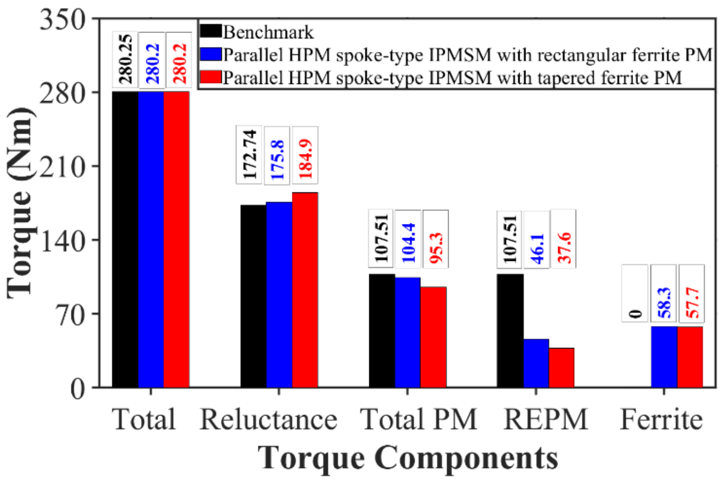

Fig. 2.12. Comparison of torque components in parallel HPM spoke-type IPMSMs with rectangular and tapered FEPMs, and those of benchmark at 625 A_{max} and 2100 r/min.

Table 2.5. Comparison of Torque and PM Volume in Parallel HPM Spoke-Type IPMSMs with rectangular and tapered FEPMs, and Benchmark

Results	**Benchmark**	**Parallel HPM IPMSM with rectangular FEPM**	**Parallel HPM IPMSM with tapered FEPM towards airgap**
Torque (Nm)	280	280	280
REPM Volume (cm^3)	249.4	108.2	99.96
FEPM Volume (cm^3)	-	817.6	784.5

Fig. 2.13 illustrates the flux densities and flux lines distributions of these machines at open circuit. As can be seen, the stator yoke saturations of the parallel HPM machines are slightly higher than that of the benchmark. In addition, the comparisons of open circuit airgap flux densities and back-EMFs at 2100 r/min are given in Figs. 2.14 and 2.15, respectively. As can be seen, the fundamental components of airgap flux density and back-emf of the proposed tapered FEPM parallel HPM spoke-type IPMSM are higher than those of the benchmark, but slightly lower than those of the rectangular FEPM counterpart. Finally, a comparison of open circuit flux linkages is presented in Fig. 2.16.

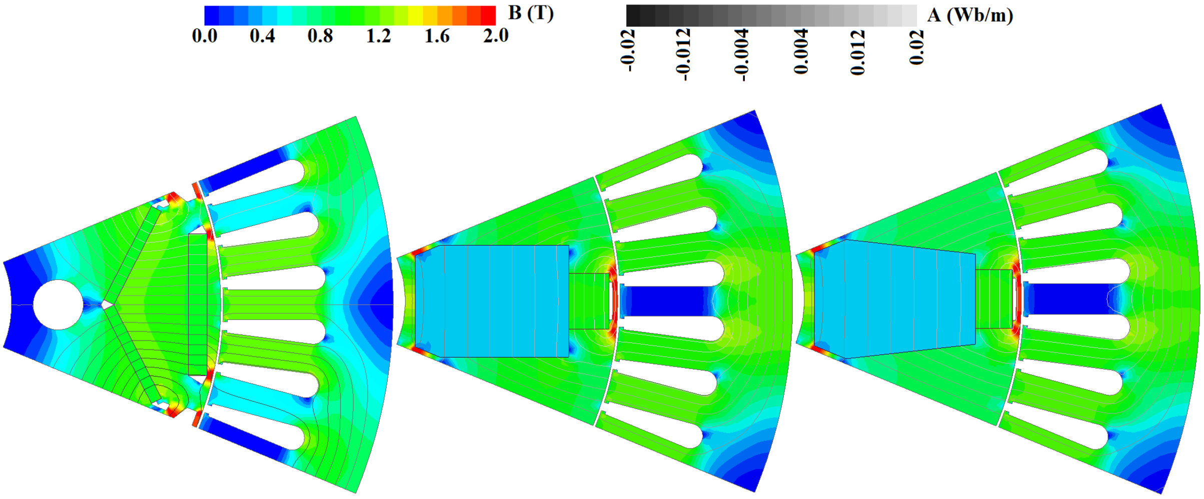

(a) (b) (c)

Fig. 2.13. Comparison of open circuit flux densities and flux lines distributions. (a) Benchmark. (b) Parallel HPM spoke-type IPMSM with rectangular FEPM. (c) Parallel HPM spoke-type IPMSM with tapered FEPM.

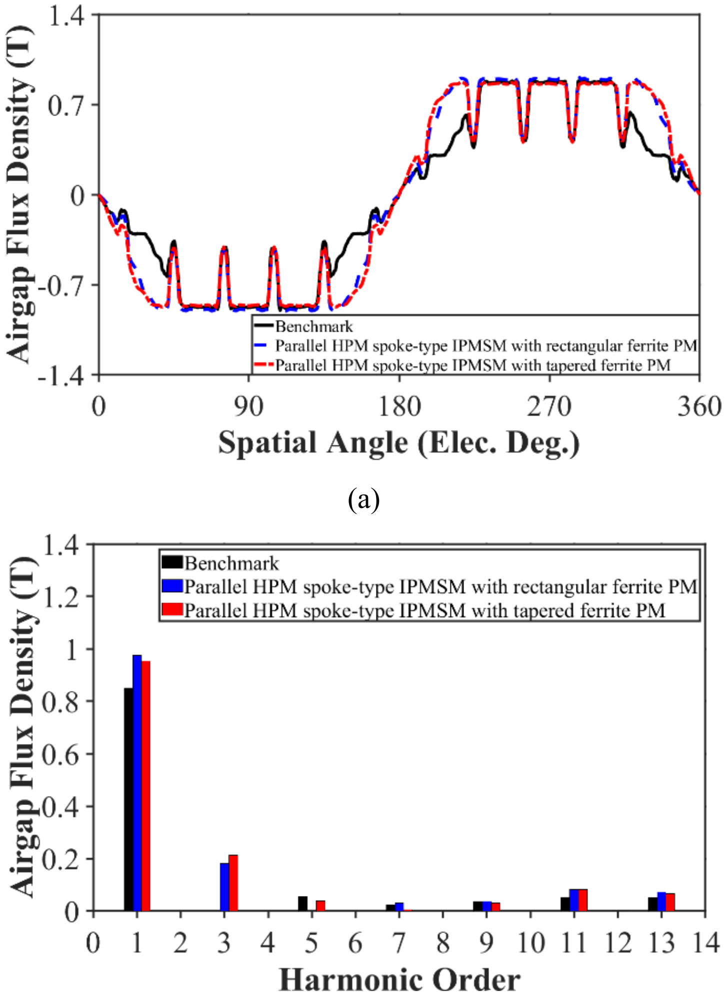

(a)

(b)

Fig. 2.14. Comparison of open circuit airgap flux densities. (a) Waveforms. (b) Spectra.

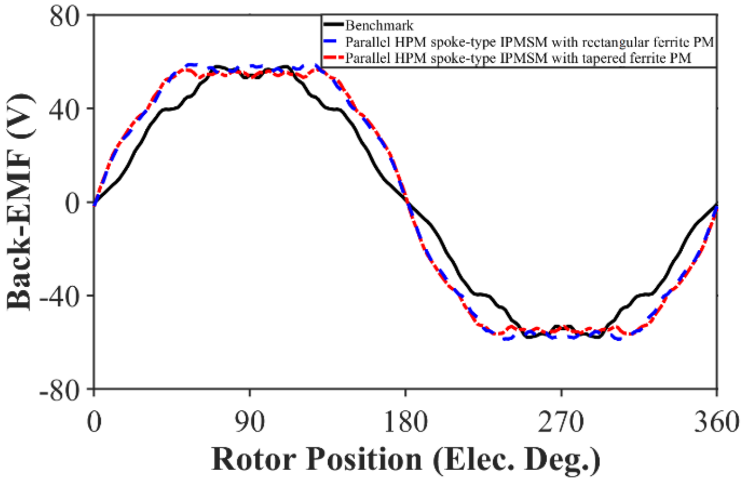

(a)

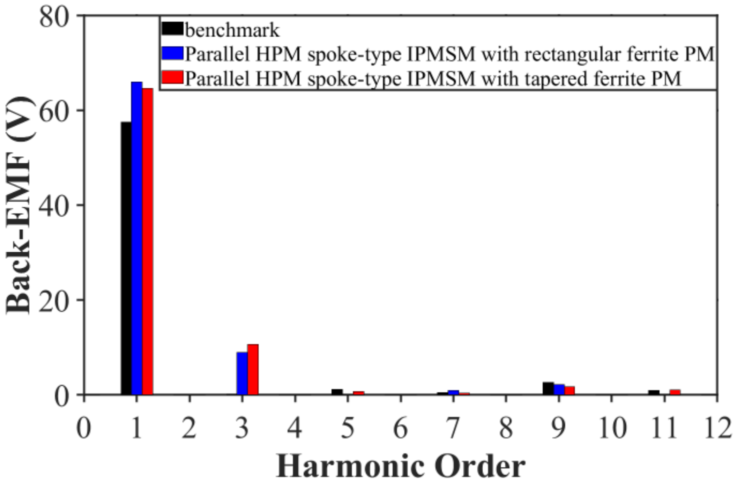

(b)

Fig. 2.15. Comparison of open circuit back EMFs at 2100 r/min. (a) Waveforms. (b) Spectra.

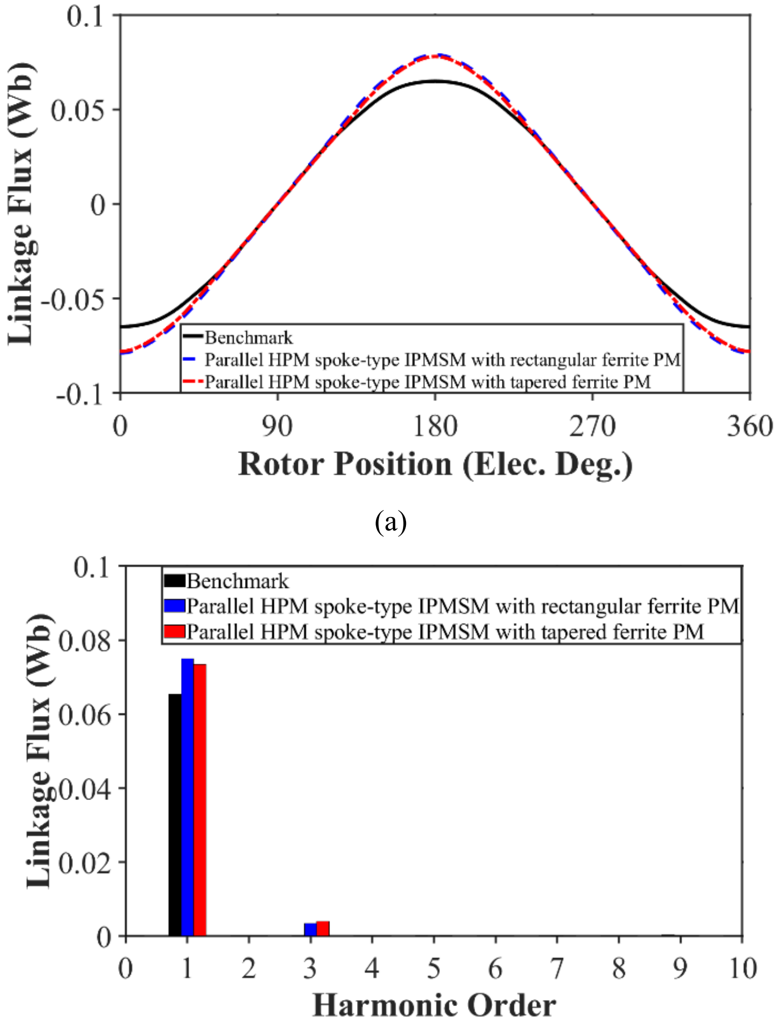

(a)

(b)

Fig. 2.16. Comparison of open circuit flux linkages. (a) Waveforms. (b) Spectra.

2.4. Mechanical Strength and Demagnetization

As a high volume of FEPM is used in the proposed parallel HPM spoke-type IPMSM with tapered FEPMs, a high mechanical strength and reliability at high speed is required. Therefore, for the sake of fair PM volume comparison, the thicknesses of the ribs are adjusted to achieve the same stress level as the benchmark. Fig. 2.17 presents the von-mises stress distributions of benchmark and the proposed machine at 10000 r/min. As can be seen, the maximum stress on outer rib in both machines reach to ~283 MPa which implies the safety factor of 1.59 at the maximum speed.

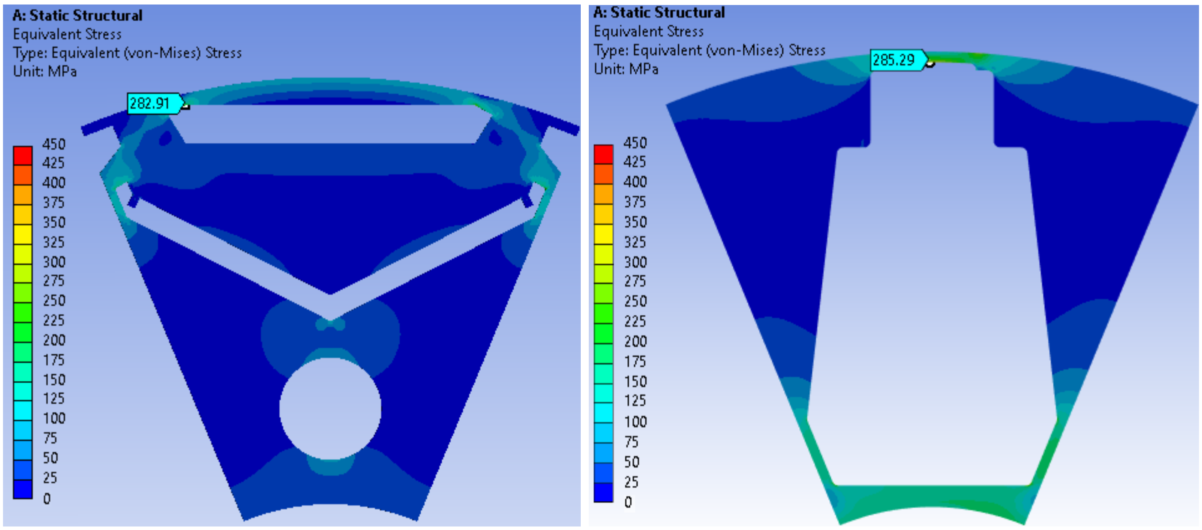

(a) (b)

Fig. 2.17. Comparison of von-mises stress distributions at 10000 r/min. (a) Benchmark. (b) Parallel HPM spoke-type IPMSM with tapered FEPM.

Furthermore, in contrast to REPM, FEPM is at a higher risk of irreversible demagnetization at low temperatures. Meanwhile, the high energy-product REPM in a parallel HPM configuration can reduce the working point of low-coercive FEPM or intensify its demagnetization vulnerability. It is worth mentioning that in literature the combination of low temperature and high d-axis current (overload condition) is used for the demagnetization withstand capability analysis of FEPMs. However, the suggested overload current varies from a low ratio, e.g. 1.3 times and 1.5 times of the rated current in [WU17B] and [ZHU17B], and a more common ratio, e.g. 2 times of the rated current in [YU19], [DU20], [ZHE21A], to a higher ratio, e.g. 2.5 times and 3 times of the rated current in [MA20] and [CHE23]. Therefore, for a comprehensive investigation of the demagnetization withstand capability of FEPMs in the proposed HPM machine, 2 times and 3 times of the rated d-axis currents are applied at -20 °C of temperature as shown in Fig. 2.18. As can be seen, a small region of FEPM near the

REPM is demagnetized when the triple of rated d-axis current is injected. It should be noted that the TDK-FB13B FEPM has a knee point of 0.04 T in its B-H curve at this temperature.

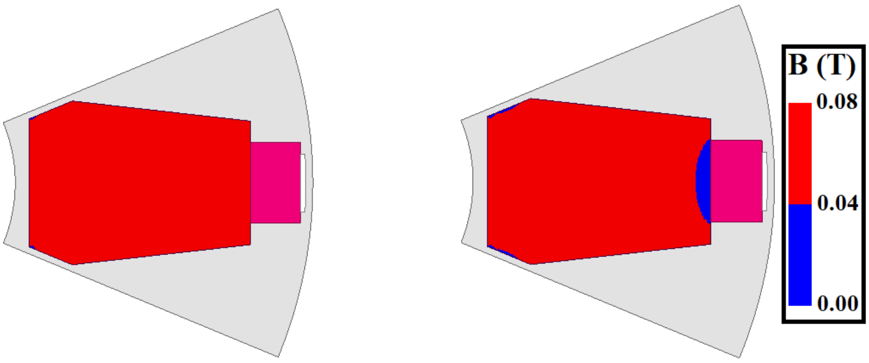

(a) (b)

Fig. 2.18. Demagnetization withstand capability of FEPM at -20 °C. (a) Twice of rated d-axis current. (b) Triple of rated d-axis current.

2.5. Experimental Validation

To validate the FEA results, a small size 24-slot/8-pole (24s8p) IPMSM is manufactured as shown in Fig. 2.19. This machine is optimized at 40 W copper loss of active part with the main dimensional parameters as listed in Table 2.6. It is tested using the static and dynamic test benches as presented in Fig. 2.20. The static test is conducted to measure the cogging torque and static torque. However, the dynamic platform is used to measure the waveforms of back-EMF and transient torque.

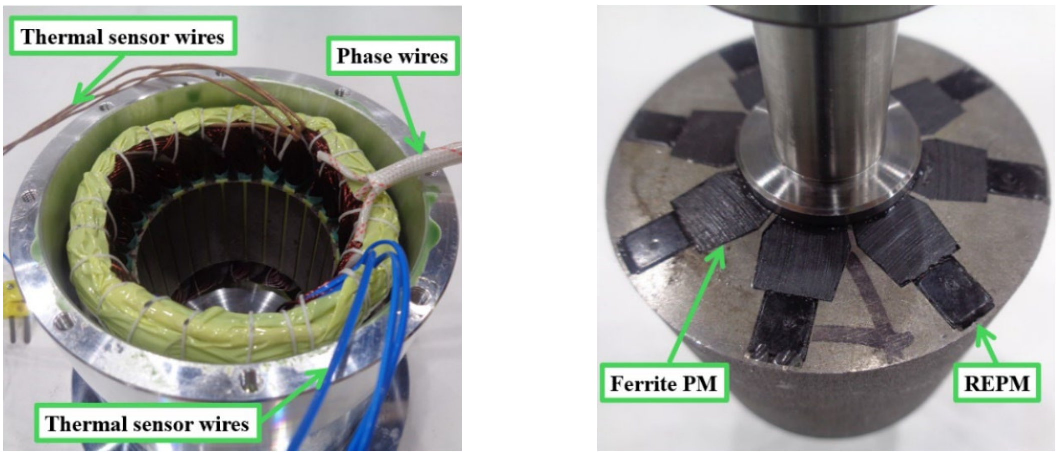

(a) (b)

Fig. 2.19. Prototype. (a) Stator. (b) Rotor.

Table 2.6. Main Dimensional Parameters of Prototype

Parameters	Values	Parameters	Values
Stator outer diameter	100 mm	Slot number	24
Stator inner diameter	63 mm	Pole number	8
Active stack length	50 mm	Turns per coil	60
Airgap length	1 mm	Phase resistance	1.6 Ω
Remanence of N28AH	1.075 T	Phase current	4 A_{max}
Remanence of TDK-FB13B	0.475 T		

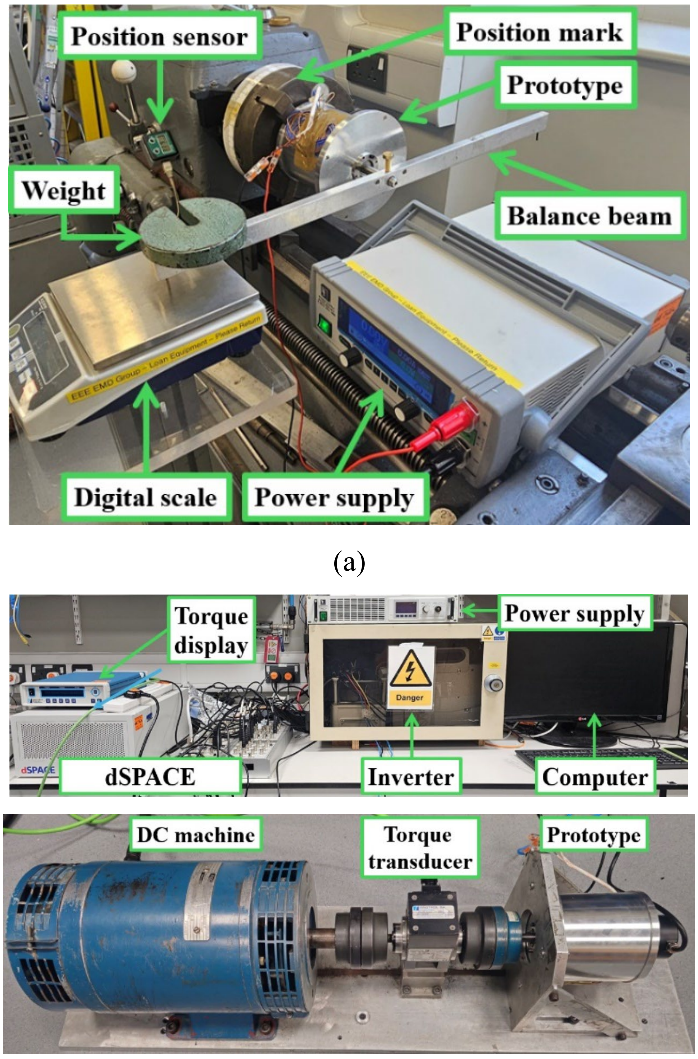

(a)

(b)

Fig.2.20. Experimental test benches. (a) Static test rig. (b) Dynamic test rig.

The open circuit line back-EMF waveforms and spectra obtained by FEA and measurement are compared at 750 r/min rotor speed in Fig. 2.21. Whereas the cogging torques are illustrated in Fig. 2.22. As can be seen, both measured back-EMF and cogging torque are in good agreement with FEA predictions. It is worth mentioning that as the cogging torque waveform in an electrical period consists of 6 periodic cycles, one-six of an electrical period is measured. In addition, Fig. 2.23 shows the variation of static torque with rotor position when DC current ($I_a = -2I_b = -2I_c = I_{DC}$) is injected into windings. The waveforms and spectra of FEA predicted and measured dynamic torques at 4 A_{max} and 250 r/min rotor speed are shown in Fig 2.24. Whereas the variation of predicted and measured average torque with current are compared in Fig. 2.25. As can be seen, the measured torques match with predictions.

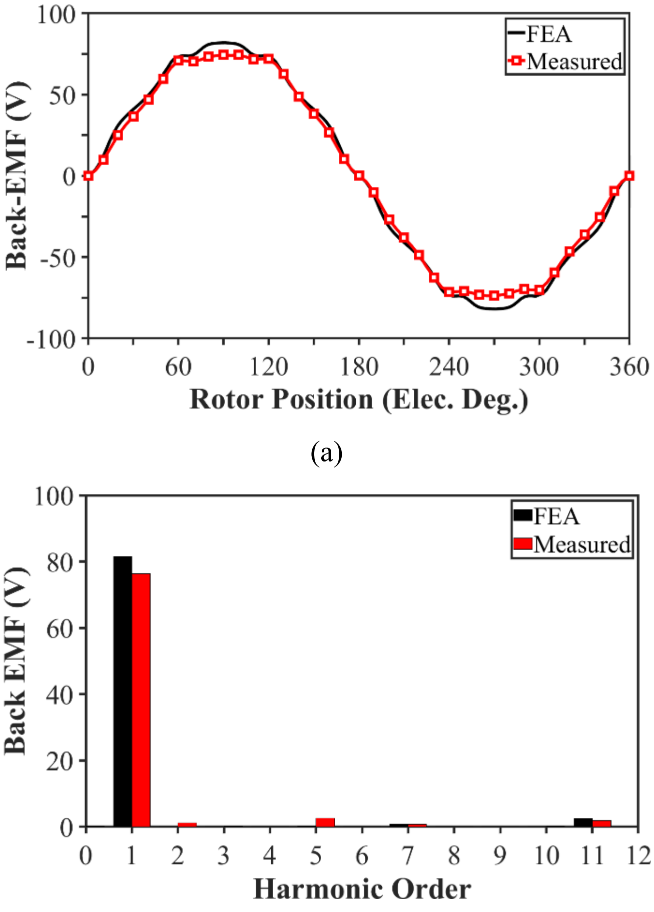

(a)

(b)

Fig. 2.21. FEA predicted and measured line back-EMFs at 750 r/min. (a) Waveforms. (b) Spectra.

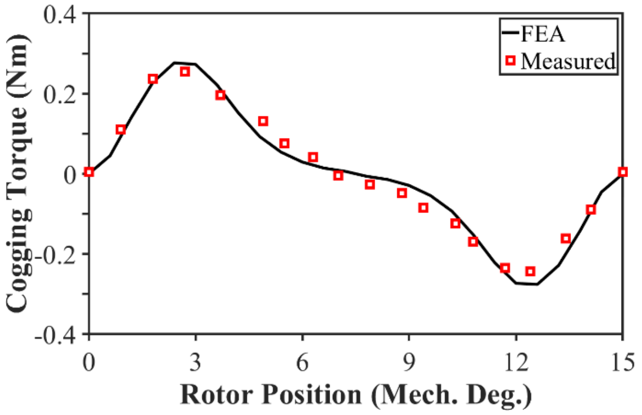

(a)

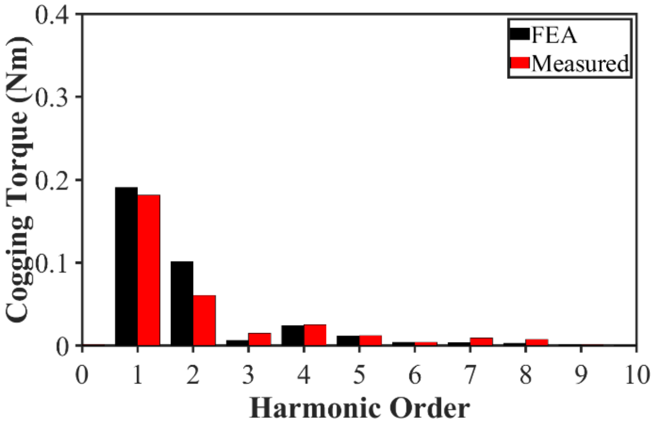

(b)

Fig. 2.22. FEA predicted and measured cogging torques at open circuit in one-six of an electrical period. (a) Waveforms. (b) Spectra.

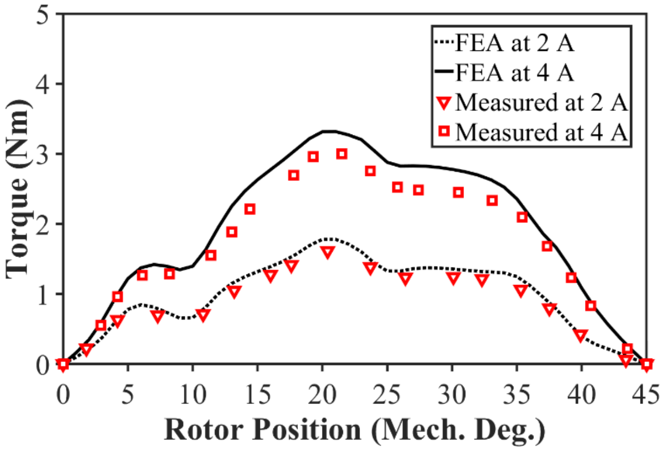

Fig. 2.23. FEA predicted and measured static torques at DC current equals to 2A and 4A.

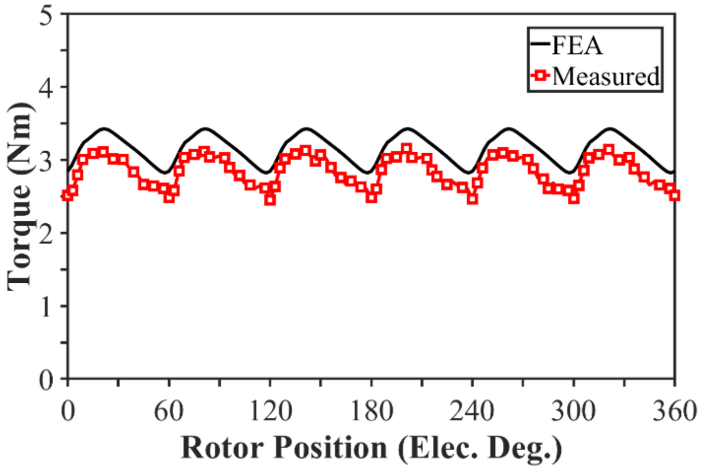

(a)

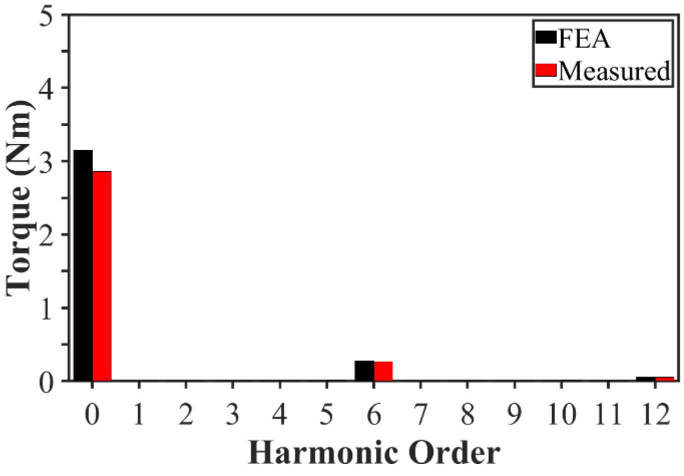

(b)

Fig. 2.24. FEA predicted and measured torques at 4 A_{max} and 250 r/min. (a) Waveforms. (b) Spectra.

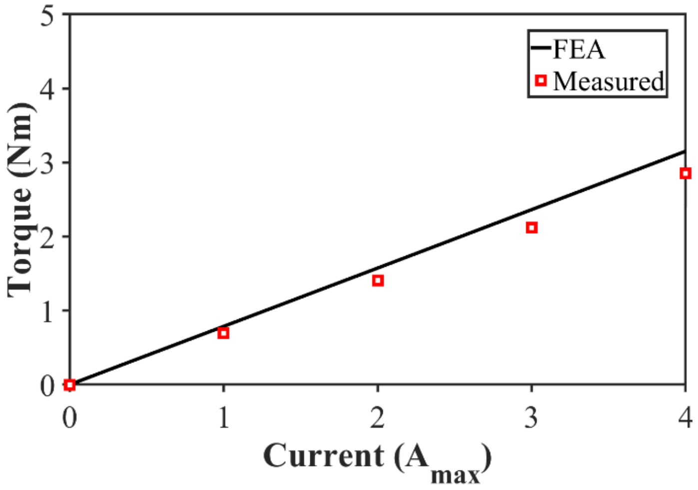

Fig. 2.25. Variation of FEA predicted and measured average torques at 250 r/min.

2.6. Conclusion

The application of tapering FEPM towards shaft and airgap in HPM spoke-type IPMSMs with the aim of torque enhancement is investigated in this chapter. The results show that the appropriate tapering FEPM towards airgap is beneficial to increase the torque per REPM volume ratio. It is revealed that by narrowing FEPM towards airgap, the increased cross section area of q-axis flux leads to a reduced saturation level, higher q-axis flux and inductance, and more reluctance torque component. Therefore, at the same total torque with an increased reluctance torque component, less REPM torque component is required leading to the reduction of REPM utilization. For a comprehensive investigation, both series and parallel HPM configurations are considered showing that the proposed tapered FEPM parallel HPM spoke-type IPMSM is the most promising cost-effective competitor to the benchmark as the torque per REPM volume ratio of this machine with 2.8 Nm/cm^3 is higher than those of the tapered FEPM series HPM counterpart with 1.24 Nm/cm^3 and benchmark with 1.12 Nm/cm^3. Assuming the cost of REPM being 10 times of FEPM, the total PM expense of the proposed parallel HPM spoke-type IPMSM with tapered FEPM is estimated to be 40 % less than that of benchmark. However, it is worth mentioning that the torque enhancement effect of tapering FEPM in a parallel HPM spoke-type IPMSM can be less than that of a series HPM counterpart. This is because the cross section area of q-axis flux in a parallel HPM spoke-type IPMSM is already increased by using a thinner REPM than the FEPM. Therefore, the q-axis flux and inductance of this machine are higher than those of series HPM counterpart leading to a higher reluctance torque component. Consequently, tapering FEPM can only lead to a further reluctance torque improvement to some extent.

CHAPTER 3

PARALLEL HYBRID MAGNET V-SHAPE SPOKE IPMSM

3.1. Introduction

A vast majority of industrial applications, e.g. electric vehicles (EVs), wind power generators, robots, home appliances, etc., are widely using high-performance PM machines, thanks to their high torque/power densities, and high efficiency, etc. [ZHU07], [KAZ23A], [KAZ18]. However, each application has specific requirements to be satisfied which can prioritize the selection of favourable PM machine topologies. For example, in EV application, different driving cycles demand high acceleration at low speed, and high maximum speed for highway driving. Meanwhile, a high coverage distance per charge and high reliability are also needed. Therefore, a PM machine with high torque density at low speed, wide speed range, high efficiency, and high reliability at all driving cycles can be a proper candidate for this application. Consequently, many researches on various topologies of PM machines for EV application can be found in literature, among which, interior PM synchronous machines (IPMSMs) play a distinguished role due to high torque density by utilizing rare-earth PMs (REPMs), wide speed range by high flux weakening capability, and ease of manufacturing [REF14], [YAN16]. Meanwhile, by searching into the EV industry, it can be found that different IPMSM topologies have been used in the wide-spread manufactured EVs on the market including V-shape PMs in Toyota Prius Gen III and Tesla Model 3, UI-shape PMs in Toyota Prius Gen IV, Δ-shape PMs in Nissan Leaf, Double V-shape PMs in Chevy Bolt, and Double I-shape PMs in BMW 225xe [RAM19].

Although the US Department of Energy (DoE) and the UK Advanced Propulsion Centre (APC) drafted the enhanced requirement targets for the future of EV traction machines [SHA20], the instabilities of REPM price and resources make a cost-effective design challenge towards the electrification transportation. Therefore, introducing high-performance PM machines at an acceptable cost has become a hot research topic in recent years. This target can be addressed by improving the torque per REPM usage either by a higher performance at the same REPM volume or the same performance at a lower REPM volume utilization. The application of Hairpin windings and asymmetric rotors are two well-known examples of developing higher performance at the same REPM usage. In the former method, the conventional stranded windings will be replaced by Hairpin windings to increase the slot fill factor, reduce DC resistance, and improve the torque which are achievable at the cost of higher AC resistance and AC losses at high speed [ZHA19]. However, the latter method employs asymmetric rotor structure to enhance the average torque at the same REPM consumption [ZHU22], [XIA22]. In this method, the maximums of PM torque and reluctance torque components are forced to merge to a specific current advancing angle. Then, as both torque components reach their maximum close to a unique current advancing angle, the summation of them will lead to a higher average torque. On the contrary, the hybrid permanent magnet (HPM) machines, which are introduced only around a dozen of years ago [CHE11B], [SHE12], [ISH13], [AFI14], employ two different PM materials including REPMs and ferrite PMs (FEPMs) in one structure. The outstanding benefit of these machines is to increase the torque per REPM usage by partially replacing the high-cost REPMs with low-cost FEPMs at the same performance [AFI16], [MA20], [JEO19]. These machines have become more attractive in the last few years as the price of REPMs unboundedly increased. Meanwhile, as two PM materials with different properties are used, their relative positions can categorize HPM machines into three configurations including parallel, series, and mixed [KAZ23B]. The name of parallel HPM configuration suggests that the flux paths of two magnets are in parallel. In other word, either of these two PMs will not see the other magnet as a magnetic reluctance of their flux path leading to a higher electromagnetic performance in the parallel HPM category [KAZ23C]. On the contrary, the performance of a series HPM configuration is expected to be lower than that of a parallel HPM counterpart due to a higher magnetic reluctance of flux path in this machine. To address this issue, increasing the output torque of a series HPM spoke-type IPMSM by using an asymmetric rotor is investigated in [ZHU23B]. However, on the upside, a series HPM configuration benefits from a higher tolerance against irreversible demagnetization of FEPMs by putting these magnets on the flux path of REPMs which increases the working point of these magnets [AFI16], [KAZ23D]. In contrast, the FEPMs in a parallel HPM configuration can suffer from a higher demagnetization risk by REPM leakage flux. As a solution to this drawback, the narrow flux barriers are used to reduce the REPM leakage flux circulating through low-coercive FEPMs in a parallel HPM machine in [WAN19]. In addition, in [ZHU17A], [DU20], the importance of proper positioning of two PM materials is emphasized by distancing FEPMs from airgap and putting REPMs in between to reduce the effect of armature reaction on the demagnetization of the FEPMs in a parallel arrangement of HPMs. Finally, the mixed configuration of HPM can naturally share the advantages and disadvantages of both HPM types. Therefore, it can be considered as a trade-off between the electromagnetic performance and the demagnetization withstand capability at the cost of structural complexity [ALQ21], [ZHE21A]. In addition to the electromagnetic performance and the demagnetization withstand capability of HPM machines, a high mechanical reliability at high-speed is also very important for EV applications which rises a mechanical concern in HPM machines due to the increased mass by a high FEPM usage.

Due to the increased popularity of HPM utilization in reducing the PM cost at the same performance, it has been used in various electrical machine topologies including switched flux PM (SFPM) machines [AFI14], [AFI16], [FAN17], [XIA18], vernier PM machines [XU17A], multi-layers PM assisted synchronous reluctance (PMASR) machines [WU17A], [YU19], and IPMSMs [LIU23B], [TU23], [SEO22]. In [MA20], the application of HPMs in a spoke-type PM machine and a two-layer IPMSM is investigated and compared to a REPM-based benchmark. It is shown that the HPM spoke-type IPMSM is the most cost-competitive design compared to the others due to the possibility of employing a high volume of low-cost FEPMs in each spoke. However, on the downside, it suffers from a low reluctance torque component and is not often suitable for high-speed applications because of mechanical concerns.

This chapter proposes a novel parallel HPM V-shape spoke IPMSM for EV application, in which, a single spoke per pole from the parallel HPM conventional spoke-type IPMSM is divided into two spokes per pole in a V-shape arrangement. In this regard, section 3.2 introduces the topology of the proposed HPM V-shape spoke IPMSM with a parallel configuration of two PM types. In section 3.3, the genetic algorithm using finite element analysis (FEA) is applied to optimize the rotor structure at the same torque performance as the benchmark using a lower volume of REPM. Then, in section 3.4, the electromagnetic performances of these two machines are compared in detail. Section 3.5 focuses on the mechanical strength at high speed and demagnetization withstand capability of FEPMs. Finally, sections 3.6 and 3.7 present the experimental results and the conclusion, respectively.

This chapter is published in IEEE - Transactions on Industry Applications [S. Kazemisangdehi, Z. Q. Zhu, Y. Zhou, H. Liu, L. Chen, and L. Yang, "Novel parallel hybrid rare-earth and FEPMs in V-spoke interior PM synchronous machine." *IEEE Transactions on Industry Applications,* Vol. 61, no. 2, pp. 2972-2982, 2025.] and presented in IEMDC2023 conference [S. Kazemisangdehi, Z. Q. Zhu, Y. J. Zhou, and H. Liu, "A new hybrid PM synchronous machine with V-shape spokes," in 2023 *IEEE Int. Electric Machines & Drives Conf. (IEMDC)*, 2023: IEEE, pp. 1-7.].

3.2. Parallel HPM V-shape Spoke IPMSM Topology

The topologies of the benchmark and the proposed parallel HPM V-shape spoke IPMSM are presented in this section.

3.2.1. Benchmark

Fig. 3.1 shows the cross section of a double V-shape IPMSM benchmark using the 48-slot/8-pole (48s8p) combination, and REPM type, i.e., NdFeB (N42UH). This benchmark is a commercial machine with specifications summarized in Table 3.1. As can be seen, this machine requires 199.08 cm^3 of REPM to generate the peak torque at peak current and rated speed.

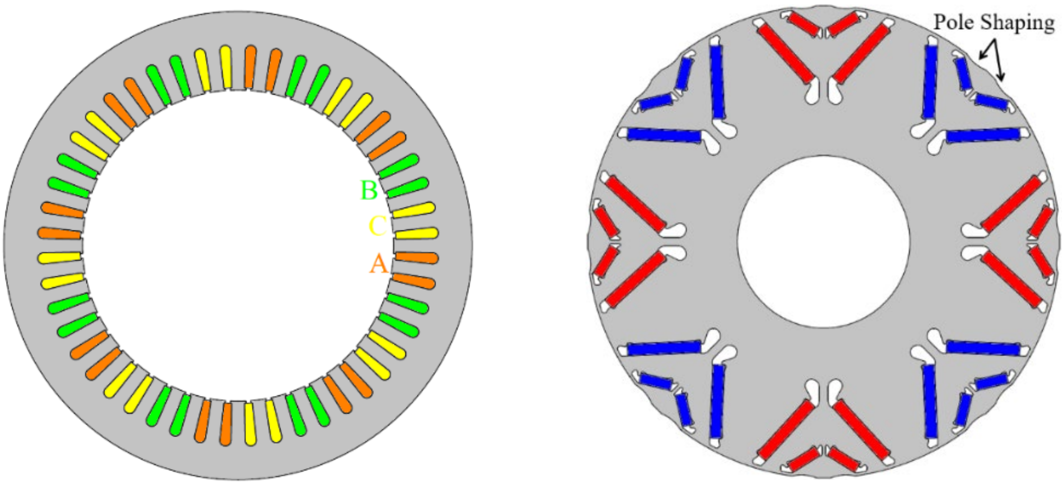

(a) (b)

Fig. 3.1. Topology of benchmark. (a) Stator. (b) Rotor.

Table 3.1. Specification of Benchmark IPMSM

Parameters	Values	Parameters	Values
Stator outer diameter (mm)	216	Peak torque (Nm)	300
Stator inner diameter (mm)	143.6	Rated torque (Nm)	150
Rotor outer diameter (mm)	142.2	Peak speed (r/min)	15000
Rotor inner diameter (mm)	52	Rated speed (r/min)	5000
Stack length (mm)	116	Peak current (A_{rms})	500
Airgap length (mm)	0.7	Rated current (A_{rms})	250
Skew angle – (6 steps V-skew) (degree)	5	Number of conductors per slot	8
REPM volume (cm^3)	199.08	Number of parallel branches	4

3.2.2. Parallel HPM V-shape spoke IPMSM Concept

Fig. 3.2 compares the proposed design with a parallel HPM conventional spoke-type IPMSM. As can be seen, each pole of the proposed machine consists of two spokes which is twice the number of spokes per pole in the conventional counterpart. Fig. 3.3 illustrates two design features of the proposed HPM machine. As can be seen in Fig. 3.3 (a), the possibility of stepping technique (verge introduction) in the proposed design can increase the integrity and reliability of rotor by leaning FEPMs to the strong core pillar via the introduced verge. Therefore, the increased mass of PMs would not lead to a higher von-mises stress on the ribs at high speed. However, the mechanical strength of the parallel HPM conventional spoke-type IPMSM is expected to be low due to the reliance on narrow ribs as shown in Fig. 3.2 (b).

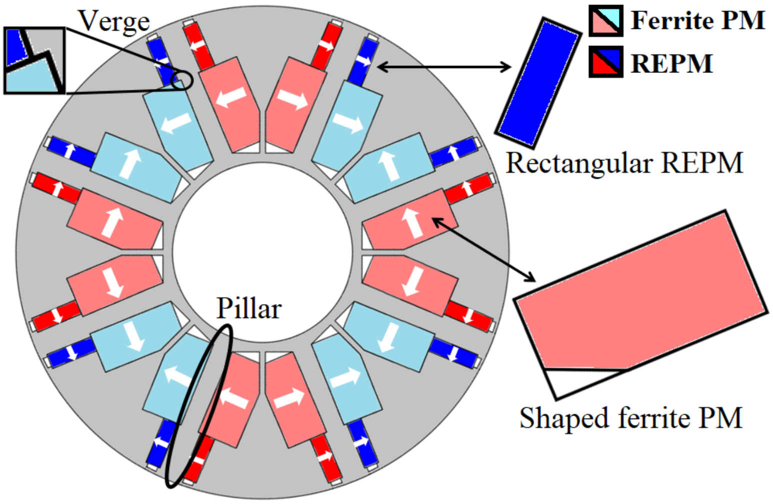

(a)

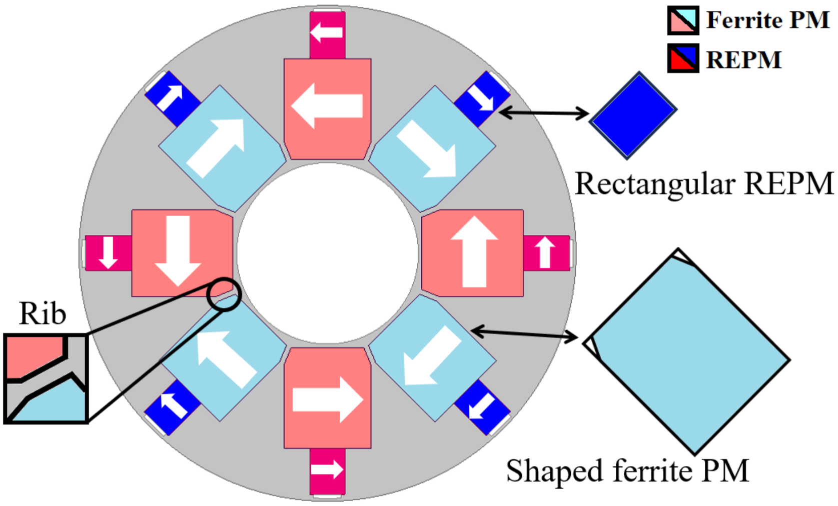

(b)

Fig. 3.2. Comparison of topologies. (a) Proposed parallel HPM V-shape spoke IPMSM. (b) Parallel HPM conventional spoke-type IPMSM.

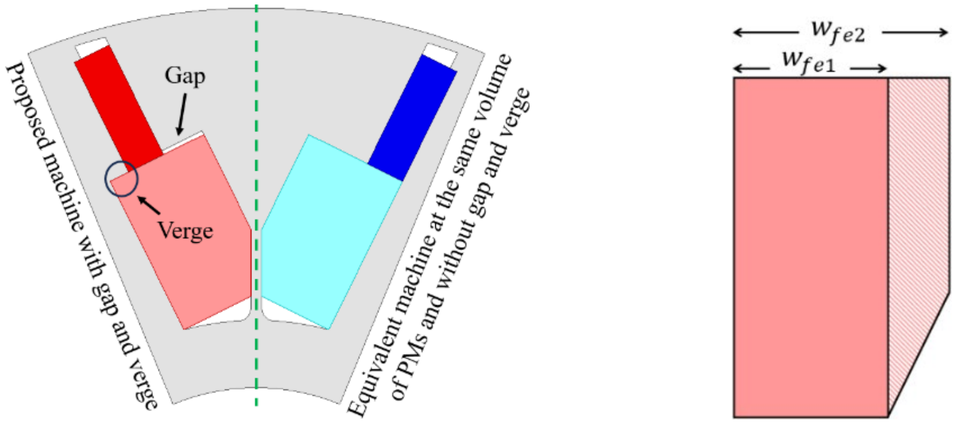

(a) (b)

Fig. 3.3. Features of the proposed HPM machine. (a) Introduction of verge and gap. (b) Thicker FEPM utilization due to the magnet shaping.

Therefore, the proposed parallel HPM V-shape spoke topology is expected to be more reliable for high-speed EV application. In addition, if FEPM was limited to a rectangular shape, a thinner PM should be used due to the geometrical limits. However, by employing the shaped FEPMs, a thicker magnet can be used as shown in Fig. 3.3 (b). Therefore, FEPMs are shaped from the shaft side to improve the feasibility of a higher FEPM volume utilization. Figs. 3.4 (a) and (b) show the flux paths of two magnet types (as will be shown later, it is achievable by open circuit flux lines and flux density vectors) and the equivalent magnetic circuit of the parallel HPM V-shape spoke IPMSM, respectively. It can be seen by selecting one PM type that the produced flux by either FEPM or REPM flows through another PM with the same PM material meaning that they are in series, i.e., the FEPM flux flows through a second FEPM and that of a REPM flows through a second REPM. However, considering the two PM types, the produced flux by either FEPM or REPM does not flow through a PM with different material, i.e., HPMs are in parallel.

The reluctances of the equivalent magnetic circuit in Fig. 3.4 (b) can be expressed as:

$$R_g = \frac{L_g}{\mu_0 S_g} \tag{3.1}$$

$$R_{nd1} = R_{nd2} = \frac{W_{nd}}{\mu_0 \mu_r S_{nd}} \tag{3.2}$$

$$R_{fe1} = R_{fe2} = \frac{W_{fe}}{\mu_0 \mu_r S_{fe}} \tag{3.3}$$

where L_g is the airgap length, W_{nd} and W_{fe} are the thicknesses of REPM and FEPM, S_g is the airgap cross section, and S_{nd} and S_{fe} are the surface areas of REPM and FEPM in their magnetization direction, respectively. In addition, μ_0 and μ_r are the air permeability and the relative permeability.

From the equivalent magnetic circuit and considering that the two REPMs are in the same size, and the two FEPMs are identical, it can be concluded that:

$$\emptyset_{fe} = \emptyset_{fe1} = \emptyset_{fe2} = \frac{F_{fe1}}{R_{fe1}} = \frac{F_{fe2}}{R_{fe2}} = \frac{F_{fe}}{R_{fe}} \tag{3.4}$$

$$\emptyset_{nd} = \emptyset_{nd1} = \emptyset_{nd2} = \frac{F_{nd1}}{R_{nd1}} = \frac{F_{nd2}}{R_{nd2}} = \frac{F_{nd}}{R_{nd}} \tag{3.5}$$

$$\emptyset_{g} = \emptyset_{1} + \emptyset_{fe} - \emptyset_{2} \tag{3.6}$$

where F_{fe} and F_{nd} are the MMF of FEPMs and REPMs, and $\emptyset_{fe}$, $\emptyset_{nd}$, and $\emptyset_{g}$ are the FEPM flux, the REPM flux, and the total flux linkage, respectively.

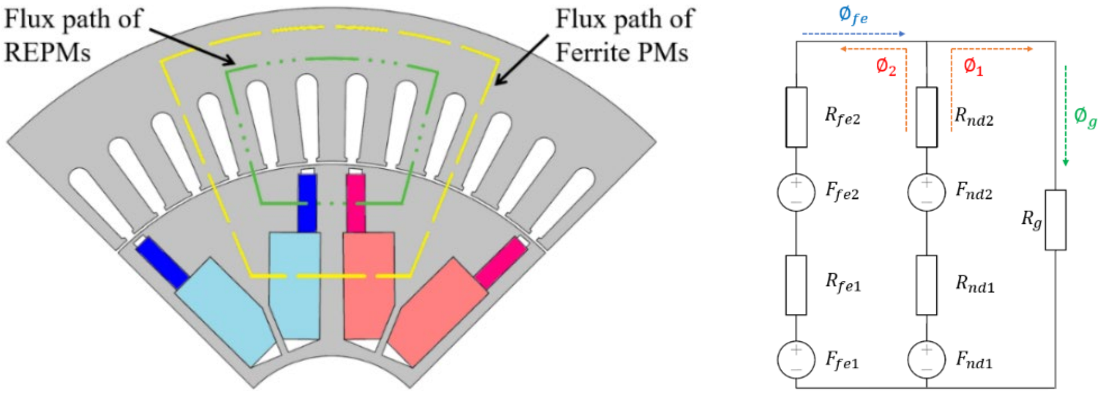

(a) (b)

Fig. 3.4. Magnetic flux path and equivalent magnetic circuit of parallel HPM V-shape spoke IPMSM. (a) Flux paths of PMs. (b) Equivalent magnetic circuit.

As shown in Fig 3.4 (b) and presented in (3.6), the flux produced by REPM can be divided into the REPM flux linkage ($\emptyset_{1}$) flowing through the airgap and the REPM leakage flux ($\emptyset_{2}$) passing through the FEPMs in a parallel configuration of HPMs. On the one hand, the leakage flux of REPM ($\emptyset_{2}$) can reduce the FEPM flux linkage ($\emptyset_{fe}$) by lowering its working point or even cause irreversible demagnetization in some area of this magnet. On the other hand, the increased thickness range of the FEPM by shaping (as shown in Fig. 3.3 (b)) means a higher W_{fe} in (3.3) leading to a higher reluctance of FEPMs (R_{fe}). Consequently, this can lead to not only a higher contribution of FEPMs, but also a lower demagnetization risk in these magnets. In addition, the REPM encounters a higher magnetic reluctance in the parallel path leading to a reduced leakage flux ($\emptyset_{2}$) and increased REPM flux linkage ($\emptyset_{1}$).

3.3. Parallel HPM V-shape spoke IPMSM Optimization

A parallel HPM V-shape spoke IPMSM is designed using the benchmark specifications with the aim of PMs' cost reduction at the same torque production. To achieve this goal, the genetic algorithm using FEA is employed for the optimization. The same REPM material as the benchmark, i.e. NdFeB (N42UH), and the FEPMs (TDK-FB13B) are used in the proposed design. To only consider the effect of hybrid PM utilization, the overall dimensions, stator structure, specifications, and the rotor outer and inner radii are considered constant as presented in Fig. 3.1 and listed in Table 3.1. Consequently, only the rotor structure is re-optimized. The rotor design parameters and their optimum values are presented in Fig. 3.5 and Table 3.2, respectively. As can be seen, d_1 describes the displacement of REPM considering the FEPM alignment as the reference. Similarly, b_1 describes the displacement of barrier considering the REPM alignment as the reference. These parameters are added with the aim of verge introduction as discussed in previous section. Then, the equations for the thicknesses of REPM and barrier can be written as:

$$w_{nd} = d_2 - d_1 \tag{3.7}$$

$$w_b = w_{nd} - b_1 \tag{3.8}$$

In addition, the angle of V-shape local coordinate can be expressed related to the V-shape angle (θ_v) and the V-shape local coordinate position (x_c) as:

$$\theta_c = \tan^{-1}\left(\frac{R_{or}\sin(\theta_v)}{(R_{or}\cos(\theta_v)) - x_c}\right) \tag{3.9}$$

It is worth mentioning that the rotor is skewed with the same method as the benchmark for torque ripple reduction and the sake of comparison. Moreover, the thickness of gap (b_2) and those of ribs (W_{mr} and W_{or}) are defined based on mechanical concerns at high speed. Although the thinner ribs are required for mitigating the leakage flux, thicker ribs may be required for mechanical strengthening purpose at high-speed applications.

Following the parametric design as described in Fig. 3.5, an optimization is carried out at the maximum current (500 A_{rms}) and the rated speed (5000 r/min) to achieve the same peak torque (300 Nm) as the benchmark with lower volume of REPMs. The third objective is to minimize the torque ripple which is also required for EV application. Taking the importance of each objective into account, the optimization function is defined as follows:

$$\begin{cases}\text{Objectives: Max } [T_{out}],\ \text{Min } [V_{NdFeB}],\ \text{Min } [T_{ripple}] \\ \text{Selection criteria of optimum point: } T_{out} \geq 300 \text{ Nm},\ V_{NdFeB} < 199.08 \text{ cm}^3,\ T_{ripple} \leq 5.5\ \% \\ \text{Weighting factors: } K_{T_{out}} = 4\text{p.u.},\ K_{V_{NdFeB}} = 2\text{p.u.},\ K_{T_{ripple}} = 1\text{p.u.}\end{cases} \qquad (3.10)$$

Variables: Listed in Table 3.2.

where T_{out}, V_{NdFeB}, and T_{ripple} are the output torque, the volume of REPM, and the torque ripple, respectively.

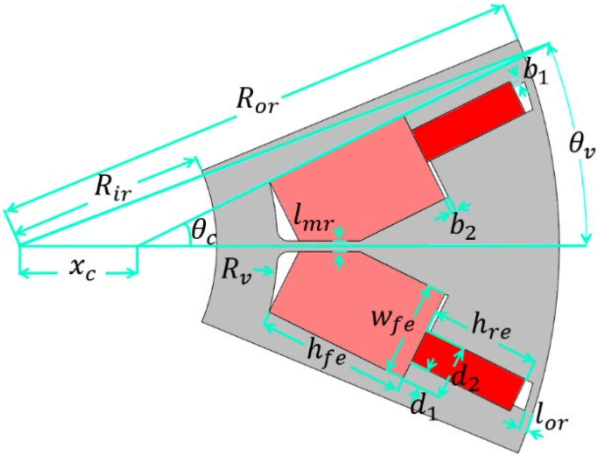

Fig. 3.5. Design parameters of parallel HPM V-shape spoke rotor structure.

Figs. 3.6 (a) and (b) show the optimization results of torque with REPM volume and torque with ripple, respectively. The cross section of the selected optimum design is illustrated in Fig. 3.6 (c). As can be seen, the desired 300 Nm torque is achievable when the volume of REPM is ~37% lower than that of the benchmark.

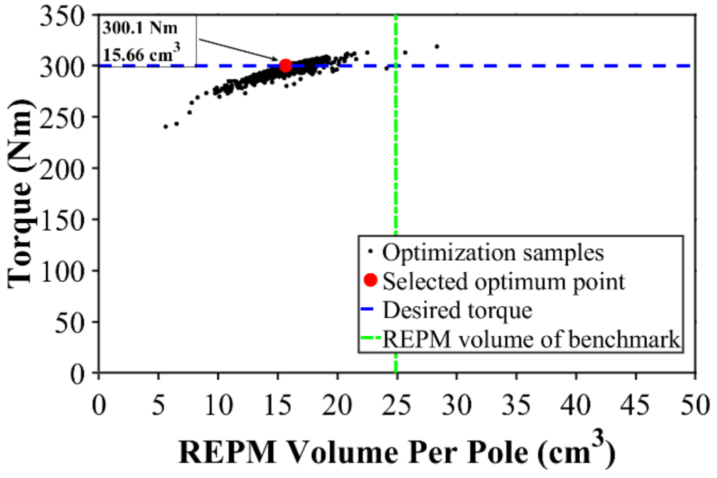

(a)

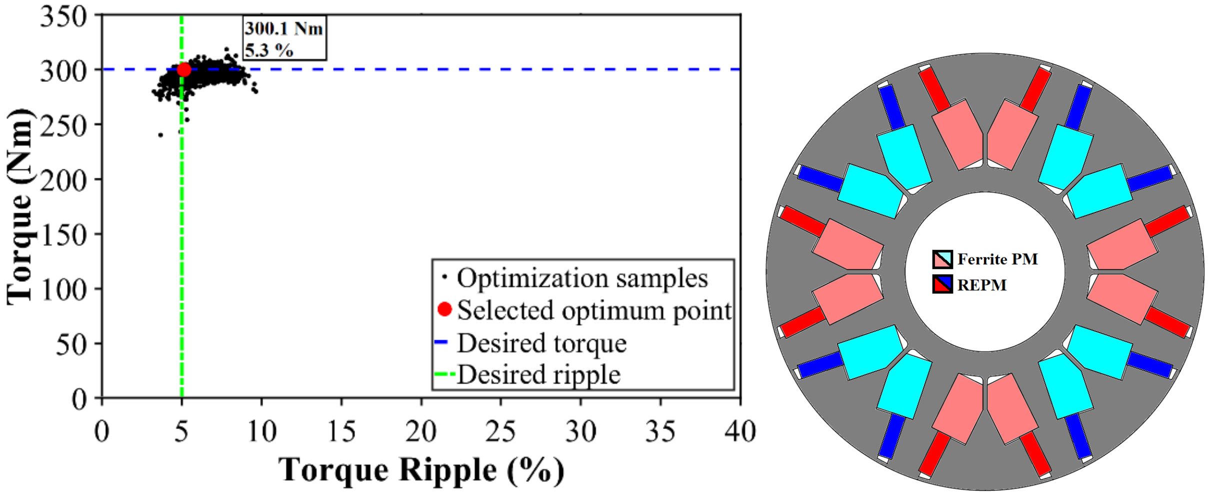

(b) (c)

Fig. 3.6. Optimization of proposed parallel HPM V-shape spoke IPMSM. (a) Torque with REPM volume. (b) Torque with ripple. (c) Cross section of selected optimum point.

Table 3.2. Design Parameters and Optimum Values of Parallel HPM V-shape Spoke IPMSM

Parameters	Symbols	Unit	Value
Rotor outer radius	R_{or}	mm	71.1
Rotor inner radius	R_{ir}	mm	26
V-shape inner radius	R_v	mm	34
V-shape angle	θ_v	degree	20.37
V-shape local coordinate angle	θ_c	degree	26.31
V-shape local coordinate position	x_c	mm	16.61
Width of FEPM	w_{fe}	mm	12.45
Height of FEPM	h_{fe}	mm	19.7
Height of REPM	h_{re}	mm	14.52
Displacement of REPM's 1st side	d_1	mm	2.44
Displacement of REPM's 2nd side	d_2	mm	7.09
Width of REPM	w_{nd}	mm	4.65
Displacement of barrier on top of REPM	b_1	mm	0.91
Width of barrier on top of REPM	w_b	mm	3.74
Thickness of gap on top of FEPM	b_2	mm	0.5
Width of middle rib	W_{mr}	mm	1.6
Width of outer rib	W_{or}	mm	1.1

3.4. Comparison of Performance

Fig. 3.7 compares the electromagnetic torque waveforms and spectra of the parallel HPM V-shape spoke and benchmark IPMSMs at 500 A_{rms} and 5000 r/min, respectively. As can be seen, both machines produce a similar output torque.

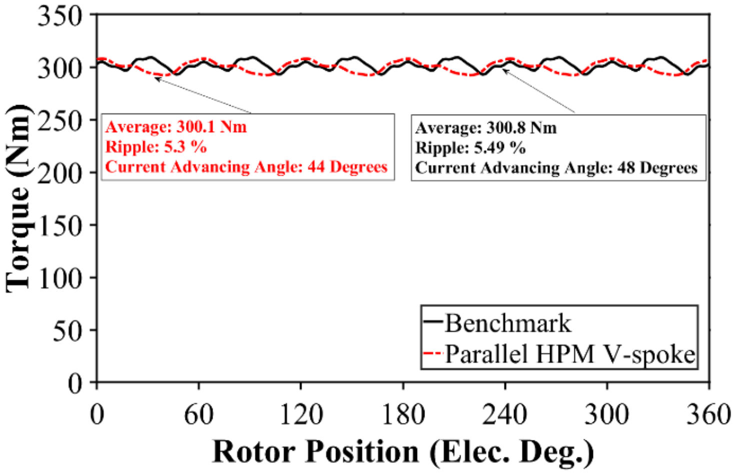

(a)

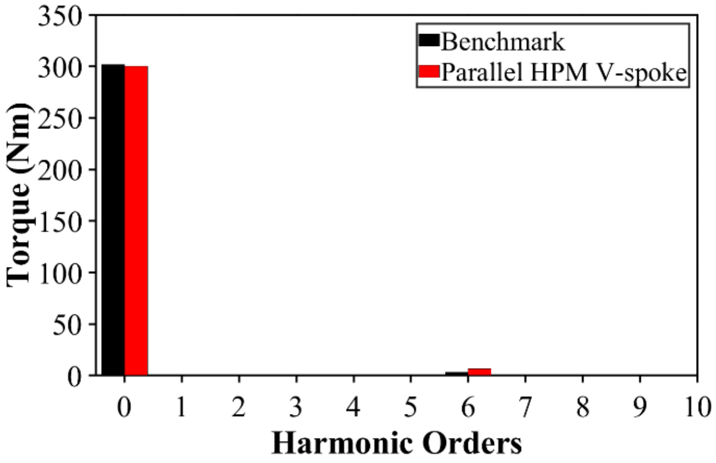

(b)

Fig. 3.7. Comparison of torques at 500 A_{rms} and 5000 r/min. (a) Waveforms. (b) Spectra.

In addition, Figs. 3.8 (a) and (b) show the variations of torques, and dq-axis inductances with current advancing angle of both machines at 500 A_{rms} and 5000 r/min, respectively. As can be seen, although the developed torques of both machines are the same, the torque variations with current advancing angle are different which results in different contributions of the torque components. It is known that the developed torque of a PM machine can be written as a summation of PM torque (T_{PM}) and reluctance torque (T_{rel}) as below:

$$T = T_{PM} + T_{rel} = \frac{3p}{2}\left(\psi_{pm} i_q + (L_d - L_q) i_d i_q\right) \tag{3.11}$$

where p is the number of pole pairs, ψ_{pm} is the PM flux linkage, L_d and L_q are d- and q-axis inductances, and i_d and i_q are d- and q-axis currents, respectively.

To accurately separate the torque components, the frozen permeability method (FPM) is used at 500 A_{rms} and 5000 r/min as shown in Fig. 3.9. As can be seen, the parallel HPM V-shape spoke IPMSM has a lower reluctance torque but a higher PM torque component than the benchmark. However, among 126.7 Nm of PM torque, 39.3 Nm is contributed by FEPMs. In addition, the suitability of these two machines for high-speed operation of EV application is investigated by comparing their torque-speed and power-speed characteristics in Fig. 3.10. As can be seen, both characteristics are matching each other with a good agreement.

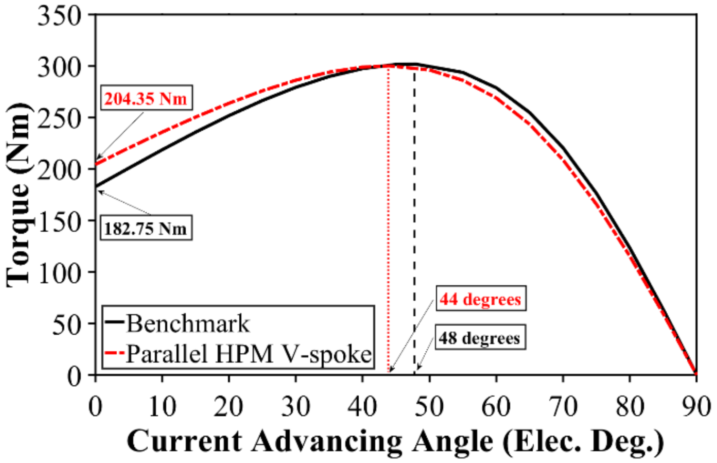

(a)

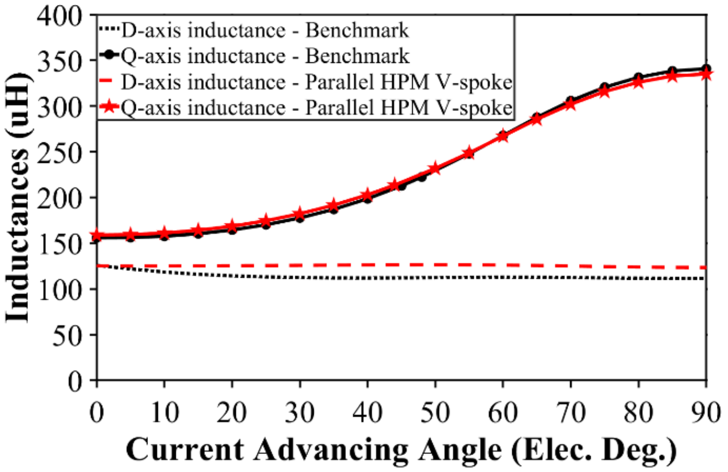

(b)

Fig. 3.8. Comparisons of torques and dq-axis inductances with current advancing angle at 500 A_{rms} and 5000 r/min. (a) Torques. (b) Dq- inductances.

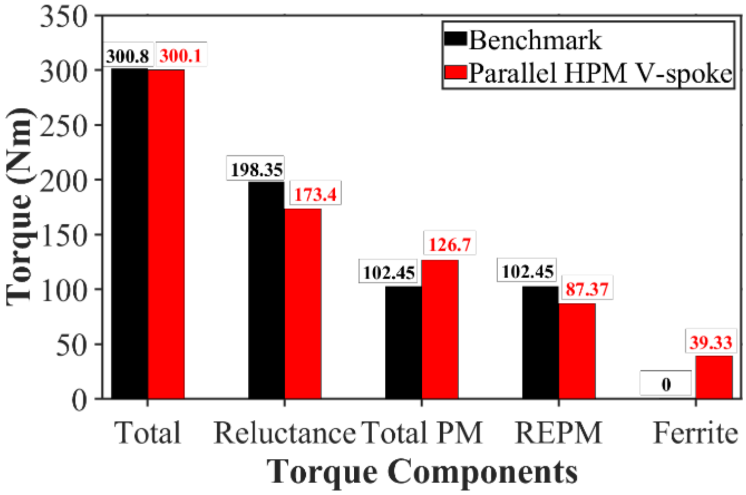

Fig. 3.9. Comparison of torque components at 500 A_{rms} and 5000 r/min.

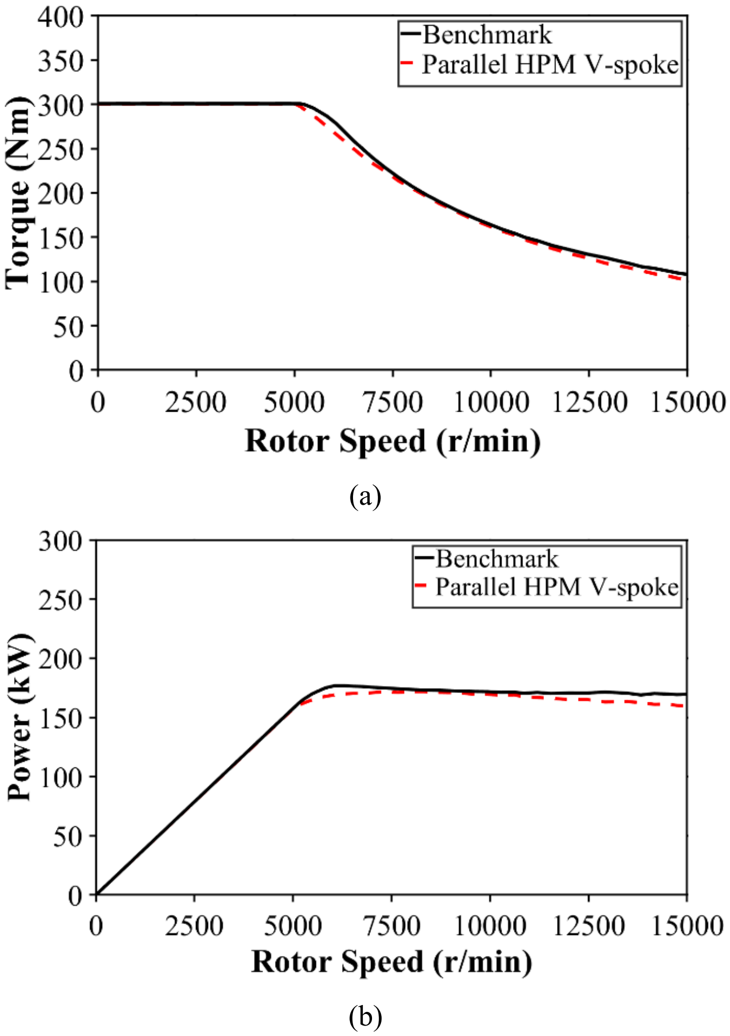

(a)

(b)

Fig. 3.10. Comparisons of speed related characteristics at 500 A_{rms}. (a) Torque-speed. (b) Power-speed.

Meanwhile, the copper loss, iron loss, and efficiency maps are compared in Fig. 3.11. As expected, the maps of copper loss are almost the same with a slight difference as the same winding specifications and stator structure are used. However, the iron loss at high-speed in the parallel HPM V-shape spoke IPMSM is higher than that of the benchmark due to the higher airgap flux density components as will be shown later. This difference in iron losses can reach to slightly more than 1kW at 15000 r/min. This is because the benchmark utilizes the rotor pole shaping method (Fig. 3.1 (b)) to reduce the harmonics of the airgap flux density. Meanwhile, this method is not applied to the proposed parallel HPM V-shape spoke IPMSM (Fig. 3.6 (c)). Finally, the efficiency maps (Fig. 3.11 (c)), are achieved using the equation below:

$$\eta = \frac{P_{out}}{P_{in}} \tag{3.12}$$

where η is the efficiency, P_{in} and P_{out} are the input and output powers, respectively.

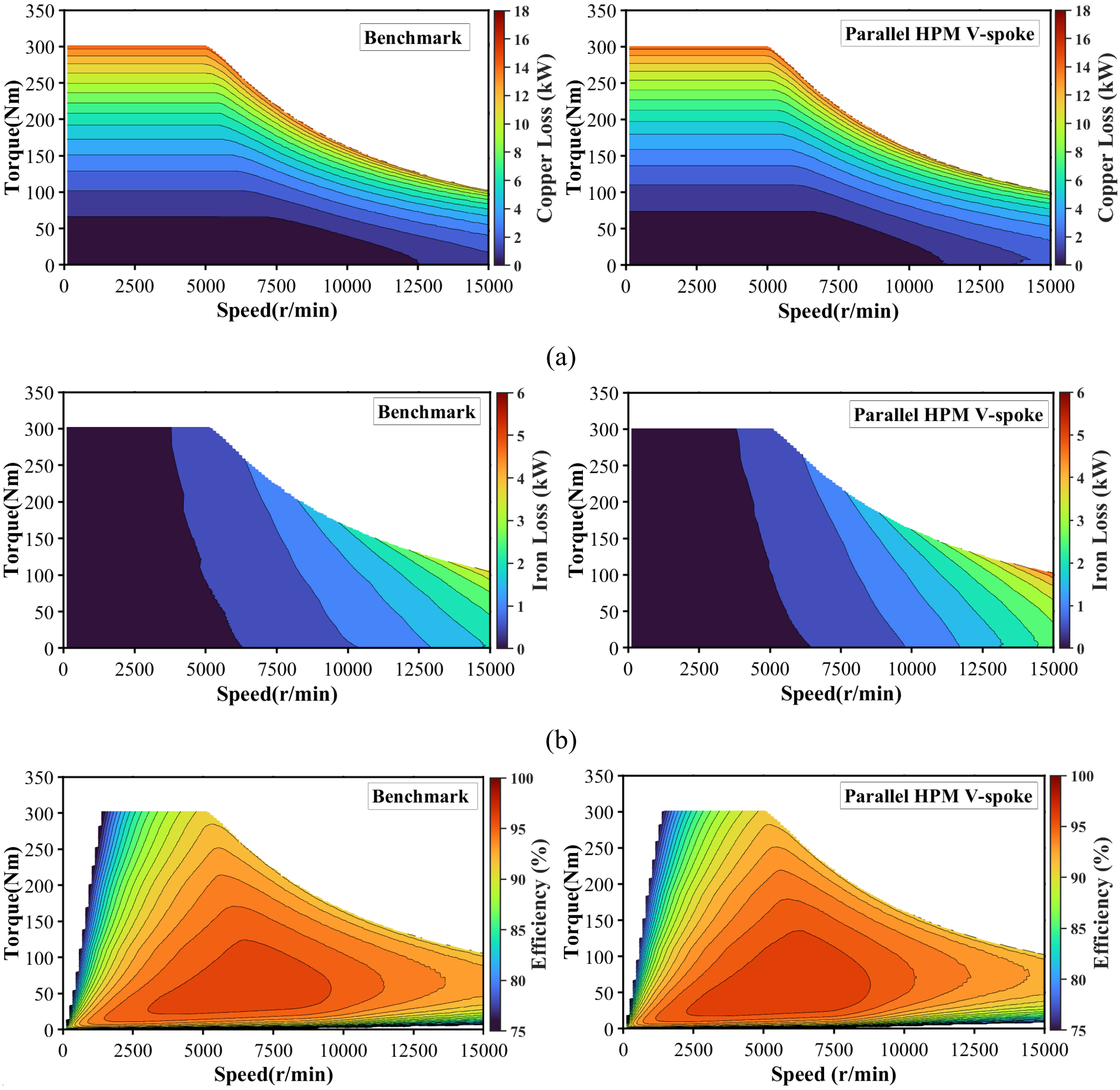

(a)

(b)

(c)

Fig. 3.11. Comparisons of loss and efficiency maps. (a) Copper loss maps. (b) Iron loss maps. (c) Efficiency maps.

As can be seen, the proposed parallel HPM V-shape spoke IPMSM benefits from a higher efficiency than benchmark at low speeds but suffers from a lower efficiency at high speeds due to the increase in iron loss.

Figs. 3.12 and 3.13 compare the open circuit airgap flux densities and back-EMFs at 5000 r/min rotor speed. As can be seen, the proposed design has higher fundamental components than the benchmark. In addition, as shown in Fig. 3.14, the parallel HPM V-shape spoke IPMSM also has a higher amplitude of the open circuit flux linkage than the benchmark leading to a higher PM torque utilization as presented in Fig. 3.9. Then, the flux density distribution and flux line comparisons of these machines are compared at open circuit in Fig. 3.15. By using Fig. 3.15 (b), the magnetic flux paths of two PMs in the proposed machine can be achieved as shown in Fig. 3.4 (a). Moreover, the open circuit saturation level on some stator teeth in the proposed parallel HPM V-shape spoke IPMSM has slightly increased to some extents. This is because the PM flux linkage of the proposed HPM machine is higher than that of the benchmark at the same tooth thickness and stator structure.

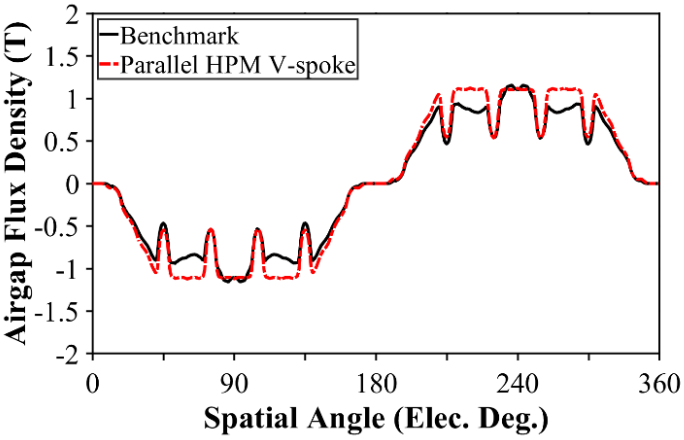

(a)

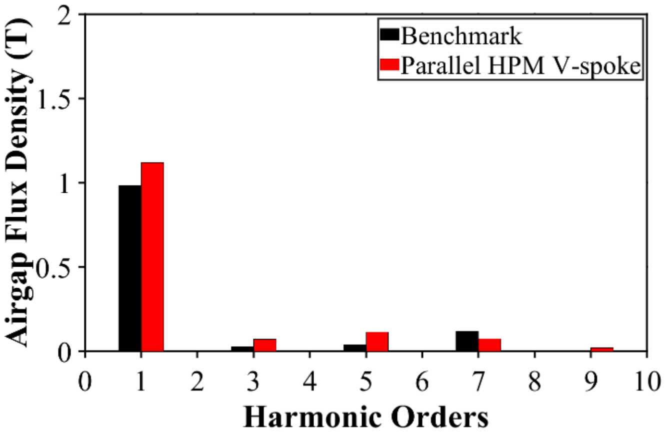

(b)

Fig. 3.12. Comparison of open circuit airgap flux densities. (a) Waveforms. (b) Spectra.

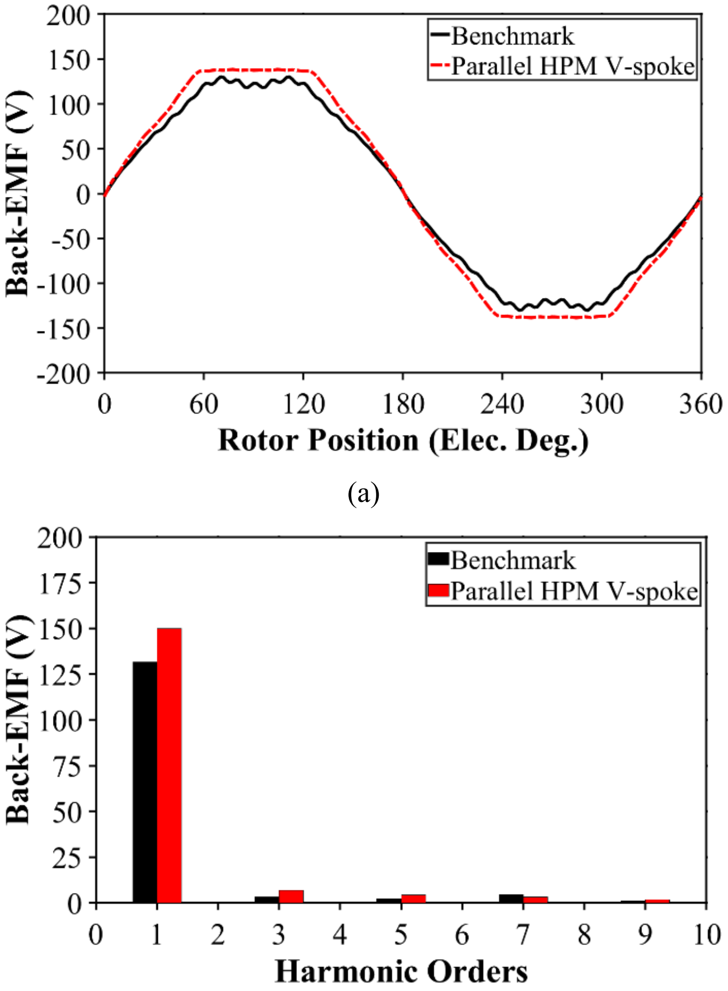

(a)

(b)

Fig. 3.13. Comparison of open circuit back-EMFs at 5000 r/min. (a) Waveforms. (b) Spectra.

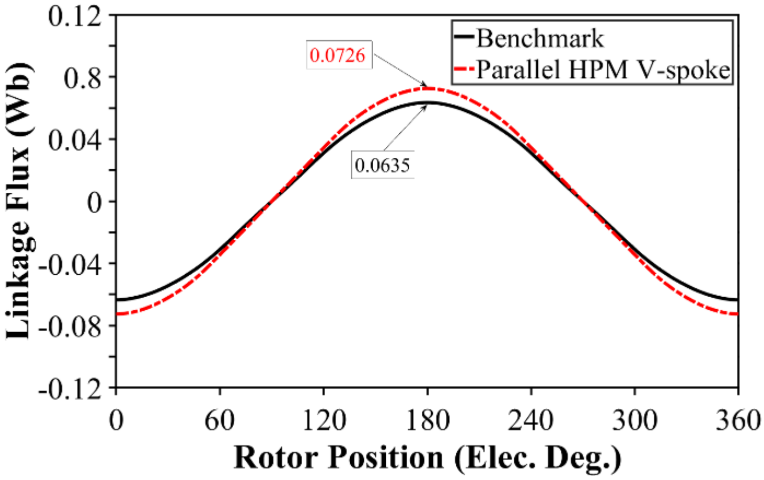

(a)

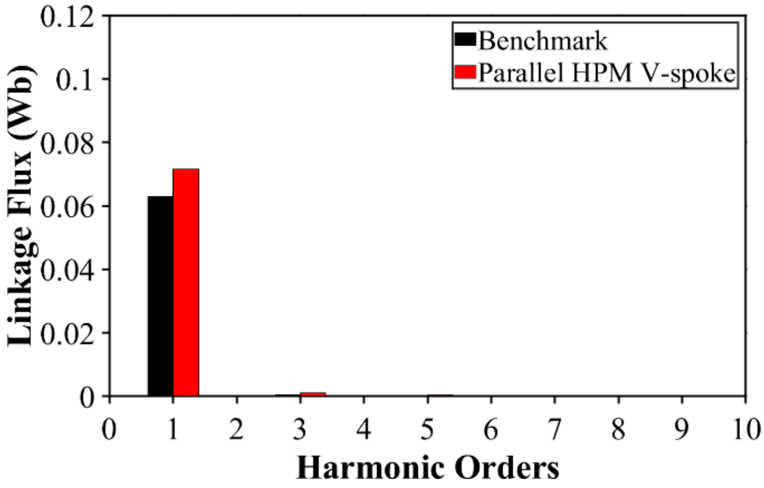

(b)

Fig. 3.14. Comparison of open circuit flux linkages. (a) Waveforms. (b) Spectra.

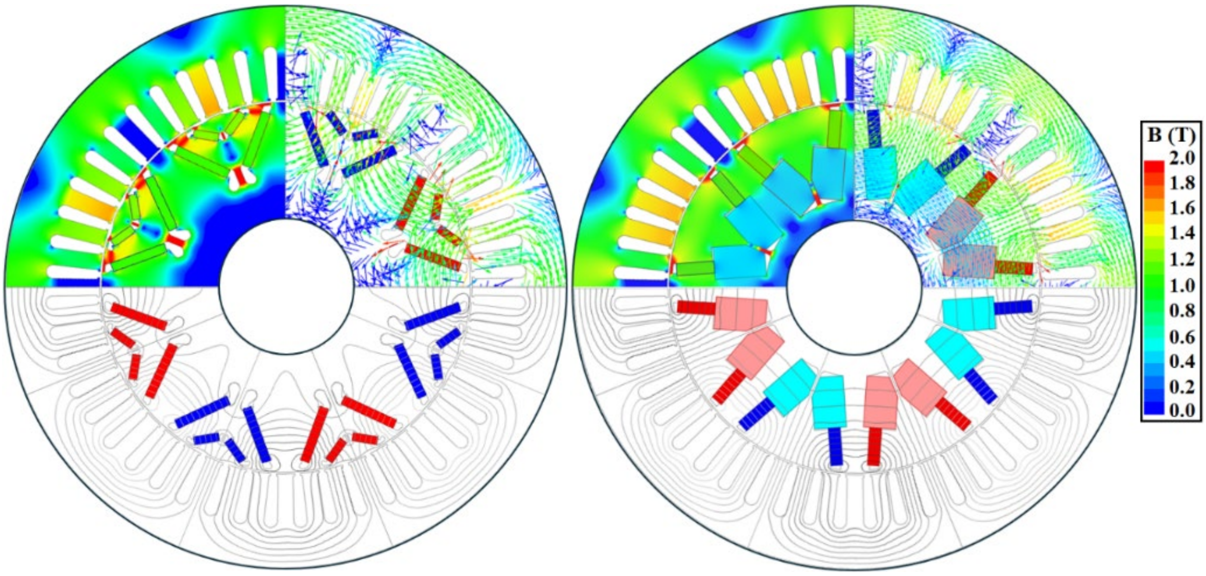

(a) (b)

Fig. 3.15. Comparison of flux lines and flux density distributions at open circuit condition. (a) Benchmark. (b) Parallel HPM V-shape spoke IPMSM.

In addition to the comparison of electromagnetic performances, a cost study has been carried out to emphasize the amount of active materials expenses which can be saved at the same performance as presented in Table 3.3. As can be seen, the volume of REPM is reduced about 37 % which leads to almost 30 % reduction of total PM cost. Moreover, the cost of electrical steel sheets is also reduced slightly due to the change of rotor design, whereas the cost of copper is constant. It is worth noting that the proposed HPM machine is optimized for the same torque at the same peak current, speed and size as the benchmark, leading to the same peak power density as listed in this table. However, the rated power density of the proposed machine is slightly higher at the rated current. On the one hand, at lower electrical loading, the on-load saturation reduces. On the other hand, the proposed design produces more PM flux linkage and therefore utilizes a higher PM torque contribution. As a result, its output torque and power are slightly higher. That is also the reason of its higher efficiency at low speed and under low electrical loading in Fig. 3.11.

Table 3.3. Comparisons of Performances and Costs in Parallel HPM V-shape Spoke and Benchmark IPMSMs

Parameters	**Unit**	**Benchmark IPMSM**	**Parallel HPM V-shape spoke IPMSM**
Volume of IPMSM	cm^3	4250.65	
Torque	Nm	300	
REPM volume	cm^3 (%)	199.08 (100 %)	125.3 (62.92%)
Torque per REPM volume	Nm/cm^3	1.507	2.394
Peak power density	W/cm^3	36.956	36.956
Rated power density	W/cm^3	18.478	18.848
FEPM volume	cm^3	-	431.263
REPM’s mass	kg	1.513	0.952
FEPM’s mass	kg	-	2.156
Total cost of PMs*	GBP (%)	68.085 (100 %)	48.231 (70.84%)
Copper mass	kg	6.356	6.356
Electrical steel sheet mass	kg	24.35	22.12
Cost of copper**	GBP	41.31	41.31
Cost of electrical steel sheet**	GBP	20.7	18.8

* Costs of REPM and FEPMs are 45 GBP/kg and 2.5 GBP/kg.

** Costs of Electrical steel and copper are 0.85 GBP/kg and 6.5 GBP/kg [DU20].

3.5. Mechanical Stress and Demagnetization

As discussed in Table 3.3, when substituting a percentage of REPM volume with FEPM, more volume and mass of FEPMs are required for the same torque. In addition, the low-coercive FEPMs can be at a higher risk of irreversible demagnetization by high-coercive REPMs in HPM machines. Therefore, the mechanical strength at high speed and the PM demagnetization withstand capability of the proposed parallel HPM V-shape spoke IPMSM and benchmark will be investigated in this section.

3.5.1. Mechanical Strength

Fig. 3.16 compares the von-mises stress distributions of both machines at 15000 r/min rotor speed when the contact regions of magnets with rotor core and that of the two magnet types are frictional. As can be seen, the proposed design with 429 MPa of maximum von-mises stress on outer rib has a similar stress to that of the benchmark with 443 MPa. Fig. 3.17 presents the variations of maximum von-mises stress on outer ribs of both machines at different speeds. Although the mass of PMs in the proposed HPM design with 3.108 kg is higher than that of the benchmark with 1.513 kg, the level of stress in both machines is almost equal.

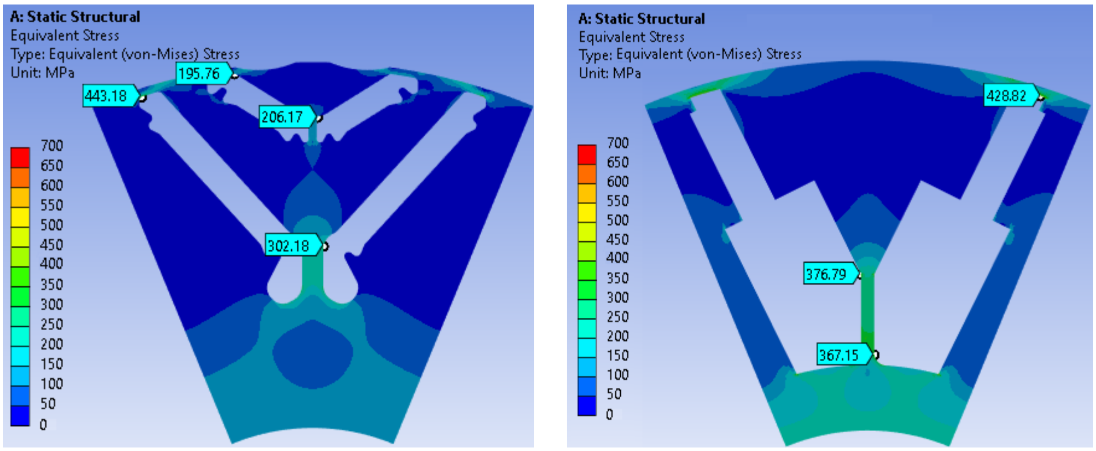

(a) (b)

Fig. 3.16. Comparison of von-mises stress distributions at 15000 r/min rotor speed. (a) Benchmark. (b) Proposed parallel HPM V-shape spoke IPMSM.

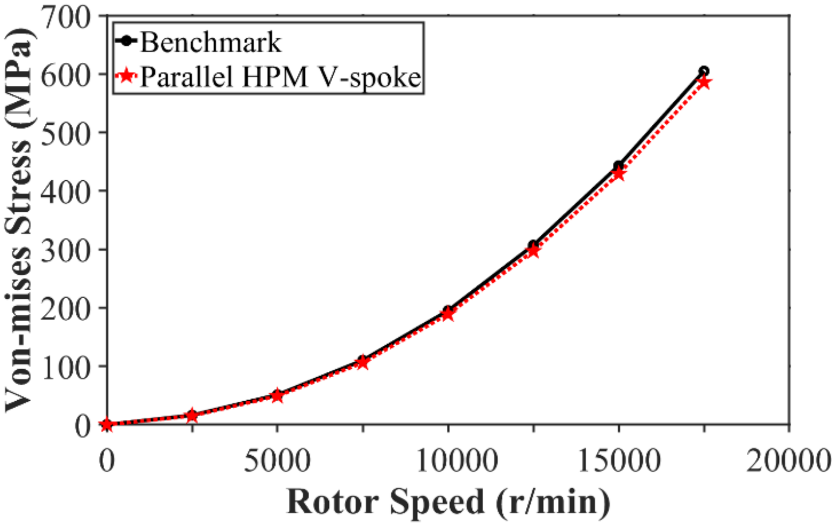

Fig. 3.17. Comparison of peak von-mises stresses on outer rib at different speed.

As discussed, the introduced verge of the proposed parallel HPM V-shape spoke IPMSM is beneficial to ban the movement of FEPMs by the strong rotor core pillar, when they tend to fly off due to the centrifugal force at high speed. Therefore, these PMs tend to rotate towards the radial axis but in opposite directions as shown in Fig. 3.18 (a). However, as these two FEPMs are in the same size, they put the same force on each other. Consequently, lower stress will be transferred to the outer ribs as shown in Fig. 3.18 (b). On the contrary, a higher stress on outer ribs can be found by removing the verges on FEPMs as shown in Fig. 3.18 (c). In this case, the strong rotor core pillar has no control on the movement of FEPMs, and thus, they can easily fly off. In addition, the mechanical effect of the introduced gap over the FEPMs can be revealed by comparing Figs. 3.18 (b) and (d). As can be seen, by removing the gap in Fig. 3.18 (d), a higher mechanical stress will be transferred to the outer ribs as the contact region between FEPMs and the central part of rotor core increases.

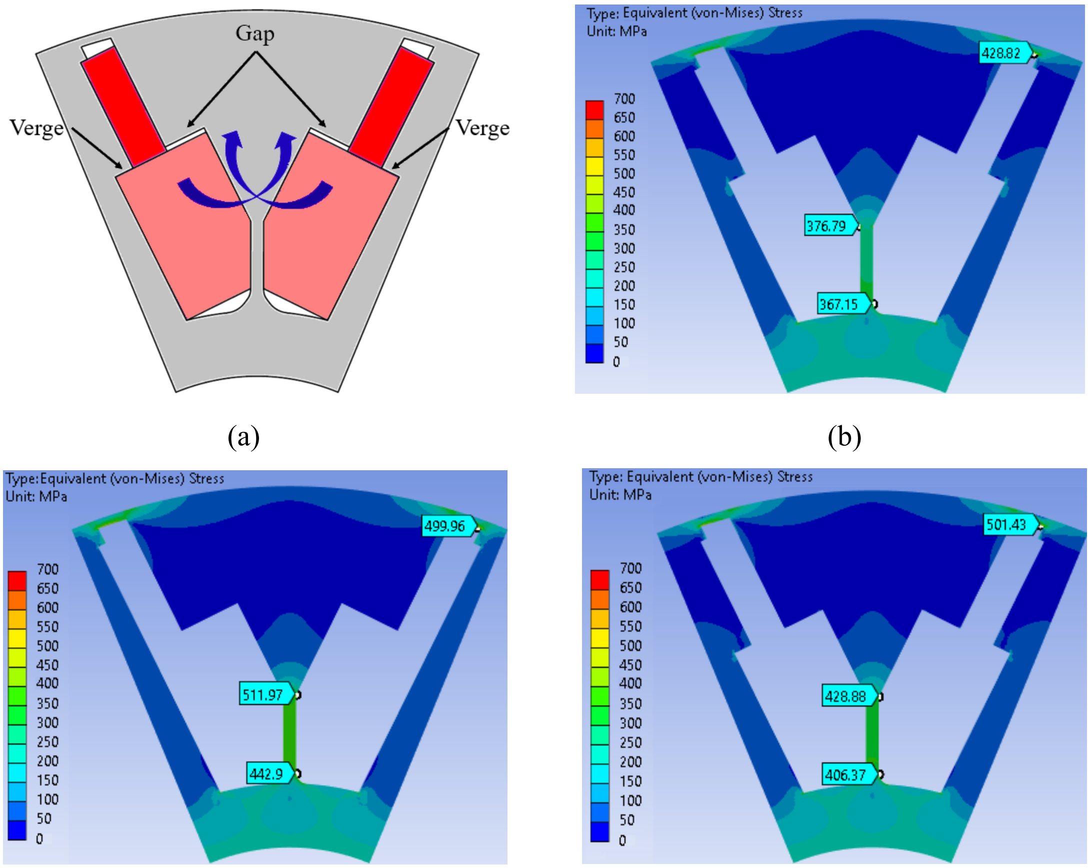

(a)

(b)

(c)

(d)

Fig. 3.18. Comparisons of von-mises stress distributions affected by verge and gap in the parallel HPM V-shape spoke IPMSM at 15000 r/min rotor speed. (a) Illustration of verge and gap. (b) Proposed design with verge and gap. (c) An equivalent design with the same volume of PMs and without verge. (d) An equivalent design with the same volume of PMs and without gap.

3.5.2. Demagnetization Withstand Capability of FEPMs

In the proposed HPM machines, where two types of PM materials are used in parallel, the REPMs can affect the demagnetization withstand capability of low-coercive FEPMs. Meanwhile, as FEPMs are more vulnerable to demagnetization at low temperature, this study is carried out at -20 ºC by applying multiple d-axis currents. It is worth noting that the knee point of B-H curve for TDK-FB13B FEPM at -20 ºC is 0.04 T. The maximum d-axis current can define the worst-case scenario in a demagnetization analysis. This current can be achieved using the active short circuit condition at high-speed operation as shown in Fig. 3.19 (a). At a certain time, the voltage pulse generator produces a signal to operate the switches and simulate the short circuit condition of AC current sources. Before fault, the proposed machine requires -619 A_{max} of d-axis current and 112.5 A_{max} of q-axis current (equivalent to the amplitude of 629 A_{max} and 79.7 Elec. Deg. of current advancing angle) at 15000 r/min to generate 104 Nm torque (Figs. 3.19 (b) to (d)). It is revealed that if the short circuit happens at 0.4 ms, the peak d-axis current reaches -1039 A_{max} (or -734.7 A_{rms}) which is almost triple of the rated current.

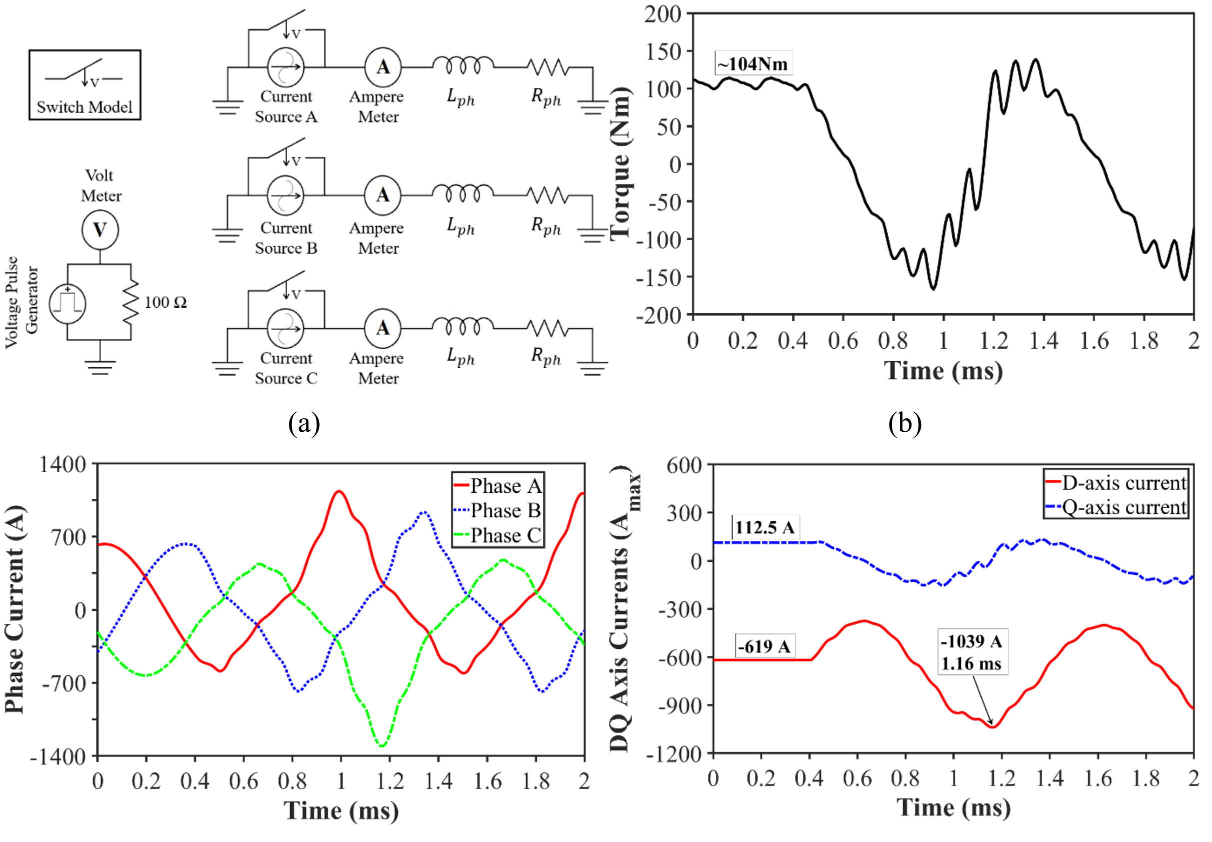

(a) (b)

(c) (d)

Fig. 3.19. Simulation of active short circuit at 15000 r/min in proposed HPM machine. (a) Circuit. (b) Torque. (c) ABC currents. (d) DQ-axis currents.

Therefore, Fig. 3.20 illustrates the decomposed flux density distribution of FEPMs into their magnetization direction under the above-mentioned condition. As can be seen, the FEPM is thick enough to tolerate extreme demagnetizing conditions, and only a small region of FEPM will be demagnetized mainly near the contact region to REPM. Consequently, to investigate the effect of REPM on the demagnetization of FEPMs, Fig. 3.21 investigates the decomposed flux density distribution of FEPMs under the same condition when REPMs are removed. Comparing Figs. 3.20 and 3.21, it can be concluded that the presence of a parallel REPM can make the FEPM be more vulnerable to demagnetization.

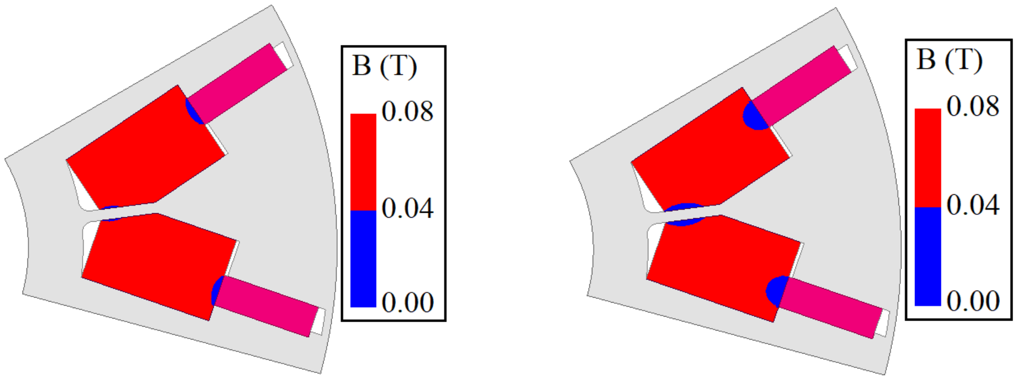

(a) (b)

Fig. 3.20. Demagnetization withstand capability of FEPM at -20 °C. (a) At twice of rated d-axis current. (b) At triple of rated d-axis current.

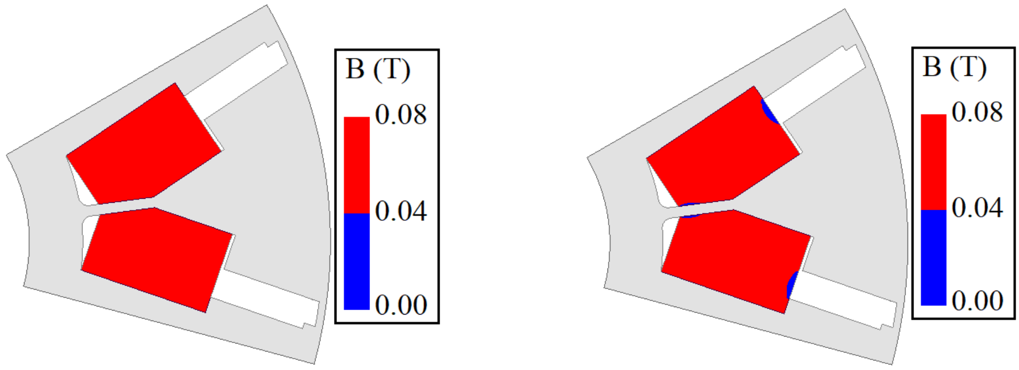

(a) (b)

Fig. 3.21. Demagnetization withstand capability of FEPM at -20 °C. (a) At twice of the rated d-axis current. (b) At triple of the rated d-axis current.

3.6. Experimental Validation

To validate the FEA results, a small size of the proposed parallel HPM V-shape spoke IPMSM with 24s8p is manufactured as shown in Fig. 3.22. This machine is optimized at 40 W copper loss of active part with the main dimensional parameters as listed in Table 3.4. It is tested using the static and dynamic test benches as presented in Fig. 3.23. The static test is conducted to measure the cogging torque and static torque. However, the dynamic platform is used to measure the waveforms of back-EMF and transient torque.

The line back-EMF waveforms and spectra obtained by FEA and measurement, are compared at 750 r/min rotor speed in Fig. 3.24. Whereas the open circuit cogging torques are illustrated in Fig. 3.25. As can be seen, both measured back-EMF and cogging torque are in good agreement with FEA predictions. It is worth mentioning that as the cogging torque waveform in an electrical period consists of 6 periodic cycles, one-six of an electrical period is measured. Fig. 3.26 shows the variation of static torque with rotor position when DC current (I_a = -2I_b = -2I_c = I_{DC} = 2 A) is injected into windings. The waveforms and spectra of FEA predicted and measured dynamic torques at 4 A_{max} and 250 r/min rotor speed are shown in Fig 3.27. As can be seen, the measured torque matches with prediction with an error rate of ~7.5%. Finally, the variation of predicted and measured average torques with current are compared in Fig. 3.28.

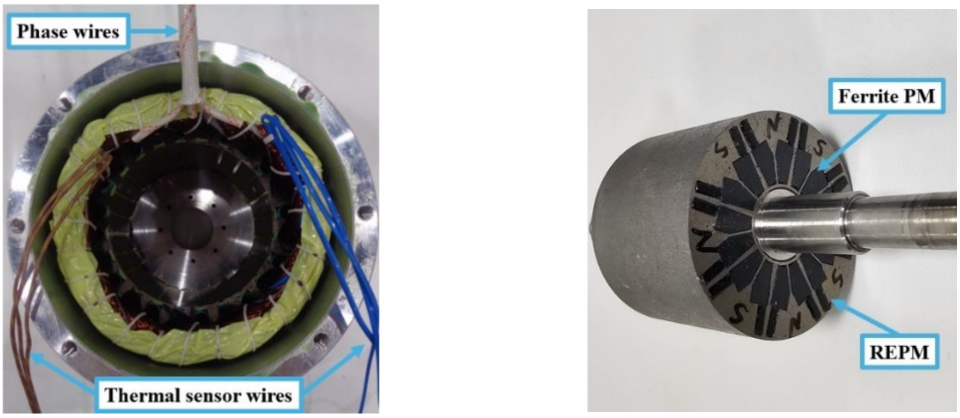

(a) (b)

Fig. 3.22. Prototype. (a) Stator. (b) Rotor.

Table 3.4. Main Dimensional Parameters of Prototype

Parameters	Values	Parameters	Values
Stator outer diameter	100 mm	Slot number	24
Stator inner diameter	63 mm	Pole number	8
Active stack length	50 mm	Turns per coil	60
Airgap length	1 mm	Phase resistance	1.6 Ω
Remanence of N42UH	1.31 T	Phase current	4 A_{max}
Remanence of TDK-FB13B	0.475 T		

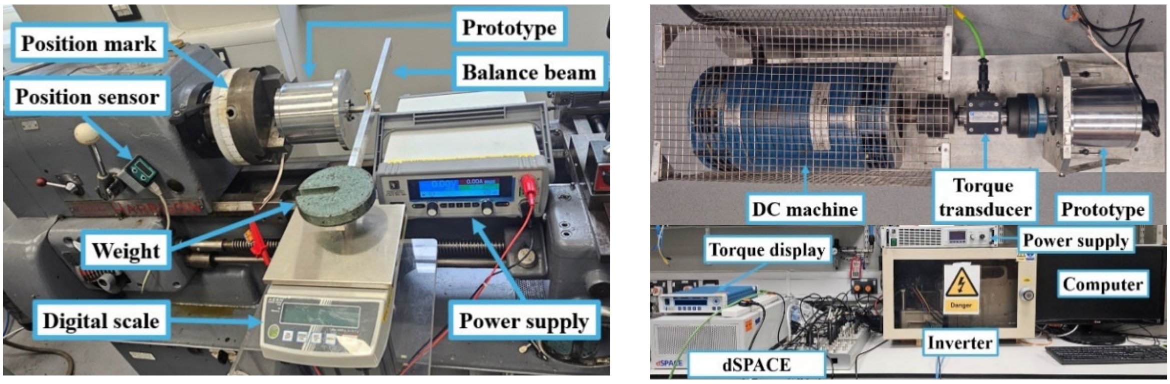

(a) (b)

Fig. 3.23. Experimental test benches. (a) Static test rig. (b) Dynamic test rig.

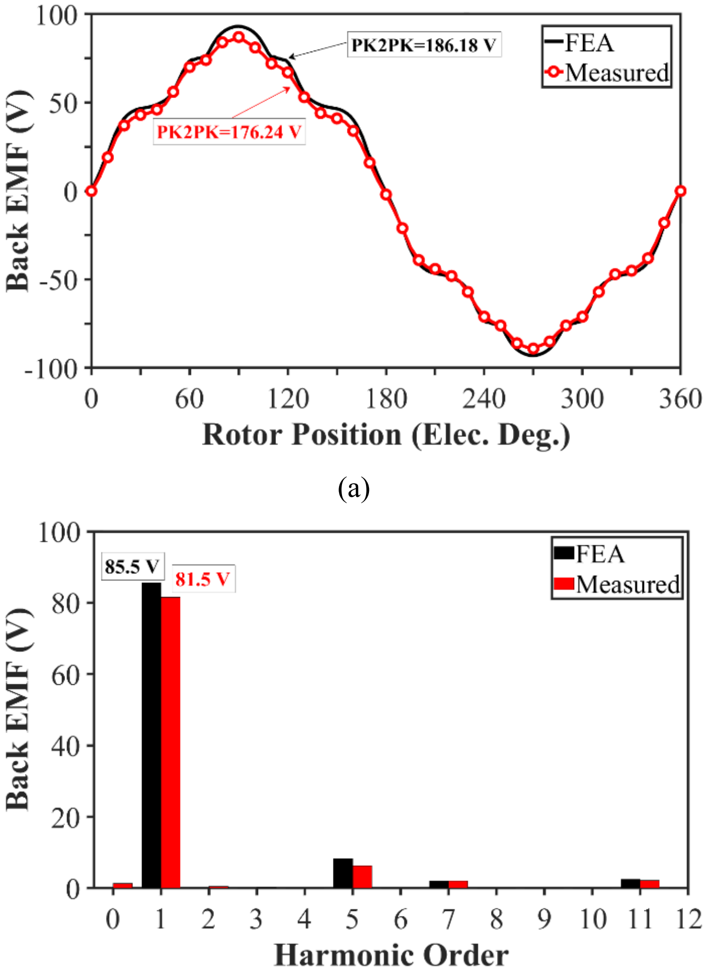

(a)

(b)

Fig. 3.24. FEA predicted and measured line back-EMFs at 750 r/min. (a) Waveforms. (b) Spectra.

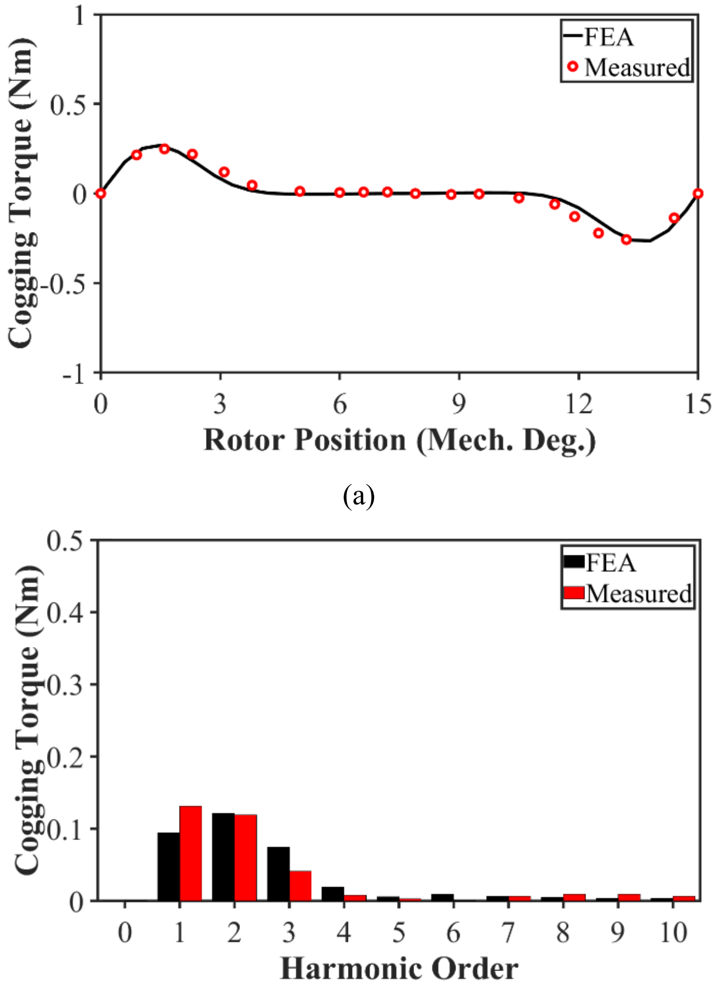

(a)

(b)

Fig. 3.25. FEA predicted and measured cogging torques at open circuit in one-sixth of electrical period. (a) Waveforms. (b) Spectra.

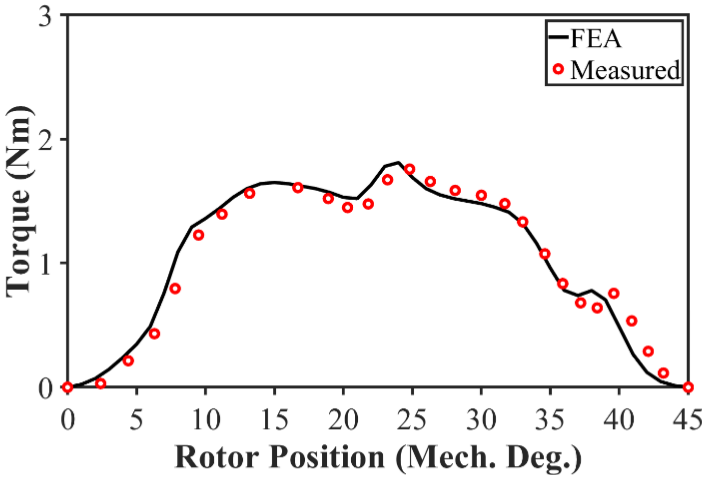

Fig. 3.26. FEA predicted and measured static torques at $I_a = -2I_b = -2I_c = 2$ A.

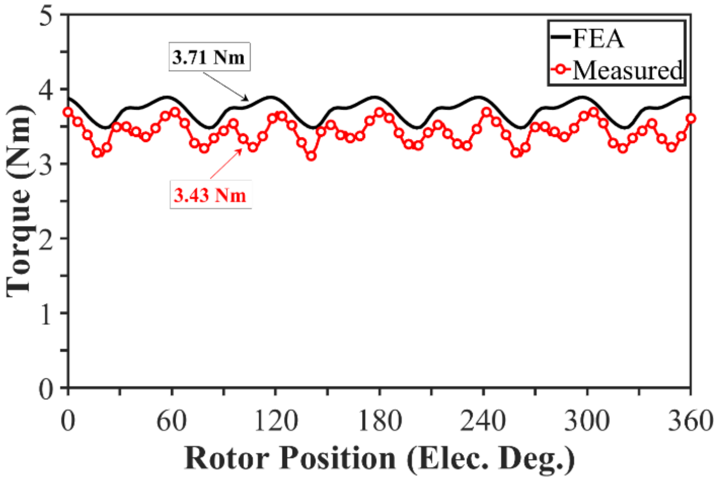

(a)

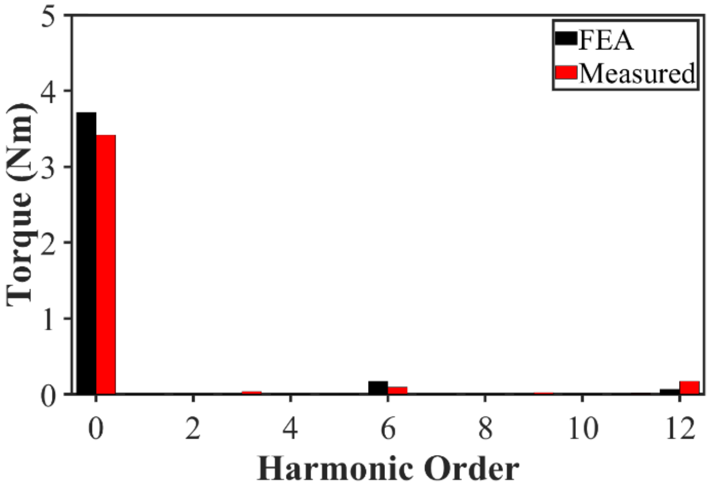

(b)

Fig. 3.27. FEA predicted and measured torques at 250 r/min and 4 A_{max}. (a) Waveforms. (b) Spectra.

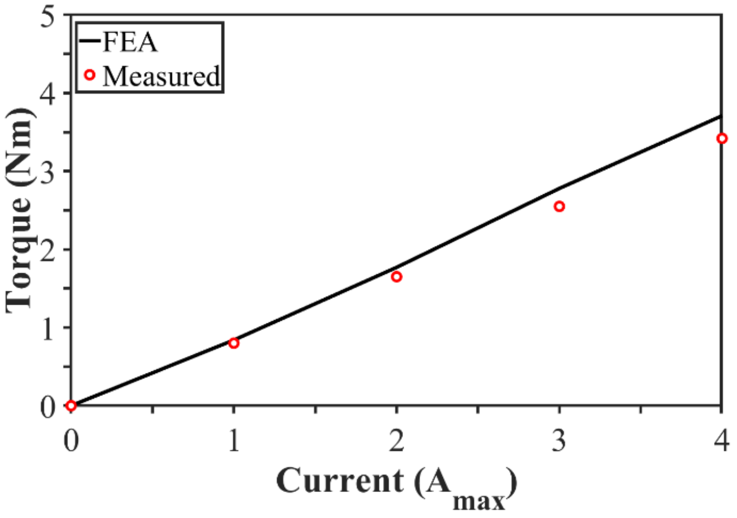

Fig. 3.28. FEA Predicted and measured average torques with current at 250 r/min.

3.7. Conclusion

In this chapter, a novel parallel HPM V-shape spoke IPMSM is proposed and analysed, together with a comparison with the commercial double V-shape IPMSM for EV application. The results show that the proposed machine can develop the same torque as the benchmark at 37% reduction of REPM volume and 30% reduction of total PM cost. Since a single V-shape spoke IPM rotor is employed, the proposed machine has a relatively lower reluctance torque component than that of the benchmark, but noticeable amount of FEPM torque contribution to produce the same resultant torque. In addition, although the total mass of PMs has been almost doubled, the introduced verge and gap in the proposed parallel HPM V-shape spoke design can significantly reduce the maximum von-mises stress on ribs and keep it close to that of the benchmark. Besides, the demagnetization withstand capability of FEPM proved a high tolerance against irreversible demagnetization except a small region close to the REPM.

Appendix – Rotor Pole Shaping

In this section, with the aim of further reduction in torque ripple, the application of rotor pole shaping technique [QI22A], [QI22B] will be investigated when the volume of magnets and all design parameters are kept constant as listed in Tables 3.2 and 3.3. To reveal the effectiveness of the method, 4 different scenarios will be considered by making combinations of skewing and shaping methods including un-skewed/un-shaped rotor (1st), skewed/un-shaped rotor (2nd), un-skewed/shaped rotor (3rd), and skewed/shaped (4th) rotor cases. Fig. 3.29 shows a parametric model for the rotor pole shaping of cases 3 and 4. As can be seen, the rotor pole surface is divided by several points with a cylindrical coordinate position as (R_i, θ_i). It is also worth noting that only the symmetrical pole shaping is considered in this study. The parameter θ_i represents the angle of the point ith with the fixed interval of 1.5° and 3° as shown in Fig. 3.29. However, the radial position parameter (R_i) of the point ith will be achieved by:

$$R_i = R_{or} - m_i \tag{3.13}$$

where m_i is the displacement length of the ith point which can be optimized between 0 to 0.8 mm.

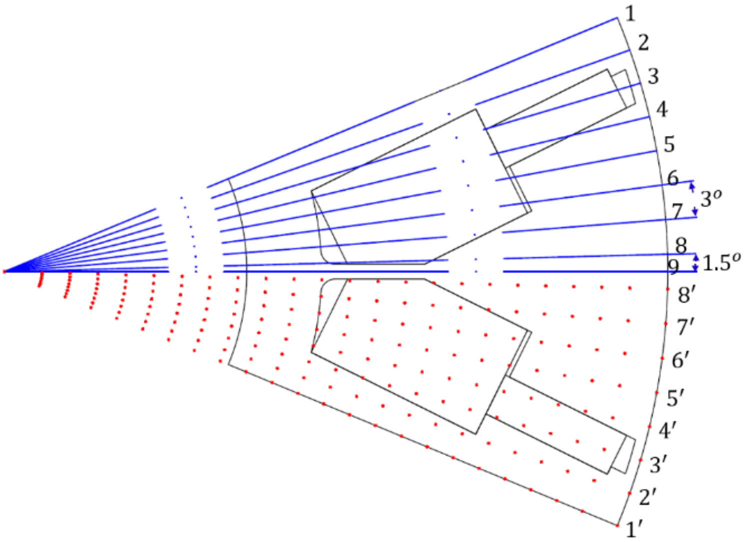

Fig. 3.29. Rotor pole shaping method.

The aim is to reduce the torque ripple at low reduction of average torque using the optimum values of the rotor pole shaping parameters in Table 3.5. Meanwhile, it should be noted that the un-manufacturable values below 0.1 mm are rounded to zero. In Figs. 3.30 (a) and (b), the developed torques and cogging torques of the un-skewed/un-shaped (1st), skewed/un-shaped (2nd), un-skewed/shaped (3rd), and skewed/shaped (4th) rotors are compared, respectively. Compared to the 1st case with un-skewed/un-shaped rotor, it can be concluded that the employed V-step-skew technique (2nd case) considerably reduces both the torque ripple and cogging torque. Meanwhile, the pole-shaped rotor (3rd case) benefits from a lower torque ripple only. Finally, the 4th case with both skewing and pole shaping technique benefits from a further reduction of torque ripple and cogging torque at the cost of losing 1.2 Nm of total torque (~-0.4%). Although this method is used for the further reduction of torque ripple in this chapter, it can also be employed for reducing the harmonics of airgap flux density in future work.

Table 3.5. Parameters of Rotor Pole Shaping Technique

Parameters	Range (mm)	3rd case with un-skewed/shaped rotor	4th case with skewed/shaped rotor
$m_1 - m_{1\prime}$	0 – 0.8	~ 0	~ 0
$m_2 - m_{2\prime}$		~ 0	~ 0
$m_3 - m_{3\prime}$		~ 0	~ 0
$m_4 - m_{4\prime}$		~ 0	~ 0
$m_5 - m_{5\prime}$		~ 0	~ 0
$m_6 - m_{6\prime}$		~ 0	~ 0
$m_7 - m_{7\prime}$		0.5	0.2
$m_8 - m_{8\prime}$		~ 0	~ 0
m_9		0.2	~ 0

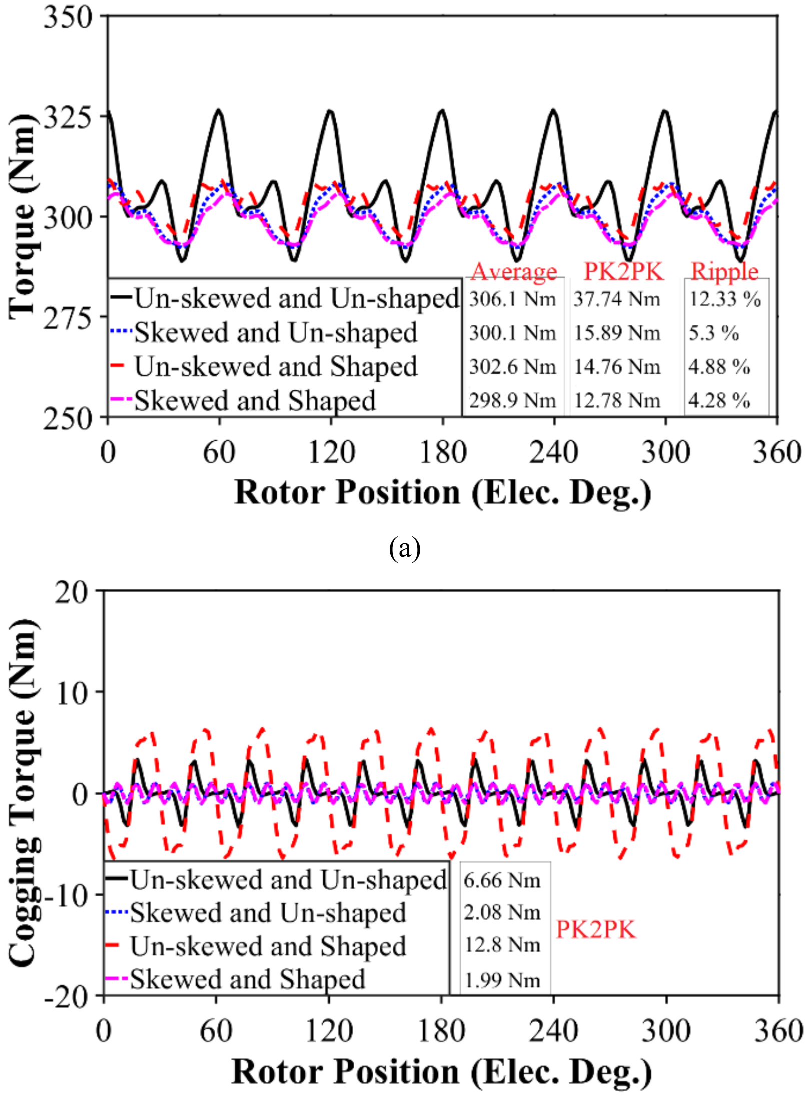

(a)

(b)

Fig. 3.30. Effect of skewing and shaping techniques on the performances of the proposed parallel HPM V-shape spoke IPMSM. (a) Torque at 500 A_{rms} and 5000 r/min. (b) Cogging torque at open circuit.

CHAPTER 4

SERIES HYBRID MAGNET DELTA-SHAPE IPMSM WITH SPLIT FERRITE SPOKE

4.1. Introduction

The increased concern of global warming in recent years has obliged many industries to achieve a sustainable system by reducing the reliance on fossil fuels [KAZ23D]. Therefore, the application of high-performance permanent magnet (PM) machines in electric vehicles (EVs), wind power generators, robots, etc., is investigated and proposed as a decent solution [ZHU07], [JIA09]. Although each application requires a variety of components including batteries and converters, etc., the PM machine plays a significant role in this transformation to replace the internal combustion engine. This is because PM machines benefit from outstanding advantages of high efficiency, high torque/power densities, etc. [ZHU07], [KAZ18] and can be designed in a variety of topologies to be suitable for a specific application. For example, in EV application, where high torque density at low speed (e.g. acceleration), wide speed range (e.g. highway driving), and high efficiency are required, the interior PM synchronous machines (IPMSMs) are widely used [YAN16]. For instance, the V-shape arrangement PMs in the Toyota Prius Gen III and Tesla Model3, the UI-shape PMs in Toyota Prius Gen IV, the Δ-shape PMs in Nissan Leaf, the double V-shape PMs in Chevy Bolt, and the double I-shape PMs in BMW 225xe are used [KRI20].

Meanwhile, on the one hand, the additive performance targets are drafted for the growing EV market in future [SHA20]. On the other hand, on the way of achieving a sustainable electrified transportation system, a cost-effective design challenge has raised as the price of rare-earth PM (REPM) is reported by the US Department of Energy (DoE) to cost from 20% to 30% of the total expenses in PM machines [ENE]. Therefore, a universal attempt towards less REPM usage in PM machines has been provoked in recent years [POU21]. To address this issue, the electromagnetic performance per cost ratio needs to be enhanced which can be done either by improving the performance at the same cost or reducing the cost at the same performance. Some researchers have dealt with the issue using the former solution by improving the output torque using the asymmetric rotor designs. In this method, the PM torque and reluctance torque components are forced to reach to their maximum at a merged current advancing angle which leads to an increased total torque [ZHU22].

However, taking the cost reduction solution into account, many studies have been carried out to replace a part of high-cost REPMs with low-cost ferrite magnets (FEPMs) at the same performance. As two different PM materials with different magnetic properties are used in one topology, this kind of PM machine is designated as hybrid PM (HPM) machine. Although the HPM machines are first introduced in almost a dozen of years ago [CHE11B], [SHE12], [ISH13], [AFI14], they have just gained a higher attraction in recent years as the cost of REPM has unboundedly increased. In general, these machines benefit from the synergies of high energy-product of REPM and low-cost of FEPM [KAZ23D]. However, the relative positions of these two magnets can affect the overall performance and categorize the HPM machines into three configurations including parallel, series, and mixed [KAZ23C]. The parallel HPM machines are known for their higher electromagnetic performance at the cost of lower demagnetization withstand capability of FEPMs [M20], [KAZ23A] compared to those of a series counterpart [AFI14]. This is because the REPM magnetic field in a series connection with FEPM can support this magnet against irreversible demagnetization. However, a series HPM machine suffers from a lower electromagnetic performance due to an increased magnetic reluctance of the flux path by using FEPMs. Finally, the mixed configuration of HPMs can have a trade-off of these features at the cost of a more complicated structure [CHE23]. Consequently, the series HPM configuration can provide a higher reliability for EV application. However, the disadvantage of its lower electromagnetic performance than a parallel HPM counterpart needs to be addressed. Thus, in [PAR22], a novel series HPM machine with improved reluctance torque is proposed. In [XU17A], a novel asymmetric rotor with unequal poles is presented in the form of a series configuration of HPMs with a mixture of surface mounted REPM-based and multilayer FEPM-based poles. Although this machine shows an improved performance, it suffers from axial leakage flux. In addition, in [KAZ23C], [ZEN19], [ZHU23B], the tapered FEPM spoke, and asymmetric rotor structures are investigated in conventional series HPM spoke-type IPMSMs, respectively.

As the extended work of [KAZ23D] and [KAZ23B], this chapter proposes a novel series HPM delta-shape IPMSM with split ferrite spoke. As will be shown, the volume of FEPM is suppressed by the q-axis flux path when a single FEPM is used in each spoke. However, using the frozen permeability method (FPM) [CHU12], it will be shown that the proposed machine benefits from higher FEPM torque and reluctance torque components leading to less required

REPM torque and resultant REPM usage. Moreover, the proposed novel design will be compared to a series HPM delta-shape IPMSM counterpart without split ferrite spoke and a commercialized REPM-based delta-shape IPMSM benchmark in terms of open-circuit and on-load characteristics, mechanical von-mises stress, demagnetization withstand capability and PM cost.

Section 4.2 presents the concept of the proposed series HPM delta-shape IPMSM with split ferrite spoke in comparison with a series HPM counterpart without split ferrite spoke and the benchmark. Then, section 4.3 discusses the finite element analysis (FEA) results whereas section 4.4 provides analyses on von-mises stress and demagnetization. Finally, sections 4.5 and 4.6 include the experimental validation of a small-size prototype and the conclusion, respectively.

This chapter is presented in ICEMS2023 conference [S. Kazemisangdehi, Z. Q. Zhu, and Y. Zhou, "Split spoke series hybrid PM delta-shape IPMSM with improved performance," in *2023 26th Int. Conf. on Electrical Machines and Systems (ICEMS)*, 2023: IEEE, pp. 678-683.] and [S. Kazemisangdehi, Z. Q. Zhu, and Y. Zhou, "Comparative study of performance improvement methods in a series hybrid PM delta-shape IPMSM," in *2023 26th Int. Conf. on Electrical Machines and Systems (ICEMS)*, 2023: IEEE, pp. 684-689.].

4.2. Split Ferrite Spoke Series HPM Delta-Shape IPMSM

A delta-shape arrangement of PM is a well-known IPMSM topology to improve the reluctance torque component of PM machines by utilizing a double-layer PM structure. In this section, the developed series HPM machines with delta-shape arrangement of PMs will be introduced.

4.2.1. Benchmark

For this study, a commercialized delta-shape IPMSM with a 48-slot/8-pole (48s/8p) combination of stator slots and rotor poles is selected as the benchmark as shown in Figs. 4.1 (a) and (b). Meanwhile, the specifications of benchmark are summarized in Table 4.1. As can be seen, this machine requires 249.4 cm^3 of REPM (N28AH) to produce 280 Nm peak torque at the maximum current of 625 A_{max} and the rotor speed of 2100 r/min.

For the sake of comparison, the same stack length and shaft diameter, the identical stator geometry and winding configurations, and the same airgap length are used for the design of HPM machines in this study. Therefore, only the rotor structure will be re-optimized by FEA using the genetic algorithm (GA). The main objective is to reduce the volume of REPM by being proportionally substituted with FEPMs type TDK- FB13B at the same peak torque of 280 Nm when 625 $A_{\max}$ and 2100 r/min are applied. Meanwhile, the second objective is to minimize the torque ripple. Taking the importance of each objective into account, the optimization function is defined as follows:

$$\begin{cases} \text{Objectives: Max } [T_{out}],\ \text{Min } [V_{NdFeB}],\ \text{Min } [T_{ripple}] \\ \text{Selection criteria of optimum point: } T_{out} \geq 280 \text{ Nm},\ V_{NdFeB} < 249.4 \text{ cm}^3 \\ \text{Weighting factors: } K_{T_{out}} = 4\text{p.u.},\ K_{V_{NdFeB}} = 2\text{p.u.},\ K_{T_{ripple}} = 1\text{p.u.} \\ \text{Variables: will be listed in a table later.} \end{cases} \tag{4.1}$$

where T_{out}, V_{NdFeB}, and T_{ripple} are the output torque, the volume of REPM, and the torque ripple, respectively.

4.2.2. Series HPM Delta-Shape IPMSM without Split Ferrite Spoke

Fig. 4.1 (c) shows the optimum design of a series HPM delta-shape IPMSM without split ferrite spoke. As can be seen, this machine employs a bar-shape REPM and a V-spoke arrangement of FEPMs. As will be shown, this machine requires a lower volume REPM than the benchmark at the same torque. However, the volume of FEPM is limited by the width due to being restricted with the q-axis flux path. Meanwhile, the length of FEPM is expanded towards the shaft to increase the FEPM utilization.

4.2.3. Series HPM Delta-Shape IPMSM with Split Ferrite Spoke

Fig. 4.1 (d) illustrates the optimum cross section of the proposed series HPM delta-shape IPMSM with split ferrite spoke. As will be shown, this machine can effectively reduce the volume of REPM compared to that of its HPM counterpart without split ferrite spoke and the benchmark due to higher FEPM and reluctance torque contributions. It is worth mentioning that the term of split in this chapter means diving each FEPM spoke into two FEPM segments with different sizes in the rotor cross section (compare Figs. 4.1 (c) and (d)).

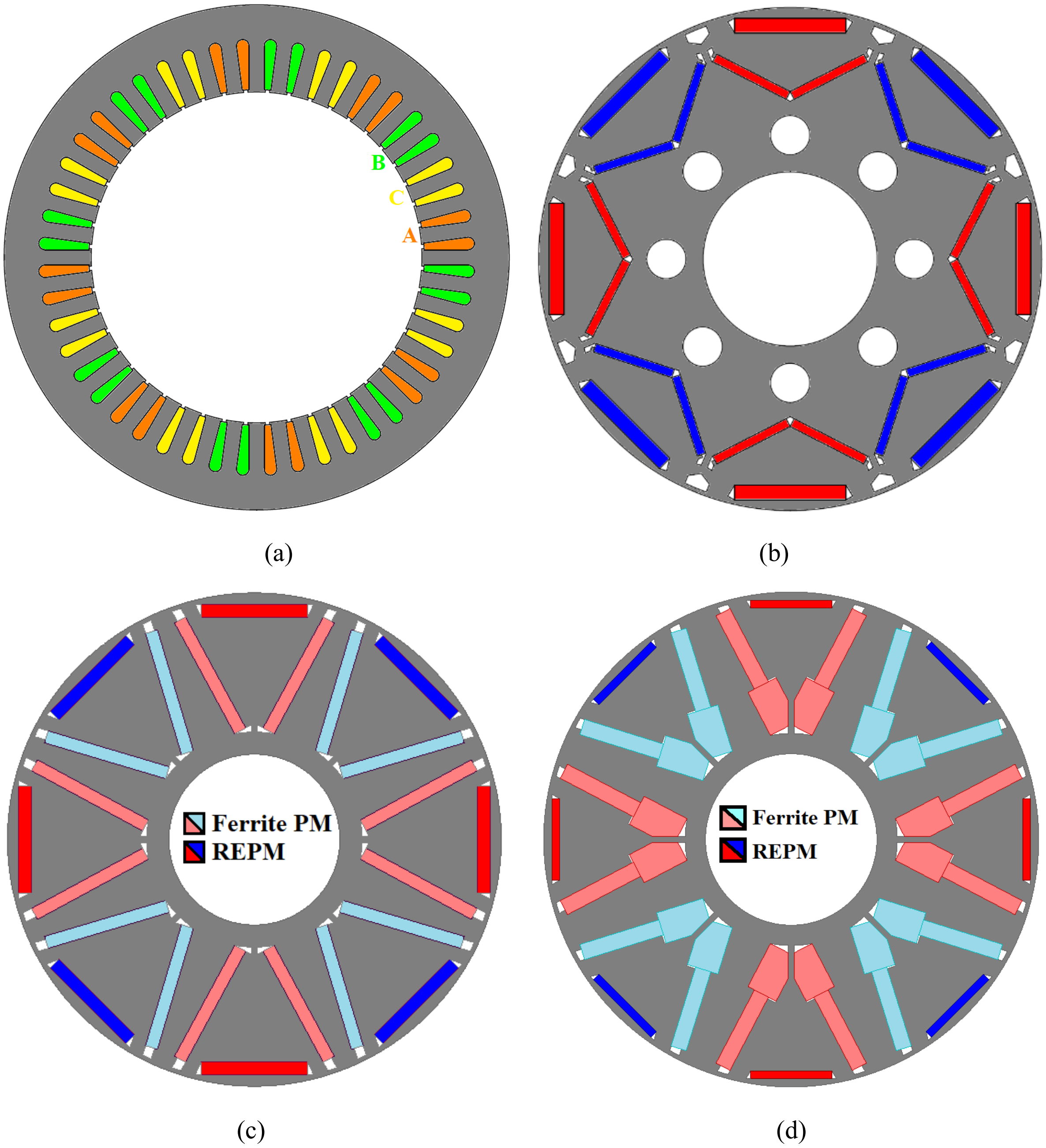

(a) (b) (c) (d)

Fig. 4.1. Schematic comparison of delta-shape IPMSMs. (a) Benchmark’s stator. (b) Benchmark’s rotor. (c) Series HPM rotor without split ferrite spoke. (d) Series HPM rotor with split ferrite spoke.

Table 4.1. Specification of Benchmark IPMSM

Parameters	Values	Parameters	Values
Stator slot no.	48	Peak speed (r/min)	10000
Rotor pole no.	8	Rated speed (r/min)	2100
Stator outer diameter (mm)	200	Peak torque (Nm)	280
Stator inner diameter (mm)	131	Peak current (A_{max})	625
Rotor outer diameter (mm)	130	Conductor no. per slot	8
Rotor inner diameter (mm)	45	Number of parallel branches	4
Stack length (mm)	151	NdFeB volume (cm^3)	249.4
Airgap length (mm)	0.5	NdFeB remanence (T)	1.075
Angle of rotor skew (degree)	3.75	Ferrite remanence (T)	0.475

4.3. FEA Results

This section focuses on FEA results. First, a series HPM delta-shape IPMSM without split ferrite spoke is optimized based on the above-mentioned optimization criteria. Second, the feasibility analysis of employing the split ferrite spoke is investigated using the optimum cross section. Third, the proposed series HPM delta-shape IPMSM with split ferrite spoke will be optimized with the same objectives. Finally, a detailed comparison of all machines will be given including the electromagnetic performances at open-circuit and on-load conditions, the von-mises stress analysis at high speed, the demagnetization withstand capability of FEPM at low temperature, and the PM cost.

4.3.1. Series HPM Delta-Shape IPMSM without Split Ferrite Spoke

Fig. 4.2 (a) presents a parametric model of the series HPM delta-shape IPMSM without split ferrite spoke. Following this parametric model, an optimization is carried out to deliver 280 Nm torque at a lower volume of REPM than that of the benchmark when 625 A_{max} and 2100 r/min are applied. Figs. 4.2 (b) and (c) show the optimization results and the optimum cross section of the rotor, whereas the optimum values of the design parameters are listed in Table 4.2. As can be seen, the volume of REPM in this design with 112.85 cm^3 is ~55% less than that of the benchmark with 249.4 cm^3. It is worth mentioning that the rotor inner and outer radii, R_{ir} and R_{or}, are constant. In addition, as will be shown later, the rib thicknesses are chosen close to those of the benchmark in a way to provide the same mechanical strength at high speed. Meanwhile, the angle of V-shape spoke local coordinate can be expressed using the V-shape angle (θ_v) and the V-shape local coordinate centre (x_c) as:

$$\theta_c = \tan^{-1}\left(\frac{R_{or}\times\sin(\theta_v)}{(R_{or}\times\cos(\theta_v))-x_c}\right) \tag{4.2}$$

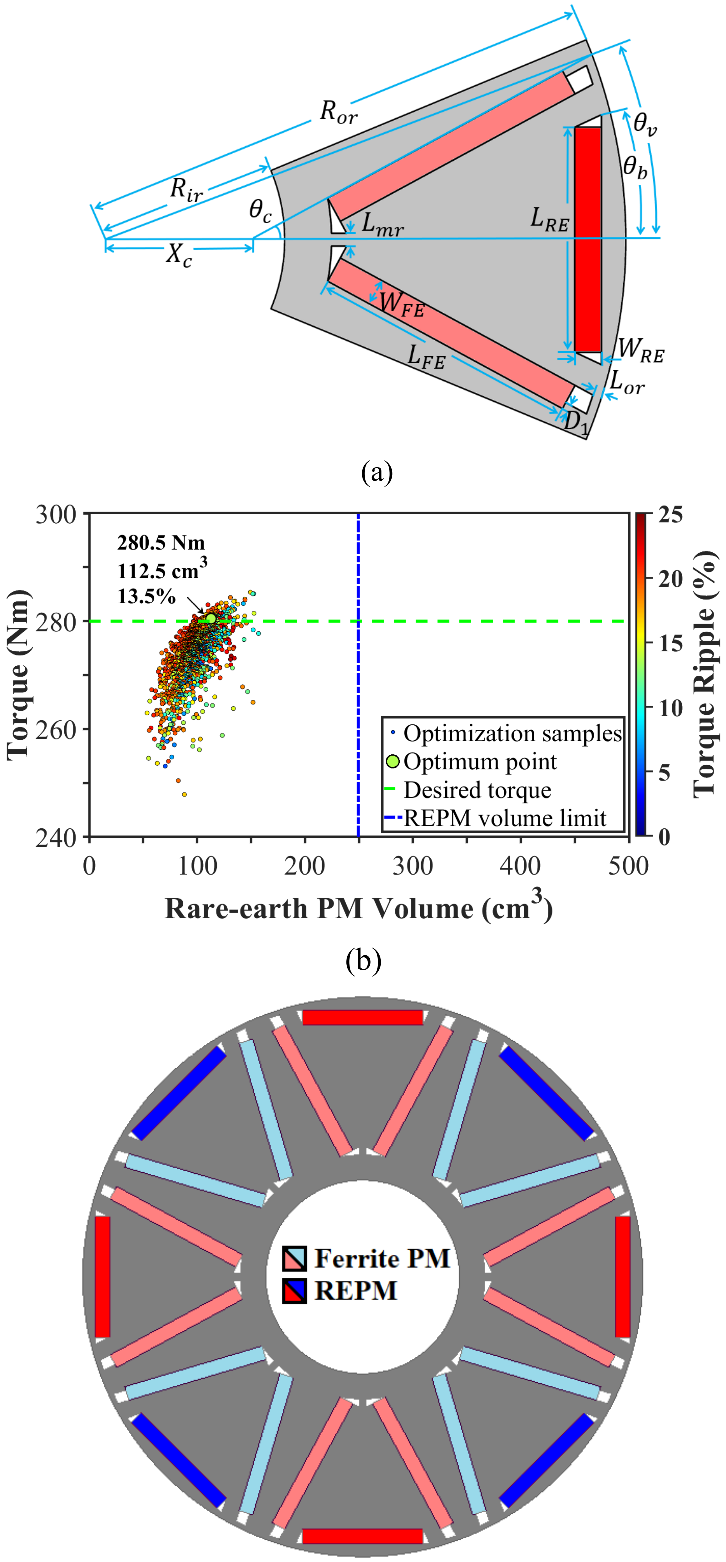

(a)

(b)

(c)

Fig. 4.2. Series HPM delta-shape IPMSM without split ferrite spoke. (a) Parametric model. (b) Optimization result. (c) Optimum cross-section.

4.3.2. Feasibility Analysis of Splitting Ferrite Spokes

To investigate the feasibility of dividing each ferrite spoke into two segments (i.e. named as split ferrite spokes in this chapter), the optimum design of the series HPM delta-shape IPMSM without split ferrite spoke is selected. As shown in Table 4.2, the optimum width of FEPM is 3.3 mm. However, it can parametrically be increased to 6.3 mm without interfering the REPM due to the geometrical limit.

Fig. 4.3 (a) shows the parametric model of dividing each spoke into two FEPMs (FE1 is the ferrite segment near airgap, and FE2 is the one near shaft). As can be seen, four variables are introduced including the lengths and widths of two magnets. Meanwhile, the position of each magnet is also an important factor which can differently affect the performance. Figs. 4.3 (b) and (c) present the variation of torque and dq-axis inductances at different FEPM length ratios. For the ratios below 0.5, the FE1 PM is longer than FE2 PM which is opposite to that of ratios above 0.5. However, at the ratio of 0.5, both segments are of the same length. As can be seen, torque would significantly drop by the increase in the thickness of FEPM without split ferrite spoke (Fig. 4.3 (b)). This is mainly due to the reduction of reluctance torque by the change of dq-axis inductances as shown in Fig. 4.3 (c). However, it can be different when the split ferrite spoke is used. When $W_{FE2} > W_{FE1}$, torque increases by an increase in L_{FE2} (enhancing the ratio) until a certain point when q-axis inductance significantly drops. This is due to the PM torque component enhancement without a negative impact on the reluctance torque component. In [KAZ23D], it is shown that at a higher W_{FE2}, the interfere with q-axis flux path happens at a lower ratio. On the contrary, when $W_{FE1} > W_{FE2}$, torque drops drastically by an increase in L_{FE1} (reducing the ratio) which is due to the sudden reduction of q-axis inductance.

This ratio can not only affect the reluctance torque but also can affect the magnetic reluctance of the REPM flux path by changing the volume of FEPMs. Therefore, it is an important parameter during the optimization. However, for the simplicity and investigating the effect of the FEPM width, the length ratio is fixed at 0.5 in Figs. 4.3 (d) and (e). This is to normalize the variation of FEPM volume per change of each segment's width. As can be seen in Fig. 4.3 (d), at $W_{FE} < 3.3$ mm in the HPM design without split ferrite spoke, the machine is not optimized yet to deliver 280 Nm torque. However, when $W_{FE} > 3.3$ mm, although a higher volume of FEPM is used, the torque would significantly drop due to the reduction of q-axis inductance as shown in Fig. 4.3 (e). On the contrary, the variation of torque with the thickness of FEPM depends on the position of this magnet in the HPM topology with the split ferrite spoke (FE1 or FE2). When $W_{FE1} > W_{FE2}$, torque reduces by the increase in the FEPM thickness. In contrast, when $W_{FE1} < W_{FE2}$, torque is enhancing. As a result, by optimizing the proposed series HPM delta-shape IPMSM with split ferrite spoke to deliver the fixed torque of 280 Nm at 625 A_{max} and 2100 r/min, a lower REPM usage is expected.

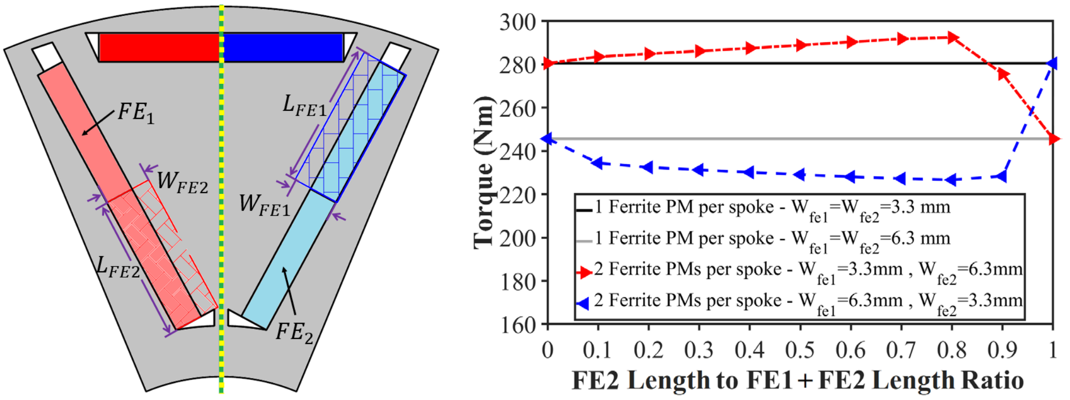

(a) (b)

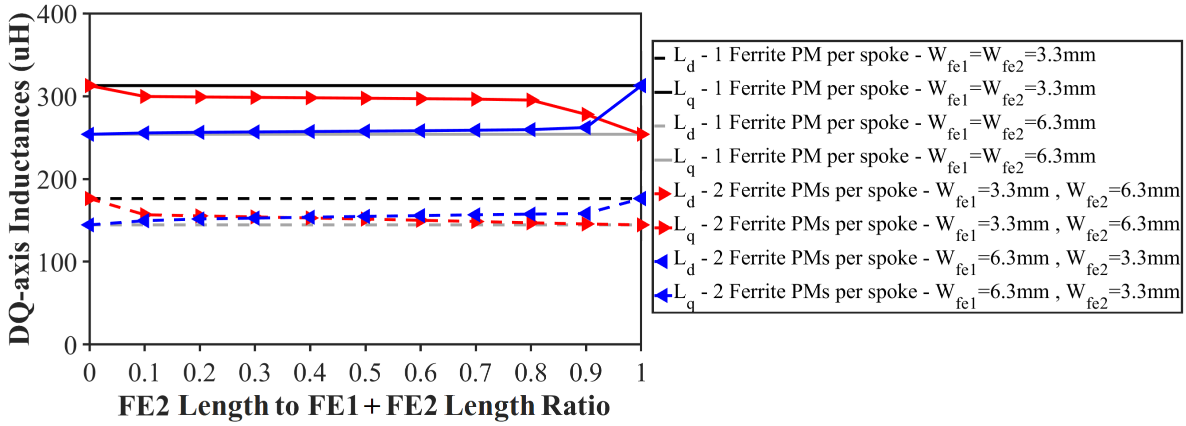

(c)

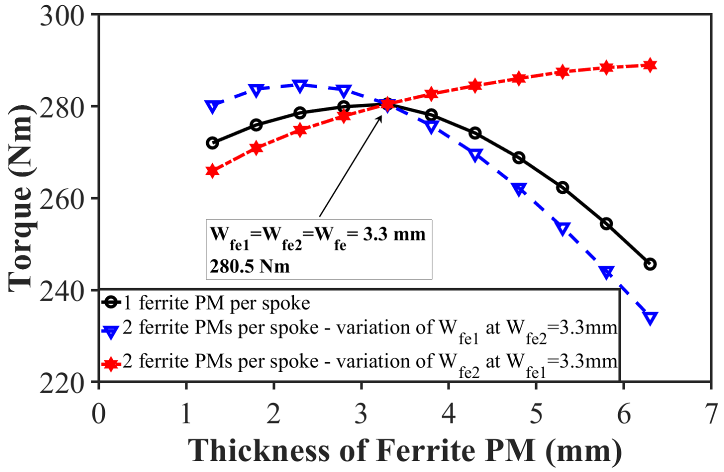

(d)

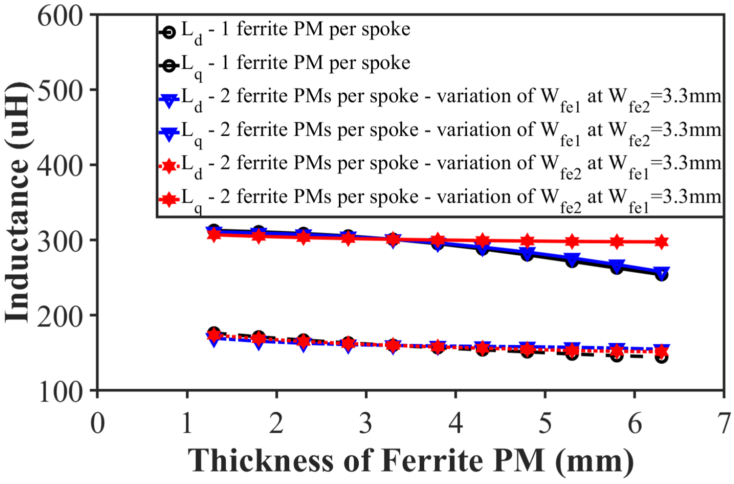

(e)

Fig. 4.3. Feasibility analysis of splitting ferrite spoke in series HPM delta-shape IPMSM. (a) Parametric model. (b) Torque at 625 A_{max} and 2100 r/min (effect of FEPMs length ratio). (c) Dq- axis inductances (effect of FEPMs length ratio). (d) Torque at 625 A_{max} and 2100 r/min (effect of FEPMs thicknesses at length ratio 0.5). (e) Dq- axis inductances (effect of FEPMs thicknesses at length ratio 0.5).

4.3.3. Series HPM Delta-Shape IPMSM With Split Ferrite Spoke

Following the feasibility analysis in the previous section, an optimization is carried out using the same objectives as before. Fig. 4.4 (a) illustrates the developed parametric model, whereas Figs. 4.4 (b) and (c) present the optimization result and the optimum cross section. As can be seen, for the same torque, the proposed series HPM delta-shape IPMSM with split ferrite spoke uses 52.1 cm^3 of REPM which is ~54% less than that of its counterpart without split ferrite spoke with 112.5 cm^3. The optimum values of the design parameters are listed in Table 4.2.

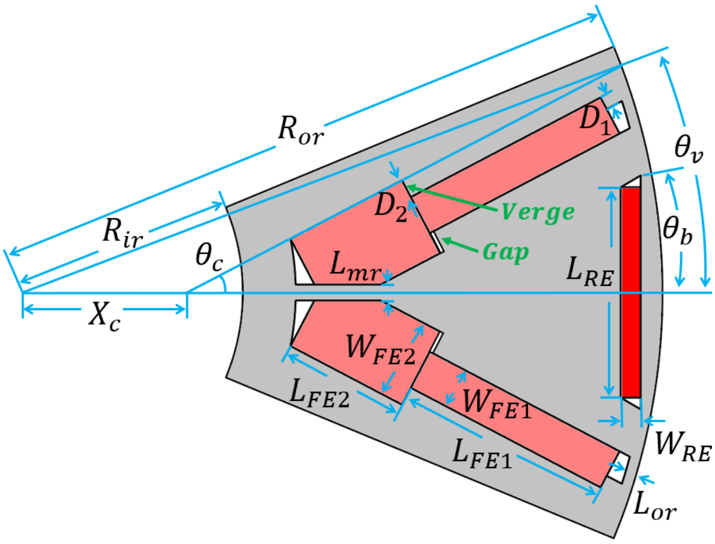

(a)

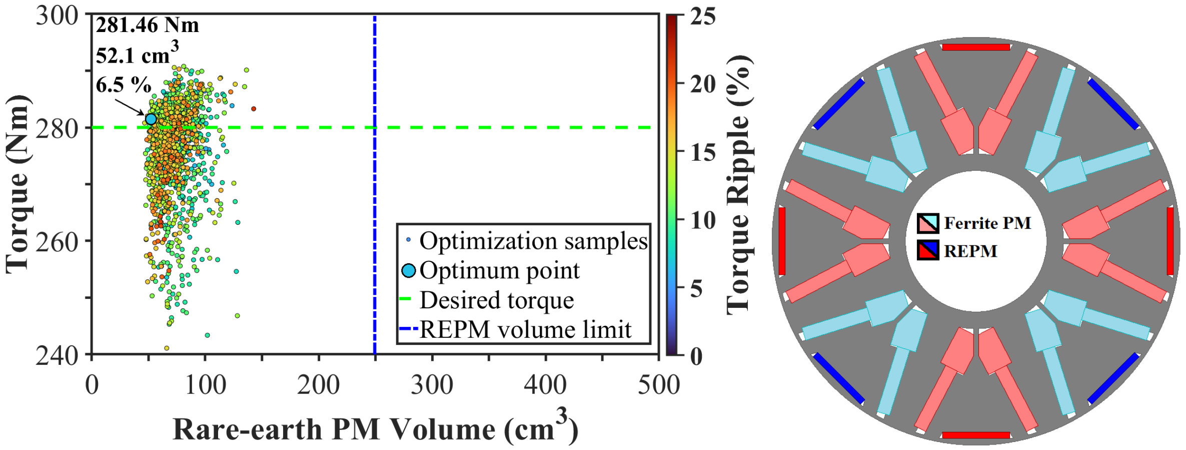

(b) (c)

Fig. 4.4. Series HPM delta-shape IPMSM with split ferrite spoke. (a) Parametric model. (b) Optimization result. (c) Optimum cross-section.

Table 4.2. Design Parameters and Their Optimum Values in proposed HPM Machines

Parameter	**Symbol**	**Unit**	**Series HPM delta-shape IPMSM without split ferrite spoke**	**Series HPM delta-shape IPMSM with split ferrite spoke**
Rotor outer radius	R_{or}	mm	65	
Rotor inner radius	R_{ir}	mm	22.5	
Local coordinate center	x_c	mm	18.78	17.5
Local coordinate angle	θ_c	Deg.	28.28	27.49
V-shape angle	θ_v	Deg.	20.41	20.35
Bar-shape angle	θ_b	Deg.	14.1	10.67
Length of FEPM	L_{FE}	mm	33.37	-
Width of FEPM	W_{FE}	mm	3.3	-
Length of REPM	L_{RE}	mm	28.05	21.3
Width of REPM	W_{RE}	mm	3.33	2.025
Length of ferrite segment 1	L_{FE1}	mm	-	21.7
Width of ferrite segment 1	W_{FE1}	mm	-	4.13
Length of ferrite segment 2	L_{FE2}	mm	-	12.75
Width of ferrite segment 2	W_{FE2}	mm	-	8.34
Length of verge near airgap	D_1	mm	1	1.2
Length of verge over FE2	D_2	mm	-	1.9
Width of middle rib	W_{mr}	mm	1.5	
Width of outer rib	W_{or}	mm	1.1	

4.3.4. Comparison of Open-Circuit Performance

The open-circuit flux density distributions and flux lines of these machines are compared in Fig. 4.5. As can be seen, in Figs. 4.5 (b) and (c), the flux lines are flowing through both PM types in a series connection. Meanwhile, Fig. 4.6 compares the open-circuit airgap flux density waveforms and spectra. As can be seen, the developed series HPM delta-shape IPMSMs have lower fundamental components but higher harmonics compared to those of the benchmark as no method for harmonic reduction is used in their structure.

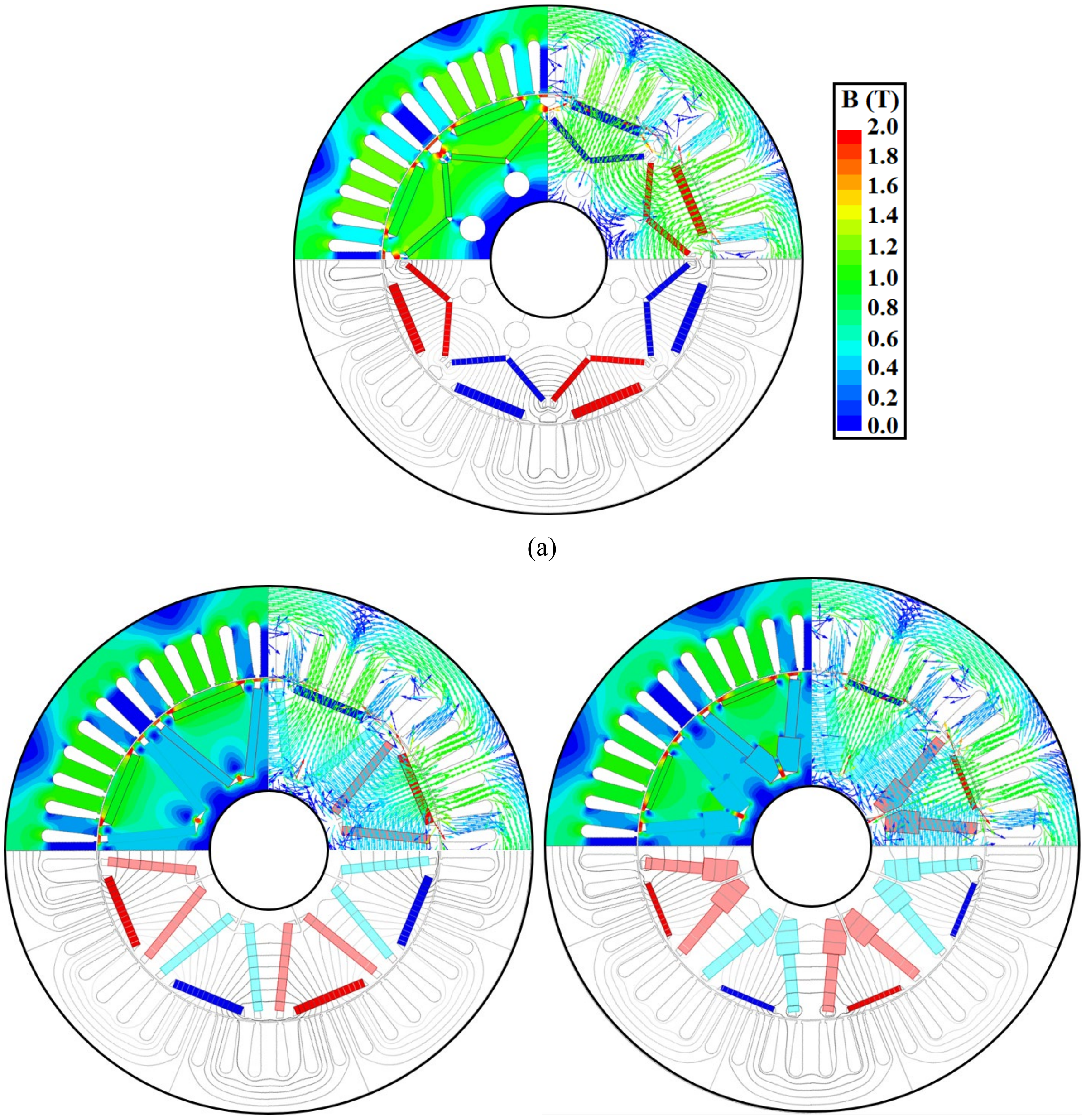

(a)

(b) (c)

Fig. 4.5. Comparison of open-circuit flux density distributions and flux lines. (a) Benchmark. (b) Series HPM delta-shape IPMSM without split ferrite spoke. (c) Series HPM delta-shape IPMSM with split ferrite spoke.

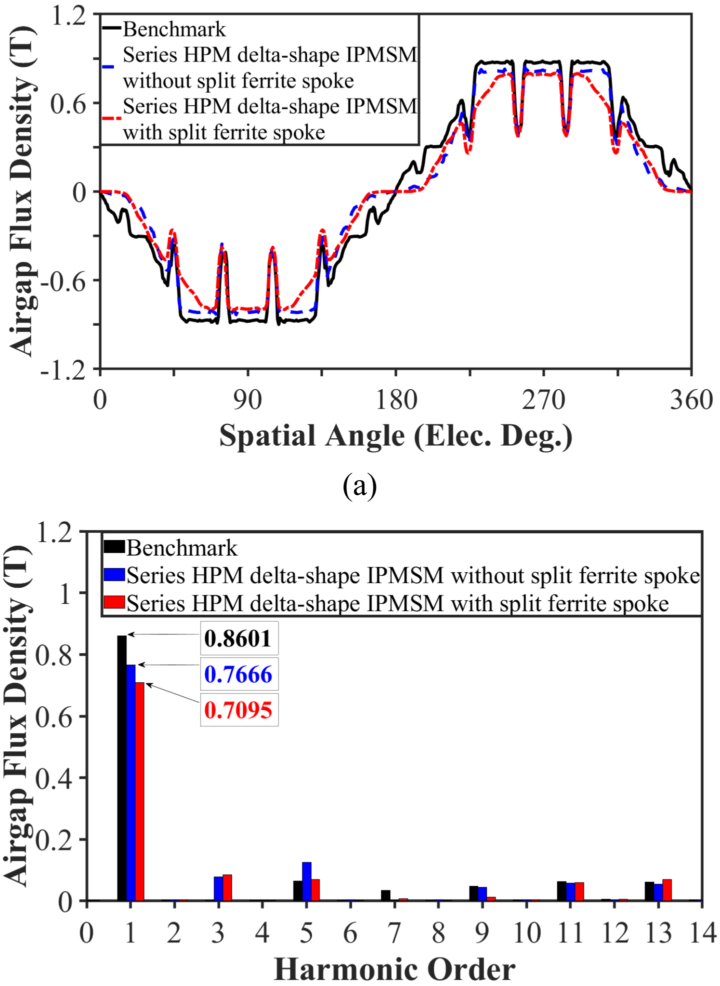

(a)

(b)

Fig. 4.6. Comparison of open-circuit airgap flux densities. (a) Waveforms. (b) Spectra.

Fig. 4.7 shows the open-circuit flux linkages. As can be seen, the proposed series HPM delta-shape IPMSM with split ferrite spoke benefits from the lowest amplitude with 0.0522 Wb which is ~19% less than that of benchmark with 0.0642 Wb. In addition, Fig. 4.8 compares the open-circuit back-emf of these three machines at 2100 r/min rotor speed. The fundamental back-EMF of the proposed machine with 47.6 V is ~7% less than that of the other HPM counterpart without split ferrite spoke with 51.33 V, and ~16% less than that of benchmark with 56.87 V. Meanwhile, the THDs of the back-EMFs in the developed series HPM delta-shape IPMSMs are higher than that of benchmark. Having the lowest back-emf amplitude can also be helpful for the safety measurement at high speed, when a fault can transfer a high voltage to the terminals of an inverter. In other words, this means a lower back-emf at high-speed, a lower risk of damage. Finally, the comparison of the cogging torque waveforms and spectra are shown in Fig. 4.9. As can be seen, the proposed series HPM delta-shape IPMSM with split ferrite spoke benefits from the lowest cogging torque.

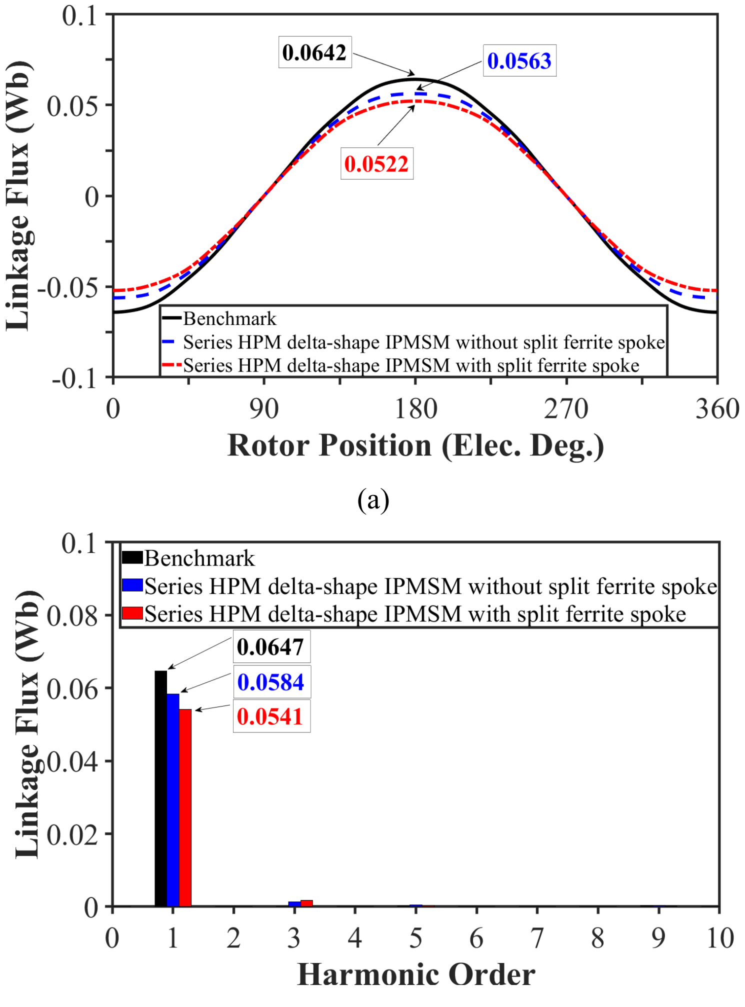

(a)

(b)

Fig. 4.7. Comparison of open-circuit flux linkages. (a) Waveforms. (b) Spectra.

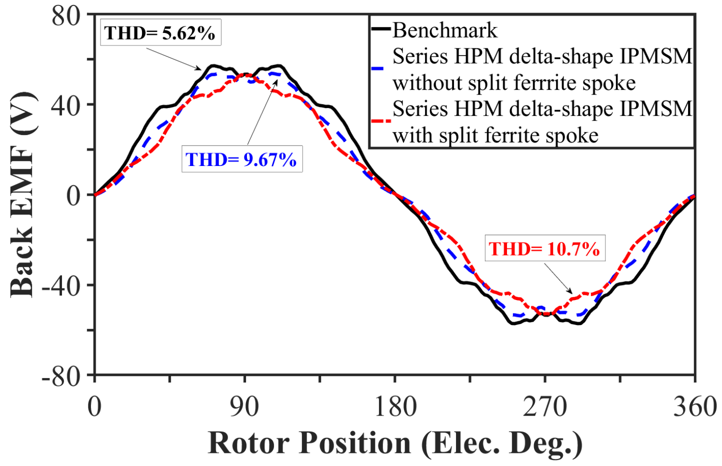

(a)

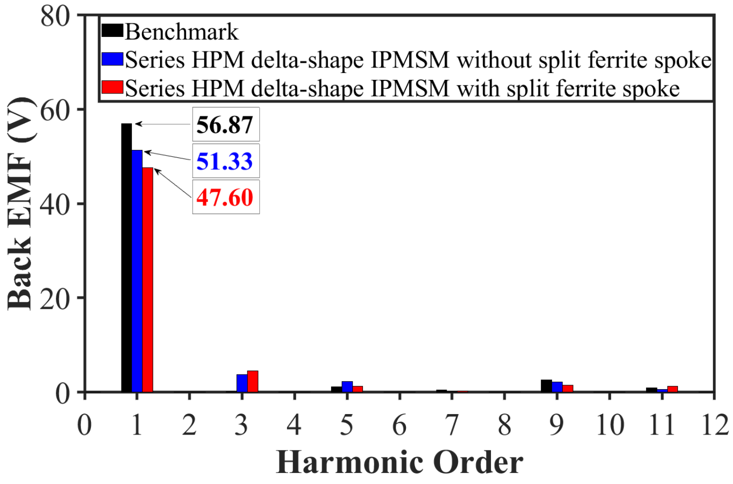

(b)

Fig. 4.8. Comparison of open-circuit back-EMFs at 2100 r/min. (a) Waveforms. (b) Spectra.

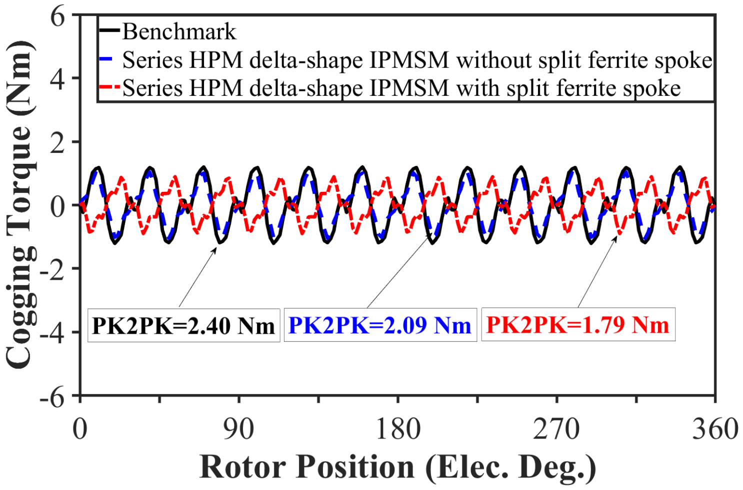

(a)

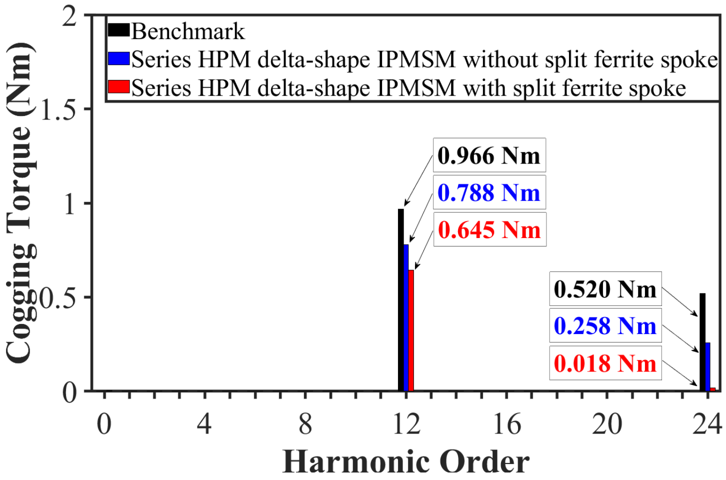

(b)

Fig. 4.9. Comparison of open-circuit cogging torques. (a) Waveforms. (b) Spectra.

4.3.5. Comparison of On-Load Performance

Fig. 4.10 compares the peak torque waveforms and spectra of these machines at 625 A_{max} and 2100 r/min. As discussed in sections 4.3.1. and 4.3.3, the developed series HPM delta-shape IPMSMs with and without split ferrite spoke are designed for the same torque as the benchmark. Therefore, a similar torque performance can be seen. However, as the rated current advancing angles of these machines are different, a different torque with current advancing angle is expected. Fig. 4.11 presents the variations of torques and dq-axis inductances with current advancing angle at 625 A_{max} and 2100 r/min. As can be seen in Fig. 4.11 (a), the torques at zero current advancing angle are different, which is in the same order as the open-circuit flux linkages. In addition, the proposed series HPM delta-shape IPMSM with split ferrite spoke is expected to have the highest reluctance torque component due to a higher difference between the dq- axis inductances as shown in Fig. 4.11 (b). Therefore, at the same output torque, this machine is expected to require the lowest PM torque component.

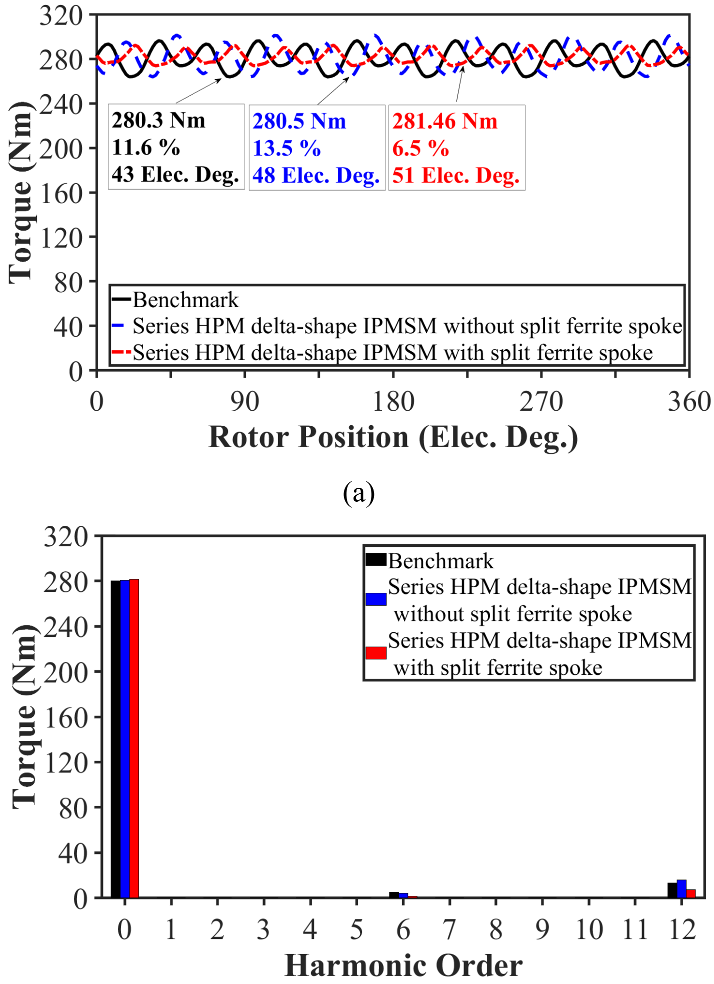

(a)

(b)

Fig. 4.10. Comparison of peak torques at 625 A_{max} and 2100 r/min. (a) Waveforms. (b) Spectra.

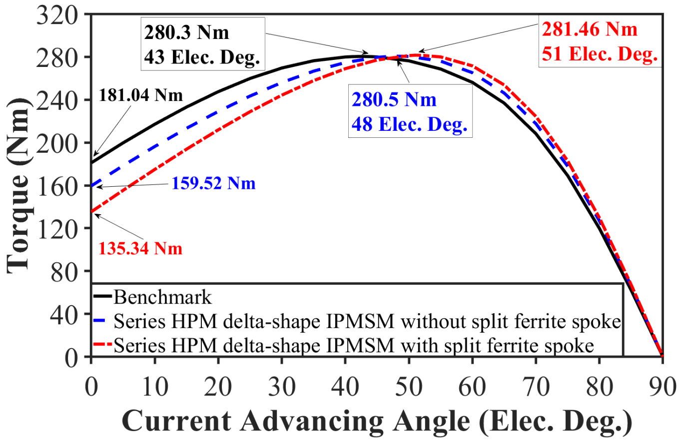

(a)

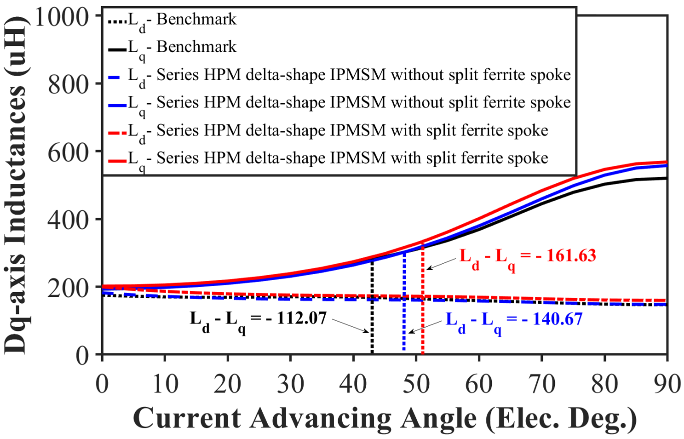

(b)

Fig. 4.11. Comparison of torques and dq-axis inductances with current advancing angle at 625 A_{max} and 2100 r/min. (a) Torque. (b) Dq-axis inductances.

For a precise decomposition of torque components into the reluctance, REPM, and FEPM torques, the FPM is applied. Fig. 4.12 compares the components of peak torques at 625 A_{max} and 2100 r/min. As discussed, the proposed series HPM delta-shape IPMSM with split ferrite spoke has the highest reluctance torque component with 200.45 Nm. Meanwhile, as expected from section 4.3.2. this machine has a higher FEPM torque component with 55.39 Nm (+35%) than its counterpart without split ferrite spoke with 41.06 Nm. As a result, the proposed topology benefits from the synergies of high reluctance torque and FEPM torque components which can effectively reduce the required REPM torque component to 24.34 Nm. Consequently, the proposed design needs to employ much less REPM volume than the others at the same torque.

Fig. 4.13 compares the torque-speed and power-speed characteristics of these machines. As the developed series HPM delta-shape IPMSMs are designed for the same peak torque as the benchmark, the similar torque and power outputs for the low-speed region are expected.

Meanwhile, these characteristics at high-speed could have been different. However, the same 80 kW output power limit as the benchmark [BUR13] is applied to the developed series HPM delta-shape IPMSMs. Therefore, as can be seen in Figs. 4.13 (a) and (b), the torque and power outputs of all machines at high-speed region become similar as well.

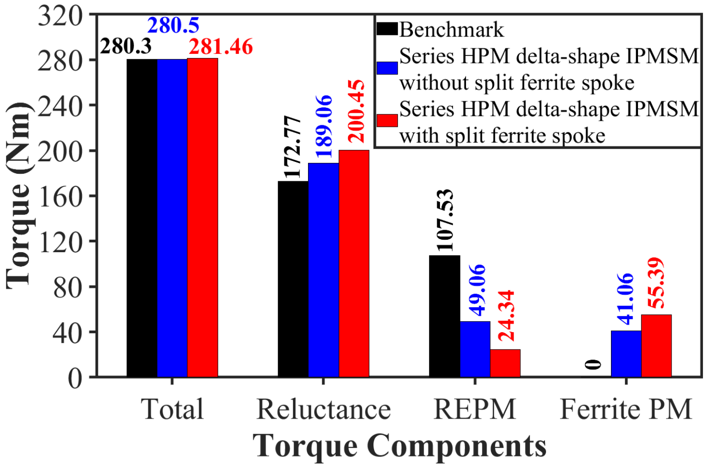

Fig. 4.12. Comparison of peak torque components at 625 A_{max} and 2100 r/min using FPM.

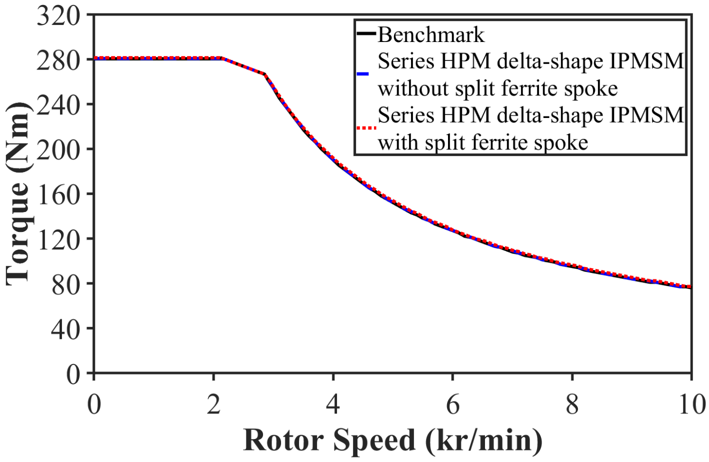

(a)

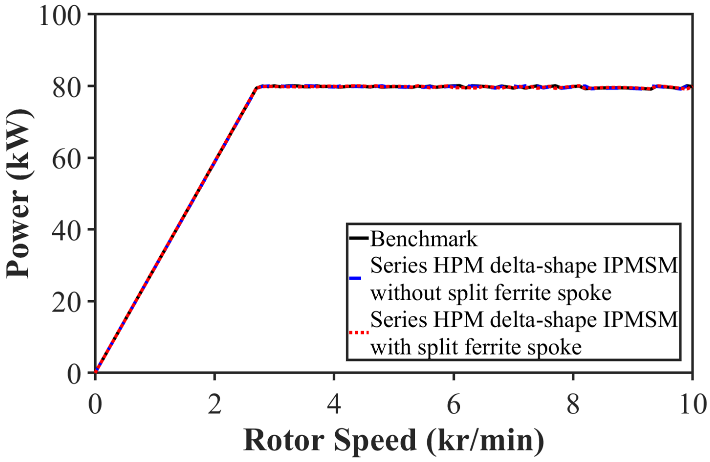

(b)

Fig. 4.13. Comparison of on-load characteristics with speed. (a) Torque. (b) Power.

The efficiency (η) of all machines can be obtained using the equation below:

$$\eta = \frac{P_{out}}{P_{out}+P_{cu}+P_{core}+P_{mec}} \times 100\ \% \tag{4.3}$$

where P_{out}, P_{cu}, P_{core}, and P_{mec} are the output power, the copper loss, the iron loss, and the mechanical loss, respectively.

As all machines share the same stator, stack length, and winding configurations, the copper losses are expected to be almost the same. In contrast, the iron losses are expected to be different due to the harmonics of the open-circuit airgap flux densities as presented in Fig 4.6. Meanwhile, the calculation of mechanical losses requires two coefficients as follows which are taken from [YAN17A]:

$$P_{mec} = k_{mec1}f + k_{mec2}f^2 \tag{4.4}$$

Figs. 4.14 (a) to (c) compare the copper loss maps, iron loss maps and efficiency maps of the benchmark, series HPM delta-shape IPMSM without split ferrite spoke and the proposed series HPM delta-shape IPMSM with split ferrite spoke. As can be seen, the variations in copper losses are almost the same. However, at high speeds, the developed series HPM delta-shape IPMSMs have slightly higher iron losses than the benchmark. As a result, as can be seen in Fig. 4.14 (c), the efficiencies of these machines are affected by less than 0.5% at high speed. However, the regions of efficiency over 97% are almost similar in all machines.

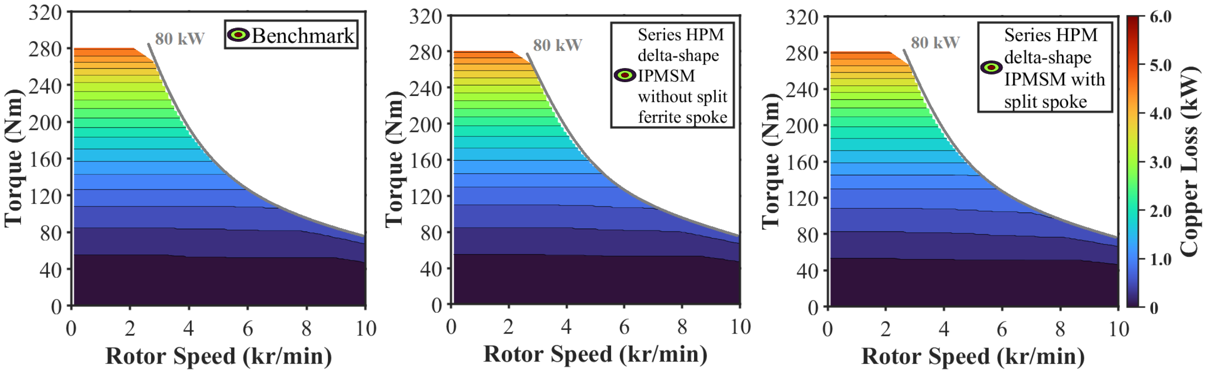

(a)

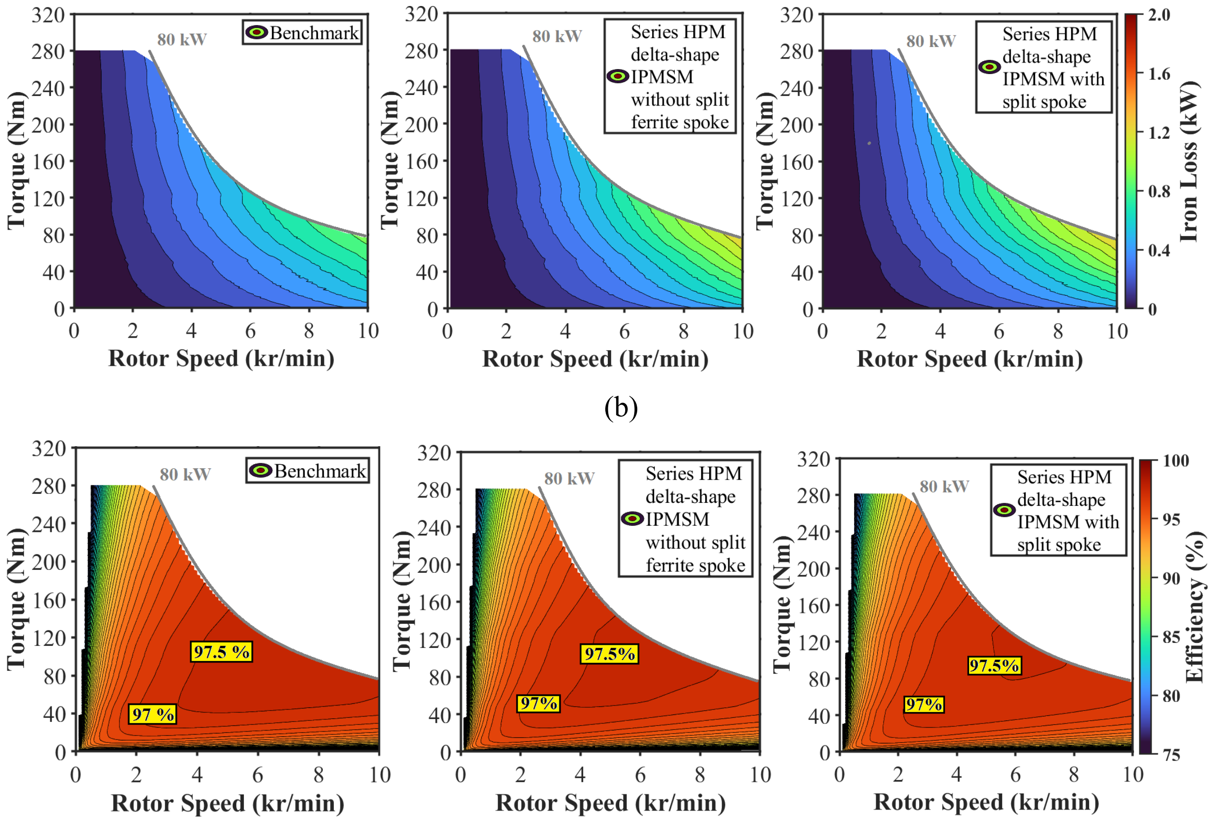

(b)

(c)

Fig. 4.14. Comparisons of copper loss, iron loss, and efficiency maps. (a) Copper loss maps. (b) Iron loss maps. (c) Efficiency maps.

4.3.6. Comparison of PM Cost

The main advantage of HPM machines is to improve the torque per REPM volume usage ratio either by achieving a higher torque at the same volume of high-cost REPMs or the same torque at a lower volume of REPM material. As the latter method is used, a comparison of PM cost can distinguish the benefit of the proposed design as shown in Table 4.3. In this comparison, it is assumed that the cost of REPM being 10 times the FEPM. As can be seen, the proposed series HPM delta-shape IPMSM with split ferrite spoke requires only ~52 cm^3 REPM which is ~54% less than that of the series HPM delta-shape IPMSM without split ferrite spoke with ~113 cm^3 and ~79% less than that of the benchmark with ~250 cm^3. As a result, the PM material cost of the proposed design is estimated to be ~67% less than that of benchmark, and ~37% less than that of its HPM counterpart without split ferrite spoke.

It should be noted that the selected benchmark for this chapter is a commercialized EV IPMSM as the aim of this thesis is to propose novel HPM machines for EV application. However, this benchmark may not be optimized against the same conditions and objectives as the proposed HPM machines in this chapter. As a result, the direct comparisons of the volumes and the cost of PMs may not be fair enough. Therefore, it is essential to declare that the benchmark is used as a reference only. However, the effectiveness of the proposed method can be validated by comparing the volumes and the total cost of PMs in the proposed HPM machines without and with split FEPMs, which are optimized at the same conditions and objectives. Meanwhile, for a fair comparison in conclusion chapter, a REPM-based baseline rotor will be optimized at the same conditions and objectives as the proposed HPM machines using the same stator, specifications, and overall dimensions as the benchmark.

Table 4.3. Comparison of PM Cost

Parameter	**Benchmark**	**Series HPM delta-shape IPMSM without split ferrite spoke**	**Series HPM delta-shape IPMSM with split ferrite spoke**
Size of machine		Same	
Torque (Nm)	280.3	280.5	281.46
REPM volume (cm^3)	249.4	112.85	52.14
FEPM volume (cm^3)	0	264.82	451.16
REPM mass (kg)	1.895	0.858	0.396
FEPM mass (kg)	0	1.324	2.256
PM cost estimation (%)	100	52.23	32.81

- Mass densities of REPM and FEPM are 7.6 and 5 g/cm^3
- Cost of REPM assumed to be 10 times of FEPM

4.4. Mechanical Strength and Demagnetization

As a high volume of FEPM is used in the developed series HPM delta-shape IPMSMs, the mechanical strength of these machines at high speed needs to be investigated. In this regard, Fig. 4.15 compares the von-mises stress distributions of benchmark and the two developed HPM machines at 10000 r/min where all contact regions are frictional with the friction coefficient of 0.2. In addition, for the sake of fair comparison in topologies with similar cross sections, the thicknesses of the ribs in the series HPM delta-shape IPMSM without split ferrite spoke are adjusted for a similar stress level as the benchmark as shown in Figs. 4.15 (a) and (b). Then, these thicknesses are kept constant in the proposed design (See Table 4.2) to investigate the advantage of the introduced gap and verge for mechanical strengthening purposes in the proposed design (See Fig. 4.4 (a)). As can be seen, the maximum stress on outer rib in the benchmark and the series HPM delta-shape IPMSM without split ferrite spoke can reach to ~280 MPa which implies the safety factor of 1.6 at the maximum speed. Meanwhile, the maximum stress on outer ribs of the proposed series HPM delta-shape IPMSM with split ferrite spoke is 255 MPa which implies the safety factor of 1.76 at the same maximum speed. Therefore, it can be concluded that although the mass of PMs has increased by ~22%, the maximum stress on the rib is reduced by ~9% compared to those of the other HPM counterpart. On the one hand, the resultant movement of FE2 magnet caused by centrifugal force at high speed, will be prohibited by the employed verges. On the other hand, a lower mechanical force will be transferred to the centre of the pole as a part of contact regions, between FE2 magnets and core, are reduced by the employed gaps. Fig. 4.16 compares the maximum von-mises stress on outer ribs of these machines at different speeds when the maximum tolerable stress of the electrical with the safety factor of 1 is 450 MPa. As can be seen, the maximum von-mises stress of the proposed machine is lower than the other topologies.

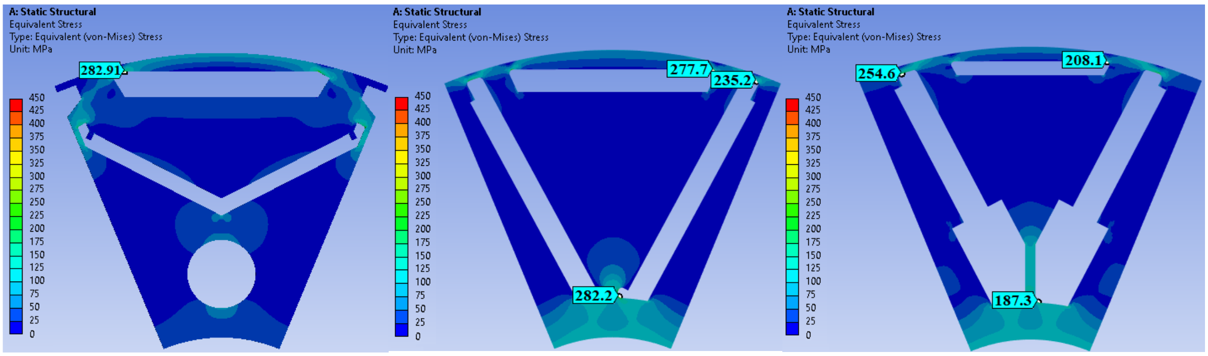

(a) (b) (c)

Fig. 4.15. Comparison of von-mises stress distributions at 10000 r/min. (a) Benchmark. (b) Series HPM delta-shape IPMSM without split ferrite spoke. (c) Series HPM delta-shape IPMSM with split ferrite spoke.

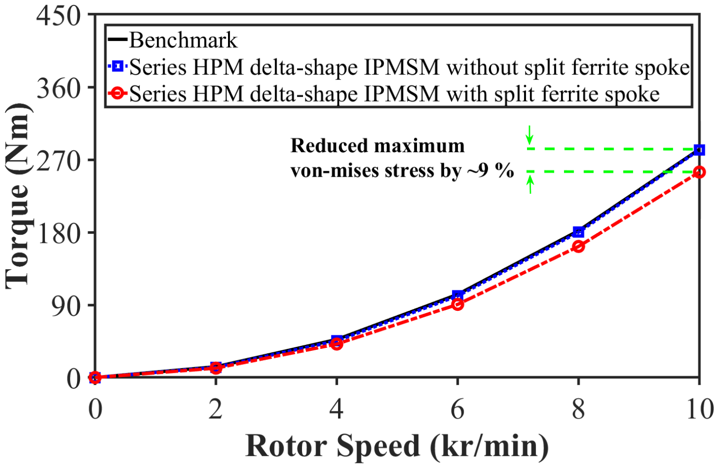

Fig. 4.16. Comparison of maximum von-mises stress on outer ribs at different speeds.

The demagnetization withstand capability of FEPMs needs to be investigated at low temperatures as they will be more vulnerable. However, these magnets can receive a magnetic field support against the irreversible demagnetization from the series REPMs. Fig. 4.17 compares the demagnetization withstand capability of FEPMs in the developed series HPM delta-shape IPMSMs at -40 °C of temperature and twice of d-axis rated current. As can be seen, both machines show an acceptable tolerance against demagnetization at this condition. However, the demagnetized region of the proposed design is slightly higher than the other counterpart. It is because the FEPMs receive less magnetic field support by the reduced volume of REPM. Moreover, a comparison of the FEPMs' demagnetization with and without stator at open circuit condition and -40 °C of temperature is presented in Fig. 4.18. It is worth mentioning that the TDK-FB13B FEPM has the knee point of 0.06 T at this temperature. As can be seen in Figs. 4.18 (a) and (b), no demagnetized region can be found at open circuit condition at the presence of stator. In addition, it can be observed that the open circuit flux linkage flows through stator. However, there is an inter-link flux path through two adjacent poles when rotor is located out of stator (e.g. during assembling stage) as shown in Figs. 4.18 (c) and (d). As can be seen, there is no demagnetized region of FEPMs in both machines as a series configuration of HPM is used. However, applying a similar condition to a parallel HPM machine may lead to a partial demagnetization region in FEPMs which can add extra tolerance to the manufacturing.

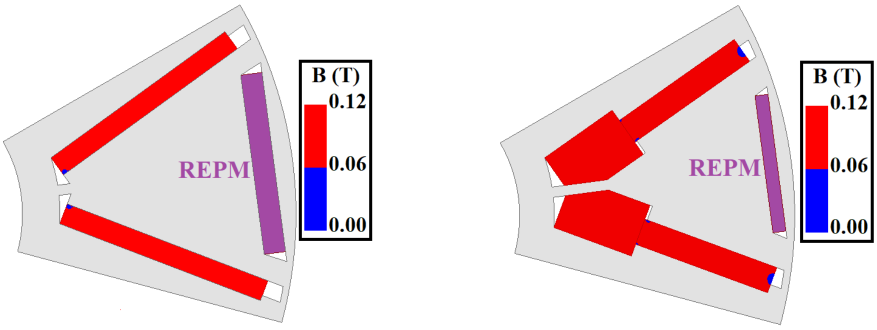

(a) (b)

Fig. 4.17. Comparison of demagnetization withstand capability of FEPMs at -40 °C and twice of rated d-axis current. (a) Series HPM delta-shape IPMSM without split ferrite spoke. (b) Series HPM delta-shape IPMSM with split ferrite spoke.

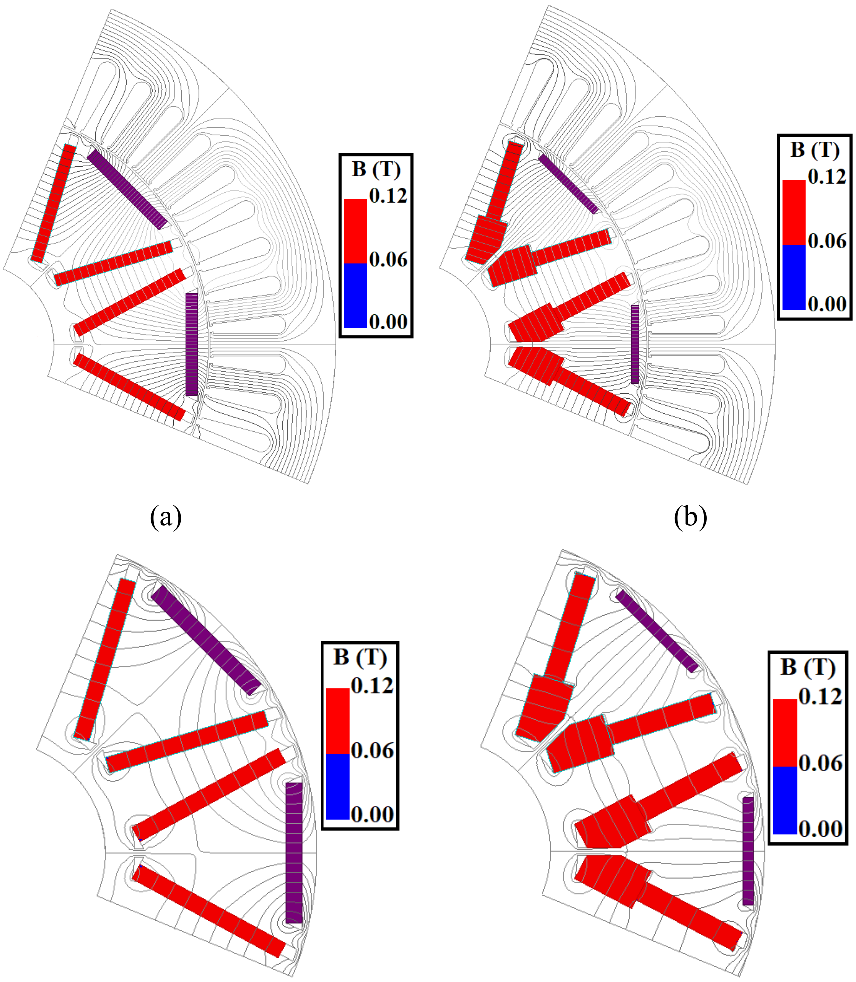

(a) (b)

(c) (d)

Fig. 4.18. Comparison of demagnetization withstand capability of FEPMs at -40 °C and open circuit condition. (a) Series HPM delta-shape IPMSM without split ferrite spoke and with stator. (b) Series HPM delta-shape IPMSM with split ferrite spoke and stator. (c) Series HPM delta-shape IPMSM without split ferrite spoke and stator. (d) Series HPM delta-shape IPMSM with split ferrite spoke and without stator.

4.5. Experimental Validation

To validate the FEA results, a small size 24-slot/8-pole (24s8p) series HPM delta-shape IPMSM with split ferrite spoke is manufactured as shown in Fig. 4.19. This machine is optimized at 40 W copper loss of active part with the main dimensional parameters as listed in Table 4.4. Then, it is tested using the dynamic and static test benches as presented in Fig. 4.20. The dynamic platform is used to measure the back-EMF and transient torque. However, the static test bench is conducted to measure the cogging torque and static torque [ZHU09].

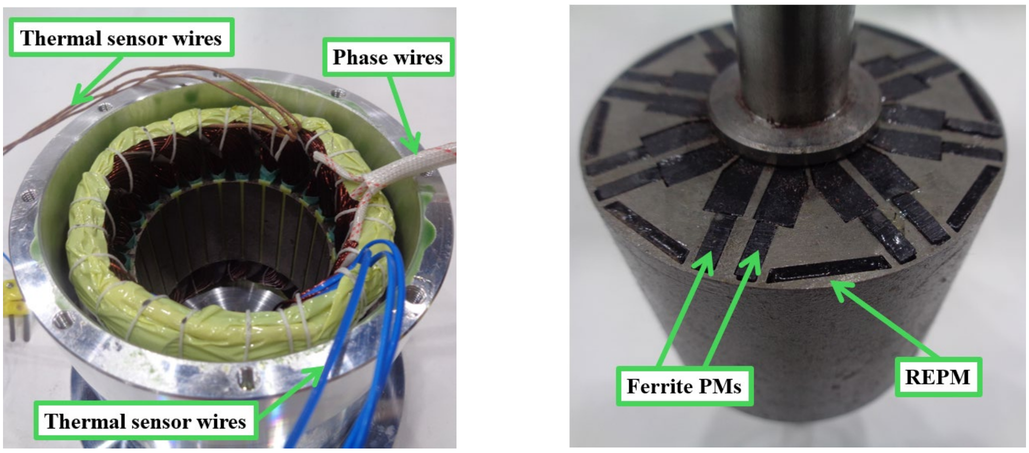

(a) (b)

Fig. 4.19. Prototype. (a) Stator. (b) Rotor.

Table 4.4. Main Dimensional Parameters of Prototype

Parameters	Values	Parameters	Values
Stator outer diameter	100 mm	Slot number	24
Stator inner diameter	63 mm	Pole number	8
Active stack length	50 mm	Turns per coil	60
Airgap length	1 mm	Phase resistance	1.6 Ω
Remanence of N28AH	1.075 T	Phase current	4 A_{max}
Remanence of TDK-FB13B	0.475 T		

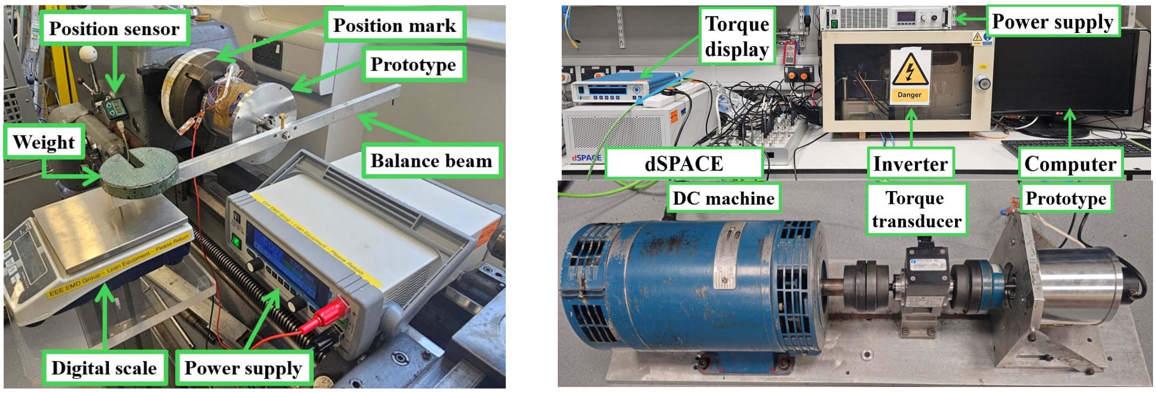

(a) (b)

Fig. 4.20. Experimental test benches. (a) Static test rig. (b) Dynamic test rig.

The open circuit line back-EMF waveforms and spectra obtained by FEA and measurement are compared at 750 r/min rotor speed in Fig. 4.21, whereas the cogging torques are compared in Fig. 4.22. As can be seen, both measured back-EMF and cogging torque waveforms and spectra are in good agreement with FEA predictions. It is worth noting that as the cogging torque waveform consists of 6 periodic cycles in one electrical period, only one-six of an electrical period is used for the measurement. Fig. 4.23 shows the variation of static torque with rotor position when DC current ($I_a = -2I_b = -2I_c = I_{DC}$) is injected into windings, whereas the variation of predicted and measured average torques with current are compared in Fig. 4.24. As can be seen, the measured torques match well with predictions with an error of ~3.5%.

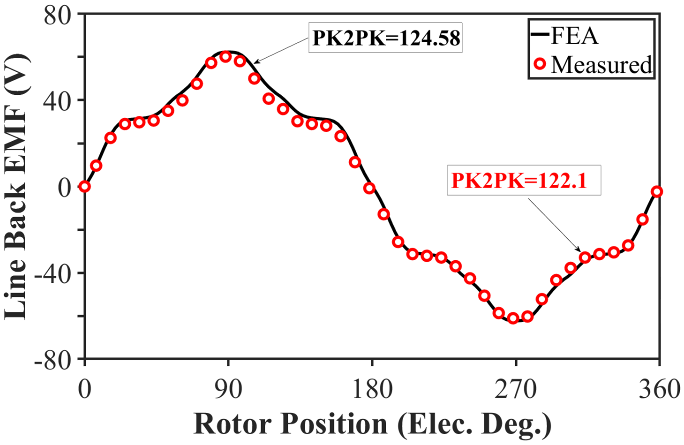

(a)

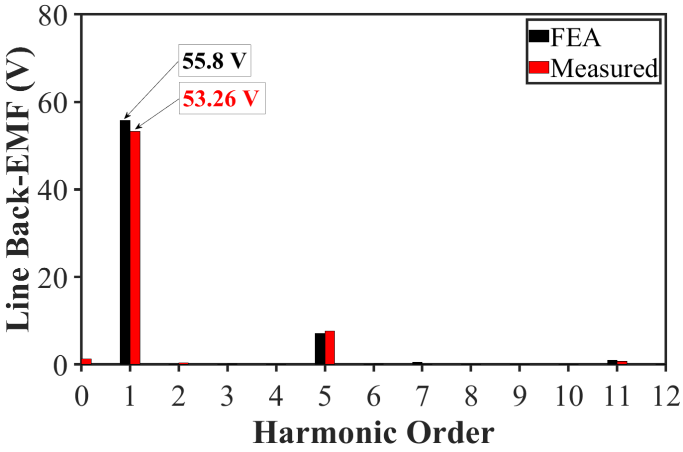

(b)

Fig. 4.21. FEA predicted and measured line back-EMFs at 750 r/min. (a) Waveforms. (b) Spectra.

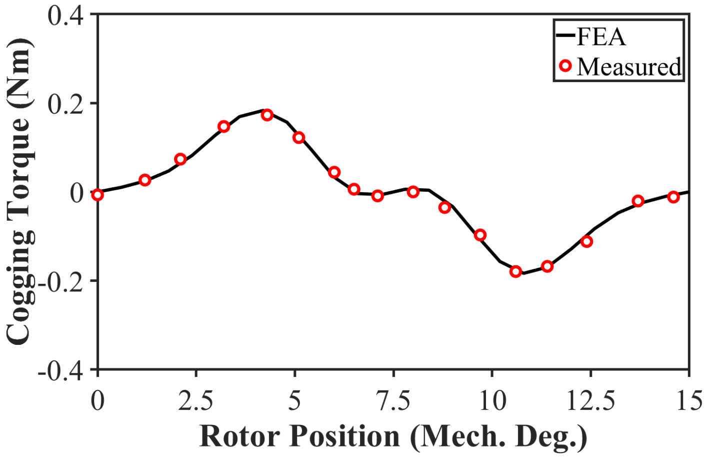

(a)

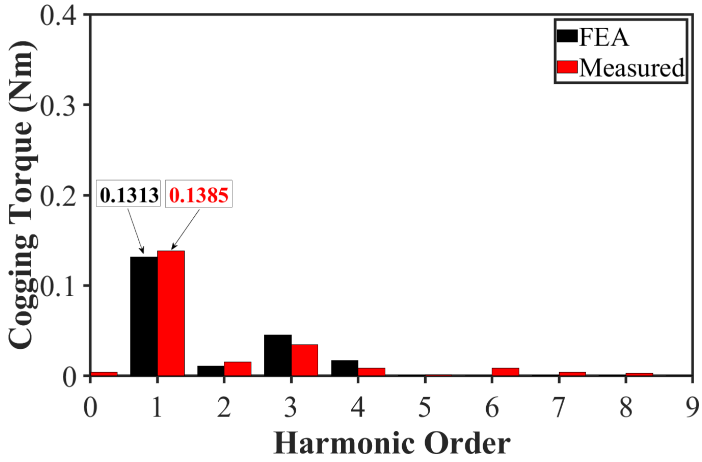

(b)

Fig. 4.22. FEA predicted and measured cogging torques at open circuit (one-six of an electrical period). (a) Waveforms. (b) Spectra.

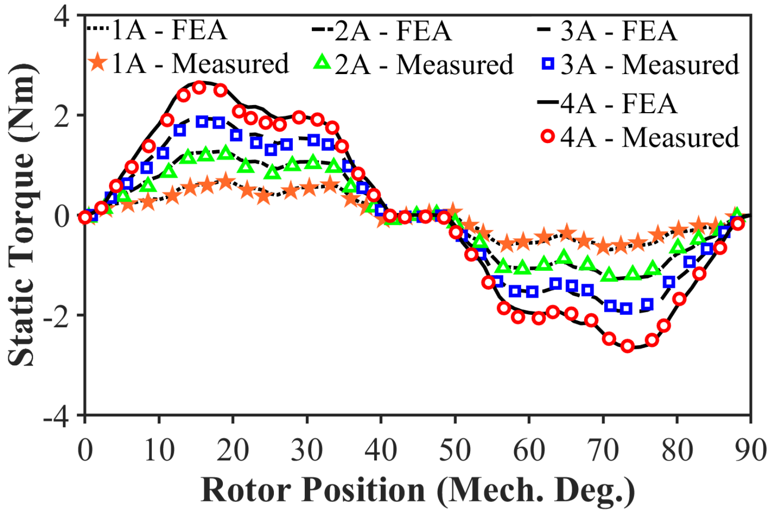

Fig. 4.23. FEA predicted and measured static torques at different DC currents.

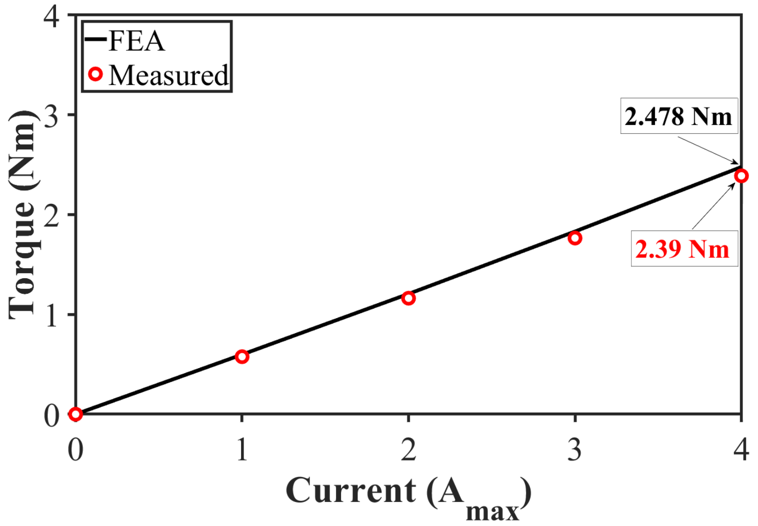

Fig. 4.24. Variation of FEA Predicted and measured average torques with current at 250 r/min.

4.6. Conclusion

In this Chapter, a novel series HPM delta-shape IPMSM with split ferrite spoke is presented. The electromagnetic performance, mechanical strength, demagnetization withstand capability of FEPM, and PM cost of the proposed machine are compared to those of a series HPM counterpart without split ferrite spoke and a commercialized REPM-based benchmark. It is shown that the series HPM delta-shape IPMSM without split ferrite spoke requires a less volume of REPM than the benchmark at the same torque. However, the FEPM usage of this machine is restricted by the q-axis flux path. To address this issue, the effect of dividing the FEPM spoke into two segments is investigated and shown that a proper splitting method can increase the output torque. Then, the performance of the optimum series HPM delta-shape IPMSM with split ferrite spoke is compared to that of the other topologies. It is shown that for the same torque, the proposed design benefits from the lowest amplitude of open circuit flux linkage and back-emf. This can also be considered as a lower risk of damage to the terminals of an inverter when a fault occurs at high speeds. Meanwhile, using the FPM, it is shown that the torque components of these machines are different even when they all generate the same peak torque. It is observed that the proposed machine has high FEPM torque and reluctance torque components and thus requires less REPM torque component and a lower resultant volume of REPM. The cost comparison shows that the PM material cost of the proposed series HPM delta-shape IPMSM with split ferrite spoke is estimated to be ~67% less than that of benchmark, and ~37% less than that of the other HPM counterpart. In addition, the comparison of von-mises stress distributions shows an improved mechanical strength in the proposed HPM topology with split ferrite spoke at the same speed and ribs' thicknesses as the other HPM counterpart without split ferrite spoke.

CHAPTER 5

NOVEL HYBRID MAGNET ASYMMETRIC V- AND U-SHAPE IPMSMS ACCOUNTING FOR DEMAGNETIZATION WITHSTAND CAPABILITY

5.1. Introduction

The rare-earth permanent magnet (REPM) machines with the outstanding benefits of high torque/power densities and high efficiency, etc., have been widely used in high performance electric vehicles (EVs) [ZHU07]. Meanwhile, as the EV market is growing, a cost-effective design challenge has been raised towards the electrification transportation. On the one hand, the competitive EV market has required the US Department of Energy (DoE) and the UK Advanced Propulsion Centre (APC) to draft higher performance targets for the future [SHA20]. On the other hand, the DoE has reported that about 20% to 30% of total expense of a PM machine belongs to the price of the costly REPMs [ENE]. To address this issue, the torque per REPM volume ratio needs to be improved in PM machines [POU21].

The magnetic field shifting (MFS) effect in an asymmetric rotor geometry and the utilization of low-cost ferrite PMs (FEPMs) in a hybrid PM (HPM) configuration are the two promising examples of torque per REPM volume ratio enhancement methods which have gained a lot of attention in recent years [ZHU22], [CHE11B]. In an asymmetric rotor PM machine, the reduced difference between the corresponding current advancing angles of the maximum PM and reluctance torque components leads to a higher resultant torque [XIA21A]. Meanwhile, the main feature of the HPM machines rely on using the high-energy product but expensive REPMs together with the low-energy product but inexpensive FEPMs in one topology. As a result, these machines can deliver a high performance at a reduced cost. The HPM utilization can be considered as a new approach in the design of PM machines which is introduced only about a dozen of years [CHE11B], [SHE12], [ISH13], and [AFI14]. These machines can be divided into three configurations including parallel, series, and mixed which are categorized by the relative positions of two PM materials in an equivalent magnetic circuit [ZHE21A], [KAZ23D]. For example, the flux paths of two PM types are in parallel in a parallel HPM configuration. Therefore, each PM type would face a lower magnetic reluctance in its flux path leading to a higher electromagnetic performance than an equivalent series HPM counterpart

[KAZ25]. On the downside, a parallel HPM arrangement suffers from a lower demagnetization withstand capability of FEPMs than that of a series HPM topology [AFI14]. Meanwhile, a mixed HPM configuration is a combination of the first two designs and can have a trade-off performance [ALQ21]. It is shown in [MA20] that a spoke-type IPMSM with a parallel configuration of HPM can significantly improve the torque per REPM volume ratio of PM machines due to the high consumption of FEPMs in each spoke. Meanwhile, a novel parallel HPM V-shape spoke IPMSM is introduced in [KAZ25] to not only maximize the FEPM usage in each spoke but also improve the reluctance torque component by using a V-shape arrangement of PMs.

Although each of these methods can separately improve the torque per REPM ratio in a PM machine, a combination of them may lead to even more enhanced benefits. For example, the application of an asymmetric bar-shape REPM in a series and a mixed HPM spoke-type IPMSMs are investigated in [ZEN19], [ZHU23B], and [CHE21], [CHE23], respectively. The proposed machines in both configurations are shown to have an enhanced torque density due to the MFS effect. In addition, an asymmetric HPM machine with unequal poles is proposed in [XU17A]. Although the performance of the proposed machine is improved, it may suffer from the axial leakage flux due to the employment of unequal north and south poles. In [LIU23B], a parallel HPM asymmetric V-shape IPMSM using a low volume of FEPM is proposed. In [JI23], a HPM IPMSM with a consequent pole asymmetric rotor structure is compared to a conventional pole asymmetric rotor counterpart. The results show that the proposed consequent pole IPMSM benefits from a higher torque per REPM volume ratio than its conventional counterpart at the cost of slightly lower overload capability.

This chapter proposes two mixed parallel and series HPM asymmetric V-shape and U-shape IPMSMs considering the demagnetization withstand capability of FEPMs. The proposed V-shape structure utilizes an enlarged barrier over FEPM to distance this magnet from the armature current. However, the proposed U-shape counterpart consists of a U-shape barrier design with PMs being filled in a L-shape arrangement. The vulnerable FEPM in this structure is removed to improve the demagnetization withstand capability and the magnetic field shifting effect. As will be shown, the demagnetization withstand capability of FEPMs is considerably improved in both machines. Meanwhile, it should be noted that the improved demagnetization is achieved at the cost of a slight reduction of torque performance which can be interpreted as a slight increase in the cost of PMs for generating the same torque. Therefore, at first, two initial topologies will be designed and optimized for the same torque at a lower volume of

REPM than that of the baseline when the demagnetization withstand capability is not considered. This is to evaluate the maximum reduction of REPM usage and PM cost saving. Afterwards, with the aim of improving the demagnetization withstand capability of FEPMs, the two final proposed topologies will be derived with the same optimization objectives. This is to evaluate the difference in the required volume of REPM and PM cost saving without and with considering the demagnetization improvement. In addition, a detailed comparison of electromagnetic performances will be presented including the open-circuit and on-load characteristics, loss/efficiency maps, and torque components decomposition using the frozen permeability method (FPM) in [WU12].

In this regard, section 5.2 introduces the initial (V-1 and U-1) and final (V-2 and U-2) proposed mixed parallel and series HPM asymmetric V-shape and U-shape IPMSMs and the REPM-based symmetrical V-shape IPMSM as the baseline. In section 5.3, the finite element analysis (FEA) is employed to investigate and compare the electromagnetic performances, mechanical strengths, and the demagnetization withstand capabilities, whereas in section 5.4 a comparison of PM cost is presented. Finally, sections 5.5 and 5.6 summarize the experimental validation and conclusion, respectively.

This chapter is submitted to IET Electric Power Applications [S. Kazemisangdehi, Z. Q. Zhu, L. Chen, L. Yang, and Y. Zhou, " Novel Hybrid Rare-earth and Ferrite Magnet Asymmetric V-shape and U-shape IPMSMs Accounting Demagnetization Withstand Capability"]

5.2. Mixed Parallel and Series HPM Asymmetric V- and U-shape IPMSMs

As this study only focuses on the design of different rotor geometries, the same specifications and stator of a commercialized IPMSM is used as presented in Table 5.1 and Fig. 5.1 (a). As can be seen this machine produces 280 Nm peak torque at its peak current (625 A_{max}) and rated speed (2100 r/min) by employing a 48-slot/8-pole (48s8p) combination of stator slots and rotor poles.

The V-shape IPMSMs are known for their simple structure with increased saliency and flux focusing effect. Therefore, the baseline of this study is designated as a REPM-based symmetrical V-shape IPMSM using the NdFeB type N28AH, as shown Fig. 5.1 (b). Then, two initial mixed parallel and series HPM asymmetric IPMSMs (V-1 and U-1) and two final mixed parallel and series HPM asymmetric IPMSMs (V-2 and U-2) without and with considering the demagnetization withstand capability of FEPMs will be designed using the same REPM material and FEPM type TDK-FB13B as shown in Figs. 5.1 (c) to (f). The main design criterion of all these HPM machines is to achieve the same torque as the baseline with a lower volume of REPM by substituting a part of this magnet with FEPM. For the sake of comparison, the inner and outer radii of rotor, the stack length, the airgap length, the stator dimensions, and the winding configurations are kept constant. Therefore, only the rotor structures will be re-designed. It is also worth mentioning that in general, the asymmetric IPMSMs are classified in four groups including symmetrical PM configuration and rotor core structure (group 1), symmetrical PM configuration but asymmetric rotor core structure (group 2), asymmetric PM configuration but symmetrical rotor core structure (group 3), and asymmetric PM configuration and rotor core structure (group 4) [ZHU22]. As can be seen in Fig. 5.1, all HPM asymmetric IPMSMs presented in this chapter can be categorized in group 4. These machines are introduced in more detail in the following subsections. For convenience, in the following discussions, all IPMSMs will have "mixed parallel and series HPMs" and hence "mixed parallel and series HPM IPMSMs" will be simply designated as "HPM IPMSMs".

Table 5.1. Specification of Commercialized IPMSM [YAN17A] and [BUR13]

Parameters	Values	Parameters	Values
Stator slot no.	48	Peak speed (r/min)	10000
Rotor pole no.	8	Rated speed (r/min)	2100
Stator outer diameter (mm)	200	Peak torque (Nm)	280
Stator inner diameter (mm)	131	Peak current (A_{max})	625
Rotor outer diameter (mm)	130	Peak current density (A/mm^2)	26.31
Rotor inner diameter (mm)	45	Conductor no. per slot	8
Stack length (mm)	151	Number of parallel branches	4
Airgap length (mm)	0.5	Active volume of machine (L)	4.76
NdFeB remanence (T)	1.075	Actual volume of machine (L)	6.06
Angle of rotor skew (degree)	3.75	Peak torque per actual volume (Nm/L)	46.2

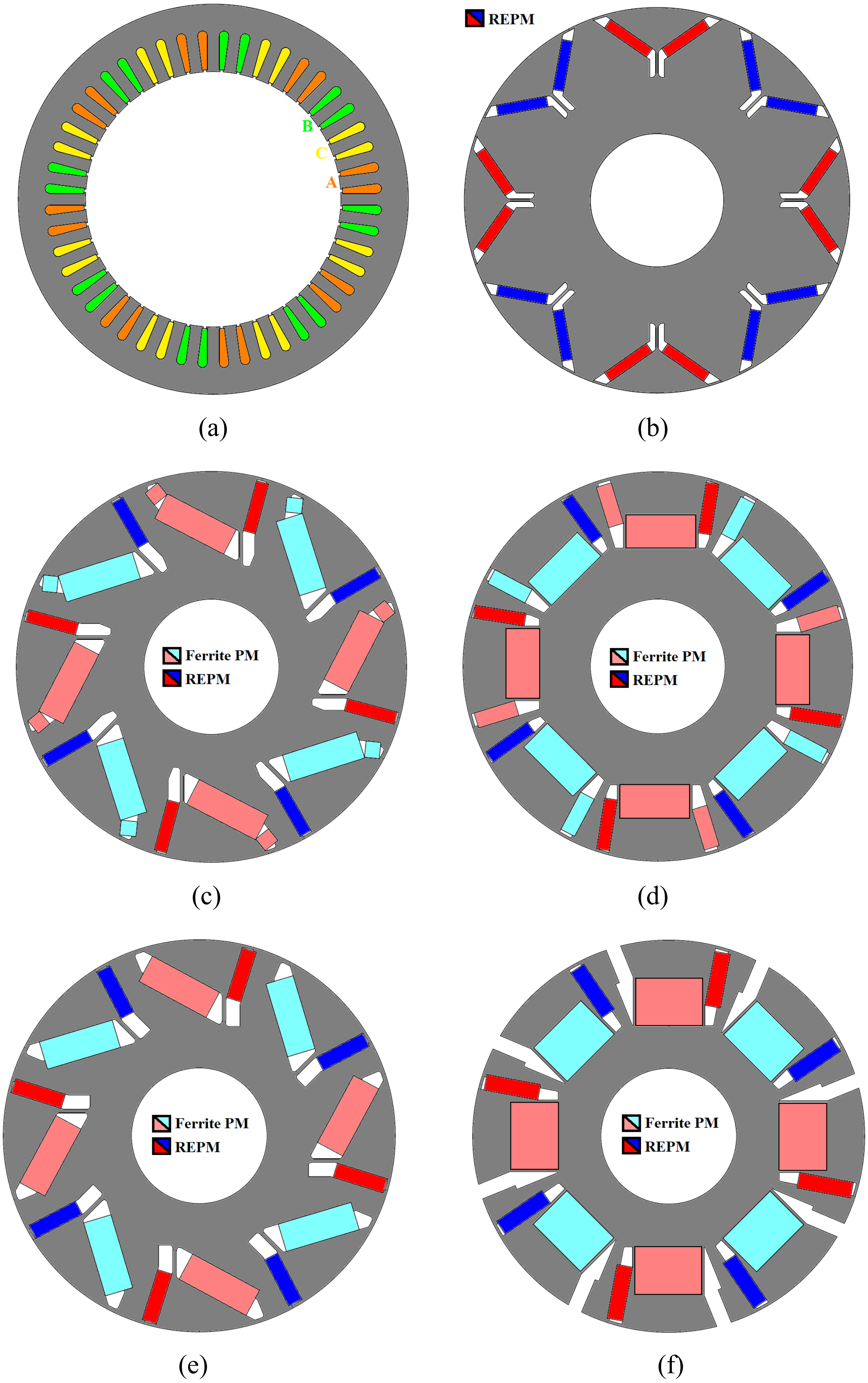

(a) (b) (c) (d) (e) (f)

Fig. 5.1. Structural comparison of IPMSMs. (a) Stator of the commercialized IPMSM. (b) REPM-based symmetrical V-shape rotor (baseline). (c) HPM asymmetric V-1 rotor (initial design). (d) HPM asymmetric U-1 rotor (initial design). (e) HPM asymmetric V-2 rotor (final design). (f) HPM asymmetric U-2 rotor (final design).

5.2.1. REPM-based Symmetrical V-shape IPMSM (Baseline)

A REPM-based symmetrical V-shape IPMSM is considered as the baseline of this study. The baseline uses neither the MFS effect nor the HPM utilization. Therefore, it is expected to have the highest required volume of REPMs among all topologies in Fig. 5.1. Consequently, it will be used as the REPM usage limit during the optimization of the others.

5.2.2. HPM Asymmetric V-1 IPMSM

The optimum design of the mixed HPM asymmetric V-1 IPMSM with two FEPM segments is presented in Fig. 5.1 (c). This machine maximizes the utilization of FEPMs along with a decent MFS effect. As a result, a high reduction of REPM usage is expected. As can be seen, the REPM is in parallel to the two FEPM segments within 1 pole. However, considering two adjacent poles, the two PM types are in a series connection. Therefore, the overall configuration of HPM in this machine is mixed (a combination of the series and parallel HPM configurations).

5.2.3. HPM Asymmetric U-1 IPMSM

Similar to the HPM asymmetric V-1 IPMSM, a counterpart with the U-shape arrangement of PMs is optimized as shown in Fig. 5.1 (d). The configuration of HPM in this machine is also considered as mixed whereas two FEPM segments are used as well.

5.2.4. HPM Asymmetric V-2 IPMSM

Accounting for the demagnetization withstand capability of FEPMs, it will be shown that the small FEPM in the mixed HPM asymmetric V-1 IPMSM suffers from a high risk. As a result, this magnet needs to be removed at the cost of a torque reduction. Therefore, the HPM asymmetric V-2 IPMSM is optimized with 1 FEPM segment per pole as shown in Fig. 5.1 (e). As will be shown, this machine would require more volume of REPM than the V-1 counterpart but at an improved demagnetization withstand capability.

5.2.5. HPM Asymmetric U-2 IPMSM

Similarly, the FEPM segment on the side of the mixed HPM asymmetric U-1 IPMSM also suffers from a high demagnetization risk. Therefore, the proposed mixed HPM asymmetric U-2 IPMSM is designed and optimized as shown in Fig. 5.1 (f). It will be shown that this machine benefits from a higher demagnetization withstand capability at the cost of an increased volume of REPM than those of the U-1 counterpart.

5.3. FEA Results

The FEA results are presented in this section. The aim is to improve the torque per REPM volume ratio by combining the HPM utilization and the MFS effect. In this regard, all HPM machines are optimized to deliver the same torque (280 Nm) as the baseline with a lower volume of REPM at 625 A_{max} and 2100 r/min. Meanwhile, the torque ripple mitigation is considered as the second objective. As there are more than one objective, the optimization function can be written as follows:

$$\begin{cases} \text{Objectives: Max } [T_{out}],\ \text{Min } [V_{NdFeB}],\ \text{Min } [T_{ripple}] \\ \text{Selection criteria of optimum point: } T_{out} \geq 280 \text{ Nm},\ V_{NdFeB} \leq 150.2 \text{ cm}^3,\ T_{ripple} < 4\% \\ \text{Weighting factors: } K_{T_{out}} = 4\text{p.u.},\ K_{V_{NdFeB}} = 2\text{p.u.},\ K_{T_{ripple}} = 1\text{p.u.} \\ \text{Variables: listed in Table II.} \end{cases} \tag{5.1}$$

where T_{out}, V_{NdFeB}, and T_{ripple} are the output torque, the volume of REPM, and the torque ripple, respectively.

Therefore, at the same torque and size, the optimization results will reveal the reduced amount of REPM volume. In addition, the cost of PMs can be compared in all machines at a fair condition by using the same size and torque. In other words, it can be used to emphasize the saved amount of money considering the price of REPM being ten times of FEPM. Then, a demagnetization withstand capability study will be conducted to investigate the risk of damage to the magnets at severe conditions. Moreover, a detailed comparison of performance in all machines will be conducted to compare their features and explain how the REPM usage and PM cost can be reduced in the proposed HPM asymmetric IPMSMs accounting for an improved demagnetization withstand capability. Meanwhile, having a similar mechanical strength is considered as a precondition for the fair comparison.

5.3.1. Optimization Results (Baseline, HPM Asymmetric V-1 and U-1 IPMSMs)

The optimization results of the baseline, HPM asymmetric V-1 and U-1 IPMSMs will be discussed in this section when they are optimized with the above-mentioned objectives. Fig. 5.2 (a) presents the parametric model of the REPM-based symmetrical V-shape IPMSM (baseline), whereas the optimization result, and the optimum cross section are shown in Fig. 5.2 (b) and (c), respectively. As can be seen, this machine requires ~150.2 cm^3 volume of REPM to deliver 280 Nm peak torque at 625 A_{max} and 2100 r/min.

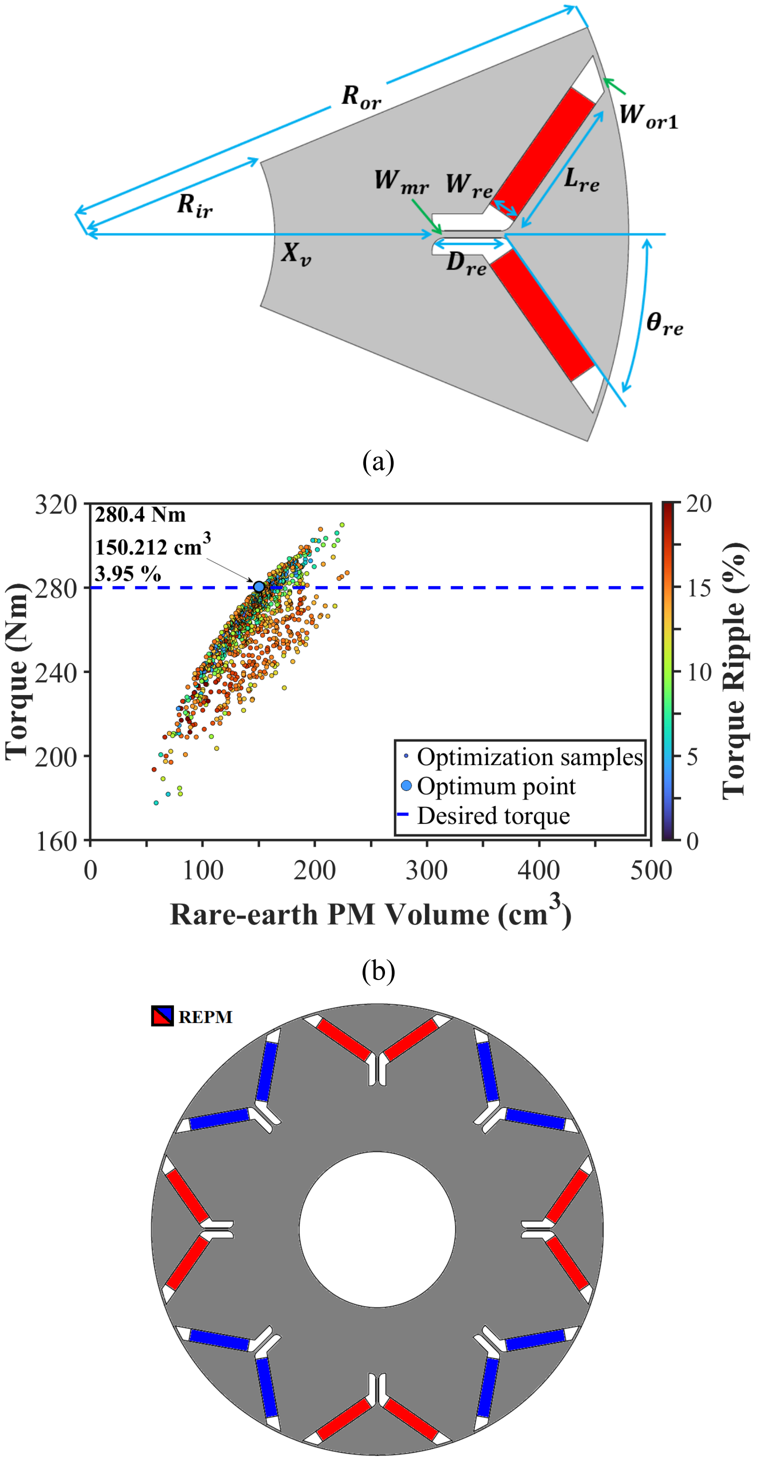

(a)

(b)

(c)

Fig. 5.2. REPM-based symmetrical V-shape IPMSM (baseline). (a) Parametric model. (b) Optimization result at 625 A_{max} and 2100 r/min. (c) Optimum cross section.

Meanwhile, Figs. 5.3 (a) to (c) present the parametric model of the HPM asymmetric V-1 IPMSM, the optimization result and the optimum cross section, respectively. As can be seen, this machine needs only ~87.3 cm^3 volume of REPM to produce 280 Nm peak torque at 625 A_{max} and 2100 r/min. Therefore, at the same torque and size, the volume of high-cost REPM can be reduced by ~42 %. In general, by using a V-shape arrangement of PMs with one FEPM and one REPM even at the same size, an asymmetric rotor can be achieved. This is due to the difference in the residual flux densities of these two PM types. However, two specific design considerations are used to effectively increase the MFS effect of the asymmetric rotor structure. Firstly, the relative angles of REPM and FEPM, which define their arcs, can be changed independently. Secondly, the centre of the V-shape arrangement can be displaced in Y-axis as shown in Fig. 5.3 (a). As will be shown, a displaced centre of V-shape arrangement causes an intentional saturation between two adjacent poles.

Finally, Figs. 5.4 (a) to (c) present the parametric model, optimization result, and optimum cross section of the HPM asymmetric U-1 IPMSM, respectively. As can be seen, to generate 280 Nm torque at 625 A_{max} and 2100 r/min, ~89.3 cm^3 volume of REPM is consumed in this structure. Therefore, at the same torque and size, the volume of high-cost REPM can be reduced by ~40.5 %. It is worth mentioning that for this design, two parameters are added to independently optimize the height of air barriers (H_{b1} and H_{b2}) as shown in Fig. 5.4 (a). This is to add more flexibility to cause an intentional saturation between two adjacent poles which helps with the MFS effect. Table 5.2 summarizes the definitions and the optimum values of the design parameters in these three machines. All parameters listed in this table are considered as the optimization variables except the constant inner and outer radii of rotor.

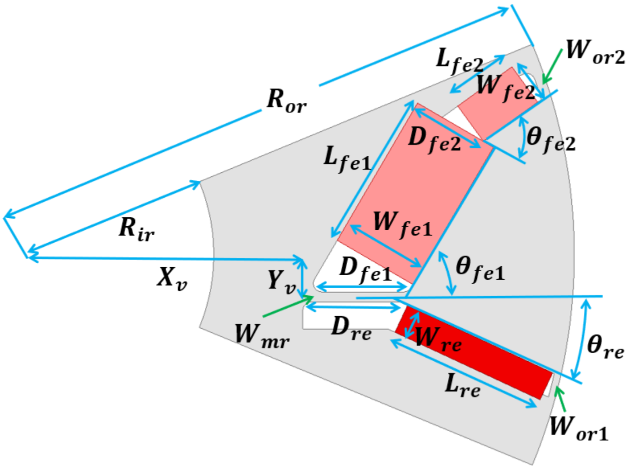

(a)

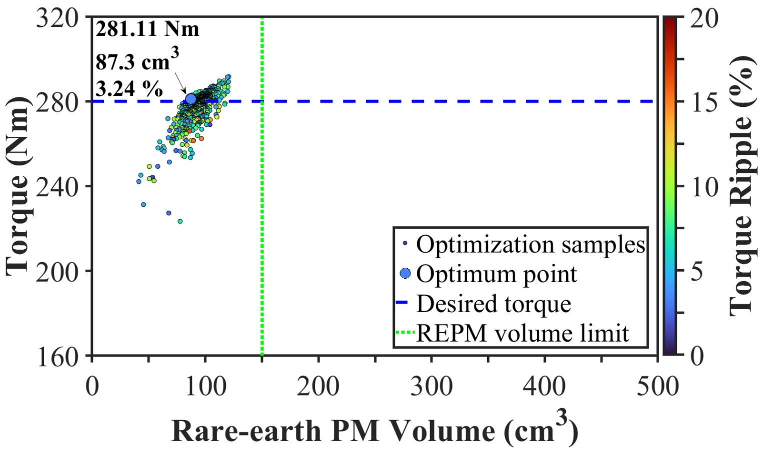

(b)

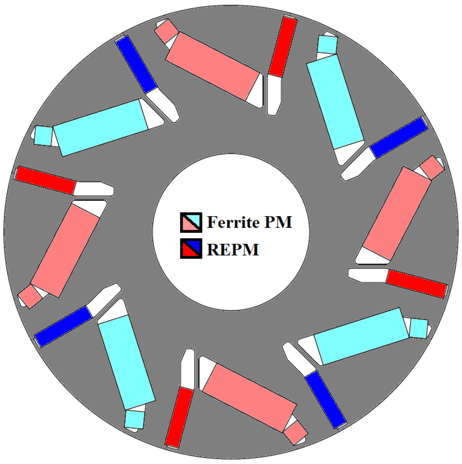

(c)

Fig. 5.3. HPM asymmetric V-1 IPMSM. (a) Parametric model. (b) Optimization result at 625 A$_{max}$ and 2100 r/min. (c) Optimum cross section.

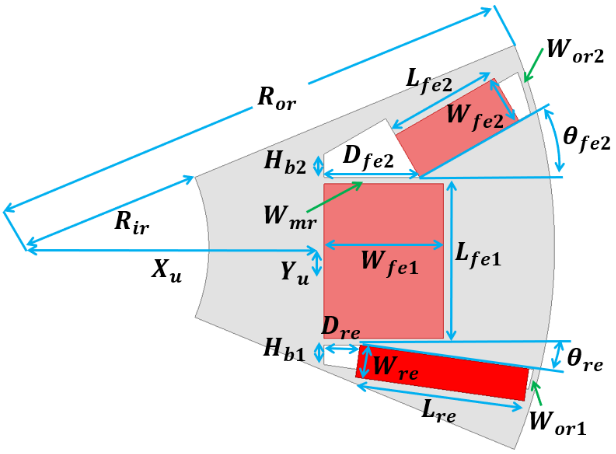

(a)

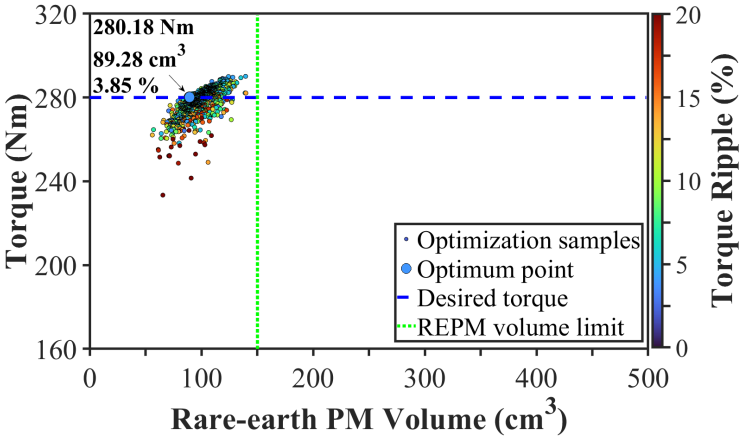

(b)

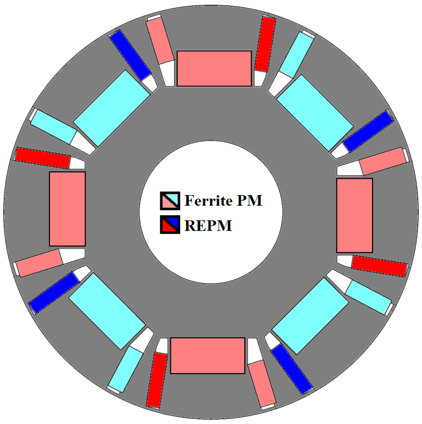

(c)

Fig. 5.4. HPM asymmetric U-1 IPMSM. (a) Parametric model. (b) Optimization result at 625 A_{max} and 2100 r/min. (c) Optimum cross section.

The widths of the ribs are defined using the mechanical strength analysis as shown in Fig. 5.5. This is to achieve a similar von-mises stress on the ribs to ensure the fair comparisons of performances and PM usage. Generally, the mechanical strength of rotor can be considered as an important factor when utilizing the HPMs. This is because replacing a certain amount of REPM at the same performance requires a higher volume of FEPM due to the difference in the magnetic properties of two PM types. Consequently, the increased mass of PMs can potentially transfer more stress on ribs. Therefore, the widths of the ribs need to be adjusted for the similar performance and mechanical strength considering that a thicker width, a higher leakage flux and thus a higher required volume of REPM. Consequently, the adjusted widths of the ribs for a similar maximum von-mises stress level are considered as a pre-condition of a fair PM usage comparison. Fig. 5.5 compares the von-mises stress distributions of these three machines at 10 kr/min rotor speed. As can be seen, the maximum stress on rib in these topologies can reach ~240 MPa which implies the safety factor of ~1.9 at the maximum speed. It is worth mentioning that the frictional contact with the friction coefficient of 0.2 is used for this analysis.

Table 5.2. Design Parameters and Their Optimum Values of Baseline, HPM Asymmetric V-1 and U-1 IPMSMs

Parameter	**symbol**	**Unit**	**REPM-based symmetrical V**	**HPM asymmetric V-1**	**HPM asymmetric U-1**
Rotor outer radius	R_{or}	mm	65		
Rotor inner radius	R_{ir}	mm	22.5		
V-shape in x-axis	X_v	mm	41.4	33.42	-
V-shape in y-axis	Y_v	mm	0	9.75	-
U-shape in X-axis	X_u	mm	-	-	39.45
U-shape in Y-axis	Y_u	mm	-	-	1.02
Width of REPM	W_{re}	mm	3.63	4.21	4.32
Length of REPM	L_{re}	mm	17.13	17.18	17.11
Width of FEPM1	W_{fe1}	mm	-	9.23	11.24
Length of FEPM1	L_{fe1}	mm	-	25.81	23.29
Width of FEPM2	W_{fe2}	mm	-	5.46	5.2
Length of FEPM2	L_{fe2}	mm	-	4.94	14.04
Angle of REPM	θ_{re}	Degree	55.13	14.91	9.04
Angle of FEPM1	θ_{fe1}	Degree	-	62.63	-
Angle of FEPM2	θ_{fe2}	Degree	-	66.29	17.13
REPM displacement	D_{re}	mm	6.05	11.04	5.14
FEPM1 displacement	D_{fe1}	mm	-	9.82	-
FEPM2 displacement	D_{fe2}	mm	-	8.95	8.41
Height of barrier 1	H_{b1}	mm	-	-	2.46
Height of barrier 2	H_{b2}	mm	-	-	2.86
Width of middle rib	W_{mr}	mm	0.8	1.2	0.8
Width of outer rib 1	W_{or1}	mm	0.6	0.8	0.8
Width of outer rib 2	W_{or2}	mm	-	1.2	0.8

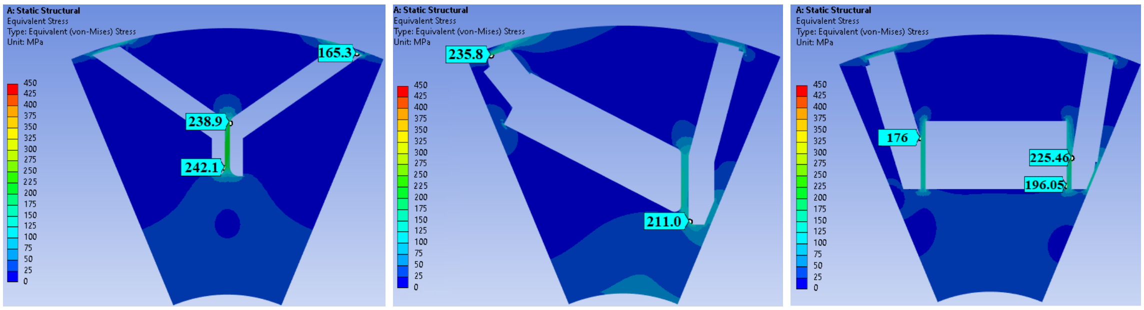

(a) (b) (c)

Fig. 5.5. Comparison of von-mises stress distributions at 10 kr/min. (a) REPM-based symmetrical V-shape IPMSM. (b) HPM asymmetric V-1 IPMSM. (c) HPM asymmetric U-1 IPMSM.

5.3.2. Comparison of HPM Asymmetric V-1 and U-1 IPMSMs

Fig. 5.6 compares the open circuit flux density and flux line distributions of the HPM asymmetric V-1 and U-1 IPMSMs. As can be seen, the d-axis is shifted in both machines. In addition, by focusing on the flux lines, the series connection of HPMs between two adjacent poles is visible. The comparison of the open circuit airgap flux density waveforms and spectra can be found in Figs. 5.7 (a) and (b), respectively. As suggested by [XIA21A], a numerical comparison of the MFS effect is achievable by comparing the shifted phase of the airgap flux density fundamental component waveforms. Therefore, Fig. 5.7 (c) presents a waveform comparison of the fundamental components of open circuit airgap flux densities in these two machines. As can be seen, the magnetic fields of the both HPM asymmetric V-1 and U-1 IPMSMs are shifted about ~10 electrical degrees.

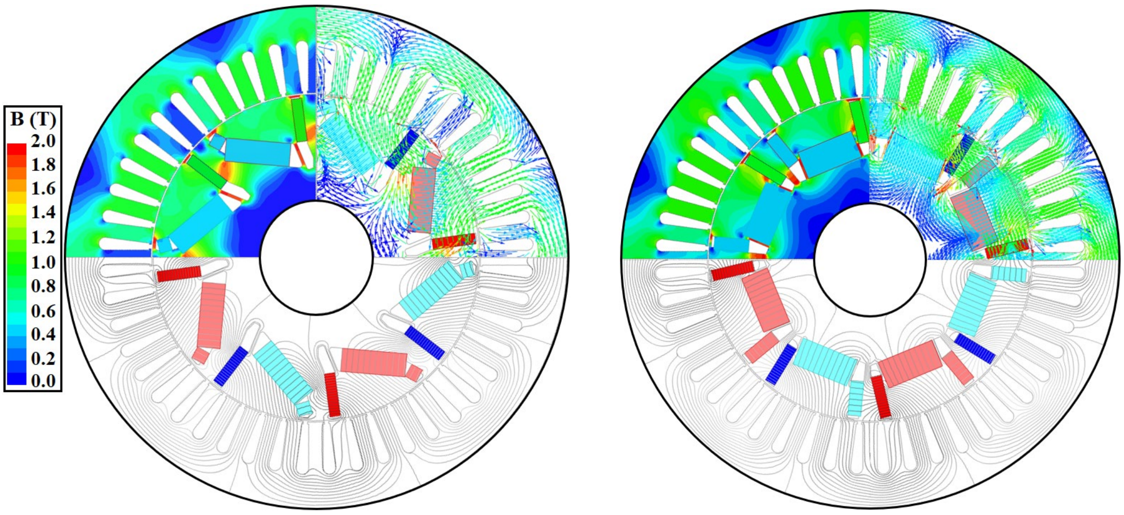

(a) (b)

Fig. 5.6. Comparison of open circuit flux density and flux line distributions. (a) HPM asymmetric V-1 IPMSM. (b) HPM asymmetric U-1 IPMSM.

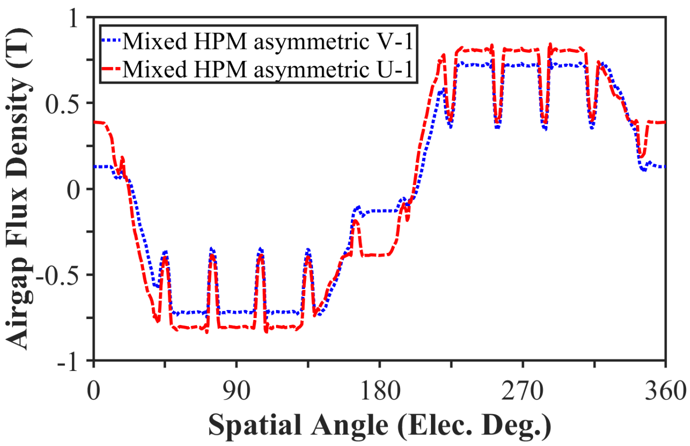

(a)

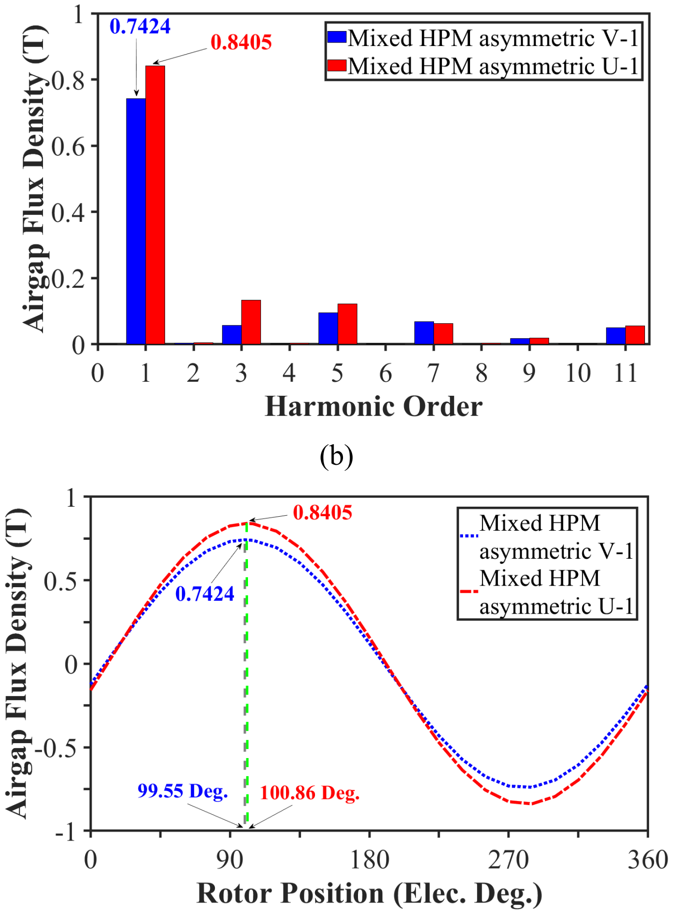

(b)

(c)

Fig. 5.7. Comparison of open circuit airgap flux densities of HPM asymmetric V-1 and U-1 IPMSMs. (a) Waveforms. (b) Spectra. (c) Fundamental component waveforms.

A comparison of the open circuit flux linkage waveforms and spectra is given in Fig. 5.8. As can be seen, the flux linkage waveforms of both machines are shifted whereas the maximum value of flux linkage in the HPM asymmetric U-1 IPMSM with 0.0663 Wb is higher than that of the HPM asymmetric V-1 IPMSM with 0.0573 Wb. Therefore, at the same speed, a higher amplitude of back-EMF is expected in the machine with U-shape arrangement of PMs. Figs. 5.9 (a) and (b) illustrate the open circuit back-EMF waveforms and spectra at 2100 r/min, respectively. As can be seen, the back-EMF's fundamental component of the HPM asymmetric U-1 IPMSM with 56.34 V is higher than that of the HPM asymmetric V-1 IPMSM with 49.7 V. A lower back-EMF may be considered as a safety measure especially at high speeds, when a fault can transfer a high voltage across the terminals of the inverter and cause damage. Therefore, Fig. 5.9 (c) compares the variations of peak-to-peak values of open circuit back-EMFs in both machines. As can be seen, the peak-to-peak value of the HPM asymmetric V-1 IPMSM at 10 kr/min with 466.74 V is 47.92 V (~9.3%) less than that of the U-1 HPM asymmetric U-1 topology.

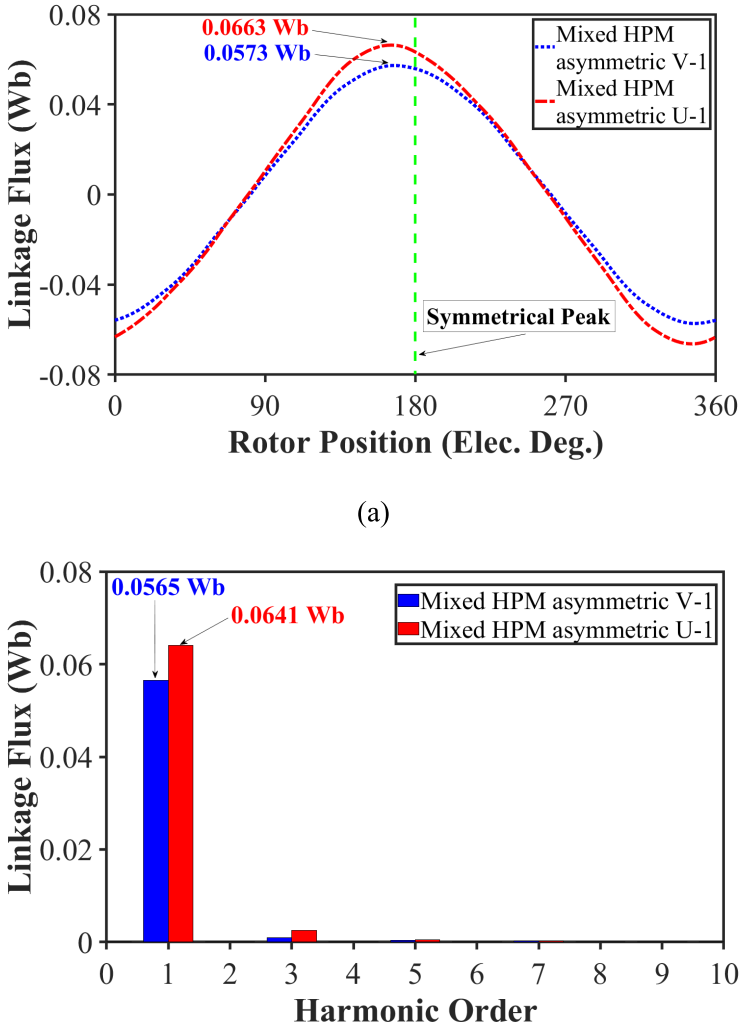

(a)

(b)

Fig. 5.8. Comparison of open circuit flux linkages in HPM asymmetric V-1 and U-1 IPMSMs. (a) Waveforms. (b) Spectra.

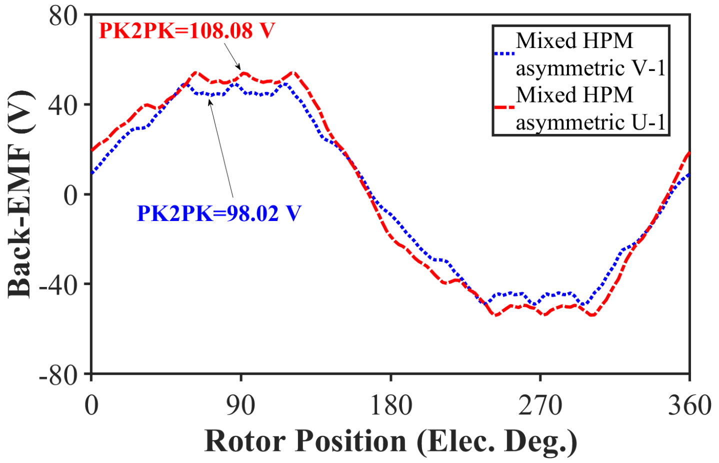

(a)

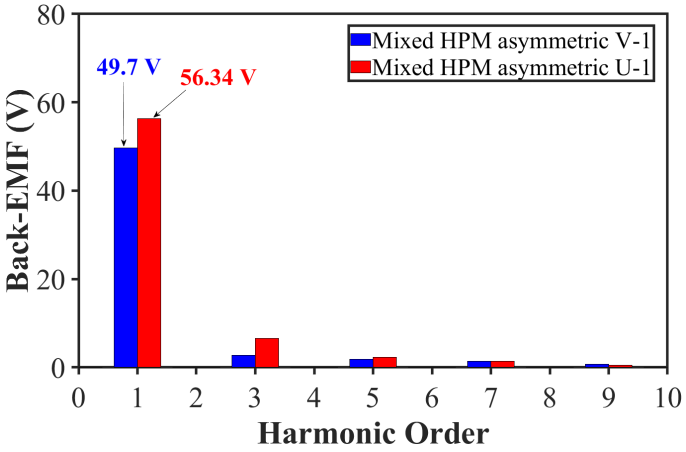

(b)

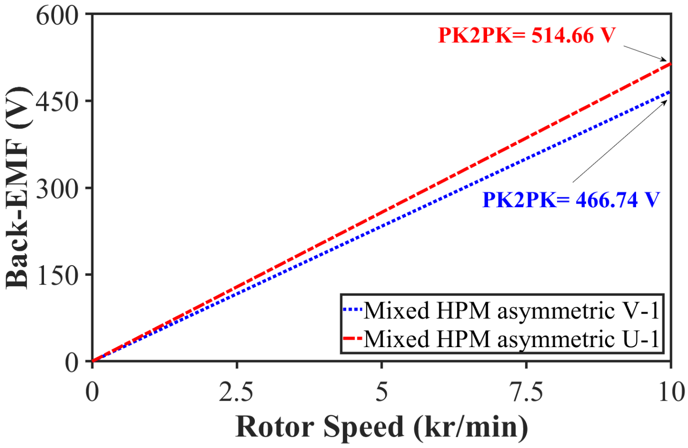

(c)

Fig. 5.9. Comparison of open circuit back-EMFs in HPM asymmetric V-1 and U-1 IPMSMs. (a) Waveforms. (b) Spectra. (c) Peak to peak values with speed.

Figs. 5.10 (a) and (b) compare the variations of torques and dq-axis inductances with the current advancing angle at 625 A_{max} and 2100 r/min. Although both machines have the same peak torque, their profiles of torque with current advancing angle are different. As a result, each machine would have a unique optimum current advancing angle.

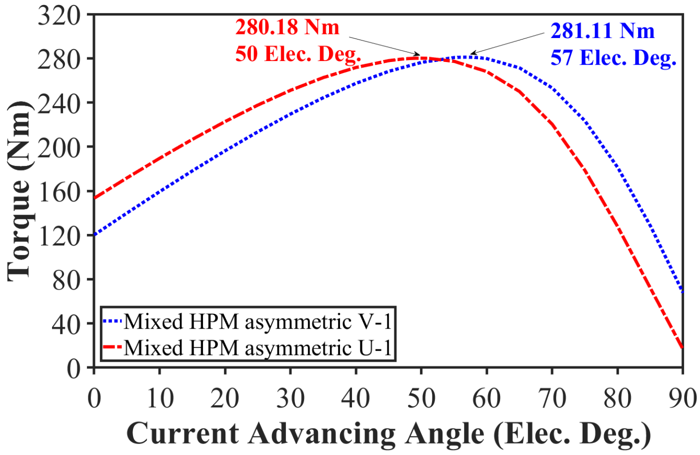

(a)

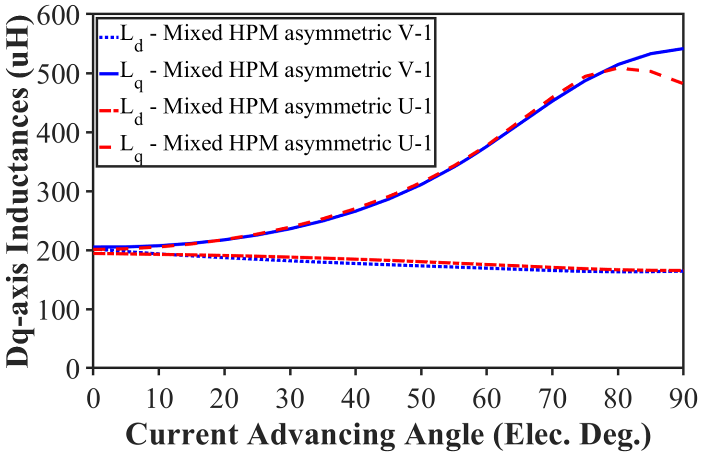

(b)

Fig. 5.10. Comparison of torque and dq-axis inductances with current advancing angle at 625 A_{max} and 2100 r/min in HPM asymmetric V-1 and U-1 IPMSMs. (a) Torques. (b) Dq-axis inductances.

Meanwhile, as the employed REPM (N28AH) has a residual flux density of 1.075 T, which is almost 2.3 times that in the FEPM (TDK-FB13B) with 0.475 T, a concern regarding the demagnetization withstand capability of FEPM rises. In addition, the difference in the magnetic properties of REPMs and FEPMs shows that, in contrast to REPMs, the FEPMs will be at a higher risk of irreversible demagnetization at low temperature. Therefore, demagnetization withstand capability study of FEPMs is conducted at -40 °C. Figs. 5.11 (a) to (d) compares the decomposed flux density distributions of FEPMs in their magnetization direction in both machines at -40 °C and open circuit condition. It is worth mentioning that in Figs. 5.11 (a) and (b), the rotors are assumed to be out of stator for example during the assembling stage or maintenance. However, in Figs. 5.11 (c) and (d), rotors are inside the stator without any injected current. In addition, the knee point of FEPMs type TDK-FB13B is equal to 0.06 T at this temperature. As can be seen, the FEPM2 suffers from regional self-demagnetized areas when rotor is outside of stator in both HPM asymmetric V-1 and U-1 IPMSMs. However, when rotors are inside the stator, the flux produced by PMs finds a lower magnetic reluctance in its path by circulating through the stator. As a result, no demagnetization occurs at this condition.

It is worth mentioning that in literature the combination of low temperature and high d-axis current (overload condition) is used for the demagnetization withstand capability analysis of FEPMs. However, the suggested overload current varies from a low ratio, e.g. 1.3 times and 1.5 times of the rated current in [WU17B] and [ZHU17B], and a more common ratio, e.g. 2 times of the rated current in [YU19], [DU20], [ZHE21A], to a higher ratio, e.g. 2.5 times and 3 times of the rated current in [MA20] and [CHE23]. Therefore, for a comprehensive investigation of the demagnetization withstand capability of FEPMs in the proposed HPM machine, multiple d-axis currents ranging from 2 times to 3 times of the rated current are applied at -40 °C of temperature as shown in Fig. 5.12. As can be seen, the FEPM2 significantly suffers from the irreversible demagnetization in both HPM asymmetric V-1 and U-1 IPMSMs. Therefore, these magnets are better to be removed to increase the demagnetization withstand capability of the proposed machines which may be at the cost of torque reduction.

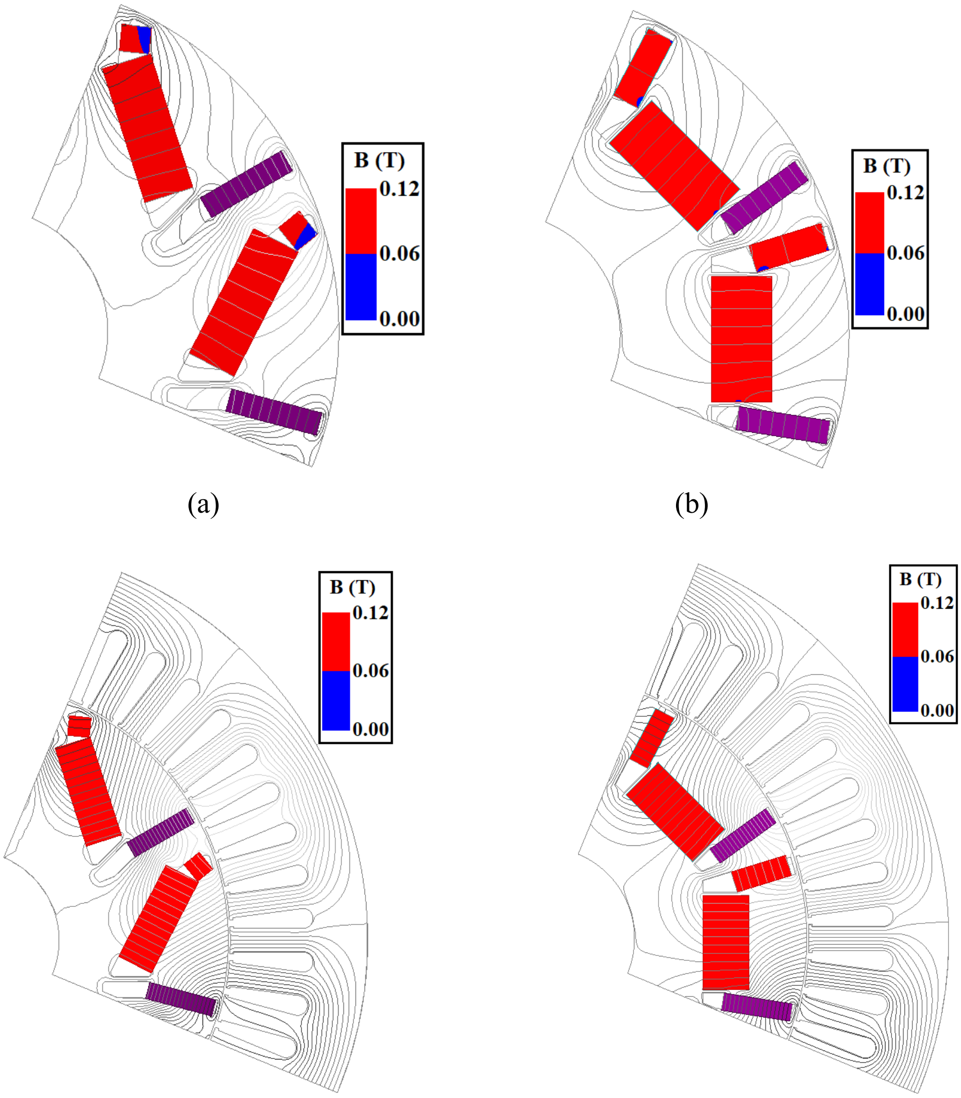

(a) (b)

(c) (d)

Fig. 5.11. Comparison of decomposed flux density distributions of FEPMs at -40 °C and open circuit condition. (a) HPM asymmetric V-1 rotor (without stator). (b) HPM asymmetric U-1 rotor (without stator). (c) HPM asymmetric V-1 rotor (with stator). (d) HPM asymmetric U-1 rotor (with stator).

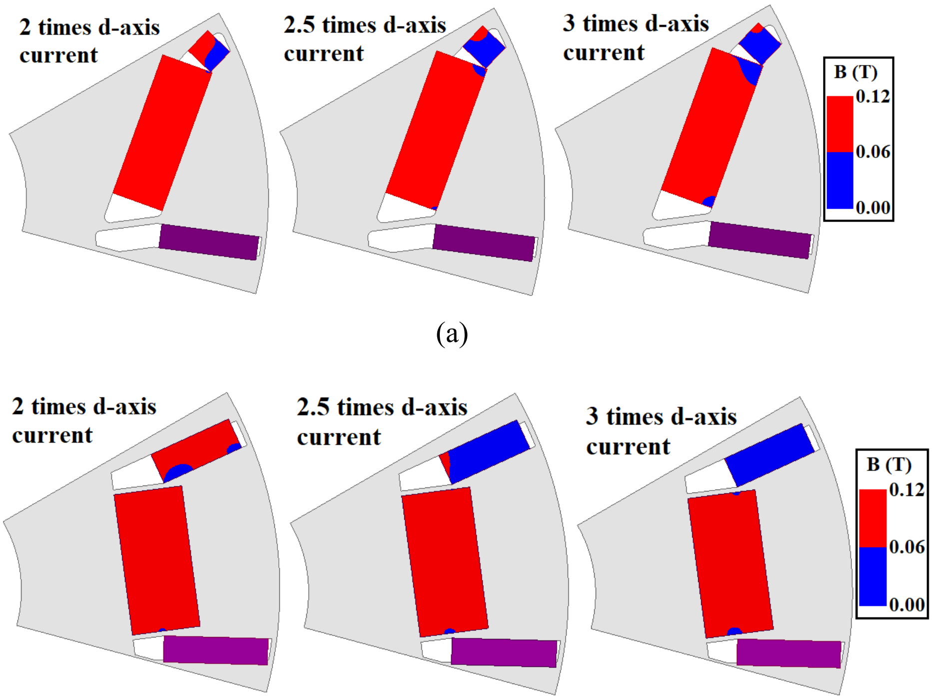

(a)

(b)

Fig. 5.12. Comparison of decomposed flux density distributions of FEPMs at -40 ºC when d-axis currents ranging from twice to triple of rated current are applied. (a) HPM asymmetric V-1 IPMSM. (b) HPM asymmetric U-1 IPMSM.

Fig. 5.13. Compares the produced torque by both HPM machines with and without FEPM2 at 625 A_{max} and 2100 r/min. As expected, both machines are producing about 280 Nm torque which they were optimized for. However, by removing the FEPM2, the developed torque of the HPM asymmetric V-1 IPMSM drops for ~9.5 Nm, and that of the HPM asymmetric U-1 IPMSM reduces about ~14.9 Nm. Consequently, the final proposed HPM asymmetric V-2 and U-2 IPMSMs are expected to use slightly more REPM volume to generate the same torque of 280 Nm, which will be discussed in more detail in the following section.

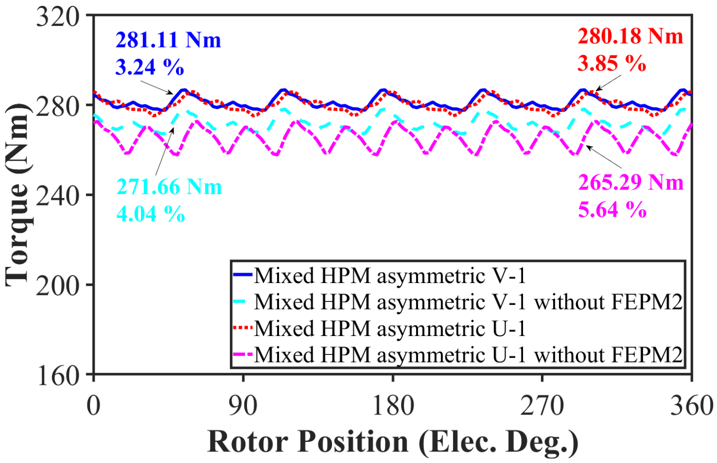

(a)

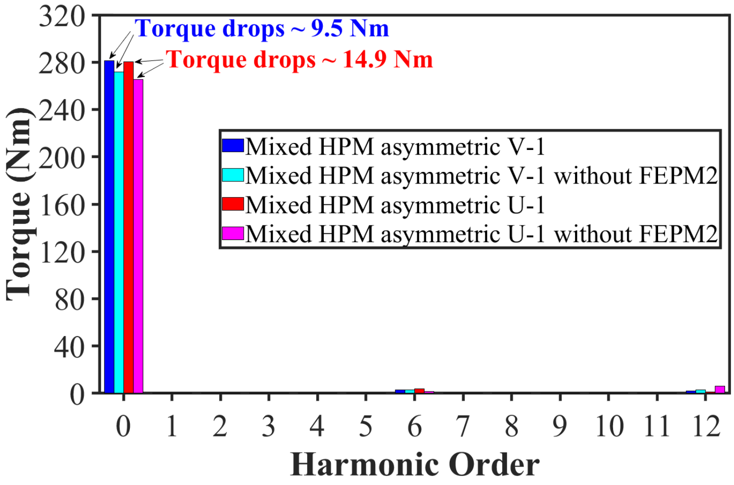

(b)

Fig. 5.13. Comparison of torque waveforms and spectra at 625 A$_{max}$ and 2100 r/min in both HPM asymmetric V-1 and U-1 IPMSMs considering the effect of FEPM2 removal. (a) Waveforms. (b) Spectra.

5.3.3. Optimization Results (HPM Asymmetric V-2 and U-2 IPMSMs)

The optimization results of the proposed HPM asymmetric V-2 and U-2 IPMSMs with an improved demagnetization withstand capability are presented in this section. In this regard, the parametric model of the HPM asymmetric V-2 IPMSM is shown in Fig. 5.14 (a), whereas the optimization result, and the optimum cross section of this machine are presented in Fig. 5.14 (b) and (c), respectively. As can be seen, this machine requires ~103.62 cm^3 volume of REPM to deliver 280 Nm peak torque at 625 A$_{max}$ and 2100 r/min. Therefore, at the same torque and size, the volume of high-cost REPM can be reduced by ~31 % compared to the baseline. Consequently, the saved volume of REPM is reduced from 42 % to 31 % compared to that of the HPM asymmetric V-1 IPMSM. However, as will be shown later, the demagnetization withstand capability of FEPM is significantly improved.

Furthermore, Figs. 5.15 (a) to (c) present the parametric model, optimization result, and the optimum cross section of the HPM asymmetric U-2 IPMSM, respectively. As can be seen, to produce 280 Nm torque at 625 A$_{max}$ and 2100 r/min, ~115.09 cm^3 volume of REPM is consumed in this structure. Therefore, at the same torque and size, the volume of high-cost REPM can be reduced by ~23.4 % compared to the baseline. Meanwhile, the saved volume of REPM is reduced from 40.5 % to 23.4 % compared to that of the HPM asymmetric U-1 IPMSM, but a higher demagnetization withstand capability of FEPM is achieved. It is worth mentioning that the parametric models of the HPM asymmetric V-2 and U-2 IPMSMs are like those of the

HPM asymmetric V-1 and U-1 IPMSMs except not employing the FEPM2 segments. In addition, the second outer rib is removed in the parametric model of the proposed HPM asymmetric U-2 IPMSM ($W_{or2} = 0$) as shown in Fig. 5.15 (a). The definitions of the design parameters and their optimum values in both machines are summarized in Table. 5.3.

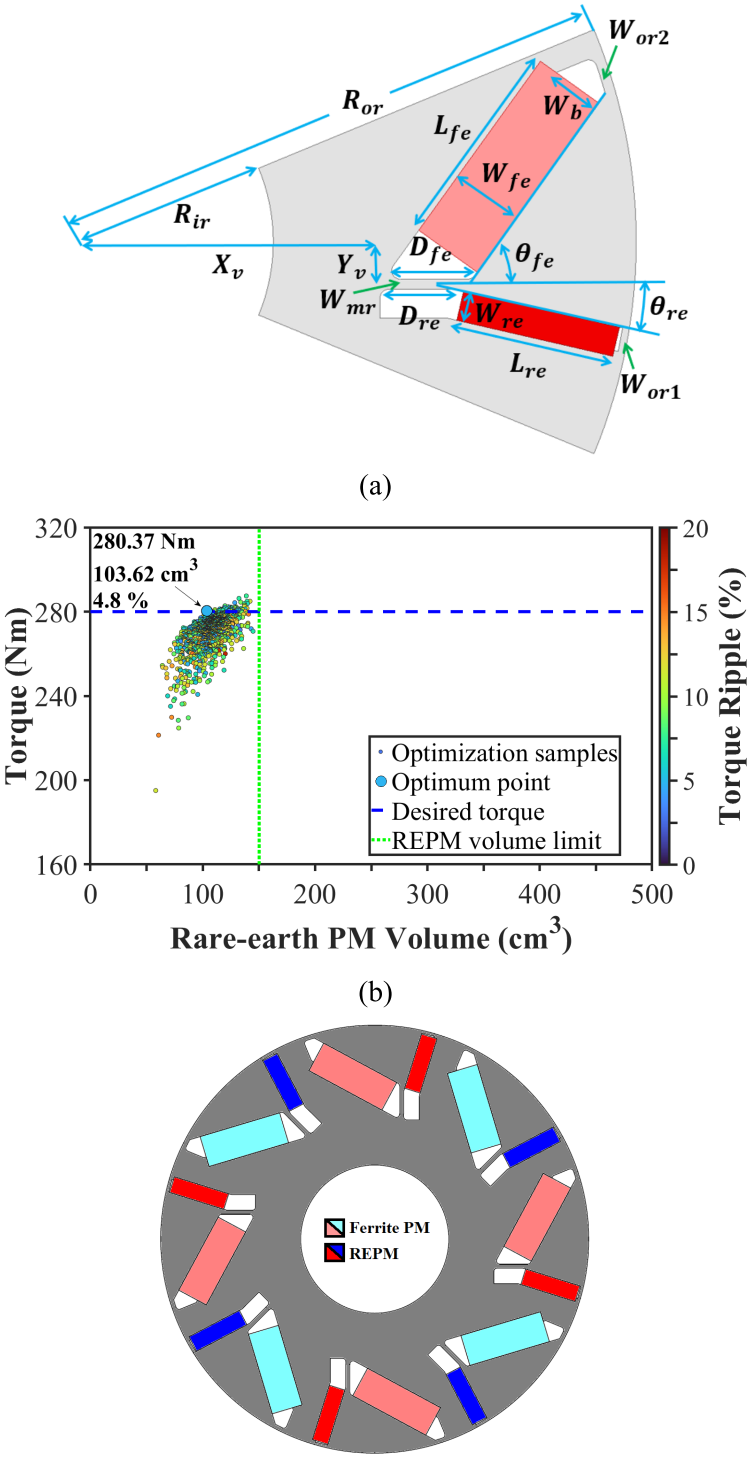

(a)

(b)

(c)

Fig. 5.14. HPM asymmetric V-2 IPMSM. (a) Parametric model. (b) Optimization result at 625 A_{max} and 2100 r/min. (c) Optimum cross section.

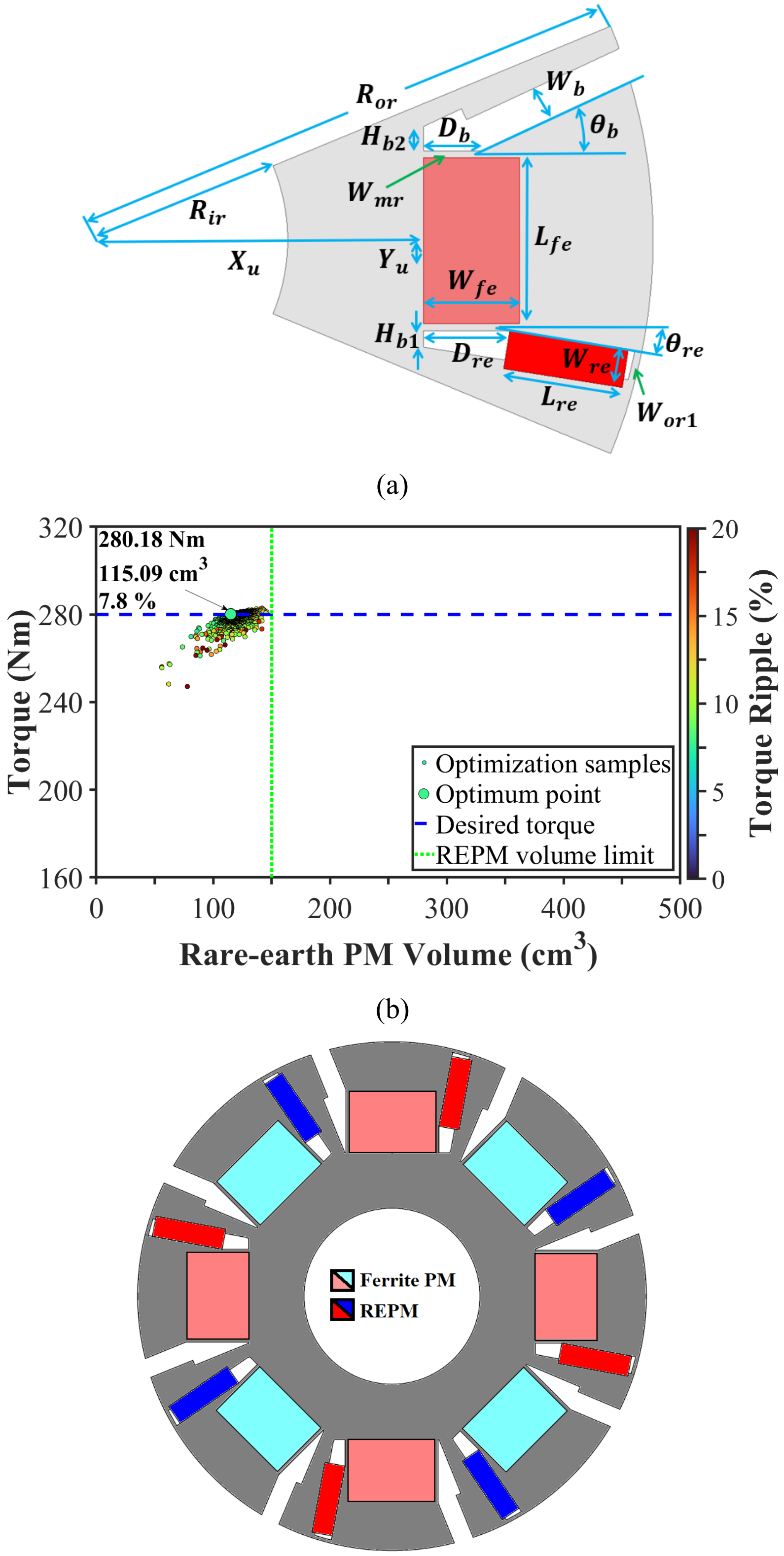

(a)

(b)

(c)

Fig. 5.15. HPM asymmetric U-2 IPMSM. (a) Parametric model. (b) Optimization result at 625 A_{max} and 2100 r/min. (c) Optimum cross section.

Table 5.3. Design Parameters and Their Optimum Values of HPM Asymmetric V-2 and U-2 IPMSMs.

Parameter	**symbol**	**Unit**	**HPM asymmetric V-2**	**HPM asymmetric U-2**
Rotor outer radius	R_{or}	mm	65	
Rotor inner radius	R_{ir}	mm	22.5	
V-shape in x-axis	X_{v}	mm	36.19	-
V-shape in y-axis	Y_{v}	mm	8.17	-
U-shape in X-axis	X_{u}	mm	-	36.62
U-shape in Y-axis	Y_{u}	mm	-	0.114
Width of REPM	W_{re}	mm	4.96	5.25
Length of REPM	L_{re}	mm	17.28	18.15
Width of FEPM	W_{fe}	mm	9.52	15.79
Length of FEPM	L_{fe}	mm	25.2	22.14
Width of barrier	W_{b}	mm	6.48	5.04
Angle of REPM	θ_{re}	Degree	17.34	10.52
Angle of FEPM	θ_{fe}	Degree	61.65	-
Angle of barrier	θ_{b}	Degree	-	22.11
REPM displacement	D_{re}	mm	8.75	6.79
FEPM displacement	D_{fe}	mm	9.93	-
Barrier displacement	D_{b}	mm	-	16.16
Height of barrier 1	H_{b1}	mm	-	2.77
Height of barrier 2	H_{b2}	mm	-	0.29
Width of middle rib	W_{mr}	mm	1.2	0.8
Width of outer rib 1	W_{or1}	mm	0.8	0.8
Width of outer rib 2	W_{or2}	mm	1.2	-

Figs. 5.16 (a) to (c) present a comparison of the von-mises stress distributions of the proposed HPM asymmetric V-2 and U-2 IPMSMs to that of the baseline at 10 kr/min when the frictional contacts with the friction coefficient of 0.2 are used. As can be seen, both proposed machines benefit from a lower maximum stress on the ribs compared to the baseline. It should be noted that the same widths of the ribs as the HPM asymmetric V-1 and U-1 IPMSMs are employed for the sake of comparison. In the proposed HPM asymmetric V-2 IPMSM, the movements of the REPM and FEPM1 are well controlled with the introduced verges. Meanwhile, by removing the FEPM2 (also means the less contact regions between PMs and core), less force is transferred to the second outer rib. Consequently, the maximum stress on this rib is reduced from ~236 MPa to ~ 205 MPa (-13 %). In addition, although the volume of REPM and FEPM1

in the HPM asymmetric U-2 IPMSM is increased, the middle ribs are only used to maintain the FEPM1 from movement when FEPM2 is removed. Meanwhile, the possible movement of REPM is also well controlled with the introduced verge. As a result, the maximum von-mises stress on these ribs remained almost unchanged. Finally, the proposed HPM asymmetric V-2 and U-2 IPMSMs and the baseline can provide the safety factors of 2.2, 2, and 1.9, respectively.

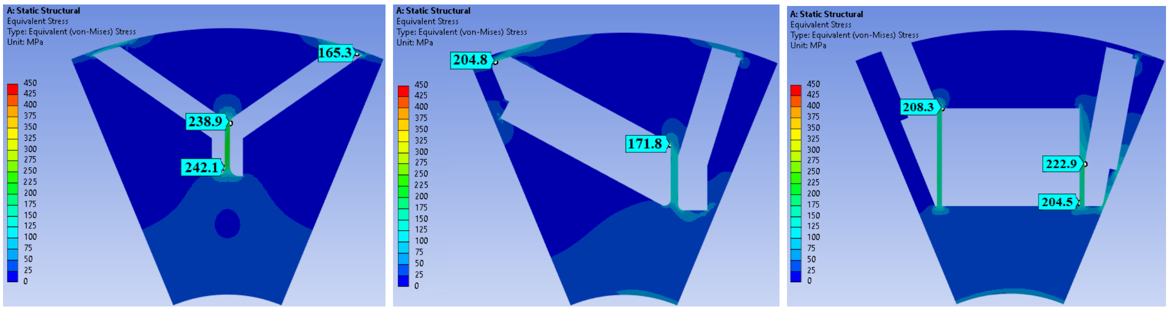

(a) (b) (c)

Fig. 5.16. Comparison of von-mises stress distributions at 10 kr/min. (a) REPM-based symmetrical V-shape IPMSM. (b) HPM asymmetric V-2 IPMSM. (c) HPM asymmetric U-2 IPMSM.

5.3.4. Comparison of HPM Asymmetric V-2 and U-2 IPMSMs with Baseline

The open circuit flux density and flux line distributions of the baseline and the proposed HPM asymmetric V-2 and U-2 IPMSMs are shown in Fig. 5.17. As can be seen, the d-axis of the proposed HPM asymmetric machines is shifted compared to that of the baseline.

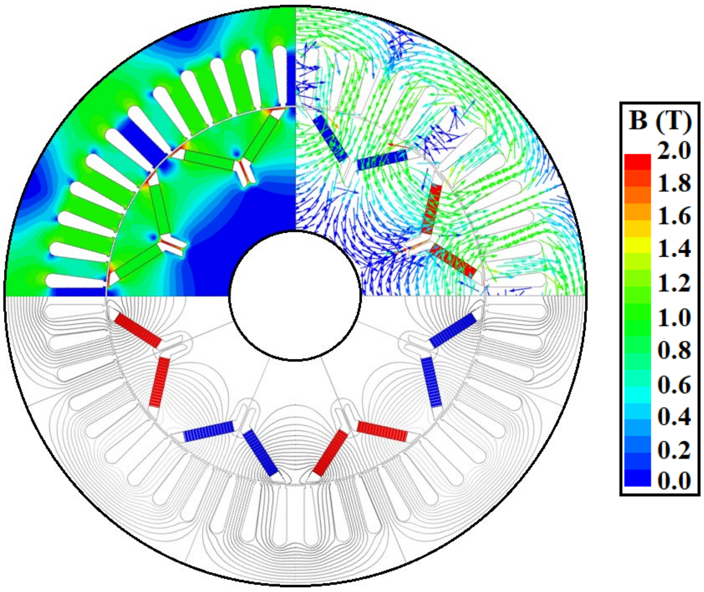

(a)

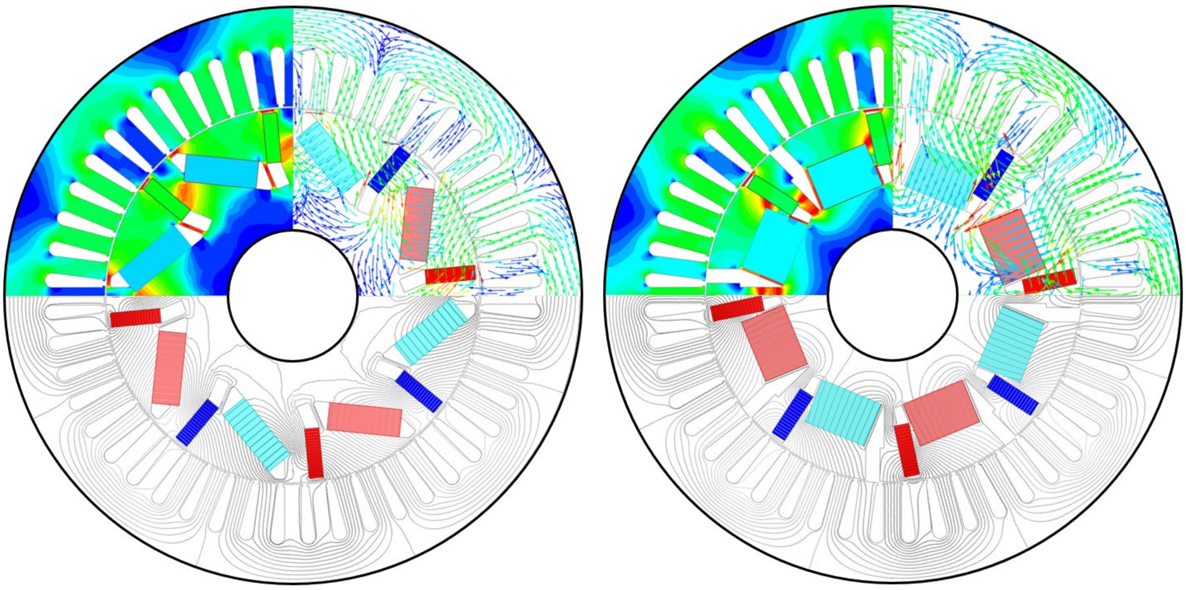

(b) (c)

Fig. 5.17. Comparison of open circuit flux density and flux line distributions. (a) REPM-based symmetrical V-shape IPMSM (baseline). (b) HPM asymmetric V-2 IPMSM. (c) HPM asymmetric U-2 IPMSM.

Moreover, the comparison of the open circuit airgap flux density waveforms, spectra, and fundamental component variations with rotor position can be found in Figs. 5.18 (a) to (c), respectively. By comparing the shifted phase of the airgap flux density fundamental component waveforms, it is revealed that the HPM asymmetric U-2 IPMSM has the highest shifted d-axis by ~22.6 electric degrees which is double of that in the HPM asymmetric V-2 IPMSM with ~11.4 electric degrees. Meanwhile, the HPM asymmetric U-2 IPMSM suffers from the highest harmonic components of airgap flux density among these three machines. Fig. 5.19 presents a comparison of the open circuit flux linkage waveforms and spectra. As can be seen, unlike the baseline, the flux linkage waveforms of the proposed HPM asymmetric machines are shifted. In addition, the fundamental components of open circuit flux linkages of the baseline and HPM asymmetric V-2 and U-2 IPMSMs are 0.0663 Wb, 0.0525 Wb, and 0.0566 Wb, respectively. Therefore, at the same speed, the amplitudes of back-EMFs in the proposed HPM asymmetric V-2 and U-2 IPMSMs are expected to be lower than that of the baseline.

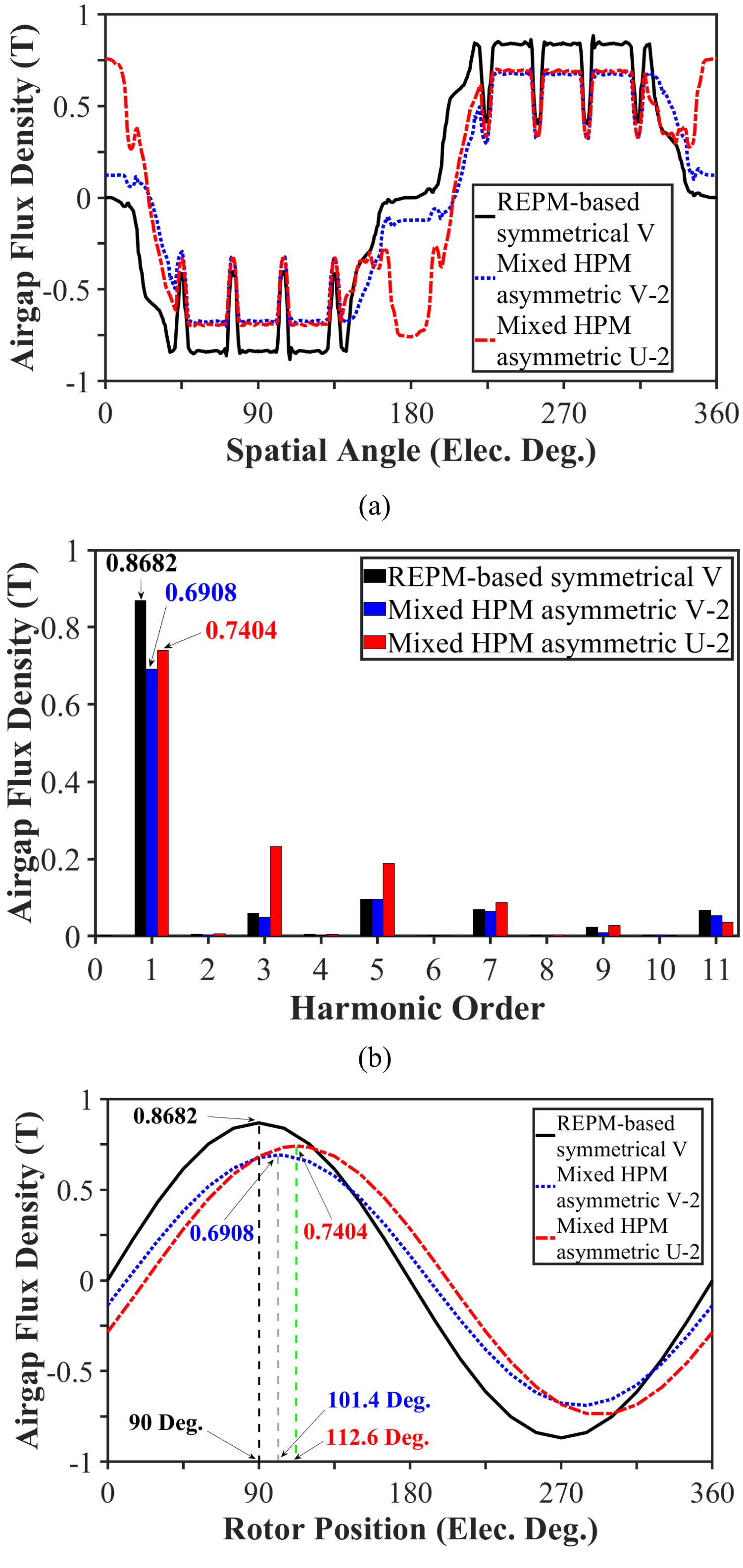

(a)

(b)

(c)

Fig. 5.18. Comparison of open circuit airgap flux densities of baseline and HPM asymmetric V-2 and U-2 IPMSMs. (a) Waveforms. (b) Spectra. (c) Fundamental component waveforms.

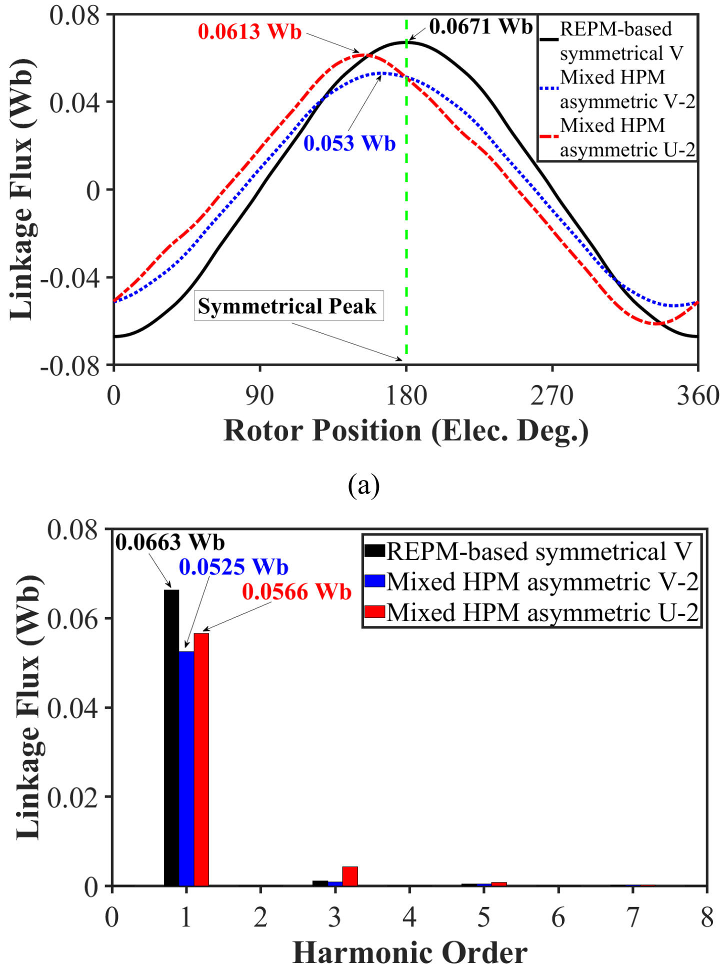

(a)

(b)

Fig. 5.19. Comparison of open circuit flux linkages of baseline and HPM asymmetric V-2 and U-2 IPMSMs. (a) Waveforms. (b) Spectra.

In this regard, the open circuit back-EMF waveforms and spectra at 2100 r/min are compared in Fig. 5.20. As can be seen, the back-EMF's fundamental component of the baseline with 58.3 V is higher than those of the HPM asymmetric V-2 and U-2 IPMSMs with 46.2 V and 49.8 V, respectively. Fig. 5.20 (c) compares the variations of open circuit back-EMFs with speed in these three machines. As can be seen, the peak-to-peak values of the both HPM asymmetric V-2 and U-2 IPMSMs at 10 kr/min are about 440 V which are ~18.8 % less than that of the baseline with 542 V. Therefore, both proposed HPM machines are expected to be safer than the baseline at high speeds in terms of having a lower back-EMF across the terminals of the inverter if a fault occurs. Meanwhile, it is worth mentioning that the proposed HPM asymmetric V-2 IPMSM is slightly better than the other counterpart with U-shape arrangement due to having lower harmonics. Finally, Fig. 5.21 compares the cogging torque waveforms and spectra of these three machines. As can be seen, the HPM asymmetric V-2 IPMSM benefits from the lowest cogging torque.

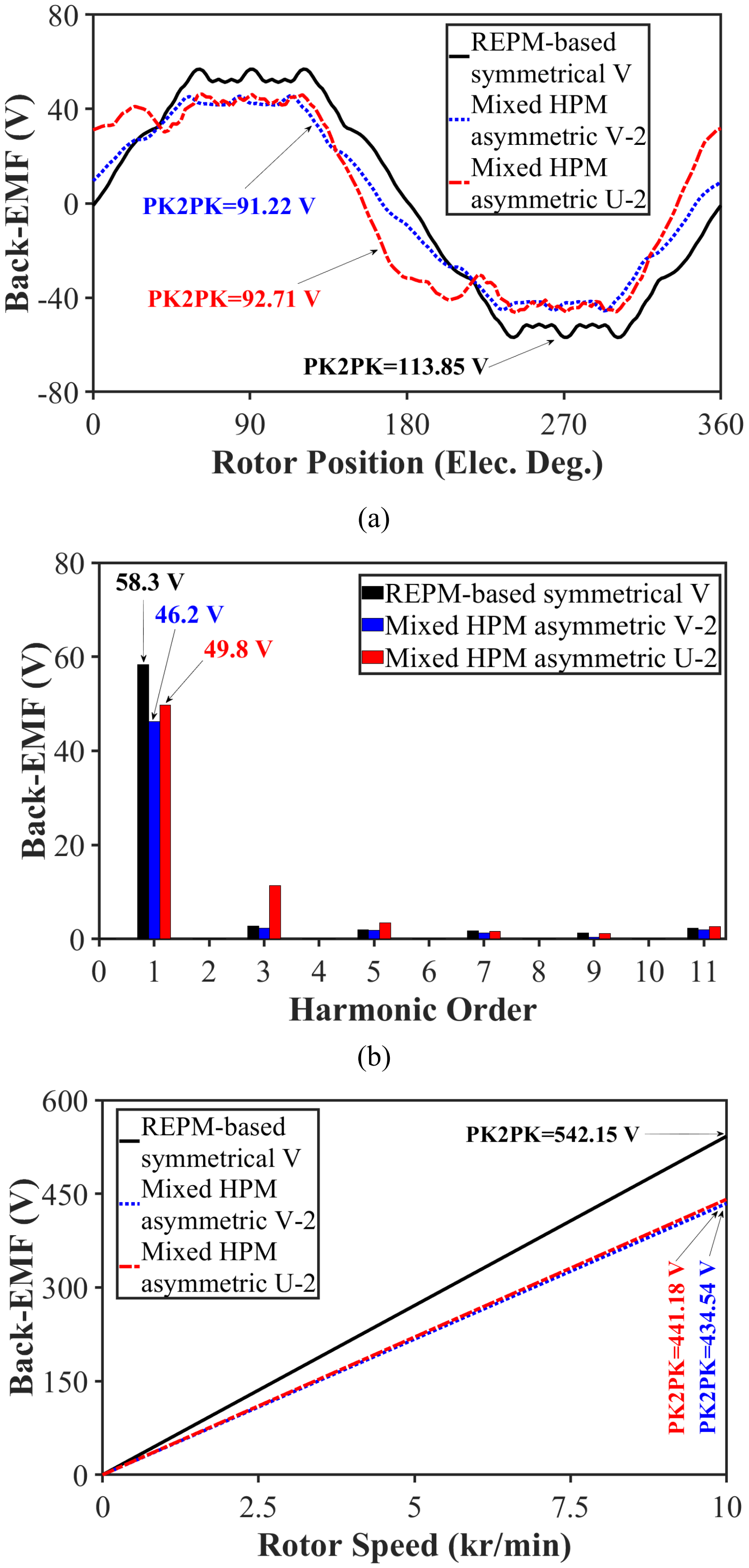

(a)

(b)

(c)

Fig. 5.20. Comparison of open circuit back-EMFs of baseline, and HPM asymmetric V-2 and U-2 IPMSMs. (a) Waveforms. (b) Spectra. (c) Peak to peak values with speed.

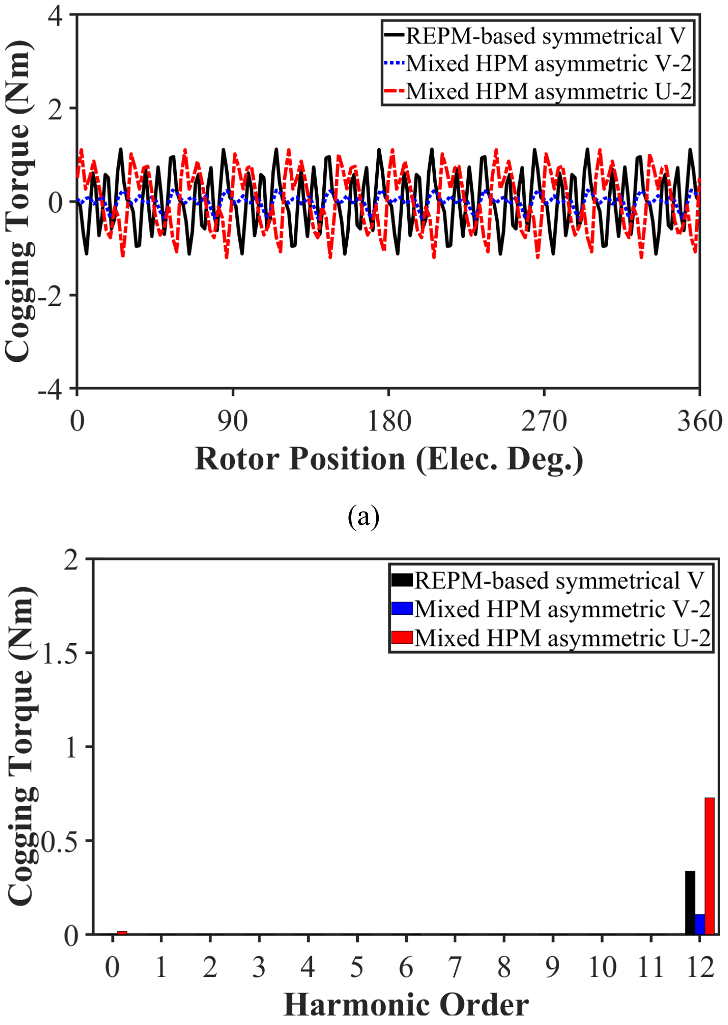

(a)

(b)

Fig. 5.21. Comparison of open circuit cogging torques of baseline and HPM asymmetric V-2 and U-2 IPMSMs. (a) Waveforms. (b) Spectra.

Fig. 5.22 compares the peak torque waveforms and spectra of these three machines at 625 A$_{max}$ and 2100 r/min. As these machines are optimized to deliver the same peak torque, a similar performance is expected. Moreover, Figs. 5.23 (a) and (b) compare the variations of torques and dq-axis inductances of these machines with the current advancing angle at 625 A$_{max}$ and 2100 r/min. As can be seen in Fig. 5.23 (a), the variations of torque with current advancing angle are different which suggests that these machines would have different reluctance torque and PM torque components. It is known that the developed torque of a PM machine can be written as a summation of PM torque (T_{PM}) and reluctance torque (T_{rel}) as follows:

$$T = T_{PM} + T_{rel} = \frac{3p}{2}\left(\psi_{pm} i_q + (L_d - L_q) i_d i_q\right) \tag{5.2}$$

where p is the number of pole pairs, ψ_{pm} is the PM flux linkage, L_d and L_q are the dq-axis inductances, and i_d and i_q are the dq-axis currents, respectively.

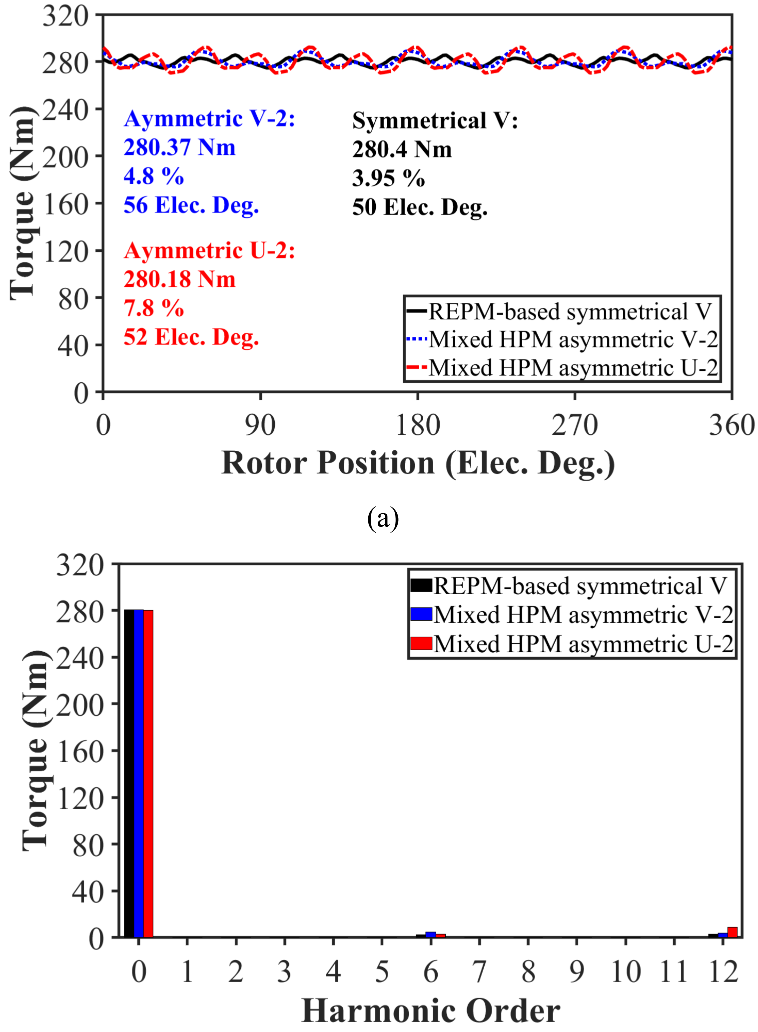

(a)

(b)

Fig. 5.22. Comparison of torque waveforms and spectra of baseline and HPM asymmetric V-2 and U-2 IPMSMs at 625 A_{max} and 2100 r/min. (a) Waveforms. (b) Spectra.

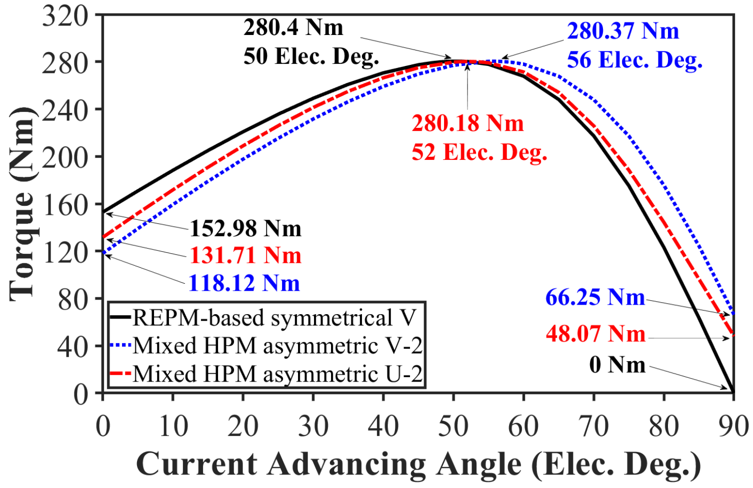

(a)

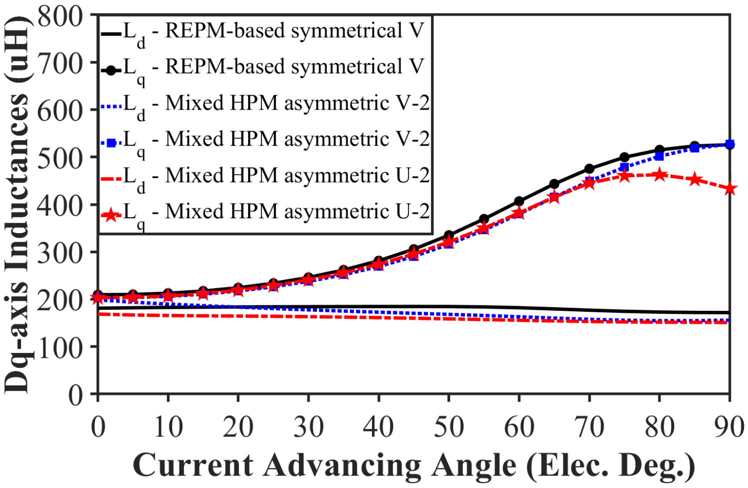

(b)

Fig. 5.23. Comparisons of torques and dq-axis inductances of baseline and HPM asymmetric V-2 and U-2 IPMSMs at 625 A_{max} and 2100 r/min. (a) Torques. (b) Dq-axis inductances.

As can be seen in Fig. 5.23 (b), the q-axis inductances of the proposed HPM asymmetric IPMSMs are slightly lower than that of the baseline. This is because in the optimum designs of these machines, the REPM is rotated towards the centre of the pole as shown in Figs. 5.14 (c) and 5.15 (c). Therefore, the cross sections of the q-axis flux path are reduced. Consequently, an increased saturation leads to a reduced q-axis inductance. Meanwhile, the d-axis inductances of the proposed machines are also lower than that of the baseline due to having thicker barriers in d-axis compared to that of the baseline. Therefore, a higher reluctance torque component is expected in the proposed HPM asymmetric V-2 and U-2 IPMSMs. Meanwhile, the FPM for a precise torque components decomposition is used at 625 A_{max} and 2100 r/min as presented in Fig. 5.24. It is worth mentioning that the current advancing angles of each machine are at their optimum value from Fig. 5.23 (a). As can be seen, the reluctance torques of the proposed HPM asymmetric V-2 and U-2 IPMSMs are ~10 Nm and ~12 Nm more than that of the baseline with 198.75 Nm, respectively. Therefore, for the same total torque, these machines would only need ~70 Nm of PM torque. Meanwhile, ~39.3 % and ~35.5 % of the required PM torques in the HPM asymmetric V-2 and U-2 IPMSMs are generated by the FEPMs, respectively. Consequently, the proposed HPM asymmetric V-2 and U-2 IPMSMs would only require 43.5 Nm and 45 Nm of REPM torques which are ~38 Nm and ~37 Nm less than that of the baseline, respectively. As a result, the volume of REPM can be reduced at no torque deterioration.

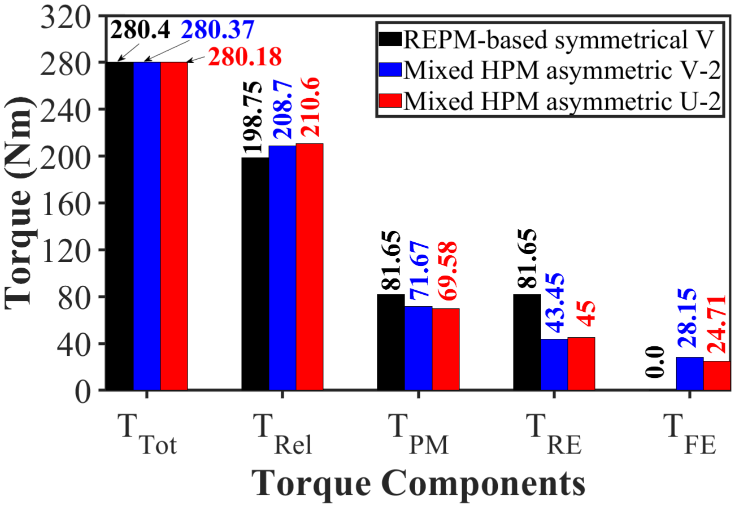

Fig. 5.24. Comparison of torque components of baseline and HPM asymmetric V-2 and U-2 IPMSMs by using FPM at 625 A_{max} and 2100 r/min.

Figs. 5.25 (a) and (b) compare the torque-speed and power-speed characteristics of these three machines. As these machines are designed for the same torque at low speed when 625 A_{max} and 2100 r/min are applied, these characteristics are expected to be the same at constant torque region. Meanwhile, the commercialized IPMSM has a maximum power cap of 80 kW [BUR13] which is also applied to these three machines. Therefore, the torque/power-speed characteristics at constant power region become the same as well.

The efficiency (η) of these machines can be obtained using the equation below:

$$\eta = \frac{P_{out}}{P_{out}+P_{cu}+P_{core}+P_{mec}} \times 100\ \% \tag{5.3}$$

where P_{out}, P_{cu}, P_{core}, and P_{mec} are the output power, the copper loss, the iron loss, and the mechanical loss, respectively.

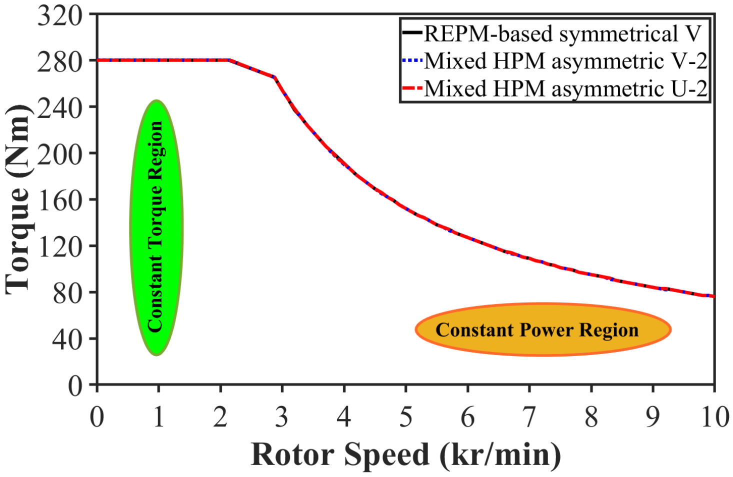

(a)

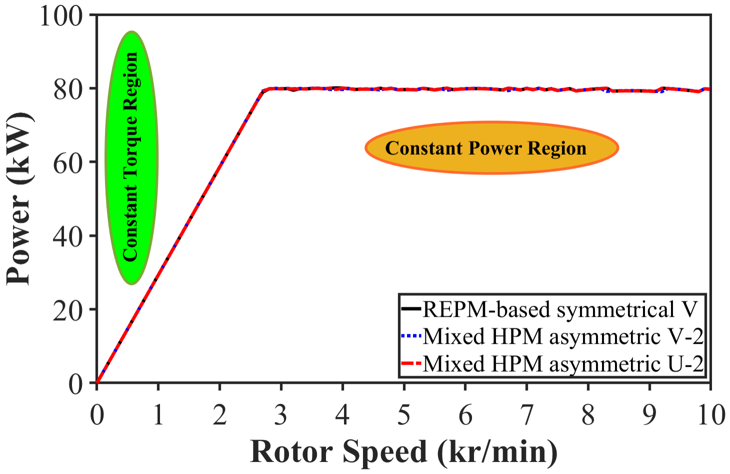

(b)

Fig. 5.25. Comparisons of torque-speed and power-speed characteristics at 625 A_{max}. (a) Torque-speed characteristics. (b) Power-speed characteristics.

The mechanical loss calculation requires two coefficients as follows which are taken from [YAN17A]:

$$P_{mec} = k_{mec1}f + k_{mec2}f^2 \tag{5.4}$$

where f is the frequency, and k_{mec1} and k_{mec2} are the mechanical loss coefficients.

By sharing the same stator, stack length, and winding configurations, the copper losses of these machines are expected to be almost the same as shown in Fig. 5.26 (a). However, the FEA results in Fig. 5.26 (b) show that the iron loss of the HPM asymmetric U-2 IPMSM is higher than that of the others due to having higher harmonic components of the airgap flux density as shown in Fig. 5.18 (b). Finally, as can be seen in Fig. 5.27 (c), the efficiencies of baseline and the proposed HPM asymmetric V-2 and U-2 IPMSMs can exceed 97 %. Meanwhile, this region in the HPM asymmetric U-2 IPMSM is smaller than the others due to an increased iron loss.

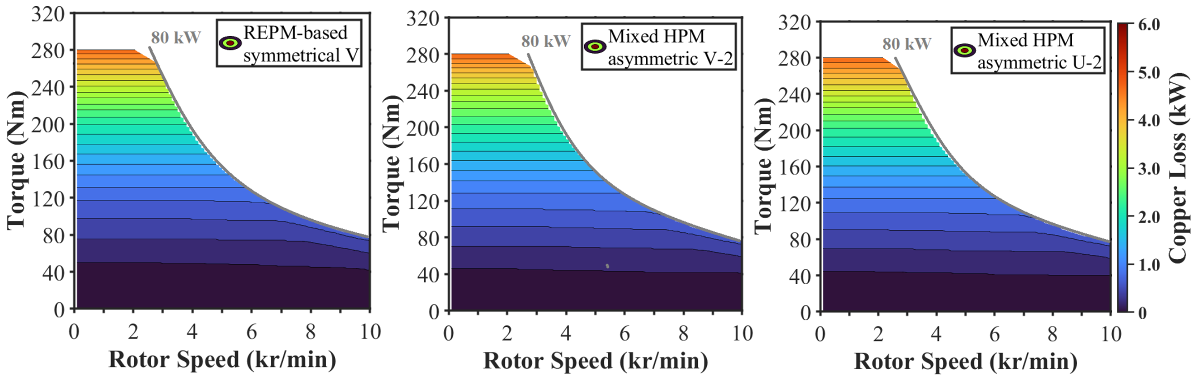

(a)

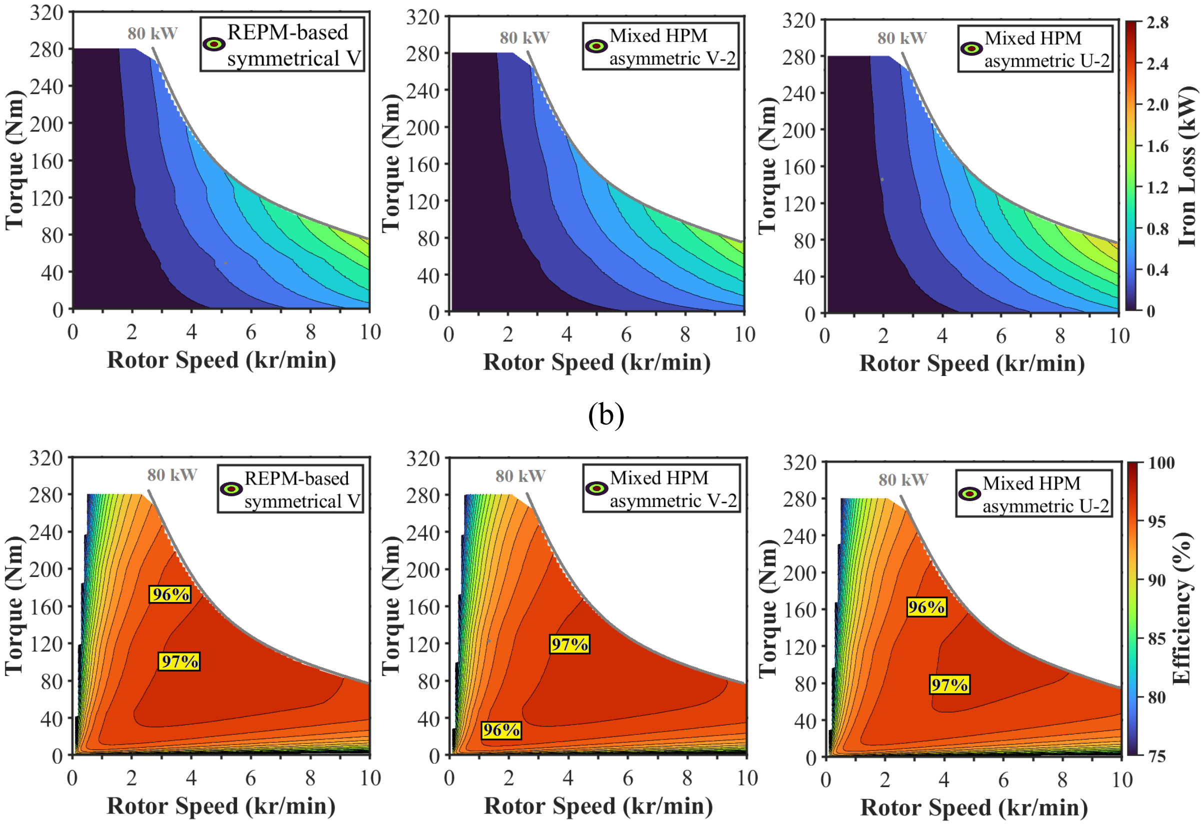

(b)

(c)

Fig. 5.26. Comparisons of copper loss, iron loss, and efficiency maps of these three machines. (a) Copper loss maps. (b) Iron loss maps. (c) Efficiency maps.

Figs. 5.27 (a) to (d) compares the decomposed flux density distributions of FEPMs in their magnetization direction in the proposed HPM asymmetric V-2 and U-2 IPMSMs at -40 °C and open circuit condition. It is worth mentioning that the knee point of FEPMs type TDK-FB13B is equal to 0.06 T at this temperature. As can be seen, no demagnetized region can be found in both machines when rotor is either inside or outside of the stator.

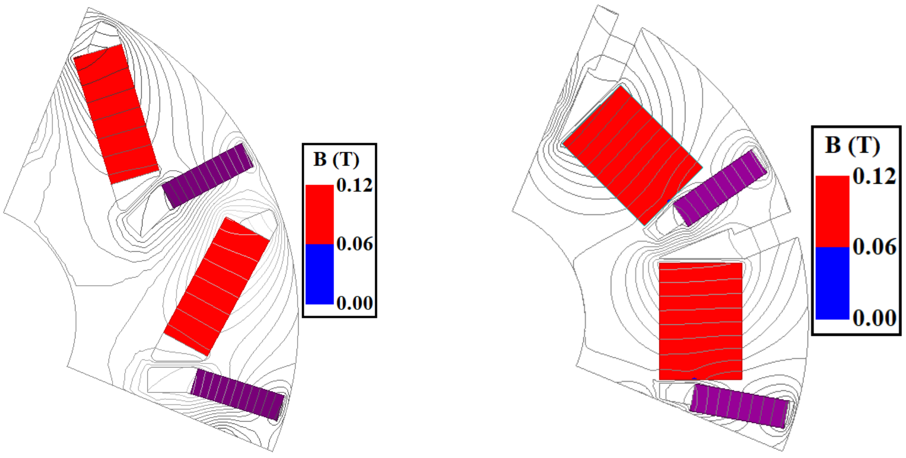

(a)

(b)

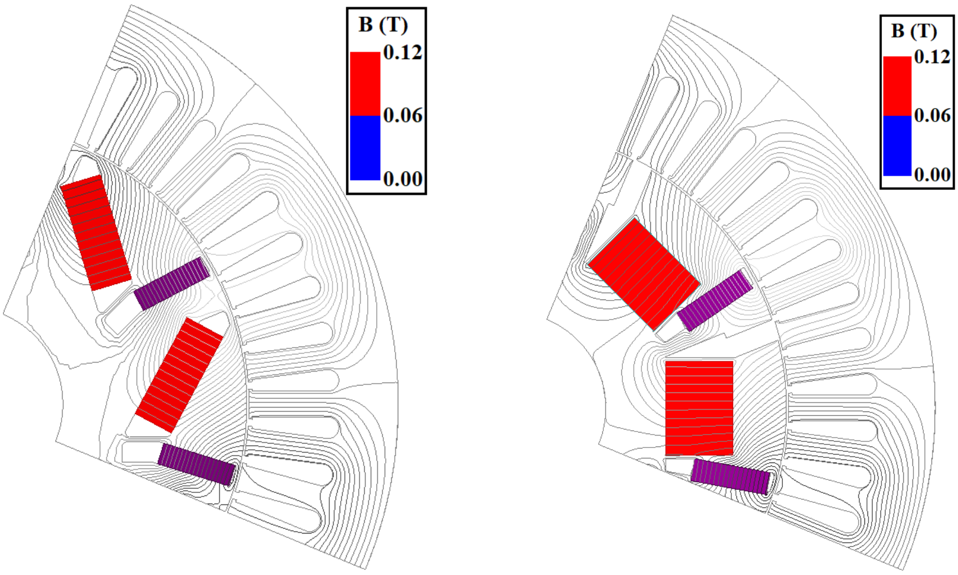

(c) (d)

Fig. 5.27. Comparison of decomposed flux density distributions of FEPMs at -40 °C and open circuit condition. (a) HPM asymmetric V-2 rotor (without stator). (b) HPM asymmetric U-2 rotor (without stator). (c) HPM asymmetric V-2 rotor (with stator). (d) HPM asymmetric U-2 rotor (with stator).

In addition, Fig. 5.28 presents a demagnetization withstand capability study of FEPMs in HPM asymmetric V-2 and U-2 IPMSMs at -40 °C when d-axis currents ranging from twice to triple of the rated current are applied. As can be seen, the regions of the irreversible demagnetized area are significantly reduced compared to those of the HPM asymmetric V-1 and U-1 IPMSMs in Fig. 5.12. Finally, Fig. 5.29 compares the decomposed flux density distribution of REPMs at 120 °C and triple of rated d-axis current. As can be seen, only a negligible area of REPMs is at the risk of irreversible demagnetization at severe conditions.

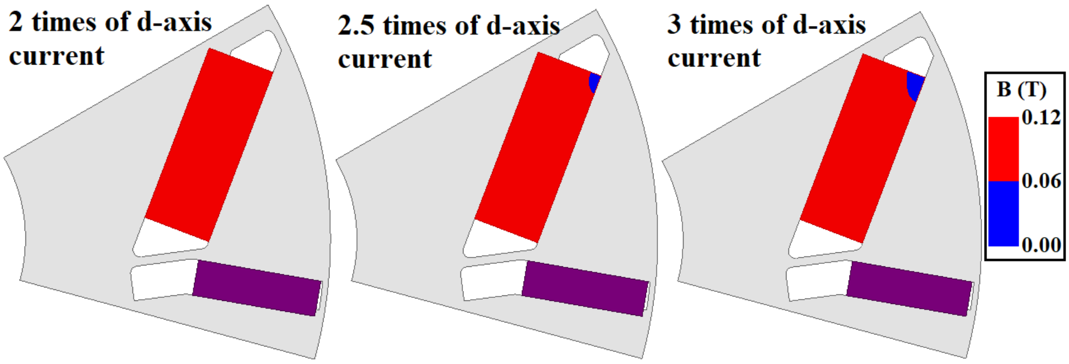

(a)

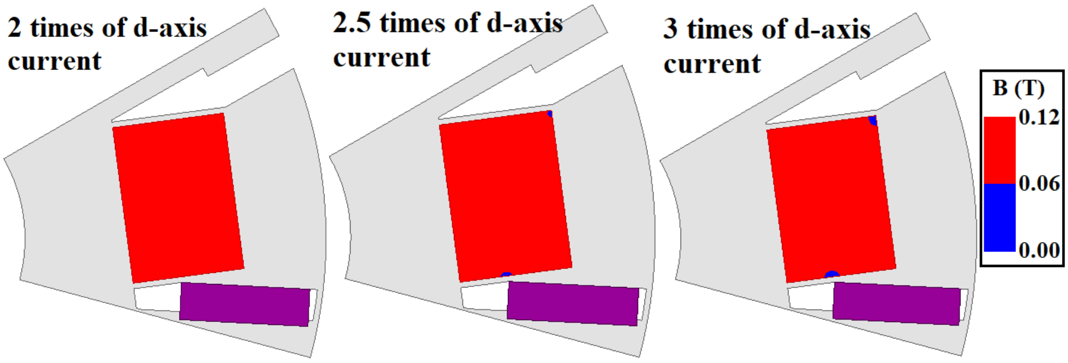

(b)

Fig. 5.28. Comparison of decomposed flux density distributions of FEPMs at -40 ºC when d-axis currents ranging from twice to triple of rated current are applied. (a) HPM asymmetric V-2 IPMSM. (b) HPM asymmetric U-2 IPMSM.

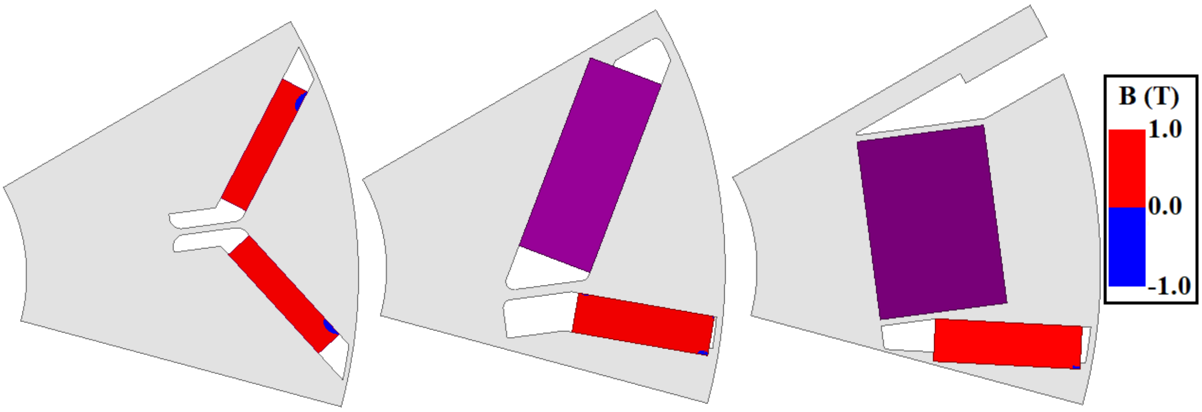

(a) (b) (c)

Fig. 5.29. Comparison of decomposed flux density distributions of REPMs at 120 ºC and triple of rated d-axis current. (a) REPM-based symmetrical V-shape IPMSM. (b) HPM asymmetric V-2 IPMSM. (c) HPM asymmetric U-2 IPMSM.

5.4. Comparison of PM Cost

The main application of HPM utilization is to improve the torque per REPM volume ratio which can be achieved either by a torque enhancement at the same volume of REPM, or by REPM volume reduction at the same torque. As the latter approach is used, all HPM asymmetric IPMSMs were expected to deliver a similar torque and power, with difference in several details including the torque components, back-EMFs, etc. However, a comparison of PM cost can emphasize these differences even more. Therefore, Table 5.4 presents a detailed comparison of the volume of both PMs and an estimation of PM cost considering the price of REPM being ten times of FEPM. As can be seen, compared to the baseline at the same torque of 280 Nm, the required volumes of REPM in the proposed HPM asymmetric V-2 and U-2

IPMSMs are reduced ~31 % and ~23.4 %, respectively. These savings are higher in the HPM asymmetric V-1 and U-1 IPMSMs with ~42 % and ~40.5 %. However, as discussed, those designs would suffer from a significant risk of irreversible demagnetization in FEPMs at low temperature. In addition, the PM cost reductions of the proposed HPM asymmetric V-2 and U-2 IPMSMs are ~18 % and ~5 %, respectively, considering the price of REPM being ten times the FEPM. Obviously, if the price of REPM increases in future, the reduced amount of the PM cost will also be higher considering the percentage of reduced volume of REPM. Finally, not only the ratios of torque per REPM volume in all HPM machines are higher than that of the baseline, but also the ratios of torque per rotor active mass of these machines are higher. This is mainly due to the low mass density of FEPMs. To employ a high volume of FEPM with the mass density of 5 g/cm^3 in a rotor with the fixed dimensions, a high volume of electrical steel with the mass density of 7.65 g/cm^3 needs to be removed. Therefore, the total mass of the rotor active parts would be lower than the baseline.

Table 5.4. Comparison of PMs' Volume, Mass, and Cost Estimation.

	Baseline	**HPM asymmetric IPMSMs**			
	V-shape	**V-1**	**U-1**	**V-2**	**U-2**
Total torque (Nm)	280.4	281.11	280.18	280.37	280.18
Volume of REPM (cm^3)	150.21	87.3	89.28	103.62	115.09
Volume of FEPM (cm^3)	-	320.32	404.41	289.67	422.22
Mass of REPM (kg)	1.142	0.663	0.679	0.788	0.875
Mass of FEPM (kg)	0.0	1.602	2.022	1.448	2.111
Volume of rotor electrical steel (cm^3)	1536.2	1253.5	1206.3	1248.8	1066.6
Mass of rotor electrical steel (kg)	11.752	9.589	9.228	9.553	8.159
Total mass of rotor active parts (kg)	12.894	11.854	11.929	11.789	11.145
Total torque per rotor active mass (Nm/kg)	21.75	23.71	23.49	23.78	25.14
Total torque per REPM volume (Nm/cm^3)	1.867	3.220	3.138	2.706	2.434
REPM volume reduction (%)	0	-41.88	-40.56	-31.02	-23.38
PM cost estimation (%)	100	72.08	77.16	81.68	95.11

* Mass densities of REPM, FEPM, and rotor electrical steel are 7.6 g/cm^3, 5 g/cm^3, and 7.65 g/cm^3.

5.5. Experimental Validation

To validate the FEA results, two small laboratory size prototypes with 24-slot/8-pole (24s8p) HPM asymmetric V- and U- shape arrangements of PMs are manufactured as shown in Fig. 5.30. These machines are optimized to deliver 2 Nm torque at lower volume of REPM with the copper loss constraint of 40 W and the same dimensional parameters as listed in Table 5.5. Then, they are tested using the dynamic and static test benches as presented in Fig. 5.31. The dynamic platform is used to measure the back-EMF and the transient torque, and the static test bench is employed to measure the cogging torque and the static torque. The volumes of REPM and FEPM are compared in Table 5.6. As can be seen at the same size and performance, the HPM asymmetric V-shape prototype requires 8.16 cm^3 volume of REPM which is ~8.5 % less than that of the HPM asymmetric U-shape prototype with 8.92 cm^3. This agrees with the conclusion of PM volume comparison in Table 5.4.

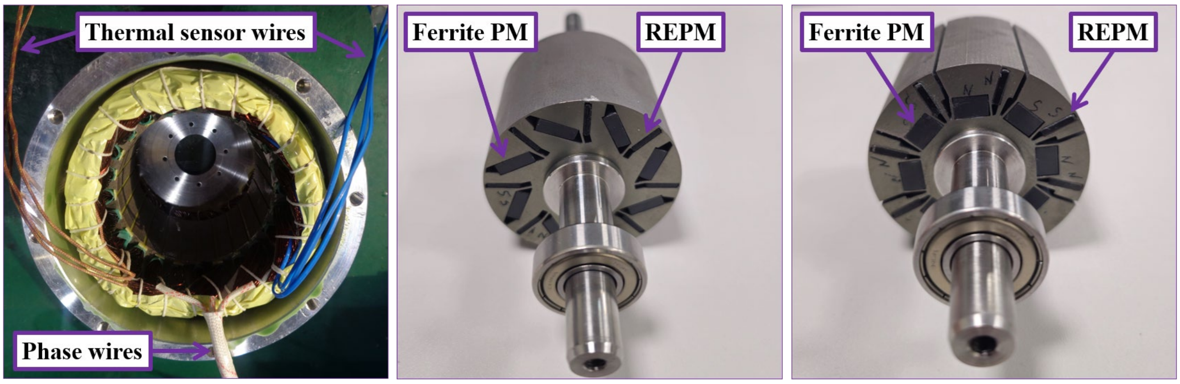

(a) (b) (c)

Fig. 5.30. Prototypes. (a) Shared stator. (b) HPM asymmetric V rotor. (c) HPM asymmetric U rotor.

Table 5.5. Main dimensional parameters for both prototypes.

Parameters	Values	Parameters	Values
Stator outer diameter	100 mm	Slot number	24
Stator inner diameter	63 mm	Pole number	8
Active stack length	50 mm	Turns per coil	60
Airgap length	1 mm	Phase resistance	1.6 Ω
Remanence of N28AH	1.075 T	Phase current	4 A_{max}
Remanence of TDK-FB13B	0.475 T		

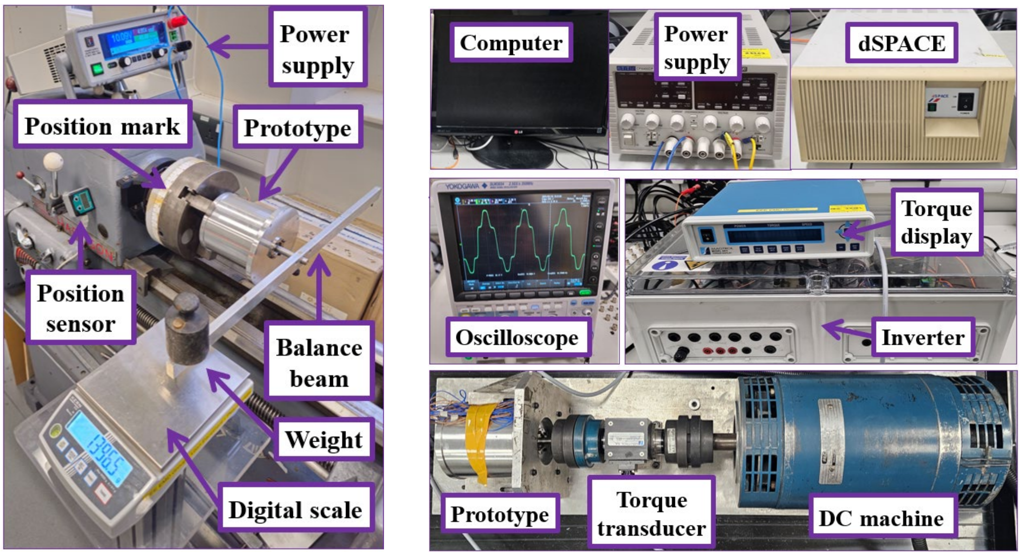

(a) (b)

Fig. 5.31. Experimental test benches. (a) Static test rig. (b) Dynamic test rig.

Table 5.6. Volume of PMs in both prototypes.

PM type	HPM asymmetric V-shape prototype	HPM asymmetric U-shape prototype
REPM (cm^3)	8.16	8.92
FEPM (cm^3)	20.9	23.3

Figs. 5.32 and 5.33 compare the open-circuit FEA predicted and measured back-EMFs at 250 r/min and open-circuit cogging torques, respectively. As can be seen in Fig. 5.32, the back-EMF of the HPM asymmetric U-shape prototype is slightly higher than that of the V-shape counterpart and matches with Fig. 5.20. In addition, the cogging torque of the HPM asymmetric V-shape IPMSM is negligible which was expected and matches with the cogging torque comparison in Fig. 5.21.

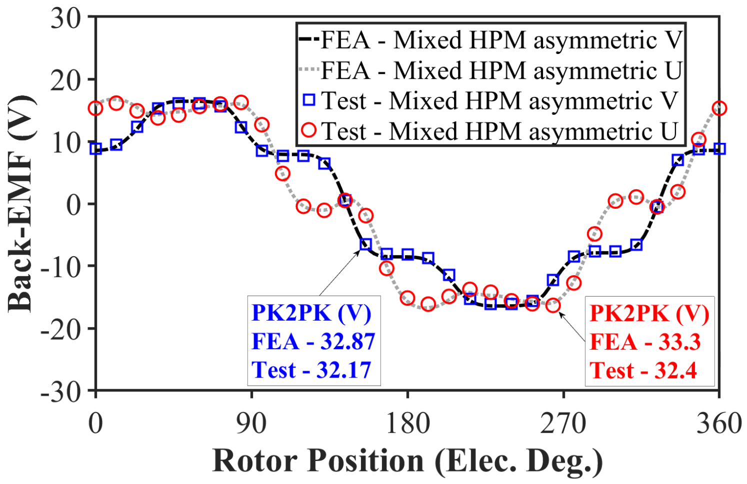

(a)

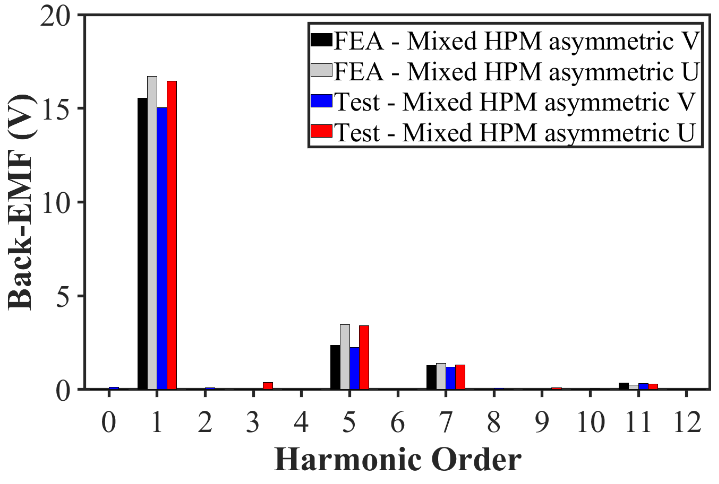

(b)

Fig. 5.32. FEA predicted and measured line back-EMFs at 250 r/min and open-circuit condition. (a) Waveforms. (b) Spectra.

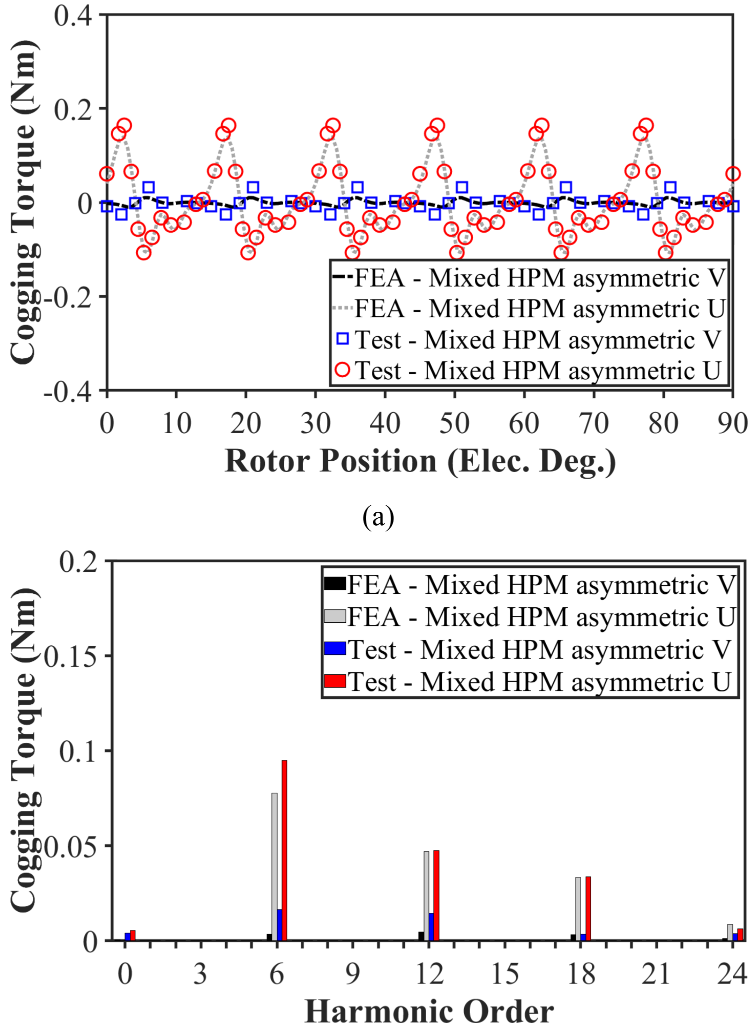

(a)

(b)

Fig. 5.33. FEA predicted and measured cogging torques at open circuit condition. (a) Waveforms. (b) Spectra.

Fig. 5.34 compares the variations of static torques with rotor position, when DC current ($I_a = -2I_b = -2I_c = I_{DC}$) is injected into the windings. Finally, Fig. 5.35 presents the variation of predicted and measured average torques with current. As can be seen, both machines can produce the required torque with a good agreement accounting for ~5 % error.

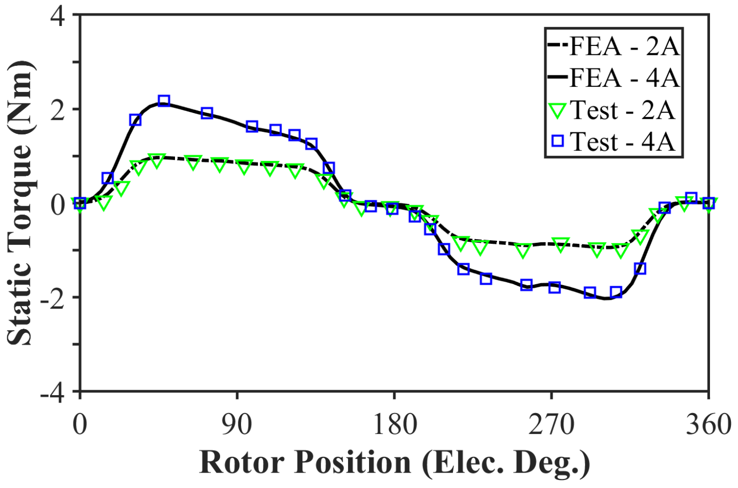

(a)

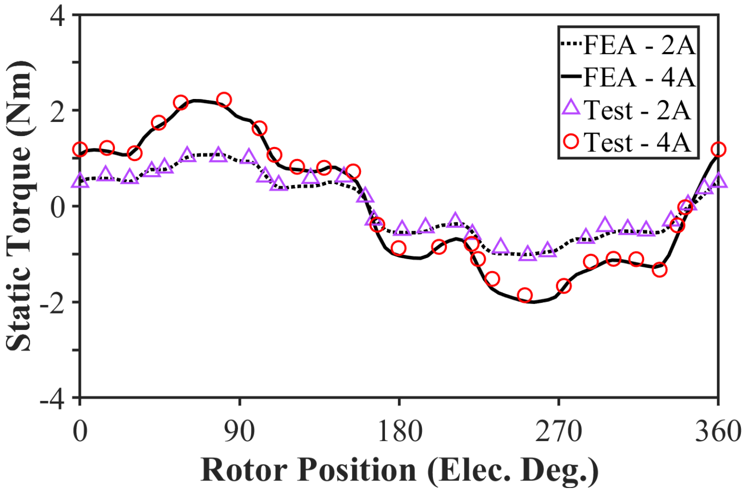

(b)

Fig. 5.34. FEA predicted and measured static torques at different DC currents. (a) HPM asymmetric V-shape prototype. (b) HPM asymmetric U-shape prototype.

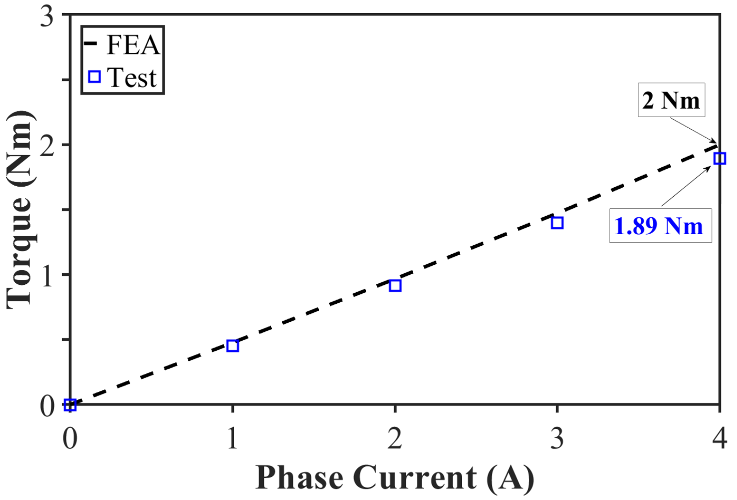

(a)

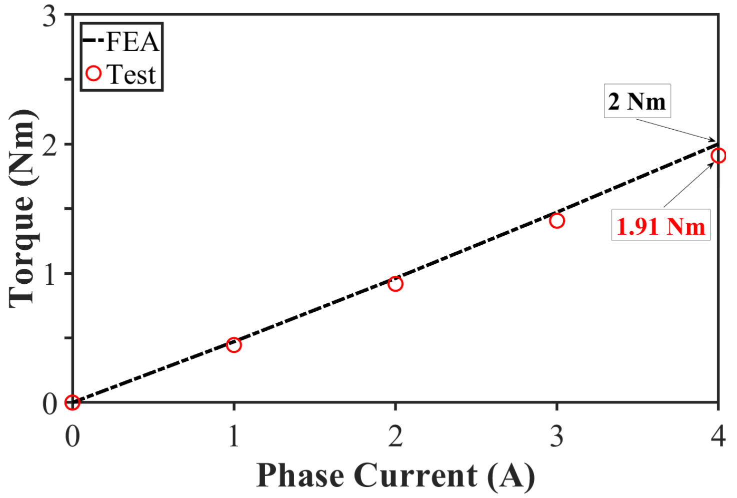

(b)

Fig. 5.35. Variation of FEA predicted and measured average torques with current at 250 r/min. (a) HPM asymmetric V-shape prototype. (b) HPM asymmetric U-shape prototype.

5.6. Conclusion

This chapter proposes two novel HPM asymmetric V-2 and U-2 IPMSMs accounting for a higher demagnetization withstand capability of FEPMs. First, two HPM asymmetric V-1 and U-1 IPMSMs are designed to effectively use the MFS effect and the FEPM utilization when the demagnetization withstand capability was not considered. It is shown that compared to a REPM-based symmetrical V-shape PMSM, these machines could have saved the required volume of REPM by ~42 % and ~40.5 %, respectively. Meanwhile, it is shown that the onload demagnetization risk of FEPMs at -40 °C and multiple d-axis currents is serious. The FEPM2 of these machines also suffers from a self-demagnetization risk when rotor is out of stator at open circuit condition. To address this issue, the HPM asymmetric V-2 and U-2 IPMSMs are proposed by modifying the designs of the previous topologies. Although the demagnetization withstand capability of FEPMs is considerably increased, the percentages of the REPM volume reduction have decreased to ~31 % and ~23.4 %, respectively. Considering the cost of REPM being ten times the FEPM, these machines can reduce the total PM cost by ~18.5 % and ~5 %, respectively. In conclusion, the proposed HPM asymmetric V-2 IPMSM benefits from a lower volume of REPM and total PM cost along with lower harmonic components and a higher efficiency than that of the HPM asymmetric U-2 IPMSM. Meanwhile, the latter topology benefits from a higher MFS effect and slightly better demagnetization withstand capability of FEPM at the cost of only ~5 % reduction of total PM expense. However, if the price of REPM increases in future, the percentages of PM cost saving in both machines will also increase. Finally, two small size prototypes of these machines are built and tested to verify the FEA results.

CHAPTER 6

NOVEL HYBRID MAGNET ASYMMETRIC V-SHAPE IPMSM

6.1. Introduction

The employment of high energy product rare-earth permanent magnets (REPMs) in electrical machines brought the advantages of high torque/power densities, high efficiency, etc., which qualified them to be used in various high-performance applications including electric vehicles (EVs) [ZHU07], [KAZ18]. However, as reported by the US Department of Energy (DoE), the cost of REPM forms 20% to 30% of total expense of a PM machine [ENE]. Therefore, the uncertain supply and the increased price of REPMs in recent years on the one hand, and the additive performance targets for the future of EVs established by DoE and the UK Advanced Propulsion Centre (APC) on the other hand [SHA20], have introduced a cost-effective design challenge towards the electrification transportation. To address this issue, many researches have been carried out to reduce the volume of REPM in PM machines at the same performance [POU21]. This means any method with the benefit of higher torque per REPM volume ratio can be used towards achieving this goal.

The asymmetric rotor design and hybrid PM (HPM) utilization are two promising examples of REPM reduction methods which have gained a lot of attention in recent years [ZHU21], [CHE11B]. An asymmetric rotor PM machine benefits from the magnetic field shifting (MFS) effect which reduces the difference between the corresponding current advancing angles of maximum PM and reluctance torque components. Therefore, the peaks of both components move towards each other and thus the resultant torque will increase [XIA21A], [ZHU22]. For example, an additional flux barrier is used in an asymmetric V-shape arrangement of PMs to enhance the MFS effect of the proposed machine in [XIA21B]. Meanwhile, the latter method relies on using two PM materials, including FEPMs and REPMs, in the same structure. As a result, a HPM machine utilizes the synergies of high-performance REPMs and low-cost FEPMs. It is known that a complete replacement of REPMs with FEPMs would not usually end up with a comparable performance. This is due to the noticeable difference in the magnetic properties of these PMs, i.e. the remanence of FEPM can be 67% lower than that of REPM. Meanwhile, a HPM machine with the advantage of a high performance at a reduced price can be a cost competitive candidate for high performance applications, e.g., EV.

The HPM machines are first introduced about a dozen years ago [CHE11B], [SHE12], [ISH13], [AFI14] and are categorized into parallel, series, and mixed configurations with different features [AFI14], [ZHE21], [KAZ23D]. As the name of parallel HPM configuration suggests, the flux paths of two PM types are in parallel. Therefore, the magnetic reluctance of each PM would not affect the flux path of the other PM [KAZ25]. However, in a series configuration of HPM, the reluctance of one PM increases the magnetic reluctance of the other PM's flux path. Consequently, a parallel HPM machine benefits from a higher electromagnetic performance than a series HPM counterpart at the cost of lower demagnetization withstand capability of FEPMs [AFI14]. Meanwhile, a mixed HPM configuration is a combination of the series and parallel HPMs and can have a traded-off performance [ALQ21]. Generally, to replace a specific volume of REPM with FEPM at the same performance, a higher volume of FEPM will be needed due to their lower energy-product. For example, in [MA20], it is shown that using a high volume of low-cost FEPM in a spoke-type IPMSM with parallel configuration of HPM is advantageous and leads to a higher torque per REPM volume ratio than the others. Meanwhile, although a spoke-type IPMSM provides more space for FEPM utilization, a V-shape IPMSM benefits from a higher reluctance torque component. Therefore, a novel high performance parallel HPM IPMSM with the V-shape spoke arrangement of PMs is introduced in [KAZ25].

A combination of the HPM utilization and the advanced MFS technique can lead to the enhanced benefits. In [ZEN19] and [ZHU23B], the application of an asymmetric bar-shape REPM in a series HPM spoke-type IPMSM is investigated. It is shown that the resultant MFS effect improves the total torque, and the demagnetization withstand capability of FEPM. Similarly, the application of an asymmetric bar-shape REPM in a spoke-type IPMSM with a mixed configuration of HPM is investigated in [CHE21], [CHE23]. The proposed machine benefits from an enhanced torque density due to MFS effect at the cost of a complicated structure. In [QIA24], a novel asymmetric HPM PM aSynRM is proposed to improve the MFS effect with a multi-layer arrangement of PMs. In [XU17A], a novel HPM asymmetric rotor using the mixture of REPM-based surface mounted poles and multilayer FEPM -based poles is proposed. Although the proposed machine shows an improved performance, it may suffer from the axial leakage flux due to the employment of unequal north and south poles. In [LIU23B], a parallel HPM asymmetric V-shape IPMSM is designed where a relatively low volume of FEPM is used in the centre of a V-shape arrangement of REPMs. In [JI23] and [JI24], a consequent pole asymmetric rotor IPMSM with HPM utilization is designed and compared to a conventional pole asymmetric rotor counterpart. The results show that the proposed consequent pole IPMSM benefits from a comparable torque and a higher torque per REPM volume ratio than its conventional counterpart at the cost of slightly lower overload capability and negligible MFS effect. In [LIU24], a novel HPM asymmetric V-shape IPMSM is proposed which benefits from an improved torque with a lower torque ripple compared to the other topologies. However, the torque per cost ratio of the proposed machine is only improved by 2% compared to that of the REPM-based asymmetric V-shape IPMSM counterpart due to the low utilization of FEPMs.

This chapter proposes a novel mixed HPM asymmetric V-shape IPMSM with a large segment of shaped FEPM that can effectively reduce the required volume of REPM by maximizing the FEPM usage and MFS effect. It will be shown that shaping the edge of FEPM can not only enable a higher usage of FEPMs but also improves the MFS effect by introducing an intentional saturation area between each two adjacent poles instead of using additional barriers as presented in literature. The effect of MFS is investigated by analysing the electromagnetic performance at open-circuit and on-load conditions. Meanwhile, the effect of HPM utilization is shown by separating the torque components of the proposed HPM machine using the frozen permeability method (FPM) in [CHU12].

In this regard, section 6.2 introduces the proposed mixed HPM asymmetric V-shape IPMSM and the REPM-based symmetrical V-shape IPMSM as the baseline. In section 6.3, the finite element analysis (FEA) is employed to investigate and compare the electromagnetic performances. Section 6.4 presents the mechanical strength, and the demagnetization withstand capability investigations. Finally, sections 6.5 and 6.6 summarize the experimental validation and conclusion, respectively.

This chapter is published in IEEE- Transactions on Transportation Electrification [S. Kazemisangdehi, Z. Q. Zhu, L. Chen, L. Yang, and Y. Zhou, "A Mixed Hybrid Rare-earth and Ferrite Magnet Asymmetric V-shape IPMSM" *IEEE Transactions on Transportation Electrification, Early Access,* 2025.]

6.2. Mixed HPM Asymmetric V-shape IPMSM

This study is carried out using the same stator and specifications of a commercialized IPMSM as presented in Fig. 6.1 (a) and Table 6.1. As can be seen, this machine uses a 48-slot/8-pole (48s8p) combination and generates 280 Nm peak torque at its peak current (625A_{max}) and rated speed (2100 r/min). It is also worth mentioning that the volume of active part in this machine is ~4.76 L. Meanwhile, it increases to ~6.06 L when considering the end winding [YAN17A].

It is known that the V-shape arrangement of PMs is a fashionable way to introduce an IPMSM with increased saliency and flux focusing effect. Therefore, a REPM-based symmetrical V-shape IPMSM, with REPM type N28AH, is designed as the baseline as shown Fig. 6.1 (b). Then, the proposed mixed HPM asymmetric V-shape IPMSM using the same REPM material and FEPM type TDK-FB13B is designed as shown in Fig. 6.1 (c). The design criterion is to achieve the same torque as the baseline with a lower volume of REPM by substituting a part of this magnet with FEPM. These machines are introduced in more detail in the following subsections.

6.2.1. REPM-based Symmetrical V-shape IPMSM (Baseline)

The baseline to this study is a REPM-based IPMSM with a symmetrical V-shape arrangement of PMs as shown in Fig. 6.1 (b). The required volume of REPMs in this machine is used as the REPM usage limit for the optimization of the proposed HPM machine.

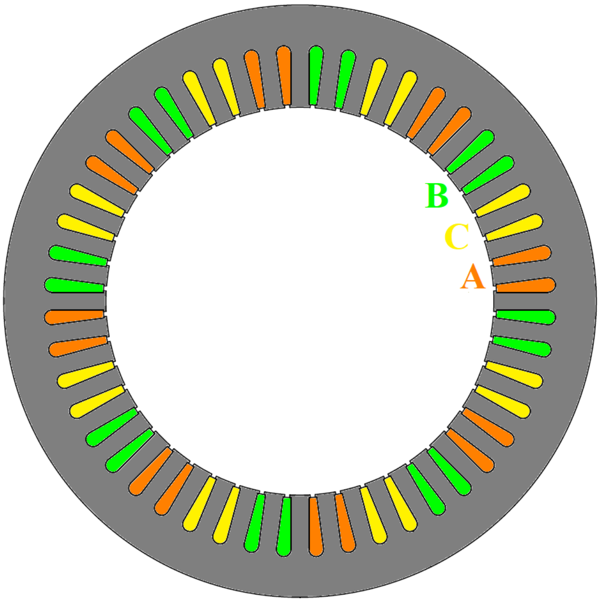

(a)

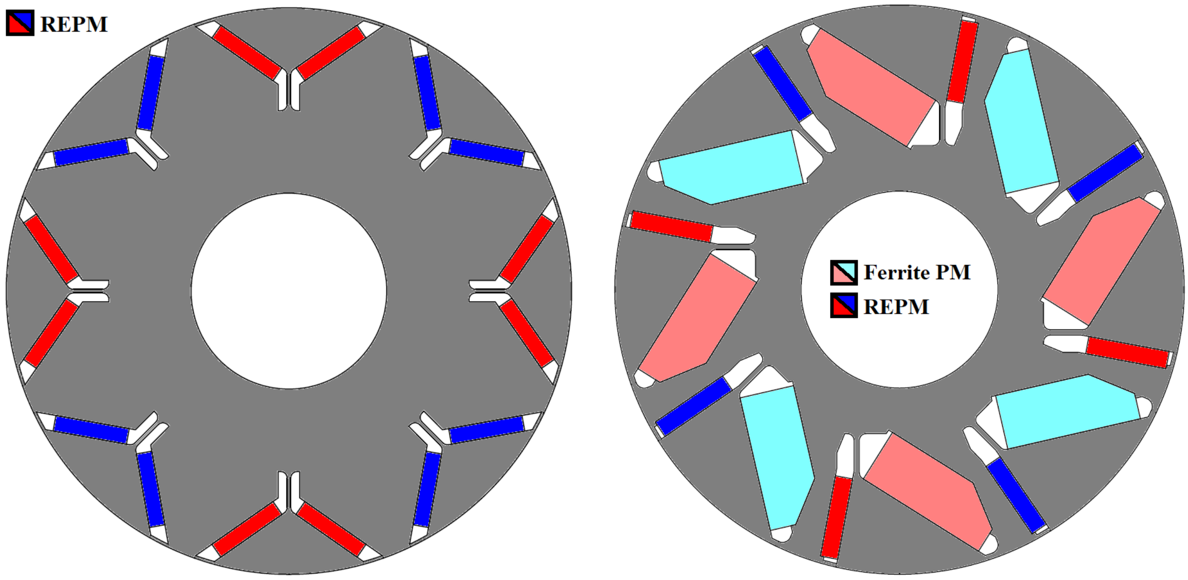

(b) (c)

Fig. 6.1. Structural comparison of V-shape IPMSMs. (a) Stator of the commercialized IPMSM. (b) REPM-based symmetrical V-shape rotor (baseline). (c) Proposed mixed HPM asymmetric V-shape rotor.

Table 6.1. Specification of Commercialized IPMSM [YAN17A] and [BUR13].

Parameters	Values	Parameters	Values
Stator slot no.	48	Peak speed (r/min)	10000
Rotor pole no.	8	Rated speed (r/min)	2100
Stator outer diameter (mm)	200	Peak torque (Nm)	280
Stator inner diameter (mm)	131	Peak current (A_{max})	625
Rotor outer diameter (mm)	130	Peak current density (A/mm^2)	26.31
Rotor inner diameter (mm)	45	Conductor no. per slot	8
Stack length (mm)	151	Number of parallel branches	4
Airgap length (mm)	0.5	Active volume of machine (L)	4.76
NdFeB remanence (T)	1.075	Actual volume of machine (L)	6.06
Angle of rotor skew (degree)	3.75	Peak torque per actual volume (Nm/L)	46.2

6.2.2. Mixed HPM Asymmetric V-shape IPMSM

The proposed mixed HPM asymmetric V-shape IPMSM is presented in Fig. 6.1 (c). As can be seen, a large FEPM segment is in parallel to a small REPM within 1 pole. However, considering two adjacent poles, the two PM types are in a series connection. Therefore, the overall configuration of HPM in the proposed machine is considered as mixed (a mixture of the series and parallel HPM configurations).

6.3. FEA Results

This section focuses on FEA results. The aim is to reduce the PM cost at the same performance by using the HPM utilization and MFS effect which leads to an improved torque per REPM volume ratio. As both methods are applied to the rotor structure, the stator dimensions including the stack length, and the winding configurations are kept constant as listed in Table 6.1 and shown in Fig. 6.1 (a) to keep the electrical loading the same. In addition, the airgap length and the inner and outer radii of rotor are kept the same during the optimization for the sake of comparison. Therefore, only the rotor structures will be re-designed and the effect of both HPM utilization and MFS on the performance will be revealed. Meanwhile, it would be useful to mention that an individual global optimization (i.e. including the stator), may lead to an ideal optimized structure for each machine if they were supposed to be optimized separately. In this chapter, an optimization is conducted when the genetic algorithm (GA) within ANSYS Maxwell FEA software is used to optimize the rotor structure in each topology. The proposed HPM machine is optimized to deliver the same peak torque (280 Nm) as the baseline with a lower volume of REPM at 625 A_{max} and 2100 r/min. Meanwhile, the second objective is to minimize the torque ripple. Taking the importance of each objective into account, the optimization function is defined as follows:

$$\begin{cases}\text{Objectives: Max } [T_{out}],\ \text{Min } [V_{NdFeB}],\ \text{Min } [T_{ripple}] \\ \text{Selection criteria of optimum point: } T_{out} \geq 280 \text{ Nm},\ V_{NdFeB} \leq 150.2 \text{ cm}^3,\ T_{ripple} < 4\% \\ \text{Weighting factors: } K_{T_{out}} = 4\text{p.u.},\ K_{V_{NdFeB}} = 2\text{p.u.},\ K_{T_{ripple}} = 1\text{p.u.} \\ \text{Variables: listed in Table II.}\end{cases} \tag{6.1}$$

where T_{out}, V_{NdFeB}, and T_{ripple} are the output torque, the volume of REPM, and the torque ripple, respectively.

Therefore, at the same torque and size, the optimization results will reveal the reduced amount of REPM volume. Then, a PM cost comparison can emphasize the amount of money which can be saved considering the price of REPM being ten times of FEPM. When the monetary privilege of HPM utilization is declared, a detailed performance comparison of the proposed HPM asymmetric V-shape IPMSM and the baseline will be conducted to compare the features of these machines and explain how the REPM usage and PM cost can be reduced in the proposed HPM machine.

It is worth mentioning that generating the same peak torque is selected as the base condition of optimization in this chapter. This is to make sure that both machines have enough magnetic loading to provide 280 Nm torque when the electrical loading is pushed to the maximum capacity (625 A_{max}). If this condition is satisfied, then all torque levels between 0 to 280 Nm are achievable by adjusting the electrical loading via maximum torque per current (MTPA) control strategy. Meanwhile, if the proposed machine is subject to be optimized solely for EV application, a global optimization accounting for the driving cycle would be privileged.

6.3.1. Comparison of Optimization Results

This section discusses the optimization results of both machines when they are optimized with the above-mentioned objectives. Fig. 6.2 (a) presents the parametric model of the REPM-based symmetrical V-shape IPMSM, whereas the optimization result, and the optimum cross section are shown in Fig. 6.2 (b) and (c), respectively. As can be seen, this machine requires ~150.2 cm^3 volume of REPM to deliver 280 Nm peak torque at 625 A_{max} and 2100 r/min. Fig. 6.3 (a) illustrates the parametric model of the proposed mixed HPM asymmetric V-shape IPMSM, whereas the optimization result, and the optimum cross section are shown in Fig. 6.3 (b) and (c), respectively. As can be seen, this machine requires only ~90.2 cm^3 volume of REPM to deliver 280 Nm peak torque at 625 A_{max} and 2100 r/min. Therefore, at the same torque and size, the volume of high-cost REPM can be reduced by ~40 %. The optimum values of the design parameters in both machines are listed in Table 6.2. It is worth mentioning that some parameters are defined by structural ratios to avoid structural conflicts during the optimization. However, they are shown as size-based parameters in this table for a better understanding when being compared to the parametric models. In addition, it should be noted that the widths of the ribs are defined using the mechanical strength analysis as will be shown in section 6.3. In addition, the inner and outer radii of rotor (R_{ir} and R_{or}) are assumed to be constant in this study.

It is worth mentioning that a V-shape arrangement of PMs with one FEPM and one REPM can generally be considered as an asymmetric rotor. This is due to the different residual flux densities of these two PM types. However, two specific design parameters are added to the parametric model of the proposed HPM machine. The first parameter which is added to change the FEPM pole arc independent from the REPM pole arc is the angle of FEPM (θ_{fe}). As will be shown, having two independent pole arc variables helps with the MFS effect. The second parameter which is used to displace the centre of the V-shape arrangement in Y-axis is Y_v. As will be shown, the combination of the displaced V-shape arrangement and tapered FEPM causes an intentional saturation between two adjacent poles which helps with the MFS effect.

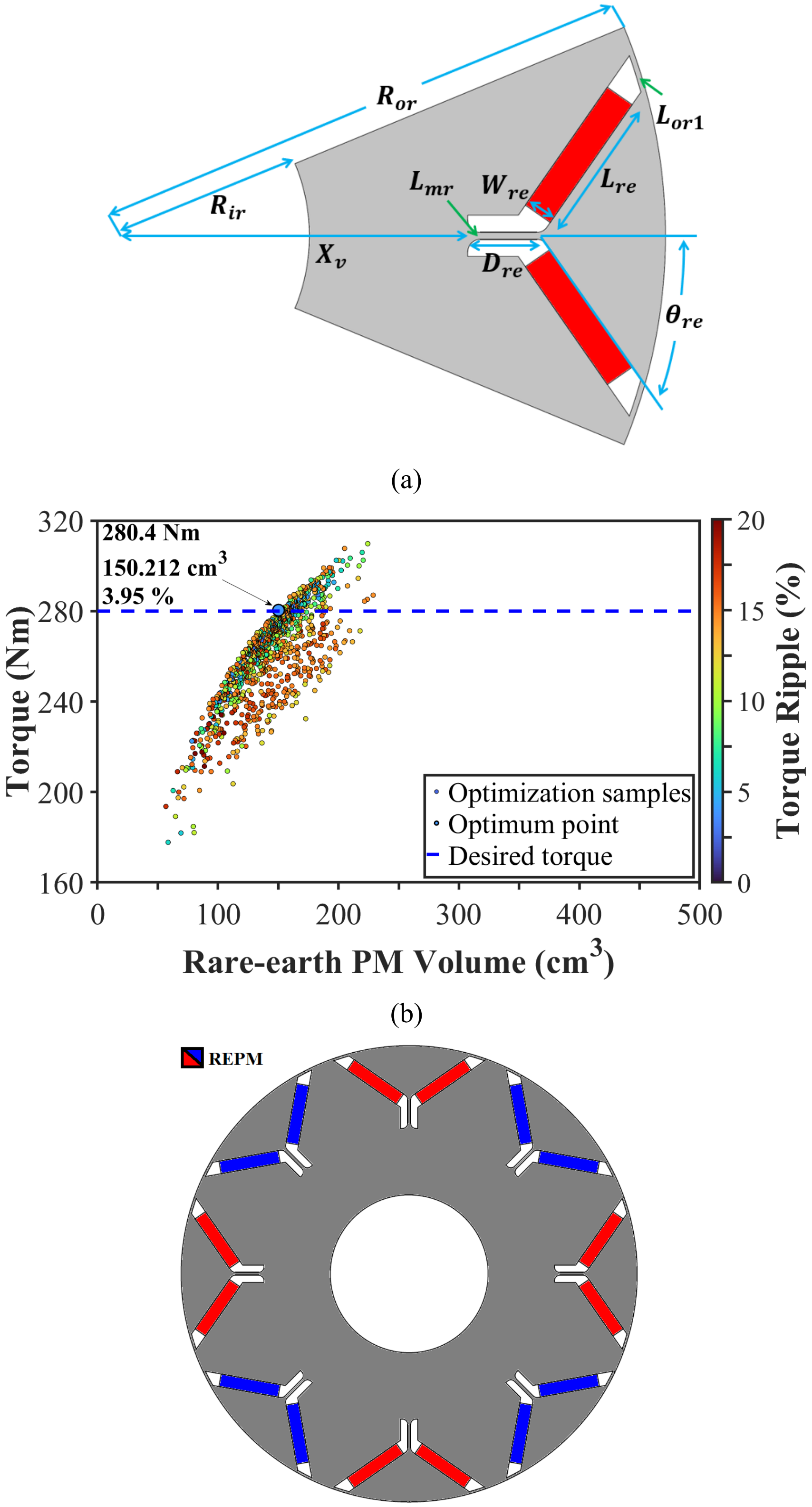
(a)

(b)

(c)

Fig. 6.2. REPM-based symmetrical V-shape IPMSM (baseline). (a) Parametric model. (b) Optimization result at 625 A_{max} and 2100 r/min. (c) Optimum cross section.

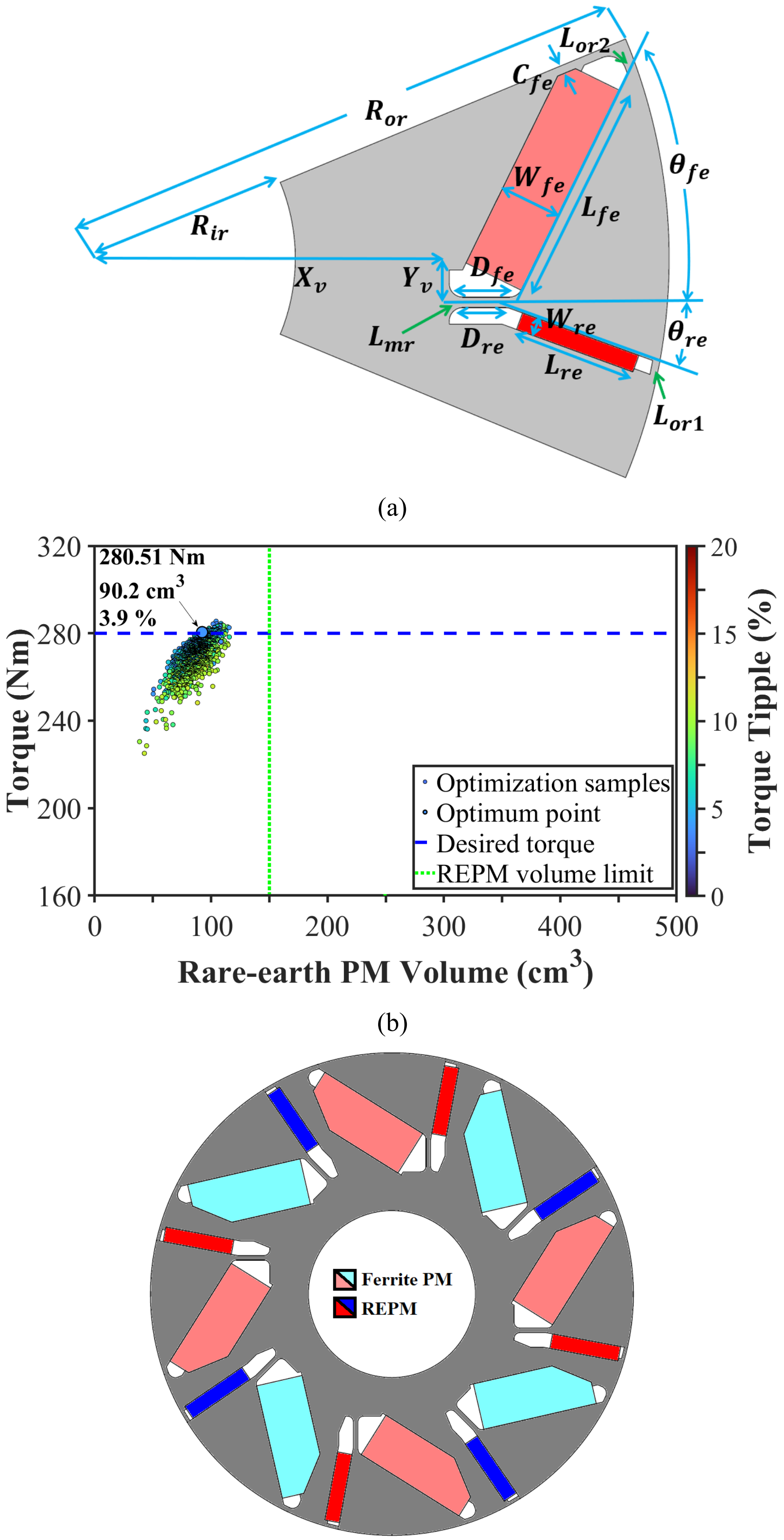

(a)

(b)

(c)

Fig. 6.3. Mixed HPM asymmetric V-shape IPMSM. (a) Parametric model. (b) Optimization result at 625 A_{max} and 2100 r/min. (c) Optimum cross section.

Table 6.2. Design Parameters of V-shape IPMSMs and Their Optimum Values.

Parameter	**Symbols**	**Unit**	**REPM-based symmetrical V-shape IPMSM**	**Mixed HPM asymmetric V-shape IPMSM**
Rotor outer radius	R_{or}	mm	65	
Rotor inner radius	R_{ir}	mm	22.5	
V-shape x-axis position	X_v	mm	41.4	32.88
V-shape y-axis position	Y_v	mm	0	9.78
Width of REPM	W_{re}	mm	3.63	4.0
Length of REPM	L_{re}	mm	17.128	18.665
Width of FEPM	W_{fe}	mm	-	12.57
Length of FEPM	L_{fe}	mm	-	30.72
Angle of REPM	θ_{re}	Degree	55.13	10.57
Angle of FEPM	θ_{fe}	Degree	-	58.10
Displacement of REPM	D_{re}	mm	6.05	8.6
Displacement of FEPM	D_{fe}	mm	-	9.7
Cut off edge of FEPM	C_{fe}	mm	-	1.47
Width of middle rib	W_{mr}	mm	0.8	1.2
Width of outer rib-1	W_{or1}	mm	0.6	0.8
Width of outer rib-2	W_{or2}	mm	-	1.2

6.3.2. Comparison of PM Cost

The outstanding advantage of the HPM utilization is to improve the torque per REPM volume ratio. This benefit can be achieved by either improving the output torque at the same REPM usage or reducing the volume of REPM at the same output torque. As the latter solution is used, a PM cost comparison can emphasize the advantage of the proposed mixed HPM asymmetric V-shape IPMSM over the REPM-based symmetrical V-shape baseline. Therefore, Table 6.3 compares the volume of both PMs and an estimation of PM costs considering the price of REPM being ten times of FEPM. As can be seen, the volume of REPM in the proposed mixed HPM asymmetric V-shape IPMSM is ~40 % less than that of the REPM-based symmetrical V-shape IPMSM which leads to ~21 % reduction of PM cost. Obviously, with an increase in the cost of REPM in future, this price gap will be even bigger.

Table 6.3. Comparison of PM Cost Estimations and Torque per REPM Volume Ratios.

	REPM-based symmetrical V-shape IPMSM	**Mixed HPM asymmetric V-shape IPMSM**
Total torque (Nm)	280.4	280.51
Volume of REPM (cm^3)	150.212	90.2
Volume of FEPM (cm^3)	-	431.15
Mass of REPM (kg)	1.14161	0.68552
Mass of FEPM (kg)	-	2.15575
Torque per REPM volume (Nm/cm^3)	1.8667	3.11
PM cost estimation (%)	**100**	**78.93**

6.3.3. Magnetic Field Shifting (MFS) Effect

The reduced volume of REPM and total PM cost are not only achieved by HPM utilization, but also due to the MFS effect. As presented in literature, the MFS effect can be shown by analysing the open circuit performances. Therefore, Figs. 6.4 (a) and 6.5 (a) investigate the effect of REPM angle and FEPM width on the open circuit flux linkage, respectively, when all the other design parameters are set to their optimum values as listed in Table 6.2. It is worth mentioning that a higher REPM angle means the pole arcs of FEPM and REPM get to a closer number (See Fig. 6.3 (a)). As can be seen, by reducing the REPM angle from 20 degrees to 0 degree, the MFS will continuously increase. However, even at 20 degrees of REPM angle, the magnetic field is already shifted. That means the REPM angle is not the only parameter affecting the MFS. It should be noted that the amplitude of flux linkage is not changing as the volumes of both PMs are constant. In addition, Figs. 6.4 (b) – (d) illustrate the open circuit flux density and flux lines distributions showing that the d-axis is rotating by the reduction of REPM angle. Meanwhile the parametric study of FEPM width is carried out to illustrate the effect of intentional saturation between two adjacent poles. As can be seen, this saturation, which is due to the displacement of V-shape arrangement of PMs and the FEPM width, can affect the MFS. As can be seen, the MFS improves in two steps by increasing the width of FEPM from 6 mm to 12 mm, whereas the amplitude of flux linkage is also enhancing as the volumes of FEPM is increasing. Meanwhile, even at low FEPM width, the magnetic field is already shifted mainly due to the REPM angle. In addition, Figs. 6.5 (b) – (d) illustrate the open circuit flux density and flux lines distributions showing that the d-axis is rotating by the increase in the FEPM width.

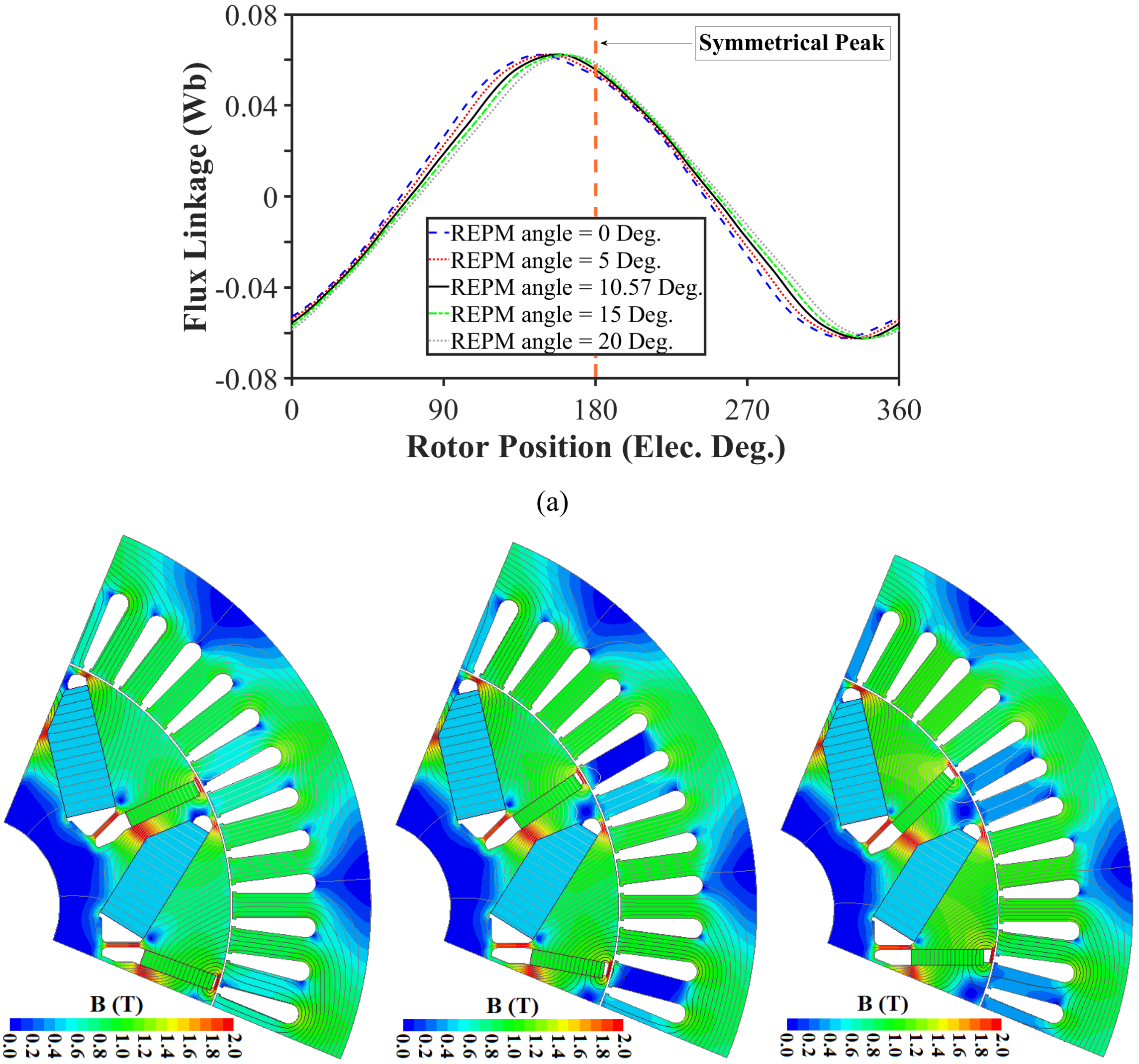

(a)

(b) (c) (d)

Fig. 6.4. MFS effect caused by REPM angle in proposed mixed HPM asymmetric V-shape IPMSM at open circuit. (a) Flux linkage waveforms. (b) Flux density and flux line distributions at θ_{re}= 20 degrees. (c) Flux density and flux line distributions at optimum θ_{re} = 10.57 degrees. (d) Flux density and flux line distributions at θ_{re} = 0 degree.

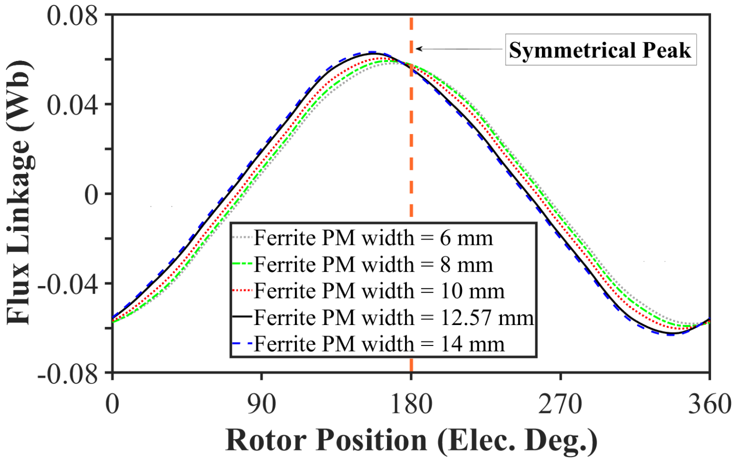

(a)

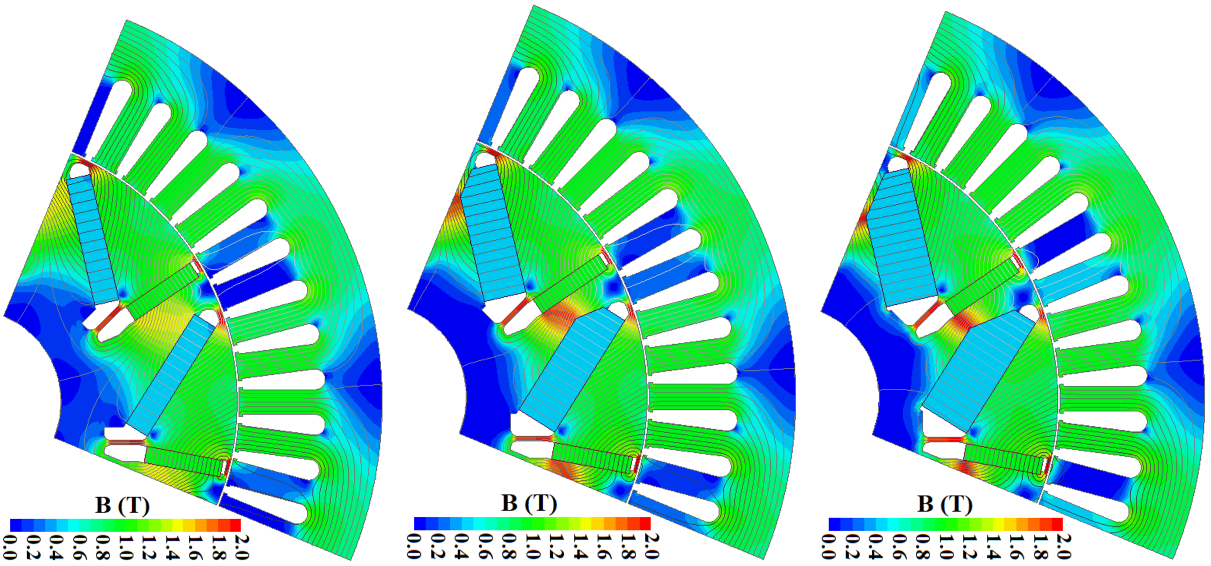

(b) (c) (d)

Fig. 6.5. MFS effect caused by intentional saturation between two adjacent poles in proposed mixed HPM asymmetric V-shape IPMSM at open circuit. (a) Flux linkage waveforms. (b) Flux density and flux line distributions at W_{fe}= 6 mm. (c) Flux density and flux line distributions at W_{fe} = 10 mm. (d) Flux density and flux line distributions at optimum W_{fe} = 12.57mm

The results of Figs. 6.4 and 6.5 suggest a lower REPM angle and a higher FEPM width leads to a higher MFS effect. However, the optimum value of each parameter is somewhere in the middle of the variation range, but not at the lowest REPM angle or the highest FEPM width. Figs. 6.6 (a) and 6.7 (a) present the variations of output torque with REPM angle and FEPM width at 625 A_{max} and 2100 r/min, respectively. Whereas the variations of onload field distributions corresponding to each study are compared in Figs. 6.6 (b) to (d) and Figs. 6.7 (b) to (d), respectively. As can be seen, by reducing the REPM angle from 20 degrees to 0 degree, the output torque increases first and then reduces significantly. Meanwhile, the increase in the FEPM width leads to a continuous increase in the output torque. It is worth mentioning that there are a few alternative points in both graphs which may satisfy the desired torque. However, they suffer from a higher torque ripple than the selected optimum point.

It is also worth mentioning that the saturations on some stator teeth are changing by the rotation of REPM, which is mainly due to the change of pole arcs and partially due to the MFS effect as can be seen in Figs. 6.6 (b) to (d). On the other hand, as can be seen in Figs. 6.7 (b) to (d), the saturation on some stator teeth is changing by the increase in the thickness of FEPM due to the increase in the PM field and the MFS effect at the same pole arc. However, the saturation between two adjacent poles is changing by the increase in the thickness of FEPMs.

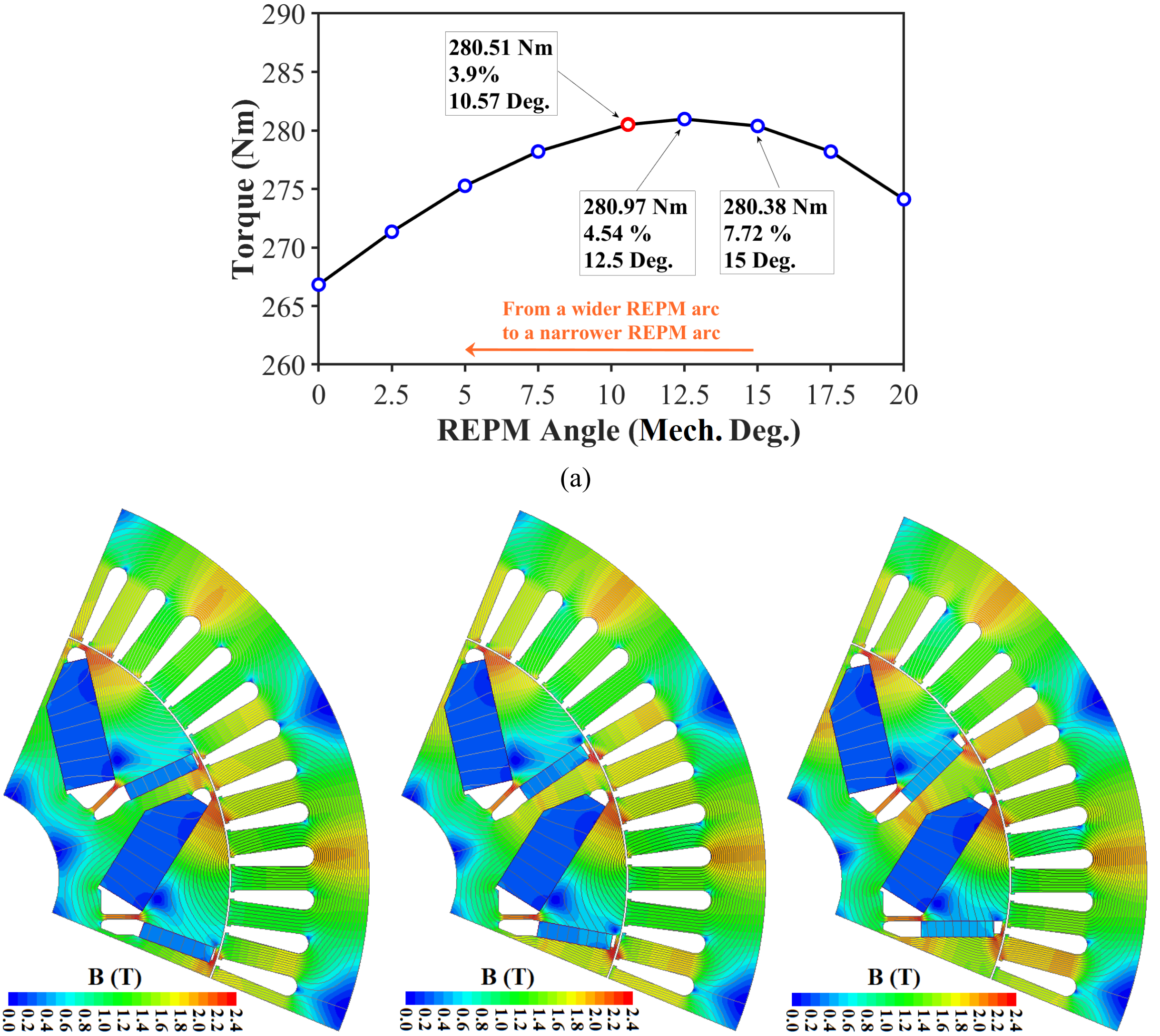

(a)

(b) (c) (d)

Fig. 6.6. Variation of output torque and on-load field distribution caused by REPM angle at 625 A_{max} and 2100 r/min in proposed mixed HPM asymmetric V-shape IPMSM. (a) Torque with REPM angle. (b) Flux density and flux line distributions at θ_{re}= 20 degrees. (c) Flux density and flux line distributions at optimum θ_{re} = 10.57 degrees. (d) Flux density and flux line distributions at θ_{re} = 0 degree.

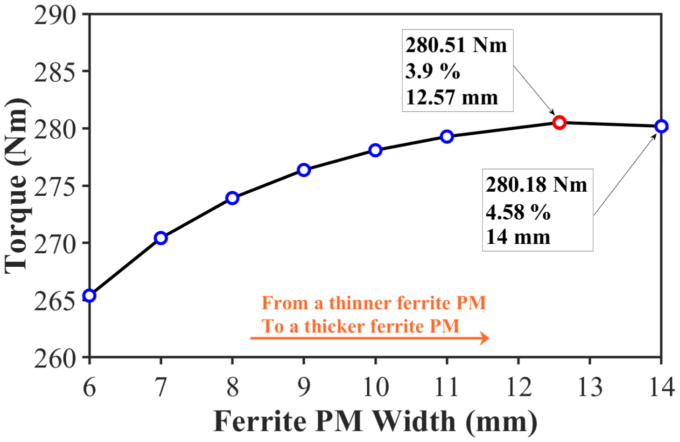

(a)

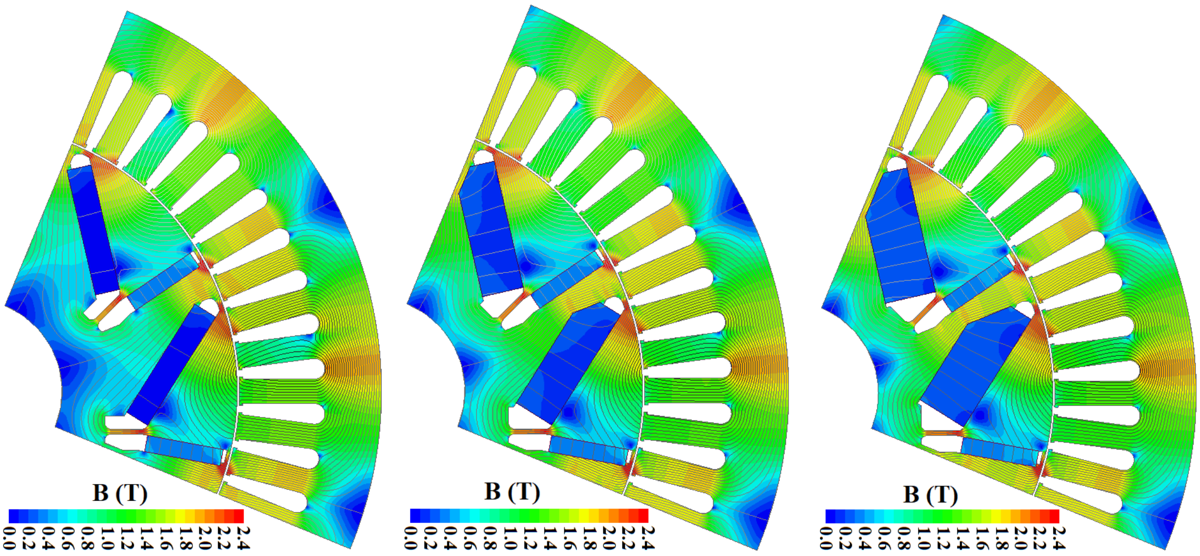

(b) (c) (d)

Fig. 6.7. Variation of output torque and on-load field distribution caused by thickness of FEPM at 625 A_{max} and 2100 r/min in proposed mixed HPM asymmetric V-shape IPMSM. (a) Torque with FEPM thickness. (b) Flux density and flux line distributions at W_{fe}= 6 mm. (c) Flux density and flux line distributions at W_{fe} = 10 mm. (d) Flux density and flux line distributions at optimum W_{fe} = 12.57mm.

For a better understanding of the torque variation with either REPM angle or FEPM width, the torque components should be separated by FPM. This is because the variation of torque components is important in an asymmetric rotor where the peak values of PM torque and reluctance torque components are tried to merge to a closer current advancing angle to maximize the output torque. In [ZHU22], the asymmetric IPMSMs are categorized into four groups including symmetrical PM configuration and rotor core structure (group 1), symmetrical PM configuration but asymmetric rotor core structure (group 2), asymmetric PM configuration but symmetrical rotor core structure (group 3), and asymmetric PM configuration and rotor core structure (group 4). Figs. 6.8 (a) and (b) show the PM configuration and rotor core structure of the proposed mixed HPM asymmetric V-shape IPMSM which is classified in group 4. Fig. 6.8 (c) presents the variation of the output torque, the reluctance torque component, and the PM torque component with REPM angle at 625 A_{max} and 2100 r/min when FPM is used. As can be seen, the PM torque increases by reducing the REPM angle which is mainly due to the MFS effect at the same volumes of both PMs. Meanwhile, as it is shown, the reluctance torque component is reducing significantly due to the reduction of q-axis inductance as shown in Fig. 6.8 (d). It is because reducing the REPM angle means lowering the REPM arc which leads to a lower q-axis cross section area, an increased q-axis saturation and therefore a lower q-axis inductance. As a result, the maximum torque of the proposed mixed HPM asymmetric V-shape IPMSM happens at a traded-off optimum point when the summation of the reduced reluctance torque and the enhanced PM torque is maximized. In addition, Fig. 6.8 (e) illustrates the variation of the output torque, the reluctance torque component, and the PM torque component with FEPM width at 625 A_{max} and 2100 r/min when FPM is used. As can be seen, the PM torque gradually increases with the increase in the FEPM width with two jumps which are due to the MFS effect as discussed in Fig. 6.5. Meanwhile, the reluctance torque is almost constant except for the last point (W_{fe}=14mm) where the difference between dq-axis inductances is reducing as shown in Fig. 6.8 (f). Although the total torque at this point can satisfy the output torque, the torque ripple is slightly higher than that of the optimum point as shown in Fig. 6.7 (a). Therefore, the maximum torque of the proposed mixed HPM asymmetric V-shape IPMSM happens at a thicker width of FEPM where both optimization objectives are satisfied. In addition, it can be said that the effect of FEPM width on the MFS may be less obvious than the REPM angle, but it is contributing to the torque enhancement.

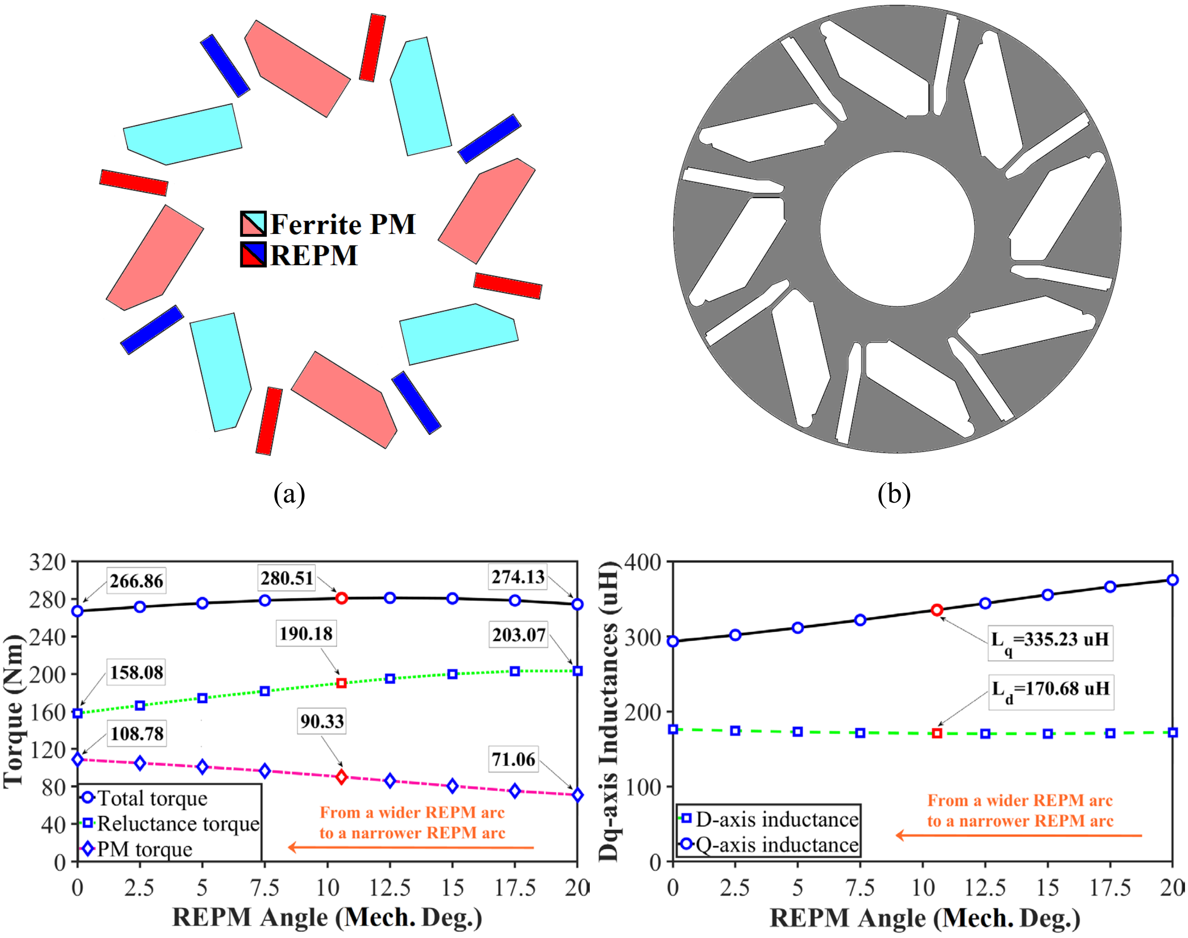

(a) (b)

(c) (d)

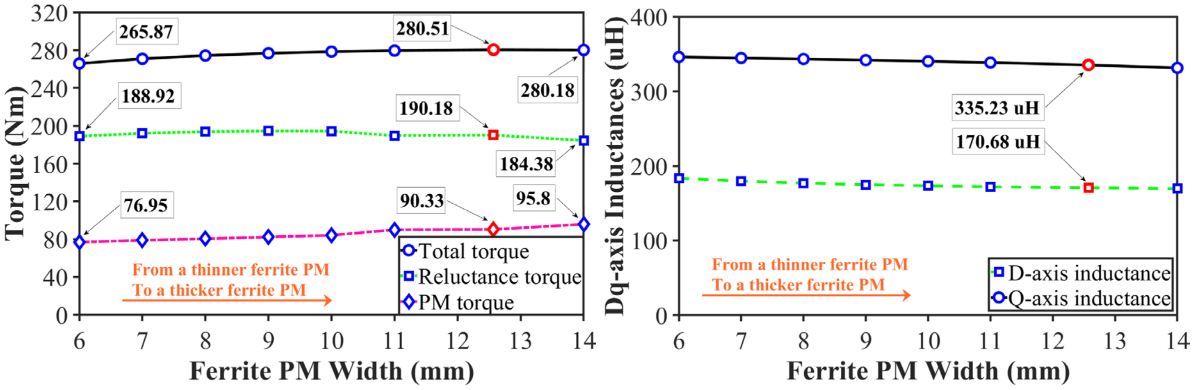

(e) (f)

Fig. 6.8. Effect of REPM angle and FEPM width on torque components using FPM at 625 A_{max} and 2100 r/min. (a) Asymmetric PM configuration. (b) Asymmetric rotor core structure. (c) Torque with REPM angle. (d) Dq-axis inductances with REPM angle. (e) Torque with FEPM width. (f) Dq-axis inductances with FEPM width.

6.3.4. Comparison of Open Circuit Performances

Fig. 6.9 compares the open circuit flux density and flux line distributions of the REPM-based symmetrical V-shape IPMSM and the proposed mixed HPM asymmetric V-shape IPMSM. As can be seen, the d-axis of the proposed machine is shifted from the symmetrical position. In addition, the series connection of two PM materials between two adjacent poles can also be seen by observing the flux lines.

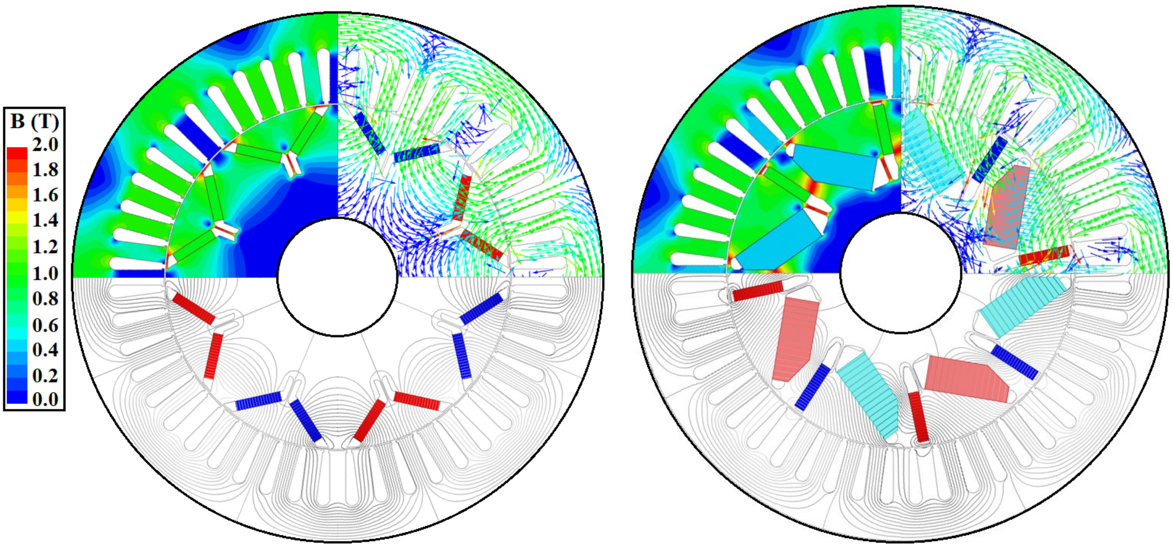

(a) (b)

Fig. 6.9. Comparison of open circuit flux density and flux line distributions. (a) REPM-based symmetrical V-shape IPMSM. (b) Proposed mixed HPM asymmetric V-shape IPMSM.

Fig. 6.10 compares the open circuit airgap flux density waveforms and spectra of these two machines in both tangential and radial directions. As [XIA21A] suggests, the numerical comparison of the MFS effect can be declared by the variation of the fundamental component of the open circuit airgap flux density in radial direction. Therefore, Fig. 6.10 (e) presents a comparison of fundamental components of the radial airgap flux densities of these two machines at open circuit. As can be seen, the magnetic field of the proposed mixed HPM asymmetric V-shape IPMSM is shifted by 20.6 elec. deg. compared to that of the baseline.

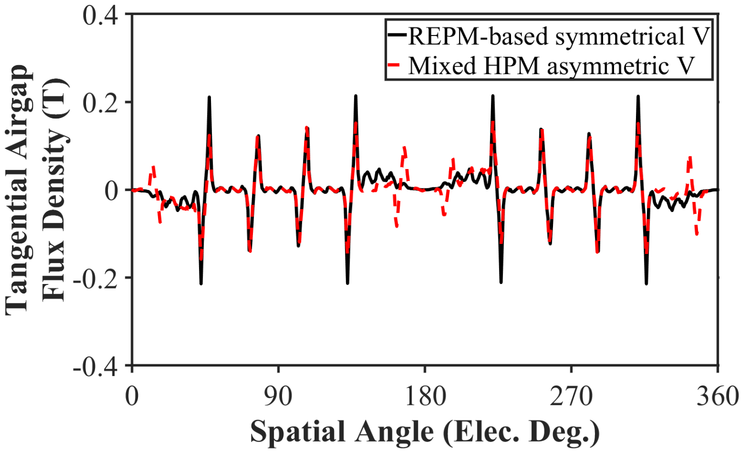

(a)

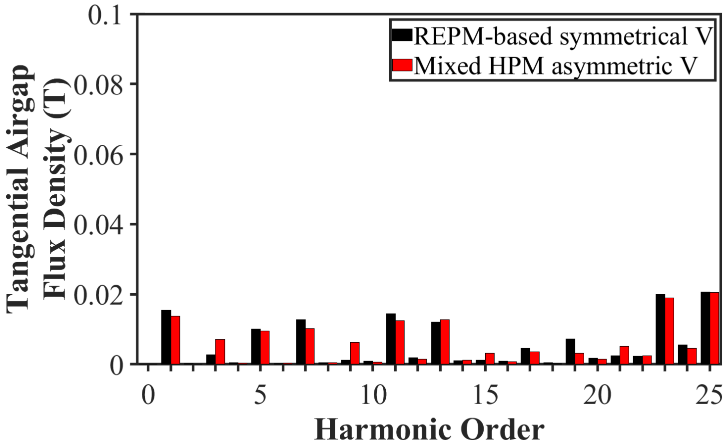

(b)

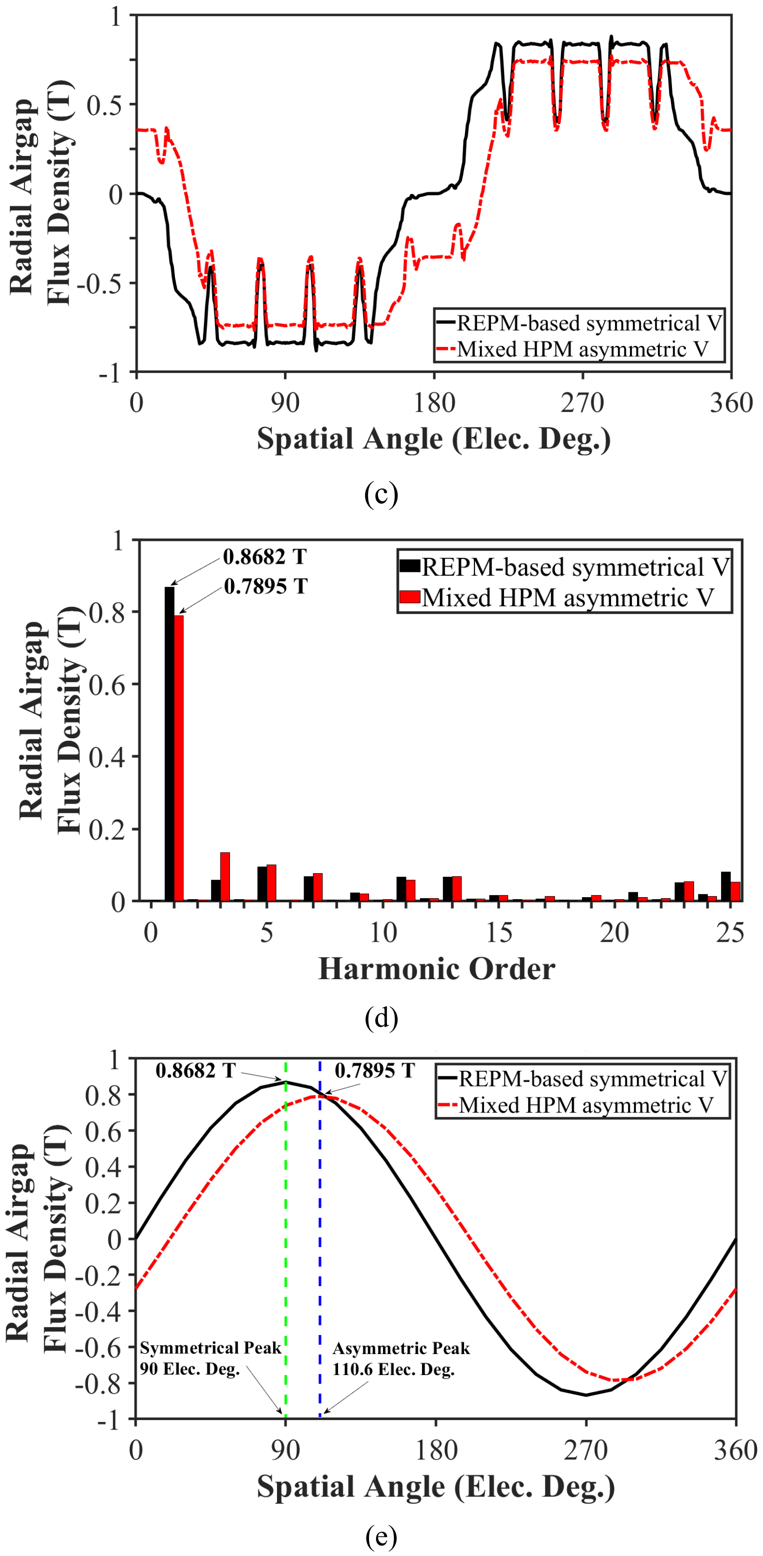

(c)

(d)

(e)

Fig. 6.10. Comparison of open circuit airgap flux densities of REPM-based symmetrical V-shape and proposed mixed HPM asymmetric V-shape IPMSMs. (a) Waveforms in tangential direction. (b) Spectra in tangential direction. (c) Waveforms in radial direction. (d) Spectra in radial direction. (e) Fundamental component waveform in radial direction.

Fig. 6.11 compares the open circuit flux linkage waveforms and spectra. As can be seen, the flux linkage of the proposed mixed HPM asymmetric V-shape IPMSM is not only shifted but also has a lower amplitude. Therefore, at the same speed, a lower amplitude of back-EMF is expected. A comparison of open circuit back-EMF waveforms and spectra at 2100 r/min is presented in Figs. 6.12 (a) and (b), respectively. As can be seen, the back-EMF's fundamental component of the proposed mixed HPM asymmetric V-shape IPMSM with 52.74 V is less than that of the REPM-based symmetrical V-shape IPMSM with 58.3 V. In general, having a higher amplitude of back-EMF at the same size could be considered as an advantage of a PM machine if a symmetrical geometry (e.g. baseline in this study) is used. This is because it can be interpreted as a higher PM torque contribution leading to a higher total torque at the same current, especially at low electrical loading when the saturation level is eased. However, although the magnetic loading and back-emf of the proposed mixed HPM asymmetric V-shape IPMSM are considerably lower than those of the baseline (see Fig. 6.12), it is capable of producing a comparable torque with a negligible margin at different currents (using MTPA control strategy) due to the reduced phase between the maximum PM and reluctance torque components by the MFS effect. On the contrary, having a lower back-EMF at high speeds is an advantage of the proposed mixed HPM asymmetric V-shape IPMSM, where a fault can transfer a high voltage across the terminals of the inverter and increase the potential risk of damage. Therefore, Fig. 6.12 (c) compares the variation of peak-to-peak values of open circuit back-EMFs in both machines. As can be seen, the peak-to-peak value of the proposed HPM machine at 10000 r/min with 476.57 V is 65.58 V (~12 %) less than that of the baseline. Finally, Fig. 6.13 presents a comparison of cogging torques. As can be seen, the cogging torque of the proposed mixed HPM asymmetric V-shape IPMSM is lower than that of the REPM-based symmetrical V-shape IPMSM.

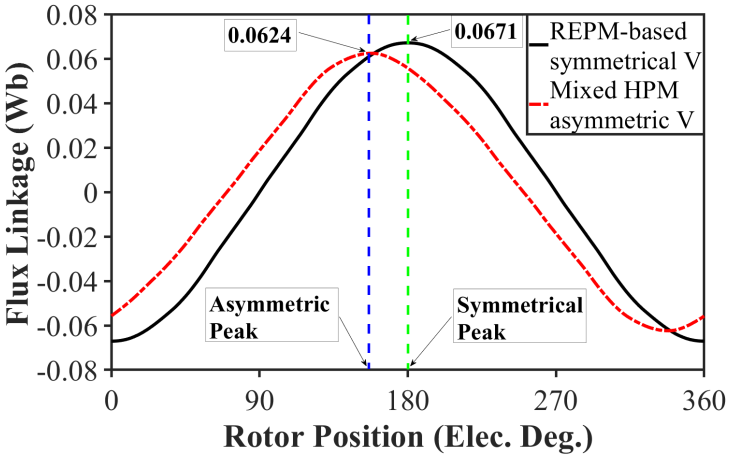

(a)

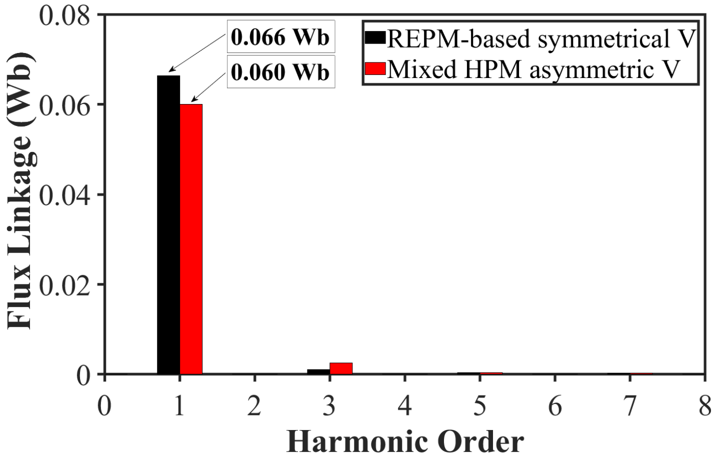

(b)

Fig. 6.11. Comparison of open circuit flux linkages of baseline and proposed mixed HPM asymmetric V-shape IPMSMs. (a) Waveforms. (b) Spectra.

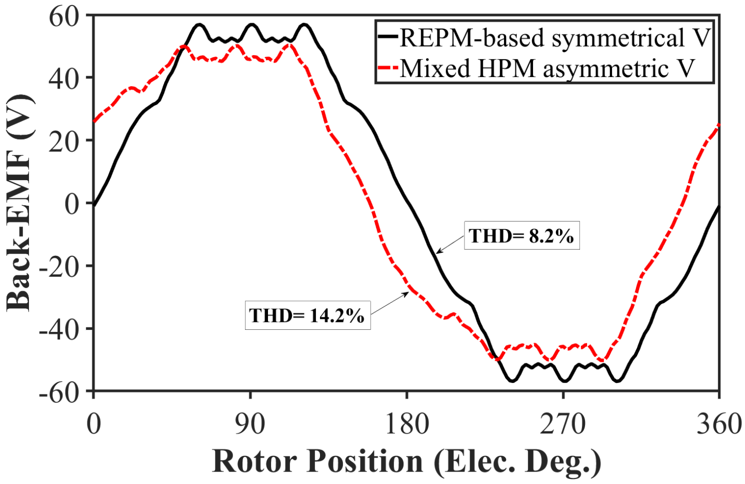

(a)

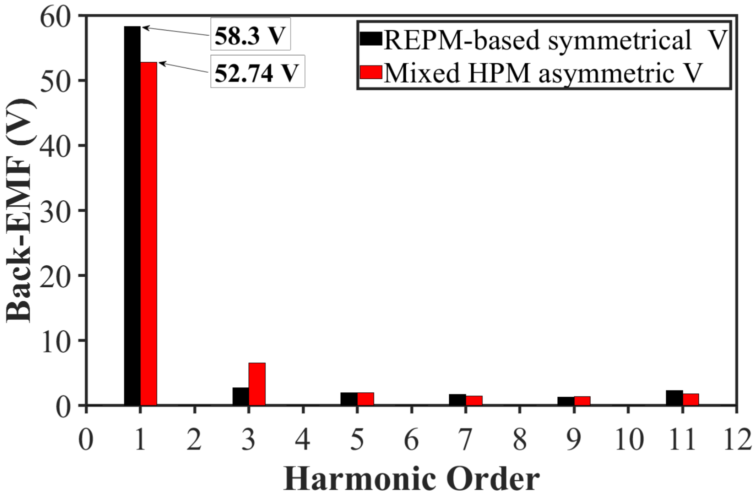

(b)

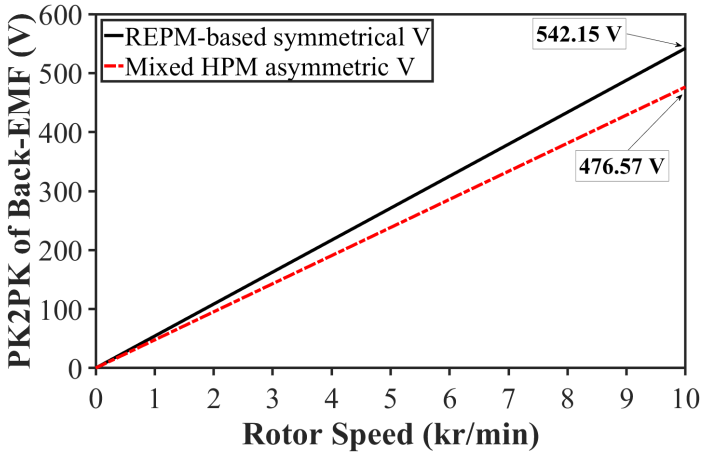

(c)

Fig. 6.12. Comparison of open circuit back-EMFs of baseline and proposed mixed HPM asymmetric V-shape IPMSMs. (a) Waveforms at 2100 r/min. (b) Spectra at 2100 r/min. (c) PK2PK values of back-EMFs with speed.

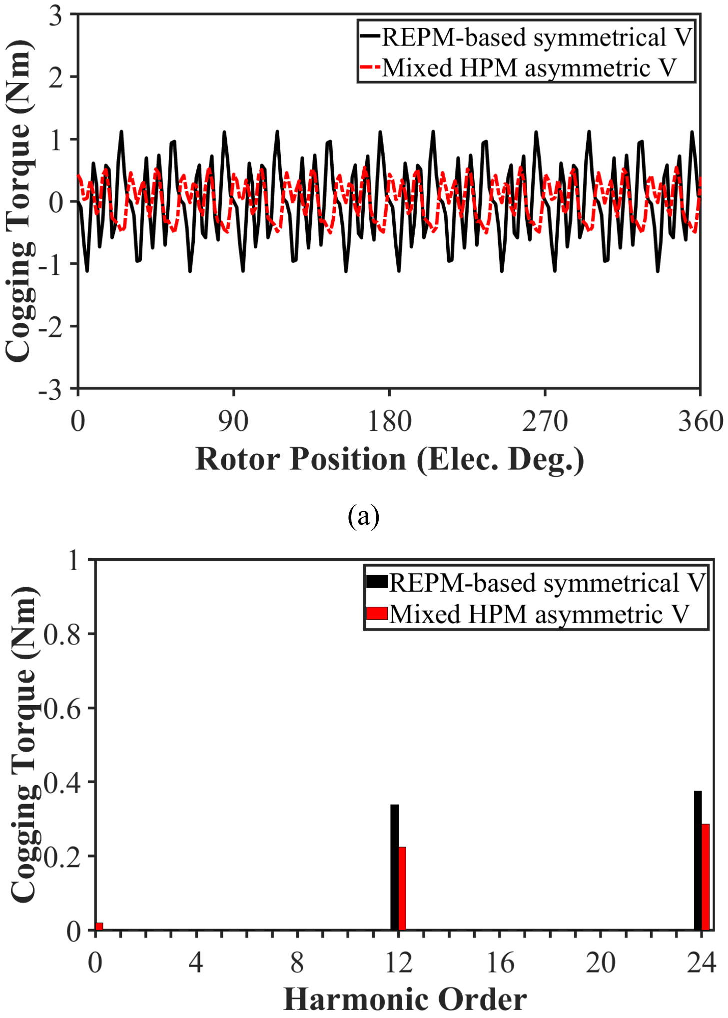

(a)

(b)

Fig. 6.13. Comparison of open-circuit cogging torques of REPM-based symmetrical V-shape and mixed HPM asymmetric V-shape IPMSMs. (a) Waveforms. (b) Spectra.

6.3.5. Comparison of On-load Performances

Fig. 6.14 compares the peak torque waveforms and spectra of these two machines at 625 A_{max} and 2100 r/min. As both machines are optimized to deliver the same peak torque, a similar performance is expected. However, as can be seen, the optimum current advancing angle of the proposed machine is higher than that of the baseline. Fig. 6.15 compares the variations of total torques with current using the MTPA control strategy at 2100 r/min. As can be seen, the proposed mixed HPM asymmetric V-shape IPMSM produces a similar torque as the baseline with the biggest margin of 1.8 Nm at 156.25 A_{max}. However, both machines are producing the same peak torque as they were optimized for.

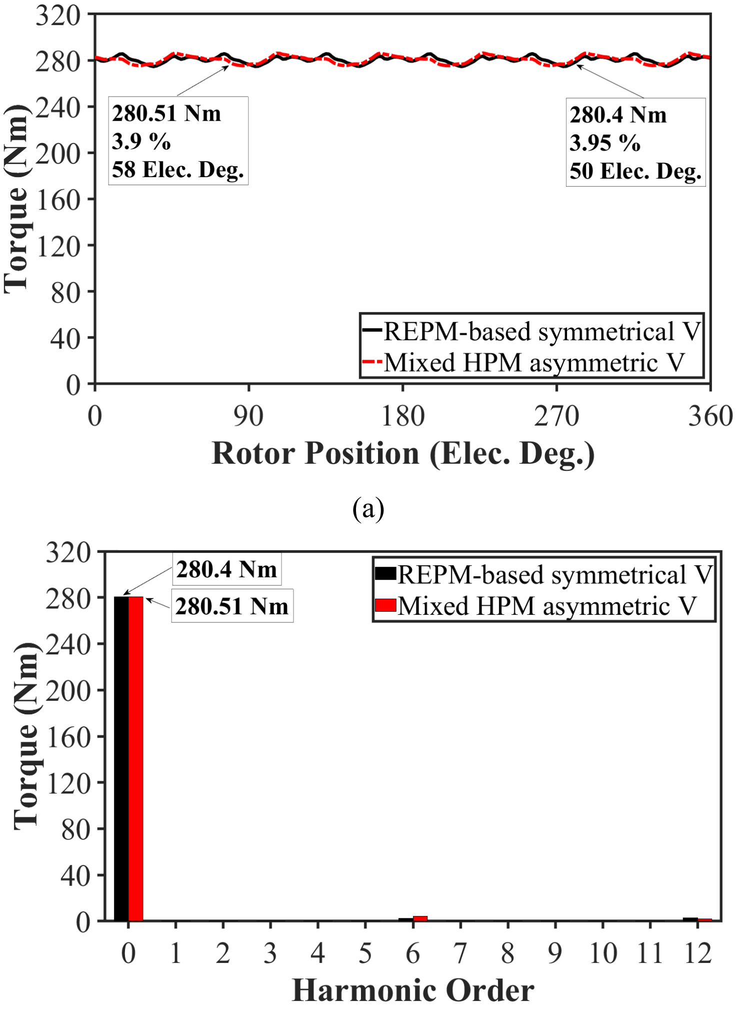

(a)

(b)

Fig. 6.14. Comparison of output torques at 625 A_{max} and 2100 r/min. (a) waveforms. (b) Spectra.

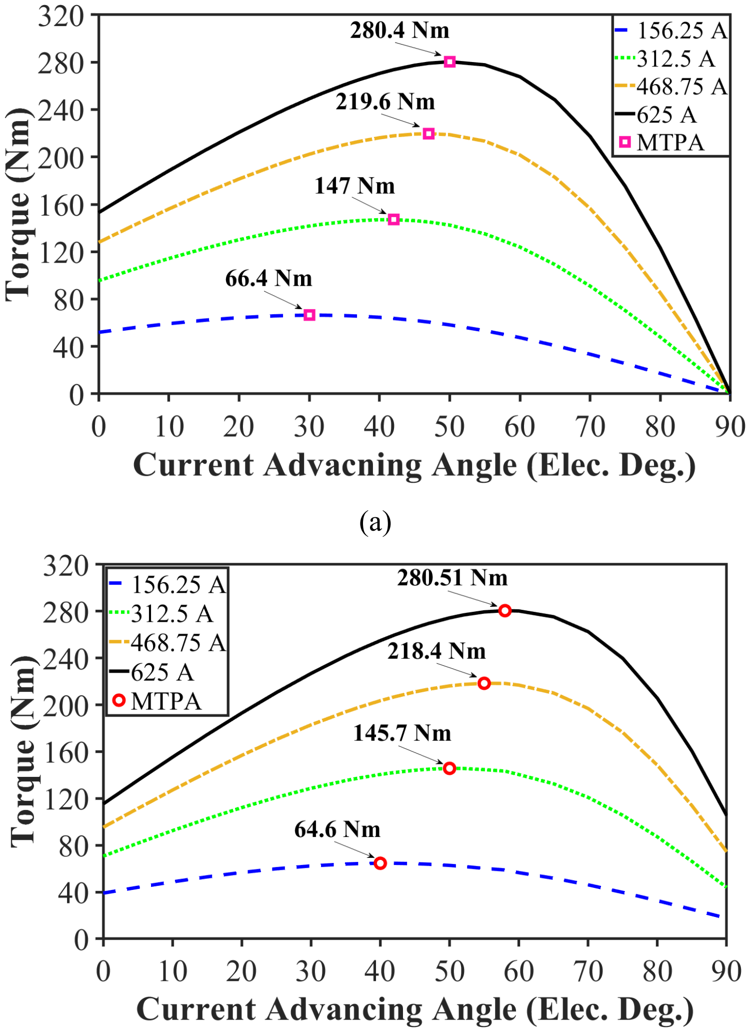

(a)

(b)

Fig. 6.15. Comparison of output torques with current advancing angle at different current amplitudes using MTPA control strategy at 2100 r/min. (a) Baseline. (b) Proposed IPMSM.

Fig. 6.16 compares the onload field distributions of both machines at 625 A_{max} and 2100 r/min when each machine is operating with its optimum current advancing angle as shown in Fig. 6.14 (a). Figs. 6.17 (a) and (b) compare the variations of torques and dq-axis inductances of these two machines with the current advancing angle at 625 A_{max} and 2100 r/min. As can be seen in Fig. 6.17 (a), the variations of torque with current advancing angle are different, which suggests that these machines would have different reluctance torque and PM torque components. In addition, as can be seen in Fig. 6.17 (b), although the d-axis inductances are almost the same, the q-axis inductance of the proposed mixed HPM asymmetric V-shape IPMSM is less than that of the REPM-based symmetrical V-shape IPMSM due to the reduction of the REPM angle. Therefore, it is expected that the proposed HPM machine has a lower reluctance torque than the baseline.

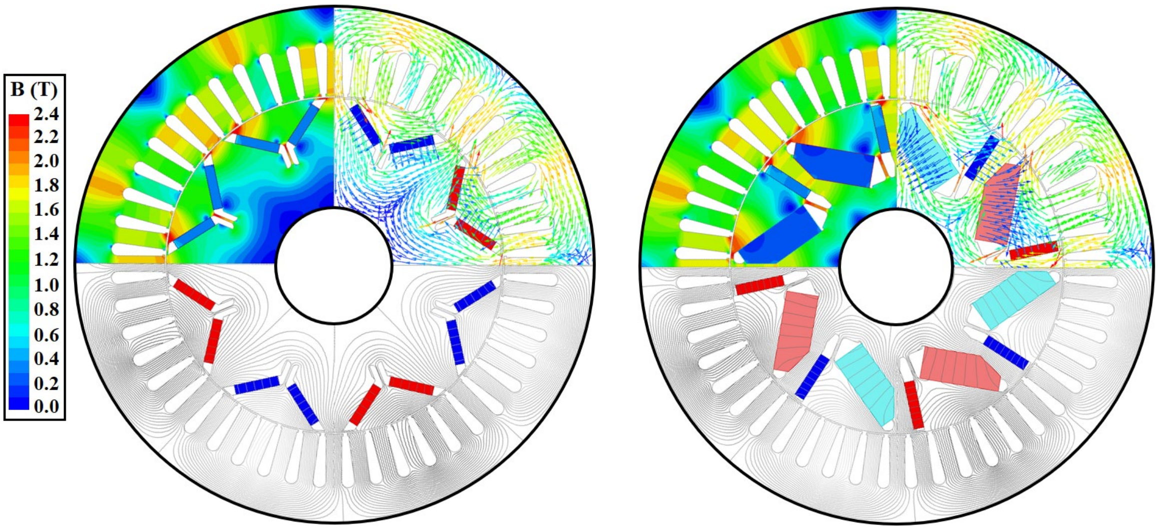

(a) (b)

Fig. 6.16. Comparison of onload flux density and flux line distributions at 625 A_{max} and 2100 r/min. (a) REPM-based symmetrical V-shape IPMSM. (b) Proposed mixed HPM asymmetric V-shape IPMSM.

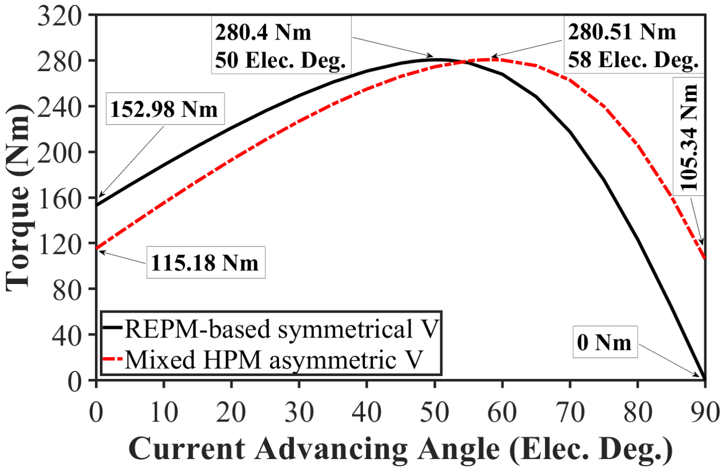

(a)

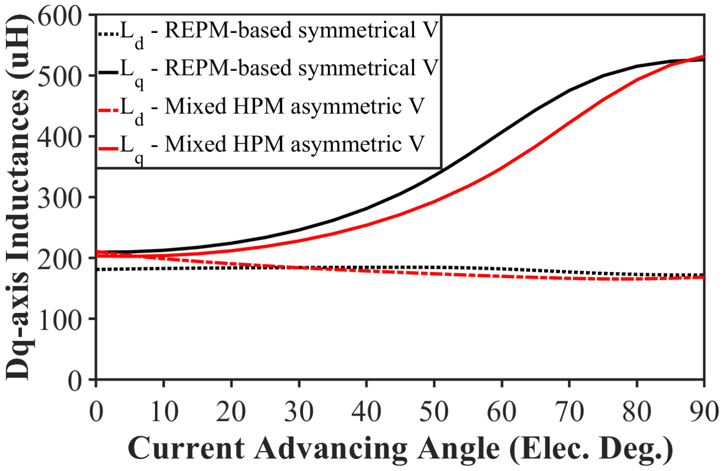

(b)

Fig. 6.17. Comparisons of on-load characteristics with current advancing angle at 625 A_{max} and 2100 r/min. (a) Torques. (b) Dq-axis inductances.

Meanwhile, for a precise torque components decomposition, Fig. 6.18 (a) compares the components of output torque in both machines at 625 A_{max} and 2100 r/min using the FPM. On the other hand, to investigate the effect of the magnetic field shifting on torque components, Fig. 6.18 (b) presents a torque components decomposition with the current advance angle at 625 A_{max} and 2100 r/min. It is worth mentioning that in Fig. 6.18 (a), the current advancing angles of each machine are at their optimum value. This graph is important to appreciate the advantage of HPM utilization. As can be seen, the reluctance torque of the proposed HPM topology with 190.18 Nm is 8.5 Nm less than that of the REPM-based symmetrical V-shape IPMSM. This means that the proposed HPM machine requires 90.33 Nm of PM torque at the same output torque. However, the one third of the required PM torque is delivered by FEPMs (30.44 Nm). Therefore, the proposed mixed HPM asymmetric V-shape IPMSM only needs 60.07 Nm of REPM torque which is ~21.5 Nm less than that of the baseline. As a result, a less volume of REPM can be used. In addition, the REPM torque per REPM volume ratio can be used as a definition to the REPM utilization. This ratio shows the amount of REPM torque produced by each 1 cm^3 of REPM material. From Fig. 6.18 (a) and Table 6.3, it can be concluded that the REPM utilization in the proposed mixed HPM asymmetric V-shape IPMSM with 0.666 Nm/cm^3 is ~22.5 % more than that of the REPM-based symmetrical V-shape IPMSM with 0.5436 Nm/cm^3.

It should also be noted that in Fig. 6.18 (b), the increase in the current advancing angle leads to the increase in the d-axis current. Consequently, the field distribution of the iron will change, and it would not be appropriate to freeze the permeability when the current advancing angle is changing from 0 to 90 elec. deg. Therefore, to plot the variation of total torque with current advancing angles, several FEA simulations are conducted to achieve the individual field distributions in iron at each current advancing angle step. Then, the contributions of the PM and reluctance torque components are separated by freezing the permeability of each individual field distribution corresponding to a unique current advancing angle. As can be seen, the difference between the corresponding current advancing angles of the PM and reluctance torque in the REPM-based symmetrical V-shape IPMSM with ~55 elec. deg. is reduced to ~25 elec. deg. in the proposed mixed HPM asymmetric V-shape IPMSM. Consequently, the output torque is delivered at the improved torque components. In other words, this means a less required volume of REPM at the same total torque. In addition, the PM torque component of the baseline reduces when current advancing angle is advancing from 0 to 50 elec. deg. accounting for MTPA control strategy at 625 A_{max}. However, the PM torque component of the proposed mixed HPM asymmetric V-shape IPMSM is almost preserved when current advancing angle is advancing from 40 to 58 elec. deg. accounting for MTPA control strategy at the same current. Therefore, at the same peak torque and size, baseline would require a higher magnetic loading than the proposed mixed HPM asymmetric IPMSM in open circuit conditions (see Figs. 6.10 to 6.12) to compensate the PM torque reduction in Fig. 6.18 (b).

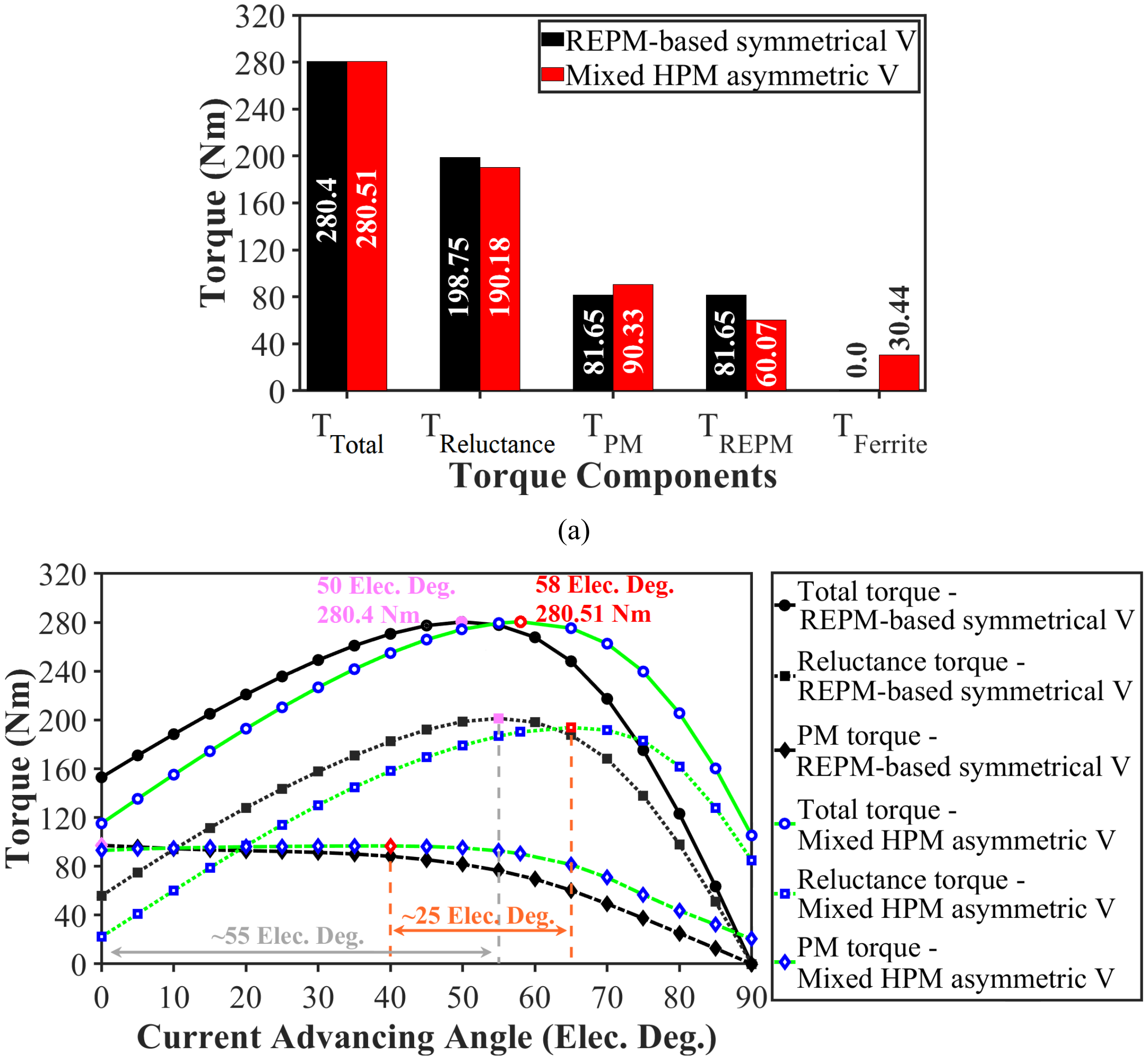

(a)

(b)

Fig. 6.18. Comparisons of torque components at 625 A_{max} and 2100 r/min using the FPM. (a) At optimum current advancing angles of baseline and proposed mixed HPM asymmetric V-shape IPMSM. (a) With current advancing angle.

Figs. 6.19 (a) and (b) compare the torque-speed and power-speed characteristics of these two machines. As both machines are designed for the same torque at low speed under 625 A_{max} and 2100 r/min, these characteristics are expected to be the same at constant torque region. However, on the one hand, the speeds of entering the flux weakening region in these machines are generally expected to be different even at the same DC link voltage of 375 V and maximum phase current of 625 A. This is due to the difference in the flux linkages of these machines which can induce different voltages at the same speed. In other words, the same DC link voltage limit is expected to meet at different speeds. On the other hand, the commercialized IPMSM has a maximum power cap of 80 kW [BUR13] which is also applied to these two machines. Therefore, both machines will have the same characteristics at constant power region after applying the power limit as shown in Figs. 6.19 (a) and (b). Meanwhile, as the torque ripple can vary at different speeds and electrical loadings, a comparison of the peak-2-peak torque variation with speed, based on [CAW23], is conducted by showing a few points within the torque-speed characteristic maps of both machines as shown in Fig. 6.20. As can be seen, the peak-2-peak values of torque in the proposed mixed HPM asymmetric V-shape IPMSM are less than those of the baseline within this map.

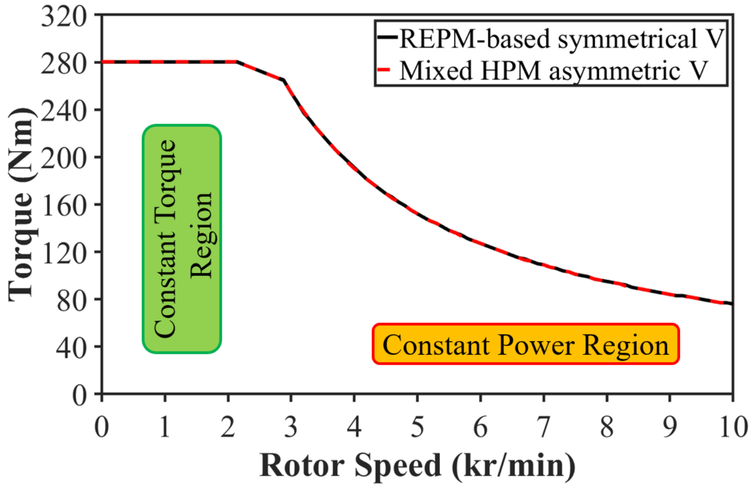

(a)

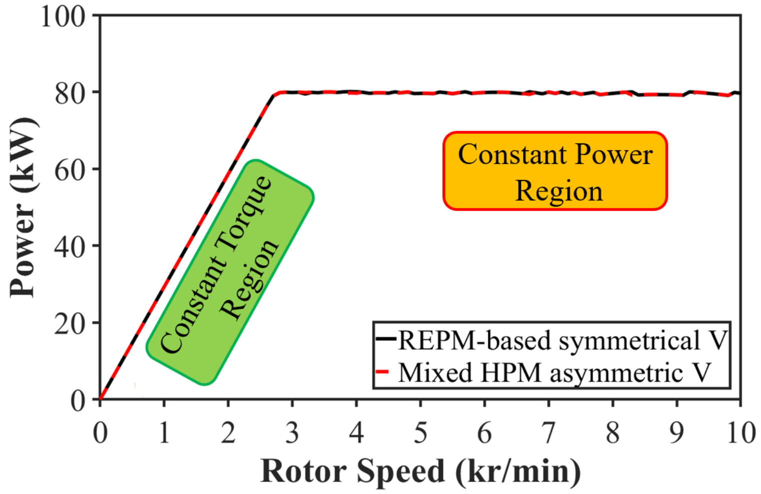

(b)

Fig. 6.19. Comparisons of torque-speed and power-speed characteristics at 625 A_{max}. (a) Torque-speed characteristics. (b) Power-speed characteristics.

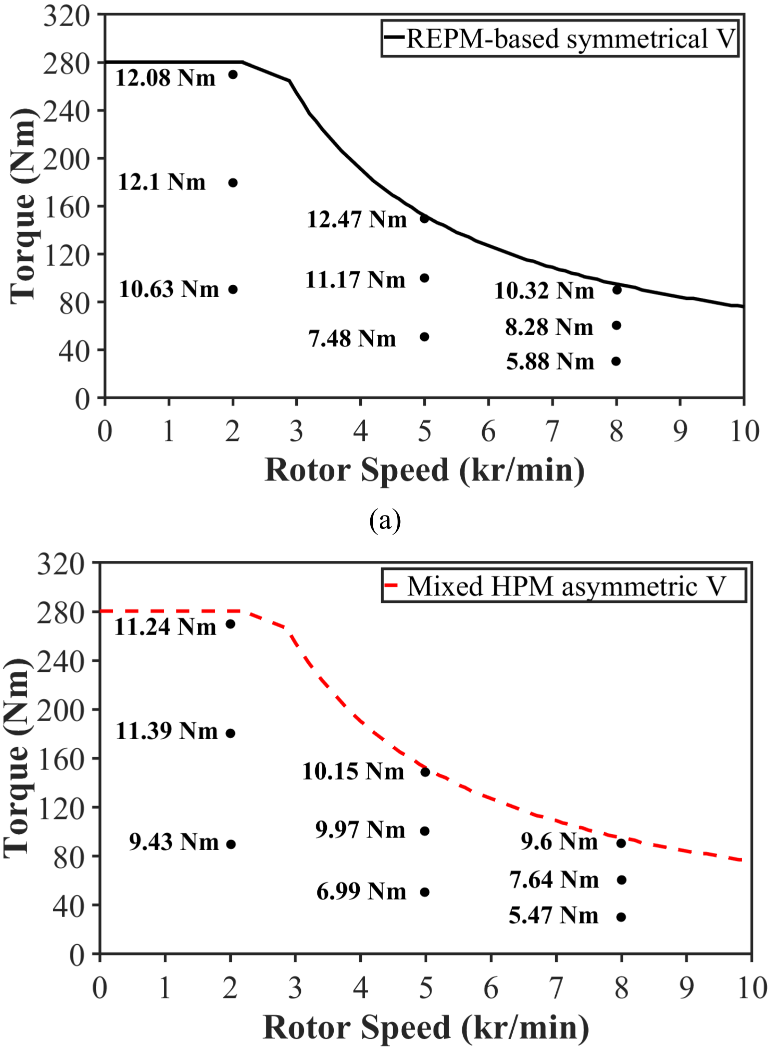

(a)

(b)

Fig. 6.20. Comparison of total peak-2-peak torque ripple magnitudes. (a) Baseline IPMSM. (b) Proposed Mixed HPM asymmetric V-shape IPMSM.

The efficiency (η) of these machines can be obtained using the equation below:

$$\eta = \frac{P_{out}}{P_{out}+P_{cu}+P_{core}+P_{mec}} \times 100\ \% \tag{6.2}$$

where P_{out}, P_{cu}, P_{core}, and P_{mec} are the output power, the copper loss, the iron loss, and the mechanical loss, respectively.

As these machines share the same stator, stack length, and winding configurations, the copper losses are expected to be almost the same as shown in Fig. 6.21 (a). It is worth mentioning that the AC copper loss is ignored in this calculation. It is because on the one hand, the commercialized IPMSM employs a distributed winding with 4 parallel branches, 8 turns per coil, and 15 strands per conductor, as can be seen in Table 6.1. In [YAN17A], the strand diameter of 0.816 mm with 0.71 mm diameter of copper is suggested which agrees with the tested phase resistance of the commercialized IPMSM with 0.4% error as reported in [BUR13]. On the other hand, at the maximum speed of 10 kr/min, the frequency of the input current increases to ~667 Hz which implies the skin depth (δ) of ~2.5 mm in copper using the equation below:

$$\delta = \sqrt{\frac{\rho}{\pi f \mu_0 \mu_r}} \tag{6.3}$$

where ρ is the resistivity of the material, μ_0 and μ_r are the air and the relative permeabilities, and f is the frequency.

As the resultant skin depth at maximum speed is more than three times the copper diameter in each strand, the AC copper loss effect can be ignored. In addition, the FEA results present that the iron loss maps are also the same as shown Fig. 6.21 (b). Meanwhile, the mechanical loss calculation requires two coefficients as follows which are taken from [YAN17A]:

$$P_{mec} = k_{mec1} f + k_{mec2} f^2 \tag{6.4}$$

where k_{mec1} and k_{mec2} are the mechanical loss coefficients.

Finally, as can be seen in Fig. 6.21 (c), the efficiency of both machines can exceed 97 %.

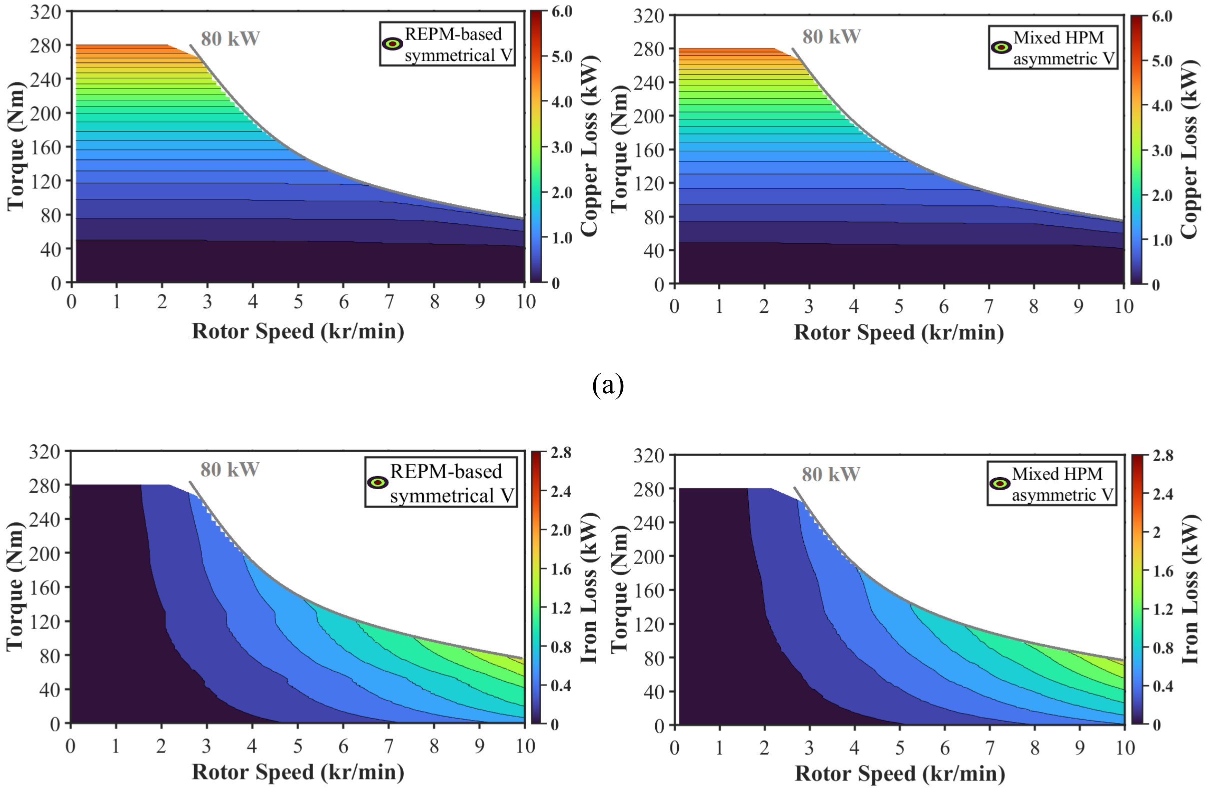

(a)

(b)

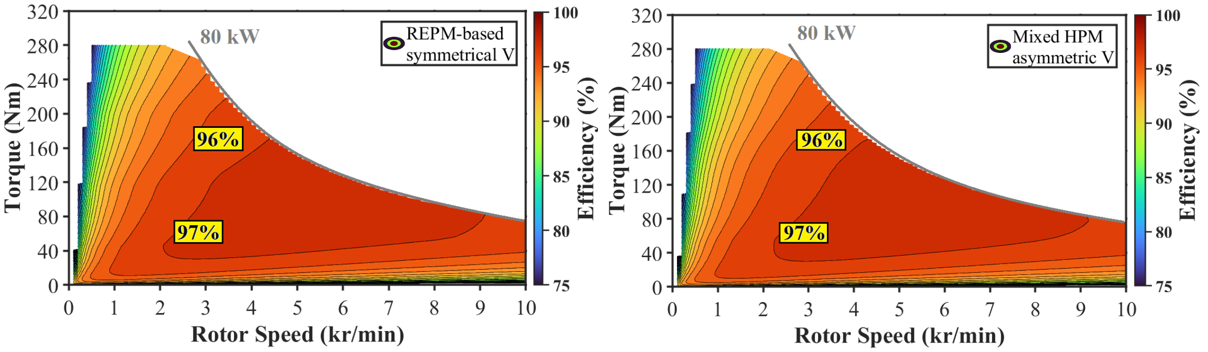

(c)

Fig. 6.21. Comparisons of copper loss, iron loss, and efficiency maps of both machines. (a) Copper loss maps. (b) Iron loss maps. (c) Efficiency maps.

6.4. Mechanical Strength and Demagnetization

In general, the substitution of REPM with FEPM can naturally increase the mechanical concern as a high volume of FEPM is required to replace a certain volume of REPM. Consequently, the increased mass of PMs can potentially transfer more stress on ribs. Changing the thickness of the ribs along with the verge introduction, fillet usage on corners, etc., are the common ways to address this issue and improve the mechanical strength of the rotor at the cost of a higher leakage flux and a lower performance. Meanwhile, to compensate the performance loss a higher volume of PMs may be required. Therefore, for a fair comparison of PM usage, the thicknesses of the ribs are adjusted to achieve a similar maximum von-mises stress levels at maximum speed in both machines. Meanwhile, the mechanical strength study at overspeed condition with 1.2 times the maximum speed is also suggested by IEC60034-1 and IEC60349-2. Therefore, the von-mises stress distributions of these machines at 10000 r/min and 12000 r/min are compared in Fig. 6.22. It is worth mentioning that the frictional contact with the friction coefficient of 0.2 is used for this analysis. As can be seen at the maximum speed, the peak von-mises stress on rib in these topologies can reach ~240 MPa which implies the safety factor of ~1.9. As the mass of PMs in the proposed machine is ~2.5 times of that of the baseline, the widths of the ribs in the proposed mixed HPM asymmetric V-shape IPMSM are selected higher than those of the REPM-based symmetrical V-shape IPMSM (see Table 6.2). However, at overspeed condition, the maximum stress in the proposed machine with 357.8 MPa is only ~6% higher than that of the baseline with 337.4 MPa. It is worth mentioning that if higher thicknesses of ribs were used in both machines, a higher safety factor would have been achieved. However, to compensate the torque reduction, a higher volume of PMs would be needed.

Meanwhile, as the proposed machine has the advantages of FEPM torque component and MFS effect over the baseline, it would be expected to require less increase in REPM usage.

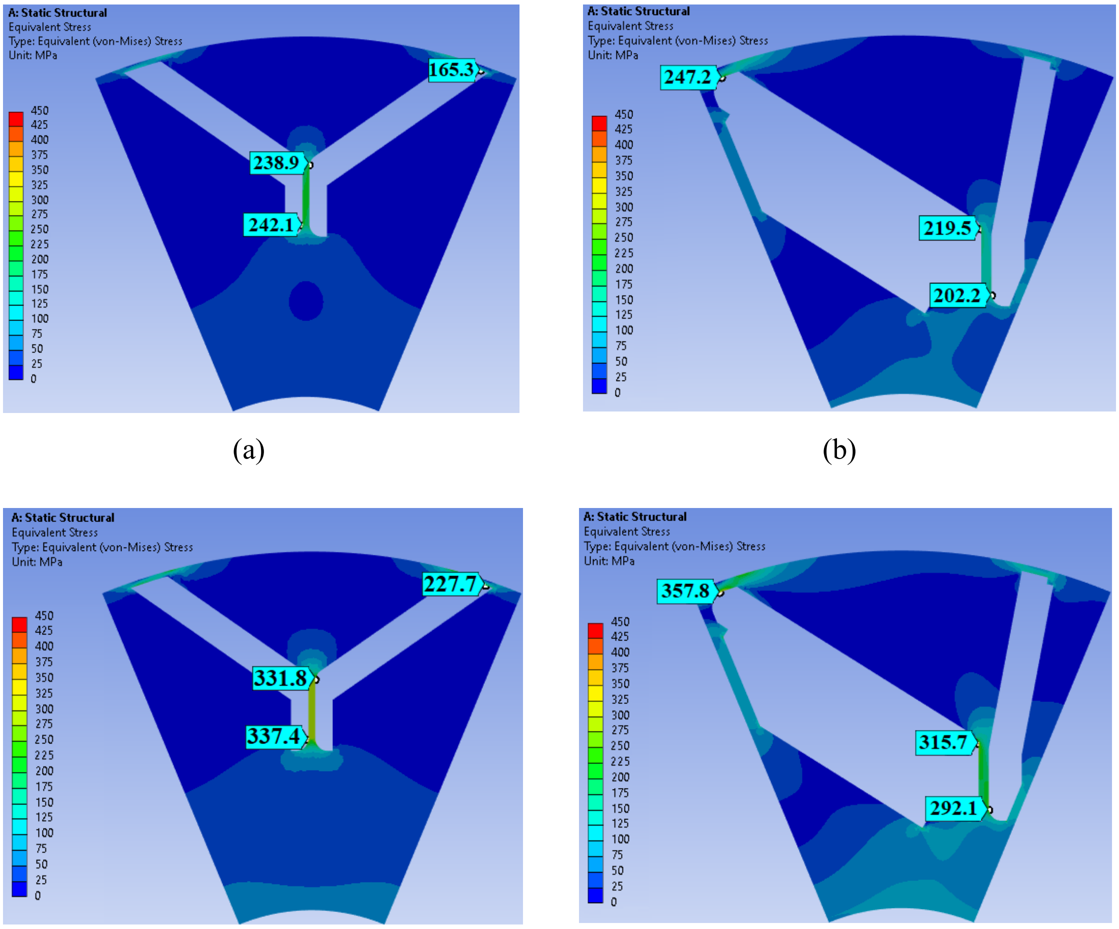

(a) (b)

(c) (d)

Fig. 6.22. Comparison of von-mises stress distributions. (a) Baseline at 10000 r/min. (b) Mixed HPM asymmetric V-shape IPMSM at 10000 r/min. (c) Baseline at 12000 r/min. (d) Mixed HPM asymmetric V-shape IPMSM at 12000 r/min.

Fig. 6.23 presents the decomposed flux density distribution of REPM in its magnetization direction at the twice of rated d-axis current and 120 °C of temperature. It is worth mentioning that the knee point of B-H curve of the N28AH is 0 T at this temperature. As can be seen, no demagnetized region can be found in REPMs of these two machines. However, the difference in the magnetic properties of REPM and FEPM shows that, in contrast to REPMs, the FEPMs will be at a higher risk of irreversible demagnetization at low temperature. Meanwhile, using a REPM in series connection can improve the demagnetization withstand capability of these magnets. Therefore, Fig. 6.24 (a) presents the decomposed flux density distribution of FEPMs in their magnetization direction at the twice of rated d-axis current and -40 °C of temperature to investigate the demagnetization withstand capability of FEPM in the proposed HPM machine. It is worth mentioning that the TDK-FB13B FEPM has a knee point of 0.06 T in its B-H curve at this temperature. As can be seen, only a small demagnetized area can be seen at the edge of FEPM near the airgap. Figs. 6.24 (b) and (c) compare the open circuit demagnetization withstand capability of FEPM with and without stator.

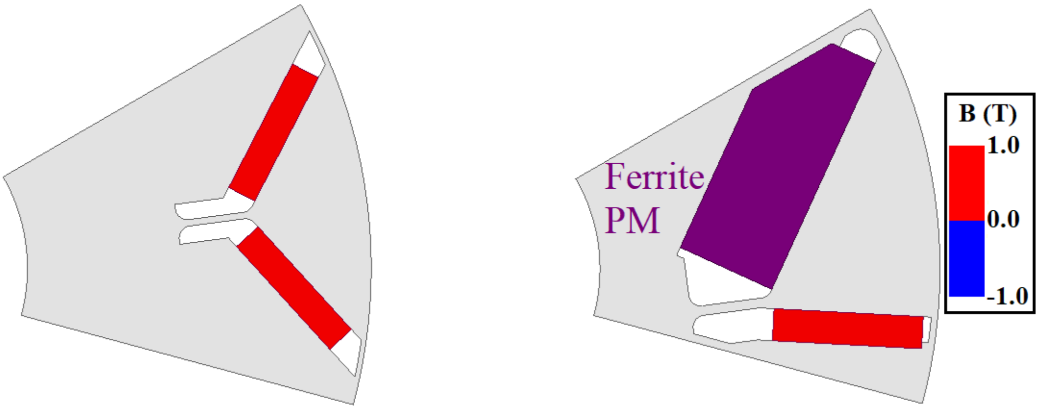

(a) (b)

Fig. 6.23. Comparison of demagnetization withstand capability of REPM at twice of rated d-axis current and 120 °C. (a) REPM-based symmetrical V-shape IPMSM. (b) Proposed mixed HPM asymmetric V-shape IPMSM.

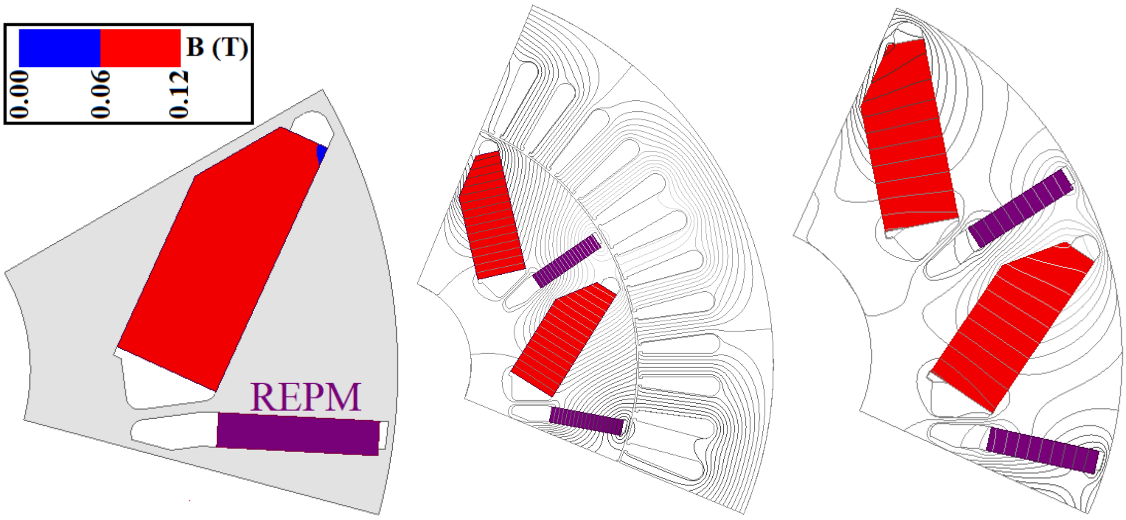

(a) (b) (c)

Fig. 6.24. Demagnetization withstand capability of FEPMs in proposed mixed HPM asymmetric V-shape IPMSM at -40 °C. (a) At twice of rated d-axis current. (b) At open-circuit condition with stator. (c) At open circuit-condition without stator.

As can be seen, no demagnetized area is found in FEPMs. Meanwhile, it is worth mentioning that the open circuit flux lines are different with presence or absence of stator. When rotor is inside the stator, the flux produced by the PMs in a north pole flow through the stator and passes through the adjacent south pole as shown in Fig. 6.24 (b). However, when the rotor is outside of the stator (for example at the stage of rotor assembling), an interpolar flux path forms between the two adjacent poles as shown in Fig. 6.24 (c). Although there is no open circuit demagnetized area in the FEPMs of the proposed mixed HPM asymmetric V-shape IPMSM, the interpolar flux path at the open circuit condition may increase the risk of open circuit demagnetization of FEPM in some HPM machine topologies at the stage of prototyping.

6.5. Experimental Validation

Although the FEA section focuses on a large size IPMSM for EV application by using the specifications of a commercialized IPMSM, a small size 24-slot/8-pole (24s8p) mixed HPM asymmetric V-shape IPMSM is optimized and manufactured as a proof of the concept accounting for the laboratory limits and funding capacities, as shown in Fig. 6.25. This machine is optimized at 40 W copper loss of active part with the main dimensional parameters as listed in Table 6.4. FEA simulation shows that this machine is expected to generate 2.6 Nm torque at 4 A_{max} current and 250 r/min. In addition, its d- and q-axis inductances are 11.5 mH and 15.7 mH, respectively.

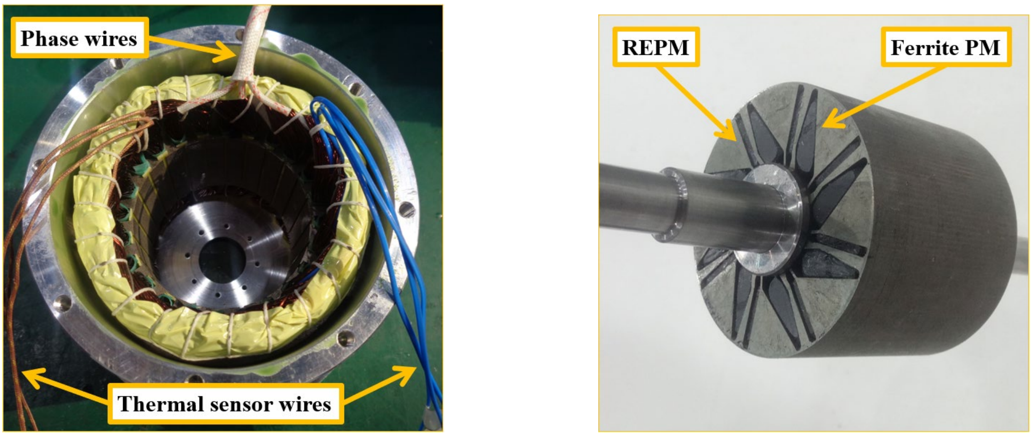

(a) (b)

Fig. 6.25. Prototype. (a) Stator. (b) Rotor.

Table 6.4. Main Dimensional Parameters of Prototype

Parameters	Values	Parameters	Values
Stator outer diameter	100 mm	Slot number	24
Stator inner diameter	63 mm	Pole number	8
Active stack length	50 mm	Turns per coil	60
Airgap length	1 mm	Phase resistance	1.6 Ω
Remanence of N28AH	1.075 T	Phase current	4 A_{max}
Remanence of TDK-FB13B	0.475 T		

Then, it is tested using the dynamic and static test benches as presented in Fig. 6.26. The dynamic platform is used to measure the back-EMF and transient torque. However, the static test bench is conducted to measure the cogging torque and static torque using the method presented in [ZHU09].

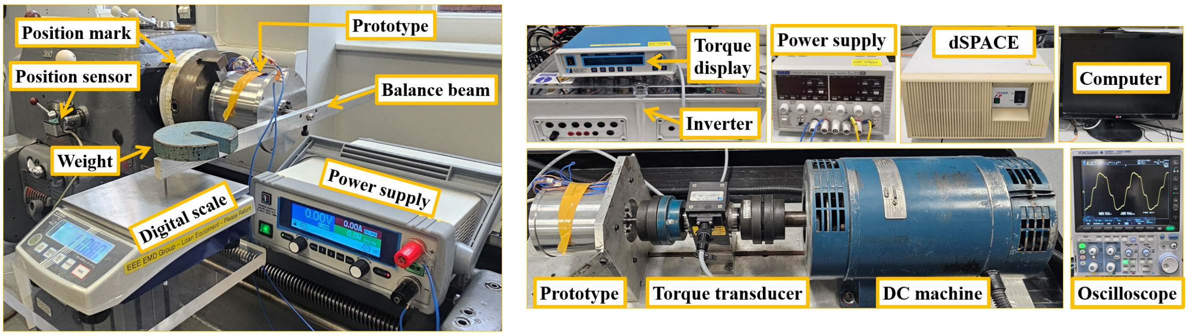

(a) (b)

Fig. 6.26. Experimental test benches. (a) Static test rig. (b) Dynamic test rig.

The open circuit line back-EMF waveforms and spectra obtained by FEA and measurement are compared at 750 r/min in Fig. 6.27, whereas the open-circuit cogging torques are compared in Fig. 6.28. As can be seen, both measured back-EMF and cogging torque waveforms and spectra are in good agreement with FEA predictions.

Fig. 6.29 shows the variation of static torque with rotor position when DC current ($I_a = -2I_b = -2I_c = I_{DC}$) is injected into windings. Meanwhile, the variation of predicted and measured average torques with current are compared in Fig. 6.30. As can be seen, the measured torque matches well with prediction with an error of ~5.6%.

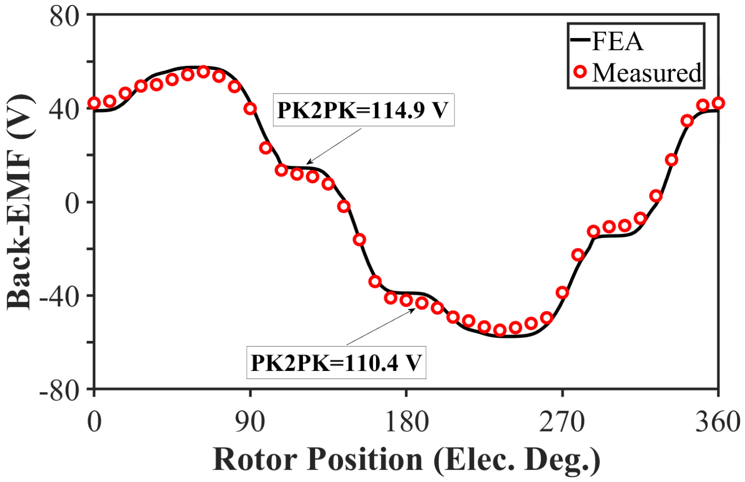

(a)

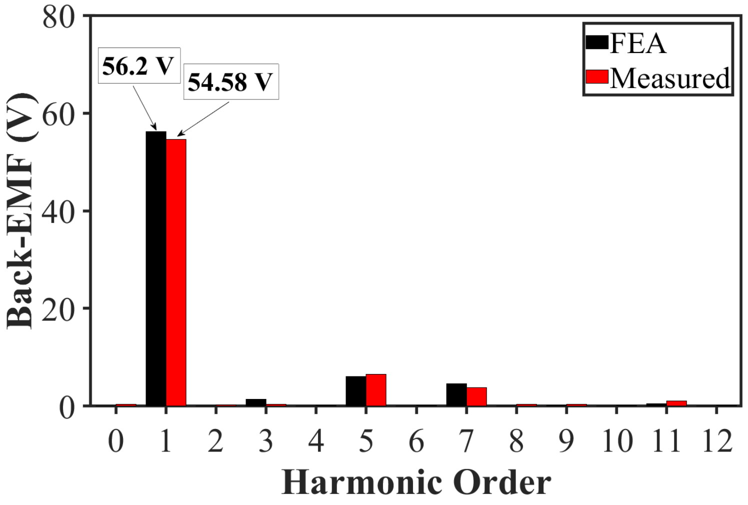

(b)

Fig. 6.27. FEA predicted and measured line back-EMFs at 750 r/min and open-circuit condition. (a) Waveforms. (b) Spectra.

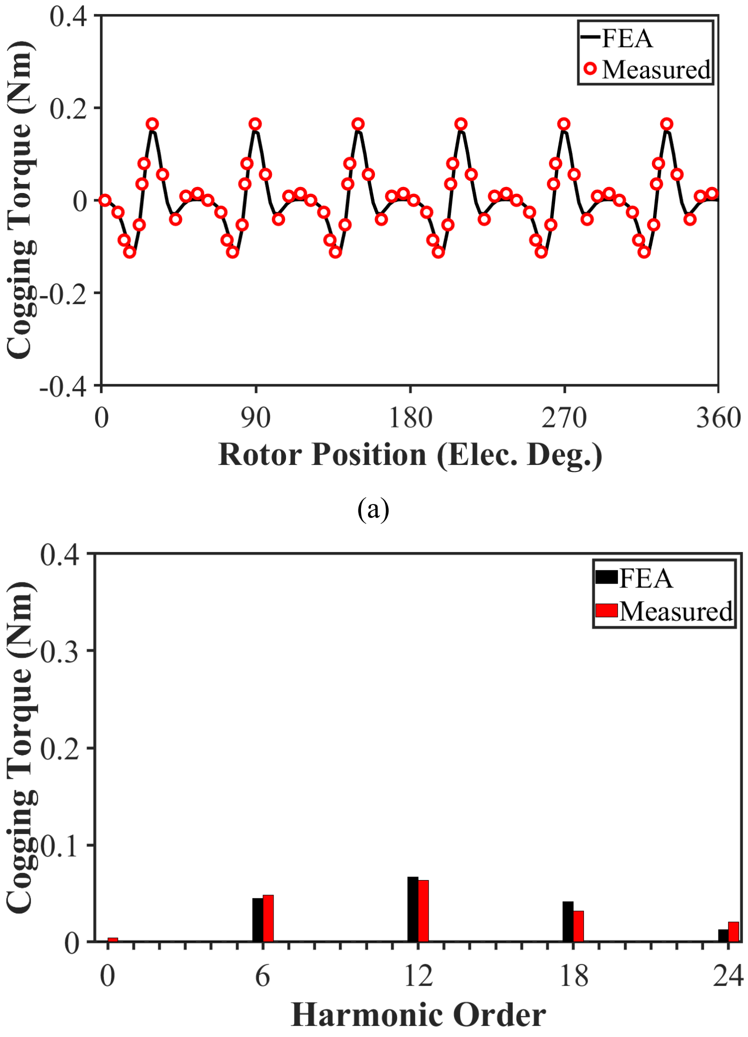

(a)

(b)

Fig. 6.28. FEA predicted and measured cogging torques at open circuit. (a) Waveforms. (b) Spectra.

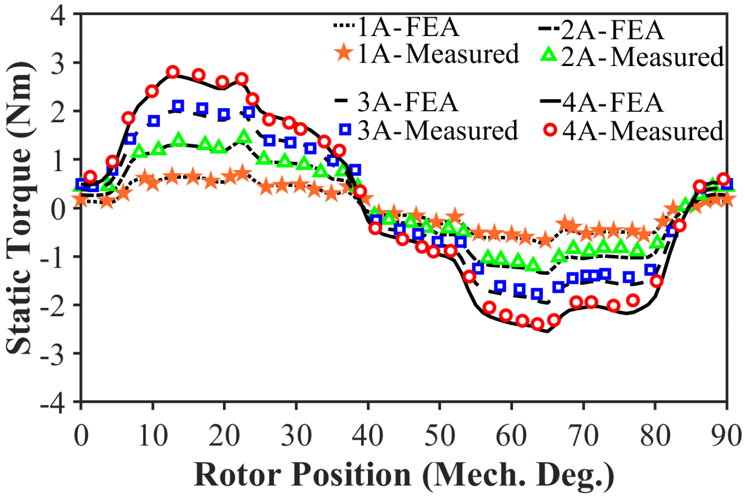

Fig. 6.29. FEA predicted and measured static torques at different DC currents.

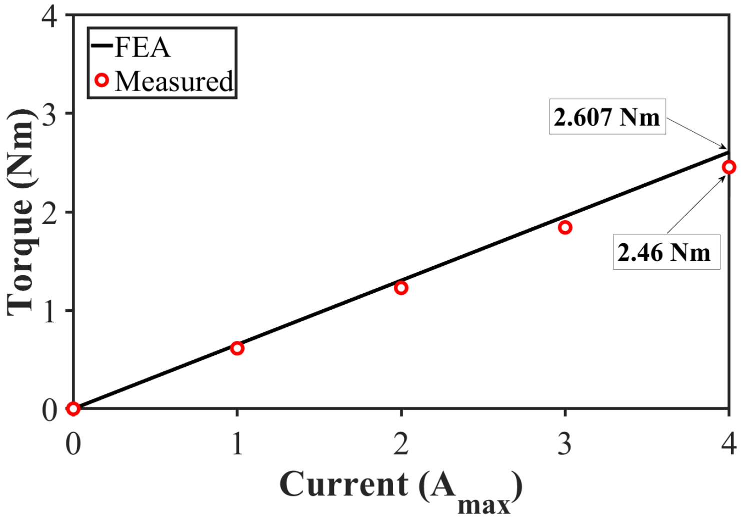

Fig. 6.30. Variation of FEA Predicted and measured average torques with current at 250 r/min.

6.6. Conclusion

This chapter presents a novel mixed HPM asymmetric V-shape IPMSM which benefits from an improved torque per REPM volume ratio by the synergies of the HPM utilization and the MFS effect. The electromagnetic performance of the proposed machine is compared to that of a REPM-based symmetrical V-shape IPMSM as the baseline. Both machines are optimized at the same torque with lower volume of REPM to declare the amount of REPM volume and the total PM cost which can be saved at the same performance and size. The results show that the proposed mixed HPM asymmetric V-shape IPMSM can save ~40 % of REPM usage and ~21% of total PM cost compared to those of the baseline.

Using the FPM, it is shown that the one third of the required PM torque in the proposed HPM machine is delivered by FEPMs. As a result, the required REPM torque in this machine is reduced to 60.07 Nm which is ~26 % less than that of the baseline. In addition, the difference between the corresponding current advancing angles of the peak PM and reluctance torque components is reduced from ~55 elec. deg. to ~25 elec. deg. which leads to a further improvement of the torque per REPM usage ratio in the proposed HPM machine. Meanwhile, the torque-speed and power speed characteristics along with the losses and efficiency maps of both machines are compared and showed a similar performance. The same mechanical strength and demagnetization withstand capability of PMs are also concluded. Finally, a small size prototype of the proposed mixed HPM asymmetric V-shape IPMSM is built and tested.

It is worth mentioning that the difference in the variation of the magnetic properties of REPM and FEPM accounting for temperature (i.e. alpha coefficients with opposite signs) can raise a challenge in HPM machine operation. This is due to the change of flux density distributions caused by the variations of PMs' properties at different rotor temperatures, even at the same operating point. This can result in different L_d and L_q, flux linkage, efficiency, etc. Therefore, the look up tables used by inverters are required to include the rotor temperature when designing the HPM machines. This challenge will be analysed in future work. In addition, the effect of using different grades of PMs on the performance and thermal analysis of the proposed machine will be also investigated.

CHAPTER 7

GENERAL CONCLUSION

In this thesis, several HPM IPMSM topologies have been proposed and investigated using the same stator, winding configuration, and specification of the commercialized Nissan Leaf 2012 IPMSM. Meanwhile, only the developed parallel HPM V-shape spoke IPMSM in chapter 3 employs different dimensions and specifications. Therefore, for the sake of a fair comparison in this chapter, this machine is also re-optimized based on the Nissan Leaf 2012 specifications in [BUR13], [YAN17A]. In addition, a REPM-based baseline with a single layer symmetrical V-shape arrangement is optimized for the comparison as most of the proposed machines are using a single layer structure as well. The main objective is to improve the torque with REPM ratio which can be done either by a higher torque at the same volume of REPM, or the same torque at a lower volume of REPM. As the latter method is used, the torque related performances are expected and also shown to be similar. However, for the clarity of the advantages of the proposed machines in REPM volume reduction, a comparison of torque with REPM ratios, volumes of both PM types, and PM cost estimations will be provided in this chapter. It is worth mentioning that all the proposed HPM machines in this thesis are experimentally validated.

7.1. Structural Comparison

7.1.1. Overview

Fig. 7.1 (a) illustrates the stator structure which is shared with the same winding configurations and dimensions among all proposed HPM machines in this chapter. In addition, Fig. 7.1 (b) presents a symmetrical REPM-based rotor which is optimized for 280 Nm at low volume of RPEM material at 625 A_{max} and 2100 r/min. As this machine does not employ HPM utilization and MFS effect, it is expected to be more reliant on REPM material. Therefore, this machine is used as the baseline for comparison to show how much REPM volume and total PM cost can be saved by using HPM and MFS effect.

The cross sections of the proposed HPM IPMSMs in this thesis are shown in Fig. 7.2, whereas the features and contributions of each machine are summarized in Table 7.1.

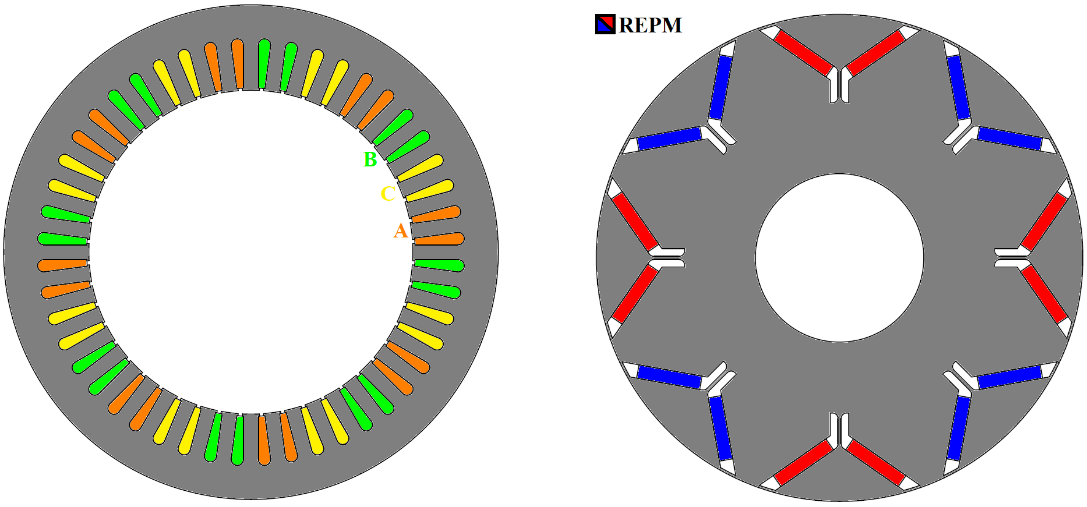

(a) (b)

Fig. 7.1. Baseline topology. (a) Shared stator selected from [BUR13], [YAN17A]. (b) Symmetrical REPM-based V-shape rotor (Baseline).

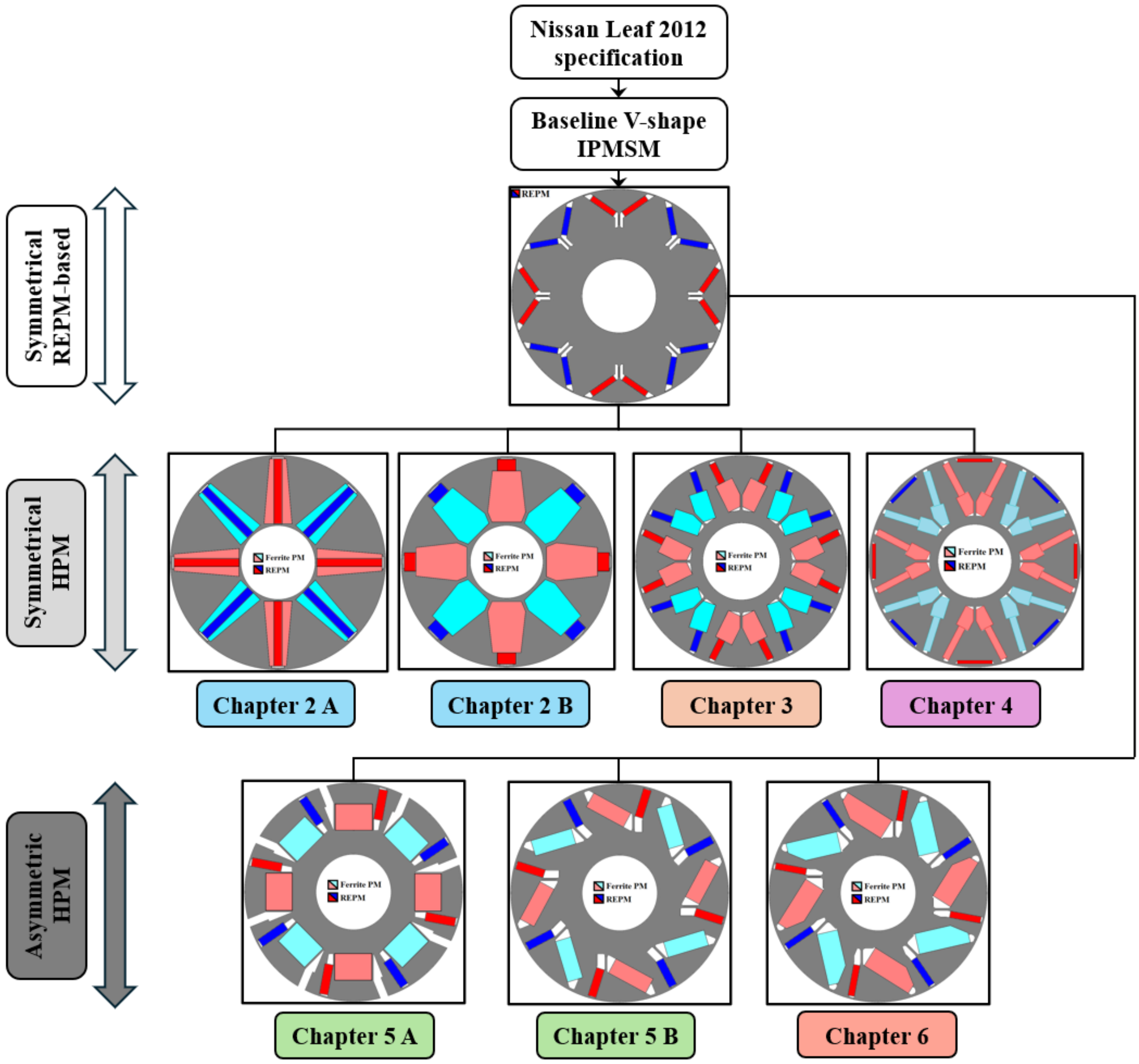

Fig. 7.2. Overview of the proposed HPM IPMSMs in this thesis.

Table 7.1. Summary of the features and contributions of proposed HPM machines in each chapter.

Chapter	Cross section	Feature	Contribution
2 A	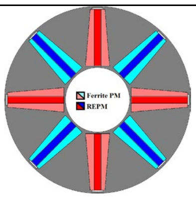	• Symmetrical • Tapered FEPM • Spoke-type structure • Series and Parallel HPMs	• Influence of tapering parameters in FEPMs on torque performance • Defining the proper tapering direction • Comparison with rectangular FEPM counterparts and a REPM baseline • Torque components decomposition • PM cost comparison • Mechanical & Demagnetization study
2 B	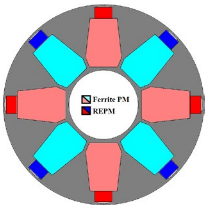		
3	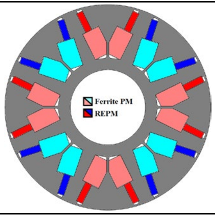	• Symmetrical • Combined V-shape and Spoke structure • Parallel HPM	• Comparison with a REPM baseline • Torque components decomposition • PM cost comparison • Mechanical & Demagnetization study
4	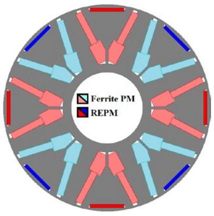	• Symmetrical • Delta-shape with split (segmented) FEPMs • Series HPM	• Influence of splitting parameters of FEPMs on torque performance • Comparison with a HPM counterpart without split FEPM and a REPM baseline • Torque components decomposition • PM cost comparison • Mechanical & Demagnetization study
5 A	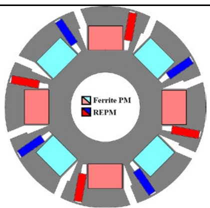	• Asymmetric • U-shape and V-shape • Mixed HPM • Rectangular FEPM • Intentional interpolar saturation between adjacent poles	• Comparison with a REPM baseline • Torque components decomposition • PM cost comparison • MFS effect • Mechanical & Demagnetization study
5 B	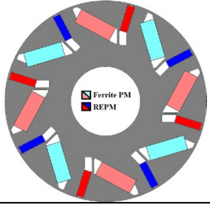		
6	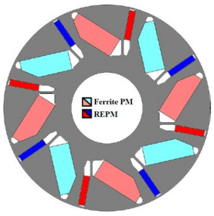	• Asymmetric • V-shape • Mixed HPM • Tapered FEPM • Intentional interpolar saturation	• Comparison with a REPM baseline • Torque components decomposition • PM cost comparison • MFS effect • Effect of saturation on MFS improvement • Mechanical & Demagnetization study

7.1.2. Parallel and Series HPM Spoke-type IPMSM with Tapered FEPM

In chapter 2, two spoke-type IPMSMs with series and parallel HPM configurations using tapered FEPMs are proposed. These machines are compared with literature in Table 7.2.

Table 7.2. Comparison of tapered FEPM series and parallel HPM spoke IPMSMs with literature.

Topologies	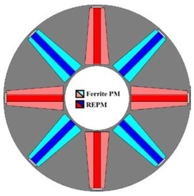 Proposed chapter 2A	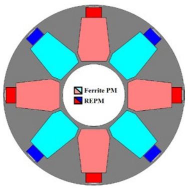 Proposed chapter 2B	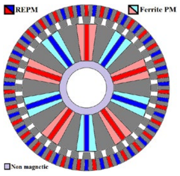 [ALQ19]	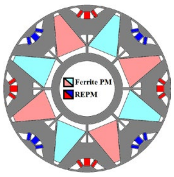 [PAR21]	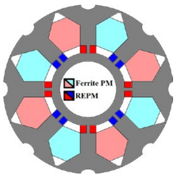 [PAR21]
Increase in torque with REPM ratio	✓	✓	✓	✓	✓
Increase in torque by tapering FEPMs	✓	✓	✗	✓	✓
Demagnetization & mechanical study	✓	✓	N/A	✓	✓
Parametric search study of tapering FEPMs	✓	✓	N/A	N/A	N/A
Torque components decomposition	✓	✓	N/A	N/A	N/A

7.1.3. Parallel HPM V-shape Spoke IPMSM

Chapter 3 proposes a parallel HPM V-shape spoke IPMSM which is compared with literature in Table 7.3.

Table 7.3. Comparison of parallel HPM V-shape spoke IPMSM with literature.

Topologies	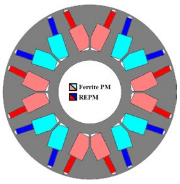 Proposed chapter 3	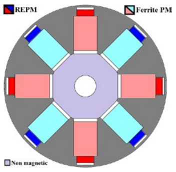 [MA20]	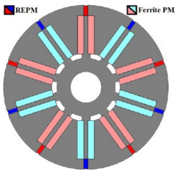 [ZHU17B]	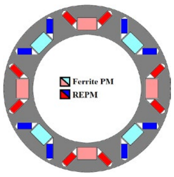 [DU20]
Increase in torque with REPM ratio	✓	✓	✓	✓
High FEPM usage	✓	✓	✓	✗
Improved reluctance torque	✓	✗	✗	✓
Demagnetization study	✓	✓	✓	✓
Mechanical study	✓	✓	N/A	✓

7.1.4. Series HPM Delta-shape IPMSM with Split Ferrite Spoke

A series HPM delta-shape IPMSM with split (segmented) ferrite spoke is proposed in chapter 4 and compared with literature in Table 7.4.

Table 7.4. Comparison of series HPM delta-shape IPMSM using split ferrite spoke with literature.

Topologies	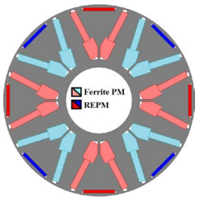 Proposed chapter 4	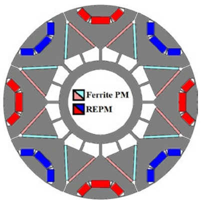 [PAR22]	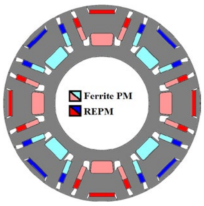 [CUI22]
Increase in torque with REPM ratio	✓	✓	✓
Flexible FEPM usage and size	✓	✗	○
High FEPM torque contribution	✓	✗	N/A
Double-layers structure	✓	✓	✓
Demagnetization study	✓	✓	N/A
Mechanical study	✓	✓	N/A

7.1.5. Mixed HPM Asymmetric IPMSMs with U- and V-shape Structures

In chapters 5 and 6, three HPM asymmetric IPMSMs including U-shape with rectangular FEPM (chapter 5a), V-shape with rectangular FEPM (chapter 5b), and V-shape with tapered FEPM (chapter 6) are proposed. These machines are compared with literature in Table 7.5.

Table 7.5. Comparison of proposed mixed HPM asymmetric IPMSMs with literature.

Topologies	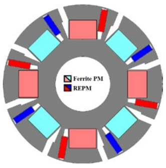 Proposed chapter 5a	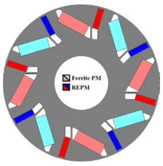 Proposed chapter 5b	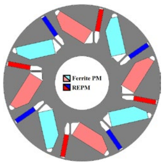 Proposed chapter 6	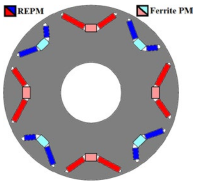 [LIU23B]	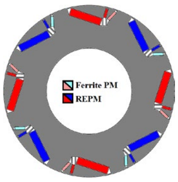 [LIU24]
Increase in torque with REPM ratio	✓	✓	✓	✓	✓
Flexible FEPM usage and size	○	✓	✓	✗	✗
High FEPM torque	✓	✓	✓	N/A	✗
Parametric search study of MFS effect	N/A	N/A	✓	N/A	N/A
High shifted magnetic field	✓	○	✓	✗	✓

Demagnetization study	✓	✓	✓	✓	✓
Mechanical study	✓	✓	✓	N/A	✓

7.2. Methodology

Fig. 7.3 presents the employed methodology in chapters 2 to 6, whereas Fig. 7.4 illustrates the static and transient test benches and Fig. 7.5 shows a diagram of prototypes.

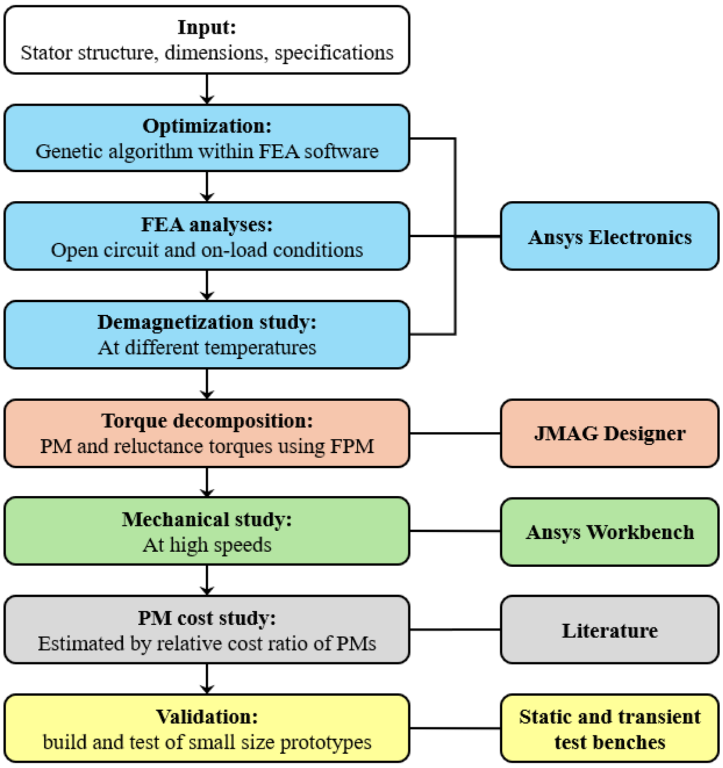

* FEA: Finite element analysis; ** FPM: Frozen permeability method

Fig. 7.3. Applied methodology to chapters 2 to 6.

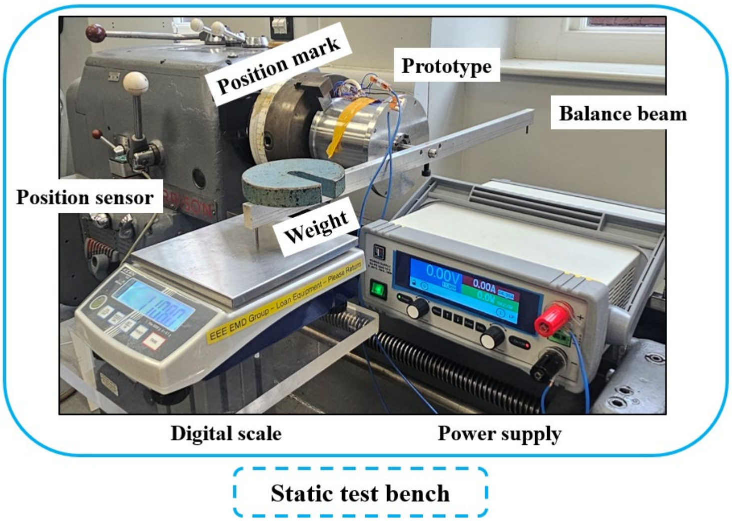

(a)

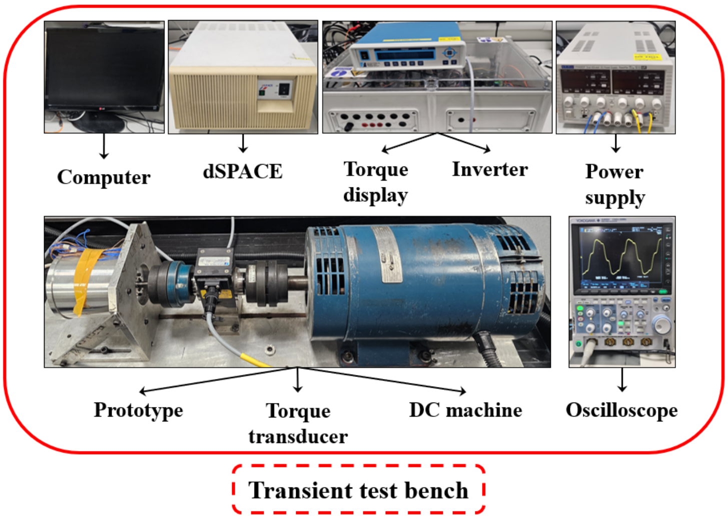

(b)

Fig. 7.4. Test benches. (a) Static test bench. (b) Transient test bench.

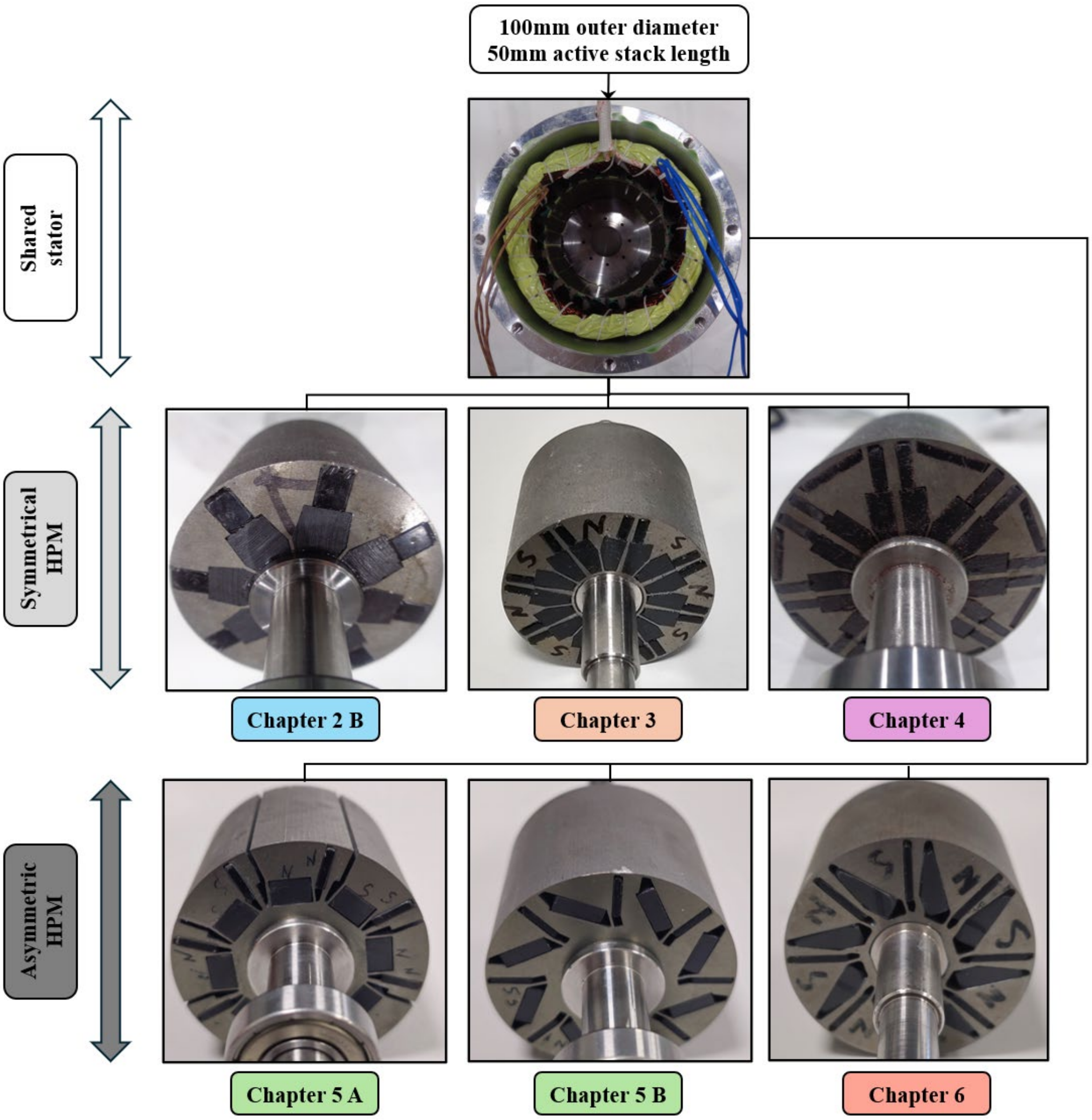

Fig. 7.5. All built prototypes in this thesis.

7.3. Electromagnetic Performance

The proposed HPM machines in this thesis are designed and compared using the same dimensions, specifications, and stator structure (see Fig. 7.1 (a)) except the introduced parallel HPM V-shape spoke IPMSM in chapter 3. Meanwhile, for the electromagnetic performance comparison in this section, this machine is re-optimized with the same objective as the others. The main objective is to produce 280 Nm torque with lower volume of REPM at 625 A_{max} and 2100 r/min by substituting this magnet with FEPMs. As the baseline employs a symmetrical REPM-based structure, it has no advantage of HPM utilization or MFS effect. As a result, the required volume of REPM in this machine with 150 cm^3 is considered as upper limit for REPM usage. Fig. 7.6 compares the output torque waveforms and spectra of proposed HPM machines with those of the baseline at 625 A_{max} and 2100 r/min. In addition, Fig. 7.7 compares the variations of average torques with current advancing angle at 625 A_{max} and 2100 r/min.

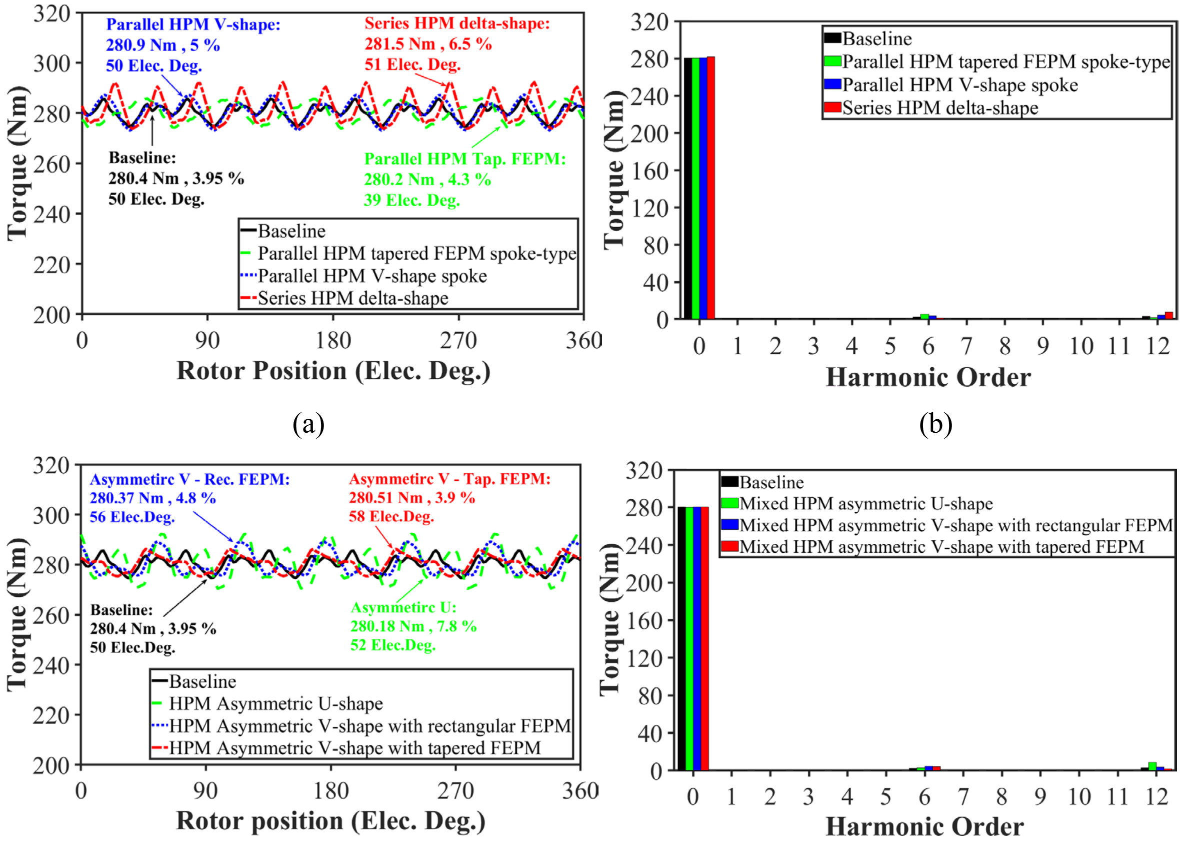

(a) (b)

(c) (d)

Fig. 7.6. Comparison of torque waveforms and spectra at 625 A_{max} and 2100 r/min. (a) Waveforms (symmetrical HPM machines). (b) Spectra (symmetrical HPM machines) (c) Waveforms (asymmetric HPM machines) (d) spectra (asymmetric HPM machines).

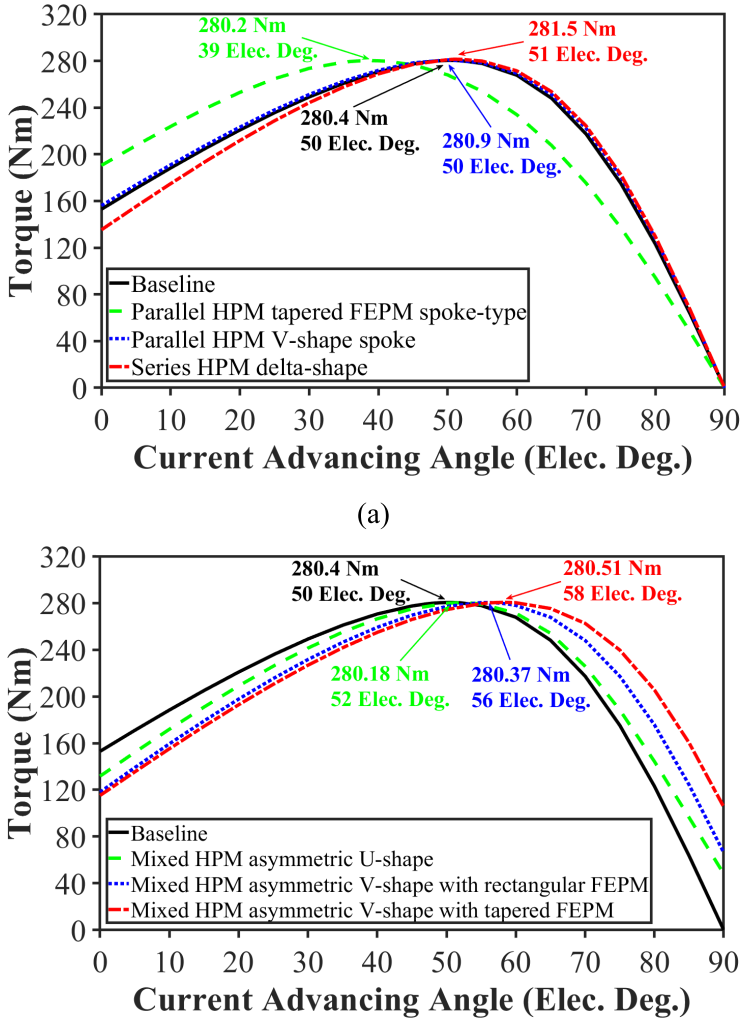

(a)

(b)

Fig. 7.7. Comparison of average torques with current advancing angle at 625 A_{max} and 2100 r/min. (a) Symmetrical HPM machines. (b) Asymmetric HPM machines.

As can be seen:

- All machines are capable of producing the same total torque with 280 Nm.
- Parallel HPM tapered FEPM spoke-type IPMSM is expected to have the highest PM loading due to the low reluctance torque contribution.
- Series HPM delta-shape IPMSM is expected to have a lower PM loading than the other symmetrical HPM machines due to having a higher reluctance torque contribution caused by double-layers arrangement of PMs.
- Unlike the symmetrical machines, the asymmetric HPM machines have a higher torque than 0 at 90 elec. deg. of current advancing angle.
- The variations of torques with current advancing angle are different which suggests that they are expected to have different PM and reluctance torque components.

Consequently, Fig. 7.8 compares the torque components of these machines at 625 A_{max} and 2100 r/min using FPM. It is worth mentioning that for this comparison, the current advancing angle of each machine is set at its optimum values as shown in Fig. 7.7.

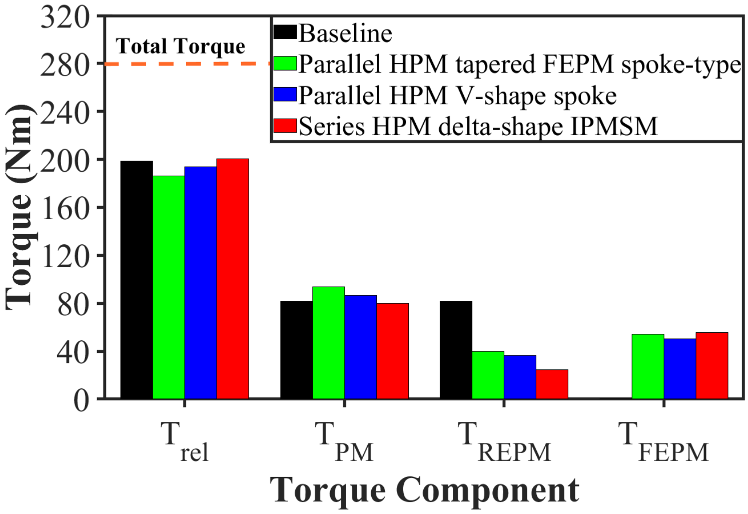

(a)

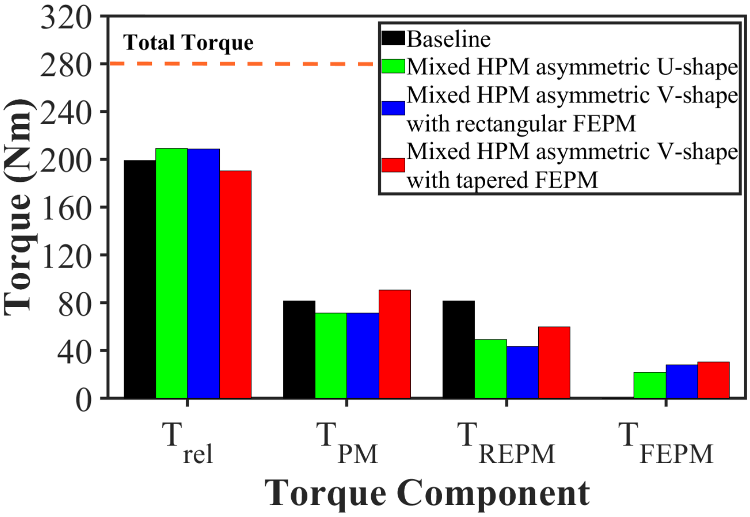

(b)

Fig. 7.8. Comparison of torque components at 625 A_{max} and 2100 r/min with optimum current advancing angle for each machine. (a) Symmetrical HPM machines. (b) Asymmetric HPM machines.

As can be seen:

- From Fig. 7.8 (a): The reluctance torque of the proposed parallel HPM tapered FEPM spoke-type IPMSM is lower than the others. Therefore, at the same torque, this machine requires a higher PM torque. However, a considerable ratio of the needed PM torque is delivered by FEPMs which means this machine is advantageous for a higher FEPM usage.

- From Fig. 7.8 (a): The reluctance torque of the proposed HPM V-shape spoke IPMSM is improved compared to that of the spoke-type IPMSM with tapered FEPMs. Therefore, this machine would require less PM torque than the latter topology. Consequently, the required volume of REPM at the same torque is expected to be lower.
- From Fig. 7.8 (a): The series HPM delta-shape IPMSM has the highest reluctance toque which results in the lowest required PM torque among all HPM machines. In addition, its FEPM torque contribution is increased to some extent due to using a higher number of FEPM segments which leads to a higher effective cross section area (perpendicular to the magnetization direction) of FEPMs. As a result, the FEPM torque contribution is ~20% of total torque. Consequently, the required volume of REPM would be the least.
- It should be noted that the less needed REPM torque in symmetrical HPM machines can be interpreted as a lower required volume of this magnet. This is because these machines do not have the advantage of torque enhancement by MFS effect.
- From Fig. 7.8 (b): The reluctance torques of the mixed HPM asymmetric U-shape and V-shape IPMSMs with rectangular FEPMs are almost the same which means they will need the same PM torque to deliver the same total torque. However, as the effective cross section area (perpendicular to the magnetization direction) of FEPMs in V-shape topology is higher than that of the U-shape counterpart, the former topology benefits from a slightly higher FEPM contribution. As a result, the required REPM torque contribution and resultant REPM usage is expected to be lower. It should also be noted that as these machines benefit from MFS effect, the required volume of REPM would be less than that of a symmetrical counterpart.
- From Fig. 7.8 (b): The reluctance torque of the proposed mixed HPM asymmetric V-shape IPMSM with tapered FEPM is less than the other two counterparts. As a result, this machine requires more PM torque. As can be seen, a considerable amount of PM torque is generated by REPMs. However, as will be shown later, this machine employs less volume of REPM than the other two asymmetric HPM machines due to more torque enhancement by an effective MFS caused by the intentional interpolar saturation.
- It should be noted that unlike the symmetrical HPM machines, the REPM torque contribution cannot be directly linked to REPM usage as it may be partially improved by MFS effect.

Fig. 7.9 compares the variations of torques with current amplitude to investigate the overload capabilities of the proposed HPM machines. As the overload capability will be restricted by the core saturation, Fig. 7.10 compares the core saturations of a few topologies.

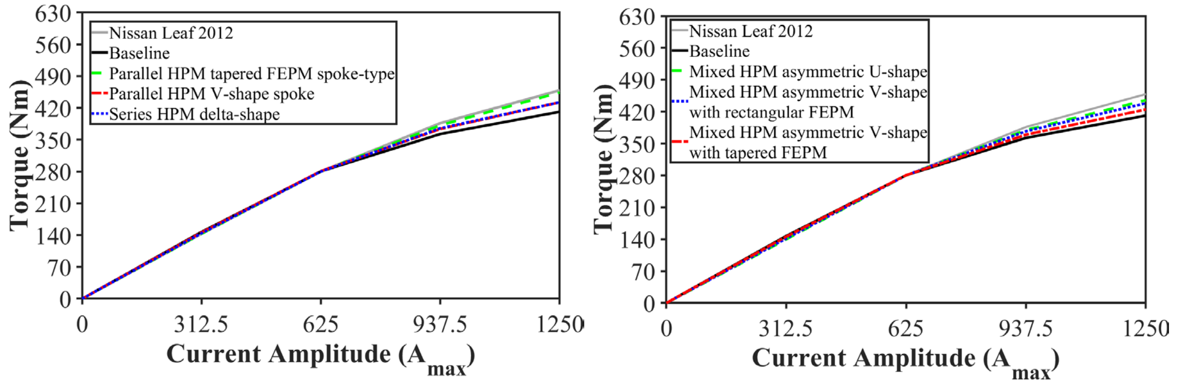

(a) (b)

Fig. 7.9. Comparison of torques with current amplitude (overload capability). (a) Symmetrical HPM machines. (b) Asymmetric HPM machines.

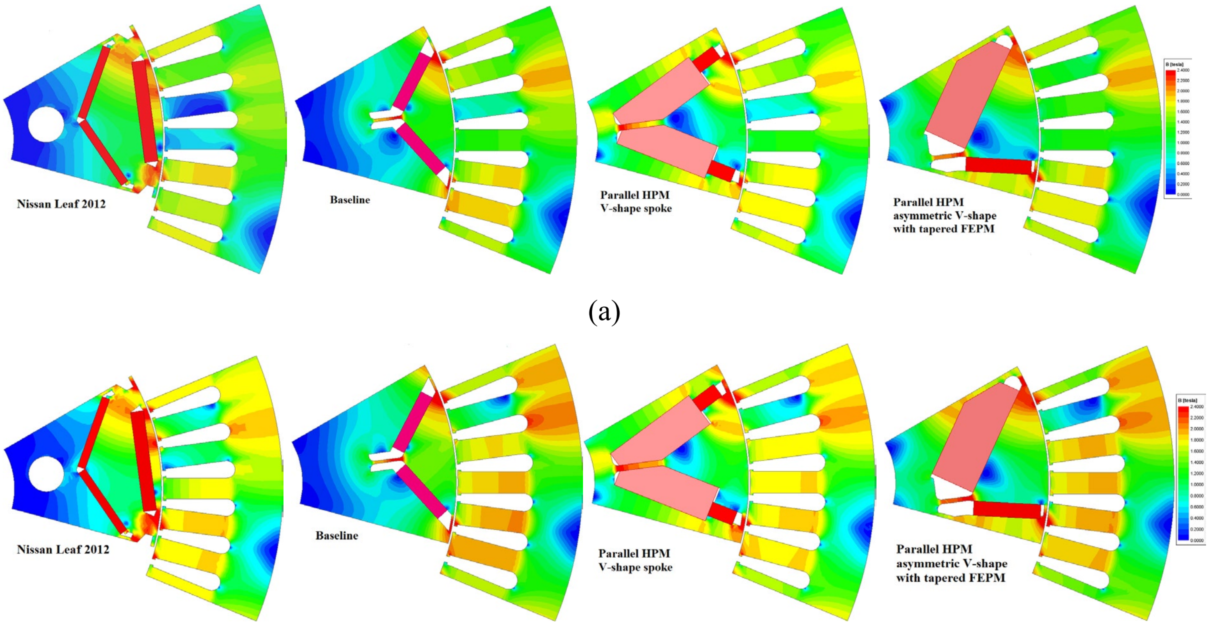

(b)

Fig. 7.10. Comparison of core saturations in a few topologies at different currents. (a) peak current (twice of rated current). (b) overload condition (4 times of rated current).

As can be seen:

- The overload capability of the baseline is less than that of the Nissan Leaf 2012 as it suffers from a higher saturation in stator at overload condition.

- In general, substituting a portion of REPM with FEPM at the same torque, requires a higher volume of FEPM consumption due to difference in the magnetic properties of two PM types, i.e. the residual flux density of FEPM can be 67% lower than that of the REPM. Meanwhile, this leads to a less cross section of rotor core at a fixed cross-sectional area. As a result, the saturation levels of rotor core in HPM machines are expected to be higher than those of the REPM counterparts (see Fig. 7.10). Consequently, the overload capabilities of the proposed HPM machines are expected to be between those of the Nissan Leaf 2012 and the REPM-based V-shape baseline.
- If the saturation level of the stator in a proposed HPM machine is closer to that of the Nissan Leaf 2012 (e.g. Parallel HPM V-shape spoke IPMSM), its overload capability is expected to be closer to the Nissan Leaf as well.
- If the saturation level of the stator in a proposed HPM machine is closer to that of the baseline (e.g. mixed HPM asymmetric V-shape IPMSM with tapered FEPM), its overload capability is expected to be closer to the baseline as well.

Fig. 7.11 compares the open circuit airgap flux density waveforms, spectra, and the fundamental component waveforms of the proposed HPM machines with those of the baseline.

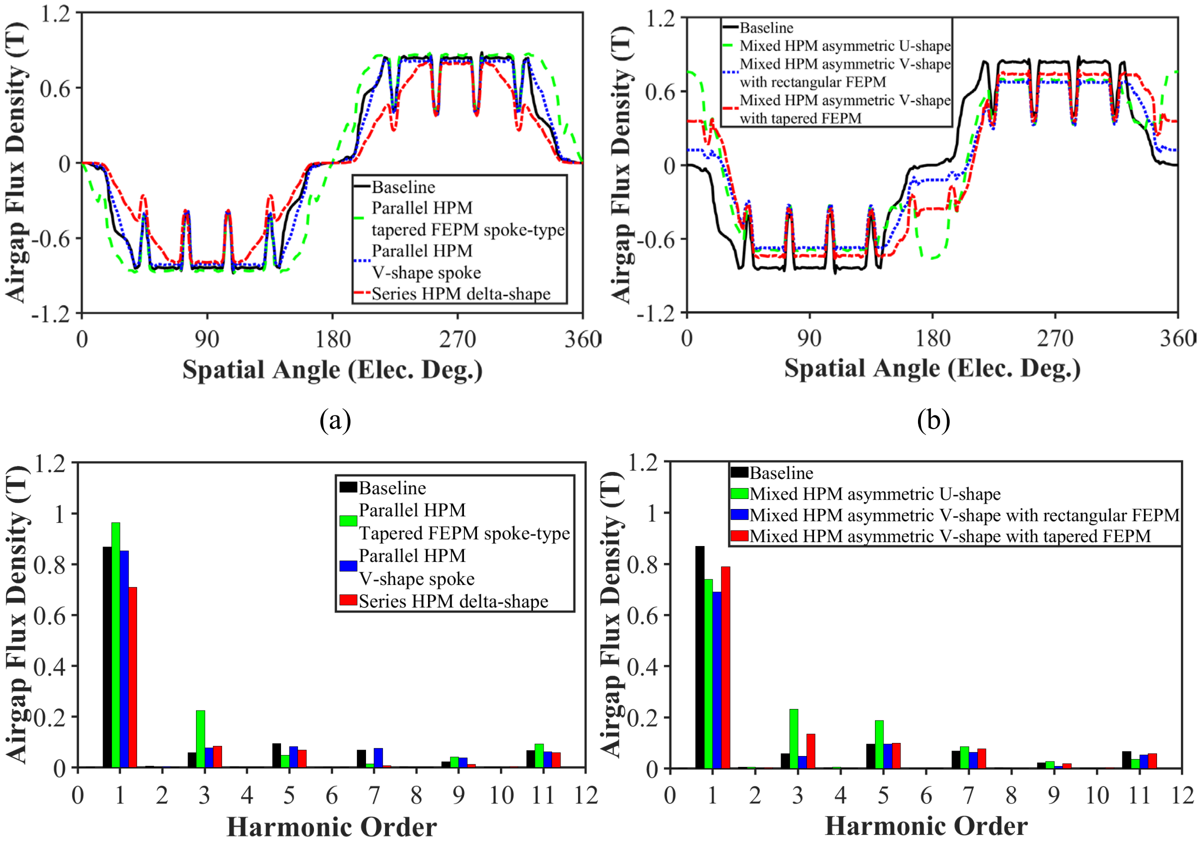

(a) (b)

(c) (d)

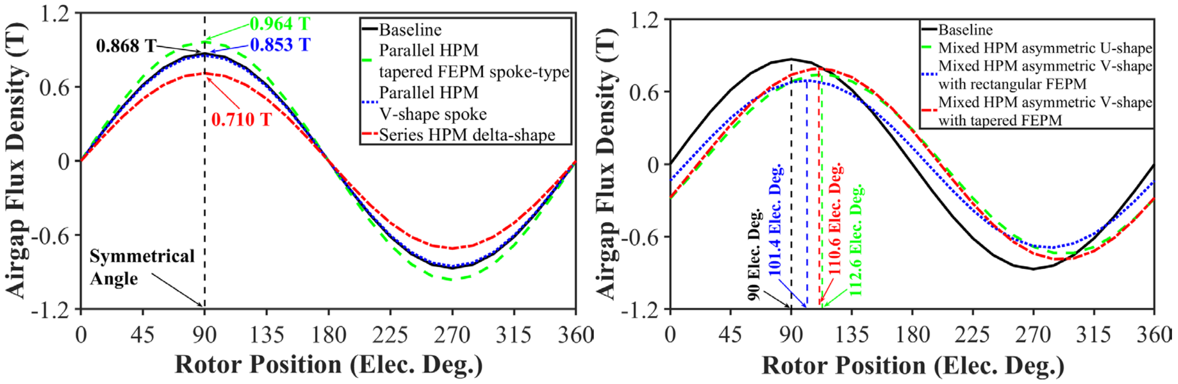

(e) (f)

Fig. 7.11. Comparison of open circuit airgap flux densities. (a) Waveforms (symmetrical HPM machines). (b) Waveforms (asymmetric HPM machines). (c) Spectra (symmetrical HPM machines). (d) Spectra (asymmetric HPM machines). (e) Fundamental (symmetrical HPM machines). (b) Fundamental (asymmetric HPM machines).

As can be seen in symmetrical HPM machines:

- The peak airgap flux densities are achieved at 90 elec. deg.
- The spoke-type HPM machine requires a higher amplitude of the airgap flux density whereas the delta-shape HPM IPMSM requires a less amplitude of the airgap flux density than that of the baseline. It is because the spoke-type HPM and the delta-shape IPMSMs have lower and higher reluctance torque components than that of the baseline, respectively. Therefore, at the same torque, the former topology needs a higher magnetic loading whereas the latter one requires less.

As can be seen in asymmetric HPM machines:

- The peak airgap flux densities are shifted from 90 elec. deg.
- The mixed HPM asymmetric V-shape IPMSM with rectangular FEPM has a lower shifted magnetic field than the other two asymmetric HPM machines.
- In general, asymmetric machines can produce the same torque as a symmetrical counterpart at a lower contribution of PM and reluctance torque components. As all proposed asymmetric HPM machines have a single layer arrangement of PMs, they have no major reluctance torque improvement compared to that of the baseline because of the same number of layers in PMs arrangement. Meanwhile, thanks to the torque enhancement by MFS effect, these machines require less magnetic loading (i.e. lower amplitude in Fig. 7.11 (f)) than that of the baseline.

Finally, Table 7.6 compares the volume of PMs and torque components of all proposed HPM machines with those of the baseline.

Table 7.6. Comparison of torque component and PM volumes in proposed HPM machines.

Chapter	**all**	**2B**	**3**	**4**	**5A**	**5B**	**6**
Topology	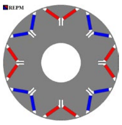	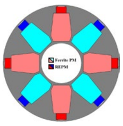	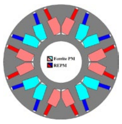	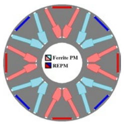	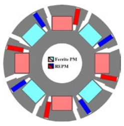	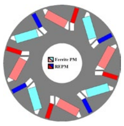	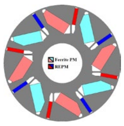
Size	Same						
Torque (Nm)	280						
Reluctance torque (Nm)	198.35	186.34	194.10	200.45	210.60	208.70	190.18
REPM torque (Nm)	81.65	39.86	36.60	24.35	45.00	43.45	60.07
FEPM torque (Nm)	-	53.80	49.30	55.20	24.40	27.85	29.75
REPM volume (cm^3)	**150.21**	**99.96**	**70.38**	**52.10**	**115.09**	**103.62**	**90.20**
FEPM volume (cm^3)	-	784.50	573.75	451.16	422.22	289.67	431.15
Total torque with REPM volume (Nm/cm^3)	1.86	2.80	3.98	5.37	2.43	2.70	3.10
REPM torque with REPM volume (Nm/cm^3)	0.546	0.399	0.520	0.467	0.390	0.419	0.666
REPM mass* (kg)	1.1416	0.7570	0.5349	0.3960	0.8747	0.7876	0.6855
FEPM mass* (kg)	-	3.9225	2.8688	2.2558	2.1111	1.4484	2.1558
PM cost estimation (%)**	**100**	**100.67**	**71.98**	**54.44**	**95.11**	**81.67**	**78.93**
REPM volume reduction (%)	**-**	**33.45**	**53.15**	**65.32**	**23.38**	**31.02**	**39.95**

* Mass densities of REPM, FEPM, and rotor electrical steel are 7.6 g/cm^3, 5 g/cm^3, and 7.65 g/cm^3.

** Cost of REPM assumed to be ten times of FEPM

As can be seen:

- All HPM machines benefit from higher torque with REPM volume ratios than the baseline.
- The proposed parallel HPM tapered FEPM spoke-type IPMSM can reduce the required volume of REPM by ~33%. However, as it suffers from low reluctance torque component, a massive volume of FEPM is used. Accounting for the cost of REPM being ten times of FEPM, the PM cost estimation is the same as that of the baseline. It is worth mentioning that by using a higher cost ratio if the price of REPM increases in future, the PM cost of this machine would be less than that of the baseline.
- The proposed topologies in chapters 3 and 4 benefit from a decent reluctance torque component along with a high FEPM toque contribution due to employing two spokes

arrangement of FEPMs per pole. As a result, they can reduce the required volume of REPM by ~53% and 65%, respectively. Accounting for the price of FEPM, total PM costs of these machines are expected to be equal to 72% and 54% of that of the baseline, respectively.

- Although the reluctance torques of the proposed machines in chapter 5 have increased, their FEPM torque contributions are drastically reduced. This is because a lower number of FEPMs are used in different arrangement than a spoke-type structure which resulted in a lower effective cross section of FEPMs (perpendicular to the magnetization direction). Meanwhile, the torque enhancement by MFS effect can compromise the reduced PM torque contribution to some extent. Consequently, topologies 5A and 5B can reduce the required volume of REPMs by 23% and 31%, respectively. That can be interpreted as having a total PM cost of 95% and 82% compared to that of the baseline, respectively.
- Although the proposed mixed HPM asymmetric V-shape IPMSM with tapered FEPM suffers from a lower reluctance torque than those topologies presented in chapter 5, it has slightly higher FEPM torque contribution due to using more FEPM materials. In addition, the REPM torque is significantly improved due to utilizing an effective MFS effect. Consequently, this machine benefits from more reduction of REPM usage with 40% which results in having 79% of total PM cost compared to the baseline.

7.4. Future Work

Based on the analyses provided in this thesis, some future work can be summarised as follows:

1) Further development of asymmetric HPM machines with multi-layers of flux barriers including double V-shape, double I-shape, delta-shape, etc.
2) Further development of asymmetric HPM machines with a combination of asymmetric V-shape and U-shape flux barriers with the spoke arrangement of FEPMs.
3) Investigation and comparison of efficiencies in HPM machines and REPM-based baselines accounting for high-speed conditions and different winding configurations which may result in a better performance in HPM machines as FEPMs benefits from a lower PM loss due to having a higher resistance against eddy current.
4) Investigation of heat transfer capability and limitations of HPM machines accounting for the thermal behaviour, lower PM loss, and different cooling strategies.
5) Investigating the performance of the HPM machines at different operation conditions considering different variations of magnetic properties in FEPMs and REPMs in response to the change of temperature.

REFERENCES

[AFI14] I. Afinowi, Z. Q. Zhu, Y. Guan, J. C. Mipo, and P. Farah, “Performance analysis of a switched-flux permanent magnet machine with hybrid NdFeB and ferrite magnet,” *The 17th Int. Conf. on Electrical Machines and Systems (ICEMS)*, 2014, pp. 3110-3116, IEEE.

[AFI16] I. Afinowi, Z. Q. Zhu, Y. Guan, J.C. Mipo, and P. Farah, “Switched-flux machines with hybrid NdFeB and ferrite magnets,” *COMPEL The International Journal for Computation and Mathematics in Electrical and Electronic Engineering*, vol. 35, no.2, pp.456-472, 2016.

[ALL20] A. Allahyari and H. Torkaman, “A novel high-performance consequent pole dual rotor permanent magnet Vernier machine,” *IEEE Transaction on Energy Conversion*, vol. 35, no. 3, pp. 1238–1246, 2020.

[ALQ19] A. Al-Qarni, F. Wu, and A. El-Refaie, “High-torque-density low-cost magnetic gear utilizing hybrid magnets and advanced materials,” *In 2019 IEEE International Electric Machines & Drives Conference (IEMDC)*, 2019, pp. 225-232, IEEE.

[ALQ21] A. Al-Qarni and A. EL-Refaie, “Magnetic gears and magnetically geared machines with reduced rare-earth elements for vehicle applications,” *World Electric Vehicle Journal*, vol. 12, no.2, pp.52-74, 2021.

[ALS15] J. Y. Alsawalhi and S. D. Sudhoff, “Effects of positioning of permanent magnet axis relative to reluctance axis in permanent magnet synchronous machines,” *In Proc. IEEE Power Energy Conf. at Illinois (PECI)*, 2015, pp. 1–8, IEEE.

[ARZ20] A. Arzillo et al., "Challenges and future opportunities of hairpin technologies," *In 2020 IEEE 29th International Symposium on Industrial Electronics (ISIE)*, 2020, pp. 277-282, IEEE.

[BER20] G. Berardi, S. Nategh, N. Bianchi, and Y. Thioliere, "A comparison between random and hairpin winding in e-mobility applications," *In IECON 2020 The 46th Annual Conference of the IEEE Industrial Electronics Society*, 2020, pp. 815-820, IEEE.

[BES12] E. K. Beser, S. Camur, B. Arifoglu, and E. Beser, “Analysis and application of a hybrid motor structure convenient to modify the magnet and reluctance torques on the rotor,” *Journal of Electrical Engineering & Technology*, vol. 7, no. 3, pp. 349–357, 2012.

[BIA09] N. Bianchi, S. Bolognani, D. Bon, and M. Dai Pre, “Rotor flux-barrier design for torque ripple reduction in synchronous reluctance and PM-Assisted synchronous reluctance motors,” *IEEE Transactions on Industry Applications*, vol. 45, no. 3, pp. 921-928, 2009.

[BIL15] B. Bilgin *et al.*, "Making the case for electrified transportation," *IEEE Transactions on Transportation Electrification,* vol. 1, no. 1, pp. 4-17, 2015.

[BIL19] B. Bilgin *et al.*, "Modeling and analysis of electric motors: state-of-the-art review," *IEEE Transactions on Transportation Electrification,* vol. 5, no. 3, pp. 602-617, 2019.

[BUR13] T. Burress, "Benchmarking state-of-the-art technologies," in Oak Ridge National Laboratory (ORNL), *2013 US DOE Hydrogen and Fuel Cells Program and Vehicle Technologies Program Annual Merit Review and Peer Evaluation Meeting*, 2013.

[CAO12] W. Cao, B. C. Mecrow, G. J. Atkinson, J. W. Bennett, and D. J. Atkinson, "Overview of electric motor technologies used for more electric aircraft (MEA)," *IEEE Transactions on Industrial Electronics*, vol. 59, no. 9, pp. 3523-3531, 2012.

[CAR14] E. Carraro, M. Degano, M. Morandin, and N. Bianchi, "PM synchronous machine comparison for light electric vehicles," *In 2014 IEEE International Electric Vehicle Conference (IEVC)*, 2014, pp. 1-8, IEEE.

[CAW23] T. Cawkwell, A. Haris, J. M. Gonzalez, L. K. Rodrigues, and V. Shirokov, "A methodology for applying skew in an automotive interior permanent magnet rotor for robust electromagnetic and noise, vibration and harshness performance," *World Electric Vehicle Journal*, vol. 14, no. 12, p. 350, 2023.

[CHA08] K. T. Chau, C. C. Chan, C. Liu "Overview of permanent-magnet brushless drives for electric and hybrid electric vehicles*," IEEE Transactions on Industrial Electronics*, Vol. 55, no. 6, pp. 2246-2257, 2008.

[CHE11A] M. Cheng, W. Hua, J. Zhang, and W. Zhao, “Overview of stator-permanent magnet brushless machines,” *IEEE Transactions on Industrial Electronics*, vol. 58, no. 11, pp. 5087-5101, 2011.

[CHE11B] J. T. Chen and Z. Q. Zhu, "A synchronous PM machine," *Siemens Gamesa Renewable Energy A/S,* European Patent Application Number 11162813.7, filed 2011-04-18, EP2515417-B1, granted 2014-04-02.

[CHE14] Q. Chen, G. Liu, W. Zhao, M. Shao, and Z. Liu, "Design and analysis of the new high-reliability motors with hybrid permanent magnet material," *IEEE Transactions on Magnetics*, vol. 50, no. 12, pp.1-10, 2014.

[CHE18A] Y. Chen, Y. Ding, X. Li, and X. Zhu, "Design and analysis of less-rare-earth double-stator modulated machine considering multioperation conditions,” *IEEE Transactions on Applied Superconductivity*, vol. 28, no.3, pp.1-5, 2018.

[CHE18B] Y. Chen, Y. Ding, J. Zhuang, X. Li, and F. Liu, "Optimization and performance improvement of multi-excitation double-stator flux-switching machine,” *In 2018 IEEE International Conference on Applied Superconductivity and Electromagnetic Devices (ASEMD)*, 2018, pp. 1-2: IEEE.

[CHE19] Y. Chen, J. Zhuang, T. Cai, Q. Wang, and W. Pu, "Design and analysis of a new less-rare-Earth permanent magnet motor with axial hybrid rotors,” *In 2019 22nd International Conference on Electrical Machines and Systems (ICEMS)*, 2019, pp. 1-4, IEEE.

[CHE20] Y. Chen, T. Cai, X. Zhu, D. Fan, and Q. Wang, "Analysis and design of a new type of less-rare-earth hybrid-magnet motor with different rotor topologies," *IEEE Transactions on Applied Superconductivity*, vol. 30, no. 4, pp.1-6, 2020.

[CHE21] Y. Chen, T. Cai, X. Zhu, and D. Yu, "Optimization of a new asymmetric-hybrid-PM machine with high torque density and low torque ripple considering the difference of magnetic materials," *IEEE Transactions on Magnetics*, vol. 58, no.2, pp.1-5, 2021.

[CHE23] Y. Chen, X. Zhou, Z. Li, and X. Zhu, "Torque performance enhancement for hybrid PM motor considering magnet characteristic difference and variation," *IEEE Transactions on Magnetics*, vol. 59, no.11, pp.1-5, 2023.

[CHE24] Y. Chen, X. Zhou, M. Lu, and Y. Xu, "Research on air-gap field modulation effect of torque enhanced hybrid permanent magnet motor," *IEEE Transactions on Magnetics*, early access, 2024.

[CHI13] K. Chiba, M. Takemoto, S. Ogasawara, and W. G. Yim, "Ferrite-magnet spoke-type IPMSM with W-shaped magnet placement," *In IECON 2013-39th Annual Conference of the IEEE Industrial Electronics Society*, 2013, pp. 2869-2874, IEEE.

[CHU11] S. U. Chung, J.W. Kim, B.C. Woo, D.K. Hong, J.Y. Lee, and D.H. Koo, “A novel design of modular three-phase permanent magnet Vernier machine with consequent pole PMSM,” *IEEE Transactions on Magnetics*, vol. 47, no. 10, pp. 4215–4218, 2011.

[CHU12] W. Chu and Z. Q. Zhu, "Average torque separation in permanent magnet synchronous machines using frozen permeability," IEEE Transactions on Magnetics, vol. 49, no. 3, pp. 1202-1210, 2012.

[CHU15] S. U. Chung, J. W. Kim, Y. D. Chun, B. C. Woo, and D. K. Hong, "Fractional slot concentrated winding PMSM with consequent pole rotor for a low-speed direct drive: Reduction of rare earth permanent magnet," *IEEE Transactions on energy conversion*, vol. 30, no.1, pp. 103-109, 2015.

[CUI22] W. Cui, L. Ren, J. Zhou, and Q. Zhang, "A new IPMSM with hybrid rotor structure for electrical vehicle with reduced magnet loss," *IEEE Transactions on Magnetics*, vol. 58, no.2, pp.1-6, 2022.

[CUI23] W. Cui, D. Wang, L. Ren, and Y. Zhang, "A new optimized IPMSM for EVs with reduced magnet loss for over-modulation operation," *IEEE Transactions on Magnetics*, vol. 59, no.2, pp.1-4, 2023.

[CUT23] G. Cutuli, S. Nuzzo, T. Zou, G. Franceschini, C. Gerada, and D. Barater, "Multi-objective optimizations of copper and aluminum hairpin windings: a comparison, " *In 2023 IEEE Energy Conversion Congress and Exposition (ECCE)*, 2023, pp. 3796-3801: IEEE.

[DIA23] C. Diao, W. Zhao, N. Wang, and X. Wang, "Analysis of a high-speed axial flux permanent magnet synchronous motor with cost-effective hybrid magnets," *IEEE Transactions on Magnetics*, vol. 59, no. 5, pp.1-4, 2023.

[DU20] Z. S. Du, and T. A. Lipo, "Cost-effective high torque density bi-magnet machines utilizing rare earth and ferrite permanent magnets," *IEEE Transactions on energy conversion*, vol. 35, no.3, pp.1577-1584, 2020.

[DUB18] C. Du-Bar and O. Wallmark, "Eddy current losses in a hairpin winding for an automotive application," *In 2018 XIII International Conference on Electrical Machines (ICEM)*, 2018, pp. 710-716: IEEE.

[ELR10] A. M. EL-Refaie, “Fractional-slot concentrated-windings synchronous permanent magnet machines: Opportunities and challenges,” *IEEE Transactions on Industrial Electronics*, vol. 57, no. 1, pp. 107–121, 2010.

[ENE] U. S. D. o. Energy. Advanced Vehicle Technologies Research Funding Opportunity Announcement. [Online] Available: https://www.energy.gov/eere/vehicles/funding-opportunities.

[FAN17] D. Fan, L. Quan, X. Zhu, Z. Xiang, and W. Wu, "Demagnetization investigation of a partitioned rotor flux switching machine with hybrid permanent magnet," *AIP Advances*, vol. 7, no. 5, 2017.

[FER15] M. Ferrari, N. Bianchi, and E. Fornasiero, "Analysis of rotor saturation in synchronous reluctance and PM-assisted reluctance motors," *IEEE Transactions on Industry Applications*, vol. 51, no. 1, pp. 169-177, 2015.

[FYH17] P. Fyhr, G. Domingues, A. Reinap, M. Andersson, and M. Alaküla, "Performance and manufacturability trade-offs of different electrical machine designs," *In 2017 IEEE International Electric Machines and Drives Conference (IEMDC)*, 2017, pp. 1-7: IEEE.

[GAO22] Y. Gao, M. Doppelbauer, J. Ou, and R. Qu, "Design of a double-side flux modulation permanent magnet machine for servo application," *IEEE J. Emerg. Sel. Topics Power Electron.*, vol. 10, no. 2, pp. 1671-1682, 2022.

[GUG13] P. Guglielmi, B. Boazzo, E. Armando, G. Pellegrino, and A. Vagati, "Permanent-magnet minimization in PM-assisted synchronous reluctance motors for wide speed range," *IEEE Transactions on Industry Applications*, vol. 49, no. 1, pp. 31-41, 2013.

[HAN22] Y. Han, and M. Lin, "Design and analysis of a novel hybrid permanent-magnet machine with less rare earth materials," *In 2022 IEEE 5th Student Conference on Electric Machines and Systems (SCEMS)*, 2022, pp. 1-5, IEEE.

[HAY19] S. Hayslett and E. Strangas, “Design and analysis of aligned axis interior permanent magnet machines considering saturation,” *In 2019 IEEE International Electric Machines and Drives Conference (IEMDC)*, 2019, pp. 686–692, IEEE.

[HUA19] Y. Hua, L. Quan, X. Zhu, L. Xu, Z. Xiang, and W. Pu, “Design and comparison of two hybrid less-rare-earth permanent magnet machines with different rotor topologies,” *In 2019 22nd International Conference on Electrical Machines and Systems (ICEMS)*, 2019, pp. 1-5, IEEE.

[HUY17] T. A. Huynh and M.-F. Hsieh, "Comparative study of PM-assisted SynRM and IPMSM on constant power speed range for EV applications," *IEEE Transactions on Magnetics*, vol. 53, no. 11, pp. 1-6, 2017.

[HUY18] T. A. Huynh, M.-F. Hsieh, K.-J. Shih, and H.-F. Kuo, "An investigation into the effect of PM arrangements on PMASynRM performance," *IEEE Transactions on Industry Applications,* vol. 54, no. 6, pp. 5856-5868, 2018.

[ISH13] S. Ishii, Y. Hasegawa, K. Nakamura, and O. Ichinokura, "Novel flux barrier type outer rotor IPM motor with rare-earth and ferrite magnets," *Journal of the Magnetics Society of Japan*, vol. 37, no. 3-2, pp. 259-263, 2013.

[ISL19] M. S. Islam, I. Husain, A. Ahmed, and A. Sathyan, "Asymmetric bar winding for high-speed traction electric machines," *IEEE Transactions on Transportation Electrification*, vol. 6, no. 1, pp. 3-15, 2019.

[JEO17] C. L. Jeong, and J. Hur, 2017, "Optimization design of PMSM with hybrid-type permanent magnet considering irreversible demagnetization," *IEEE Transactions on Magnetics*, vol. 53, no.11, pp.1-4, 2017.

[JEO19] C. L. Jeong, Y. K. Kim, and J. Hur, "Optimized design of PMSM with hybrid-type permanent magnet for improving performance and reliability," *IEEE Transactions on Industry Applications*, vol. 55, no.5, pp.4692-4701, 2019.

[JI23] Y. Ji, Y. Li, and Q. Lu, 2023, "Investigation of a novel hybrid less-rare-earth consequent-pole interior permanent magnet machine with asymmetric rotor," *In 2023 26th International Conference on Electrical Machines and Systems (ICEMS)*, 2023, pp. 5354-5359, IEEE.

[JI24] Y. Ji, Q. Lu, Y. Li, and Y. Fang, "An efficient design optimization method for consequent-pole asymmetric rotor hybrid interior permanent magnet synchronous machine," *In 2024 Third International Conference on Sustainable Mobility Applications, Renewables and Technology (SMART)*, 2024, pp. 1-8, IEEE.

[JIA09] L. Jian, K. Chau, and J. Jiang, "A magnetic-geared outer-rotor permanent-magnet brushless machine for wind power generation," *IEEE Transactions on Industry Applications*, vol. 45, no.3, pp. 954-962, 2009.

[JIA22] J. Jiang, and S. Niu, "A novel slot-pm-assisted consequent-pole-PM machine with hybrid magnets of FEPMs and rare earth PMs," *IEEE Transactions on Magnetics*, vol. 58, no.8, pp.1-6, 2022.

[KAK13] W. Kakihara, M. Takemoto, and S. Ogasawara, "Rotor structure in 50 kW spoke-type interior permanent magnet synchronous motor with ferrite permanent magnets for automotive applications," *In 2013 IEEE Energy Conversion Congress and Exposition*, 2013, pp. 606-613, IEEE.

[KAN22] M. Kang, L. Xu, J. Ji, and, X. Zhu, "Design and analysis of a high torque density hybrid permanent magnet excited vernier machine," *Energies*, vol. 15, no. 5, pp 1723-1738, 2022.

[KAZ18] S. Kazemisangdehi, S. E. Abdollahi, and S. A. Gholamian, "Analysis of a novel transverse laminated rotor flux switching machine," *IEEE Transactions on Energy Conversion*, vol. 33, no. 3, pp. 1193-1202, 2018.

[KAZ23A] S. Kazemisangdehi, Z. Q. Zhu, Y. Zhou, and H. Liu, "A new hybrid permanent magnet synchronous machine with V-shape spokes," *In 2023 IEEE Int. Electric Machines & Drives Conference (IEMDC)*, 2023, pp. 1-7, IEEE.

[KAZ23B] S. Kazemisangdehi, Z. Q. Zhu, and Y. Zhou, "Comparative study of performance improvement methods in a series hybrid PM delta-shape IPMSM," *In 2023 26th Int. Conference on Electrical Machines and Systems (ICEMS)*, 2023, pp. 684-689, IEEE.

[KAZ23C] S. Kazemisangdehi, Z. Q. Zhu, Y. Zhou, and H. Liu, "Improved performance of series and parallel hybrid permanent magnet spoke-type PM machines using tapered magnets," *In 2023 IEEE Int. Electric Machines & Drives Conference (IEMDC)*, 2023, pp. 1-7, IEEE.

[KAZ23D] S. Kazemisangdehi, Z. Q. Zhu, and Y. Zhou, "Split spoke series hybrid PM delta-shape IPMSM with improved performance," *In 2023 26th Int. Conference on Electrical Machines and Systems (ICEMS)*, 2023, pp. 678-683, IEEE.

[KAZ25] S. Kazemisangdehi, Z. Q. Zhu, Y. Zhou, H. Liu, L. Chen, and L. Yang, "Novel parallel hybrid rare-earth and ferrite magnets in V-spoke interior PM synchronous machine," *IEEE Transactions on Industry Applications*, early access, 2025.

[KNY14] L. Knypiñski, L. Nowak, and A. Demenko, "Optimization of the synchronous motor with hybrid permanent magnet excitation system," *COMPEL: The International Journal for Computation and Mathematics in Electrical and Electronic Engineering*, vol. 34, no. 2, pp.448-455, 2015.

[KRI20] A. Krings and C. Monissen, "Review and trends in electric traction motors for battery electric and hybrid vehicles," *In 2020 International Conference on Electrical Machines (ICEM)*, 2020, pp. 1807-1813, IEEE.

[KUM20] R. R. Kumar, G. Vakil, D. Gerada, C. Gerada, K. Paciura, B. G. Fernandes, and L. Yan, "Hybrid magnet configuration to reduce the content of rare earth elements in a pm-synrel machine," *In 2020 IEEE Transportation Electrification Conference & Expo (ITEC)*, 2020, pp. 352-357, IEEE.

[KWO18] J.-W. Kwon and B.-I. Kwon, “Investigation of dual-stator spoke-type Vernier machine for EV application,” *IEEE Transactions on Magnetics*, vol. 54, no. 11, pp. 1–5, 2018.

[LI16A] D. Li, R. Qu, J. Li, L. Xiao, L. Wu, and W. Xu, “Analysis of torque capability and quality in Vernier permanent-magnet machines,” *IEEE Transactions on Industry Applications*, vol. 52, no. 1, pp. 125–135, 2016.

[LI16B] X. Li, L. Quan, Y. Chen, X. Zhu, and Q. Chen, “Electromagnetic performance analysis of a new hybrid excited stator-partitioned flux switching permanent magnet machine,” *In 2016 19th International Conference on Electrical Machines and Systems (ICEMS)*, 2016, pp. 1-6, IEEE.

[LI18] J. Li, K. Wang, and C. Liu, “Torque improvement and cost reduction of permanent magnet machines with a dovetailed consequent-pole rotor,” *IEEE Transactions on Energy Conversion*, vol. 33, no. 4, pp. 1628–1640, 2018.

[LI19] Y. Li, H. Yang, H. Lin, S. Fang, and W. Wang, “A novel magnet-axis-shifted hybrid permanent magnet machine for electric vehicle applications,” *Energies*, vol. 12, no. 4, p.641-653, 2019.

[LIN22] Y. Lin, Y. Sun, Y. Wang, and J. Shen, “A hybrid PM-assisted SynRM with ferrite and rare-earth magnets,” *Transactions of China Electrotechnical Society*, vol. 37, no. 5, pp.1145-1157, 2022.

[LIU14] G. Liu, M. Shao, W. Zhao, Q. Chen, and L. Mo, “Cost reduction of a new fault-tolerant Halbach permanent magnet machine using ferrite magnet,” *IEEE Transactions on Magnetics*, vol.50, no.11, pp.1-4, 2014.

[LIU17] G. Liu, G. Xu, W. Zhao, X. Du, and Q. Chen, “Improvement of torque capability of permanent-magnet motor by using hybrid rotor configuration,” *IEEE Transactions on Energy Conversion*, vol. 32, no. 3, pp. 953–962, Sep. 2017.

[LIU18] F. Liu, L. Quan, X. Zhu, Z. Xiang, and W. Wu, W, “Investigation of reverse saliency characteristic in flux-intensifying hybrid permanent magnet motor considering various operation conditions,” *In 2018 IEEE International Conference on Applied Superconductivity and Electromagnetic Devices (ASEMD)*, 2018, pp. 1-2, IEEE.

[LIU23A] C.T. Liu, W. L. Chen, S. C. Yen, Y. W. Hsu, P. C. Shih, and T. Y. Luo, “Effective performance improvement designs of a hybrid permanent-magnet-assisted synchronous reluctance motor,” *In 2023 IEEE International Magnetic Conference-Short Papers (INTERMAG Short Papers)*, 2023, pp. 1-2, IEEE.

[LIU23B] K. Liu, L. Shi, Z. Liu, W. Wang, and H. Ding, “Analysis and optimization of asymmetric hybrid permanent magnet motor for electric vehicle,” *Journal of Electrical Engineering & Technology*, vol. 18, no.5, pp.3555-3567, 2023.

[LIU24] L. Liu, Y. Ma, K. Shuai, Y. Xiao, H. Kang, Z. Ou, and H. Zhao, “A comparative study of V-shaped IPMSMs with asymmetric and symmetric rotors,” *In 2024 The 9th International Conference on Power and Renewable Energy (ICPRE)*, 2024, pp. 108-113, IEEE.

[LU16] T. Lu, L. Quan, X. Zhu, D. Fan, and Y. Chen, “Electromagnetic performance analysis of less rare-earth double-stator permanent magnet machine,” *In 2016 IEEE Vehicle Power and Propulsion Conference (VPPC)*, 2016, pp. 1-6, IEEE.

[LV23] B. Lv, L. Shi, K. Liu, L. Li, and H. Ding, “Optimization and pole-slot analysis of a new type of permanent magnet hybrid pole motor for electric vehicles,” *Journal of Electrical Engineering & Technology*, vol. 18, no.5, pp.3593-3602, 2023.

[MA20] Q. Ma, A. El-Refaie, and B. Lequesne, “Low-cost interior permanent magnet machine with multiple magnet types,” *IEEE Transactions on Industry Applications*, vol 56, no.2, pp.1452-1463, 2020.

[MA21A] Q. Ma, A. EL-Refaie, and A. Fatemi, “Multi-objective design optimization of a blended permanent magnet assisted synchronous reluctance machine,” *In 2021 IEEE International Electric Machines & Drives Conference (IEMDC)*, 2021, pp. 1-7, IEEE.

[MA21B] Q. Ma, A. EL-Refaie, and A. Fatemi, and T. Nehl, “Comparative analysis of two different types of blended permanent magnet assisted synchronous reluctance machine,” *In 2021 IEEE Energy Conversion Congress and Exposition (ECCE)*, 2021, pp. 4189-4196, IEEE.

[MIR20] S. A. Mirnikjoo, K. Abbaszadeh, and S. E. Abdollahi, "Multi-objective design optimization of a double-sided flux switching permanent magnet generator for counter-rotating wind turbine applications," *IEEE Transactions on Industrial Electronics*, Vol. 60, no. 8, pp. 6640-6648, 2020.

[NAG16] S. Nagano, M. Takemoto, and S. Ogasawara, "An examination for improvement of constant output characteristics at high-speed region in a spoke-type IPMSM using ferrite permanent magnet by changing the shape of rotor surface," *In 2016 IEEE Energy Conversion Congress and Exposition (ECCE)*, 2016, pp. 1-8, IEEE.

[PAR21] J. Park, R. Tsunata, M. Takemoto, K. Orikawa, and S. Ogasawara, "Investigation of Dy-free hybrid PM motor based on spoke-type rotor for automotive applications," *In 2021 IEEE International Electric Machines & Drives Conference (IEMDC)*, 2021, pp. 1-8, IEEE.

[PAR22] J. Park, R. Tsunata, M. Takemoto, K. Orikawa, and S. Ogasawara, "Hybrid-type PM motor for electric vehicle traction with improved reluctance torque," *Journal of the Japan Society of Applied Electromagnetics and Mechanics*, vol. 30, no.3, pp.324-334, 2022.

[POL13] H. Polinder, J. A. Ferreira, B. B. Jensen, A. B. Abrahamsen, K. Atallah, and R. A. McMahon, "Trends in wind turbine generator systems," *IEEE J. Emerg. Sel. Topics Power Electron.*, vol. 1, no. 3, pp. 174-185, 2013

[POU21] B. Poudel, E. Amiri, P. Rastgoufard, and B. Mirafzal, "Toward less rare-earth permanent magnet in electric machines: A review," *IEEE Transactions on Magnetics*, vol.57, no.9, pp.1-19, 2021.

[POU22] B. Poudel, E. Amiri, and P. Rastgoufard, "Analytical investigation and heuristic optimization of surface mounted permanent magnet machines with hybrid magnetic structure, " I*EEE Open Journal of Industry Applications*, vol.3, pp.152-163, 2022.

[PRE21] E. Preci et al., "Segmented hairpin topology for reduced losses at high frequency operations," *IEEE Transactions on Transportation Electrification*, vol.8, no.1, pp. 688-698, 2021.

[QI22A] J. Qi, Z. Q. Zhu, L. Yang, G. W. Jewell, C. Gan, Y. Ren, S. Brockway, and C. Hilton, "Effect of pole shaping on torque characteristics of consequent pole PM machines," *IEEE Transactions on Industry Applications*, vol. 58, no. 3, pp. 3511-3521, 2022.

[QI22B] J. Qi, Z. Q. Zhu, L. Yang, G. W. Jewell, C. Gan, Y. Ren, S. Brockway, and C. Hilton, "Suppression of torque ripple for consequent pole PM machine by asymmetric pole shaping method," *IEEE Transactions on Industry Applications*, vol. 58, no. 3, pp. 3545-3557, 2022.

[QIA24] Z. Qiao, L. Shi, F. Li, H. Xu, T. Zhou, and W. Wang, "Characteristics analysis of magnetic-pole-shift in an asymmetric hybrid pole-permanent magnet assisted synchronous reluctance motor," *IEEE Journal of Emerging and Selected Topics in Power Electronics*, early access, 2024.

[RAM19] P. Ramesh and N. Lenin, "High power density electrical machines for electric vehicles—Comprehensive review based on material technology," *IEEE Transactions on Magnetics*, vol.55, no.11, pp. 1-21, 2019.

[REF14] A. M. El-Refaie, J. P. Alexander, S. Galioto, P. B. Reddy, K. K. Huh, P. D. Bock, and X. Shen, "Advanced high-power-density interior permanent magnet motor for traction applications," *IEEE Transactions on Industry Applications*, vol. 50, no. 5, pp. 3235-3248, 2014.

[REN15] W. Ren, Q. Xu, and Q. Li, “Asymmetrical V-shape rotor configuration of an interior permanent magnet machine for improving torque characteristics,” *IEEE Transactions on Magnetics*, vol. 51, no. 11, pp. 1–4, 2015.

[SEO22] C. H. Seok, S. Y. Yoon, H. S. Choi, H. Y. Lee, and J. Seo, “Analysis and modelling of axial leakage for spoke-type hybrid permanent magnet machines,” *IEEE Access*, vol. 11, pp.6385-6393, 2022.

[SHA20] L. Shao, A. E. H. Karci, D. Tavernini, A. Sorniotti, and M. Cheng, "Design approaches and control strategies for energy-efficient electric machines for electric vehicles—A review," *IEEE Access*, vol. 8, pp. 116900-116913, 2020.

[SHE12] Y. Shen and Z. Q. Zhu, "Analysis of electromagnetic performance of Halbach PM brushless machines having mixed grade and unequal height of magnets," *IEEE Transactions on Magnetics*, vol. 49, no. 4, pp. 1461-1469, 2012.

[SHI24] L. Shi, J. Jing, W. Wang, Z. Liu, and F. Li, "Electromagnetic characteristic analysis of a negative-salient hybrid permanent magnet motor for electric vehicles," *IEEE Journal of Emerging and Selected Topics in Industrial Electronics*, vol. 5, no. 3, pp. 1283-1291, 2024.

[TAH20] H. Tahanian, M. Alimahdi, and J. Faiz, "Ferrite permanent magnets in electrical machines: opportunities and challenges of a non-rare-earth alternative," *IEEE Transactions on Magnetics*, vol. 56, no. 3, pp. 1-20, 2020.

[TU23] R. Tu, H. Yang, H. Lin, H. Zhan, D. Wu, and M. Yu, "Design and optimization of a novel delta-type consequent-pole hybrid magnet memory machine," *IEEE Transactions on Energy Conversion*, 2023.

[VAG14] A. Vagati, B. Boazzo, P. Guglielmi, and G. Pellegrino, "Design of ferrite-assisted synchronous reluctance machines robust toward demagnetization," *IEEE Transactions on Industry Applications*, vol. 50, no. 3, pp. 1768-1779, 2014.

[VID24] B. D. S. G. Vidanalage, Z. Li, A. Lombardi, and N. C. Kar, "A novel winding design for EV traction motors: hybrid Hairpin winding layout containing both copper and aluminum windings," *In 2024 IEEE International Magnetic Conference (INTERMAG)*, 2024, pp. 1-6: IEEE.

[WAN15] K. Wang, Z. Q. Zhu, G. Ombach, M. Koch, S. Zhang, and J. Xu, "Torque ripple reduction of synchronous reluctance machines," *COMPEL–The international journal for computation and mathematics in electrical and electronic engineering*, vol. 34, no. 1, pp. 3-17, 2015.

[WAN17] Y. Wang, G. Bacco, and N. Bianchi, "Geometry analysis and optimization of PM-assisted reluctance motors," *IEEE Transactions on Industry Applications*, vol. 53, no. 5, pp. 4338-4347, 2017.

[WAN19] M. Wang, C. Tong, P. Zheng, L. Cheng, S. Zhang, G. Qiao, and Y. Sui, "Analysis of a novel hybrid-PM variable-flux machine using new magnet material CeFeB," *IEEE Transactions on Magnetics*, vol. 55, no. 7, pp.1-7, 2019.

[WAN22] H. Wang, H. Zhu, S. Ding, C. He, Z. Jin, and Z. Wei, " A new hybrid magnet dual stator field modulation machine with different split ratios of stators," *IEEE Transactions on Magnetics*, vol. 58, no.8, pp.1-6, 2022.

[WAN24] W. Wang, L. Fu, N. Wang, L. Zhu, X. Zhao, and J. Wei, "Structure comparison and performance analysis of multi-layer flux-barrier hybrid-pole permanent-magnet synchronous machine," *In 2024 IEEE 7th International Electrical and Energy Conference (CIEEC)*, 2024, pp. 4935-4939, IEEE.

[WU16] W. Wu, X. Zhu, L. Quan, Z. Xiang, D. Fan, and S. Yang, "Performance evaluation of a U-shaped less-rare-earth hybrid permanent magnet assisted synchronous reluctance motor," *In 2016 IEEE Vehicle Power and Propulsion Conference (VPPC)*, 2016, pp. 1-6, IEEE.

[WU17A] W. Wu, X. Zhu, L. Quan, Y. Du, Z. Xiang, and X. Zhu, "Design and analysis of a hybrid permanent magnet assisted synchronous reluctance motor considering magnetic saliency and PM usage," *IEEE Transactions on Applied Superconductivity*, vol. 28, no.3, pp.1-6, 2017.

[WU17B] W. Wu, X. Zhu, L. Quan, D. Fan, and Z. Xiang, "Characteristic analysis of a less-rare-earth hybrid PM-assisted synchronous reluctance motor for EVs application," *AIP Advances*, vol. 7, no. 5, 2017.

[WU21] J. Wu, X. Zhu, D. Fan, Z. Xiang, L. Xu, and L. Quan, "Robust optimization design for permanent magnet machine considering magnet material uncertainties," *IEEE Transactions on Magnetics*, vol. 58, no.2, pp.1-7, 2021.

[XIA18] Z. Xiang, X. Zhu, L. Quan, and D. Fan, "Optimization design and analysis of a hybrid permanent magnet flux-switching motor with compound rotor configuration," *CES Transactions on Electrical Machines and Systems*, vol. 2, no. 2, pp.200-206, 2018.

[XIA20A] Y. Xiao, Z. Q. Zhu, J. T. Chen, D. Wu, and L. M. Gong, “A novel asymmetric rotor interior PM machine with hybrid-layer PMs,” *In Proc. IEEE Energy Conversion Congress Expo. (ECCE)*, 2020, pp. 2286–2291, IEEE.

[XIA20B] Y. Xiao, Z.-Q. Zhu, J.-T. Chen, D. Wu, and L.-M. Gong, “A novel spoke-type asymmetric rotor interior PM machine,” *In Proc. IEEE Energy Conversion Congress Expo. (ECCE)*, 2020, pp. 4050–4057, IEEE.

[XIA21A] Y. Xiao, Z. Q. Zhu, S. S. Wang, G. W. Jewell, J. T. Chen, D. Wu, and L. M. Gong, “A novel asymmetric interior permanent magnet machine for electric vehicles,” *IEEE Transactions on Energy Conversion*, vol. 36, no.3, pp.2404-2415, 2021.

[XIA21B] Y. Xiao, Z. Q. Zhu, G. W. Jewell, J. T. Chen, D. Wu, and L. M. Gong, "Influence of armature reaction on magnetic-field-shifting effect in asymmetric interior permanent magnet machines," *IEEE Transactions on Energy Conversion*, vol. 37, no. 2, pp. 1475-1488, 2021.

[XIA22] Y. Xiao, Z. Q. Zhu, G. W. Jewell, J. T. Chen, D. Wu, and L. M. Gong, "A novel asymmetric interior PM synchronous machine," *IEEE Transactions on Industry Applications*, vol. 58, no. 3, pp. 3370-3382, 2022.

[XIE22] Y. Xie, J. Shao, S. He, B. Ye, F. Yang, and L. Wang, “Novel PM-assisted synchronous reluctance machines using asymmetrical rotor configuration,” *IEEE Access*, vol. 10, pp.79564-79573, 2022.

[XU17A] G. Xu, G. Liu, M. Chen, X. Du, and M. Xu, “Cost-effective Vernier permanent-magnet machine with high torque performance,” *IEEE Transactions on Magnetics*, vol. 53, no.11, pp.1-4, 2017.

[XU17B] G. Xu, G. Liu, X. Du, and F. Bian, “A novel PM motor with hybrid PM excitation and asymmetric rotor structure for high torque performance,” *AIP advances*, vol. 7, no.5, 2017.

[XU25] H. Xu, Z. Q. Zhu, Y. Zhou, and L. Chen, "Contributions of stator and rotor PMs in torque production of multi-tooth dual-PM machines with different stator/rotor pole number combinations," *IEEE Transactions on Industry Applications, early access*, 2025.

[YAN16] Y. Yang S. M. Castano, R. Yang, M. Kasprzak, B. Bilgin, A. Sathyan, H. Datkhah, and A. Emadi, "Design and comparison of interior permanent magnet motor topologies for traction applications," *IEEE Transactions on Transportation Electrification*, vol. 3, no. 1, pp. 86-97, 2016.

[YAN17A] R. Yang, "Electrified vehicle traction machine design with manufacturing considerations," PhD dissertation, College of Mechanical Engineering, McMaster University, Hamilton, Canada, 2017. Accessed on: July 28, 2021. [Online]. Available: https://macsphere.mcmaster.ca/bitstream/11375/20895/2/Yang_Rong_2016December_Ph.D..pdf

[YAN17B] H. Yang et al., “Novel reluctance axis shifted machines with hybrid rotors,” *In Proc. IEEE Energy Conversion Cong. Expo. (ECCE)*, 2017, pp. 2362–2367, IEEE.

[YAN24A] K. Yang, L. Zhang, M. Wang, and C. Du, ”Performance comparison and optimization of a PMSM based on hybrid-type permanent magnet with two kinds of rotor topology,” *Energies*, vol. 17, no. 3, pp. 557-574, 2024.

[YAN24B] M. Yang, L. Quan, X. Zhu, Z. Xiang, D. Fan, W. Fan, and M. Jiang,” Design and analysis of a hybrid permanent magnet variable leakage flux motor for low core loss and wide speed range," *AIP Advances*, vol. 14, no.1, 2024.

[YU19] D. Yu, X. Huang, X. Zhang, J. Zhang, Q. Lu, and Y. Fang,” Optimal design of outer rotor interior permanent magnet synchronous machine with hybrid permanent magnet," *IEEE Transactions on Applied Superconductivity*, vol. 29, no. 2, pp.1-5, 2019.

[ZEN18] X. Zeng, L. Xu, and C. Zhang, “Design and optimization of a less-rare earth permanent magnet brushless motor considering cost effective,” *In 2018 21st International Conference on Electrical Machines and Systems (ICEMS)*, 2018, pp. 488-492, IEEE.

[ZEN19] X. Zeng, L. Quan, X. Zhu, L. Xu, and F. Liu, “Investigation of an asymmetrical rotor hybrid permanent magnet motor for approaching maximum output torque,” *IEEE Transactions on Applied Superconductivity*, vol. 29, no.2, pp.1-4, 2019.

[ZHA18] W. Zhao, H. Shen, T. A. Lipo, and X. Wang, “A new hybrid permanent magnet synchronous reluctance machine with axially sandwiched magnets for performance improvement,” *IEEE Transactions on Energy Conversion*, vol. 33, no. 4, pp. 2018–2029, Dec. 2018.

[ZHA19] Y. Zhao, D. Li, T. Pei, and R. Qu, "Overview of the rectangular wire windings AC electrical machine," *CES Transactions on Electrical Machines and Systems*, vol. 3, no. 2, pp. 160-169, 2019.

[ZHA20] Z. Zhang, "High torque density spoke-type ferrite permanent magnet synchronous machine assisted by rare-earth magnets for traction applications," *In 2020 IEEE Energy Conversion Congress and Exposition (ECCE)*, 2020, pp. 1806-1813, IEEE.

[ZHA21] Y. Zhang, Z. Xiang, X. Zhu, L. Quan, and M. Jiang, "Anti-demagnetization capability research of a less-rare-earth permanent-magnet synchronous motor based on the modulation principle," *IEEE Transactions on Magnetics*, vol. 57, no. 2, pp.1-6, 2021.

[ZHE19] J. Zhenxing, L. Hongmei, C. Zhiwei, Y. Tian, L. Liwen, and M. Mingna, “Design and optimization of permanent magnet assisted synchronous reluctance motor for better torque performance,” *In Proc. 22nd International Conference on Electrical Machines and Systems (ICEMS)*, 2019, pp. 1–4, IEEE.

[ZHE21A] S. Zheng, X. Zhu, L. Xu, Z. Xiang, L. Quan, and B. Yu, “Multi-objective optimization design of a multi-permanent-magnet motor considering magnet characteristic variation effects,” *IEEE Transactions on Industrial Electronics*, vol. 69, no. 4, pp.3428-3438, 2021.

[ZHE21B] S. Zheng, X. Zhu, L. Xu, T. Zhu, and D. Wu, “Comparative analysis and multi-objective optimization of hybrid permanent magnet motors considering different saliency characteristics,” *IEEE Transactions on Applied Superconductivity*, vol. 31, no. 8, pp.1-5, 2021.

[ZHU07] Z. Q. Zhu and D. Howe, "Electrical machines and drives for electric, hybrid, and fuel cell vehicles," *Proc. IEEE*, vol. 95, no. 4, pp. 746-765, 2007

[ZHU09] Z. Q. Zhu, "A simple method for measuring cogging torque in permanent magnet machines," *In 2009 IEEE Power & Energy Society General Meeting*, 2009, pp. 1-4, IEEE.

[ZHU11] Z. Q. Zhu, “Fractional slot permanent magnet brushless machines and drives for electric and hybrid propulsion systems,” *COMPEL The International Journal for Computation and Mathematics in Electrical and Electronic Engineering*, vol. 30, no. 1, pp. 9–31, 2011.

[ZHU14] Z. Q. Zhu, "Permanent magnet machines for traction applications," *Encyclopedia of Automotive Engineering*, 1-20, 2014.

[ZHU17A] Z. Q. Zhu, W. Chu, and Y. Guan, “Quantitative comparison of electromagnetic performance of electrical machines for HEVs/EVs,” *CES Transactions on Electrical Machines and Systems*, vol. 1, no. 1, pp. 37-47, Jul. 2017.

[ZHU17B] X. Zhu, X. Wang, C. Zhang, L. Wang, and W. Wu, “Design and analysis of a spoke-type hybrid permanent magnet motor for electric vehicles,” *IEEE Transactions on Magnetics*, vol. 53, no. 11, pp.1-4, 2017.

[ZHU19] X. Zhu, W. Wu, L. Quan, Z. Xiang, and W. Gu, “Design and multi-objective stratified optimization of a less-rare-earth hybrid permanent magnets motor with high torque density and low cost,” *IEEE Transactions on Energy Conversion*, vol. 34, no.3, pp.1178-1189, 2019.

[ZHU22] Z. Q. Zhu and Y. Xiao, "Novel magnetic-field-shifting techniques in asymmetric rotor pole interior PM machines with enhanced torque density," *IEEE Transactions on Magnetics*, vol. 58, no. 2, pp. 1-10, 2022.

[ZHU23A] X. Zhu, S. Zheng, S. Niu, L. Xu, H. Liu, and M. Jiang, "Torque quality enhancement of a multi-permanent-magnets motor considering different role-plays of permanent magnets," *IEEE Transactions on Industrial Electronics*, vol. 71, no.9, pp.10173-10183, 2023.

[ZHU23B] X. Zhu, S. Li, S. Zheng, L. Quan, D. Fan, X. Zeng, and C. H. Lee, "Torque component redistribution and enhancement for hybrid permanent magnet motor with permanent magnet offset placement," *IEEE Transactions on Transportation Electrification*, vol. 9, no.1, pp.631-641, 2022.

APPENDIX A – CAD DRAWINGS OF PROTOTYPES

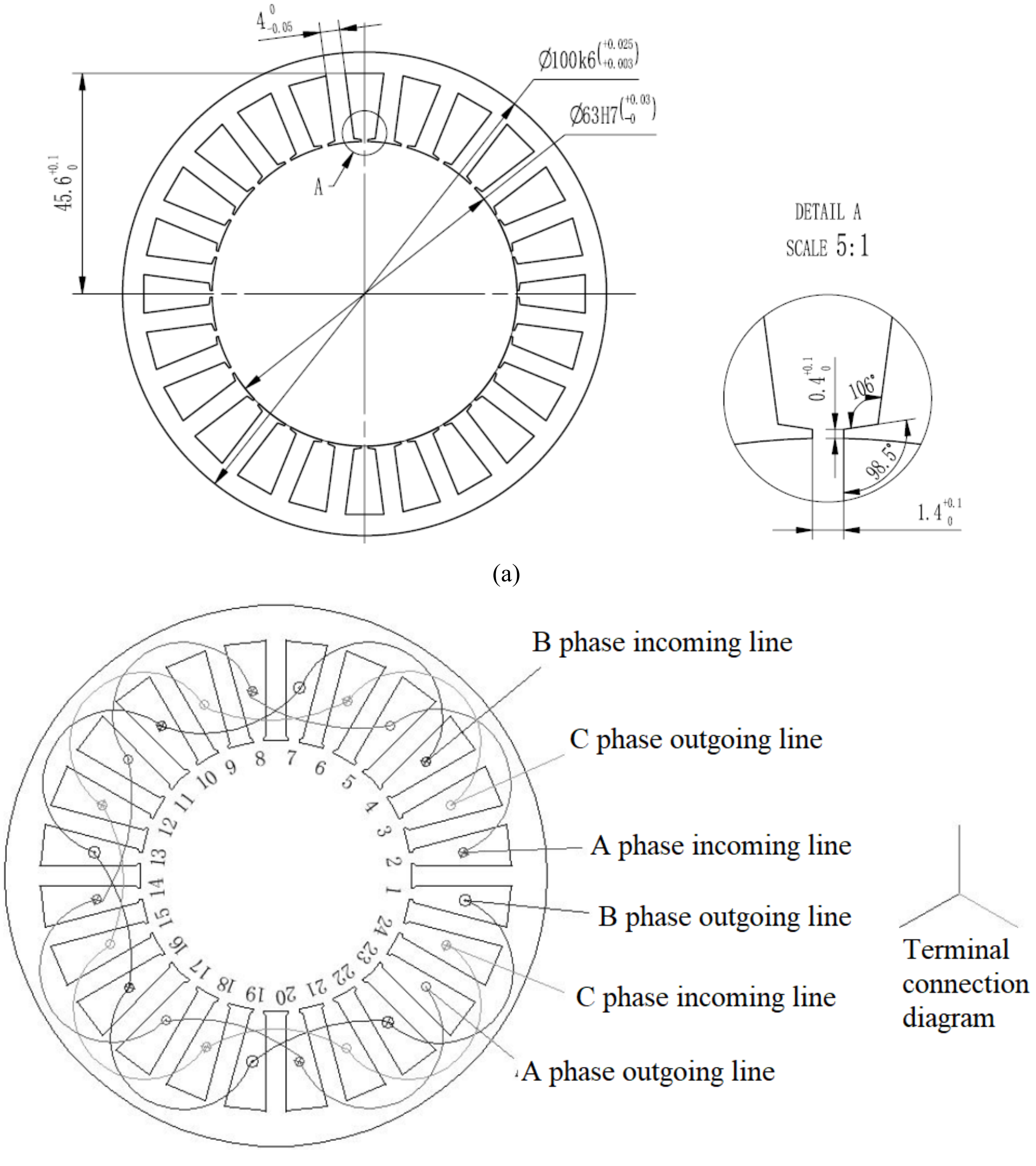

(a)

(b)

Fig. a.1. Shared stator between all prototypes. (a) Stator core. (b) Winding configuration.

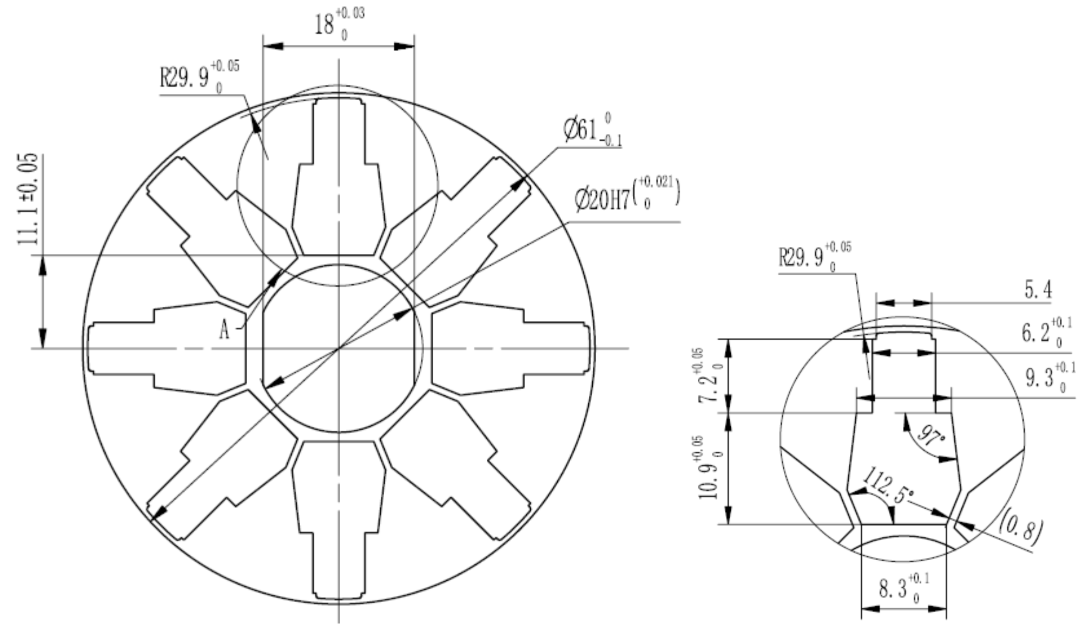
18 +0.03 0
R29.9 +0.05 0
Ø61 0 -0.1
Ø20H7 (+0.021 0)
11.1±0.05
A
R29.9 +0.05 0
5.4
6.2 +0.1 0
9.3 +0.1 0
7.2 +0.05 0
10.9 +0.05 0
97°
112.5°
(0.8)
8.3 +0.1 0

(a)

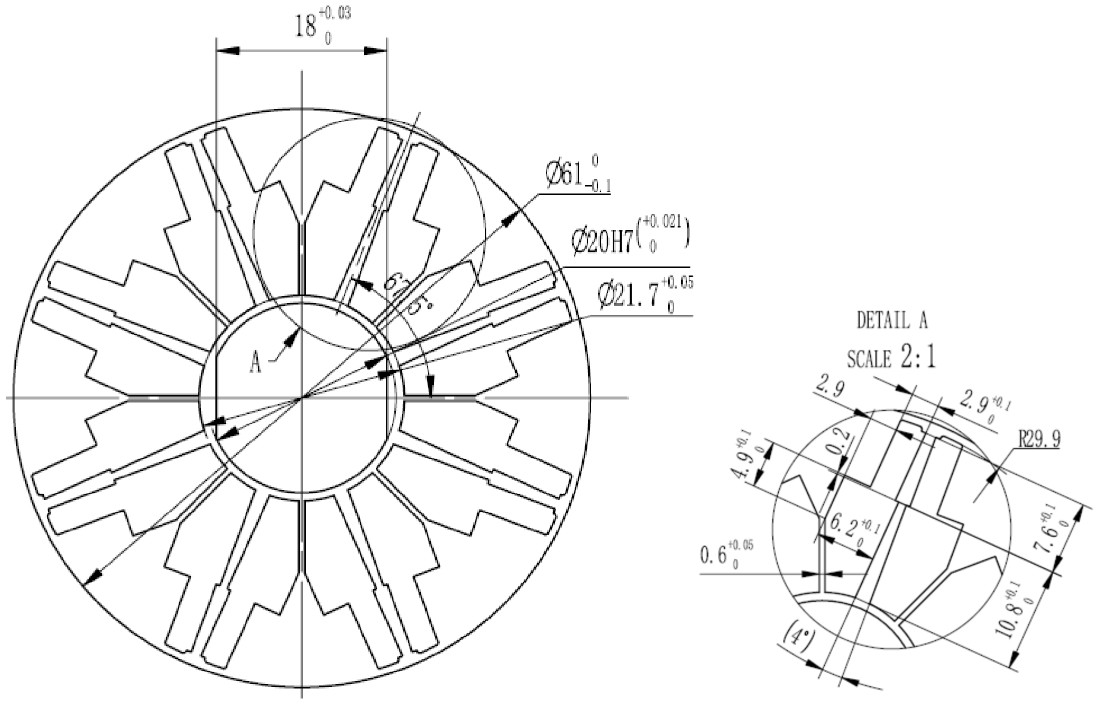
18 +0.03 0
Ø61 0 -0.1
Ø20H7 (+0.021 0)
Ø21.7 +0.05 0
67.5°
A
DETAIL A
SCALE 2:1
2.9
2.9 +0.1 0
R29.9
0.2
4.9 +0.1 0
6.2 +0.1 0
0.6 +0.05 0
7.6 +0.1 0
10.8 +0.1 0
(4°)

(b)

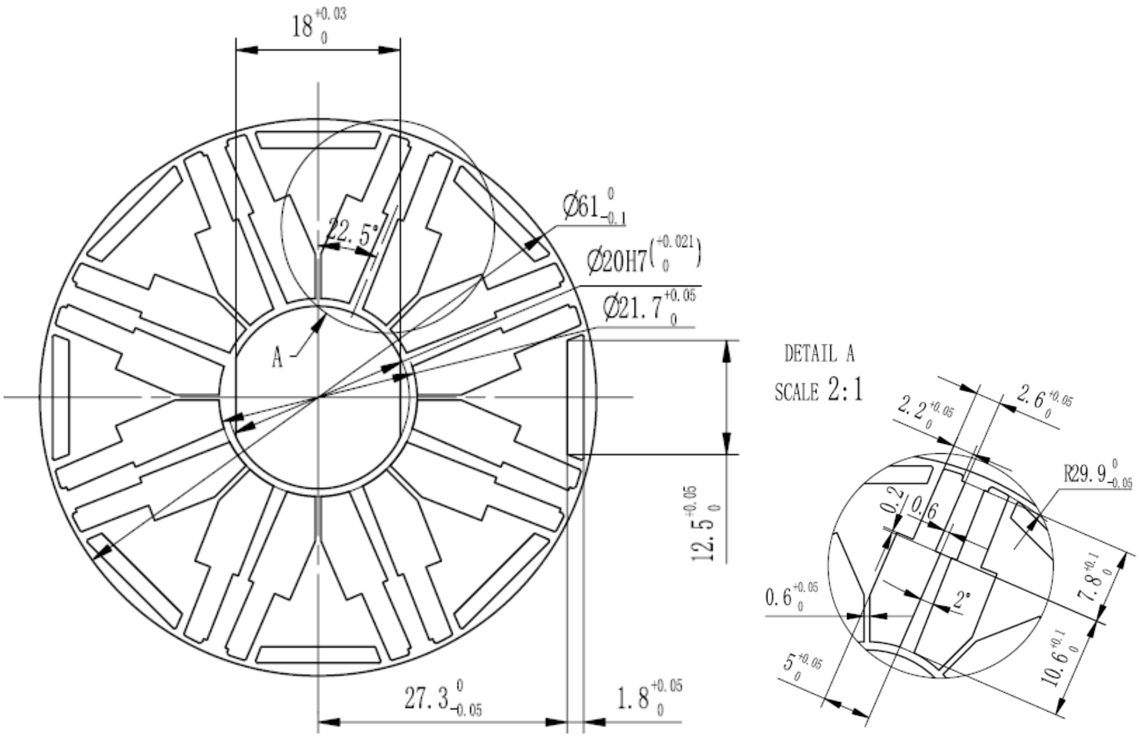
18 +0.03 0
22.5°
Ø61 0 -0.1
Ø20H7(+0.021 0)
Ø21.7 +0.05 0
A
12.5 +0.05 0
27.3 0 -0.05
1.8 +0.05 0
DETAIL A
SCALE 2:1
2.2 +0.05 0
2.6 +0.05 0
R29.9 0 -0.05
0.2
0.6
7.8 +0.1 0
0.6 +0.05 0
2°
5 +0.05 0
10.6 +0.1 0

(c)

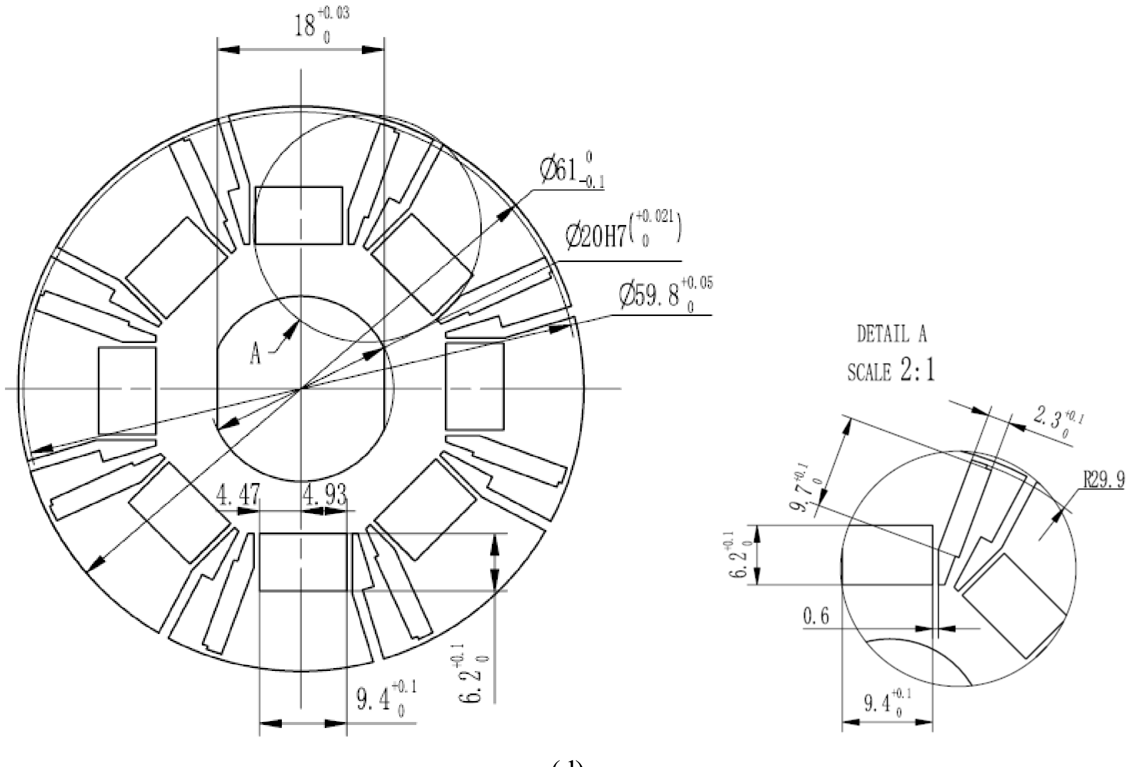
18 +0.03 0
Ø61 0 -0.1
Ø20H7(+0.021 0)
Ø59.8 +0.05 0
A
4.47
4.93
9.4 +0.1 0
6.2 +0.1 0
DETAIL A
SCALE 2:1
2.3 +0.1 0
9.7 +0.1 0
R29.9
6.2 +0.1 0
0.6
9.4 +0.1 0

(d)

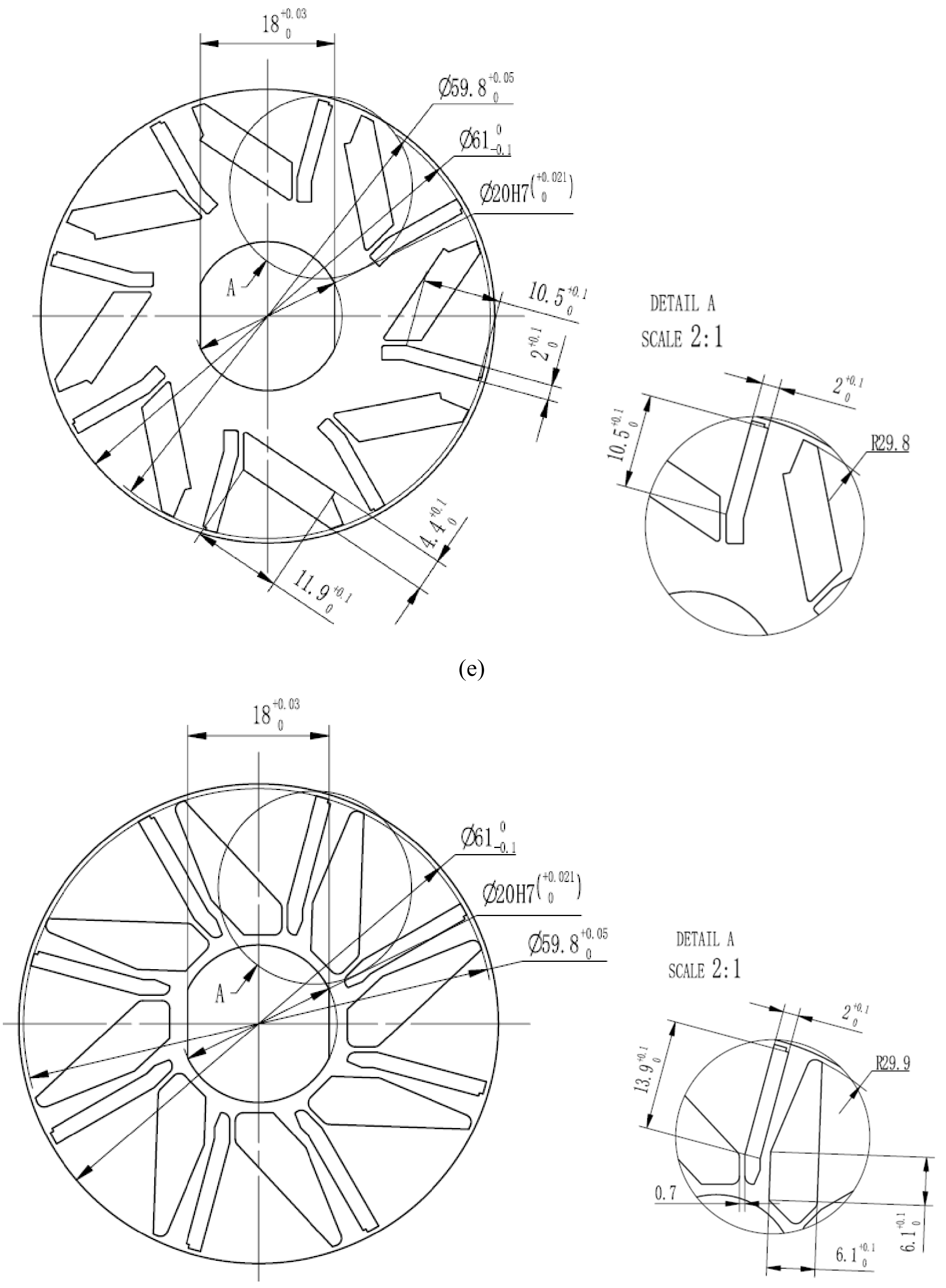

(e)

(f)

Fig. a.2. Rotor drawings of prototyped HPM machines based on chapters. (a) Chapter 2B. (b) Chapter 3. (c) Chapter 4. (d) Chapter 5A. (e) Chapter 5B. (f) Chapter 6.

APPENDIX B - RESEARCH OUTCOMES

List of Papers

Published and Submitted Journal Papers

[1] **S. Kazemisangdehi**, Z. Q. Zhu, Y. Zhou, H. Liu, L. Chen, and L. Yang, "Novel parallel hybrid rare-earth and ferrite magnets in V-spoke interior PM synchronous machine," *IEEE Transactions on Industry Applications,* Vol. 61, no. 2, pp. 2972-2982, 2025. (**Chapter 3**)

[2] **S. Kazemisangdehi**, Z. Q. Zhu, Y. Zhou, L. Chen, and L. Yang, "Series hybrid rare-earth and ferrite magnets delta-shape IPMSM with split ferrite spoke," *IEEE Transactions on Industry Applications,* Under review. (**Chapter 4**)

[3] **S. Kazemisangdehi**, Z. Q. Zhu, L. Chen, L. Yang, and Y. Zhou "Novel hybrid rare-earth and ferrite magnet asymmetric V-shape and U-shape IPMSMs accounting for demagnetization withstand capability," *IET Electric Power Applications*, Under review. (**Chapter 5**)

[4] **S. Kazemisangdehi**, Z. Q. Zhu, L. Chen, L. Yang, and Y. Zhou "A mixed hybrid rare-earth and ferrite magnet asymmetric V-shape IPMSM," *IEEE Transactions on Transportation Electrification*, *early access*, 2025. (**Chapter 6**)

Conference Papers

[1] **S. Kazemisangdehi**, Z. Q. Zhu, Y. Zhou, and H. Liu, "Improved performance of series and parallel hybrid permanent magnet spoke-type PM machines using tapered magnets," *In 2023 IEEE International Electric Machines & Drives Conference (IEMDC)*, 2023, pp. 1-7, IEEE. (**Chapter 2**)

[2] **S. Kazemisangdehi**, Z. Q. Zhu, Y. Zhou, and H. Liu, "A new hybrid permanent magnet synchronous machine with V-shape spokes," *In 2023 IEEE International Electric Machines & Drives Conference (IEMDC)*, 2023, pp. 1-7, IEEE.

[3] **S. Kazemisangdehi**, Z. Q. Zhu, and Y. Zhou, "Split spoke series hybrid PM delta-shape IPMSM with improved performance," *In 2023 26th International Conference on Electrical Machines and Systems (ICEMS)*, 2023, pp. 678-683, IEEE.

[4] **S. Kazemisangdehi**, Z. Q. Zhu, and Y. Zhou, "Comparative study of performance improvement methods in a series hybrid PM delta-shape IPMSM," *In 2023 26th International Conference on Electrical Machines and Systems (ICEMS)*, 2023, pp. 684-689, IEEE.

[5] Q. Wei, Z. Q. Zhu, **S. Kazemisangdehi**, J. Feng, S. Guo, Y. Li, and S. Feng, "A novel asymmetric U-shaped variable flux memory machine," *In 2024 Third International Conference on Sustainable Mobility Applications, Renewables and Technology (SMART)*, 2024, pp. 1-8, IEEE.

[6] Q. Wei, Z. Q. Zhu, **S. Kazemisangdehi**, J. Feng, S. Guo, Y. Li, and S. Feng, “A novel asymmetric variable flux memory machine with hybrid-layer permanent magnets,” *In 2024 Third International Conference on Sustainable Mobility Applications, Renewables and Technology (SMART)*, 2024, pp. 1-9, IEEE.

List of Patents

[1] Z. Q. Zhu, **S. Kazemisangdehi**, L. Chen, and G. Wu, "An asymmetric hybrid permanent magnet rotor and motor," *Midea Group Co. Ltd.*, Chinese Patent Proposal Number MD202411731, Jan. 2025.

[2] Z. Q. Zhu, Y. Zhou, and **S. Kazemisangdehi**, "Rotor and Motor," *Midea Group Co. Ltd.*, Chinese Patent Application Number 2023116209459, filled 2023-11-29.